

NASA-CP-3158-PT-1

NASA Conference Publication 3158  
Part 1

# Sixteenth International Laser Radar Conference



*Abstracts of papers presented  
at a conference and held at the  
Massachusetts Institute of Technology  
Cambridge, Massachusetts  
July 20-24, 1992*

**AMS**

**USAF**

**OSA**

**NASA**

3 1176 01356 0678

*NASA Conference Publication 3158  
Part 1*

# Sixteenth International Laser Radar Conference

*Edited by*  
M. P. McCormick  
*NASA Langley Research Center*  
*Hampton, Virginia*

Abstracts of papers presented at a conference sponsored by the United States Air Force Office of Scientific Research, NASA Langley Research Center, the United States Air Force Phillips Laboratory, the American Meteorological Society, and the Optical Society of America, and held at the Massachusetts Institute of Technology Cambridge, Massachusetts July 20–24, 1992

**NASA**

National Aeronautics and  
Space Administration  
Office of Management  
Scientific and Technical  
Information Program

**1992**

## Preface

Abstracts of papers presented at the Sixteenth International Laser Radar Conference (ILRC), held on the campus of the Massachusetts Institute of Technology in Cambridge, Massachusetts, July 20-24, 1992, are contained in this publication. These conferences, held biennially, bring together an interdisciplinary group of scientists working in the field of laser remote sensing as applied to the atmosphere, earth and oceans. At the 16th ILRC, 100 oral papers and 95 poster papers were presented during 16 sessions. Topics covered include: the worldwide measurements of aerosols produced from the June 1991 eruption of the Pinatubo volcano; the role of lidars in global change research, including long-term stratospheric ozone measurements and the Network for the Detection of Stratospheric Change (NDSC); measurements from space by the Laser Atmospheric Winds Sensor (LAWS) and the Lidar In-space Technology Experiment (LITE); stratospheric and mesospheric temperature and wind measurements; mesospheric sodium and ion measurements; cloud measurements, including the Experimental Cloud Lidar Pilot Study (ECLIPS); laser imaging and ranging; tropospheric water vapor and aerosol measurements; and, the description of new systems and facilities. Although no abstracts are included herein, a NASA-sponsored special session on  $2\mu\text{m}$  solid state doppler lidar technology for remote sensing of winds took place also.

The conference was held under the auspices of the International Coordination group for Laser Atmospheric Studies (ICLAS) of the International Radiation Commission, International Association of Meteorology and Atmospheric Physics. ICLAS is the parent organization for these ILRC's which are held during even years. Through the cooperation of many societies and organizations, national lidar conferences and conferences/workshops associated with specific or related aspects of lidar research are held during odd years. The conference was co-sponsored by the U.S. Air Force Phillips Laboratory, U. S. Air Force Office of Scientific Research, NASA, the American Meteorological Society, and the Optical Society of America. The 16th ILRC was organized under the leadership of Robert A. McClatchey (General Chairman), R. Earl Good (Technical Program Chairman), and Gilbert Davidson (Local Organizing Committee Chairman). They are to be commended for the excellent venue and selection of scientific papers.

This volume was prepared for publication through the efforts of the staff of the Research Information and Applications Division, NASA Langley Research Center. Special thanks go to Natalie Bennett of PhotoMetrics and Gayle Fitzgerald, Marie Seamon and Trish Ezekiel of the MIT Conference Services Office for attending to the diverse tasks required for the success of this conference.

The use of trade names or manufacturers' names in this publication does not constitute endorsement, either expressed or implied, by the National Aeronautics and Space Administration.

M. Patrick McCormick  
Chairman, International Coordination  
Group for Laser Atmospheric Studies  
International Radiation Commission

**Robert A. McClatchey, General Chairman**  
*Phillips Laboratory*

**Technical Program Committee**

**R. Earl Good, Program Chairman**  
*Phillips Laboratory*

**Steven B. Alejandro**  
*Phillips Laboratory*

**Allan I. Carswell**  
*York University, Canada*

**Marie-Lise Chanin**  
*CNRS, France*

**Edwin W. Floranta**  
*University of Wisconsin*

**R. Michael Hardesty**  
*NOAA*

**Dennis K. Killinger**  
*University of South Florida*

**M. Patrick McCormick**  
*NASA Langley Research Center*

**Harvey Melfi**  
*NASA Goddard Space Flight Center*

**Norman Menyuk**  
*MIT Lincoln Laboratory (ret.)*

**John W. Meriwether**  
*Phillips Laboratory*

**C. Martin Platt**  
*CSIRO, Australia*

**Ronald G. Prim**  
*Massachusetts Institute of Technology*

**Wolfgang Renger**  
*DLR, Germany*

**Duane D. Smith**  
*Kaman Aerospace Corporation*

**J. William Snow**  
*Phillips Laboratory*

**Nobuo Takeuchi**  
*Chiba University, Japan*

**Vladimir E. Zuev**  
*Institute of Atmospheric Optics, Russia*

**Local Organizing Committee**

**Gilbert Davidson, Chairman**  
*PhotoMetrics, Inc.*

**Donald E. Bedo**  
*Phillips Laboratory*

**Phan D. Dao**  
*Phillips Laboratory*

**Paul L. Kelley**  
*MIT Lincoln Laboratory*

**LTC George G. Koenig**  
*Phillips Laboratory*

## ICLAS MEMBERSHIP

Dr. Al Carswell  
York University  
Dept. of Physics & CRESS  
4700 Keele St.  
North York Ontario  
M3J 1P3 CANADA

Professor Giorgio Fiocco  
Dipto di Fisica  
Citta Universitaria  
Pizzale Aldo Moro #2  
00185-Roma  
ITALY

Dr. Pierre H. Flamant  
Laboratoire de Meteorologie  
Dynamique du CNRS  
Ecole Polytechnique  
91128 Palaiseau  
FRANCE

Dr. R. Michael Hardesty  
NOAA/ERL Propagation Laboratory  
U. S. Department of Commerce  
325 Broadway  
Boulder, CO 80303

Dr. Benjamin M. Herman  
School of Atmospheric Sciences  
University of Arizona  
Tucson, AZ 85721

Dr. M. Patrick McCormick  
NASA Langley Research Center  
Mail Stop 475  
Hampton, VA 23665-5225

Dr. Gerard Megie  
Service d'Aeronomie CNRS  
BP n° 3  
91371 Verrieres Le Buisson  
FRANCE

Dr. S. Harvey Melfi  
NASA Goddard Space Flight Center  
Mail Code 917.0  
Greenbelt, MD 20771

Dr. C. M. R. Platt  
CSIRO  
Div. of Atmos. Physics  
Aspendale, Victoria  
AUSTRALIA

Dr. Wolfgang Renger  
DLR Institut für Physik der  
Atmosphäre  
D-8031 Oberpfaffenhofen  
GERMANY

Dr. Leopoldo Stefanutti  
Ist. di Ricerca sulle Onde  
Elettro Magnetiche of CNR  
Via Panciatichi 64  
Firenze 50127  
ITALY

Dr. Lance Thomas  
Department of Physics  
Univ. of College of Wales  
Penglais, Aberystwyth  
Dyfed SY23 3BZ  
UNITED KINGDOM

Dr. Christian Werner  
Ins. of Atmos. Physics  
German Aerospace Estab.  
D8031 Oberpfaffenhoffen  
GERMANY

Dr. V. E. Zuev  
Instit. of Atmos. Optics  
1 Akademichesky Av.  
Tomsk 634055  
RUSSIA

Dr. Takao Kobayashi  
Dept. of Electronics  
Fukui University 3-9-1  
Bunkyo Fukui 910  
JAPAN



**AGENDA**

**16TH INTERNATIONAL LASER RADAR CONFERENCE**

**Monday, 20 July 1992**

**PART 1**

8:30	<b>OPENING CEREMONIES</b>		
8:45	<b>Thirty Years of Optical Radar Work: Reminiscences and Perspectives</b> <i>Giorgio Fiocco</i>		
9:30-11:45	<b>SESSION A: Volcanic (Mt. Pinatubo) Dust Layer Measurements</b>		
	<b>Session Chair:</b> <i>Allan Carswell</i>		
9:30	A1	(Invited) Long Term Stratospheric Aerosol Lidar Measurements in Kyushu . . . . <i>Motow Fujiwara</i>	1
10:00-10:30	<b>COFFEE BREAK</b>		
10:30	A2	Southern Hemisphere Lidar Measurements of the Aerosol Clouds from Mt. Pinatubo and Mt. Hudson . . . . . <i>Stuart A. Young, Peter J. Manson, and Graeme R. Patterson</i>	3
10:45	A3	Stratospheric Backscatter, Extinction, and Lidar Ratio Profiling After the Mt. Pinatubo Eruptions . . . . . <i>Albert Ansmann, Christoph Schulze, Ulla Wandinger, Claus Weitkamp, and Walfried Michaelis</i>	7
11:00	A4	Measurements of Stratospheric Pinatubo Aerosol Extinction Profiles by a Raman Lidar . . . . . <i>Makoto Abo and Chikao Nagasawa</i>	11
11:15	A5	Raman Lidar Measurements of Pinatubo Aerosols Over Southeastern Kansas During November-December 1991 . . . . . <i>R. A. Ferrare, S. H. Melfi, D. N. Whiteman, and K. D. Evans</i>	13
11:30	A6	Lidar Observations of Stratospheric Aerosol Layer After the Mt. Pinatubo Volcanic Eruption . . . . . <i>Tomohiro Nagai, Osamu Uchino, and Toshifumi Fujimoto</i>	17
11:45-1:15	<b>LUNCH</b>		
1:15-4:30	<b>SESSION B: Global Change/Ozone Measurements</b>		
	<b>Session Chairs:</b> <i>Paul Kelley</i> <i>Ronald Prinn</i>		

1:15	B1	(Invited) The Role of LIDARs in Global Change Research ..... <i>Ronald G. Prinn</i>	21
1:45	B2	Interpretation of DIAL Measurements of Lower Stratospheric Ozone in Regions with Pinatubo ..... <i>William B. Grant, Edward V. Browell, Marta A. Fenn, Carolyn F. Butler, Vincent G. Brackett, Robert E. Veiga, Shane D. Mayor, Jack Fishman, D. Nganga, A. Minga, B. Cros, and Larry L. Stowe</i>	23
2:00	B3	Correcting for Interference of Mt. Pinatubo Aerosols on DIAL Measurements of Stratospheric Ozone ..... <i>W. Steinbrecht and A. I. Carswell</i>	27
2:15	B4	A New Raman DIAL Technique for Measuring Stratospheric Ozone in the Presence of Volcanic Aerosols ..... <i>Upendra N. Singh, Thomas J. McGee, Michael Gross, William S. Heaps, and Richard Ferrare</i>	31
2:30	B5	The JPL Table Mountain and Mauna Loa Stratospheric Ozone LIDARs ..... <i>I. Stuart McDermid</i>	35
2:45-3:15	<b>COFFEE BREAK</b>		
3:15	B6	The NDSC Primary Site at the Observatoire de Haute-Provence: Ozone and Aerosols Observations (1986-1992) ..... <i>G. Mégie, S. Godin, G. Ancellet, M. Beekmann, and A. M. Lacoste</i>	39
3:30	B7	Lidar Atmosphere Observatory in the Canadian Arctic ..... <i>Arkady Ulitsky, Tin-Yu Wang, Martin Flood, and Brent Smith</i>	43
3:45	B8	Observation of Stratospheric Ozone with NIES Lidar System in Tsukuba, Japan ..... <i>H. Nakane, S. Hayashida, Y. Sasano, N. Sugimoto, I. Matsui, and A. Minato</i>	45
4:00	B9	Observations of Ozone-Aerosol Correlated Behavior in the Lower Stratosphere During the EASOE Campaign ..... <i>P. Di Girolamo, M. Cacciani, A. di Sarra, G. Fiocco, D. Fuà, T. S. Joergensen, B. Knudsen, and N. Larsen</i>	49
4:15	B10	First Results from TROLIX '91: An Intercomparison of Tropospheric Ozone LIDARs ..... <i>A. Apituley, J. Bösenberg, G. Ancellet, H. Edner, B. Galle, J. B. Bergwerff, G. von Cossart, J. Fiedler, C. N. de Jonge, J. Mellquist, V. Mitev, T. Schaberl, G. Sonnemann, J. Spakman, D. P. J. Swart, and E. Wallinder</i>	53

4:30-5:15

**SESSION C: GLOBE**

Session Chair:

*Nobuo Takeuchi*

4:30	C1	Global Backscatter Experiment (GLOBE) Results: Aerosol Backscatter Global Distribution and Wavelength Dependence ..... <i>David A. Bowdle</i>	57
4:45	C2	The Global Backscatter Experiment Airborne Pulsed Lidar Measurements ..... <i>James D. Spinhirne, S. Chudamani, Robert T. Menzies, and David M. Tratt</i>	61
5:00	C3	Multi-Wavelength Airborne Lidar Intercomparisons of Aerosol and CIRRUS Backscatter over the Pacific Ocean ..... <i>Robert T. Menzies, David M. Tratt, James D. Spinhirne, and S. Chudamani</i>	63

5:15-7:00

**SESSION D: POSTER PARTY #1**

D1	Airborne Lidar Observations of the Stratosphere After the Pinatubo Eruption .. <i>David M. Winker, Mary T. Osborn, and Robert J. DeCoursey</i>	67
D2	Multiwavelength Measurements of the Stratospheric Aerosol Layer Made at Hampton, Virginia (37N, 76W) ..... <i>G. S. Kent, G. M. Hansen, and K. M. Stevens</i>	71
D3	Three-Wavelength Lidar Measurements of Pinatubo Aerosol and its Optical Properties ..... <i>Y. Sasano, I. Matsui, and S. Hayashida</i>	75
D4	Lidar Observations of the Pinatubo Stratospheric Aerosol Cloud Over Frascati, Italy ..... <i>Fernando Congeduti, Alberto Adriani, Gian Paolo Gobbi, and Sante Centurioni</i>	79
D5	L625 Lidar Measurements of Pinatubo Volcanic Cloud at Hefei ..... <i>Huanling Hu and Jun Zhou</i>	83
D6	Two Wavelength Measurements of the Pinatubo Aerosol above Toronto, Canada ..... <i>W. Steinbrecht, D. Donovan, and A. I. Carswell</i>	87
D7	Lidar Observations of the Pinatubo Volcanic Cloud Over Hampton, Virginia .. <i>M. T. Osborn, D. M. Winker, D. C. Woods, and R. J. DeCoursey</i>	91

D8	Ozone Measurements with the U.S. EPA UV-DIAL: Preliminary Results .....	95
	<i>H. Moosmüller, D. Diebel, D. H. Bundy, M. P. Bristow, R. J. Alvarez II, V. A. Kovalev, C. M. Edmonds, R. M. Turner, and J. L. McElroy</i>	
D9	Lidar Development for the Atmospheric Radiation Measurement (ARM) Program .....	99
	<i>J. Griffin and M. Lapp</i>	
D10	Lidar Measurements of Stratospheric Ozone, Temperature and Aerosol During 1992 UARS Correlative Measurement Campaign .....	103
	<i>Thomas J. McGee, Upendra N. Singh, Michael Gross, William S. Heaps, and Richard Ferrare</i>	
D11	Airborne DIAL Remote Sensing of the Arctic Ozone Layer .....	107
	<i>Martin Wirth, Wolfgang Renger, and Gerhard Ehret</i>	
D12	Lidar Measurements of Stratospheric Ozone at Hohenpeissenberg -An Improved Evaluation Method- .....	109
	<i>W. Vandersee, F. Schönenborn, and H. Claude</i>	
D13	A Multi-Wavelength Ozone Lidar for the EASOE Experiment .....	113
	<i>S. Godin, G. Ancellet, C. David, J. Porteneuve, C. Leroy, V. Mitev, Y. Emery, C. Flesia, V. Rizi, G. Visconti, and L. Stefanutti</i>	
D14	Correction of DIAL Stratospheric Ozone Measurements in the Presence of Pinatubo Aerosols .....	117
	<i>Marta A. Fenn, Syed Ismail, Edward V. Browell, and Carolyn F. Butler</i>	
D15	The Laser Atmospheric Wind Sounder (LAWS) Preliminary Error Budget and Performance Estimate .....	121
	<i>David L. Kenyon and Kent Anderson</i>	
D16	Lag Angle Compensation in a Space Borne Scanning Lidar .....	125
	<i>A. B. Wissinger</i>	
D17	Lidar In-Space Technology Experiment (LITE) Electronics Overview .....	129
	<i>Michael P. Blythe, Richard H. Couch, Carroll W. Rowland, Wayne L. Kitchen, Curtis P. Regan, Michael R. Koch, Charles W. Antill, William T. Stevens, Courtney H. Rollins, Edward H. Kist, David M. Rosenbaum, Ruben W. Remus, and Clayton P. Turner</i>	
D18	Laser Transmitter Module (LTM) for LITE .....	133
	<i>John Chang, Marc Cimolino, Edmond Joe, Mulgeta Petros, Karl Reithmaier, Ray Thompson, and Ron Villane</i>	

D19	Intercomparisons of Lidar Backscatter Measurements and In-Situ Data from GLOBE .....	137
	<i>S. Chudamani and James D. Spinhirne</i>	
D20	Simulation of the Performances of WIND an Airborne CO <sub>2</sub> Lidar .....	141
	<i>D. Oh, A. Dabas, F. Lieutaud, C. Loth, and P. H. Flamant</i>	
D21	Sampling and Representativeness for a Spaceborne Wind Lidar .....	145
	<i>F. Lieutaud, A. Dabas, P. H. Flamant, G. Sèze, and Ph. Courtier</i>	
D22	Laboratory Velocimeter Measurements Using the Edge Technique .....	149
	<i>Bruce M. Gentry and C. Laurence Korb</i>	
D23	Identification of Critical Design Points for the EAP of a Space-Based Doppler Lidar Wind Sounder .....	153
	<i>G. D. Emmitt and S. A. Wood</i>	
D24	Wind Profiles Derived from Volume Imaging Lidar Data: Enhancements to the Algorithm and Comparisons with In-situ Observations .....	157
	<i>A. K. Piironen and E. W. Eloranta</i>	
D25	Measurements of Wind Divergence with Volume Imaging Lidar .....	161
	<i>P. W. Young and E. W. Eloranta</i>	
D26	DIAL Mapping of Atmospheric Atomic Mercury of Geophysical Origin .....	165
	<i>H. Edner, P. Ragnarson, S. Svanberg, and E. Wallinder</i>	
D27	Lidar Tracking of Multiple Fluorescent Tracers: Method and Field Test .....	169
	<i>Wynn L. Eberhard and Ron J. Willis</i>	
D28	Lidar Monitoring of Mexico City's Atmosphere During High Air Pollution Episodes .....	173
	<i>C. R. Quick, Jr., F. L. Archuleta, D. E. Hof, R. R. Karl, Jr., J. J. Tjee, W. E. Eichinger, D. B. Holtkamp, and L. Tellier</i>	
D29	Lab-Scale Lidar Sensing of Diesel Engines Exhausts .....	177
	<i>A. Borghese</i>	
D30	Infrared Pulse-Laser Long-Path Absorption Measurement of Carbon Dioxide Using a Raman-Shifted Dye Laser .....	181
	<i>Atsuchi Minato, Nobuo Sugimoto, and Yasuhiro Sasano</i>	
D31	Transportable Lidar for the Measurement of Ozone Concentration and Flux Profiles in the Lower Troposphere .....	185
	<i>Yanzeng Zhao, James N. Howell, and R. Michael Hardesty</i>	

D32	Remote Detection of Biological Particles and Chemical Plumes Using UV Fluorescence Lidar .....	189
	<i>J. J. Tjee, D. E. Hof, R. R. Karl, R. J. Martinez, C. R. Quick, D. I. Cooper, W. E. Eichinger, and D. B. Holtkamp</i>	
D33	Signal Quality Influence on Averaging Procedure for DIAL Pollution Monitoring .....	193
	<i>S. Egert</i>	
D34	Extraction of Aerosol and Rayleigh Components from Doppler Lidar Return Signal .....	195
	<i>John E. Barnes, Ken W. Fischer, Vincent J. Abreu, and Wilbert R. Skinner</i>	
D35	Application of Laser Imaging for Bio/Geophysical Studies .....	199
	<i>J. R. Hummel, S. M. Goltz, N. L. DePiero, D. P. DeGloria, and F. M. Pagliughi</i>	
D36	ARCLITE: The Arctic Lidar Technology Facility at Søndre Strømfjord, Greenland .....	201
	<i>J. P. Thayer</i>	
D37	Rotational Raman Lidar for Lower Tropospheric Temperature Profiling .....	205
	<i>Takao Kobayashi, Takunori Taira, Takano Y. Yamamoto, Akihiro Hori, and Toshinobu Kitada</i>	
D38	One Year of Rayleigh Lidar Measurements at Toronto .....	209
	<i>James A. Whiteway and Allan I. Carswell</i>	
D39	Lidar Observations of Aerosol and Temperature Stratification over Urban area During the Formation of a Stable Atmospheric PBL .....	213
	<i>I. Kolev, O. Parvanov, B. Kaprielov, V. Mitev, V. Simeonov, and I. Grigorov</i>	
D40	A Comparison Between Raman Lidar and Conventional Contact Measurements of Atmospheric Temperature .....	217
	<i>V. M. Mitev, V. B. Simeonov, and I. V. Grigorov</i>	
D41	Efficiencies of Rotational Raman, and Rayleigh Techniques for Laser Remote Sensing of the Atmospheric Temperature .....	221
	<i>I. D. Ivanova, L. L. Gurdev, and V. M. Mitev</i>	
D42	Lidar Investigation of Aerosol Pollution Distribution Near a Coal Power Plant ..	225
	<i>Ts. Mitsev and G. Kolarov</i>	
D43	Laser Remote Sensing of Pollution on Water Surfaces .....	229
	<i>A. F. Bunkin and A. I. Surovegin</i>	
D44	Correlation Analysis of Wind Lidar Data .....	233
	<i>R. P. Avramova</i>	

D45	A Developing Multiple-Wavelength Lidar for Detecting Mainly Ozone and Aerosol Distributions in the Stratosphere .....	237
	<i>Zheng Siping, Qiu Jinhuan, Wang Shufang, Huang Qirong, Wang Wenming, and Wu Shaoming</i>	
D46	An Extension of the Raman-Lidar Technique to Measure the Velocity and Temperature of the Atmospheric Emission Jets from Stacks .....	239
	<i>Yu. F. Arshinov, S. M. Bobrovnikov, V. K. Shumskii, A. G. Popov, and I. B. Serikov</i>	
D47	Lidar Observations of Stratospheric Clouds After Volcanic Eruption of Pinatubo .....	243
	<i>Sun Jinhui, Qiu Jinhuan, Xia Qilin, and Zhang Jinding</i>	
D48	In Vivo and In Vitro Chlorophyll-a and Pheophytin-a Concentration Measurements by Laser Fluorometry .....	247
	<i>A. A. Demidov, E. V. Baulin, and E. A. Chernyavskaya</i>	

8:30-10:15            **SESSION E: LAWS/LITE**

**Session Chairs:**

*Donald Bedo*

*William Vickery*

8:30	E1	Science Goals and Mission Objectives of NASA's Laser Atmospheric Wind Sounder Program ..... <i>Wayman E. Baker</i>	251
8:45	E2	The Laser Atmospheric Wind Sounder (LAWS) Phase II Preliminary System Design ..... <i>John C. Petheram, David L. Kenyon, Alan B. Wissinger, and T. Rhidian Lawrence</i>	257
9:00	E3	The Laser Atmospheric Wind Sounder (LAWS) Phase II Preliminary Laser Design ..... <i>T. Rhidian Lawrence, Albert L. Pindroh, Mark S. Bowers, Terence E. DeHart, Kenneth F. McDonald, Ananda Cousins, and Stephen E. Moody</i>	261
9:15	E4	G. E.'s Mobile, Coherent Doppler Lidar Test/Evaluation Facilities ..... <i>J. T. Sroga, J. W. Scott, S. C. Kiernan, F. J. Weaver, J. E. Trotta, J. C. Petheram</i>	265
9:30	E5	e-Beam Sustained Laser Technology for Space-Based Doppler Wind Lidar ..... <i>M. J. Brown, W. Holman, R. J. Robinson, P. M. Schwarzenberger, I. M. Smith, S. Wallace, M. R. Harris, D. V. Willetts, and S. C. Kurzius</i>	269

9:45-10:15

**COFFEE BREAK**

10:15	E6	(Invited) The Lidar In-Space Technology Experiment (LITE) ..... <i>M. Patrick McCormick</i>	273
10:45	E7	System Testing and Performance Characterization of the LITE Laser Transmitter Module at NASA ..... <i>Marc C. Cimolino and Mulugeta Petros</i>	277
11:00	E8	Mechanical and Thermal Issues in the Development of a Spaceborne Lidar System ..... <i>Joseph F. DeLorme</i>	281

11:15-12:15

**SESSION F: Stratospheric Measurements**

**Session Chair:**

*Dennis Killinger*

Tuesday, 21 July 1992

11:15	F1	Lidar Measurements of Aerosol and Ozone Distributions During the 1992 Airborne Arctic Stratospheric Expedition .....	285
		<i>E. V. Browell, C. F. Butler, M. A. Fenn, W. B. Grant, and A. F. Carter</i>	
11:30	F2	Airborne Lidar Measurements of Stratospheric Aerosols During the European Arctic Stratospheric Ozone Experiment (EASOE) .....	289
		<i>Wolfgang Renger, Gerhard Ehret, Peter Moerl, and Martin Wirth</i>	
11:45	F3	Aerosols and Polar Stratospheric Clouds Measurements During the EASOE Campaign .....	291
		<i>D. Haner, S. Godin, G. Mégie, C. David, and V. Mitev</i>	
12:00	F4	Lidar Observations of Polar Stratospheric Clouds and Stratospheric Temperatures at the South Pole .....	293
		<i>Richard L. Collins, Kenneth P. Bowman, and Chester S. Gardner</i>	

**Tuesday Afternoon and Evening—Optional Activities**

NASA has scheduled a special session on:

**2 $\mu$ m Solid State Doppler Lidar Technology for Remote Sensing of Winds**

The session will be held in Huntington Hall (Room 10-250) from 1:30-5:00 p.m. on Tuesday, and is open to all interested conference attendees.

8:30-2:00	<b>SESSION G: Sodium, the Mesosphere, and the Middle Atmosphere</b>		
	<b>Session Chairs:</b>		
		<i>Marie-Lise Chanin</i>	
		<i>Phan Dao</i>	
8:30	G1	(Invited) Development of Mesospheric Sodium Laser Beacon for Atmospheric Adaptive Optics .....	297
		<i>T. H. Jeys</i>	
9:00	G2	Characterization of Artificial Guidestars Generated in the Mesospheric Sodium Layer .....	301
		<i>M. P. Jelonek, R. Q. Fugate, W. J. Lange, A. C. Slavin, R. E. Ruane, and R. A. Cleis</i>	
9:15	G3	Optical Pumping of Mesospheric Sodium: A New Measurement Capability ...	305
		<i>R. M. Heinrichs, T. H. Jeys, K. F. Wall, J. Korn, and T. C. Hotaling</i>	
9:30	G4	Lidar Probing of the Mesosphere: Simultaneous Observations of Sporadic Sodium and Ion Formations, Calcium Ion Layers, Neutral Temperature and Winds .....	309
		<i>Timothy J. Kane, Jun Qian, Daniel R. Scherrer, Daniel C. Senft, W. Matthew Pfenninger, George C. Papen, and Chester S. Gardner</i>	
9:45	G5	Lidar Measurements of Metallic Species in Mesopause Region .....	313
		<i>Chikao Nagasawa and Makoto Abo</i>	
10:00-10:30	<b>COFFEE BREAK</b>		
10:30	G6	Narrowband Lidar System for Measurement of Upper Mesosphere Temperatures and Winds .....	315
		<i>Daniel R. Scherrer, William M. Pfenninger, Daniel C. Senft, George C. Papen, and Chester C. Gardner</i>	
10:45	G7	Error Analysis of Wind Measurements for the University of Illinois Sodium Doppler Temperature System .....	317
		<i>W. Matthew Pfenninger and George C. Papen</i>	
11:00	G8	Sodium Doppler Temperature Lidar Observations of the Mesopause Region Temperature and Wind Structure .....	321
		<i>Daniel C. Senft, Daniel R. Scherrer, and Chester S. Gardner</i>	
11:15	G9	Airborne Sodium and Rayleigh Lidar Observations from ALOHA-90 .....	325
		<i>Chris A. Hostetler and Chester S. Gardner</i>	

11:30	G10	Rayleigh/Raman Greenland Lidar Observations of Atmospheric Temperature During a Major Arctic Stratospheric Warming Event .....	329
		<i>John W. Meriwether, Robert Farley, Ross McNutt, Phan D. Dao, Warren P. Moskowitz, and Gilbert Davidson</i>	
11:45	G11	Elastic and Raman Lidar Temperature Measurements from Poker Flat, Alaska During February 1992 .....	333
		<i>Michael Burka, Phan Dao, Gilbert Davidson, Robert Farley, John Meriwether, and Alex Wilson</i>	
12:00-1:15	<b>LUNCH</b>		
1:15	G12	(Invited) Rayleigh/Raman Lidars: Intercomparisons and Validation .....	337
		<i>Marie-Lise Chanin</i>	
1:45	G13	Wind Measurements from 15 to 50 KM with a Doppler Rayleigh Lidar .....	341
		<i>A. Garnier and M. L. Chanin</i>	
2:00-4:15	<b>SESSION H: Clouds</b>		
	<b>Session Chairs:</b>		
	<i>G. G. Koenig</i>		
	<i>Martin Platt</i>		
2:00	H1	Lidar Studies of Extinction in Clouds in the ECLIPS Project .....	345
		<i>C. M. R. Platt</i>	
2:15	H2	Lidar Studies of Clouds at Toronto During the ECLIPS Program .....	349
		<i>S. R. Pal, A. I. Carswell, A. Y. Fong, I. Pribluda, and W. Steinbrecht</i>	
2:30	H3	Adaptation of the University of Wisconsin High Spectral Resolution Lidar for Polarization and Multiple Scattering Measurements .....	353
		<i>E. W. Eloranta and P. K. Piironen</i>	
2:45	H4	Polarization Lidar Liquid Cloud Detection Algorithm for Winter Mountain Storms .....	357
		<i>Kenneth Sassen and Hongjie Zhao</i>	
3:00-3:15	<b>COFFEE BREAK</b>		
3:15	H5	Measurement of Mean or Effective Radius of Cloud Drop Size Distributions with a 10.6- $\mu$ m Wavelength Lidar .....	361
		<i>Wynn L. Eberhard</i>	

Wednesday, 22 July 1992

3:30	H6	Observations of CIRRUS Clouds over the Pacific Region by the NASA Multiwavelength Lidar System ..... <i>Syed Ismail, Edward V. Browell, Marta A. Fenn, and Greg D. Nowicki</i>	365
3:35	H7	Diode - Pumped Nd: YAG Lidar for Airborne Cloud Measurements ..... <i>A. Mehnert, Th. Halldorsson, H. Herrmann, R. Häring, W. Krichbaumer, J. Streicher, and Ch. Werner</i>	369
4:00	H8	Remote Sensing by Spaceborne Lidar Aided by Surface Returns ..... <i>J. A. Reagan and T. W. Cooley</i>	373
4:15	H9	NWP Impact of Cloud Top and Boundary Layer Winds from a Satellite Borne Lidar: An Observing System Simulation Experiment ..... <i>R. G. Isaacs, C. Grassotti, R. N. Hoffman, M. Mickelson, T. Nehr Korn, and J. -F. Louis</i>	377
4:30-5:30		<b>Open Meeting of ICLAS</b>	
7:00		<b>BANQUET</b>	

PART 2\*

8:30-12:00	<b>SESSION I: Winds (Systems and Measurements)</b>		
	<b>Session Chairs:</b>		
		<i>Steven Alejandro</i>	
		<i>William Snow</i>	
8:30	I1	Boundary Layer Structure over the Ocean Observed by Leandre During a Tramontane Event ..... <i>C. Flamant, J. Pelon, P. Flamant, and P. Durand</i>	381
8:45	I2	Low-Level Atmospheric Flows Studied by Pulsed Doppler Lidar ..... <i>Robert M. Banta, Lisa D. Olivier, and R. Michael Hardesty</i>	385
9:00	I3	On the Existence of Convectively Produced Gravity Waves ..... <i>Stephen P. Palm and S. H. Melfi</i>	389
9:15	I4	Doppler Lidar Wind Measurement with the Edge Technique ..... <i>C. Laurence Korb and Bruce M. Gentry</i>	393
9:30	I5	Tropospheric and Stratospheric Wind Profiling with a Direct Detection Doppler Lidar ..... <i>Vincent J. Abreu, John E. Barnes, Ken W. Fischer, Wilbert R. Skinner, and Matt J. McGill</i>	397
9:45	I6	Atmospheric Wind Sensing with a 1 and 2 $\mu\text{m}$ Coherent Lidar ..... <i>R. Milton Huffaker and Sammy W. Henderson</i>	401
10:00-10:30	<b>COFFEE BREAK</b>		
10:30	I7	Design of a Near-IR Coherent Lidar for High Spatial and Velocity Resolution Wind Measurement ..... <i>Christian J. Grund and Madison J. Post</i>	405
10:45	I8	Boundary Layer Monitoring with a Compact Pulsed CO <sub>2</sub> Doppler Lidar ..... <i>Guy N. Pearson</i>	409
11:00	I9	A Compact High Repetition Rate CO <sub>2</sub> Coherent Doppler Lidar ..... <i>S. Alejandro, R. Frelin, B. Dix, and P. J. McNicholl</i>	413
11:15	I10	Simplified Signal Processing for an Airborne CO <sub>2</sub> Doppler Lidar ..... <i>R. L. Schwiesow and M. P. Spowart</i>	417
11:45	I11	Phase Noise in Pulsed Doppler Lidar and Limitations on Achievable Single- Shot Velocity Accuracy ..... <i>P. McNicholl and S. Alejandro</i>	421

---

\*Part 2 is presented under separate cover.

12:00	I12	A Comparison of Ultra-Sensitive Coherent Detection (USCD) and Heterodyne Detection for a Wind Sensing Application ..... <i>Sherwin Amimoto, Rolf Gross, Bob Lacy, Lissa Garman-DuValle, and Tom Good</i>	425
12:00-1:30	<b>LUNCH</b>		
1:30-3:00	<b>SESSION J: Laser Imaging and Ranging</b>		
	<b>Session Chair:</b> <i>Duane Smith</i>		
1:30	J1	(Invited) Diversity Imaging Techniques in Lidar ..... <i>K. I. Schultz</i>	429
2:00	J2	A Range-Resolved Bistatic Lidar Using a High-Sensitive CCD Camera ..... <i>K. Yamaguchi, A. Nomura, Y. Saito, and T. Kano</i>	431
2:15	J3	Fluorescence Lidar Multi-Color Imaging of Vegetation ..... <i>J. Johansson, E. Wallinder, H. Edner, and S. Svanberg</i>	433
2:30	J4	A Geodetic Laser Radar Rangefinder with $10^{-7}$ Resolution ..... <i>Y. Mizushima, M. Takeichi, Y. Warashima, A. Takeshima, I. Ogawa, and K. Ichie</i>	437
2:45	J5	Altimetry and Lidar Using AlGaAs Lasers Modulated with Pseudo-Random Codes ..... <i>James B. Abshire, Jonathan A. R. Rall, and Serdar S. Manizade</i>	441
3:00-3:15	<b>COFFEE BREAK</b>		
3:15-5:00	<b>SESSION K: Multiple Scattering</b>		
	<b>Session Chair:</b> <i>Michael Hardesty</i>		
3:15	K1	(Invited) Multiple Scattering Technique Lidar ..... <i>Luc R. Bissonnette</i>	447
3:45	K2	Multiple Scattering Effects on Spaceborne Lidar ..... <i>David M. Winker and Lamont R. Poole</i>	451
4:00	K3	Measurement of Multiple Scattering Effects with a Polarization Raman Elastic-Backscatter Lidar ..... <i>Ulla Wandinger, Albert Ansmann, Claus Weitkamp, and Walfried Michaelis</i>	455

4:15	K4	Determining Water Cloud Particle Sizes from Lidar Depolarization Measurements and Time Dependent Multiple Scattering Calculations .....	459
		<i>R. C. Garner and G. G. Koenig</i>	
4:30	K5	Multiple Scattering Lidar Returns from Stratus Clouds .....	463
		<i>D. L. Hutt and L. R. Bissonnette</i>	
4:45	K6	Analytical Multiple Scattering Correction to the Mie Theory: Application to the Analysis of the Lidar Signal .....	467
		<i>C. Flesia and P. Schwendimann</i>	
5:00-7:00	<b>SESSION L: POSTER PARTY #2</b>		
	L1	Airborne Lidar and Radiometric Observations of PBL-and Low Clouds .....	471
		<i>P. H. Flamant, R. Valentin, and J. Pelon</i>	
	L2	ECLIPS at LMD: Preliminary Results of Phase 2 .....	475
		<i>R. Valentin, L. Menenger, S. Elouragini, P. H. Flamant, and J. Pelon</i>	
	L3	The 2nd Phase of the LEANDRE Program: Water-Vapor DIAL Measurement .	479
		<i>P. Quaglia, D. Bruneau, and J. Pelon</i>	
	L4	Advanced Raman Water Vapor Lidar .....	483
		<i>David N. Whiteman, S. Harvey melfi, Richard A. Ferrare, Keith A. Evans, Luis Ramos-Izquierdo, O. Glenn Staley, Raymond W. DiSilvestre, Inna Gorin, Kenneth R. Kirks, William A. Mamakos, Lewis S. Wan, Nita W. Walsh, James M. Marsh, and Richard L. Aldridge</i>	
	L5	Water Vapor Variance Measurements Using a Raman Lidar .....	485
		<i>K. Evans, S. H. Melfi, R. Ferrare, and D. Whiteman</i>	
	L6	Airborne Remote Sensing of Tropospheric Water Vapor Using a Near Infrared DIAL System .....	489
		<i>G. Ehret, C. Kiemle, W. Renger, and G. Simmet</i>	
	L7	Trial of a Slant Visual Range Measuring Device .....	493
		<i>J. Streicher, C. Munkel, and H. Borchart</i>	
	L8	Lidar Depolarization by Nonspherical Particles: Potential of Combined Depolarization/Backscattering Measurements for PSC's Characteristics .....	497
		<i>C. Flesia, A. Mugnai, L. de Schoulepnikoff, and L Stefanutti</i>	
	L9	Coherent CO <sub>2</sub> Lidar: A Superior System for Observing Clouds? .....	501
		<i>Wynn L. Eberhard and R. Michael Hardesty</i>	
	L10	Measurements of Aerosol Profiles Using High-Spectral-Resolution Rayleigh-Mie Lidar .....	505
		<i>D. A. Krueger, R. J. Alvarez, II, L. M. Caldwell, and C. Y. She</i>	
	L11	Laboratory Scaled Simulation of Lidar Cloud Sounding Experiments .....	509
		<i>G. Zaccanti, P. Brusaglioni, M. Guriolo, and P. Sansoni</i>	

L12	An Alexandrite Regenerative Amplifier for Water Vapor and Temperature Measurements .....	513
	<i>P. -Y. Thro, J. Bösenberg, and V. Wulfmeyer</i>	
L13	Wavemeter Measurements of Frequency Stability of an Injection Seeded Alexandrite Laser for Pressure and Temperature Lidar .....	517
	<i>C. R. Prasad, G. K. Schwemmer, and C. L. Korb</i>	
L14	Conically Scanned Lidar Telescopes Using Holographic Optical Elements .....	521
	<i>Geary K. Schwemmer and Thomas D. Wilkerson</i>	
L15	Optics of the Ozone Lidar ELSA .....	525
	<i>J. Porteneuve</i>	
L16	Interferometers Adaptations to Lidars .....	529
	<i>J. Porteneuve</i>	
L17	An Ultra-Sensitive Coherent Detector Capable of Single Photon Detection for LIDAR Applications .....	533
	<i>Sherwin Amimoto, Rolf Gross, Bob Lacy, Lissa Garman-DuValle, and Tom Good</i>	
L18	A High Speed Signal Processing System for A Diode-Pumped YAG Lidar .....	537
	<i>H. Okumura, T. Sugita, H. Matsumoto, N. Takeuchi, and S. Kuwashima</i>	
L19	Pulsed Laser Spectral Measurement Using a Fabry-Perot Interferometer: Limits to Resolution .....	541
	<i>Anthony Notari and Bruce M. Gentry</i>	
L20	Tunable Electro-Optic Modulators for Lidar Systems and Atmospheric Applications .....	545
	<i>R. S. Eng, N. W. Harris, C. L. Summers, and B. Lax</i>	
L21	Injection Seeded Single Mode Alexandrite Ring Laser for Lidar Applications ..	549
	<i>H. Sang Lee and Anthony Notari</i>	
L22	Tm,Ho:YAG Laser with Tunable Range of 2.08-2.12 $\mu\text{m}$ and its Applications to Spectroscopy .....	553
	<i>Kazuhiro Asai and Toshikazu Itabe</i>	
L23	Theoretical Simulation of a 2 $\mu\text{m}$ Airborne Solid State Laser Anemometer .....	555
	<i>Béatrice Imbert and Jean-Pierre Cariou</i>	
L24	Comparison of Eye-Safe Solid State Laser Dial with Passive Gas Filter Correlation Measurements from Aircraft and Spacecraft .....	559
	<i>Robert V. Hess, Leo D. Staton, H. Andrew Wallio, and Liang-Guo Wang</i>	

L25	Lidar Multiple Scattering: Dependence on Atmospheric Parameters .....	563
	<i>Matthias Weigner</i>	
L26	Verification Measurement of a Polarization Raman Elastic-Backscatter Lidar ..	567
	<i>Christoph Schulze, Ulla Wandinger, Albert Ansmann, Claus Weitkamp, and Walfried Michaelis</i>	
L27	Time and Polarization Dependent Double Scattering Calculations of Lidar Returns from Water Clouds .....	571
	<i>R. C. Garner</i>	
L28	Multiple Scattering Wavelength Dependent Backscattering of Kaolin Dust in the I. R.: Measurements and Theory .....	575
	<i>Avishai Ben-David</i>	
L29	Aureole Lidar: Design, Operation, and Comparison with In-Situ Measurements.	579
	<i>William P. Hooper and D. R. Jensen</i>	
L30	Effect of Atmospheric Extinction on Laser Rangefinder Performance at 1.54 and 10.6 $\mu\text{m}$ .....	581
	<i>D. L. Hutt, J. -M. Thériault, V. Larochelle, and D. Bonnier</i>	
L31	A Study of Atmospheric Optical Scattering Parameters at 1.5 and 2 Micron Region for Solid State Doppler Lidar Applications .....	585
	<i>Eli Margalit, Farzin Amzajerjian, Rodney Benoist, and Richard Dubinsky</i>	
L32	A Cable Detection Lidar System for Helicopters .....	589
	<i>Benoist Grossmann, Alain Capbern, Martin Defour, and Rémi Fertala</i>	
L33	Lidar Analysis Techniques for Use in the Atmospheric Boundary Layer .....	593
	<i>William E. Eichinger, Daniel I. Cooper, Doug Hof, David Holtkamp, Robert Quick, Jr., Joe Tee, and Robert Karl</i>	
L34	Correction for Nonlinear Photon Counting Effects in Lidar Systems .....	597
	<i>D. P. Donovan, J. A. Whiteway, and A. I. Carswell</i>	
L35	High Background Photon Counting Lidar .....	601
	<i>W. J. Lentz</i>	
L36	Development of a Raman Lidar Simulation Tool .....	605
	<i>R. J. Grasso and J. R. Hummel</i>	
L37	A Variable Phase Function Approach for the Inversion of Lidar Return Signals .	607
	<i>V. A. Kovalev and H. Moosmüller</i>	

L38	A Comparison of Lidar Inversion Methods for CIRRUS Applications .....	611
	<i>Salem Elouragini and Pierre H. Flamant</i>	
L39	Time and Wavelength Domain Algorithms for Chemical Analysis by Laser Radar .....	613
	<i>David L. Rosen and James B. Gillespie</i>	
L40	Lidar Receivers for Picosecond Remote Sensing .....	617
	<i>D. V. Stoyanov and T. N. Dreischuh</i>	
L41	Acousto-Optic Filtering of Lidar Signals .....	621
	<i>G. Kolarov, A. Deleva, and Ts. Mitsev</i>	
L42	Ground-Based Doppler Lidar of Increased Laser Instability: Conception and Design .....	625
	<i>D. V. Stoyanov, B. M. Bratanov, V. N. Naboko, and M. D. Angelova</i>	
L43	Analytical Estimates of the PP-Algorithm at Low Number of Doppler Periods Per Pulse Length .....	629
	<i>M. D. Angelova, E. V. Stoykova, and D. V. Stoyanov</i>	
L44	A Considerable Effect of Stratospheric Aerosol on Lidar-Detected Ozone Profile and a Three-Wavelength Inversion Technique for Both Ozone and Aerosol .....	633
	<i>Qiu Jinhuan</i>	
L45	High-Resolution Processing of Long-Pulse-Lidar Data .....	637
	<i>L. L. Gurdev, T. N. Dreischuh, and D. V. Stoyanov</i>	
L46	Lidar Measurements of Cloud Extinction Coefficient Distribution and its Forward Scattering Phase Function According to Multiply Scattered Lidar Returns .....	641
	<i>Qiu Jinhuan and Huang Qirong</i>	
L47	Measurements of the Backscattering Phase Matrices of Crystal Clouds with a Polarization Lidar .....	643
	<i>B. V. Kaul, A. L. Kuznetsov, and E. R. Polovtseva</i>	

8:30-10:00            **SESSION M: Systems and Facilities**

Session Chair:  
*Richard Schotland*

8:30	M1	(Invited) Measurement Capabilities of Giant Lidars for Middle and Upper Atmospheric Applications .....	647
		<i>Chester S. Gardner</i>	
9:00	M2	Lidar Sounding of Ozone and Aerosols .....	649
		<i>V. E. Zuev</i>	
9:15	M3	Atmospheric Measurements Using the LAMP Lidar During the LADIMAS Campaign .....	651
		<i>C. R. Philbrick, D. B. Lysak, T. D. Stevens, P. A. T. Haris, and Y. -C. Rau</i>	
9:30	M4	Lidar Measurements Using Large Liquid Mirror Telescopes .....	655
		<i>R. J. Sica, S. Sargoytchev, S. Flatt, E. Borra, and L. Girard</i>	
9:45	M5	Spectroscopic Method for Earth-Satellite-Earth Laser Long-Path Absorption Measurements Using Retroreflector In Space (RIS) .....	659
		<i>Nobuo Sugimoto, Atsuchi Minato and Yasuhiro Sasano</i>	

10:00-10:30            **COFFEE BREAK**

10:30-12:00           **SESSION N: Water Vapor Measurements**

Session Chair:  
*Wolfgang Renger*

10:30	N1	Raman Lidar Measurements of Water Vapor and Aerosol/Clouds During the FIRE/SPECTRE Field Campaign .....	663
		<i>S. H. Melfi, D. Whiteman, R. Ferrare, K. Evans, J. E. M. Goldsmith, M. Lapp, and S. E. Bisson</i>	
10:45	N2	Performance Modeling of Daytime Raman Lidar Systems for Profiling Atmospheric Water Vapor .....	667
		<i>J. E. M. Goldsmith and Richard A. Ferrare</i>	
11:00	N3	BELINDA: Broadband Emission Lidar with Narrowband Determination of Absorption - A New Concept for Measuring Water Vapor and Temperature Profiles .....	671
		<i>F. A. Theopold, C. Weitkamp, and W. Michaelis</i>	
11:15	N4	DIAL Simulations for Satellite Water Vapor Profile Measurements within the BEST Project .....	675
		<i>P. Chazette, J. Pelon, and G. Megie</i>	

11:30	N5	Airborne Water Vapor DIAL Research: System Development and Field Measurements ..... 679 <i>Noah S. Higdon, Edward V. Browell, Patrick Ponsardin, Thomas H. Chyba, Benoist E. Grossmann, Carolyn F. Butler, Marta A. Fenn, Shane D. Mayor, Syed Ismail, and William B. Grant</i>	679
11:45	N6	Alexandrite Lidar for the Atmospheric Water Vapor Detection and Development of Powerful Tunable Sources in IR ..... 683 <i>M. Uchiuni, M. Maeda, K. Muraoka, and O. Uchino</i>	683
12:00-1:30	<b>LUNCH</b>		
1:30-3:15	<b>SESSION O: Devices and Techniques</b>		
	Session Chair: <i>Norman Menyuk</i>		
1:30	O1	(Invited) Emerging Solid-State Laser Technology for LIDAR/DIAL Remote Sensing ..... 687 <i>Dennis Killinger</i>	687
2:00	O2	Coherent Summation of Spatially Distorted Doppler Lidar Signals Using a Two-Dimensional Heterodyne Detector Array ..... 689 <i>Kin Pui Chan and Dennis K. Killinger</i>	689
2:15	O3	The Role of Laser Coherence in Long-Range Vibration Measurements ..... 691 <i>R. S. Eng, C. Freed, R. H. Kingston, K. I. Schultz, A. L. Kachelmyer, and W. E. Keicher</i>	691
2:30	O4	A Portable Lidar Using a Diode-Pumped YAG Laser ..... 695 <i>N. Takeuchi, H. Okumura, T. Sugita, H. Matsumoto, and S. Yamaguchi</i>	695
2:45	O5	Investigations on Atomic-Vapor-Filter High-Spectral-Resolution Lidar for Temperature Measurements ..... 699 <i>E. Voss and C. Weitkamp</i>	699
3:00	O6	HgCdTe Photomixers for CO <sub>2</sub> Laser Radar Systems ..... 703 <i>Peter R. Bratt</i>	703
3:15-3:30	<b>COFFEE BREAK</b>		
3:30-5:00	<b>SESSION P: Tropospheric Measurements</b>		
	Session Chair: <i>Harvey Melfi</i>		
3:30	P1	Airborne Lidar Mapping of Vertical Ozone Distributions in Support of the 1990 Clean Air Act Amendments ..... 707 <i>Edward E. Uthe, Norman B. Nielsen, and John M. Livingston</i>	707

3:45	P2	Measurements of Fugitive Hydrocarbon Emissions with a Tunable Infrared DIAL .....	711
		<i>M. J. T. Milton, P. T. Woods, B. W. Jolliffe, N. R. W. Swann, and R. A. Robinson</i>	
4:00	P3	The ENEA CO <sub>2</sub> LIDAR/DIAL Station Activity in a Tropospheric Remote Sensing Program .....	715
		<i>R. Barbini, F. Colao, A. Palucci, and S. Ribezzo</i>	
4:15	P4	Lidar Observation of Marine Mixed Layer .....	719
		<i>Susumu Yamagishi, Hiroshi Yamanouchi, and Masayuki Tsuchiya</i>	
4:30	P5	Aerosol Extinction Measurements with CO <sub>2</sub> -Lidar .....	723
		<i>Arne Hågård and Rolf Persson</i>	
4:45	P6	Dense Fog on the Highway Visual Range Monitoring in Cars? .....	727
		<i>W. Hahn, W. Krichbaumer, J. Streicher, and Ch. Werner</i>	
5:00	<b>ADJOURN</b>		



## THIRTY YEARS OF OPTICAL RADAR WORK: REMINISCENCES AND PERSPECTIVES

Giorgio Fiocco  
University of Rome "La Sapienza"

The work carried out at MIT between 1962 and 1969 towards the development of lidar and the subsequent evolution of some of those ideas will be outlined, starting from the successful experiments to obtain lunar echoes (Smullin & Fiocco 1962). For the purpose of studying the atmosphere several concepts appeared feasible. Some were demonstrated or studied to a certain depth: the basic measurement of the molecular and aerosol cross sections, the Raman technique, Doppler retrievals by either heterodyning or interferometric techniques of wind velocity, temperature and aerosol to molecules ratio, and feedback controlled telescopes to achieve large gains. Some geophysical results were also produced. Long series of observations of the stratospheric aerosol in the aftermath of the Mt. Agung eruption were carried out in 1964 and 1965. In 1964 and 1966, lidars were deployed in Sweden, Alaska and Norway, in attempts to detect stratospheric and noctilucent clouds. Much of the activity, however, had to be dedicated to the solution of new and sometimes unexpected technical problems, both in the hardware and in the software; and a large share of the credit for those projects that were successful, should be given to a few brave and hard-working graduate students of the time, particularly to Gerald Grams and Bart De Wolf. Many other groups had in the meanwhile progressively become active, all over the world. In perspective, continued support has been a key to success.

After a jump of more than 20 years, some new ideas and recent developments will be discussed. Among those, observations in the polar regions regarding ozone-aerosol interactions will be shown and compared with earlier work.

Keynote Speaker

<

# Long Term Stratospheric Aerosol Lidar Measurements in Kyushu

Motowo Fujiwara

Department of Applied Physics, Fukuoka University

Fukuoka 814-01, Japan

Lidar soundings of the stratospheric aerosols have been made since 1972 at Fukuoka (33.5N, 130.4E) , Kyushu Island of Japan.

Although the accuracy of the measurements in the early years was not good, with a ruby laser of weak power and a small receiver, the first remarkable disturbance on the stratospheric aerosols could be detected in November, 1974, which was attributed to the serious eruptions of Fuego volcano in Guatemala. A typical variation of the observed aerosol backscattering among the subsequent major volcanic events, in which a sudden increase of the the total backscattering coefficient was followed by the large fluctuations in a few months with a period of several weeks and then gradual decrease for years to the background level, was found already at this Fuego event.

Among the volcanic events in the stratosphere after the Fuego, many of which have been detected by lidar in Fukuoka, El Chichon in Mexico in 1982 and Pinatubo in Philippine in 1991 are two of the most important events in the sense that the volcanic cloud originated from them spread almost all over the world and should have given some important effects on the radiation budget of the earth's atmosphere.

In 1979 a Nd-YAG laser and a 50 cm receiving telescope were introduced into our lidar system and much more accurate measurements became available using mainly the fundamental wavelength of the laser, 1064 nm. Volcanic clouds from the eruptions of La Soufriere, Sierra Negra, St. Helens, Uluwan, Alaid, unknown volcano, and El Chichon were detected one after another in only three years from 1979 to 1982.

The most striking disturbance in this period was that from the eruptions of El Chichon in April 1982 the total backscattering coefficient of which exceeded ten times those of the previous events. A sudden increase of the total backscattering was followed by the large fluctuations while decreasing to the temporal minimum in summer. The profiles of scattering ratio showed that from April to August the volcanic cloud stratified into two layers: the upper one with fine structure and sharp edges in the easterly wind region and the lower dumpy one in the westerly region. Layers in these two regions merged into one broad layer as the westerly wind prevailed in the whole region in fall of that year, when the total backscattering began to increase toward winter-spring.

The increase of the total backscattering and the change in the shape of the layers accompanied by the variation of wind field could also be seen in the subsequent years superposed on the gradual decay from winter-spring of 1983 to the Nevado del Ruiz event in the end of 1985. Measurements were made also with the second harmonic wavelength of 532 nm though less frequently than with the fundamental wavelength. Ratio of the backscattering coefficient for 532 nm to that for 1064 nm had its minimum value around the height of the layer peak. This indicates that the aerosols were relatively larger at the layer peak than the lower or higher regions. A slight seasonal variation was also found in this ratio.

The observations above mentioned were made at Kyushu University, Fukuoka until 1989. The author moved from Kyushu University to Fukuoka University in 1988 and constructed a compact lidar with Nd-YAG laser. The observation have been made with the second harmonic wavelength.

In July 1991 strong scattering layers which were originated from the serious eruptions of Pinatubo in June and were almost comparable to the El Chichon clouds were detected. Similar to the El Chichon event, upper layers appeared at heights between 20 and 35 km and the lower layer around 17 km in the initial stage from July to August. The various heights of the layer peaks corresponded to only three narrow intervals in the value of potential temperature. In some cases the inversion of temperature appeared at the same altitude as a strong scattering layer. The behavior of the layers up to this time are fairly similar to those of the El Chichon clouds but the difference in the fine structure of vertical profiles are remarkable especially after fall.

Volcanic clouds from Pinatubo and other volcanos (especially El Chichon) are examined carefully and compared to each other and to the wind and temperature which were measured by Fukuoka Meteorological Observatory almost at the same time as the lidar observation were made.

# Southern Hemisphere Lidar Measurements of the Aerosol Clouds from Mt Pinatubo and Mt Hudson

Stuart A. Young, Peter J. Manson and Graeme R. Patterson,  
CSIRO, Division of Atmospheric Research,  
Private Bag No 1, Mordialloc, Vic, Australia, 3195.

## Initial Stratospheric Lidar Measurements of 19th July 1991.

On 19th July 1991, during tests to determine the ability of the newly-modified CSIRO Nd:YAG lidar to measure signals from the stratosphere before the arrival of dust from the eruption of Mt Pinatubo, a strongly scattering layer was detected at an altitude of 22km. That evening, the spectacular sunset and twilight were typical of volcanically disturbed conditions.

Lidar measurements at 532nm were made between 1400 and 1500 EST (0400 - 0500 UT) on 19th July through broken cloud. Approximately 3800 laser firings were averaged in 256 shot blocks. These and subsequent data have been analysed to produce profiles of aerosol volume backscatter function and scattering ratio (total backscatter / molecular backscatter). The scattering ratio for 19th July is shown in Fig. 2 where a peak ratio of 6.5 can be seen in a 2km thick layer at an altitude of 22km. The corresponding peak aerosol backscatter is  $4.5 \cdot 10^{-7} (m \cdot sr)^{-1}$ . The vertically integrated aerosol backscatter (18 - 27km) is  $9 \cdot 10^{-4} sr^{-1}$ . The peaks in the profile above the main layer are not significant. They are mainly the result of noise and low signal levels in the lidar system which had not yet been optimised for stratospheric measurements.

Clouds again prevented a clear view of the twilights on the next two nights, although there was some evidence for an enhanced glow. The sunset on the third night however, appeared normal, although again it was cloud-affected. During setting up, the lidar also showed no evidence of any stratospheric layer. Unfortunately the arrival of heavy cloud stopped operations before any data could be recorded and these conditions persisted for several days.

The evidence suggested that the aerosol layer had disappeared. An explanation for this disappearance and the earlier than expected arrival of the layer over Melbourne (38°S) was required. Nimbus 7 TOMS data for 23rd June (Smithsonian, 1991a) showed that the SO<sub>2</sub> from the eruption had extended at least 11000 km to the west and that the southern boundary of the cloud had reached 15°S just 8 days after the climactic eruption. It can be assumed that this cloud also contained dust and sulphuric acid aerosol. It was proposed that a section had then been broken away from the main cloud and carried south by a large scale eddy between the low latitude easterlies and the strong mid-latitude westerlies which finally carried the aerosol cloud over southern Australia. This hypothesis was later supported by SAGE II data supplied by M. P. McCormick and recently published (McCormick and Viega, 1992). Accompanying 30mb wind data showed a counter clockwise circulation, responsible for the transport, located in the South Atlantic Ocean.

Clear weather next permitted lidar observations on the 5th August (Fig. 3) when it was found that the layer had reappeared and deepened and that there were now two layers between 20km and 27km, each with much vertical structure. The vertically integrated aerosol backscatter had increased to  $2.0 \cdot 10^{-3} \text{ sr}^{-1}$ .

### **Wavelength Dependence of the Aerosol Backscatter.**

Our first observations at 355nm were made on 11th October. Profiles of aerosol backscatter at 355nm and 532nm are shown in Fig. 4, where the wavelength exponent for scattering ( $\alpha$ , where  $\beta = \lambda^\alpha$ ) derived from these data is also plotted. Some caution needs to be taken in interpreting these data as 75 minutes elapsed while the system was being converted to operate at 355nm. Fewer shots were fired at the shorter wavelength, hence the noisier profile and the greater consequent normalisation uncertainty. For this reason the spiky and positive values of  $\alpha$  in the regions of very low backscatter (particularly between 13 - 19km) are most likely not significant. In most of the regions where the backscatter is strong,  $\alpha$  lies between 0 and 1. The layer at 12km is due to Mt Hudson while a very variable Ci layer is below 10km.

A similar study was performed on 29/30 January 1992 (Fig. 5) when the layer was less variable. Peak backscatter at 355nm is approximately twice that at 532nm and  $\alpha$  values in this region are -1.6 to -1.7. The exponent  $\alpha$  increases steadily above the main layer reaching values of about -4 at 30 km. (Low backscatter and noisy data occur above this height.) A region of enhanced backscatter just above the tropopause (8 - 14 km) also shows low  $\alpha$  values. It is suggested that this region and the main layer contain larger particles than the regions near 15 km and above 25 km.

### **Depolarisation Measurements.**

Profiles of scattering ratio, depolarisation ratio (total cross polarised power / total parallel polarised power) and mean monthly temperature for 6th December 1991 and 21st February 1992 are plotted in Figures 6 and 7 respectively. The depolarisation data have been scaled to a value of 0.014 for the clear air below the tropopause (approx. 10 km). Most noticeable is the very low depolarisation in the region of the main Pinatubo layer (19 - 25 km) and the relatively highly depolarising layer around 16 km. The fact that the layer is still present at the same height on both dates and is not falling suggests that it is not the primarily the result of fallout of irregular dust particles. Other possible explanations for the enhanced depolarisation are the agglomeration of partially frozen droplets or a complete phase change (E. Browell, personal communication). Support for this latter suggestion comes from the temperature profiles which show a minimum at the height of peak depolarisation.

### **Lidar Measurements of Aerosols from Mt Hudson.**

During the period 12 - 15 August 1991, Mt Hudson in southern Chile erupted violently sending material into the lower stratosphere. The volcanic cloud was transported around the globe within 8 days, (Smithsonian, 1991b) reaching southern Australia on 20th August. Persistent low cloud over Melbourne prevented lidar observations on this date but aircrew and passengers on the Melbourne to Sydney route reported encounters with a strong sulphurous haze layer at about 11 - 12 km altitude. NOAA AVHRR imagery showed the cloud north of Melbourne (Barton et al, 1992). Lidar data for the 19th and 20th August (Fig. 1(a)) show no evidence of the layer, but measurements made on the morning of 28th August show the presence of a very strong layer

between 12 - 14 km with a weaker layer between 8 - 10 km (Fig.1(b)), indicating that the volcanic cloud had returned. This layer varied in strength and height during the day, which was cloud free apart from evidence of a high haze seen near the sun.

The Mt Hudson layer was observed consistently between 28th August and 6th December at heights between 10 km and 13 km, but with decreasing scattering ratios. Scattering ratio profiles for 9th September and 11th October are plotted in Fig. 1(c) and 1(d) respectively.

### Conclusions

During the 9 months since the first detection of the Mt Pinatubo aerosol layer over Melbourne, the early large variation in the structure of the layer has decreased although some sporadic layers still occur, while the main layer has generally deepened. Low depolarisation ratios indicative of spherical droplet scatterers were found in the main Pinatubo layer. A layer of high depolarisation centred at the height of the temperature minimum has been tentatively attributed to a phase change in the sulphuric acid aerosol. Dual wavelength data will be studied further in terms of the change of the aerosol size distribution with height and time.

### References

1. Barton I. J., A. J. Prata, I. G. Watterson and S. A. Young. (1992) *Identification of the Mt Hudson volcanic cloud over SE Australia*. Submitted to Geophys. Res. Letts.
2. McCormick, M. P. and R. E. Viegas (1992) *SAGEII Measurements of Early Pinatubo Aerosols*. Geophys. Res. Letters. 19,2,155 - 158.
3. Smithsonian Institute (1991a), *Pinatubo.*, Bulletin of the Global Volcanism Network, 16, 5, 2 - 8.
4. Smithsonian Institute (1991b), *Hudson.*, Bulletin of the Global Volcanism Network, 16, 7, 2 - 5.

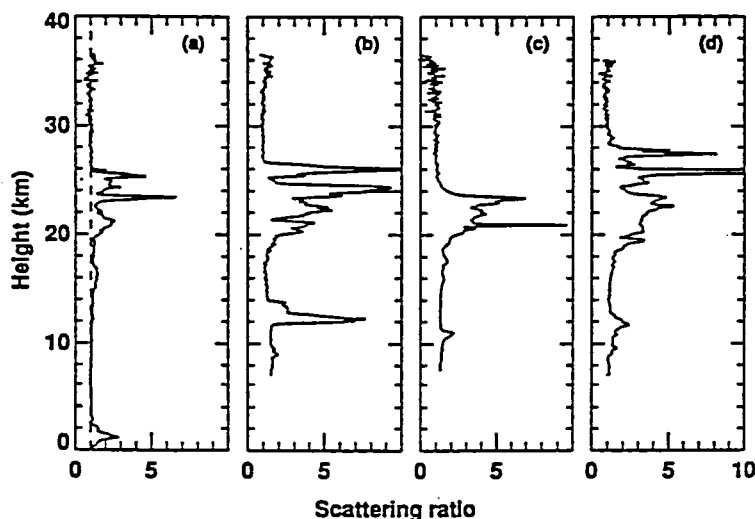


Fig 1

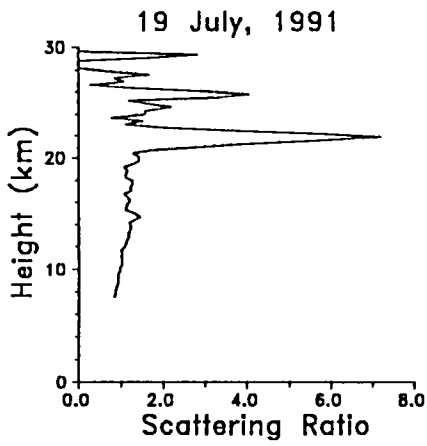


Fig 2

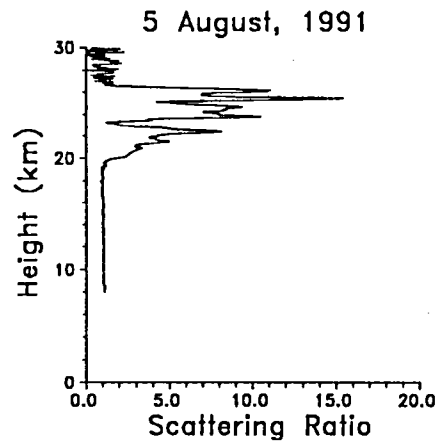


Fig 3

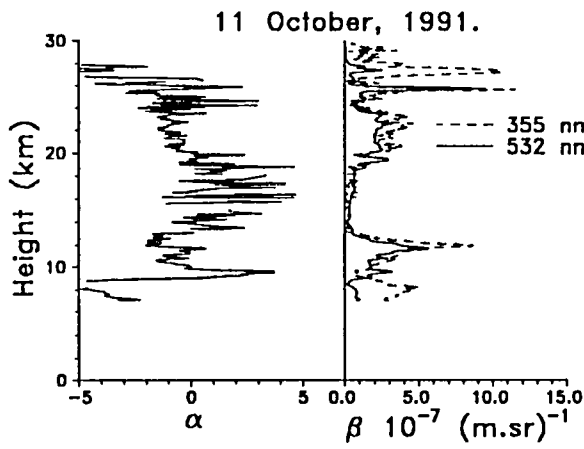


Fig 4

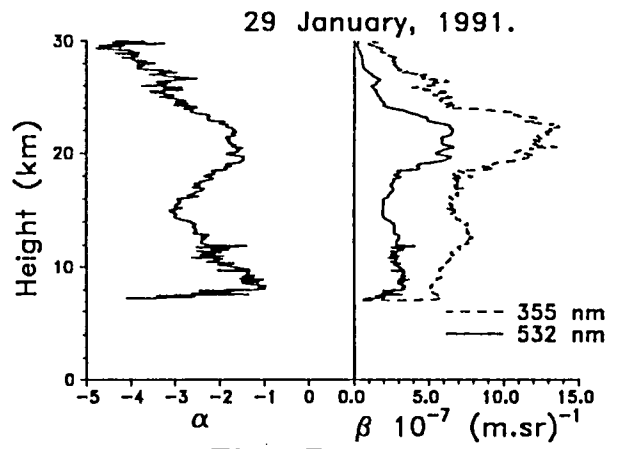


Fig 5

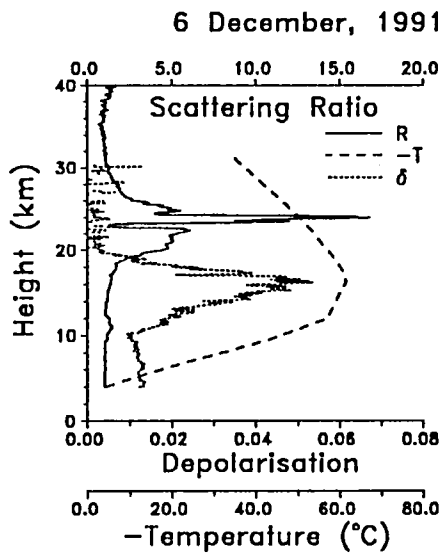


Fig 6

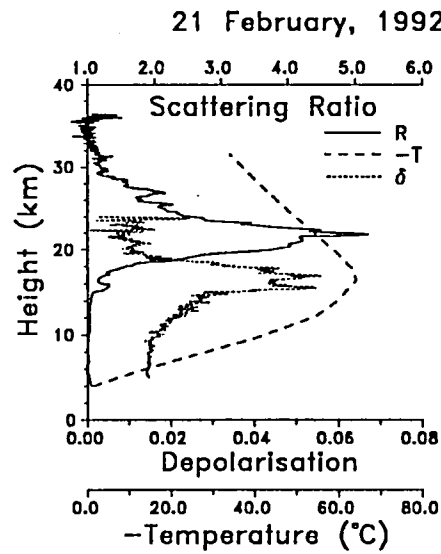


Fig 7

# Stratospheric backscatter, extinction, and lidar ratio profiling after the Mt.-Pinatubo eruptions

Albert Ansmann, Christoph Schulze, Ulla Wandinger,  
Claus Weitkamp, Walfried Michaelis  
GKSS-Forschungszentrum, W-2054 Geesthacht, Germany

Since August 1991 the stratospheric aerosol layer is continuously monitored with a combined Raman elastic-backscatter lidar. The groundbased system, described in detail in Ref. 1, is located at GKSS Research Center in North Germany (53.5°N, 10.5°E). A 308-nm XeCl excimer laser is used as the radiation source. Signals elastically backscattered from air molecules and particles and inelastically Raman backscattered from nitrogen molecules at 332 nm (rotation-vibrational branch) are detected. The measurement of these two signal profiles up to 35 km height allows the separate and independent determination of aerosol extinction and backscatter properties in the perturbed lower stratosphere. The extinction coefficient is derived from the nitrogen Raman signal profile, while the backscatter coefficient is obtained from the elastic-to-inelastic backscatter signal ratio (ref. 2). In this way, also the extinction-to-backscatter, or lidar, ratio profile is determined. For the first time, lidar ratios are determined in the perturbed stratospheric layer by the use of remote sensing only. The lidar ratio contains information about the size range of the stratospheric particles which are assumed to be sulfuric acid droplets, and it is needed in the calculation of aerosol optical properties from data taken with a typical backscatter lidar (ref. 3).

Figure 1 gives an overview of the stratospheric situation in terms of the particle backscatter coefficient for the time period from August 1991 to February 1992. Until November the particle density of the aerosol layer is moderately enhanced. Optical depth values between 0.02 and 0.15 for  $\lambda = 308$  nm are measured. The total-to-Rayleigh backscatter ratio (scattering ratio) is below 2 which corresponds to values below 6, 12, and 35 for  $\lambda = 550$  nm, 700 nm, and 1  $\mu$ m, respectively.

The base height of the layer coincides with the tropopause. Very clean air is observed in the upper troposphere most of the time. This may indicate the very efficient removal of sinking aerosol particles by ice clouds. During the first months of observation the top height of the stratospheric layer is between 21 and 25 km.

A sudden and rapid increase of the particle backscatter intensity is observed at the beginning of December 1991. On 8 December, the aerosol layer reaches up to 30.5 km. The optical depth is 0.3 and the maximum scattering ratio is nearly 3 for  $\lambda = 308$  nm. The rapid increase of the aerosol content results from the change of the stratospheric circulation. Strongly perturbed air masses begin to move northward in autumn 1991 and obviously reach 53°N in December. In the presence of the denser aerosol layer the stratosphere gets cooler. Radiosonde stations in the vicinity of Geesthacht measure very low temperatures down to -83°C between 25 and 33 km height during the winter months December and January.

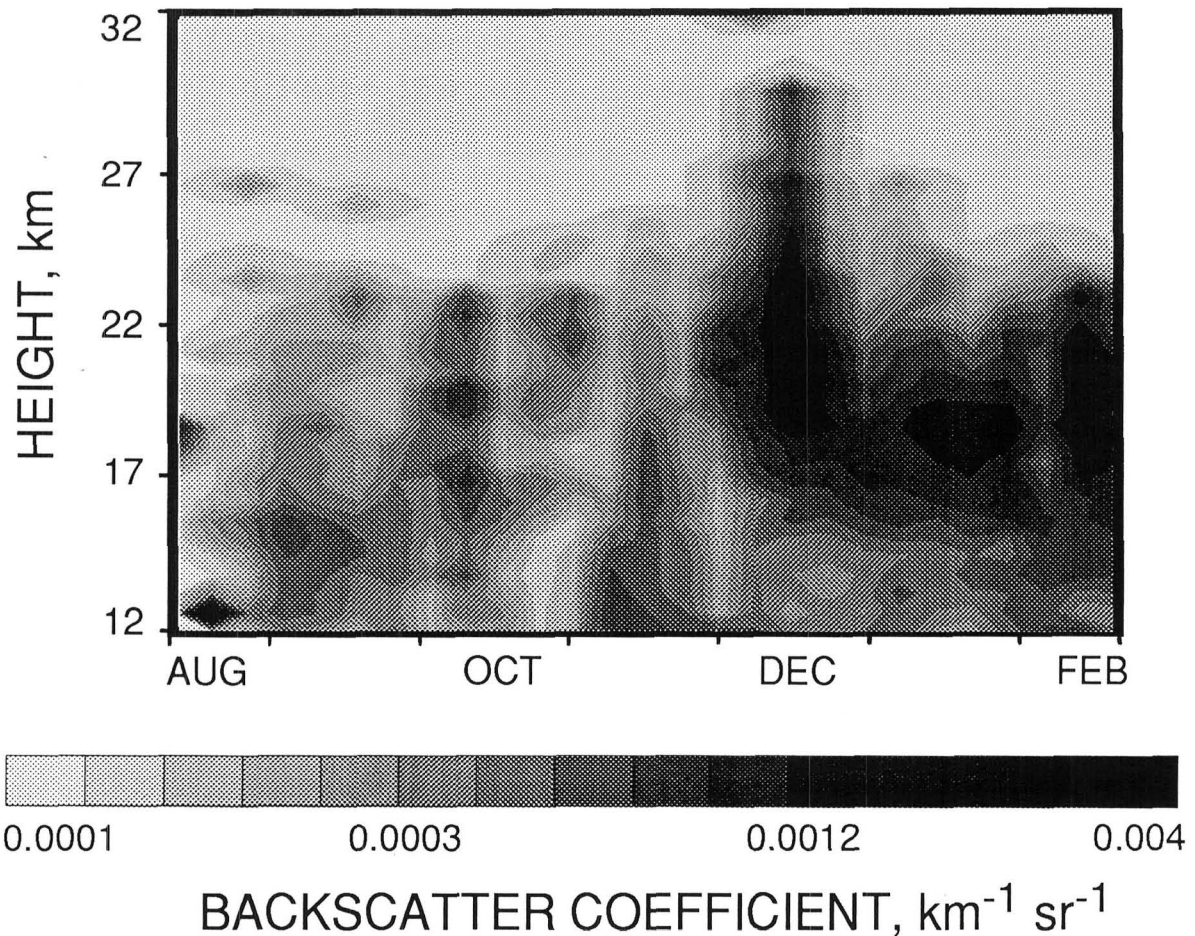


Fig. 1: Temporal development of the stratospheric aerosol layer in terms of the particle backscatter coefficient at 308 nm. The measurements are taken above North Germany (53.5°N) between 12 August 1991 and 19 February 1992. Time resolution is 1 week, range resolution is 600 m. Each lidar signal profile is based on about  $1.5 \times 10^6$  laser shots sampled within 2 hours. Changing stratospheric circulation conditions caused a rapid increase of the particle density at the beginning of December 1991.

Figure 2 shows a measurement of 17 January 1992. The stratospheric aerosol layer extends from the tropopause at 12 km to 24 km. A range-independent backscatter coefficient indicates the main layer between 17.5 and 22 km. Lidar ratios roughly between 20 and 30 sr are determined for this height range (cf. Fig. 2, between 19 and 20.5 km). The total optical depth of the stratospheric layer is 0.15. Since the measurement is made at 308 nm, ozone absorption is significant and has to be considered, especially in the calculation of particle extinction. In Fig. 2, the mean ozone density profile for January 1992 measured at Mt. Hohenpeißenberg in South Germany at 48°N (ref. 4) is used for the determination of the data represented by the solid lines. By varying the ozone density by +10 and -10 % the left-hand and right-hand side dashed curves of the lidar ratio are obtained.

At the beginning of the measurements in August 1991, very low lidar ratios around 5 sr are found. Such low values are probably caused by nonspherical particles like ice crystals. Since October 1991 the extinction-to-backscatter ratios are between 10 and 30 sr. Several months after the strong eruptions of Mt. Pinatubo in June 1991 the aerosol layer is believed to consist of spherical sulfuric droplets only. Heavy and, possibly, nonspherical particles have left the stratosphere. Under these conditions, Mie scattering calculations can be used to interpret the measured lidar ratios in terms of the mean particle radius since the extinction-to-backscatter ratio depends on particle size. This will be done, but has not been carried out yet. However, our measurement findings agree well with results derived from numerical calculation for a wavelength of  $\lambda = 532$  nm based on measured particle size spectra (ref. 5). After the volcanic eruption of Mt. El Chichon in 1982, a rapid decrease of the lidar ratio from a background value of 60 sr to 20 sr due to the increased mean particle size was found.

More details of the measurements during the past year will be presented at the conference.

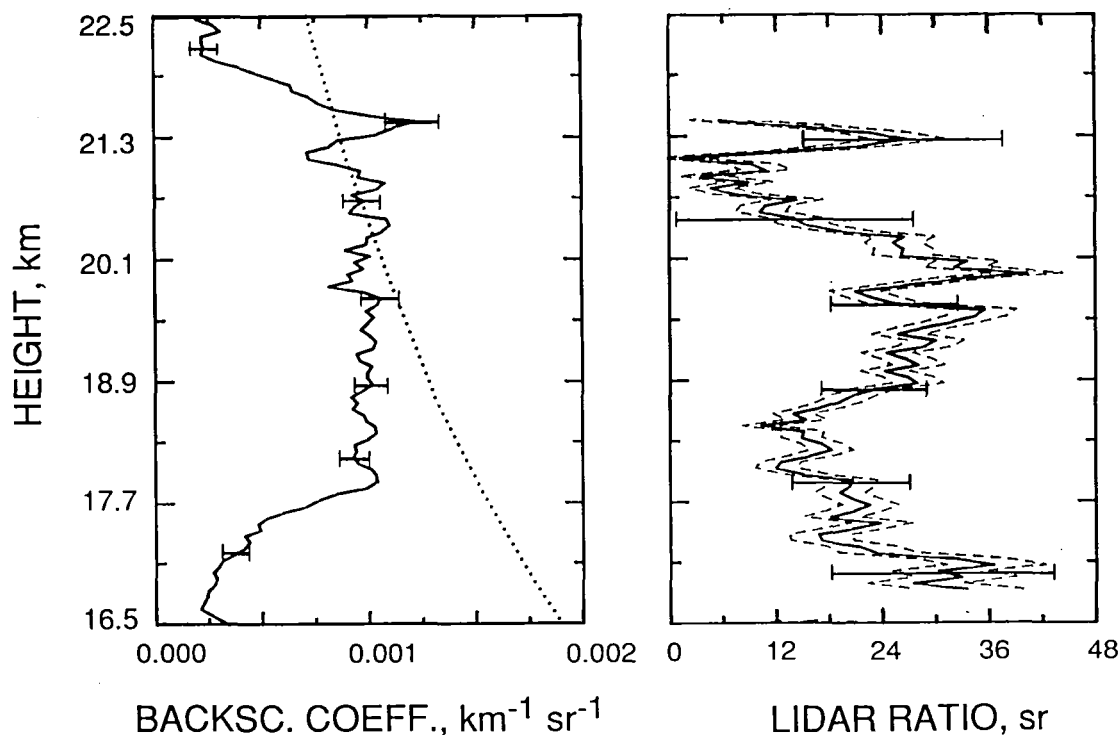


Fig. 2: Particle backscatter coefficient and extinction-to-backscatter ratio determined from a combined lidar measurement at 308 nm on 17 January 1992. Rayleigh backscatter coefficients (dotted line) are shown for comparison, derived from radiosonde data. About  $1.7 \times 10^6$  laser shots are averaged, sampling time is 2 hours and 10 minutes. Before calculating optical parameters, the signal profiles are smoothed with a sliding average length of 300 m for the backscatter coefficient and 1500 m for the extinction-to-backscatter ratio. Calculation step width is 60 m. Error bars and thin dashed curves indicate the standard deviation due to signal noise and the systematic error from a  $\pm 10\%$  uncertainty in the estimated ozone absorption, respectively.

## References

1. A. Ansmann, M. Riebesell, U. Wandinger, C. Weitkamp, E. Voss, W. Lahmann, W. Michaelis, "Combined Raman elastic-backscatter lidar for vertical profiling of moisture, aerosol extinction, backscatter, and lidar ratio", *Appl. Phys. B* 54, in press (1992)
2. A. Ansmann, M. Riebesell, U. Wandinger, C. Weitkamp, W. Michaelis, "Independent measurement of extinction and backscatter profiles in cirrus clouds using a combined Raman elastic-backscatter lidar," to be published in *Appl. Opt.*
3. F. G. Fernald, "Analysis of atmospheric lidar observations: some comments", *Appl. Opt.* 23, 652-653 (1984)
4. H. Claude, Meteorologisches Observatorium Hohenpeißenberg, Deutscher Wetterdienst (pers. communication),
5. H. Jäger and D. Hofmann, "Midlatitude lidar backscatter to mass, area, and extinction conversion model based on in situ aerosol measurements," *Appl. Opt.* 30, 127-138 (1991)

# Measurements of Stratospheric Pinatubo Aerosol Extinction Profiles by a Raman Lidar

Makoto ABO, Chikao NAGASAWA  
 Department of Electronics and Information Engineering  
 Tokyo Metropolitan University  
 Minami-Osawa, Hachioji, Tokyo 192-03, Japan

The Raman lidar has been used for remote measurements of water vapor, ozone and atmospheric temperature in the lower troposphere because the Raman cross section is three orders smaller than the Rayleigh cross section. We estimated the extinction coefficients of the Pinatubo volcanic aerosol in the stratosphere using a Raman lidar. If the precise aerosol extinction coefficients are derived, the backscatter coefficients of a Mie scattering lidar will be more accurately estimated.

The Raman lidar has performed to measure density profiles of some species using Raman scattering. Here we used a frequency-doubled Nd:YAG laser (532nm) for transmitter and received nitrogen vibrational Q-branch Raman scattering signal (607nm). The block diagram of our Nd:YAG Raman lidar system is shown in Fig.1 and specifications of the experimental setup are described in Table I.

Ansmann et al.(1990) derived tropospheric aerosol extinction profiles with a Raman lidar. We think that this method can apply to dense stratospheric aerosols such as Pinatubo volcanic aerosols. As dense aerosols are now accumulated in the stratosphere by Pinatubo volcanic eruption, the error of Raman lidar signal regarding the fluctuation of air density can be ignored. The Raman lidar equation is written as

$$P(z, \lambda_L, \lambda_R) = K\beta(z, \lambda_L, \lambda_R) \exp\left\{-\int_0^z [\alpha(\lambda_L, x) + \alpha(\lambda_R, x)] dx\right\} / z^2,$$

where  $P(z, \lambda_L, \lambda_R)$  is the received power from distance  $z$ ,  $K$  is the system constant,  $\beta(z, \lambda_L, \lambda_R)$  is the Raman backscatter coefficient and  $\alpha$  is the total extinction coefficient at the laser wavelength  $\lambda_L$  and the Raman wavelength  $\lambda_R$ .  $\alpha$  consists of the extinction coefficients due to absorption and scattering by molecules and aerosols.

Assuming a wavelength dependence of the aerosol extinction such as

$$\alpha_{aer}(\lambda_L) / \alpha_{aer}(\lambda_R) = \lambda_R / \lambda_L,$$

then the aerosol extinction coefficient profile

$$\alpha_{aer}(\lambda_L, z) = \left\{ \frac{d}{dz} [\ln(N(z)/z^2 P(z)) - \alpha_{mol}(\lambda_L, z) - \alpha_{mol}(\lambda_R, z)] \right\} / \{1 + (\lambda_L / \lambda_R)\}.$$

where  $N(z)$  is molecular density.

The calculated extinction coefficient profile is shown in Fig.2 and the scattering ratio profile on the same day ( $\lambda=532\text{nm}$ ) is shown in Fig.3.

## Reference

Ansmann, A., M.Riebesell and C.Weitkamp (1990), Optics Lett., 15, 13, 746-748.

Table I. Specifications of Raman lidar

Transmitter	
Primary wavelength	: 532nm
Pulse energy	: 300mJ
Repetition rate	: 10Hz
Beam divergence	: 0.2mrad
Receiver	
Telescope	: 280mm
Detector	: PMT(R666S HAMAMATSU)
Filter width	: 1.8nm(532nm) 3.7nm(607nm)
Data acquisition	
Type	: Photon counting
Range resolution	: 20m(min.)

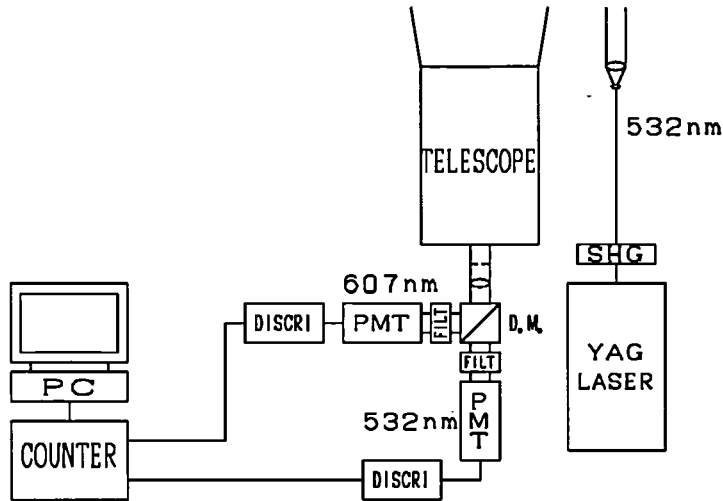


Fig.1. Block diagram of the Raman lidar

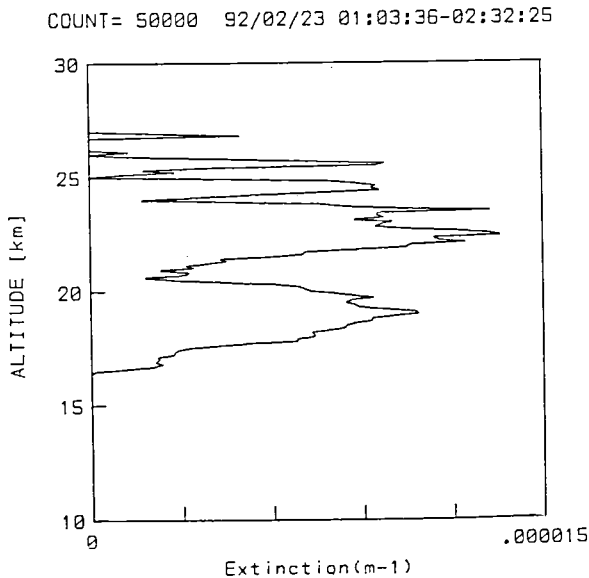


Fig.2. Aerosol extinction coefficient derived from N<sub>2</sub> Raman profile

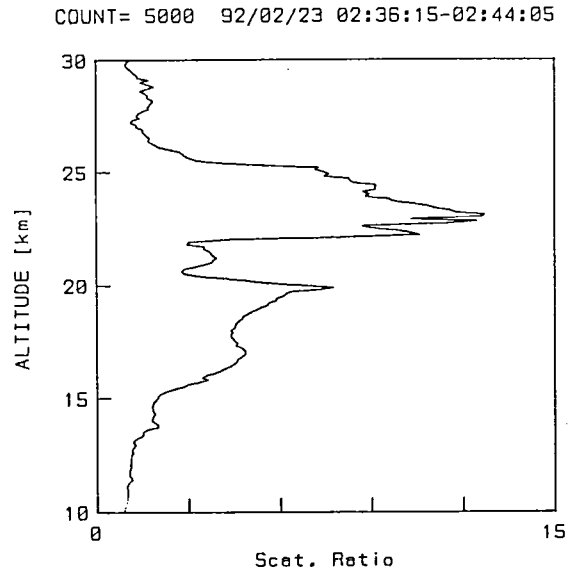


Fig.3 Scattering ratio profile(532nm)

# Raman Lidar Measurements of Pinatubo Aerosols over southeastern Kansas during November-December 1991

R. A. Ferrare<sup>1,2</sup>, S. H. Melfi<sup>2</sup>, D. N. Whiteman<sup>3</sup>, and K. D. Evans<sup>4,2</sup>

NASA/Goddard Space Flight Center, Greenbelt, Maryland 20771

The eruptions of the Philippine volcano Pinatubo during June 1991 produced large amounts of stratospheric aerosols that could significantly affect earth's climate [Hansen et al. 1992] as well as trigger stratospheric ozone depletion through heterogeneous chemical reactions [Brasseur et al, 1990]. Information regarding the physical and optical properties of these aerosols is required to quantify these effects. By measuring both the elastically backscattered signal and the inelastic signal produced by Raman scattering from nitrogen molecules, Raman lidar can provide some of this information. In this presentation we discuss Raman lidar measurements of the scattering ratio, backscattering, extinction, extinction/backscattering ratio, and optical thickness of the Pinatubo aerosols over southeastern Kansas (37.10 N, 95.57 W) made on 10 nights during November and December, 1991.

The Raman lidar developed at GSFC is a trailer-based system which uses an XeF excimer laser to transmit light at 351 nm. System details are shown in Table 1. The light backscattered by molecules and aerosols at this wavelength is detected as well as Raman scattered light from water vapor, nitrogen, and oxygen molecules. Since background skylight interferes with the detection of the Raman signals (which are about 3 orders of magnitude weaker than the elastically backscattered signal), the data discussed in this paper were acquired only at night.

The aerosol scattering ratio  $R(\lambda, z)$ , written as  $R(\lambda, z) = 1 + [\beta_a(\lambda, z)/\beta_m(\lambda, z)]$  where  $\beta_a(\lambda, z)$  and  $\beta_m(\lambda, z)$  are the aerosol and molecular volume backscattering coefficients, is derived from the Raman nitrogen return signal and the signal detected at the laser wavelength [Whiteman et al. 1992]. The aerosol backscattering coefficient  $\beta_a(\lambda, z)$  is then computed from  $R$  and from the molecular backscattering coefficient  $\beta_m(\lambda, z)$  obtained from a molecular number density profile computed using coincident radiosonde pressure and temperature data.

**Table 1. Raman Lidar Specifications**

Transmitted Wavelength	351 nm	Detected Wavelengths	351 nm
Pulse Repetition Rate	400 Hz		372 nm (Raman O <sub>2</sub> )
Energy/Pulse	35 mJ		383 nm (Raman N <sub>2</sub> )
Transmitter Divergence	~0.5 mr		403 nm (Raman H <sub>2</sub> O)
Receiver Diameter	0.76 m	Detectors	Photomultiplier
Receiver Field of View	2 mr	Detection Method	Photon Counting
Range Resolution	75 m		

<sup>1</sup> Universities Space Research Association

<sup>2</sup> NASA/Goddard Space Flight Center, Laboratory for Atmospheres, Code 917

<sup>3</sup> NASA/Goddard Space Flight Center, Laboratory for Terrestrial Physics, Code 924

<sup>4</sup> Hughes STX Corporation, 4400 Forbes Blvd., Lanham, MD 20706

The aerosol extinction coefficient  $\alpha_a(\lambda, z)$  is computed using the derivative of the Raman nitrogen return signal with respect to altitude [Ansmann et al. 1990; 1991]. Note that the current system utilizes wavelengths where gaseous (i.e. ozone) absorption is negligible.

Profiles of aerosol scattering ratio  $R(\lambda, z)$ , backscattering coefficient  $\beta_a(\lambda, z)$ , extinction coefficient  $\alpha_a(\lambda, z)$ , and extinction/backscatter ratio  $k(\lambda, z)$  at  $\lambda=351$  nm have been computed for 10 nights between November 18 and December 7. Examples for 4 nights are shown in figure 1. The vertical resolution of  $R$  and  $\beta_a$  is 300 meters; for  $\alpha_a$  and  $k$  the resolution increases from 1.35 km at 13 km to 1.95 km at 23 km. The statistical errors in the backscattering and extinction profiles are generally less than 10% for altitudes below about 23 km.

Figure 1 shows aerosol scattering and extinction generally increasing to a maximum at altitudes between 19-22 km. Figure 2 shows the derived aerosol extinction/backscatter ratio  $k(\lambda, z)$  generally ranges between 18-28 sr for altitudes between 15 and 25 km. The vertical bars in figure 2 represent the range of values measured in this altitude range.

Extinction/backscattering ratios were computed using Mie theory to determine if the values derived from the present Raman lidar measurements are consistent with the expected size distribution of sulfuric acid droplets produced by the Pinatubo volcanic eruption. These computations were made for 351 and 694 nm assuming the aerosols to be sulfuric acid droplets. These theoretical extinction/backscatter ratios are shown in figure 2 as a function of the mode radii of lognormal aerosol size distributions. Two standard deviations ( $\sigma = 0.1$  and  $0.3$ ) of the size distributions were used. Estimates of the mode radii of El Chichon and Pinatubo aerosols obtained from in situ data indicate that the mode radii generally range between 0.2 to 0.5  $\mu\text{m}$  [Jäger and Hofmann, 1991; Deschler et al., 1992]. Figure 3 indicates that for mode radii between 0.3 to 0.5  $\mu\text{m}$ ,  $k(\lambda=351 \text{ nm}, z)$  will vary between 10-30 sr in agreement with the Raman lidar measurements shown in figure 2. The wavelength dependence of  $k$  between 351 and 694 nm implies that, for this stratospheric aerosol distribution at least, aerosol extinction scales as  $\lambda^{-0.6}$  while backscattering scales as  $\lambda^{-1.7}$ .

The increase in  $k$  for decreasing particle size shown in figure 3 may also explain some of the variability of the extinction/backscatter ratios above and below 15 km shown in figure 1. Aerosol backscattering shown in figure 1 decreases for decreasing altitude below 20 km. Assuming the decrease in aerosol backscattering shown in figure 1 indicates that the mean particle radius decreases to approach that more representative of small ( $< 0.1 \mu\text{m}$ ) particles corresponding to a background aerosol distribution, then  $k$  should increase to values near 50 and 60 sr as shown in figures 1 and 3.

The aerosol extinction profiles were integrated between 15 and 25 km to obtain aerosol optical thickness. These values varied between 0.04 and 0.06. The lidar values may underestimate the total aerosol optical thickness if significant amounts of aerosols were present above 25 km. However, the lidar data generally show a rapid decrease in aerosol scattering above the layers of maximum aerosol scattering which were located between 21-23 km.

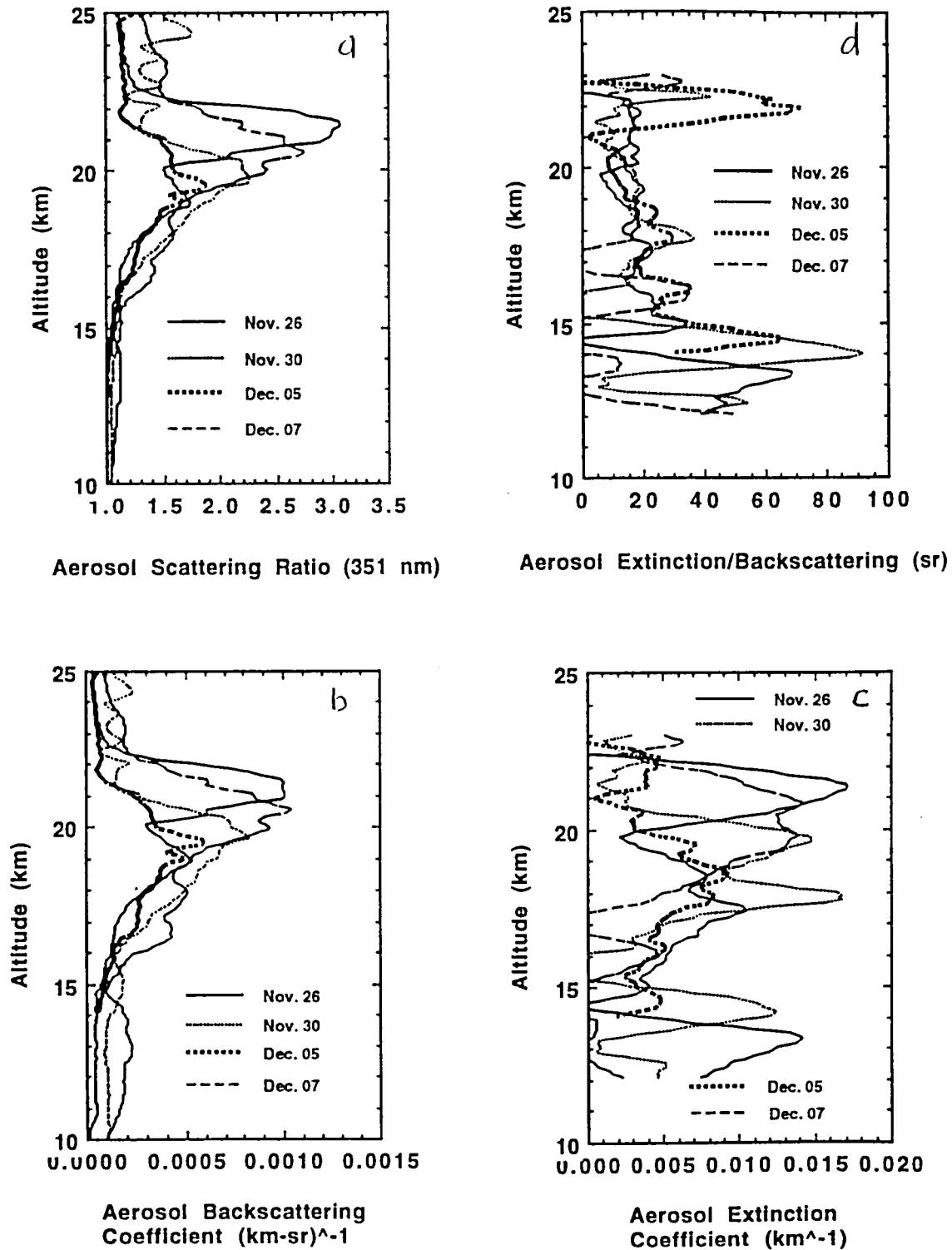


Figure 1. a) Aerosol scattering ratio  $R$ , b) backscattering coefficient  $\beta$ , c) extinction coefficient  $\alpha$ , and d) extinction/backscattering ratio  $k$  for November 26 (00:23-04:23 UT), November 30 (04:03-06:30 UT), December 5 (00:15-02:15 UT), and December 7 (00:20-05:20 UT) 1991 derived from the lidar data at 351 nm. For a) and b) vertical resolution is 300 meters while for c) and d) resolution increases from 1.35 km at an altitude of 13 km to 1.95 km at 23 km.

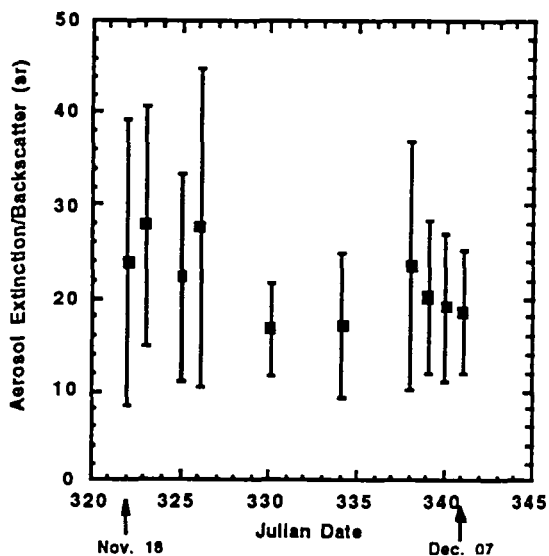


Figure 2. Aerosol extinction/backscatter ratios  $k$  derived from the lidar data at 351 nm for the altitude range 15-25 km. Vertical bars represent the range of values measured between these altitudes.

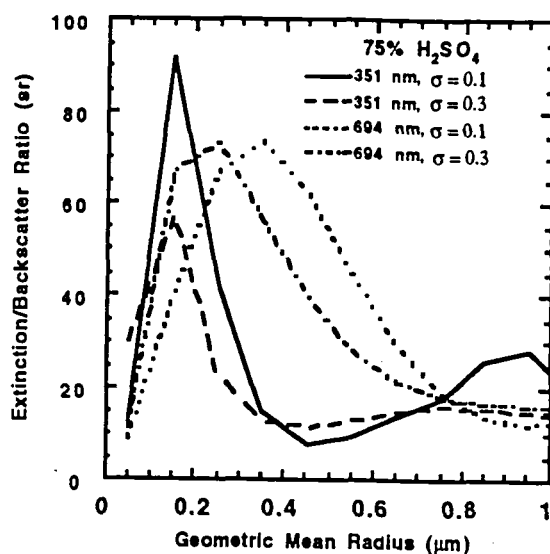


Figure 3. Aerosol extinction/backscatter ratios computed from Mie theory for spherical droplets consisting of 75%  $\text{H}_2\text{SO}_4$  aqueous solution. The droplet size distributions were assumed to be lognormal; two standard deviations ( $\sigma = 0.1$  and  $0.3$ ) were used.

## References

- Ansmann, A., M. Riebesell, and C. Weitkamp, Measurement of atmospheric aerosol extinction profiles with a Raman lidar, *Optics Letters*, **15**, No. 3, 746-748, 1990.
- Ansmann, A., U. Wandinger, C. Schulze, C. Weitkamp, and W. Michaelis, Stratospheric aerosol measurements with a combined Raman elastic-backscatter lidar, in *Proceedings of Optical Remote Sensing of the Atmosphere*, November 1991, Williamsburg, VA, 1991.
- Brasseur, G.P., C. Granier, and S. Walters, Future changes in stratospheric ozone and the role of heterogeneous chemistry, *Nature*, **348**, 626-628, 1990.
- Deschler, T., D.J. Hofmann, B.J. Johnson, and W.R. Rozier, Balloonborne measurements of the Pinatubo aerosol size distribution and volatility at Laramie, Wyoming during the summer of 1991, *Geophys. Res. Letters*, **19**, No. 2, 199-202, 1992.
- Hansen, J., A. Lacis, R. Ruedy, and M. Sato, Potential climate impact of Mount Pinatubo eruption, *Geophys. Res. Letters*, **19**, No. 2, 215-218, 1992.
- Jager, H. and D. Hofmann, Midlatitude lidar backscatter to mass, area, and extinction conversion model based on *in situ* aerosol measurements from 1980 to 1987, *Applied Optics*, **30**, No. 1, 127-138, 1991.
- Whiteman, D.N., S.H., Melfi, and R.A. Ferrare, Raman lidar system for the measurement of water vapor and aerosols in the earth's atmosphere, to appear in *Applied Optics*, May, 1992.

# *Lidar Observations of Stratospheric Aerosol Layer after the Mt. Pinatubo Volcanic Eruption*

By Tomohiro Nagai, Osamu Uchino and Toshifumi Fujimoto  
Meteorological Research Institute, Tsukuba, Ibaraki, 305 Japan

## 1. Introduction

The volcano Mt. Pinatubo (15.14°N, 120.35°E) located on the Luzon Island, Philippines, had explosively erupted on June 15, 1991. The volcanic eruptions such as volcanic ash, SO<sub>2</sub> and H<sub>2</sub>O reached into the stratosphere over 30km altitude by the NOAA-11 satellite observation and this is considered one of biggest volcanic eruptions in this century (Smithsonian Institution, Bull. Glob. Volc. Net., 1991). A grandiose volcanic eruption influences the atmosphere seriously and causes many climatic effects globally. There had been many impacts on radiation, atmospheric temperature and stratospheric ozone after some past volcanic eruptions such as Mt. Agung (1963), Mt. Fuego (1974) and Mt. El Chichón (1982) (Quiroz; 1983, Wendler; 1984, Hofmann; 1987, Angell and Korshover; 1984, Uchino; 1985, Uchino et al; 1988). Main cause of volcanic influence depends on stratospheric aerosol, that stay long enough to change climate and other meteorological conditions. Therefore it is very important to watch stratospheric aerosol layer carefully and continuously.

Standing on this respect, we do not only continue stratospheric aerosol observation at Tsukuba (36.05°N, 140.13°E) but also have urgently developed another lidar observational point at Naha (26.20°N, 127.68°E) in Okinawa Island. This observational station could be thought valuable since there is no lidar observation station in this latitudinal zone and it is much nearer to the Mt. Pinatubo. Especially, there is advantage to link up these two stations on studying the transportation mechanism in the stratosphere.

In this paper, we present the results of lidar observations at Tsukuba and Naha by lidar systems with Nd:YAG laser of 532nm wavelength.

## 2. Observational Results

The observation at Tsukuba has being carried out continuously and that at Naha started on September 19, 1991. The vertical profiles of scattering ratio of aerosol are shown in Fig. 1a and 1b. Stratospheric aerosols from Mt. Pinatubo had reached to Tsukuba on late of June or early July after about 2 weeks of the eruption and already reached to Naha at the beginning of this observation.

The aerosol layer appeared just above the local tropopause in early period, then, dense and thin layers could be seen on mid of July and early August at the altitude of about 21km. After that, the dense and thick layer appeared at about 21-27km altitude range and the layer grew day by day at Tsukuba. The layer between 30 and 33km arose on mid or late November at Naha and similar kind of layer was also observed at Tsukuba a few days later.

Integrated backscattering coefficient (IBC) are plotted in Fig. 2a and 2b. The IBC begun to increase on late of September suddenly at Tsukuba and it was increasing basically until late February. The IBC at Naha also begun to increase on mid of November as corresponding to the first look of the upper layer above 30km. These increases may correspond to wind field change in stratosphere. After this increase, IBC begun to decrease to the value of

beginning of the observation at Naha even though the IBC was still enhancing up with somewhat large fluctuation at Tsukuba on December and January. These phenomena may reflect the transportation processes of aerosols from low latitude zone to higher latitude.

The depolarization ratio observation are shown in Fig. 3. In this observation, the observation was done the two polarization component sequentially like as P-Component, S-Component, P-Component, ..., P-Component, due to using a single channel photon counter, so that the data could be taken just on fine and stable weather without many clouds. The profiles of depolarization ratio of the aerosol are shown in Fig. 3a and the scattering ratio profiles are also shown in Fig. 3b. The scattering ratio profiles were used to subtract the depolarized backscatter by the atmospheric molecules from the illusive depolarization ratio. Comparing with the two kinds of profiles, the layer having higher depolarization ratio can be seen in the lowest side of the aerosol layer and the top of the layer came down gradually. The depolarization ratio reflects the shape of the objects and it shows higher value when the light is reflected by particles deformed from sphere and/or with rough surface. These results shows that the irregular particles were in the lowest side of the aerosol layer and spherical ones have been in upper side since the start of this observation. The non spherical particles could be considered as the primitive volcanic ash and spherical one could be the liquid state sulfate particles, they are expected to be spherical, made from SO<sub>2</sub> by chemical reactions.

### 3. Concluding Remarks

The new observational station was urgently developed at Naha and two station monitoring of the stratospheric aerosol layer has been executed. The total amount of the aerosols began to increase on late September at Tsukuba and late November at Naha. The aerosols existed just above local tropopause at early period, extended to about 30km in late August at Naha and the layer above 30km appeared on late November at each station with some time rag. These phenomena reflects one of the transportation mechanism in the stratosphere. By the observation of depolarization ratio, the primitive volcanic ash particles were in the lower side of the aerosol layer and the top height of the volcanic ash particles moved down gradually. It shows that spherical sulfate particles were in the aerosol layer since the beginning of the observation on late September 1991 and the time variation and spatial distribution of the layer give some informations for chemical reaction in stratosphere.

#### < Acknowledgements >

The authors would like to thank Mr. Yoshinobu Sai, Mr. Kazuo Tamaki, Mr. Ryuichi Nomura and Mr. Tomokazu Sunagawa, Okinawa Weather Station, Japan Meteorological Agency, for their efforts on lidar observations at Naha.

#### < Reference >

- Angell, J. K. and J. Korshover, 1984: Mon. Weather Rev., 112, 1457-1463.  
Hofmann, D. J., 1987: Rev. Geophys., 25, 743-759.  
Quiroz, R. S., 1983: J. Geophys. Res., 88, 6773-6780.  
Smithsonian Institution, 1991: Bull. Global Vol. Net., 16, No.5, 2-8.  
Uchino, O., 1985: J. Met. Soc. Japan, 63, 288-293.  
Uchino, O., I. Tabata, K. Kai and I. Akita, 1988: J. Met. Soc. Japan, 66, 635-643.  
Wendler, G., 1984: Bull. Amer. Met. Soc., 65, 216-218.

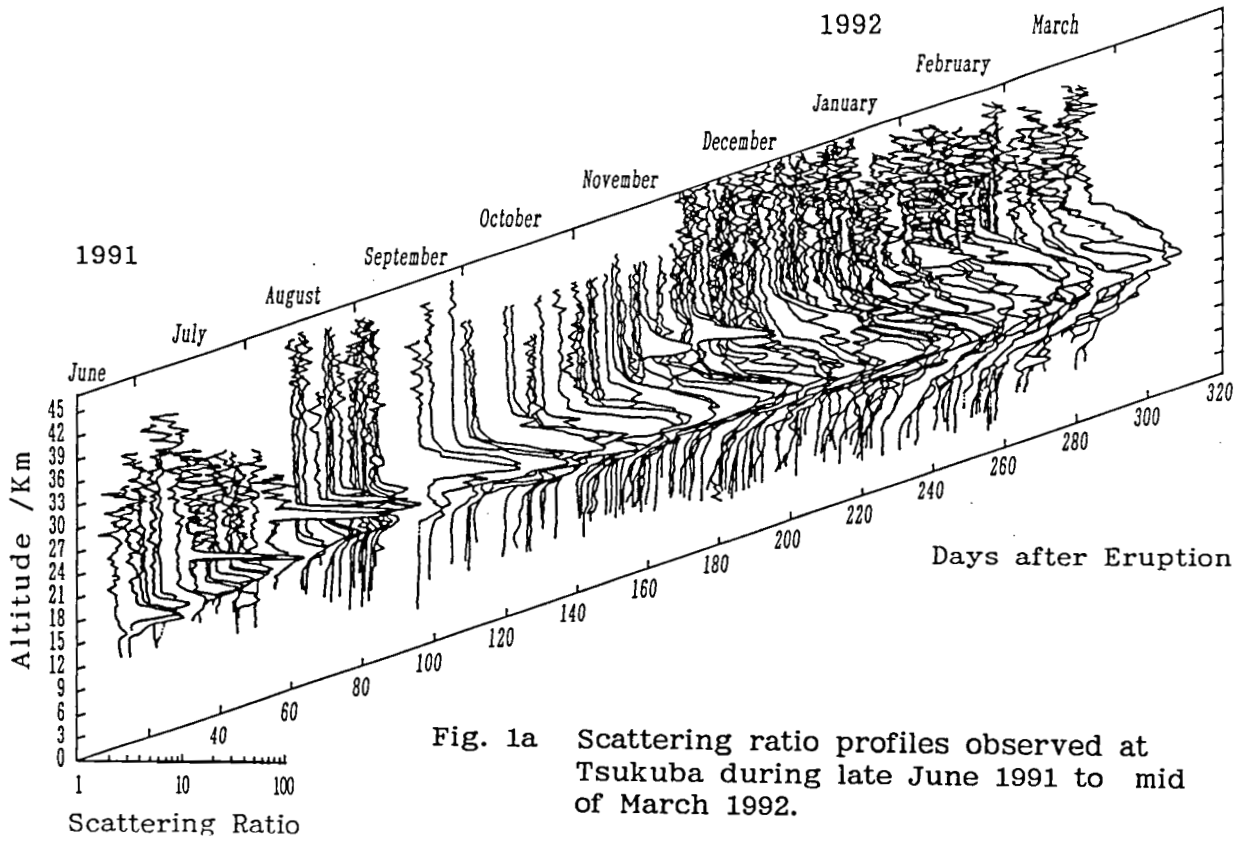


Fig. 1a Scattering ratio profiles observed at Tsukuba during late June 1991 to mid of March 1992.

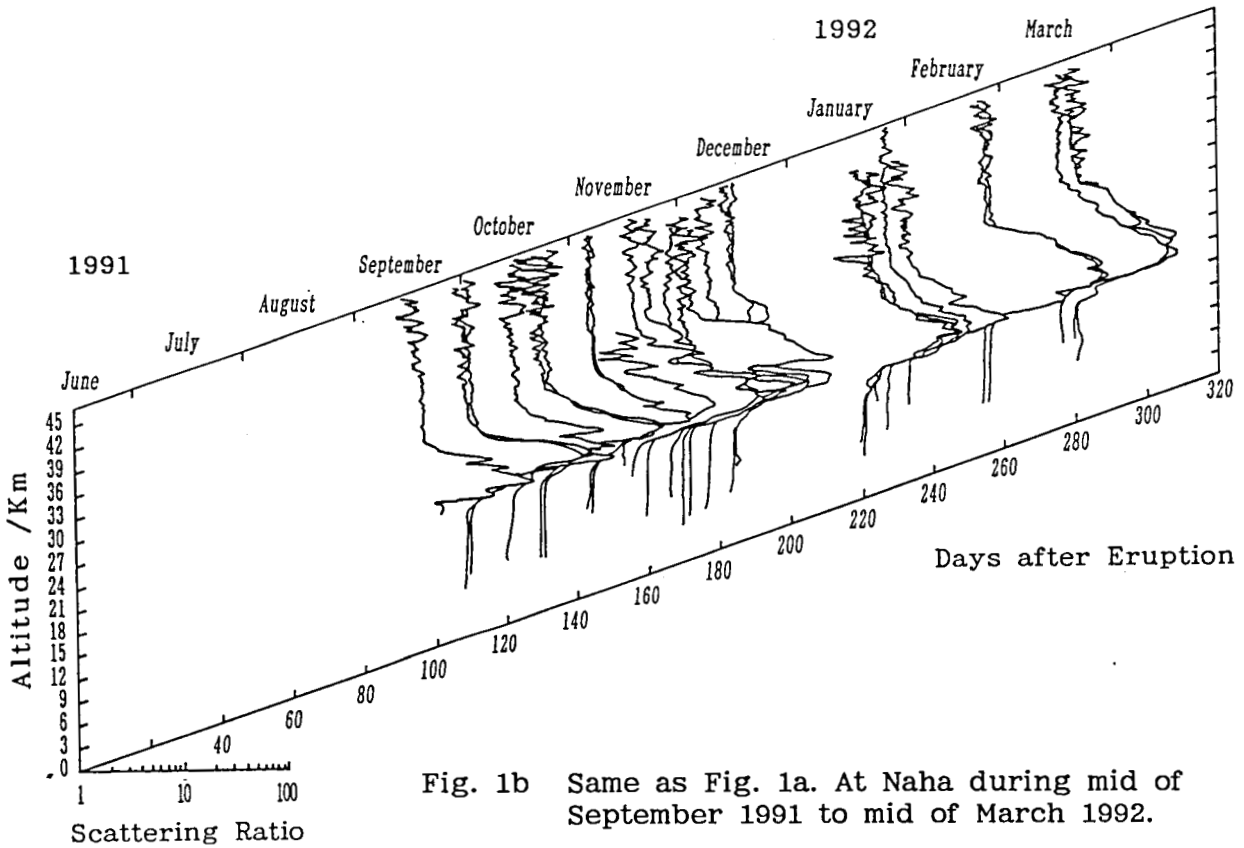


Fig. 1b Same as Fig. 1a. At Naha during mid of September 1991 to mid of March 1992.

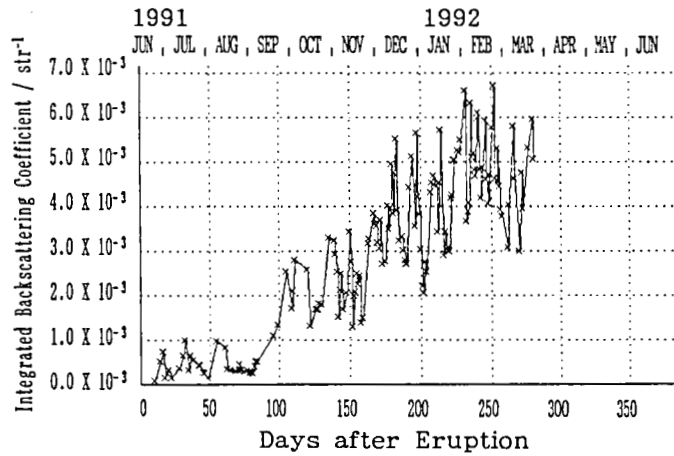


Fig. 2a Time variation of integrated backscattering coefficient (IBC) at Tsukuba.

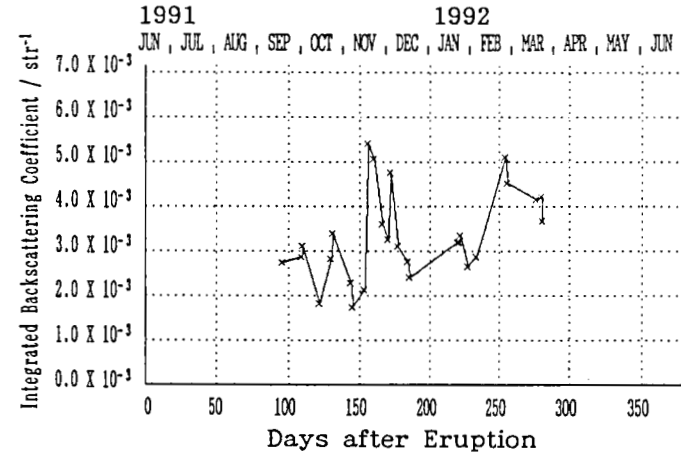


Fig. 2b Same as Fig. 2a. At Naha.

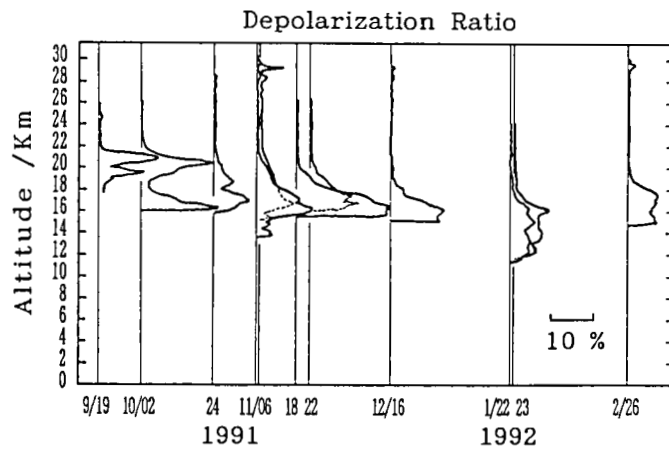


Fig. 3a Depolarization ratio profiles of stratospheric aerosols at Naha.

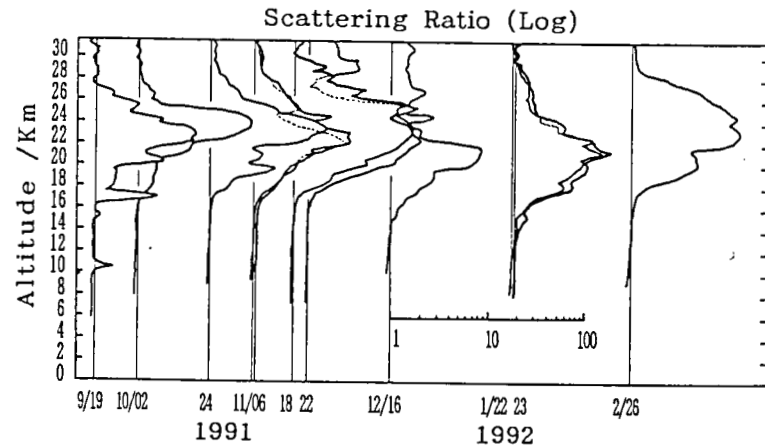


Fig. 3b Backscattering ratio profiles used to calculate true depolarization ratio of aerosols by subtracting the depolarized backscatter by the atmospheric molecules from illusive depolarization ratio.

## **The Role of Lidars in Global Change Research**

Ronald G. Prinn, Center for Global Change Science

MIT, 54-1312, Cambridge, MA 02139

Recent research has solidified a view of the Earth as a global scale interactive system with complex chemical, physical, biological, and dynamical processes that link the ocean, atmosphere, land (soils, ice, snow) and marine and terrestrial living organisms. These processes both within and between the major parts of the system help determine global and regional climate and control the biogeochemical and hydrologic cycles essential to life. The study of the Earth System requires measurements ranging from the microscales of the smallest processes to the global scale.

The complexity and intriguing nature of the Earth System is amply illustrated by a number of closely coupled processes occurring within it. These include: (a) clouds, precipitation, and vegetation, (b) ocean circulation, sea-surface temperature, and phytoplankton, (c) coupled oceanic and atmospheric circulation: the Southern Oscillation, (d) biological activity, atmospheric chemistry, and climate, and (e) biological emissions and the ozone layer. The need to understand better these complex Earth System processes has led to the development of an internationally integrated plan for action for the scientific study of our global environment. The goal is to determine the processes governing its present state and to predict how this state might change due to human and natural forcing. The international plan is embodied in the sister programs of The World Climate Research Program (WCRP) and the International Geosphere-Biosphere Program (IGBP).

The major goal of IGBP is “to describe and understand the interactive physical, chemical, and biological processes that regulate the total Earth System, the unique environment that it provides for life, the changes that are occurring in this system and the manner in which they are influenced by human actions.” Examples of major IGBP projects are the International Global Atmospheric Chemistry (IGAC) Project, the Joint Global Ocean Flux Study (JGOFS) and the Global Change and Terrestrial Ecosystems (GCTE) Project. The major goal of WCRP is “to determine to what extent climate can be predicted and the extent of man’s influence on climate”. Examples of major WCRP Projects are the Tropical Oceans and Global Atmosphere (TOGA) project, the World Ocean Circulation Experiment (WOCE), and the Global Energy and Water Cycle Experiment (GEWEX).

An important aspect of Earth System Science studies in the future is the need to observe simultaneously the physical, chemical, biological, and dynamical processes involved in highly

coupled phenomena such as those mentioned earlier. The wide variety of simultaneous satellite observations planned as a part of the Earth Observing System (EOS) later this decade along with airborne, surface, and submarine observations will be an important contributor to our understanding of these coupled phenomena on the global scale.

Lidars operating from the surface, aircraft and satellites provide a powerful observational technique to study processes and observe trends important in global change. Being active techniques they greatly reduce the need to understand the natural radiation processes inherent in passive techniques. They can operate at high frequency to look at rapidly varying phenomena (gravity waves, chemical fluxes, stratospheric warmings, polar ozone holes, storm systems, etc.). They also operate at specific wavelengths providing specificity for composition measurements (O<sub>3</sub>, hydrocarbons, water vapor, clouds, aerosols, etc.).

Lidar observations have already played important roles in helping understand processes controlling stratospheric ozone and aerosols, tropospheric clouds, water vapor, ozone, gaseous pollutants, and aerosols, and winds and temperatures throughout the atmosphere. Specific recent examples are provided by the use of this technique in studying the Arctic and Antarctic Spring ozone depletion and the global dispersion of the aerosols derived from the Mt. Pinatubo eruption.

In this paper I will review the science of global change and highlight the potential roles for lidars in studying the Earth System over the next decade.

## Interpretation of DIAL Measurements of Lower Stratospheric Ozone in Regions with Pinatubo Aerosols

William B. Grant, Edward V. Browell, Marta A. Fenn<sup>1</sup>, Carolyn F. Butler<sup>1</sup>, Vincent G. Brackett<sup>1</sup>, Robert E. Veiga<sup>1</sup>, Shane D. Mayor<sup>1</sup>, Jack Fishman, D. Nganga<sup>2</sup>, A. Minga<sup>2</sup>, B. Cros<sup>2</sup>, Larry L. Stowe<sup>3</sup>

NASA Langley Research Center, Atmospheric Sciences Division, MS 401A, Hampton, VA 23665-5225;

1 - Hughes ST Systems Corp., 28 Research Drive, Hampton, VA 23666

2 - Universite Maïen Ngouabi, Brazzaville, Congo

3 - NOAA - NESDIS, World Weather Bldg., Washington, DC 20233

The influence of volcanic aerosols on stratospheric ozone is a topic of current interest, especially with the June 15, 1991, eruption of Mt. Pinatubo in the Philippines [e.g., Prather, 1992]. Lidar has been used in the past to provide aerosol profiles which could be compared with ozone profiles measured using ozonesondes [Mast and Saunders, 1962; Komhyr, 1969] to look for coincidences between volcanic aerosols and ozone decreases [Grams and Fiocco, 1967; Adriani et al., 1987; Jäger and Wege, 1990; Grant et al., 1992].

The differential absorption lidar (DIAL) technique has the advantages of being able to measure ozone and aerosol profiles simultaneously as well as being able to cover large geographical regions rapidly [e.g., Browell, 1989]. While there are problems associated with correcting the ozone profiles for the presence of aerosols, the corrections can be made reliably when the wavelengths are closely spaced and the Bernoulli method is applied [Browell et al., 1985; Fenn et al., 1992].

Three questions come immediately to mind when applying the DIAL technique to the study of the effect of volcanic aerosols on stratospheric ozone: (1) How accurate are the measurements; (2) What can be determined about the changes in ozone caused by the presence of the aerosols; and (3) Can the DIAL system be used to provide correlative measurements for use by other instruments?

The DIAL measurements considered in this paper are those obtained in the tropical stratosphere in January 1992 during the Airborne Arctic Stratospheric Expedition (AASE-II). The determination of ozone profiles in the presence of Pinatubo aerosols is discussed in a companion paper by Fenn et al. [1992].

The accuracy of the airborne UV DIAL system measurements of ozone can be addressed by reviewing the comparison of DIAL measurements with measurements made by other instruments that are not affected by the presence of the aerosols. On many missions, the DIAL measurements have been compared to those made using onboard in situ instruments during spiral flights over a regions where the DIAL made a profile measurement. The UV DIAL system has been shown to make measurements with an accuracy of about 10% in the troposphere and lower stratosphere [Browell, 1989]. For the middle stratosphere, a pair of instruments can be used to check the accuracy. One is SAGE-II, which is a solar occultation

instrument that has been making measurements since 1984 [McCormick et al., 1989]. It has a single-occultation measurement accuracy of 7% to 10% in the 15- to 50-km region. Another is the electrochemical concentration cell (ECC) developed by Komhyr [1969]. Air containing ozone is bubbled through a KI solution and causes the release of electrons from the iodine, from which the amount of ozone present can be determined. The accuracy of the ECC sonde is 10% or better in the stratosphere and the precision is 5% to 8% between 10 and 31 km, [Barnes et al., 1985]. Figure 1 shows a comparison of SAGE I values between 10° S and 10° N for the month of April from 1985 to 1991 with ECC sonde values for the second quarter 1991. The bars on the SAGE-II data represent one standard deviation of the mean. The agreement between the two sets of values indicates that the mean values generally agree within 5% to 10% except at lower altitudes, which is very good considering that they did not measure the same air parcels.

A similar comparison can be made between SAGE-II values and UV DIAL values of ozone for a region relatively unaffected by the Mt. Pinatubo volcanic aerosols. Such a region was encountered in January from 20° N to 25° N. Again, a climatology of SAGE-II values was developed from the historical record before Pinatubo, using the months of January and February. The DIAL values are from a flight on January 30, 1992. There was moderate aerosol loading of the stratosphere, shown in arbitrary units. Figure 2 shows a comparison of the two data sets. The bars on the DIAL data represent one standard error of the mean. Note that the DIAL values generally occur at about one standard deviation above the SAGE mean, except at 18.5 km, where the aerosol loading was greatest. Considering again that the same air parcels were not measured, the agreement is very good.

Given that the SAGE-II measurements of ozone agree with both the ECC sonde and UV DIAL measurements under comparable conditions, what can be said about changes in ozone as a result of the Mt. Pinatubo volcanic eruption? Let us turn first to a comparison between the ozonesondes and SAGE-II. Figure 3 shows a comparison of the September and October 1985 to 1990 SAGE ozone data with ozonesonde values from Brazzaville for the third and fourth quarter of 1991. The reduction in ozone as measured by the sondes is significant from 20 to 27 km where the aerosol loading is greatest. The details about the reduction of ozone following the eruption using the sonde measurements for the change and SAGE-II data for the long-term trends have been described elsewhere [Grant et al., 1992]. (The reductions near the peak of the aerosol layer were about 20%, and the total column reduction was about 7%.) Finally, we can turn to the DIAL data in the presence of significant volcanic aerosol loading. Figure 4 shows the SAGE-II values between 10° N and 15° N for January and February 1985 to 1991 compared with DIAL values for January 30, 1992, from 10.8° N to 14.9° N. (SAGE-II cannot measure ozone in regions where the aerosol loading is large.) Note that the reduction in ozone has a similar profile to that measured by the sondes, although the magnitude of the decrease is less since SAGE-II climatology indicates that there should be less ozone in this region in this time frame than in the September/October time frame. Using the AVHRR aerosol optical depth map [see, also, Stowe et al., 1992], it is apparent that the volcanic optical depth at 500 nm has decreased from just over 0.4 during the former time frame at 4° S to just over 0.3 during the second time frame in the 10° N to 15° N region.

Now that good agreement between the SAGE-II, ECC sonde, and DIAL measurements of ozone in the absence of Mt. Pinatubo aerosols and the latter two in the presence of Mt. Pinatubo aerosols has been established, measurements from all three instruments can be used in a correlative fashion to help validate ozone measurements by various other optical remote sensing instruments that may be affected by the presence of the aerosols [Grant, 1989]. In addition, the UV DIAL system can be used to investigate the relationship between ozone loss and aerosol mass or area loading of the stratospheric layers.

#### References

Adriani, A., G. Fiocco, G. P. Gobbi, F. Congeduti, "Correlated behavior of the aerosol and ozone contents of the stratosphere after the El Chichon eruption," *J. Geophys. Res.* 92, 8365-8372 (1987).

Barnes, R. A., A. R. Bandy, A. L. Torres, "Electrochemical concentration cell ozonesonde accuracy and precision," *J. Geophys. Res.* 90, 7881-7887, 1985.

Browell, E. V., "Differential absorption lidar sensing of ozone," *Proc. IEEE* 77, 419-432, 1989.

Browell, E. V., S. Ismail and S. T. Shipley, "Ultraviolet measurements of O<sub>3</sub> profiles in regions of spatially inhomogeneous aerosols," *Appl. Opt.* 24, 2827-2836, 1985.

Fenn, M. A., S. Ismail, E. V. Browell and C. F. Butler, "Correction of DIAL ozone measurements in the presence of stratospheric Pinatubo aerosols," paper presented at 16 ILRC, MIT, July 20-24, 1992.

Grams, G., and G. Fiocco, "Stratospheric aerosol layer during 1964 and 1965," *J. Geophys. Res.* 72, 3523-3542, 1967.

Grant, W. B., ed., Ozone Measuring Instruments for the Stratosphere, Vol. 1 of Collected Works in Optics, 438 pp, Opt. Soc. Am., Washington, D.C., 1989.

Grant, W. B., J. Fishman, E. V. Browell, V. Brackett, C. F. Butler, M. A. Fenn, G. D. Nowicki, R. E. Veiga, D. Nganga, A. Minga, and B. Cros, "Observations of reduced ozone concentrations in the tropical stratosphere after the eruption of Mt. Pinatubo," submitted to *Geophys. Res. Lett.*, 1992.

Jäger, H., and K. Wege, "Stratospheric ozone depletion at northern midlatitudes after major volcanic eruptions," *J. Atmos. Chem.* 10, 273-287, 1990.

Komhyr, W. D., "Electrochemical concentration cells for gas analysis," *Ann. Geophys.* 25, 203-210, 1969.

Mast, G. M., H. E. Saunders, "Research and development of the instrumentation of ozone sensing," *ISA Transactions* 1, 325-328, 1962.

McCormick, M. P., J. M. Zawodny, R. E. Veiga, J. C. Larsen, and P.-H. Wang, "An overview of SAGE I and SAGE II ozone measurements," *Planet. Space Sci.* 37, 1567-1586, 1989.

Prather, M., "Catastrophic loss of stratospheric ozone in dense volcanic clouds," submitted to *J. Geophys. Res.*, 1992.

Stowe, L. L., R. M. Carey, P. P. Pellegrino, "Monitoring the Mt. Pinatubo aerosol layer with NOAA/11 AVHRR data," *Geophys. Res. Lett.* 19, 159-162, 1992.

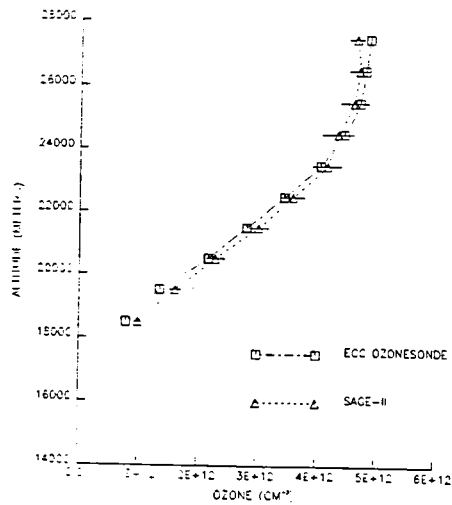


Figure 1. A comparison of ECC sonde (Brazzaville, 4° S, 2d quarter, 1991) and SAGE-II (10° S to 10° N, April, 1985-1991) stratospheric ozone measurements prior to the eruption of Mt. Pinatubo.

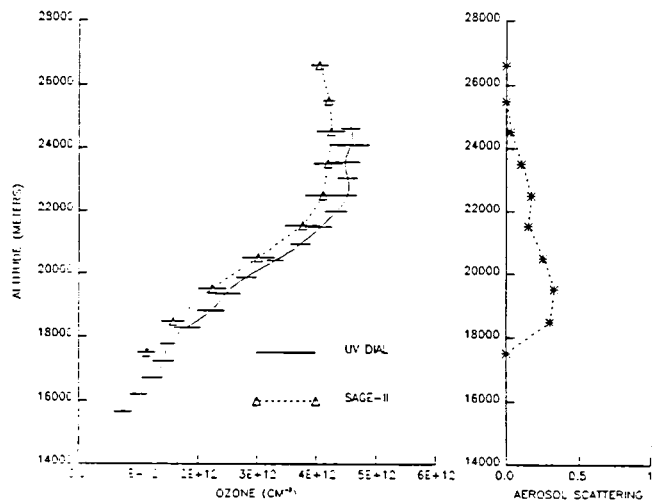


Figure 2. A comparison of UV DIAL (January 30, 1992) and SAGE-II (January and February, 1985-1991) stratospheric ozone measurements in a region (20° N to 25° N) relatively unaffected by volcanic aerosols.

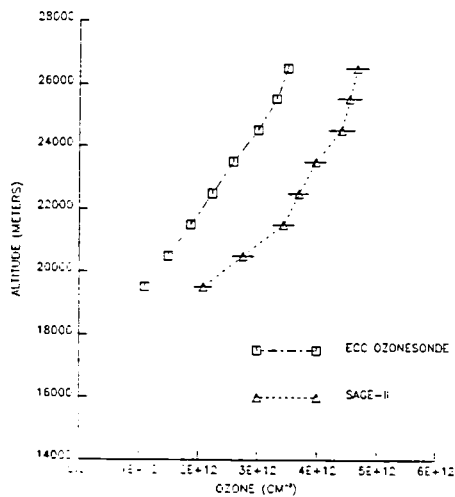


Figure 3. Same as for Figure 1, but for the 3d and 4th quarter 1991 for the sondes, and September and October, 1985-1990 for SAGE-II.

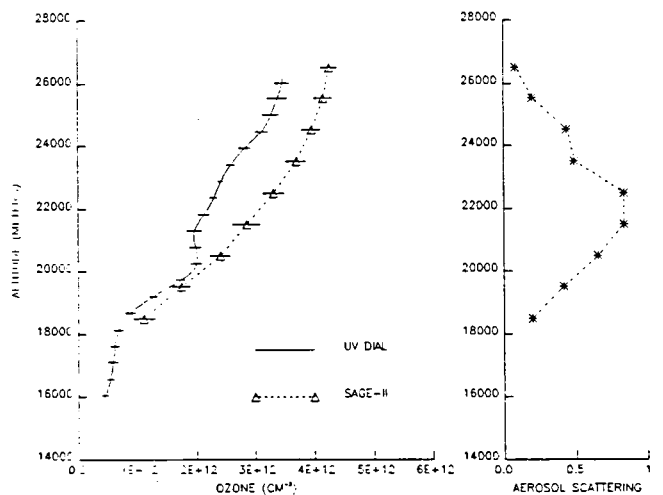


Figure 4. Same as for Figure 2, but for a region strongly affected by Mt. Pinatubo volcanic aerosols (10° N to 15° N).



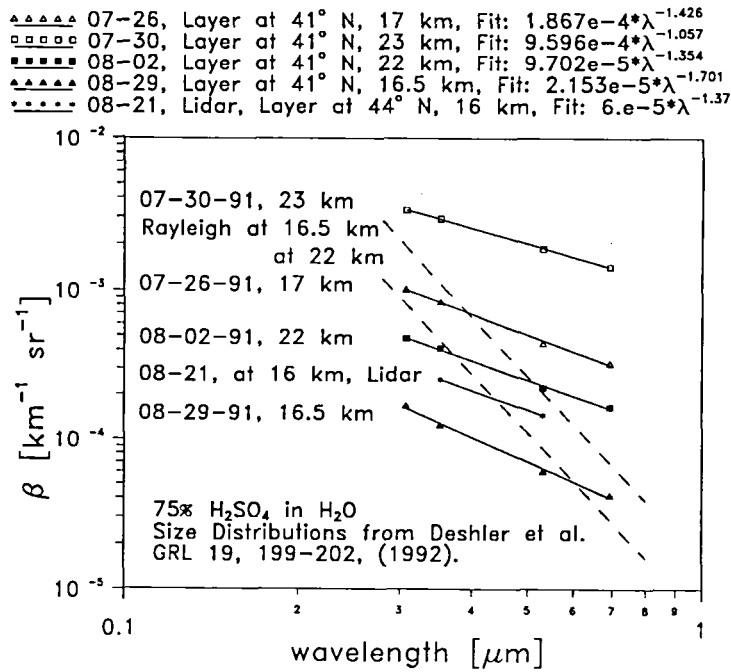


Figure 1:  $\beta_{Mie}$  as a function of wavelength, calculated for the four size distributions, as well as  $\beta_{Mie}$  measured by lidar. The dashed lines show  $\beta_{Rayleigh}$  at 16.5 and 22 km for comparison.

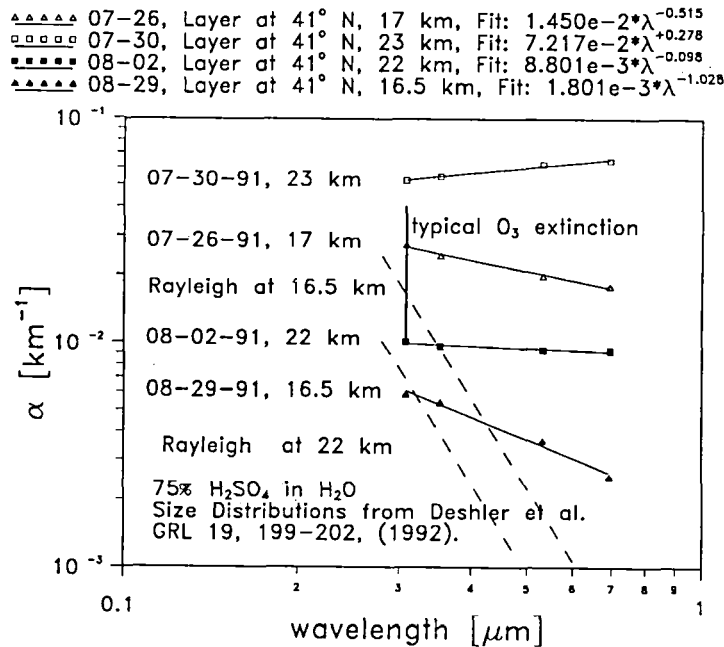


Figure 2:  $\alpha_{Mie}$  as a function of wavelength, calculated for the four size distributions. The dashed lines show  $\alpha_{Rayleigh}$  at 16.5 and 22 km for comparison. The vertical bar shows the typical range of ozone extinction in the stratosphere.

important. Careful assessment of their contribution is essential if accurate ozone concentrations are to be derived. We have undertaken this by computing the aerosol  $\alpha$  and  $\beta$  values using Mie theory and recently reported [2, 3] balloon sonde measurements of the Pinatubo aerosol. In our calculations we assumed that the aerosol is comprised of homogeneous spherical droplets of  $H_2SO_4$  in water. Folding the measured size distribution with the Mie scattering cross sections gives the values of  $\alpha_{Mie}$  and  $\beta_{Mie}$  at the wavelengths of interest. Figures 1 and 2 show plots of  $\beta_{Mie}$  and  $\alpha_{Mie}$  respectively, as a function of wavelength. Calculations were done at 308, 353, 532 and 694 nm and the points are shown for the four size distributions of [2] (corresponding to different layers at different times during July and August of 1991). Also shown in Fig. 1 is an example (August, 21 1991) of the  $\beta_{Mie}$  values measured by our DIAL lidar at 353 nm and our YAG lidar at 532 nm. In Figures 1 and 2 the dashed lines show for comparison the  $\beta_{Rayleigh}$  and  $\alpha_{Rayleigh}$  plots for the molecular component at 16.5 (upper line) and 22 km (lower line). In Fig. 2 we indicated the typical range of the ozone absorption coefficient in the stratosphere with a vertical bar at 308 nm.

In the evaluation of the correction terms of Eq. 1, (c) presents little difficulty if density profile data are available since the wavelength dependance of the Rayleigh attenuation is well known ( $\propto \lambda^{-4}$ ). Remaining errors from this term should probably be no more than 1 or 2 %. The errors from terms (b) and (d) are more difficult to quantify. From Fig. 2 we see that  $\Delta\alpha_{Mie}$  is quite variable, because of the varying nature of the size distribution observed. However, making use of the available sonde information, we anticipate that it should be possible to reduce the errors arising from term (d) to less than 5–10%. If not carefully corrected the term could lead to errors of up to 50%.

For term (b) we note that  $\beta(r, \lambda) = \beta_{Rayleigh}(r, \lambda) + \beta_{Mie}(r, \lambda)$ , since it is necessary to combine the differential behaviour of the Mie and Rayleigh contributions to the volume backscattering coefficient. We have done this using a power law ( $\lambda^{-\eta}$ ) wavelength dependance for the Mie scattering, deriving  $\eta$  from the data as shown in Fig. 1. If we define  $R^*(r) = \beta_{Mie}(r, \lambda_{off})/\beta_{Rayleigh}(r, \lambda_{off})$  we can write term (b) as

$$\frac{d}{dr} \ln \left( \frac{\beta(r, \lambda_{off})}{\beta(r, \lambda_{on})} \right) = \frac{\left( \frac{\lambda_{off}}{\lambda_{on}} \right)^{\eta-4} - 1}{\left[ 1 + R^* \left( \frac{\lambda_{off}}{\lambda_{on}} \right)^{\eta-4} \right] [1 + R^*]} \frac{d}{dr} R^*(r) = \varepsilon_{back}(r) \quad (2)$$

Figure 3 shows the size of the correction  $\varepsilon_{back}$  in the ozone concentration due to term (b) in Eq. 1. The calculations were done using Eq. 2 for lidar measurements at 353 nm on the nights of August, 21 1991 (left side) and October, 23 1991 (right side). For comparison a typical ozone profile is included (solid line). The backscatter ratio  $R = R^* + 1$  for each night is shown as a dashed line. The calculations have been done for three values of  $\eta$  in the relation  $\beta_{Mie}(\lambda) \propto \lambda^{-\eta}$ , and although the values used cover quite a wide range (1.1 – 1.8) it can be seen that the influence of  $\eta$  on the size of the term (b) is small.  $\varepsilon_{back}$  depends mostly on the slope of the scattering ratio profile, but also on the magnitude of the scattering ratio. It can be seen that neglecting term (b) in Eq. 1 generally leads to errors of 50% to over 100%. We also found that numerical differentiation leads to significant errors, especially in sharp layers. It seems to be advisable to first sum terms (a) and (b) in Eq. 1 and then perform the differentiation.

Currently we are trying to find a way of correcting for the effects of terms (b) and (d) on a routine basis. We are hoping to reduce the remaining error in the ozone concentration

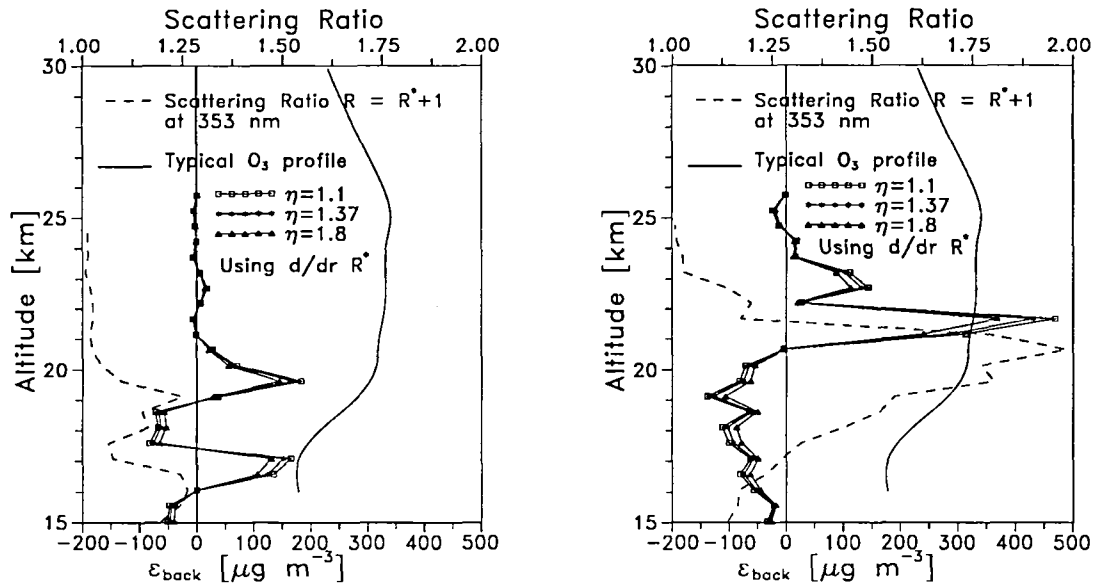


Figure 3: Correction  $\epsilon_{back}$  of the ozone concentration due to the differential backscatter term, for lidar measurements on the night of August, 21 and October, 23 1991. Calculations have been done for three values of  $\eta$ . For reference the scattering ratio  $R = R^* + 1$  (dashed line) and a typical ozone profile (solid line) are shown also.

to about 10% – 20%. However for very sharp layers the remaining error will probably be larger.

## References

- [1] A. I. Carswell, S. R. Pal, W. Steinbrecht, J. A. Whiteway, A. Ulitsky, and T-Y. Wang. Lidar Measurements in the Middle Atmosphere. *Can. J. Phys.*, **69**(8):1076 – 1086, 1991.
- [2] T. Deshler, D. J. Hofmann, B. J. Johnson, and W. R. Rozier. Balloonborne Measurements of the Pinatubo Aerosol Size Distribution and Volability at Laramie, Wyoming During the Summer of 1991. *Geophys. Res. Lett.*, **19**(2):199 – 202, January 1992.
- [3] P. J. Sheridan, R. C. Schnell, D. J. Hofmann, and T. Deshler. Electron Microscope Studies of Mt. Pinatubo Aerosol Layers over Laramie Wyoming During Summer 1991. *Geophys. Res. Lett.*, **19**(2):203 – 206, January 1992.
- [4] D. J. Hofmann. Aerosols from Past and Present Emissions. In P. V. Hobbs and M. P. McCormick, eds., *Aerosols and Climate*, pages 195 – 214. A. Deepak Publishing, Hampton Virginia, USA, 1988.
- [5] E. V. Browell. Ultraviolet Dial Measurements of  $O_3$  Profiles in Regions of Spatially Inhomogeneous Aerosols. *Appl. Opt.*, **24**:2827 – 2836, 1985.

# A NEW RAMAN DIAL TECHNIQUE FOR MEASURING STRATOSPHERIC OZONE IN THE PRESENCE OF VOLCANIC AEROSOLS

Upendra N. Singh<sup>1</sup>, Thomas J. McGee<sup>2</sup>, Michael Gross<sup>1</sup>, William S. Heaps<sup>2</sup>,  
and Richard Ferrare<sup>3</sup>

1. Hughes STX Corporation,  
4400 Forbes Blvd.  
Lanham, MD 20706

2. Environmental Sensor Branch, Code 917  
NASA/Goddard Space Flight Center  
Greenbelt, MD 20771

3. Universities Space Research Association  
Laboratory for Atmospheres, Code 917  
NASA/Goddard Space Flight Center  
Greenbelt, MD 20771

## ABSTRACT

This paper describes a new lidar scheme to measure stratospheric ozone in the presence of heavy volcanic aerosol loading. The eruptions of the Philippine volcano Pinatubo during June 1991 ejected large amounts of sulfur dioxide into the atmosphere to altitudes of at least 30 km. The resulting aerosols have severely affected the measurements of stratospheric ozone when using traditional Rayleigh differential absorption lidar (DIAL) technique, in which the scattering mechanism is almost entirely Rayleigh and which assumes a small amount or no aerosols. In order to extract an ozone profile in the regions below about 30 km where the Rayleigh lidar returns are contaminated by aerosol scattering from the Mt. Pinatubo cloud, we have used a Raman lidar technique, where the scattering mechanism depends solely on molecular nitrogen. In this scheme there is no aerosol scattering component to the backscattered lidar return. Using this technique in conjunction with the Rayleigh DIAL measurement, the GSFC stratospheric ozone lidar has measured ozone profiles between 15 and 50 km during the recently held UARS correlative measurement campaign (February-March 1992) at JPL's Table Mountain Facility in California.

## INTRODUCTION

As a part of the international Network for the Detection of Stratospheric Change (NDSC) which is made up of state-of-the-art ground based research instruments with capability to detect chemical and physical changes in the stratosphere (*Kurylo and Solomon, 1990*), we at NASA's Goddard Space Flight Center have developed a mobile, dual-wavelength Rayleigh/Raman DIAL system capable of making precise measurements of ozone concentration between 15 and 50 km.

The differential absorption lidar (DIAL) technique for the measurement of ozone consists of the transmission of at least two wavelengths into the atmosphere, one of which is strongly absorbed by ozone, and the other less significantly absorbed. Backscattered returns at these wavelengths are collected and the ratio of signal at each altitude bin is used to calculate ozone concentrations (*McGee et al., 1991*). The presence of appreciable amounts of volcanic aerosol makes the ozone profile retrieval through Rayleigh DIAL highly inaccurate since the aerosol backscatter and extinction terms in the lidar equation are no longer negligible. In our recent measurements, we have employed the Raman lidar technique, which uses Raman scattering from nitrogen molecules to provide the backscatter signal for the retrieval of an ozone profile in the region with heavy concentrations of aerosol. This technique is valid, since the Raman lidar return is dependent upon only upon molecular terms and aerosol extinction, but contains no component due to scattering from aerosols. In this new scheme, Rayleigh lidar returns at 308 and 351 nm, and corresponding N<sub>2</sub>-Raman return at 332 and 382 nm are received. The sum of 382 and 351 nm aerosol extinction can be obtained from the 382 nm channel (*Ansmann et al., 1990*). Since the difference between 332 and 382 is nearly the same as the difference between 308 and 351, a wavelength dependence is assumed between the sum of 382 and 351 nm aerosol extinction and the sum of 308 and 332 nm aerosol extinction. This information is then used for ozone computation. Signals returned are strong enough to permit a continuous profile from 15 to 50 km using both the Raman and Rayleigh techniques. We will present the results from the data taken during February-March 1992 UARS correlative measurement campaign at JPL's TMO facility. If time permits, intercomparisons with other instruments deployed during the aforesaid campaign will also be presented.

## LIDAR SYSTEM

The NASA/GSFC STROZ LITE (Stratospheric Ozone Lidar Trailer Experiment) instrument is a mobile, trailer-based system designed primarily to measure stratospheric ozone using the DIAL technique. The three major components of this system: the transmitter, the detection system, and the data acquisition system, have each been described in detail (*McGee et al., 1991*).

Both the transmitter and receiver had to be modified for this experiment. The "reference" laser was replaced with a XeF laser (351 nm), operating at a pulse repetition rate of 70 Hz, and an energy of 150 mJ/pulse.

The change in the transmitter led to corresponding modifications in the optical section of the detector package. Beamsplitters which had been used to increase the dynamic range of the referenced system were replaced with dichroic beamsplitters which separated the Rayleigh and Raman scattered wavelengths. Rayleigh lidar returns at 308 and 351, and Raman lidar returns at 332 and 382 were recorded for analysis. It was discovered, during the initial setup and operation of the lidar, that the 332 nm Raman channel filter did not adequately block the 351 nm Rayleigh return and thus in turn "contaminated" the Raman channel. To overcome this problem, we collected the Raman data sequentially by firing only one laser at a time. In each sequence, data were collected in 100,000 shots increments and were summed separately at the end of evening run. A total of 600,000 shots were collected and summed at each wavelength.

## RESULTS AND DISCUSSION

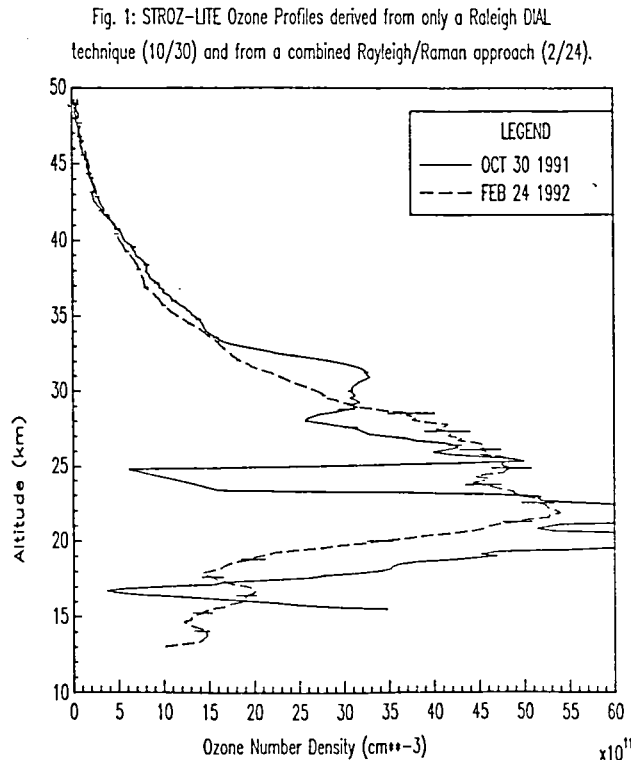
The GSFC lidar system as described above was deployed at the JPL-Table Mountain Facility, during February and March 1992. A typical ozone profile for February 24, 1992, taken at JPL-TMO is shown in Figure 1. Aerosol corrected Raman data is being used to derive the ozone profile from 15 to 28 km and Rayleigh data for 28 to 50 km. Also plotted on Figure 1 is a profile from October 30, 1991, taken at GSFC, using only Rayleigh data. The presence of aerosols in the 15-30 km region has made the ozone measurements at these altitudes meaningless. Several profiles will be presented and results will be discussed in detail.

## ACKNOWLEDGEMENTS

The authors wish to thank S.H. Melfi and D. Whiteman for helpful discussions in the design and development of this experiment. We also wish to thank them for the loan of several optics necessary to the design. The research has been supported by the NASA Upper Atmosphere Program. Thanks also to the staff of the JPL Table Mountain Facility where the data were taken.

## REFERENCES

- Ansmann, A., M. Riebesell, and C. Wietkamp, "Measurement of atmospheric aerosol extinction profiles with a Raman lidar," *Optics Letters*, **15**, No. 3, 746-748, 1990.
- Kurylo, M.J., and S. Solomon, "Network for the Detection of Stratospheric Change. A Status and Implementation Report", issued by *NASA Upper Atmosphere Research Program and NOAA Climate and Global Change Program*, January, 1990.
- McGee, T.J., D. Whiteman, R. Ferrare, J.J. Butler and J. Burris, "STROZ-LITE: Stratospheric Ozone Lidar Trailer Experiment", *Opt. Eng.* **30**, 31-39, 1991.





# The JPL Table Mountain and Mauna Loa Stratospheric Ozone Lidars

## I. Stuart McDermid

Table Mountain Facility  
Jet Propulsion Laboratory  
California Institute of Technology  
P. O. Box 367, Wrightwood, CA 92397

### Introduction

The development of a differential absorption lidar (DIAL) system for long-term measurements of stratospheric ozone and for potential inclusion in the Network for the Detection of Stratospheric Change (NDSC) [Kurylo and Solomon, 1990] began at JPL in 1986, concurrent with the first workshop that considered the priorities and appropriate measurement techniques for such a network. The DIAL system at the JPL Table Mountain Facility (TMF, 34.4° N, -117.7° W) was developed specifically to have the characteristics suitable for long-term measurements as proposed for NDSC. Regular measurements of stratospheric ozone concentration profiles commenced in February 1988 and this system has been fully described elsewhere [McDermid *et al*, 1990].

### Table Mountain Lidar

For long-term measurement programs to be successful it is necessary to ensure the quality of the results by rigorous calibration procedures and intercomparisons. To evaluate the TMF ozone lidar it has participated in a number of intercomparisons, culminating in the first formal NDSC sponsored intercomparison, Stratospheric Ozone Intercomparison Campaign 1989, (STOIC'89). These studies compared results from a large number of ozone profiling instruments and showed that agreement at the 5% level could be achieved provided that the measurements were made at approximately the same time and at the same location. Following the successful launch of the Upper Atmosphere Research Satellite (UARS) the TMF lidar has provided correlative measurements of ozone (and temperature) profiles for comparison with the satellite instruments. Some examples of the results from these various intercomparisons will be presented.

Over the first four years of operation of the TMF lidar more than 450 independent profiles have been measured. These are fairly evenly distributed throughout the years and there is only a small increase in the number of summertime measurements compared to wintertime. These results show clearly the seasonal variations in the ozone profile and an example of these variations, for 30 km altitude, is shown in Figure 1.

The long-term measurements at TMF have also allowed us to establish a mean monthly climatology for ozone at this location which is slightly different than that suggested by various model atmospheres, e.g., MAP 1985 [Keating *et al*, 1987].

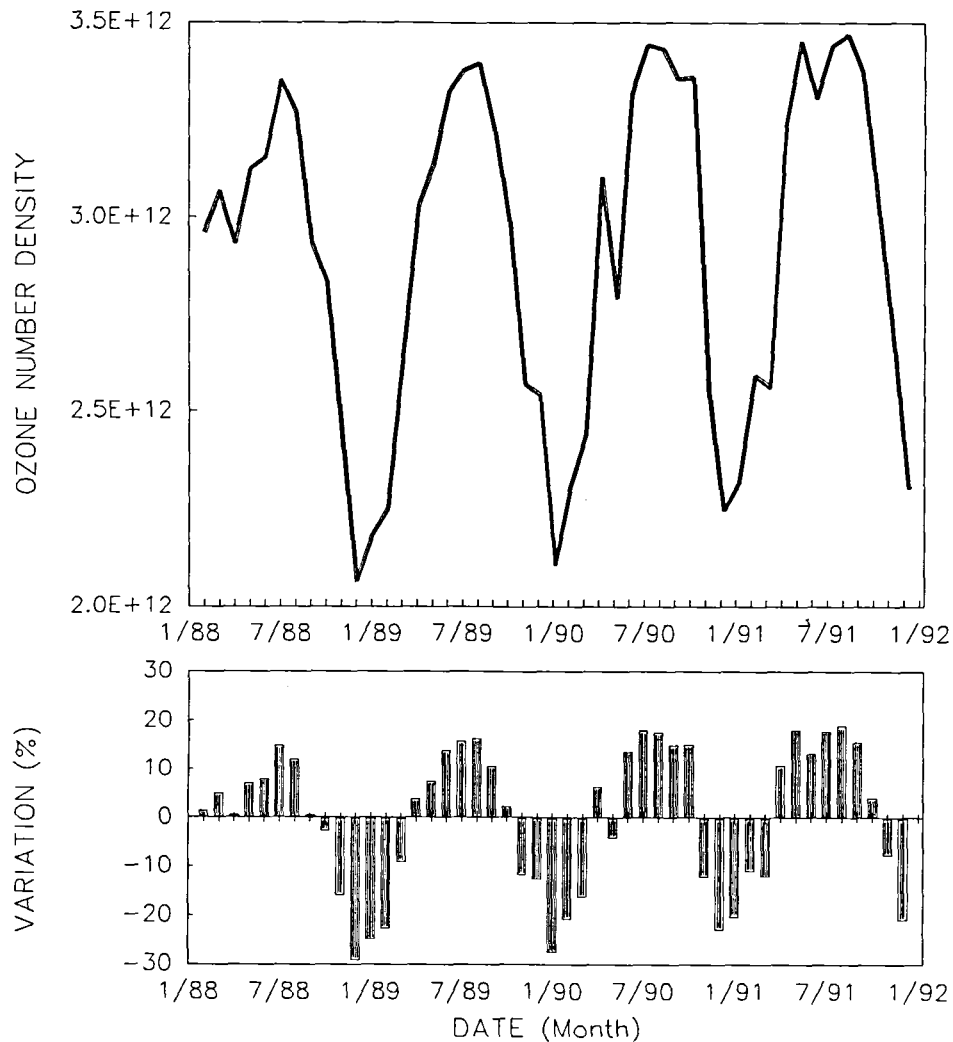


**Figure 1.** Seasonal variations, at 30 km altitude, of the monthly mean ozone concentration.

### Mauna Loa Lidar

Based on the successful demonstration and evaluation of the DIAL system at TMF, a new lidar was commissioned for deployment at the Mauna Loa, Hawaii, station of the NDSC. This system will temporarily be housed in a mobile facility pending the completion of the new observatory at Mauna Loa. This system is presently under construction and should be in operation before summer 1992. This new system incorporates some new developments compared to the TMF system and details of the new design will be presented.

Stratospheric aerosols resulting from the volcanic eruption of Mount Pinatubo have been observed in the lidar measurements at TMF since July 1991. The presence of these aerosols has a profound effect on measurements of stratospheric ozone profiles by the conventional DIAL method and essentially precludes reliable measurements in these regions. A modification to the DIAL technique using the atmospheric nitrogen Raman signal has been suggested and demonstrated by the NASA GSFC Lidar Group [McGee *et al*, 1992]. This

method, similar to the Raman augmentation technique for temperature measurements [Moskowitz *et al*, 1988], provides return signals from molecular scattering only and thus eliminates the problems caused by the differential aerosol backscattering. A small correction for differential aerosol extinction may still be required. This technique is easily implemented by adding two extra channels to the lidar receiver, which is shown in figure 2.

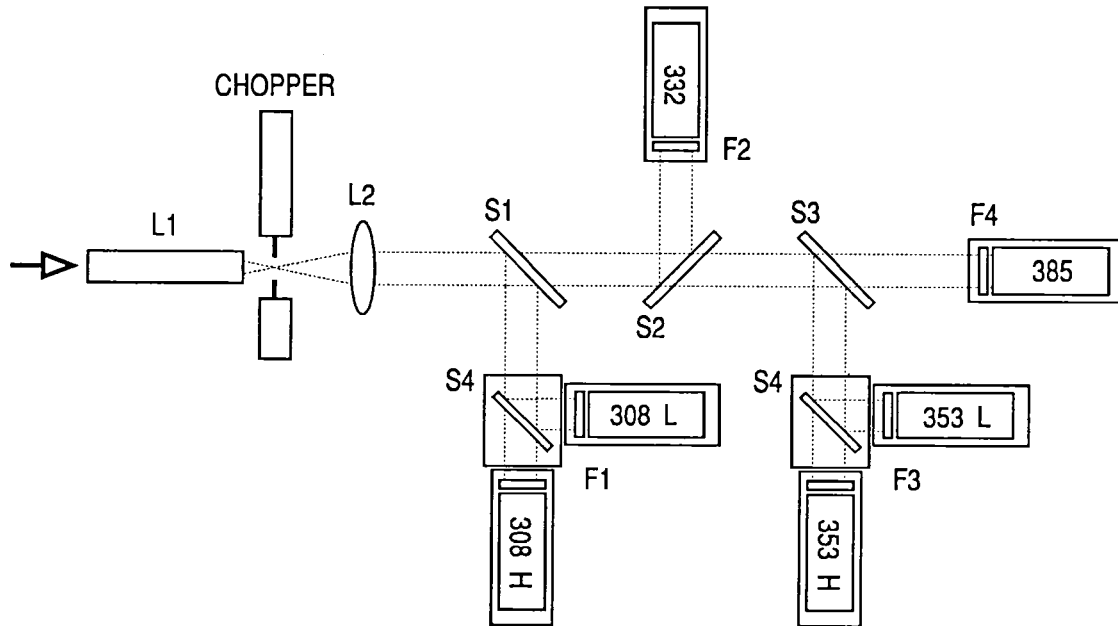


**Figure 2.** Schematic diagram of the receiver optical detection system.

Since it was necessary previously to attenuate the signal from altitudes below about 30 km, the lower efficiency for Raman scattering is largely compensated by eliminating the attenuation in these channels.

The data acquisition system in the MLO lidar employs a new PC-based photon counting/MCS system. This allows counting to much higher rates, 250 MHz, than in the TMF system and also ensures absolute synchronization between all of the counting channels. A block diagram of the data acquisition system is shown in figure 3.

Similar to the TMF lidar, the MLO system uses a 100 Watt, tuned, low-divergence, xenon chloride excimer laser for the transmitter. The reference wavelength at 353 nm is generated by stimulated Raman scattering in hydrogen. The receiver telescope is slightly larger at 1.0 m, compared to 0.9 m, and is of significantly higher optical quality. This factor, coupled with a 5x expansion of the transmitted laser beams, should allow the return signal to be mechanically chopped in less than 10  $\mu$ s. Initial results from this new system, together with more details of its design, will be presented.

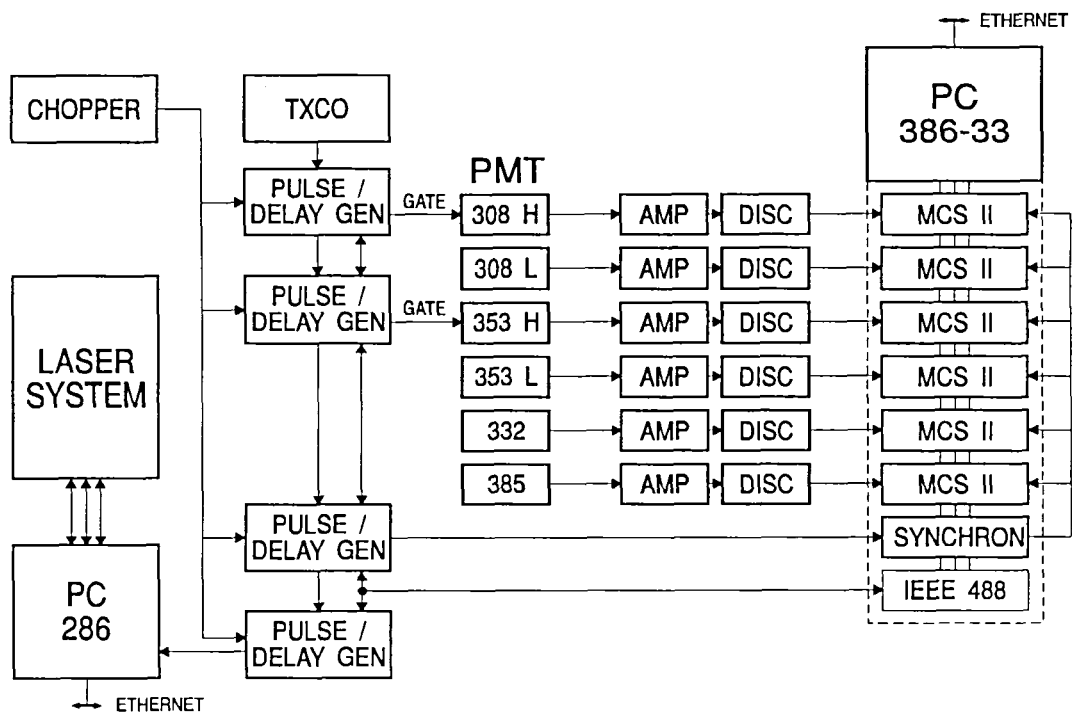


**Figure 3.** Block diagram of the receiver and data acquisition system electronics.

**Acknowledgment.** The work described in this paper was carried out at the Jet Propulsion Laboratory, California Institute of Technology, under a contract with the National Aeronautics and Space Administration. The author is also grateful for the assistance of Dan Walsh and Marty Schmoe and for interesting discussions with Tom McGee regarding the Raman augmentation to the DIAL technique.

**References.**

Keating, G. M., D. F. Young, and M. C. Pitts, 1987, Ozone reference model for CIRA, *Adv. Space Res.*, 7, 105-115.

Kurylo, M. J. and S. Solomon, 1990, *Network for the Detection of Stratospheric Change - A Status and Implementation Report*, Issued by NASA Upper Atmosphere Research Program and NOAA Climate and Global Change Program.

McDermid, I. S., S. M. Godin, and L. O. Lindqvist, 1990, Ground-based laser DIAL system for long-term measurements of stratospheric ozone, *Appl. Opt.*, 29, 3603-3612.

McGee, T. J., 1992, Private Communication.

Moskowitz, W. P., G. Davidson, D. Sipler, C. R. Philbrick, and P. Dao, 1988, Raman augmentation for Rayleigh lidar, 14th ILRC, *Conference Abstracts*, 284-286.

**The NDSC primary site at the Observatoire de Haute-Provence :  
ozone and aerosols observations (1986-1992)**

*G. Mégie, S. Godin, G. Ancellet,  
M. Beekmann, A.M. Lacoste*

*Service d'Aéronomie du CNRS - Université Pierre et Marie Curie  
B 102 - 4, Place Jussieu - 75252 Paris Cedex 05 -France*

The first primary site of the newly implemented Network for Detection of Stratospheric Changes (NDSC) includes three main sites in the alpine regions of southern Europe : the Observatoire de Haute-Provence, the Jungfrauoch high altitude station for infra-red spectrometric measurements and the Plateau de Bures for microwave spectrometric measurements. At the Observatoire de Haute-Provence (44°N, 5°E), a coherent set of experimental systems has been established to monitor on a long-term basis ozone, aerosols, minor constituents and temperature vertical distributions in the troposphere and stratosphere. Such techniques include several lidar systems, ballon-borne sondes and UV-visible spectrometry.

Lidar measurements of stratospheric aerosols are performed on a routine basis, since 1980. These include the vertical distribution of the extinction and backscattering coefficients from the tropopause up to 30 km, with an accuracy better than 10% and an altitude resolution of .5 km. The experimental system is based on a Nd-Yag laser operating at 532 nm. Routine measurements of the ozone vertical distribution are also performed, since 1986 in the stratosphere from 15 to 48 km, and since 1991 in the troposphere. Two differential absorption lidar systems are operated. The stratospheric lidar is an excimer (XeCl) based system emitting at 308 nm for the absorbed wavelength, whereas the reference wavelength is provided by the third harmonic (355 nm) of a Nd-Yag laser. The tropospheric lidar uses the fourth harmonic emission of two ND-Yag lasers (266 nm), to generate by stimulated Raman effect in hydrogen and deuterium cells, the appropriate wavelengths for ozone measurements (289 nm - 299 nm). All systems use 80-cm diameter receiving telescope and appropriate specifically designed spectrometers to separate the various received wavelengths. The temporal analysis of the signals are made both in the photon counting mode (300 MHz) and in the analogical mode using in-house built transient waveform recorders, to adapt to the signal dynamics. Specific systems, using mechanical choppers, have also been implemented to account for the signal induced noise in high altitude-low signal measurements.

The data base obtained at the Observatoire de Haute-Provence from these lidar measurements and from the ancillary experiments, such as sondes and spectrometers, allows several type of studies to be performed. Instrument comparisons can be made, based on the various instruments existing on the site itself. These include lidar-ozonosondes and lidar-Umkehr comparisons of the ozone vertical distribution, which can be adressed on a statistical basis, taking into account the large number of measurements. A comprehensive study of the biases and precision of the lidar as compared to the two types of sondes presently in use (Brewer-Mast sondes and ECC sondes) has been made, which demonstrates the fiability of lidar measurements for the determination of both the tropospheric and stratospheric ozone vertical profiling.

Lidar measurements and Umkehr observations, performed using the Automated Dobson spectrometer located at the Observatoire de Haute-Provence, correspond to a data base which includes, from 1985 to 1987, more than 1 000 Umkehr observations and 200 lidar profiles, allowing a comparison between the two methods over a large number of coincidences. The analysis shows that the ozone vertical distributions, as retrieved by the new-conventional Umkehr method, which takes into account more accurately the natural variability of the ozone concentration and the temperature influence on the ozone absorption coefficients, are in rather good agreement with the lidar measurements. No statistically significant bias can be observed in the layers 4 to 7 between the two methods of measurement. In layer 8, a positive bias between the Umkehr retrievals and the lidar measurements can be observed, mainly during the winter months, which can be accounted for by signal induced noise effects leading to an underestimate of the ozone concentration from the lidar measurements, and by the large variability in the daily temperature profiles as observed during the same period of the year. These measurements are of particular values for the determination of long term trends in ozone vertical distribution, as the Umkehr method provides yet the longest time-record of ozone profiles. Similarly, comparisons with the Sage II instrument have been performed, which show a very good agreement between the satellite-borne system and the lidar measurements within  $\pm 2\%$ , between 20 and 42 km.

Taking into account the large number of profiles already available from the lidar measurements, studies of the natural variability of the ozone vertical distribution have been undertaken which cover various temporal and spatial scales. The seasonal variation of stratospheric ozone has been shown to evoluate from an annual cycle at the 30 km level, to a semi-annual cycle at the higher altitudes giving evidence for the increasing imortance of temperature dependent chemical processes

in the upper stratosphere. In the troposphere, correlative studies of ozone and related meteorological fields, such as potential vorticity, geopotential and relative humidity, provide indication of the causes of the variability observed in the ozone vertical distribution. The intra-annual variation of the ozone content is shown to reflect the influence of the two main sources : the anthropogenically driven photochemical source, and the dynamical source related to stratosphere-troposphere exchange processes. Cases studies of such events, including tropopause folds and cut-off lows, allow to quantify the annual fluxes of stratospheric ozone into the troposphere from the various processes. No evidence for an ozone trend in the troposphere, between 1985 and 1991, can be assessed from these measurements.

Recently, measurements performed in 1991, following the major eruption of the Mount Pinatubo volcano in the Philippines in May 1991, have allowed to follow the time-evolution of the aerosol cloud in middle latitude regions. One observes a limited increase in the aerosols scattering ratio below 20 km until mid-october 1991. Much larger values, ranging from 10 to 15 at 532 nm, are then observed, related to the meridional transport of the cloud. This increase in the aerosol content can be related to the observation of the ozone vertical distribution and total content as performed by the differential absorption lidar, balloon-borne ozonsondes and the Dobson spectrophotometer. Although the total ozone content observed in December 1991 and January 1992, is low as compared to the climatological mean at the Observatoire de Haute-Provence, it is rather difficult to establish a direct relation with the aerosol cloud. A more comprehensive study of the extension and temporal variability of the Mount Pinatubo volcanic cloud in the mid- and high-latitude regions, is still required to draw definitive conclusions.



# LIDAR ATMOSPHERIC OBSERVATORY IN THE CANADIAN ARCTIC.

Arkady Ulitsky, Tin-Yu Wang, Martin Flood, Brent Smith

Optech Incorporated  
701 Petrolia Rd., Downsview,  
Ontario, M3J 2N6, Canada,  
Tel: (416) 661-5904, FAX: (416) 661-4168

## ABSTRACT

During the last decade there have been growing concerns about a broad variety of atmospheric properties. Among these, a depletion of the stratospheric ozone layer has attracted considerable attention from the general public, politicians and scientists due to its vital impact for the entire global biosphere. One of the major warning signs was the discovery of the "ozone hole" in the Antarctic region where the concentration of the ozone in the stratosphere was significantly reduced. At present the stratospheric ozone layer in this region is being continuously monitored by groups of scientists from around the world and numerous observations of the ozone layer on the global scale have clearly demonstrated the process of ozone depletion. Recent observations by NASA have shown a significant depletion in the Arctic region.

This paper provides an initial description of two lidars that are planned to be installed in a new observatory for atmospheric studies in the Canadian Arctic. This observatory is being constructed under the supervision of the Atmospheric Environment Services (AES) of Canada as a part of the Green Plan - an initiative of the Federal Government of Canada. The station is located at Eureka on Ellesmere Island at a latitude of 80°N and a longitude of 86°W.

Two laboratories of this facility will be occupied by two new LIDARS: a stratospheric ozone DIAL and a Polar Stratospheric Clouds / Arctic Haze Lidar (PSC/Haze). Both systems are being designed and constructed by Optech Inc. The receiving telescope of each lidar is enclosed inside a small compartment which is thermally insulated from the rest of the laboratory and is kept

at the outside ambient temperature. Each compartment is equipped with a motorized roof-top hatch which will open when the lidar is to be operated. This approach minimizes thermal disturbance of the telescope when the hatch is opened.

The ozone DIAL system will be able to operate in daylight conditions and will provide stratospheric ozone concentration profiles all year. It will also allow studies of the ozone layer interactions with solar radiation under the unique illumination conditions of this location. A preliminary description of this lidar system is found in ref. [1]. The transmitter of the system is based on a XeCl excimer laser operating at 308 nm for the "ON" wavelength and a pressurized hydrogen Raman shifter to provide 353 nm radiation for the "OFF" wavelength. It will provide about 60 watt of average power at 300 Hz. The system's receiver is a Newtonian telescope of one meter aperture equipped with several special features to permit daytime operation.

The second lidar, jointly sponsored by the Canadian Government and the Japanese Government through its Communications Research Laboratories and Meteorological Research Institute, is to monitor PSC and the arctic haze. It will use a two-wavelength (1064 nm and 532 nm) Nd YAG source providing about 10 watts output at 20 Hz. Separate receivers are used for the PSC and the low altitude haze measurements. Polarization measurement capabilities are available at both wavelengths.

The new Eureka station with the lidar facilities and other atmospheric sensors will be part of the global Network for Detection of Stratospheric Change (NDSC). It will make a valuable contribution to our understanding of the complex processes affecting the ozone layer. The observatory at Eureka is planned to begin operation in early 1993. This paper will present details of the lidar equipment and give an outline of the planned measurement program.

#### References:

[1]. Differential Absorption LIDAR for Monitoring Stratospheric Ozone; B.Smith, A. Ulitsky, Tin-Yu Wang; Conference on Optical Remote Sensing and Applications to Environmental and Industrial Safety Problems; Proceedings; April 1992.

# Observation of stratospheric ozone with NIES lidar system in Tsukuba, Japan

H. Nakane, S. Hayashida, Y. Sasano, N. Sugimoto, I. Matsui and A. Minato

The National Institute for Environmental Studies  
Onogawa, Tsukuba, Ibaraki 305 Japan

Lidars are expected to play important roles in an international monitoring network of the stratosphere such as the Network for the Detection of Stratospheric Change (NDSC). The National Institute for Environmental Studies (NIES) in Tsukuba (36°N, 140°E) constructed an ozone lidar system in March 1988 and started observation in August 1988.

The lidar system has a 2-m telescope and injection locked XeCl (308 nm) and XeF (351 nm) excimer lasers which can measure ozone profiles (15 - 45 km) and temperature profiles (30 - 80 km). A block diagram of the lidar system is shown in Fig. 1. Another wavelength (339 nm) is generated using a deuterium Raman shifter from the XeCl laser radiation. Then ozone profiles are obtained from both 308 - 351 nm (A-) and 308 - 339 nm (B-) signal pairs. From December 1991, lidar observation at 313 nm has been carried out in which the second Stokes line of the stimulated Raman scattering of a KrF laser (248 nm) has been used.

Agreement between ozone profiles from A- and B-wavelength pairs had been good until the stratospheric aerosols due to the eruption of Mt. Pinatubo arrived above Tsukuba, indicating that aerosol effects on ozone lidar measurements had been negligible till the arrival of the Pinatubo aerosols. A typical ozone profiles obtained from the A- and B-wavelength pairs are shown in Fig. 2 and a temperature profile obtained from the 351 nm signal is in Fig. 3.

Ozone profiles obtained with the NIES lidar system are compared with the data provided by the SAGE II satellite sensor. Results showed good agreement for the individual and the zonal mean profiles. A part of the results is shown in Fig. 4.

Variations of ozone with various time scales at each altitude can be studied using the data obtained with the NIES ozone lidar system which is shown in Fig. 5. Seasonal variations are easily found at 20 km, 30 km and 35 km, which are qualitatively understood as a result of dynamical and photochemical effects.

Systematic errors of ozone profiles due to the Pinatubo stratospheric aerosols have been detected using multi-wavelength observation. Fig. 6 is an example of ozone profiles affected by the aerosols. The scattering ratio of the aerosols has its peak at about 20 km in February 26, 1992. Negative deviations of ozone concentration are clearly seen, which is largest in the case of 308 - 351 nm pair (A-pair) and smallest in the case of 308 - 313 nm pair (C-pair). This wavelength dependence of the ozone profiles could be used for the correction of the systematic errors due to the stratospheric aerosols (Sasano, 1988).

## References

- Nakane H., S. Hayashida, Y. Sasano, N. Sugimoto, I. Matsui, and A. Minato, Vertical profiles of temperature and ozone observed during DYANA campaign with the NIES ozone lidar system at Tsukuba, submitted to *J. Geomag. Geoelectr.*, 1992.
- Nakane, H., Y., Sasano, S. Hayashida-Amano, N. Sugimoto, I. Matsui, A. Minato, and M.P. McCormic., comparison of ozone profiles obtained with NIES DIAL and SAGE II measurements, submitted to *J. Meteorol. Soc. Japan*, 1992.
- Sasano, Y., N. Sugimoto, H. Nakane, S. Hayashida-Amano, I. Matsui, A. Minato, Multiple-wavelength differential absorption lidar (DIAL) for measuring the ozone profiles in the stratosphere and the troposphere, *abstracts of First Tsukuba Workshop on Ozone DIAL, Tsukuba, Japan*, December 6 and 7, 1989.
- Sasano, Y., Simultaneous determination of aerosol and gas distribution by DIAL measurements, *Appl. Opt.*, 27, 2640 - 2641, 1988.
- Sugimoto, N., Y. Sasano, H. Nakane, S. Hayashida-Amano, I. Matsui, and A. Minato, Multiple wavelength laser radar for measuring the stratospheric and tropospheric ozone profiles, *Oyobutsuri (in Japanese)*, 56, 1385 - 1397, 1989.

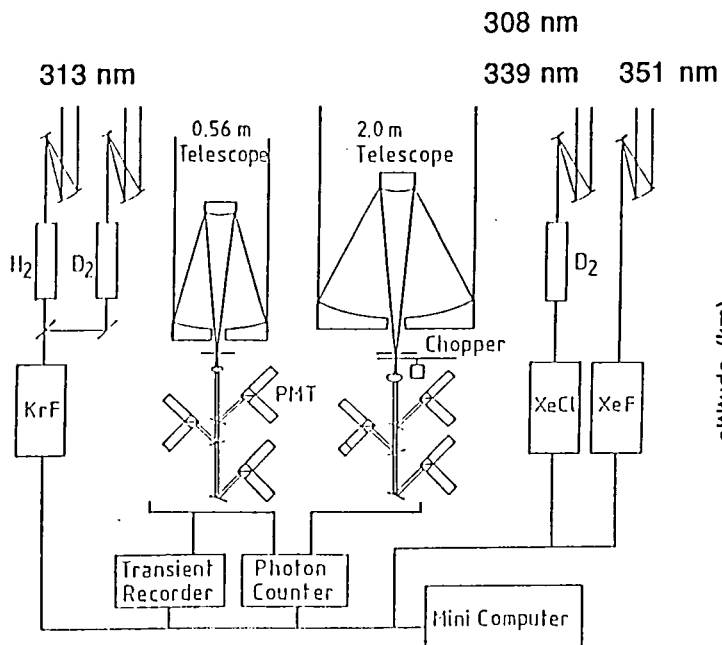


Fig. 1 Schematic diagram of the NIES lidar system (Sugimoto et al., 1988, Sasano et al., 1989).

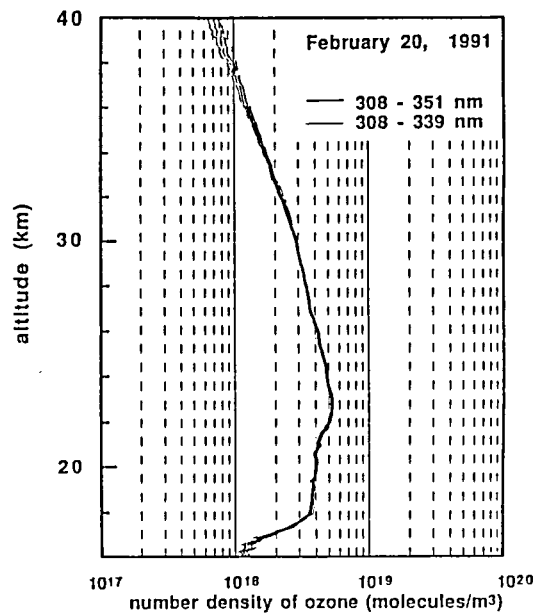


Fig. 2 Ozone profiles with random errors observed with the NIES ozone lidar.

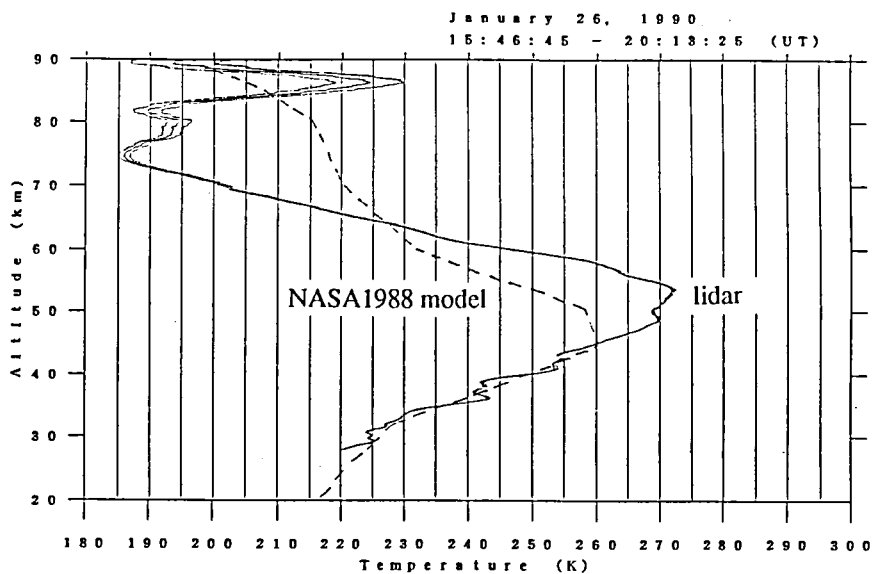


Fig. 3 A temperature profile observed with NIES ozone lidar system (Nakane et al., 1992).

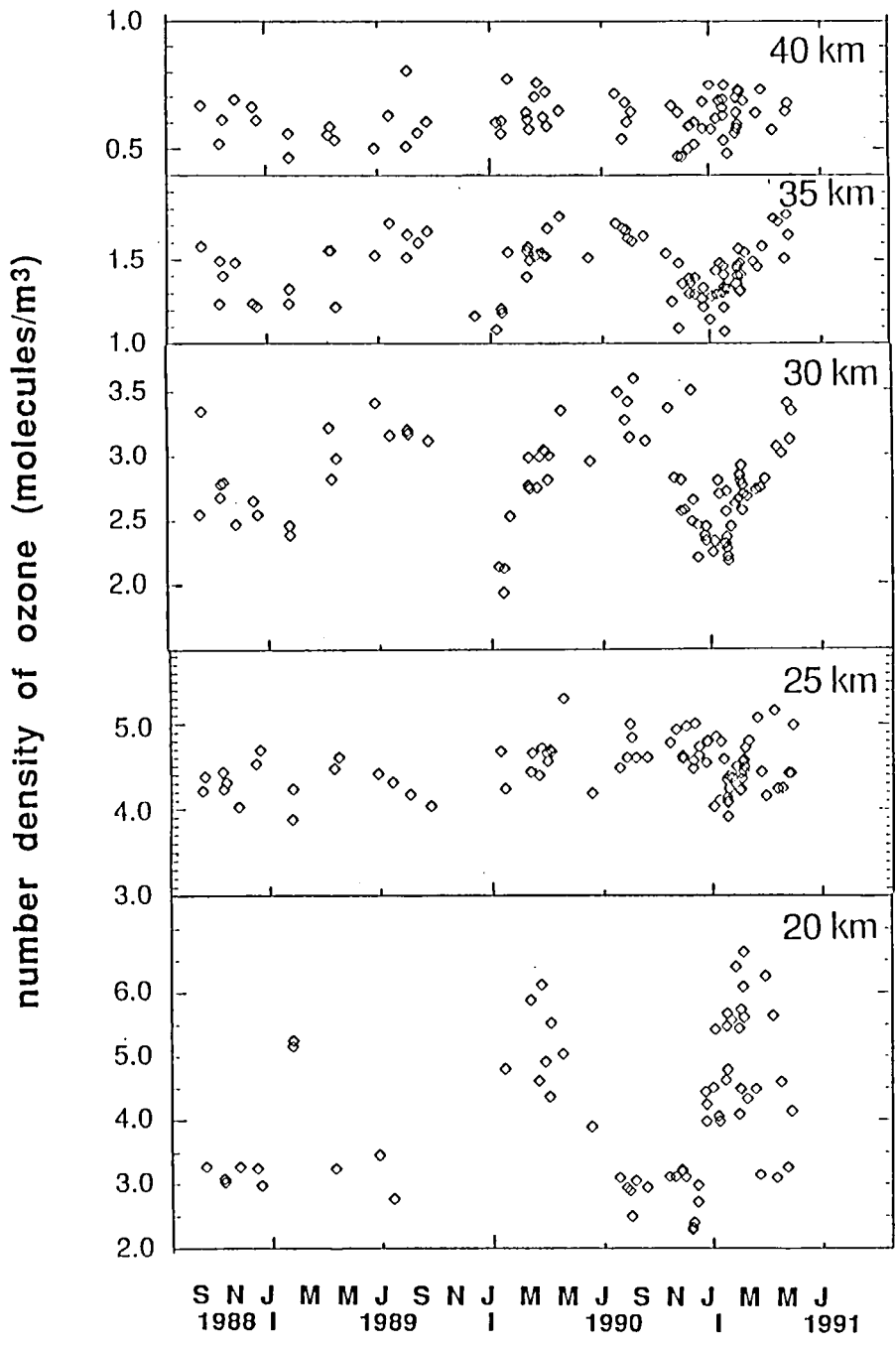


Fig. 5 Variations of ozone at 20 km, 25 km, 30 km, 35 km and 40 km observed with NIES ozone lidar.

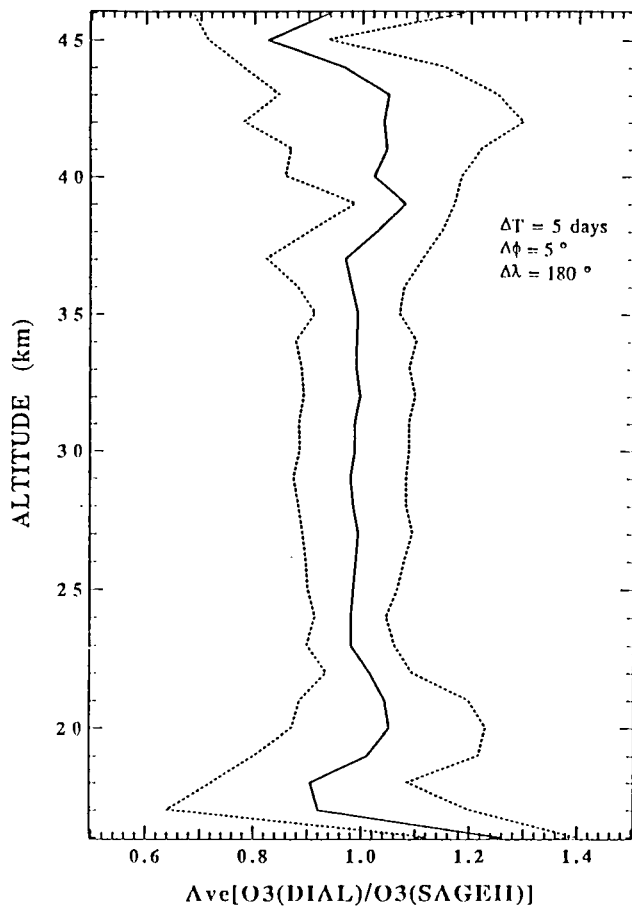


Fig. 4 Comparison of ozone profiles with the NIES ozone lidar and SAGE II measurements. The average of the ratios between the lidar data and their variabilities are shown (Nakane et al, 1992).

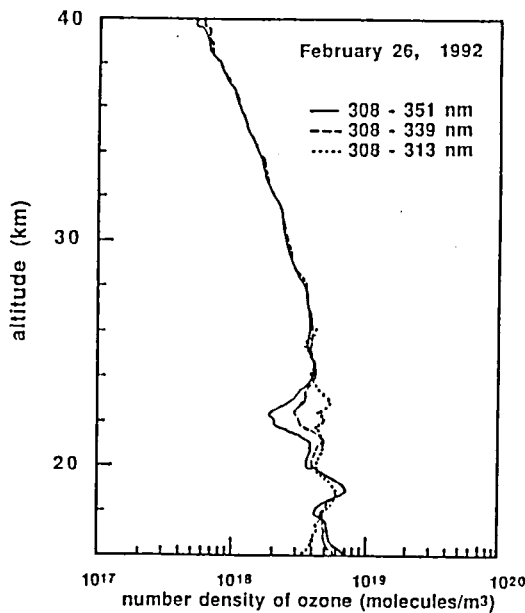


Fig. 6 Ozone profiles obtained from A-, B- and C-signal pairs. The peak of the Pinatubo aerosol layer was at about 20 km.

# OBSERVATIONS OF OZONE-AEROSOL CORRELATED BEHAVIOUR IN THE LOWER STRATOSPHERE DURING THE EASOE CAMPAIGN

P. Di Girolamo<sup>1</sup>, M. Cacciani<sup>1</sup>, A. di Sarra<sup>1,2</sup>, G. Fiocco<sup>1</sup>,  
D. Fuà<sup>1,3</sup>, T.S. Joergensen<sup>4</sup>, B. Knudsen<sup>4</sup>, N. Larsen<sup>4</sup>.

<sup>1</sup> Department of Physics, University "La Sapienza", Rome.

<sup>2</sup> AMB ENEA, S. Maria di Galeria, Rome.

<sup>3</sup> IFA CNR, Rome.

<sup>4</sup> Danish Meteorological Institute, Copenhagen.

## Introduction.

The question of possible interactions between ozone and stratospheric aerosol has been open for a long time. Measurements carried out after the Mt. Agung and El Chichón eruptions showed evidence of negative correlations between the presence of volcanic stratospheric aerosols and ozone concentration (Pittock, 1965; Fiocco and Grams, 1967; Adriani et al., 1987). Evidence for negative correlations in the polar winter has been also found (Fiocco et al., 1989). It is only after the discovery of the Antarctic ozone hole that catalytic effects related to low temperature heterogeneous chemistry have become the object of much investigation, now extended to the role of volcanic aerosol in the ozone reduction. These phenomena can be the object of various interpretations, not mutually exclusive, including the effect of transport, diffuse radiation (see e. g. Fiocco et al., 1978) as well as heterogeneous chemistry (Hofmann and Solomon, 1989; Arnold et al., 1990).

The present paper provides preliminary results of simultaneous measurements of ozone and aerosol, carried out at Thule, Greenland (76.5°N, 68.8°W), during winter 1991-92. The European Stratospheric Ozone Experiment (EASOE), that begun in mid November 1991 and ended in March 1992, was aimed at monitoring the winter Arctic stratosphere in order to obtain a deeper insight of the ozone destruction processes taking place in the polar regions. During the campaign a large set of ground based, balloon and airborne instruments were deployed in the Arctic.

A large amount of aerosol was injected into the lower stratosphere by the recent eruption of Volcano Pinatubo (Philippines, June 1991). A lidar system, already operational in Thule since November 1990, has provided detailed measurements of the stratospheric aerosol concentration during EASOE. In the same period, a large number of ozonesondes were launched. Although no PSC formation was detected over Thule, the simultaneous measurement of the stratospheric aerosol and ozone profiles give the possibility to study interactions occurring in the stratosphere between these two constituents.

## Instrumentation.

The Thule lidar system uses a Nd:YAG laser with second harmonic generator capable of

emitting pulses at 532 nm of approximately 300 mJ at 10 Hz. The system is however run more conservatively at 100 mJ, 4 Hz. The receiver consists of a vertically pointing Cassegrain telescope with a 800 mm diameter primary mirror.

The backscattered radiation is passed through a narrow band interference filter, it is divided by a polarizing beam-splitter cube and detected by two photomultipliers. A mechanical chopper prevents detectors' overloading by the echoes from the lowest altitudes. Both signals are amplified and sent simultaneously to photon counting chains and A/D converters.

The system is ordinarily set up to provide measurements of both aerosol backscattering coefficient and aerosol depolarization ratio in the range 6-40 km. Night-time operation allowed high signal-to-noise ratios up to the higher levels. About 40 conventional ECC sondes were launched from Thule during the 1991-92 winter, and quasi-simultaneous lidar measurements were carried out when weather conditions allowed.

## Results.

Lidar observations were carried out in the period December 1991 - March 1992 for a total of about 150 hour operation. In this period no evidence of stratospheric cloud formation has been observed. This is consistent with the relatively high values of temperature, which were almost at every time above 200 K, measured over Thule.

At the same time, the large amount of aerosols injected in the stratosphere by the eruption of Volcano Pinatubo (Philippines, June 1991) was measured. In order to study the correlated behaviour of ozone and aerosol, simultaneous backscattering and ozone profiles were compared.

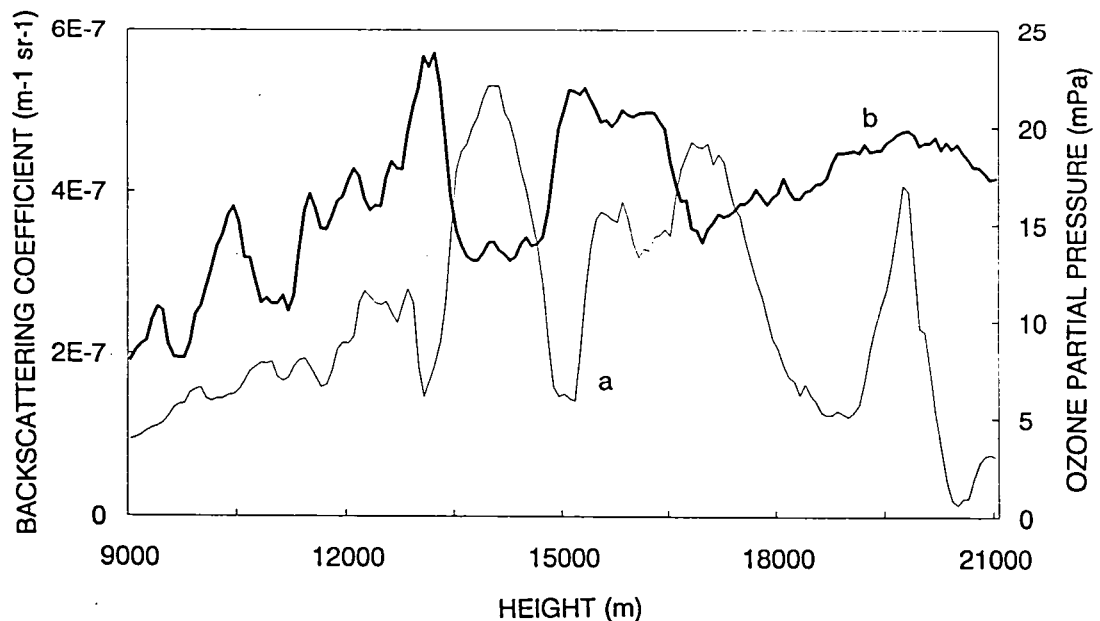


Fig. 1. Backscattering coefficient (curve a) and ozone partial pressure (curve b) as a function of height over Thule for February 6, 1992.

In figure 1 ECC (as ozone partial pressure) and lidar (as backscattering coefficient) profiles are shown for February 6, 1992. The lidar profile is the result of 1 hour averaging, almost the same time the ozonesonde takes to reach its maximum elevation. The ozone and aerosol profiles show a correlated behaviour, the ozone minima corresponding to aerosol maxima and viceversa.

Cross correlation coefficients between the ozone and aerosol deviations from the average were computed in +/- 2 km height intervals around a given level for 25 couples of backscattering and ozone measurements. For single cases, values of the negative cross correlation coefficient as high as 0.97 (February 24, height 17 km) were observed. The average coefficient are consistently negative in the lower stratosphere, and show larger values (around -0.5) in the 13-18 km height range.

A study of the trajectories was carried out to establish the thermal and radiative history of the air-mass prior to its passing over Thule. Trajectories could be reconstructed from the analysis up to ten days before transit over Thule. Although the air-masses often encountered cold regions, such that PSC formation was possible, the relationship between the ozone fluctuations and the thermal minima does not unequivocally show that ozone depletion were associated to PSC development.

## References.

Adriani, A., G. Fiocco, F. Congeduti, and G.P. Gobbi, Correlated behaviour of the aerosol and ozone contents of the stratosphere after the El Chichón eruption, *J. Geophys. Res.*, **92**, 8365-8372, 1987.

Arnold, F., Th. Bürke, and S. Qiu, Evidence for stratospheric ozone-depleting heterogeneous chemistry on volcanic aerosols from El Chichón, *Nature*, **348**, 49-50, 1990.

Fiocco, G., W. Komhyr, and D. Fuà, Is ozone destroyed during the Antarctic polar night in the presence of polar stratospheric clouds?, *Nature*, **341**, 426-427, 1989.

Fiocco, G., A. Mugnai, and W. Forlizzi, Effects of radiation scattered by aerosols on the photodissociation of ozone, *J. Atmos. Terr. Phys.*, **40**, 949-961, 1978.

Grams, G., and G. Fiocco, Stratospheric aerosol layer during 1964 and 1965, *J. Geophys. Res.*, **72**, 3523-3542, 1967.

Hofmann, D.J., and S. Solomon, Ozone destruction through heterogeneous chemistry following the eruption of El Chichón, *J. Geophys. Res.*, **94**, 5029-5041, 1989.

Pittock, A.B., Possible destruction of ozone by volcanic material at 50 mbar, *Nature*, **207**, 182, 1965.



## **First Results from TROLIX '91: An Intercomparison of Tropospheric Ozone LIDARs**

A. Apituley<sup>1</sup>, J. Bösenberg<sup>2</sup>, G. Ancellet<sup>3</sup>, H. Edner<sup>4</sup>, B. Galle<sup>5</sup>, J.B. Bergwerff<sup>1</sup>,  
G. von Cossart<sup>6</sup>, J. Fiedler<sup>6</sup>, C.N. de Jonge<sup>1</sup>, J. Mellquist<sup>5</sup>, V. Mitev<sup>3</sup>, T. Schaberl<sup>2</sup>,  
G. Sonnemann<sup>6</sup>, J. Spakman<sup>1</sup>, D.P.J. Swart<sup>1</sup>, E. Wallinder<sup>4</sup>

1: Rijksinstituut voor Volksgezondheid en Milieuhygiëne (RIVM), Bilthoven, The Netherlands

2: Max-Planck-Institut für Meteorologie (MPI), Hamburg, Germany

3: CNRS/Service d'Aéronomie (CNRS/SA), Paris, France

4: Lund Institute of Technology (LIT), Lund, Sweden

5: Institutet för Vatten- och Luftvardsforskning (IVL), Göteborg, Sweden

6: Institut für Atmosphärenphysik Kühlungsborn (IAK), Kühlungsborn, Germany

Within the framework of the European environmental research programme EUROTRAC, LIDAR systems for routine measurement of vertical ozone profiles throughout the planetary boundary layer and the free troposphere are currently under development. Several of these systems are now operational and an intercomparison experiment was undertaken in the period from June 10 to June 28, 1991 in Bilthoven, the Netherlands. The main scientific objectives defined for the campaign are:

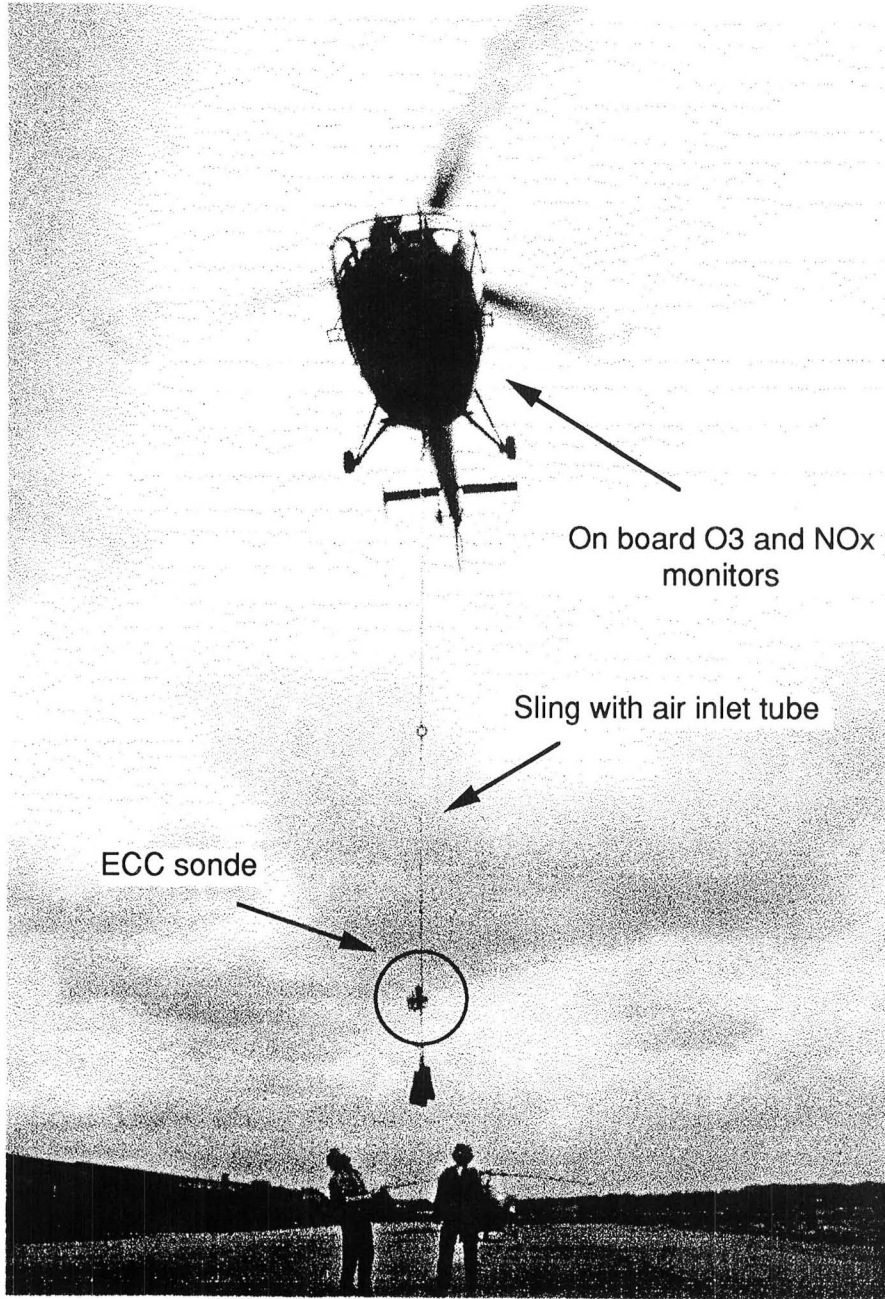
- compare the LIDAR measurements to in situ measurements of the ozone concentration,
- determine how many and which wavelengths are needed for a sufficiently accurate ozone retrieval in the lower troposphere under realistic conditions,
- assess the accuracy that can be achieved under realistic conditions,
- compare the performance of the participating systems.

Four different O<sub>3</sub>-DIAL systems participated in the campaign, all operating in the UV at wavelengths ranging from 248 to 313 nm. Two of the systems (RIVM and CNRS/SA) are Nd:YAG based, utilizing stimulated Raman shifting (SRS) in H<sub>2</sub> and D<sub>2</sub> for generation of the DIAL wavelengths. One system (MPI) is KrF excimer based, also utilizing SRS in H<sub>2</sub> or D<sub>2</sub> for generation of the needed wavelengths and the fourth system (LIT) is based on a Nd:YAG pumped dye laser system. In addition, ground level measurements of standard chemistry and meteorological parameters were obtained, as well as vertical temperature and humidity profiles from meteorological balloon soundings from a nearby meteorological station.

One of the main problems involved in DIAL measurements of ozone in the UV region is the interference of spatially inhomogeneous aerosol. To address this problem, intercomparison experiments have been carried out with all LIDAR systems pointing vertically while in situ measurements were obtained with an UV photometric ozone analyzer and an ECC-sonde carried by a helicopter. The aircraft circled around the measurement site while the LIDAR systems were operating. In addition, LIDAR measurements were made simultaneously in the 450 and 1064 nm region. Altogether a set of LIDAR measurements at up to 12 wavelengths — of which eight are in the UV— were obtained for these measurement periods.

Also, experiments were conducted with LIDARs pointing horizontally along a path closely matched by the long path of a differential optical absorption spectroscopy (DOAS) instrument. In this way, the average ozone concentration over the path covered by the DOAS could be compared to the values obtained from the DIAL systems.

Preliminary results show that accurate high resolution measurements can be obtained, at least under favorable conditions. Adverse effects, like sensitivity to steep gradients in aerosol concentration and interference with SO<sub>2</sub> are presently being studied. The collected data set is particularly suited for the assessment of these sensitivities. In this paper, the first results from the evaluation of the data will be presented.





GLObal Backscatter Experiment (GLOBE) Results:  
Aerosol Backscatter Global Distribution and Wavelength Dependence

David A. Bowdle  
Earth System Science Laboratory  
University of Alabama in Huntsville  
Huntsville Alabama 35899

INTRODUCTION

The GLObal Backscatter Experiment (GLOBE) was initiated by the National Aeronautics and Space Administration (NASA) in 1986 as an interagency and international research effort to characterize tropospheric aerosol backscatter properties. The primary objective of the GLOBE program is to develop realistic aerosol backscatter inputs to design and simulation studies for NASA's prospective Laser Atmospheric Wind Sounder (LAWS), a major instrument in the planned international Earth Observing System (EOS). To achieve this objective, GLOBE incorporates several different types of aerosol sensors, which operate from a variety of sensor platforms, cover a wide range of spatial and temporal scales, and measure a diverse set of aerosol physical, chemical, and optical properties.

Innovative data visualization methods have been developed to facilitate quality control and data analysis on the GLOBE database. The results of this analysis have provided important new information on the life cycles and physicochemical properties of global-scale tropospheric aerosol systems. GLOBE results are also applicable for design studies on a wide variety of other lidar systems that depend on backscattered signals from atmospheric aerosol tracers. In addition, GLOBE analytical methods will be useful for EOS and other studies that involve the assimilation of large, complex atmospheric aerosol databases.

RATIONALE

The design of GLOBE assumes the existence of a ubiquitous, quasi-steady-state, quasi-well-mixed global-scale aerosol background system for aerosol particles between roughly 0.05 and 5  $\mu\text{m}$  diameter. This assumption leads to several key predictions: (1) that the background system will occupy a large volume fraction of the middle and upper troposphere, especially over the remote oceans; (2) that background aerosol properties (such as backscatter coefficients) at any given altitude will vary lognormally in space and time, with a relatively small geometric standard deviation (e.g., ~2-3); and (3) that the geometric mean background backscatter mixing ratio (backscatter coefficient divided by local atmospheric density) will be approximately constant with altitude. This well-mixed pattern need not characterize any given instantaneous vertical profile of a given aerosol parameter; however, it will inevitably appear in the ensemble statistics for any suitably large aerosol data set in the middle and upper troposphere.

The existence of such a background would have profound implications for the design optimization and performance simulation on many lidar remote sensing systems, and particularly for LAWS. Background backscatter values are expected to be near the threshold for the most sensitive LAWS instrument that can be built with current technology. In addition, background conditions are expected to dominate the very regions of the atmosphere where new wind measurements from LAWS are most needed. Under these conditions, small changes in the atmospheric aerosol system, coupled with small degradations in LAWS engineering performance, could result in drastic losses in LAWS wind retrieval performance and scientific utility. Simulation of these effects in design studies for LAWS and related lidar systems requires, at minimum, verification of the background concept, realistic estimates for background backscatter magnitudes, and realistic estimates for the volume fraction of the LAWS sample domain that is characterized by background conditions. More sophisticated simulation studies would require detailed information on the structure and meteorological setting of the background aerosol field over a wide range of spatial and temporal scales.

## APPROACH

GLOBE uses several different types of measurement, analysis, and modeling strategies to accomplish these diverse objectives. The measurement phase involves acquiring suitable non-GLOBE data sets and conducting GLOBE measurement programs to fill in critical gaps in existing aerosol databases. First, global-scale data sets for aerosols or aerosol surrogates are sought to verify the existence of the global aerosol background system and to estimate its frequency of occurrence. Large data sets are needed to avoid sample bias and to ensure that background features can be readily detected and quantified. Second, direct measurements are sought for aerosol backscatter coefficients at or near selected lidar design wavelengths. These stand-alone data sets are most useful as climatologies from a single location over an extended period of time. This need has been met during much of the 1980's by a loosely-coordinated network of several CO<sub>2</sub> lidars, all operating near the primary design wavelength for LAWS. Third, coordinated data sets are sought from intensive field programs with several collocated aerosol sensors, to develop empirical links between the direct backscatter measurements and the global-scale aerosol databases, and to provide comprehensive aerosol physicochemistry information for backscatter modeling. High priority is given to field programs in remote locations. Several major GLOBE or GLOBE-related field programs of this kind have been conducted since the inception of the GLOBE program. The largest of these was the series of GLOBE airborne Survey Missions over the remote Pacific Ocean in Fall 1989 and Spring 1990. Fourth, GLOBE instruments that are used in any of these measurement programs are calibrated using standard methods (calibration for non-GLOBE data sets is not considered part of GLOBE).

GLOBE analysis and modeling efforts are directed at incorporating these diverse data sets into an aerosol model framework that can be used in LAWS design and simulation studies. First, GLOBE and GLOBE-related data sets are compiled into a centralized database, where they are transcribed into standard logical formats and carefully reviewed for quality and completeness. This process makes extensive use of innovative data display formats on modern data visualization workstations. Second, quality-controlled data sets are analyzed and assimilated into an empirical global-scale aerosol backscatter model. Depending on the data type, this step may involve comparisons of collocated aerosol measurements, aerosol correlations with meteorological conditions, backscatter modeling using Mie theory, or detailed statistical analysis. This process is designed to isolate, identify, and characterize the life cycles and backscatter properties of the major tropospheric aerosol systems, and particularly the background aerosol system. The ultimate goal of this effort is to expand the empirical model into a quasi-steady-state theoretical model of the global background aerosol system. Ideally, the model should be driven by boundary conditions that can be monitored from satellite-based sensors or other global-scale monitoring systems. This goal will be pursued by combining global-scale aerosol statistics with process-scale case-study results and ancillary information.

This comprehensive aerosol research program synthesizes the cooperative efforts of a large number of investigators from a broad international, interagency, corporate, and university base. These contributions are implicitly recognized in the above discussion. Explicit recognition of each key investigator is beyond the scope of this brief paper. The programmatic structure that coordinates these investigators and their diverse research efforts is continually evolving to meet changing requirements in the LAWS development effort and new insights in the aerosol science community.

## PRELIMINARY RESULTS

Significant portions of earlier GLOBE results have already appeared in the literature. The discussion here focuses on results from the GLOBE Pacific Survey missions and their relationship to the earlier results.

The primary finding of the GLOBE program has been the qualitative verification of the existence of the quasi-steady-state, quasi-well-mixed global-scale background aerosol system (e.g., *Rothermel et al., 1989*). Background features have been found in numerous independent aerosol data sets. Moreover, background aerosol properties from these independent data sets,

when converted to a common aerosol parameter (e.g., backscatter coefficients at selected CO<sub>2</sub> wavelengths), have all led to similar estimated values of that parameter.

Over and near the continents, and especially during the local spring/summer season, background backscatter values appear to be slightly higher, with background conditions limited to the middle and/or upper troposphere. However, over the remote oceans, and especially during the local fall/winter season, background backscatter values are slightly lower, and background conditions may characterize the entire troposphere from ~1-2 km below the tropopause to ~1-2 km above the surface. In the tropics and subtropics, where the tropopause may reach 16-17 km altitude, this pattern leads to a very deep background layer, with somewhat lower background backscatter values than at higher latitudes.

However, within the same tropical and subtropical regions, extremely low aerosol backscatter values characterize aerosol-regeneration regions immediately adjacent to quasi-steady-state convergence and precipitation zones. The mechanisms that produce and maintain these low-backscatter regions are not fully understood. However, the process is probably initiated by extremely efficient removal of aerosol material, and somewhat less efficient removal of sulfur-bearing gaseous aerosol precursors, in these precipitation zones (*Chatfield and Crutzen, 1990*). GLOBE results showed that very high concentrations ( $\gg 10,000 \text{ cm}^{-3}$ ) of new ultrafine ( $\ll 0.01 \mu\text{m}$ ) sulfuric acid particles can be nucleated by gas-to-particle conversion in the ultra-clean air parcels that are detrained from these precipitation regions (*Clarke, 1992*). Under the proper conditions, which may include sunlight and trace chemical catalysis, this nucleation step can occur quite rapidly. These ultrafine particles initially grow rapidly by coagulation, and perhaps condensation, until particle concentrations are substantially reduced. Subsequent growth proceeds much more slowly, over time scales of a few days, until the particles reach their quasi-steady-state size of ~0.1-0.3  $\mu\text{m}$ . During this regeneration process, the aerosols are advected away from the precipitating clouds and slowly subside toward the boundary layer.

These processes have a profound effect on the backscatter properties of a regenerating aerosol system. For ultrafine particles, such as the freshly nucleated aerosols, backscatter cross-sections increase as  $\sim r^6$ , where  $r$  is the typical particle size. However, for an aerosol system growing by coagulation alone (i.e., where aerosol mass is conserved), particle concentration decreases as  $\sim r^{-3}$ . The backscatter coefficient of a coagulating aerosol therefore increases as  $\sim r^3$  during the initial growth phase. However, as the particle size increases still further, backscatter cross-sections eventually increase only as  $\sim r^2$ . During this phase, therefore, the backscatter coefficient of a coagulating aerosol population decreases as  $\sim r^{-1}$ .

The maximum backscatter coefficient for a coagulating aerosol system will generally occur for a critical particle size between ~0.1  $\mu\text{m}$  and ~1.0  $\mu\text{m}$ . The critical size depends on wavelength and aerosol composition, with smaller critical sizes generally corresponding to shorter wavelengths. However, as indicated above, particle growth slows down dramatically in this same size range. Therefore, the backscatter coefficient of any given coagulating aerosol system will soon reach a quasi-steady-state value, which depends primarily on the aerosol mass concentration in the initial burst of nucleation. That limiting value can only be increased by non-conservative processes, such as growth by condensation or mixing with another air parcel that has a higher backscatter coefficient. In the atmosphere, we would expect a modest range of initial mass concentrations, condensation rates, and mixing fluxes, and a corresponding range of quasi-steady-state backscatter values, which we will identify as the predicted "background" backscatter feature. It appears, then, that a quasi-steady-state aerosol regeneration process will generally lead to low backscatter near the detrainment zones for deep precipitating cloud systems, and increasing backscatter, tending toward typical background values, at greater distances and lower altitudes. Similar features will undoubtedly characterize regions with efficient precipitation scavenging processes in transitory or migrating cloud systems at other latitudes.

The background aerosol population appears to be comprised of complex combinations of sulfate and crustal constituents. Sulfates are generally found in the smaller particles, ~0.1  $\mu\text{m}$  diameter, and irregular crustal grains in the larger particles, >1.0  $\mu\text{m}$  diameter. Particles of intermediate size often appear to be internal mixtures of sulfate and crustal constituents. Sulfate

molecular forms include sulfuric acid, ammonium bisulfate, and ammonium sulfate, as well as the entire range of intermediate acid sulfate mixtures. Sulfuric acid tends to dominate conditions with low aerosol loading and low backscatter, indicative of fresh *in-situ* aerosol regeneration. Ammonium sulfate, often accompanied by crustal or soot particles, usually dominates conditions with higher aerosol loading and higher backscatter, indicative of diluted aged continental aerosols.

The background features described above are periodically perturbed by several other types of aerosol processes in the free troposphere. Ubiquitous cumuliform and stratiform clouds in various stages of their life cycle (incipient, active, and dissipated) obviously produce regions with very high backscatter. Mineral dust and other high-backscatter continental aerosols can occasionally be found as massive plumes, sometimes up to several thousand km across. In addition, major volcanic eruptions produce large backscatter enhancements over a long period of time in several regions of the troposphere. These post-volcanic enhancements appear to be ubiquitous just below the tropopause at all latitudes, frequent in the mid-troposphere in mid-latitudes, and ubiquitous at all tropospheric altitudes in high latitudes. However, in the tropics and subtropics, the quasi-steady-state cleansing process rapidly restores most of the troposphere to pre-volcanic conditions, even when a massive volcanic aerosol pall remains overhead in the tropical lower stratosphere.

### CONCLUSIONS

A large body of atmospheric aerosol observations, combined with sound theoretical considerations, has provided strong qualitative support for the existence of a global-scale tropospheric background aerosol system. However, several key uncertainties remain in the characterization of the background. First, the existence of the background has not been rigorously verified by objective statistical tests. Second, the physical mechanisms that produce, maintain, and perturb the background have not been rigorously identified, verified, and quantified, at least to the degree required for incorporating them in a predictive theoretical model. Third, the spatial and temporal representativeness of the current GLOBE observations has not been adequately verified, so the frequency of occurrence of background conditions is not well known. Fourth, the fine structure of the background aerosol field has not been determined over the wide range of spatial and temporal scales and meteorological settings that will affect the performance of LAWS and similar lidar sensors. Fifth, backscatter perturbations at various wavelengths, due to subtle changes in aerosol composition and particle morphology, have not been adequately elucidated. And finally, backscatter estimation biases and errors due to sample volume discrepancies and other instrument effects have not been fully assessed.

Exploration of these issues will require detailed analyses of the comprehensive GLOBE survey data base, including extensive data validation for both survey missions -- initially to quantify sensor sensitivities, sampling biases, and correction factors, and ultimately to develop more robust estimates of background backscatter properties. These analyses, combined with studies using the overall GLOBE database, will provide important new insights into the structure, dynamics, and optical properties of the global aerosol system.

### ACKNOWLEDGMENTS

The assistance of Dr. Ramesh Kakar, Director of the Global Scale Processes Research Program at NASA Headquarters, is gratefully acknowledged. This work was supported in part by the University of Alabama, Huntsville, under NASA contract NAS8-37585.

### REFERENCES

- Chatfield, R. B., and P. J. Crutzen, 1990: Are there interactions of iodine and sulfur species in marine air photochemistry? J. Geophys. Res., **95**, D13, 22319-22341.
- Clarke, A. D., 1992: Atmospheric nuclei in the remote free troposphere. Submitted to J. Atmos. Sci.
- Rothermel, J., D.A.Bowdle, J.M.Vaughan, and M.J.Post, 1989: Evidence of a tropospheric aerosol background backscatter mode. Appl. Opt., **28**, 1040-1042.

## THE GLOBAL BACKSCATTER EXPERIMENT AIRBORNE PULSED LIDAR MEASUREMENTS

James D. Spinhirne, S. Chudamani\*  
Laboratory for Atmospheres  
NASA Goddard Space Flight Center  
Greenbelt, MD 20769 USA

Robert T. Menzies and David Tratt  
Jet Propulsion Laboratory  
California Institute of Technology  
4800 Oak Grove Drive  
Pasadena, CA 91109

The Global Backscatter Experiment (GLOBE) was intended to provide data on prevailing values of atmospheric backscatter cross section. The primary intent was predicting the performance of space borne lidar systems, most notably the Laser Atmospheric Wind Sounder (LAWS). A second and related goal was to understand the source and characteristics of atmospheric aerosol particles. The major components of the experiment were flight surveys throughout the Pacific region by the NASA DC-8 aircraft. Pulsed lidar systems were operated on the missions. The pulse lidars were the JPL 9  $\mu\text{m}$   $\text{CO}_2$  airborne backscatter lidar (ABL) and the GSFC visible and near IR lidar (VIRL) which obtained aerosol backscatter cross section at the fundamental and doubled Nd:YAG laser wavelengths of 1.064 and 0.532  $\mu\text{m}$  and, in addition, at a wavelength of 1.54  $\mu\text{m}$ . The GLOBE missions were in November 1989 and May-June 1990. In this paper we will give a summary of measurement results with emphasis on the magnitude, structure, characteristics and variability of the observed atmospheric aerosol and cloud scattering. A companion paper will describe in detail the wavelength dependence of the observed aerosol and cloud scattering.

The VIRL system on the GLOBE mission was a incoherent, elastic scattering instrument based on a Nd:YAG laser transmitter. The 1.54  $\mu\text{m}$  transmitted pulse was generated by Raman shifted down conversion of the 1.064  $\mu\text{m}$  radiation by transmitting the 1.064  $\mu\text{m}$  pulse through a Raman cell containing 300 psi of methane gas. The receiver telescope was designed to be rotated in order that observations could be acquired in either the nadir or zenith direction from the aircraft. All detectors were solid state. The pulse repetition frequency of the VIRL system was 50 Hz but data was averaged in real time and recorded at 2 Hz. The ABL instrument employed a one Joule injection-seeded TEA- $\text{CO}_2$  laser transmitter and a coherent receiver. The pulse repetition frequency was 3-5 Hz for the GLOBE missions. The ABL instruments could also be pointed alternately in nadir or zenith modes. An important factor for lidar backscatter measurements is accurate calibration. Both the ABL and VIRL system were calibrated by hard target calibration procedures. The calibration procedures and more detail on the instruments are given by Spinhirne et al. (1991) and Menzies and Tratt (1991).

The GLOBE observations of 1989 and 1990 were carried out on missions of three weeks duration. The region of the central and eastern Pacific was traversed by the NASA DC-8 at an altitude range of roughly 8 to 10 km. Latitudes from approximately 70°N to 70°S were covered. In addition to point-to-point traverse flights, there were local flights where vertical

flight patterns were flown and measurements from different heights could be intercompared. The intercomparison included measurements by in-situ particle probes on board the DC-8.

A summary of the results from the GLOBE missions will be presented. Four tropospheric aerosol layers may be defined that were characteristic of the GLOBE results in general. The lowest atmospheric layer is the mixed boundary layer. From the GLOBE flights extensive data has been obtained on the structure of the marine planetary boundary layer. A notable result for all observations is the strong increase in scattering that was found for the boundary layer, typically one or more orders of magnitude above the aerosol cross section in the upper troposphere. In the case where there are clouds forming in the mixed layer, there is a 'cloud pumped' aerosol layer found above the mixed layer which most probably results from particles left behind after droplet evaporation. The cloud pumped layer may extend upward several kilometers above the mixed layer. The cloud pumped layer was prevalent over much of the Pacific. Above the cloud pumped layer very low cross sections are found in the upper troposphere which may be considered the background tropospheric aerosol layer. In addition there is the fourth type of tropospheric layer. In the upper troposphere layers of elevated particulate scattering are often found that are apparently the result of transport from another region. The upper tropospheric layers were especially prevalent for the east Pacific basin in the northern hemisphere. The variability of backscatter cross section for the cloud free upper troposphere was over three orders of magnitude. It may be generally stated that the upper troposphere aerosol scattering cross section were low in the Southern hemisphere for the May-June flights and low for the Northern hemisphere for the November flights. The GLOBE pulsed lidars also observed the stratospheric aerosol layer over the range of latitudes flown.

Low and high altitude clouds were observed in abundance during both GLOBE missions. For a large fraction of the cloud observations, lidar return signals were obtained through extended layers. In most all cases both the short and long wavelength lidar systems were able to penetrate through to top of cirrus that was under flown. Large areas of clouds with vertical structure from 4 to 8 km thick were observed. The potential for extended signal returns through clouds is a potentially significant factor for laser wind measurements.

The GLOBE pulsed lidar measurements provide an extensive data set on the magnitude and variability of aerosol and cloud backscatter of the atmosphere. The data defines atmospheric aerosol scattering characteristics and should prove to be an important resource for determination of the performance and design of laser remote sensing instruments.

## V. REFERENCES

Menzies, R. T. and D. M. Tratt, 1991: Aerosol and cloud observations with a CO<sub>2</sub> backscatter lidar on the NASA DC-8 GLOBE Pacific missions. Preprint Volume of the Seventh Symposium on Meteorological Observations and Instrumentation, American Meteor. Society, Boston Mass.

Spinhirne, J. D., S. Chudamani and J. F. Cavanaugh, 1991: Visible and near IR lidar backscatter observations on the GLOBE Pacific survey missions. Preprint Volume of the Seventh Symposium on Meteorological Observations and Instrumentation, American Meteor. Society, Boston Mass.

\*Science Systems Applications Inc., Lanham, MD

MULTI-WAVELENGTH AIRBORNE LIDAR INTERCOMPARISONS  
OF AEROSOL AND CIRRUS BACKSCATTER OVER THE PACIFIC OCEAN

Robert T. Menzies  
David M. Tratt  
Jet Propulsion Laboratory  
California Institute of Technology  
4800 Oak Grove Drive  
Pasadena, CA 91109 USA

James D. Spinhirne  
S. Chudamani  
NASA Goddard Space Flight Center  
Greenbelt MD 20769 USA

Airborne CO<sub>2</sub> and Nd:YAG lidar instruments were flown on the NASA DC-8 research aircraft during two extended missions over the Pacific. These two missions, namely the GLOBE 1989 and GLOBE 1990 Missions, consisted of 15 flights between November 6 and November 30, 1989, and 13 flights between May 12 and June 5, 1990. The objectives during these Pacific circumnavigations were to characterize aerosol backscatter levels at infrared wavelengths in relatively pristine regions of the troposphere, and to observe cloud effects on lidar signals. For both lidars, the responsivities were calibrated on several occasions, using a hard target methodology (Kavaya and Menzies, 1985; Menzies and Tratt, 1991; Spinhirne, et al., 1991), in order to provide quantitative aerosol volume backscatter coefficients and reflectances from clouds and the sea surface. In addition, the three wavelength Nd:YAG data (0.53, 1.06, and 1.54  $\mu\text{m}$ ) were processed using independent temperature profile information, in order to deduce the Rayleigh scattering component of the total backscatter at each wavelength.

We report results of the intercomparison of the Nd:YAG lidar data primarily at  $1.06 \mu\text{m}$  and the  $\text{CO}_2$  lidar data at  $9.25 \mu\text{m}$  over a large number of common volume data sets taken from several flights, viewing a variety of aerosol and cirrus cases. Lidar data at these two wavelengths indicate a combination of high sensitivity and spatial resolution. The high sensitivity is important for comparisons over a wide dynamic range of backscatter levels. The high spatial resolution is desirable for intercomparisons in conditions for which spatial variability along the flight track is significant. This is certainly the case for most cirrus observations, for example. The  $0.53 \mu\text{m}$  wavelength channel sensitivity was comparable to that at  $1.06 \mu\text{m}$ ; however, the presence of the relatively large molecular Rayleigh backscatter component in the mid-visible results in larger uncertainties in the aerosol component of the backscatter signal at low aerosol levels.

The JPL Airborne Backscatter Lidar (ABL) instrument and the GSFC Visible and Near IR Lidar (VIRL) instrument both had the capability of observing in either the nadir or zenith directions during the DC-8 GLOBE missions. With the aircraft typically flying at altitudes between 25,000 ft (8 km) and 40,000 ft (12 km) the use of both nadir and zenith pointing resulted in high sensitivity observations throughout the troposphere. The ABL instrument consists of an injection-seeded TEA- $\text{CO}_2$  transmitter with output pulse energy of 1 Joule and prf of 4 Hz. The receiver is a heterodyne receiver designed for sensitive detection of the atmospheric backscatter signal. During the first GLOBE mission video detection was used following the amplification and bandpass filtering stages. A complex demodulator was fabricated and installed between the two GLOBE missions and used exclusively during the second mission in place of the video detection. Doppler information can be retrieved from the complex demodulator configuration. The VIRL instrument uses an incoherent, elastic backscattering receiver and a transmitter system which generates the fundamental and doubled Nd:YAG frequencies, and  $1.54 \mu\text{m}$  pulses by Raman shifted down-conversion in a cell containing high pressure methane gas. The VIRL range-gated backscatter profile data were stored at a rate of one per second. The ABL backscatter profile data were stored on each shot, although for most data comparison purposes, the processed data are averaged over intervals of 2 seconds or longer.

The lidar data at 1.06  $\mu\text{m}$  and 9.25  $\mu\text{m}$  show remarkable spatial correlation in regions of extensive layering and horizontal inhomogeneity. This provides confidence that valid data intercomparisons of aerosol and cloud backscatter can be made for a variety of circumstances. The Pacific circumnavigations offered lidar sampling over a variety of atmospheric aerosol conditions, including a wide range of boundary layer conditions, clean free troposphere environments, and regions of the atmosphere over the Pacific which had been significantly influenced by continental dust transport.

These intercomparisons provide insight into the wavelength dependence of atmospheric aerosol and cloud backscatter. The data can be used to better understand the capabilities of various airborne or Earth-orbiting lidar designs to provide backscatter information from aerosols and clouds, or to provide Doppler or DIAL information from aerosol and cloud backscatter.

A portion of the research described in this paper was carried out by the Jet Propulsion Laboratory, California Institute of Technology, under contract with the National Aeronautics and Space Administration.

## REFERENCES

Kavaya, M.J., and R.T. Menzies, 1985: Lidar aerosol backscatter measurements: systematic, modeling, and calibration error considerations, *Appl. Optics*, 24, 3444-3453.

Menzies, R.T., and D.M. Tratt, 1991: Aerosol and cloud observations with a CO<sub>2</sub> backscatter lidar on the NASA DC-8 GLOBE Pacific missions. Preprint Volume of the Seventh Symposium on Meteorological Observations and Instrumentation, American Meteor. Soc., Boston, MA.

Spinhirne, J.D., S. Chudamani and J.F. Cavanaugh, 1991: Visible and near IR lidar backscatter observations of the GLOBE Pacific survey missions. Preprint Volume of the Seventh Symposium on Meteorological Observation and Instrumentation, American Meteor. Soc., Boston, MA.



# Airborne Lidar Observations of the Stratosphere After the Pinatubo Eruption

DAVID M. WINKER<sup>1</sup>, MARY T. OSBORN<sup>2</sup>, AND ROBERT J. DECOURSEY<sup>2</sup>

<sup>1</sup>Atmospheric Sciences Division, NASA Langley Research Center, Hampton, VA

<sup>2</sup>Hughes STX Corporation, Hampton, VA

## INTRODUCTION

The eruption of Mt. Pinatubo (15°N, 120°E) in June 1991 injected the largest mass of gases and ash into the stratosphere observed since lidar and satellite monitoring of the stratosphere became possible in the middle 1960's. Because of early indications of the significance of the eruption, NASA mounted an airborne mission to survey the stratospheric plume soon after the eruption. The NASA Wallops Electra aircraft was outfitted with a depolarization lidar, a correlation spectrometer (for SO<sub>2</sub> measurements), a total-direct-diffuse spectral radiometer, and a Fourier transform spectrometer. As shown in Figure 1, six flights were made during the period July 7-14.

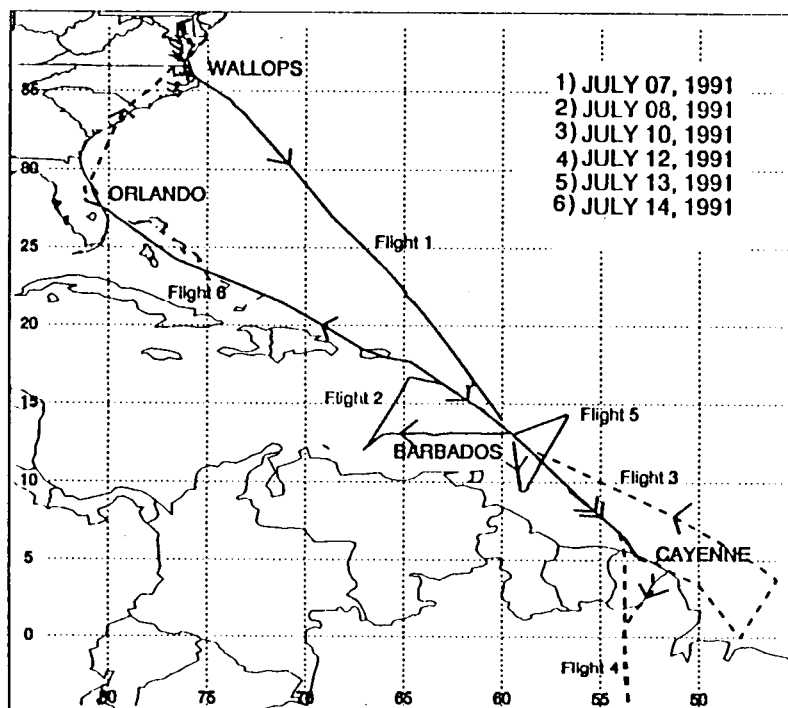


Figure 1. Flight tracks flown during the July 1991 Pinatubo survey mission.

## OBSERVATIONS

Lidar observations were made using the dual-polarization Nd:YAG airborne lidar operated by the NASA Langley Aerosol Research Branch. Backscattered light polarized parallel and perpendicular to the transmitted beam is sampled simultaneously at a resolution of 15 m. All observations were made at a wavelength of 532 nm. The lidar returns were normalized in clean regions of the upper troposphere and profiles of scattering ratio,  $R$ , and depolarization ratio,  $\delta$ , were computed. The scattering ratio profiles were corrected iteratively for transmission losses due to molecular and aerosol extinction. Due to the large aerosol loadings produced by Pinatubo, proper correction for aerosol extinction is essential for accurate determination of backscatter profiles.

The flights were conducted 21-28 days after the largest eruption events, which occurred on June 15-16. At this early stage of dispersal the volcanic material was observed to be highly stratified and horizontally inhomogeneous. Volcanic aerosols were observed at altitudes between 17 km and 26 km, generally occurring in well-defined layers. The vertical extent of the layers ranged from less than a kilometer to several kilometers. As an example, Figure 2 shows a gray-scale cross-section of  $R - 1$  taken on a northward flight leg from 4.5°S to 12.5°N. The tropopause was at about 16 km with cirrus clouds visible below this level and stratified aerosol layers above.

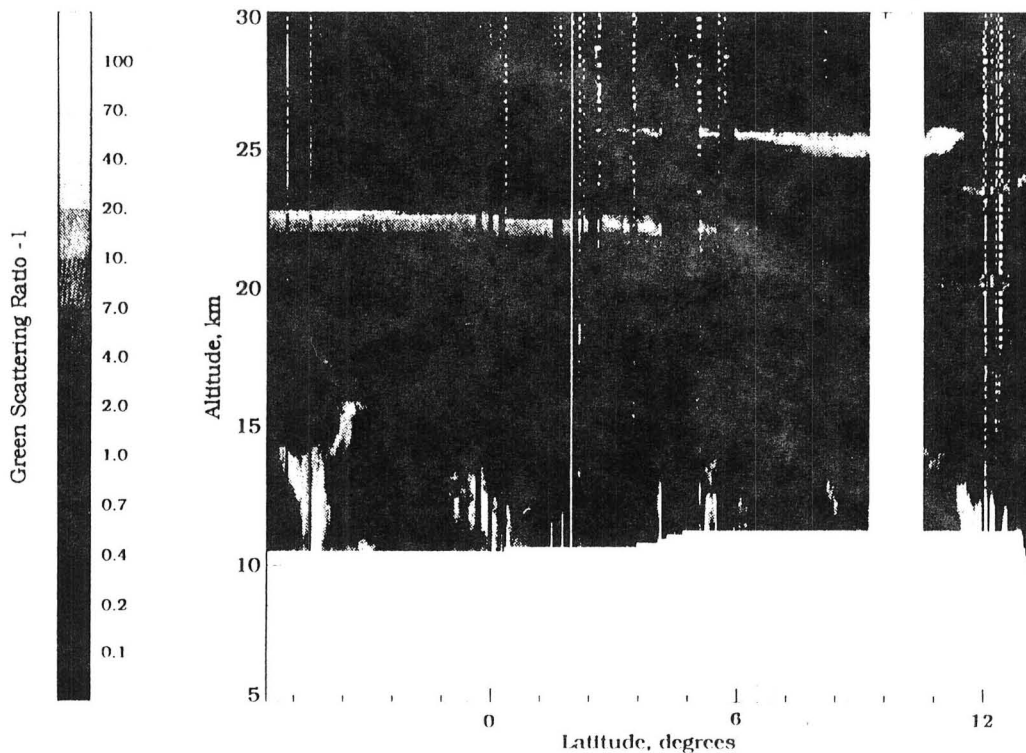


Figure 2. Lidar observations of  $R - 1$  at 532 nm from 4.5°S to 12.5°N taken on July 12-13, 1991.

The layer at 25 km between 2°N and 11°N represents the leading edge of a dense aerosol layer being advected across the path of the aircraft. It was encountered again the next day on a short flight near the latitude of Barbados (13.07°N), when the northern edge was observed at about 14°N. This layer exhibited scattering ratios as high as 80, the highest ratios observed during the mission. The layering of the aerosol is associated with wind shear. Figure 3 shows a wind profile over Barbados on July 13. Aerosols in the layer at 25 km are being transported more rapidly than the lower layers. Upper air winds and SAGE II data later confirmed that the layer at 25 km observed here corresponded to the leading edge of the volcanic plume after having circled the earth  $1\frac{1}{2}$  times since the eruption.

Figure 4 shows integrated backscatter values observed on the last three flights of the mission. The large values seen on July 13 are due to the dense layer at 25 km first seen on the previous day. Most of the volcanic aerosol was confined south of 14°N, and integrated backscatter values observed on the return flight to Wallops were relatively low. Using a mass-to-backscatter conversion ratio of 17.3 g-sr/m<sup>2</sup>, these data were used to estimate a stratospheric aerosol mass loading of 8 megatonnes (MT) [Winker and Osborn, 1992a]. SAGE II data were used to estimate the geographic extent of the plume. Since the SO<sub>2</sub> injected into the stratosphere had only partially converted to aerosol this soon after the eruption, the eventual mass loading is expected to be at least double this number. The total stratospheric aerosol mass under background conditions is on the order of 0.1 MT.

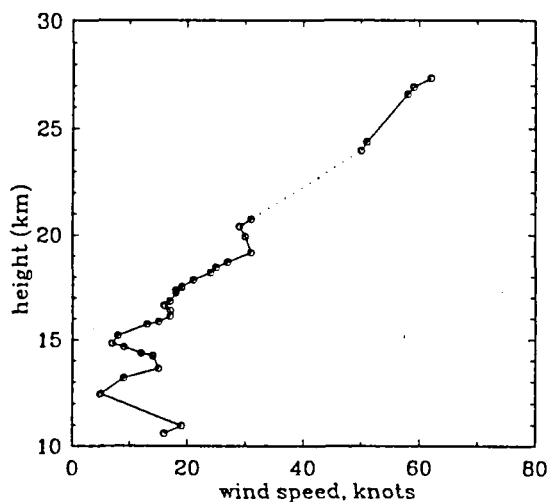


Figure 3. Profiles of wind speed and direction over Barbados, 00Z, July 13, 1991.

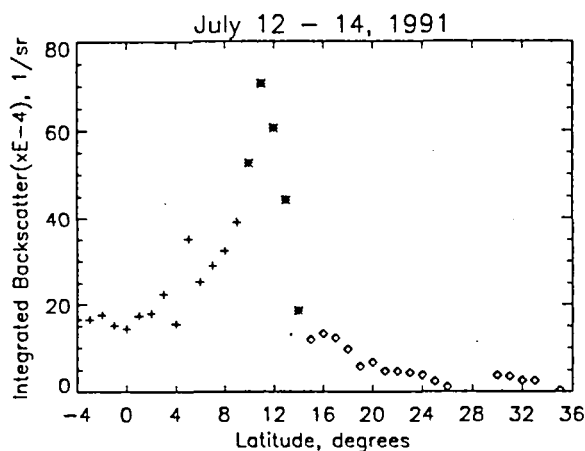


Figure 4. Latitudinal variation of stratospheric integrated backscatter (532 nm) observed on three successive days. (+ - July 12-13, \* - July 13, o - July 14).

Figure 5 shows two pairs of scattering ratio and depolarization profiles. The large depolarization values observed below the tropopause (at about 16 km) are characteristic of cirrus clouds. In the stratosphere, both depolarizing and non-depolarizing layers were observed [Winker and Osborn, 1992b]. Figure 5a shows significant depolarization at near the lower edge of the 22 km layer, probably due to the sedimentation of irregular ash particles. On the other hand, the 25 km layer, shown in Figure 5b, exhibits even stronger scattering but depolarization less than that expected from a molecular atmosphere, indicating it is composed of spherical sulfuric acid droplets with very little ash or other irregular particles.

More complete details on the observations made will be presented. A second survey mission is planned for May 1992, and preliminary results from this mission will also be presented.

#### REFERENCES

D. M. Winker and M. T. Osborn, 1992a: "Airborne lidar observations of the Pinatubo volcanic plume," *Geophys. Res. Lett.* **19**, 167-170.

D. M. Winker and M. T. Osborn, 1992b: "Preliminary analysis of observations of the Pinatubo volcanic plume with a polarization-sensitive lidar," *Geophys. Res. Lett.* **19**, 171-174.

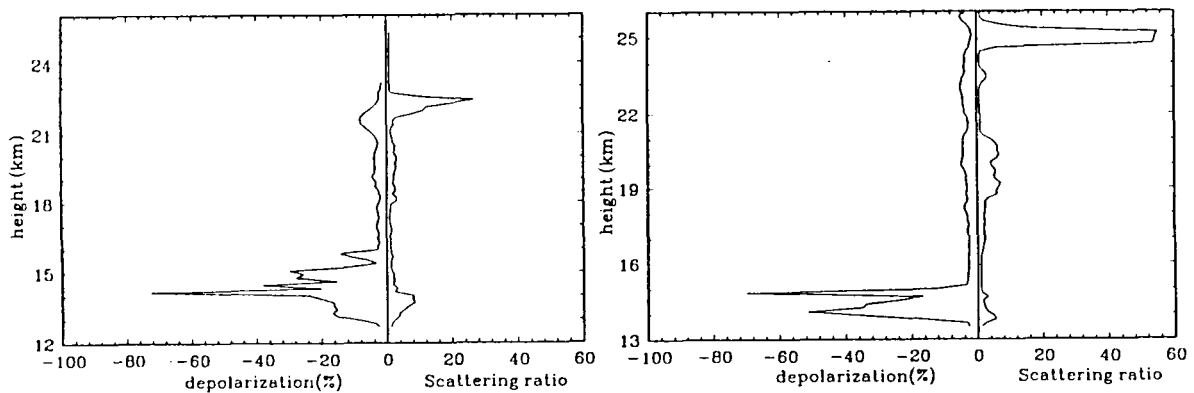


Figure 5. Profiles of scattering ratio and depolarization recorded July 12-13, 1991. Left curve - depolarization. Right curve - scattering ratio. a) 4.3°S, 53.6°W; b) 8.4°N, 55.5°W.

# MULTIWAVELENGTH MEASUREMENTS OF THE STRATOSPHERIC AEROSOL LAYER MADE AT HAMPTON, VIRGINIA (37N, 76W)

G.S. Kent, G.M. Hansen, and K.M. Skeens  
Science and Technology Corporation,  
Hampton, Virginia, USA

Atmospheric observations have recently commenced using a new lidar system, designed and constructed by the Science and Technology Corporation. The lidar, intended for the study of clouds and aerosols in the upper troposphere and stratosphere, is presently being installed at NASA Langley Research Center in Hampton. The system employs a three-wavelength Nd-YAG laser with a total output of about 500 mJ at 30 Hz, and a 14.5-inch receiving telescope with gated photomultiplier detectors at the two shortest wavelengths (532 nm and 355 nm), and an avalanche photodiode detector at the longest wavelength (1064 nm). The system also includes a rotating shutter in front of the receiving optics. A beam scanning assembly and video camera are currently being installed for off-zenith cloud studies. When completed, the lidar will also be capable of polarization diversity measurements and, as an aid to cloud investigations, the laser, rotating shutter, PMT gating, and the video camera are synchronized to a single frequency standard. The principal parameters of the lidar system are listed in Table 1.

Although all the lidar subsystems are not yet in place, a program of three-wavelength observations of the stratospheric aerosol layer was begun in late February 1992. This layer is currently very greatly enhanced as a result of the eruption of the Philippine Mt. Pinatubo volcano in June 1991 (*Geophysics Research Letters*, 19, 149-218, 1992); it shows considerable vertical structure and day-to-day changes are readily visible. The use of three lidar wavelengths to study the layer enables deductions to be made about the aerosol size distribution, which leads to improved estimates of mass loading, as well as a better understanding of the microphysical and dynamical processes taking place. An example of an early data set taken with the lidar system is shown in Fig. 1. On this occasion, cirrus cloud was present at an altitude of about 9 km and the aerosol layer extended from the tropopause (at 10.6 km) to about 25 km. The layer profile is quite irregular and shows a similar vertical structure at all three wavelengths. The enhanced layer visibility at 1064 nm, as compared to the other wavelengths, illustrates the very different wavelength dependence of the aerosol backscatter from that of the background molecular atmosphere. Inversion of these and other profiles to obtain the aerosol to molecular backscatter ratio  $R$  is being carried out. The results of these inversions, as applied to the data in Fig. 1, are shown in Fig. 2. Because of the low signal-to-noise ratios at altitudes above 25 km, where the scattering can be expected to be predominantly molecular, profile normalization has been carried out in the upper troposphere. A model for the amount of aerosol present at the normalization altitude had to be assumed, as well as a model for the extinction to backscatter ratio, causing

structure on all three wavelengths, which shows a relatively homogeneous layer below 20 km and the presence of several thin discrete layers above that altitude. At the time these data were taken it was not possible to make measurements at all three wavelengths simultaneously, and the data were taken over a period of about 40 minutes. Some of the differences observable in the upper layers are attributable to layer shape changes over the period of observation. The peak scattering ratios at 532 nm are similar to those observed by Jäger (1992) at Garmisch-Partenkirchen in October 1991 and are considerably smaller than those seen by Winker and Osborn (1992) at much lower latitudes in July 1991.

The profiles in Fig. 2 have been used to calculate the wavelength power law exponent  $\alpha$  for the aerosol backscatter, where  $\alpha$  is defined as

$$\alpha = -(\log \beta_{\lambda_1} - \log \beta_{\lambda_2}) / (\log \lambda_1 - \log \lambda_2)$$

where  $\beta_{\lambda_1}$  and  $\beta_{\lambda_2}$  are the backscatter cross sections at wavelengths  $\lambda_1$  and  $\lambda_2$ . Comparing the data at 1064 nm and 355 nm, values of  $\alpha$  are found to lie between 0.7 and 1.2 with a mean value of approximately 1.0. No significant variation in  $\alpha$  was observed over the altitude range 15-23 km but the value of  $\alpha$  for the wavelength range 1064 nm to 532 nm was found to be slightly larger than that for the range 532 nm to 355 nm. These values of  $\alpha$  are somewhat smaller than those measured by Post et al. (1992) in September 1991, who reported values of  $\alpha$  of about 1.5. Comparison of the present value of  $\alpha$  with those calculated for a sulfuric acid aerosol, using Mie theory, indicate that a uniform distribution of aerosol radii up to at least a few tenths of a micrometer would be required to explain the observational result. This conclusion is compatible with the range of particle radii reported by Deshler et al. (1992).

The present series of observations is continuing and work is currently in progress to improve the inversion algorithm used to obtain the backscatter profiles. The profiles will then be further used, in conjunction with suitable aerosol models, to derive the size distribution parameters and to make estimates of the column mass loading. These results will be presented at the 16th International Laser Radar Conference.

#### Acknowledgments

This work has been carried out under NASA contracts NAS1-18851 and NAS1-18676. We are grateful to M.P. McCormick and J.M. Alvarez for their support during the construction of the lidar system and for making available facilities at NASA/LaRC for its testing and use. We would also like to thank R.J. Allen and E. Acton for their work on the system design and control circuitry and P. Naranjo for his assistance with the lidar construction and installation.

## References

- Deshler, T., D.J. Hofmann, B.J. Johnson, and W.R. Rozier, 1992: Balloonborne measurements of the Pinatubo aerosol size distribution and volatility at Laramie, Wyoming during the summer of 1991, *Geophys. Res. Lett.* **19**, 199-202.
- Jäger, H., The Pinatubo eruption cloud observed by lidar at Garmisch-Partenkirchen, *Geophys. Res. Lett.* **19**, 191-194.
- Post, M.J., C.J. Grund, A.O. Langford, and M.H. Proffitt, 1992: Observations of Pinatubo ejecta over Boulder, Colorado by lidars of three different wavelengths, *Geophys. Res. Lett.* **19**, 195-198.
- Winker, D.M. and M.T. Osborn, 1992: Airborne lidar observations of the Pinatubo volcanic plume, *Geophys. Res. Lett.* **19**, 167-170.

Table 1. STC Scanning Lidar - Main System Parameters

Wavelengths and output energy per pulse	300 mJ (1064 nm) 105 mJ (532 nm) 75 mJ (355 nm)
Pulse repetition rate	30 Hz
Receiver aperture and field of view	37 cm, 0.5-2.0 mr
Receiver bandwidth and detectors used	20 nm, APD (1064 nm) 10 nm, PMT (532 nm) 20 nm, PMT (355 nm)
Maximum range resolution	15 m
Signal processing	Analog to digital conversion, signal averaging capability
Special features	a) Shutter in receiver optical path, opening time, 20 $\mu$ s b) Fast altitude/azimuth scanning capability c) Polarization diversity at 532 nm d) Synchronization of laser, PMT gating, rotating shutter, and video camera

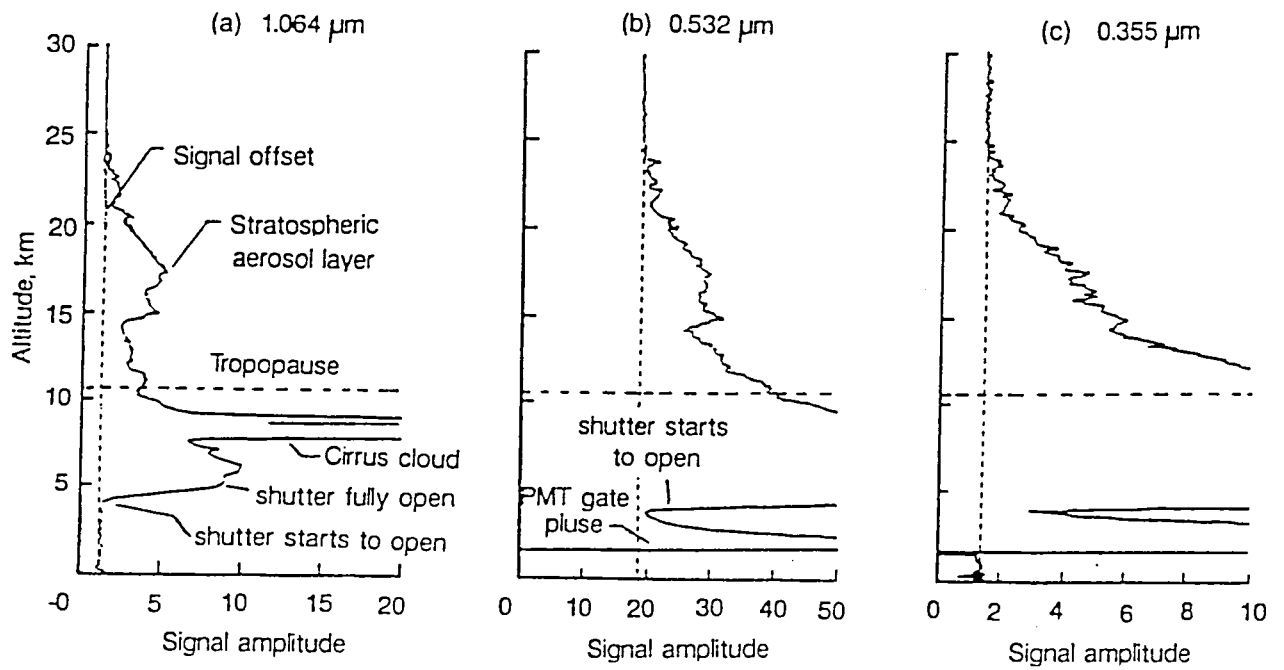


Figure 1. Examples of three-wavelength lidar profiles obtained on February 27, 1992. Data have been averaged for 1000 laser firings at 1,064 nm and 532 nm, and for 5,000 laser firings at 355 nm.

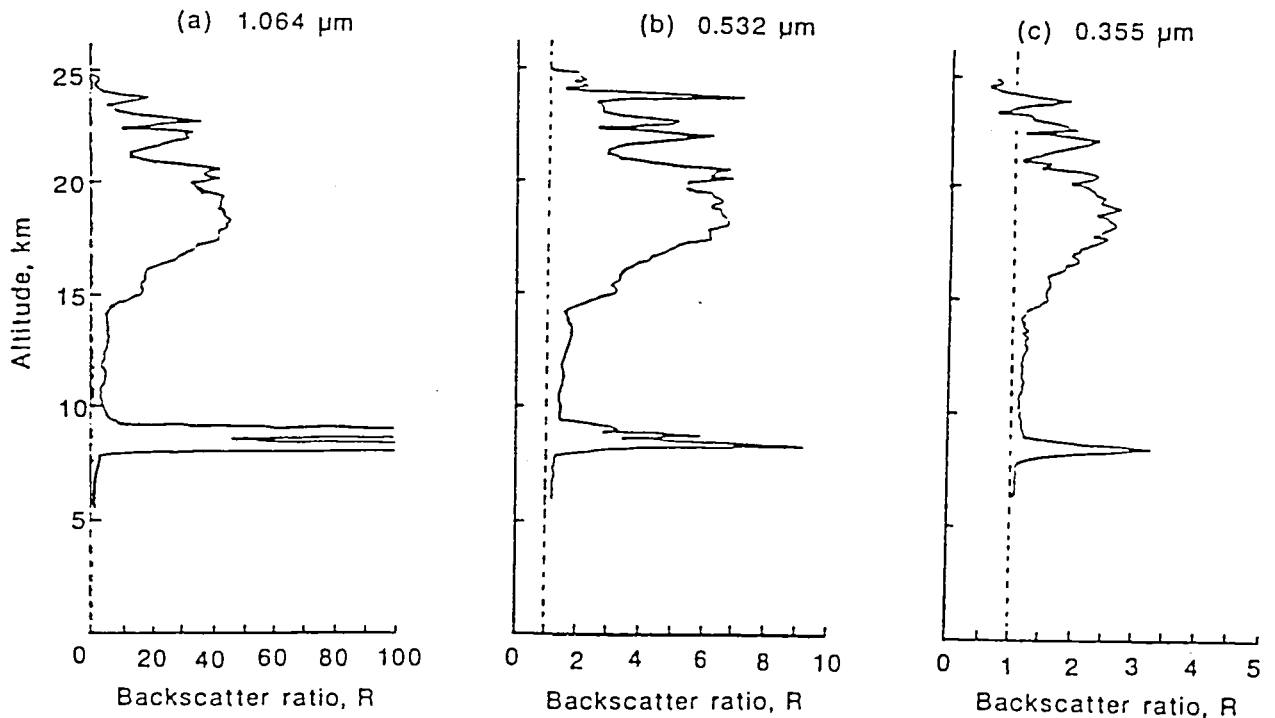


Figure 2. Aerosol to molecular scattering ratio profiles, R derived from the data shown in Fig. 1. Normalization has been carried out in the upper troposphere.

# Three-wavelength lidar measurements of Pinatubo aerosol and its optical properties

Sasano, Y., I. Matsui and S. Hayashida

The National Institute for Environmental Studies

Tsukuba, Ibaraki 305 Japan

## 1. Introduction

Enhanced stratospheric aerosols due to Mt. Pinatubo eruption has been measured using a YAG laser-based three-wavelength (1064, 532, and 355 nm) lidar and a YAG laser-based large-scale lidar (532 nm) at NIES, Tsukuba, Japan (36N, 140E) since June 1991. Temporal variation of integrated backscatter coefficient (IBC) derived from backscatter coefficient profiles which were obtained with the latter lidar system at NIES is depicted in Fig.1. The figure indicates that the main body of aerosol clouds first came over Japan in the fall of 1991 although some aerosol patches sporadically had appeared since a half month after the eruption.

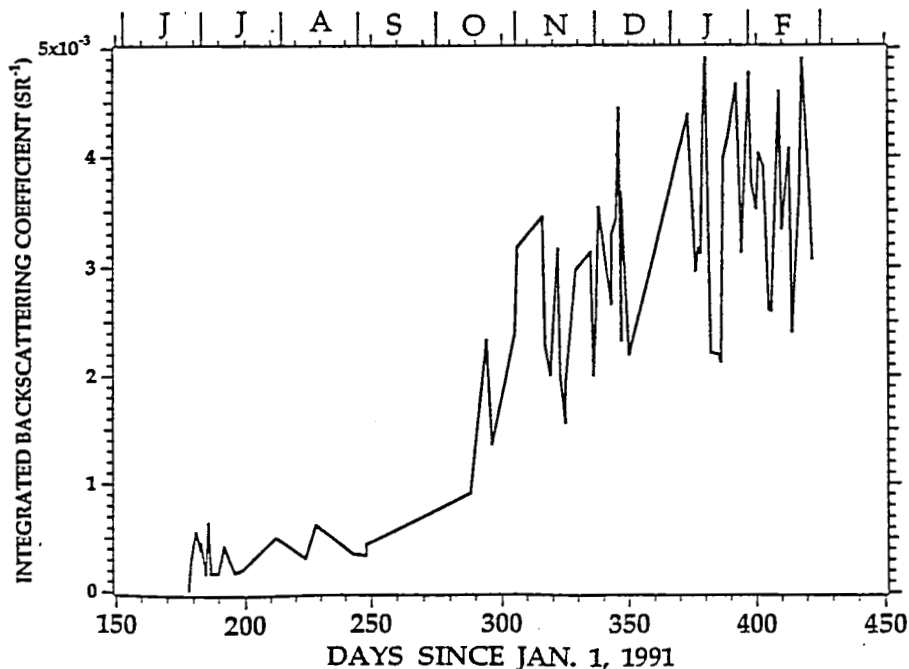


Fig.1 Temporal changes in the integrated backscatter coefficient for 532 nm between 15 km and 30 km.

The present paper describes some results of optical properties analysis using the lidar data obtained since December, 1991 when the main body of aerosols started to appear over Japan. The derived properties of the Pinatubo aerosols are extinction to backscatter ratios, wavelength dependencies of backscatter coefficients and extinction coefficients, and optical thickness. The analysis method is basically the same as that proposed by

Sasano and Browell (1989) and based on the assumption of similarity in backscatter profiles for three wavelengths (1064, 532 and 355 nm) which are derived from lidar signals using the Fernald equation (Fernald, 1984) with assumed extinction to backscatter ratios.

## 2. Method

Assuming a constant aerosol extinction to backscatter ratio  $S_1$ , a lidar signal can be solved to give an aerosol backscatter  $\beta_1$  (and an aerosol extinction  $\alpha_1$ ) profile corrected for attenuation due to aerosols using the Fernald equation. The subscript 1 is used to express the quantities related to aerosols. The subscript 2 (not used in this abstract) is reserved for quantities related to air molecules. Since a boundary condition needs to be specified, the well-known matching method can be applied to the signal in the region higher than the aerosol layer of interest under the assumption of no aerosols there.

The aerosol profile (backscatter coefficient) thus obtained for each wavelength signal depends on  $S_1$ . Fig. 2 shows aerosol backscatter profiles for 1064 nm and 532 nm obtained for different values of  $S_1$ . We notice that the larger  $S_1$  produces larger correction to the attenuation. Backscatter profiles of 1064 nm lidar signals corrected for attenuation are much less sensitive to the value of  $S_1^*$  used in the Fernald's solution than the cases for 355 nm and 532 nm.

When we can assume that profiles for different wavelength are similar to each other in their shape, we can deduce the best estimate for  $S_1$ . Let us define a performance function  $J$  as a sum of square of difference between the backscatter profiles for wavelength  $\lambda$  and  $\lambda^*$  as follows:

$$J(S_1, S_1^*) = \sum_{j_1}^{j_2} [\ln \beta_1(z_j; S_1) - \ln \{ A \cdot \beta_1^*(z_j; S_1^*) \}]^2$$

where  $S_1$  and  $S_1^*$  are the extinction to backscatter ratio for  $\lambda$  and  $\lambda^*$ , respectively;  $z_j$  is the altitude level;  $j_1$  and  $j_2$  are the lower and upper limits for estimating the performance function; and  $A$  is a constant that is determined to minimize  $J(S_1, S_1^*)$  for the combination of  $S_1$  and  $S_1^*$ . In the present analysis, the simplest mapping procedure is applied to determine  $S_1$  and  $S_1^*$  which would produce the minimum  $J$ .

Assuming the wavelength dependence of backscatter and extinction are expressed as

$$\beta_1 = \beta_1^* (\lambda / \lambda^*)^{-\delta} \quad \text{and} \quad \alpha_1 = \alpha_1^* (\lambda / \lambda^*)^{-\gamma}$$

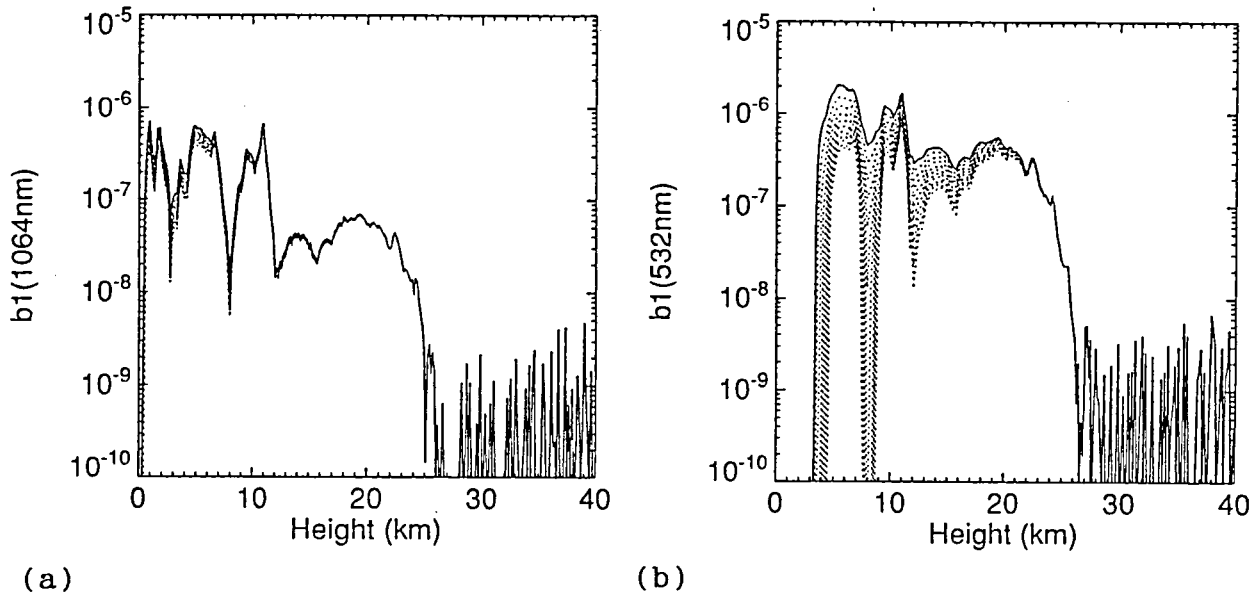


Fig.2 Backscatter coefficient profiles corrected for attenuation due to aerosols using the Fernald equation: (a) for 1064 nm, (b) for 532 nm. The dotted curves are the corrected profiles with  $S_1$  from 10 (top) to 90 (bottom). The solid curve is for no attenuation correction ( $S_1 = 0$ ).

then

$$S_1 = S_1^* (\lambda / \lambda^*)^{-(\gamma - \delta)}.$$

The exponents  $\delta$  and  $\gamma$  can be estimated in an average sense from  $\beta_1$  and  $\beta_1^*$  which are the solutions for the best estimates of  $S_1$  and  $S_1^*$ , respectively.

### 3. Results

Preliminary analysis was done for the data obtained during the period from December 1991 to March 1992. The US Standard Atmosphere was used to calculate an air molecule (Rayleigh) backscatter coefficient profile for use in the Fernald's solution.

Fig. 3(a-c) shows contour maps of  $J(S_1, S_1^*)$  calculated for combinations of the lidar signals of (a) 355 nm and 1064 nm, (b) 532 nm and 1064 nm, and (c) 355 nm and 532 nm which were obtained during the night of March 4, 1992 (JST). Altitude ranges for calculating the performance function is from 15 km to 22 km. The best estimate for  $S_1$  for 355 nm ranges from 10 to 12 (Fig.3a) and that for 532 nm ranges from 32 to 42 (Fig.3b), corresponding to  $S_1^* = 0$  and 100 for 1064 nm, respectively.

Fig.3c indicates that the best estimate for  $S_1$  (355 nm) and  $S_1^*$  (532 nm) are 11 and 37, respectively. The value of  $\delta$  and  $\gamma$  is estimated as 1.4 and -1.6, and optical thickness for 532 nm for the stratospheric aerosols (from 15 km to 30 km) is 0.104 for this particular case.

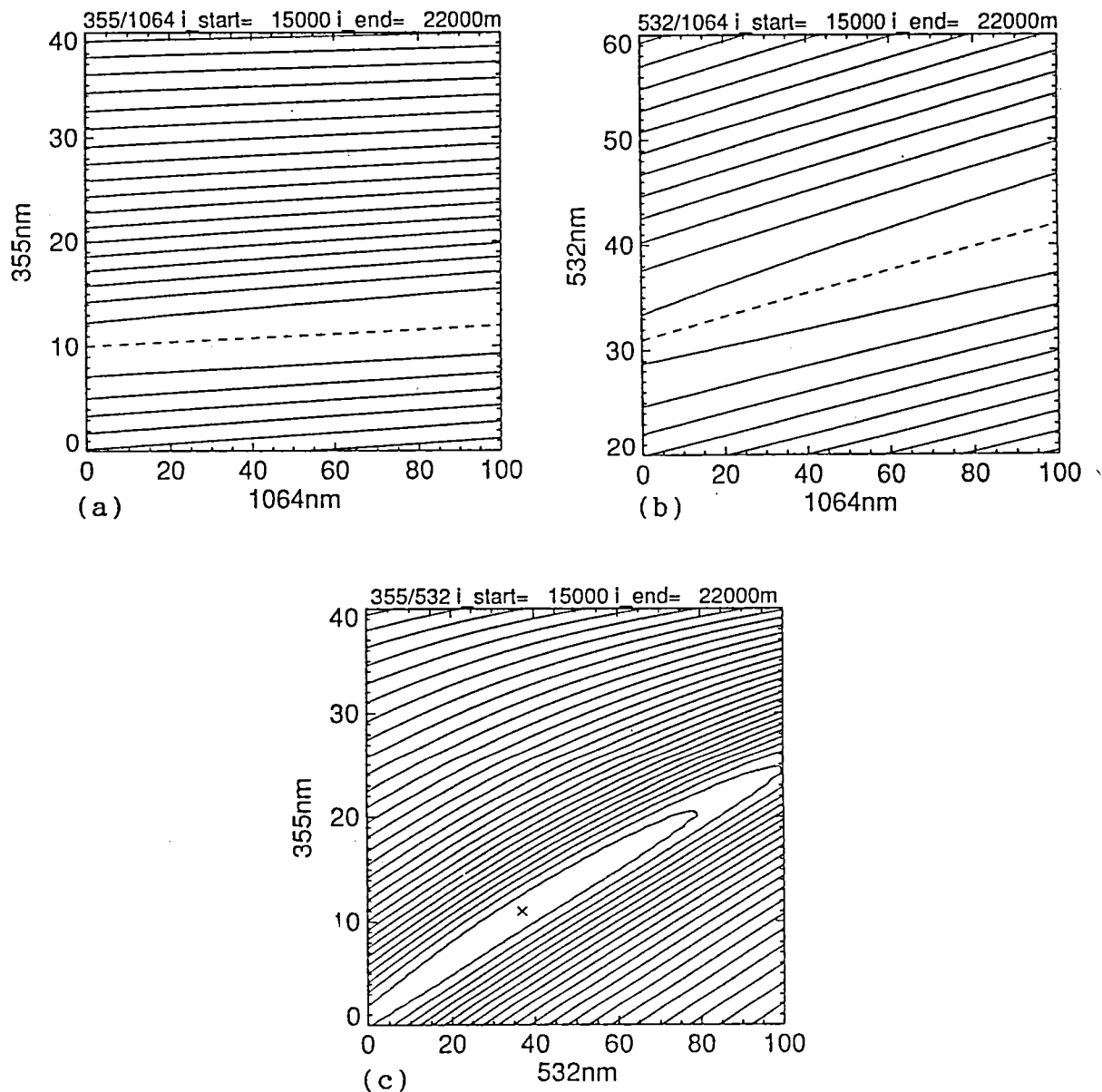


Fig.3 A contour map for the performance function  $J(S_1, S_1^*)$  calculated for the lidar signals: (a) 355 nm and 1064 nm, (b) 532 nm and 1064 nm, (c) 355 nm and 532 nm.

Reference

Fernald, F. G.: Appl. Opt., 23, 652 (1984)  
 Sasano, Y. and E. V. Browell: Appl. Opt., 28,1670 (1989)

## LIDAR OBSERVATIONS OF THE PINATUBO STRATOSPHERIC AEROSOL CLOUD OVER FRASCATI, ITALY.

Fernando Congeduti, Alberto Adriani, Gian Paolo Gobbi and Sante Centurioni  
Istituto Fisica dell'Atmosfera, CNR, C.P. 27, Frascati, Italy

The Pinatubo eruptions of June 1991 introduced large plumes (EOS, 1991) into the local stratosphere. On several occasions, volcanic gases and particles reached altitudes of about 30 km, quickly spreading to the west.

A lidar system has been almost continuously operated in Frascati (41.8N, 12.7E), Italy, to monitor the evolution of the stratospheric aerosol cloud. It employs a frequency doubled Nd-YAG laser (200 mJ @532 nm), and a 50 cm diameter Cassegrain telescope. The signal is digitized by means of a 12 bit, averaging transient recorder, and stored on PC for successive analysis. Vertical resolution of the traces is 300 m. Pressure and temperature soundings are also used to calculate the air density values needed in the calibration of the lidar trace.

The evolution of the Pinatubo cloud was depicted in fig. 1. The backscattering ratio profiles of eight different measurements taken during the period July '91 - March '92 were chosen to summarize the most significative, occurrences of the event. The backscattering ratio,  $R$ , is defined as the ratio of the lidar signal (aerosol plus molecule backscatter) to the expected pure molecular one retrieved by pressure and temperature sounding. Radiosonde temperature as well as CIRA model profiles (dotted line) (Rees et al., 1990) are also reported in fig. 1. Twenty days after the first eruption, the first signature of the volcanic aerosol cloud was detected by the lidar 14 km over Frascati. The upper portion of the cloud at an altitude of 23 km, was observed above our site on September 4, 1991. The maximum scattering ratio ( $R \approx 14$ ) was measured on October 17th. A first analysis (fig. 2) shows that, three and a half months after the eruption, the aerosol perturbation generated by Pinatubo reached and exceeded the maximum loads, observed 11 months after the El Chichon (Gobbi et al., 1989) event. At that time the volcanic cloud over Frascati extended from the tropopause up to 30 km. Since the beginning of the stronger winter planetary wave activity, the Pinatubo cloud integrated backscatter exceeded El Chichon's. Such behavior followed a monthly pattern. In

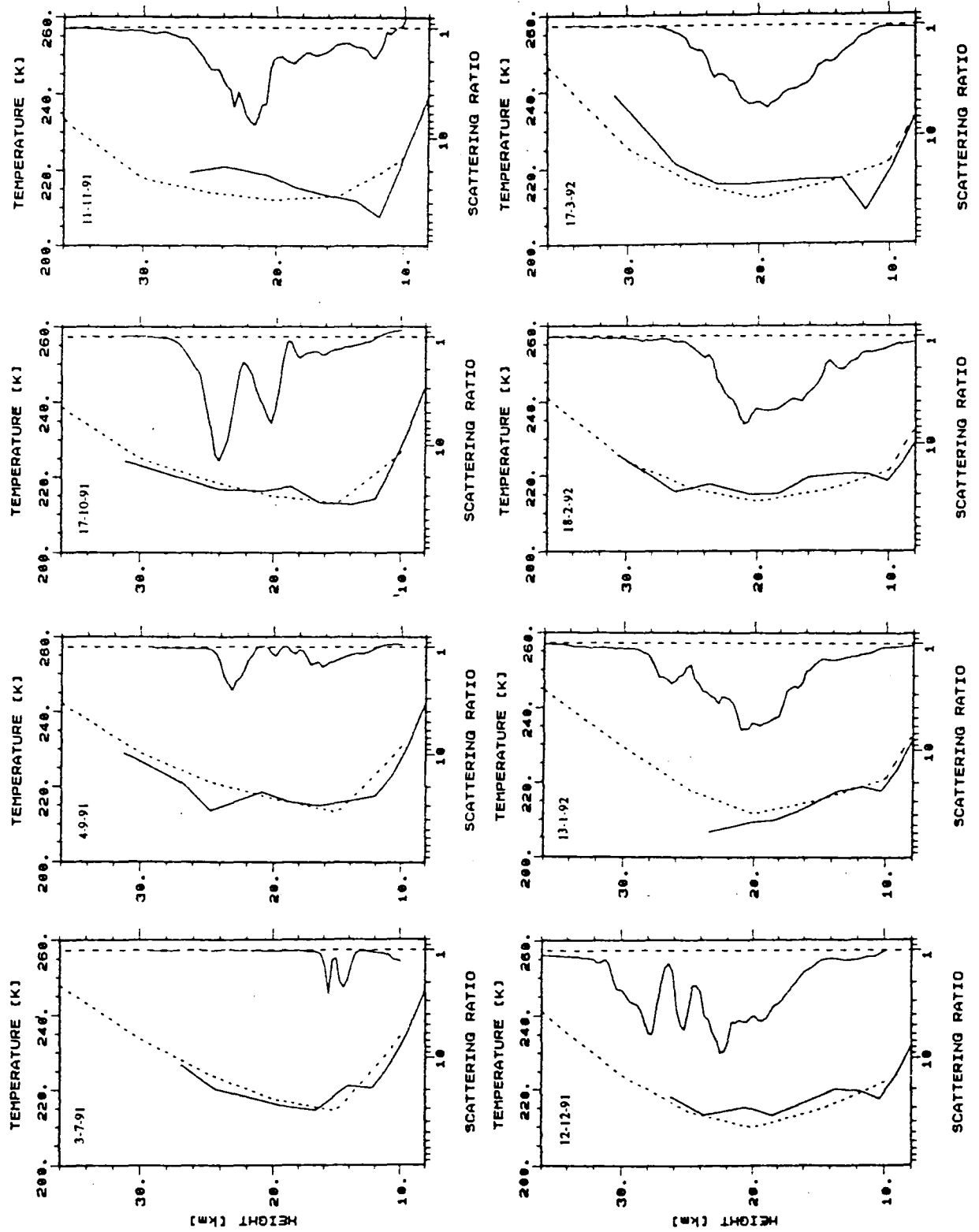


Fig. 1

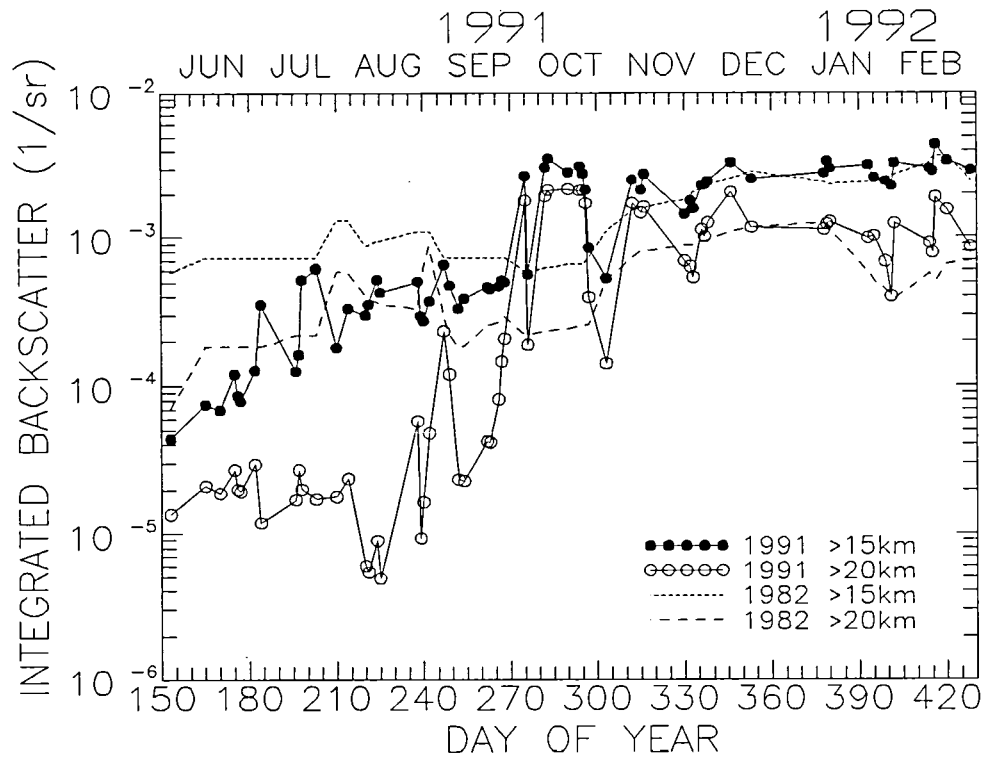


Figure 2

spite of an aerosol integrated backscatter 4 times larger than El Chichon's in October, the column content for the two events seemed to converge by the end of the year. In this context, the perturbation generated by El Chichon's can only be assumed as a lower limit of the one which will follow the Pinatubo eruption.

The highest altitudes of the aerosol cloud were observed in mid-December when the upper layers extended beyond 31 km. Observations of the event are still in progress.

#### References

- EOS, Pinatubo cloud measured, *Trans.Am.Geophys.Un.*, 72, 305-306, 1991.
- Gobbi, G.P., A. Adriani, and F. Congeduti, Stratospheric aerosol mass content estimated by lidar after El Chichon eruptions, *J.Geophys.Res.*, 94, 9909-9916, 1989.
- Rees, D., J.J. Barnett and K. Labitzke, CIRA (COSPAR International Reference Atmosphere) 1986, *Adv. Sp. Res.*, 10, 12, Pergamon Press, 1990.



# L625 Lidar Measurements of Pinatubo Volcanic Cloud at Hefei

Huanling Hu     Jun Zhou  
Anhui Institute of Optics and Fine Mechanics  
Hefei, Anhui 230031 China

## I. Introduction

Pinatubo volcano (15.14°N, 120.35°E) erupted violently between June 9-17, 1991, whose eruption was much larger than El Chichon volcano in April of 1982. Because of its important effects on the globe environment, much attention was focused on the measurements of the volcanic cloud. The 84 scattering-ratio profiles of the volcanic cloud have been obtained by our L625 lidar system at Hefei (31.32°N, 117.17°E) between July 19, 1991 and March 8, 1992.

## II. L625 Lidar System and Measurement Method

L625 lidar system[1] consists of a double frequency YAG laser (wavelength 532nm), emitting 120mj per pulse at a repetition rate of 1 Hz, a receiving telescope of diameter 625mm, and a photon counting unit. A high-speed mechanical chopper can cut the strong-intensity signal before it is amplified by the PMT (RCA 31034A02). The height resolution is 600m, normally. The whole system, which is controlled by an IBM/PC computer, is set on the top floor of a building with a dome ceiling.

In order for one PMT to cover the whole signal range of about three orders of magnitude from 6km to 35km, the measurement is divided into two steps. In the first step, an averaged profile, for 500 laser shots, of return signal is obtained at relatively low altitudes (about 6-25km), when the chopper opens at 6km and a neutral attenuator with transmittance of 38% is inserted in front of the PMT. Thus, the photon arrival rate is small enough to eliminate the pulse-pair error. At the second step, the chopper is adjusted to cut off the return signals from the altitudes below 10km, and the attenuator is taken away, so that the return signal can be recorded from higher altitudes (10-35km). The whole measurement takes about 40 minutes. A 'grand composite' profile spanning the altitude region of interest between 6km and 35km can be formed by matching the above two profiles.

The lidar backscattering ratio (or scattering ratio) is defined as

$$R(z)=[B_a(z)+B_m(z)]/B_m(z)=1+B_a(z)/B_m(z) \quad (1)$$

where  $B_m(z)$  and  $B_a(z)$  are, respectively, the molecular and aerosol backscattering functions. The  $B_m(z)$  is calculated from radiosonde data or Elterman model[2]. The scattering ratio  $R(z)$  is calculated by evaluating

$$R(z)=kN_s(z)Z^2/B_m(z)/Q^2(z) \quad (2)$$

where  $N_s(z)$  is photon number of return signal,  $Q^2(z)$  is the

two-way atmospheric transmittance, and  $k$  is a system constant determined by normalizing the right-hand side of Eq. (2) to an expected minimum value ( $R_{min}=1.01$ ) of  $R$  over a specified altitude range (10-15km or 28-32km). In calculation of the transmittance  $Q^2(z)$ , molecular extinction is from radiosonde or model, and aerosol extinction is calculated directly from the aerosol backscattering function by using extinction-backscattering ratio values of 22, 40, 43 over the height ranges of 15-20km, 20-25km, and 25-30km[3] respectively. The Eq. (2) is solved using updated value for aerosol extinction for iterations.

### III. Features of Pinatubo volcanic cloud measured at Hefei

The 84 profiles of Pinatubo volcanic cloud have been obtained by L625 lidar since July 19, 1991. Figs. 1,2,3 show the variations of peak scattering ratio, cloud thickness (ratio > 2.0), and aerosol optical depth between 10km and 30km with the day number after Pinatubo eruption (June 9, 1991).

Pinatubo volcanic cloud was observed at Hefei for the first time on July 19, 1991. Its peak scattering ratio, at the height of 21.3km, was upto 8.80, about 7 times of the normal one (for example, May 16 of 1991). From July 19 to Aug. 21, 1991, the cloud thickness was thin (0.6-1.8km), the peak ratio and the optical depth were only 2-3 times of normal ones except Aug. 8, which indicates that Pinatubo cloud invaded at Hefei not long before July 19, although no measurements were taken for about one month before July 19 because of the serious flood and cloudy sky in the area.

The peak scattering ratio values varied violently in a large range from 2.0 to 44.1 in the period from July 19 to Sep. 5. The fact reveals that the cloud was extremely inhomogeneous in the beginning. The peak ratio kept a high level from Sep. 13 of 1991 to Jan. 13 of 1992. Most of the values were between 10.0 and 20.0. Since Jan. 14, 1992, the peak ratio kept a relatively low level, whose values were between 5.0 and 9.0.

The cloud top expanded slightly from about 21km to 25km during the first 33 days, and then kept a nearly same level of about 25km. But, the cloud bottom declined slowly and steadily from about 20km to 15km.

Since the 80th day after the eruption, the optical depth was almost one order of magnitude larger than the one before the eruption (for example, 0.013 on May 16, 1991). In comparison of Fig.3 with Fig.1, there is close correlation between optical depth and the peak scattering ratio. Thus, the large optical depth depends mainly on the dense part of the cloud.

#### Conclusion:

(1) Pinatubo volcanic cloud was present over Hefei after about 40 days from its eruption.

(2) The peak scattering ratio varied violently in July and August of 1991 with largest one of 44.1 on Aug. 8, oscilated mildly between about 10 and 20 from September to middle of January of 1992, and then kept a relatively stable low level with mean value of 7.16 from Jan. 14 to March 8, 1992.

(3) The height of the peak scattering ratio is between about 18km and 25km. The cloud thickness increased from 0.6km to 10km approximately. The cloud top expanded upward slightly, and the cloud bottom declined downward steadily from about 20km to 15km.

(4) Since Aug. 28, 1991, the optical depth was about one order of magnitude larger than before the eruption.

### References

- [1] Hu, H., R. Xue, K. Tan, J. Zhou, Proc. II of 15th ILRC, 284, 1990
- [2] Elterman, L., AFCRL-68-0153, 1968.
- [3] Jager, H. and D. Hofmann, Appl. Opt., 30, 127(1991).

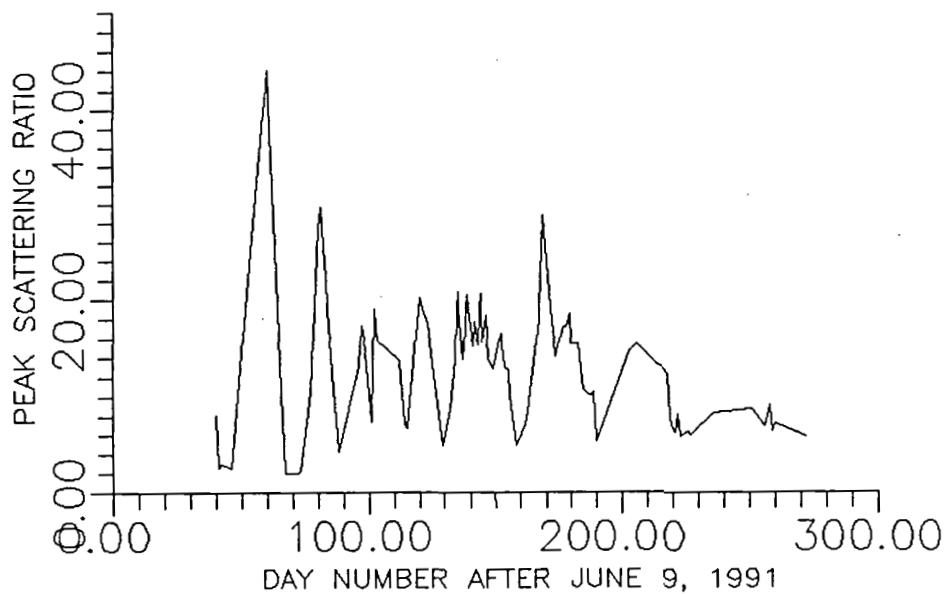


FIG.1 VARIATION OF PEAK SCATTERING RATIO

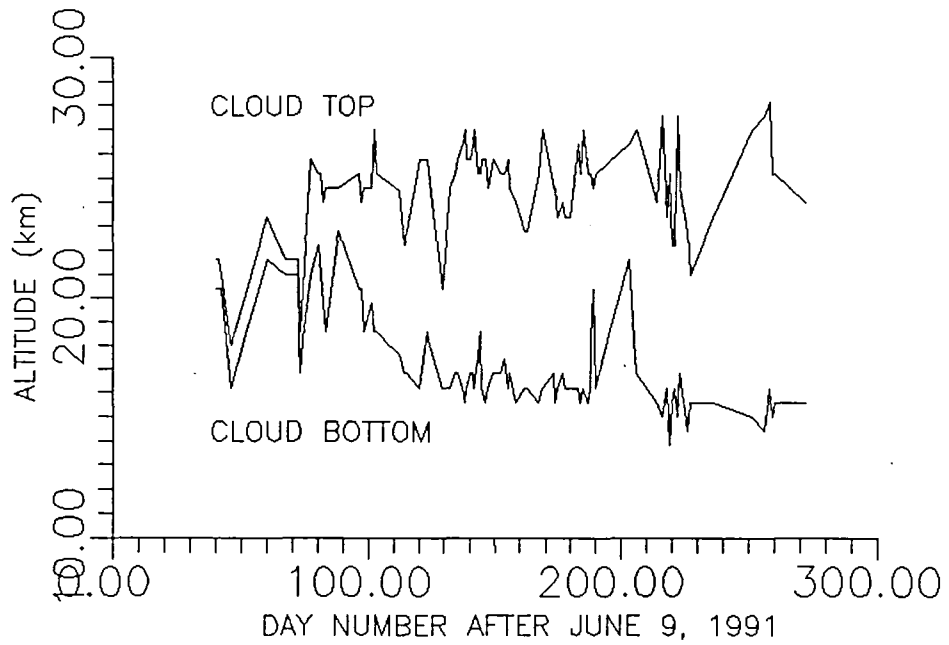


FIG.2 CLOUD THICKNESS (SCATTERING RATIO 2.0)

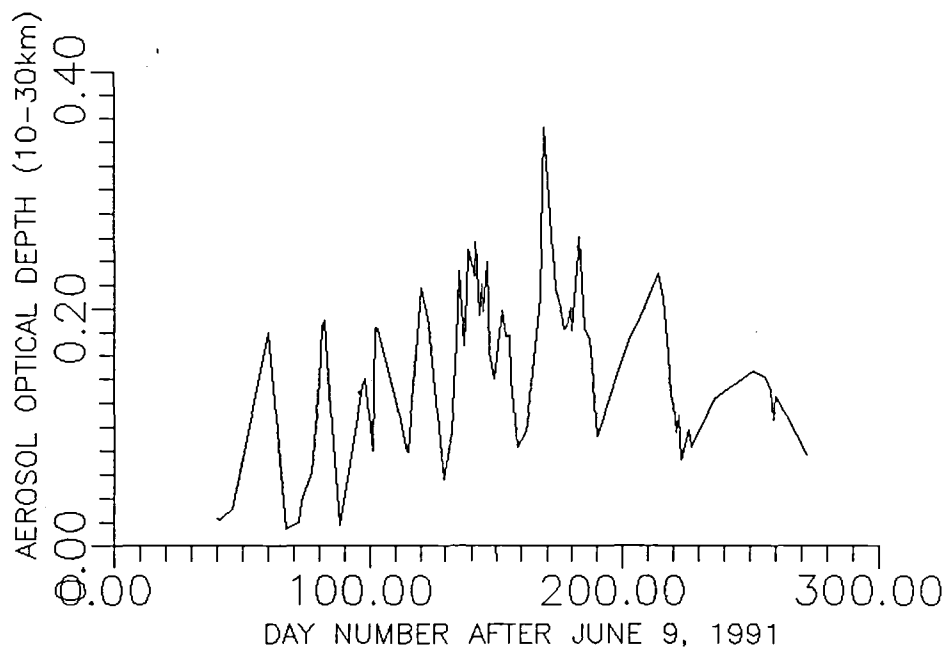


FIG.3 VARIATION OF AEROSOL OPTICAL DEPTH (10km - 30km)

# Two Wavelength Measurements of the Pinatubo Aerosol above Toronto, Canada

W. Steinbrecht, D. Donovan and A.I. Carswell

Institute for Space and Terrestrial Science and

Department of Physics and Astronomy, York University

4700 Keele Street, North York, Ont., Canada M3J 1P3, 416-736-5249, Fax: -736-5516

## 1 Introduction

Since March 1991 our group has been routinely operating a Differential Absorption Lidar system in Toronto, Canada (42.80 N, 79.50 W, 200 m). The system is based on a XeCl Excimer laser. We have also been running a Backscatter Lidar based on a NdYAG laser. The parameters of both systems are given in [1].

In the period from March 1991 to March 1992 measurements have been taken during about 40 nights with the DIAL system and more than 90 nights with the NdYAG system. In all measurements after July 21, 1991 we have observed aerosol layers in the stratosphere, resulting from the Mt. Pinatubo (15.14 N, 120.35 E) eruptions around June 15, 1991. These aerosol layers interfere significantly with many optical remote sensing techniques, and we have been investigating their properties with our two Lidar systems. In this paper we present a summary of these measurements.

## 2 Aerosol Backscatter Ratio

The backscatter ratio  $R(r)$  compares the measured total aerosol plus molecular backscattering coefficient ( $\beta_{tot}(r) = \beta_{Mie} + \beta_{Rayleigh}$ ) at each altitude with the molecular backscatter coefficient  $\beta_{Rayleigh}$ .

$$R(r) = \frac{\beta_{Mie}(r) + \beta_{Rayleigh}(r)}{\beta_{Rayleigh}(r)} \quad (1)$$

For a purely molecular atmosphere  $R = 1.0$  and additional backscattering from aerosols increases the backscatter ratio to  $R > 1.0$ .

The formula used to derive the backscatter Ratio,  $R(r)$ , from lidar signals is

$$R(r) = \frac{r^2 P(r)}{C' \beta_{Rayleigh}(r)} \exp \left\{ -2 \int_r^{r_{norm}} \alpha(r') dr' \right\} \quad (2)$$

where  $P(r)$  is the Lidar return signal from altitude  $r$ ,  $\alpha(r)$  is atmospheric extinction coefficient and  $C'$  is a constant including the instrument constant of the lidar as well as the two

way transmission of the atmosphere from ground to the normalization altitude  $r_{norm}$ .  $C'$  is chosen to give  $R(r_{norm}) = 1$ .

The molecular backscatter coefficient  $\beta_{Rayleigh}(r)$  is calculated using data from balloonsondes launched about 2 km east of the lidar site every weekday at 11 am (EST) by the Atmospheric Environment Service in Toronto. The sondes usually reach a maximum altitude of about 34 km. Since the lidar return signals from this altitude are quite strong we are able to normalize our backscatter profiles above the Pinatubo aerosol layers at altitudes where only the molecular backscattering is significant. This is preferable to a normalization at the altitude of the tropopause, where significant amounts of aerosol may be present.

### 3 Measurements

Figure 1 shows three dimensional representations of the backscatter ratio measured at 532 nm between June 29 1991 (Julian day 180) and October 7 1991 (Julian day 280). Fig.2 shows the same measured at 353 nm between September 2 1991 (Julian day 245) and October 31 1991 (Julian day 304). The backscatter ratio in both plots has not been corrected for aerosol extinction, so the backscatter ratio below strong layers may be underestimated by up to 40 %. It should be noted that the last part in Fig. 1 overlaps with the first part of Fig. 2. The large peak at about 24 km and around day 270, shows up at the end of Fig. 1, but in the beginning (foreground) of Fig. 2. Note how all the features are enhanced at 532 nm, because the cross sections change less dramatic with wavelength for Mie scattering ( $\propto \lambda^{-\eta}$ ,  $\eta \approx 1.6$ ) than for Rayleigh scattering ( $\propto \lambda^{-4}$ ). The Pinatubo aerosol cloud arrived over Toronto in the third week of July 1991, in two layers at 17 and 22 km. The layer at 17 km existed throughout the whole period from July to the end of October. The average backscatter ratio in this layer is about 1.3 at 353 nm and 2.2 at 532 nm, increasing with time at both wavelengths. The layer at 22 km disappears at around day 240. The average backscatter ratio in this layer is about 2.7, higher than in the lower layer. Around day 260 a layer appears for a few days at about 23 km. This layer can hardly be seen in Fig. 2, but shows up quite clearly at 532 nm (Fig. 1). At the end of September (around day 270) a very strong layer arrives at about 24 km, with a peak backscatter ratio of 2 at 353 nm and 5 at 532 nm. This layer seems to return around day 305 (see Fig. 2), however the maximum has now increased to over 5 at 353 nm and the whole layer has grown more intense. It is possible that the layer has been travelling around the earth in 35 days, with the particles growing, thereby increasing the backscatter ratio. If this is the case this particular cloud would have been travelling  $\approx 830$  km/day or  $10^6$  m/s or  $10^6$ /day. Stowe et al. [2] and McCormick et al. [3] found that the main eruption plume was moving east in westerly winds at about 17-20 km with speeds of 30 m/s and 20 m/s in the second week of July 1991 and first week of August 1991 respectively. This transport, however, was in a different wind regime, at low latitudes and altitudes below 21 km.

### 4 Depolarization

The YAG lidar transmits linearly polarized light at 532 nm and the receiver has two channels, recording the backscattered intensity with polarization parallel ( $P_{\parallel}(r)$ ) and perpendicular

Lidar Backscatter Ratio at 532 nm

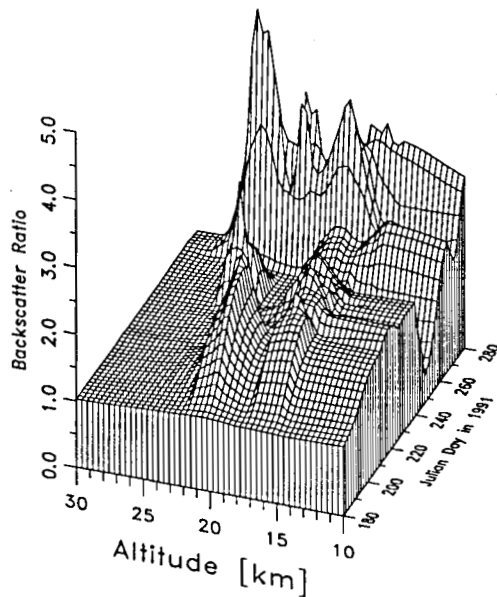


Figure 1: Backscatter ratio at 532 nm between 29 June 1991 (day 180) and 7 Oct. 1991 (day 280).

Lidar Backscatter Ratio at 353 nm

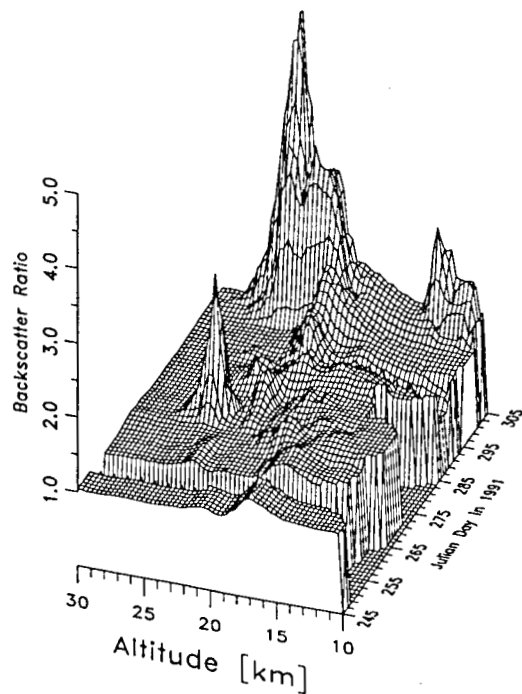


Figure 2: Backscatter ratio at 353 nm between 2 Sept. 1991 (day 245) and 31 October 1991 (day 304).

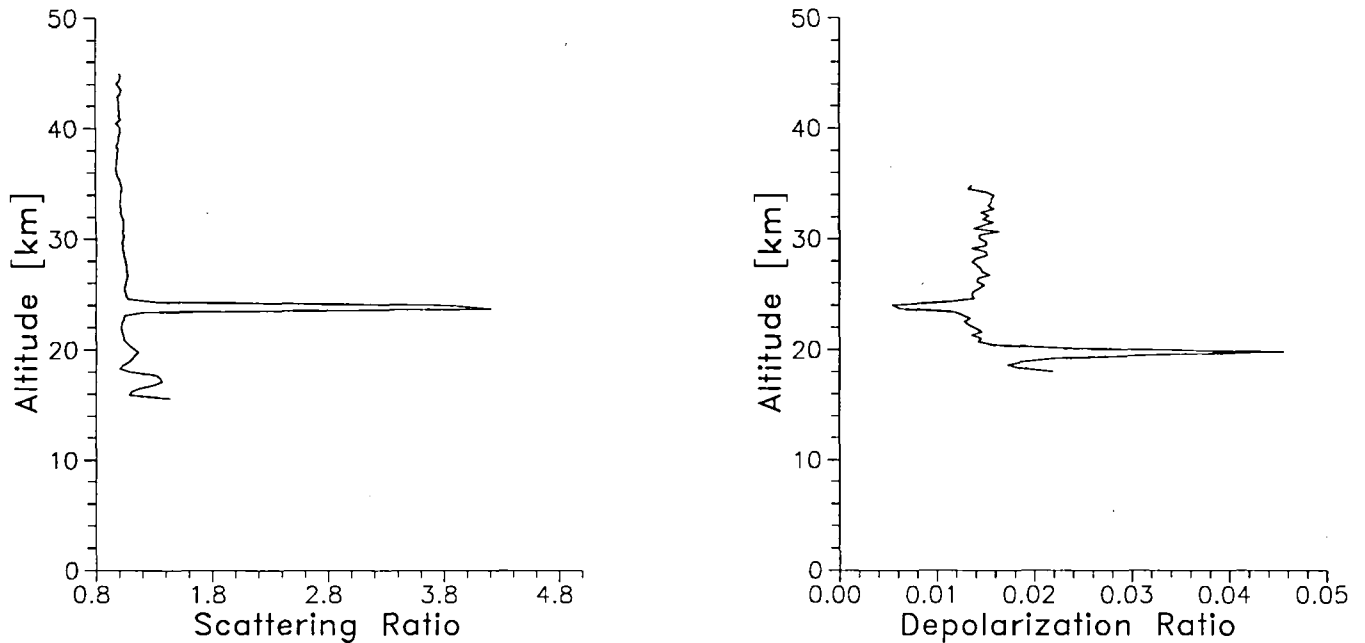


Figure 3: Backscatter Ratio and Depolarization at 532 nm measured above Toronto on September 4th 1991

( $P_{\perp}(r)$ ) to the transmitted polarization. Since backscattering from spherical particles does not change the polarization, a departure of the linear depolarization ratio  $\delta(r) = P_{\perp}/P_{\parallel}(r)$  from zero indicates scattering from nonspherical particles (or multiple scattering). Figure 3 shows an example of measured depolarization. There is a layer with a very high backscatter ratio at 24 km, and another layer of enhanced backscattering at 19 km. The depolarization of the lower layer is about 5 %, the depolarization of the purely molecular atmosphere outside the layers is about 1.4 %. However the layer at 24 km has a depolarization of only 0.6 %, less than the Rayleigh depolarization. This indicates that the scatterers in the upper layer are spherical (probably  $H_2SO_4/H_2O$  droplets), whereas the lower layer contains a significant amount of nonspherical scatterers. These may be either be frozen particles, or solid crustal material.

## References

- [1] A. I. Carswell, S. R. Pal, W. Steinbrecht, J. A. Whiteway, A. Ulitsky, and T-Y. Wang. Lidar Measurements in the Middle Atmosphere. *Can. J. Phys.*, **69**(8):1076 – 1086, 1991.
- [2] L. L. Stowe, R. M. Carey, and P. P. Pellegrino. Monitoring the Mt. Pinatubo Aerosol Layer with NOAA/11 AVHRR Data. *Geophys. Res. Lett.*, **19**(2):159 – 162, 1992.
- [3] M. P. McCormick and R. E. Veiga. SAGE II Measurements of Early Pinatubo Aerosols. *Geophys. Res. Lett.*, **19**(2):155 – 158, 1992.
- [4] A. T. Young. Rayleigh Scattering. *Physics Today*, **35**(1):42 – 48, 1982.

# Lidar Observations of the Pinatubo Volcanic Cloud Over Hampton, Virginia

M. T. Osborn<sup>1</sup>, D. M. Winker<sup>2</sup>, D. C. Woods<sup>2</sup>, and R. J. DeCoursey<sup>1</sup>

<sup>1</sup> Hughes STX Corporation, Hampton, VA

<sup>2</sup> Atmospheric Sciences Division, NASA Langley Research Center, Hampton, VA

## *Introduction*

A series of eruptions of the Philippine Mt. Pinatubo volcano in June 1991 climaxed in cataclysmic eruptions on June 15-16, which greatly perturbed the stratospheric aerosol layer. These eruptions yielded an estimated 20 megatonnes of SO<sub>2</sub>, which is about three times the amount produced by the eruptions of El Chichon in 1982 (Bluth et al., 1991). Lidar measurements taken at 694 nm by the 48-inch lidar system at Langley Research Center (LaRC) in Hampton, Virginia, show the vertical distribution, intensity and spread of the Pinatubo aerosol layers over this mid-latitude location. A few observations have also been made from Hampton using the 14-inch airborne lidar, which measures scattering and depolarization at 532 nm. The magnitude and transport time of the volcanic aerosol layers following Pinatubo and El Chichon are compared. In addition, comparisons are made between the ground-based lidar measurements and near-coincident Stratospheric Aerosol and Gas Experiment (SAGE) II satellite observations of the Pinatubo aerosol layers.

## *48-Inch Lidar System*

Routine ground-based ruby lidar measurements have been taken at LaRC, Hampton, Virginia (37.1°N, 76.3°W), since May 1974. These lidar measurements provide high-resolution vertical profiles of the stratospheric and upper tropospheric aerosols. The lidar system, often referred to as the 48-inch lidar system because of its 48-inch telescope, has evolved over the years and provides a valuable long-term history of the mid-latitude stratospheric aerosol (Fuller et al., 1988).

In mid-1990 the system was taken out of operation to be moved from a mobile trailer to a laboratory setting. During the move, the telescope primary and secondary mirrors were polished and recoated. The system was reassembled in late spring of 1991 and routine observations commenced on June 13. A new data acquisition system became operational on August 6, just a few days after the first aerosol layers from the Pinatubo eruption were observed. The new system employs 12-bit CAMAC-based digitizers controlled by a PC clone computer. The new system replaced a 10-bit Biomation transient recorder, providing greatly improved stability and accuracy.

## *Observations*

The lidar scattering ratio, defined as the ratio of the aerosol plus Rayleigh backscattering function to the Rayleigh backscattering function, is the primary result of the analysis of the lidar measurements. The Rayleigh backscatter is obtained from pressure and temperature profiles from radiosondes launched at Wallops Island, Virginia (120 km northeast of the lidar system). Lidar profiles, consisting of approximately 100-400 laser shots, are averaged to a vertical resolution of 0.15 km and normalized to a scattering ratio of 1. All profiles are adjusted iteratively for transmission losses due to aerosol extinction.

An aerosol layer from Pinatubo was first detected at LaRC on August 3, 1991. The last observation showing background conditions was made on July 18. Clouds prevented observations between July 18 and August 3. Between August 3 and March 11, 1992, 40 sets of lidar measurements were taken and analyzed, showing the vertical distribution, intensity, and

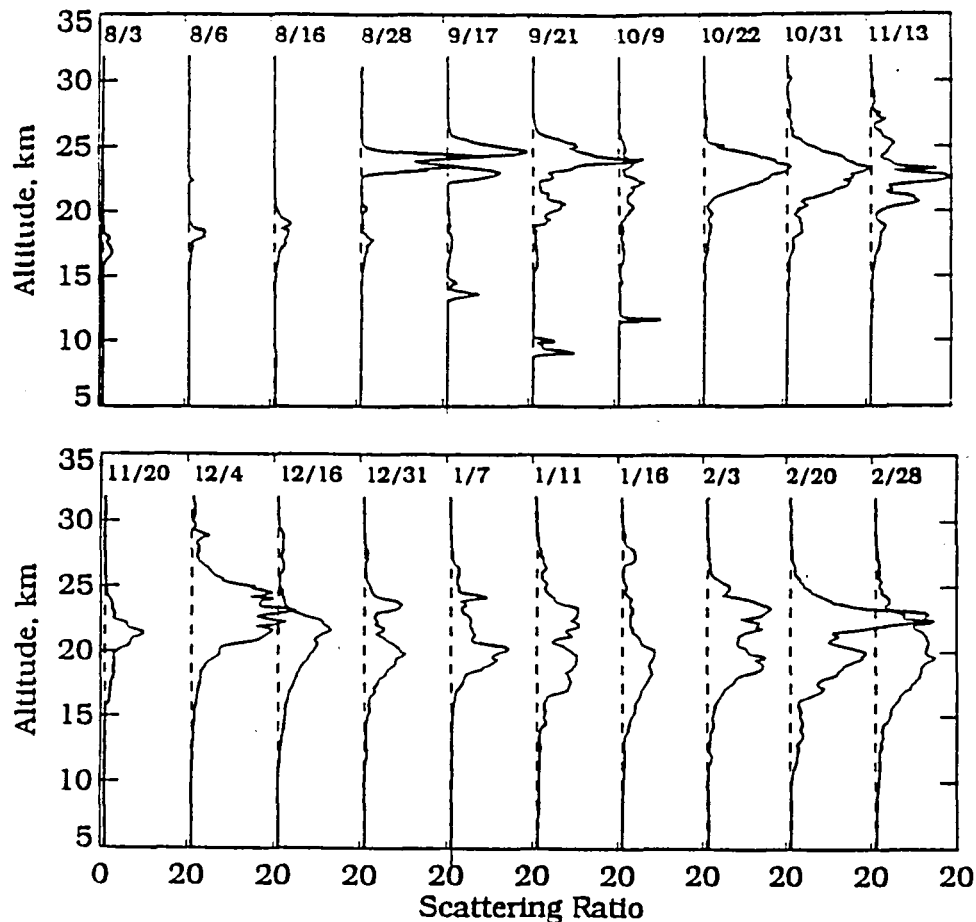


Figure 1. Lidar scattering ratio profiles taken by the LaRC 48-inch lidar system between August 3, 1991, and February 28, 1992.

spread of the Pinatubo aerosol layers over this mid-latitude location. Figure 1 summarizes these measurements by showing the scattering ratio profiles obtained on 20 of the measurement dates. As can be seen in this figure, low altitude layers (< 20 km) from Pinatubo were the first to arrive over LaRC. The first sighting of a layer above 24 km occurred on August 28. The magnitude and vertical distribution of the aerosol layers varied widely from one measurement date to the next, but there is a general increase in the amount of aerosol detected throughout this period (August 1991-February 1992). Pinatubo aerosol layers above 30 km were first detected on October 31. Starting in about December it was necessary to normalize scattering ratio profiles above 30 km since there was a significant amount of aerosol in the troposphere. Typical minimum tropospheric scattering ratios were greater than 1.2, a value which corresponds to the maximum stratospheric scattering ratio obtained just prior to the eruption of Mount Pinatubo. The lidar measurement on February 20 was the largest observed to date, exhibiting a peak scattering ratio of 34 at 22.4 km. It is likely that this relatively high altitude layer was tropical in origin and combined with lower altitude Pinatubo layers present throughout the winter.

A contour plot of scattering ratio versus altitude and time (days since eruption on June 15) is shown in Figure 2. This figure includes all of the lidar profiles obtained through March 11, 1992, and illustrates the gradual descent and broadening of the Pinatubo aerosol layer over time.

The integrated aerosol backscatter, defined here as the integral of the aerosol backscattering function from the tropopause to 30 km, provides a good measure of the amount of stratospheric aerosol loading at a given location. Figure 3 compares the time history of integrated backscatter at

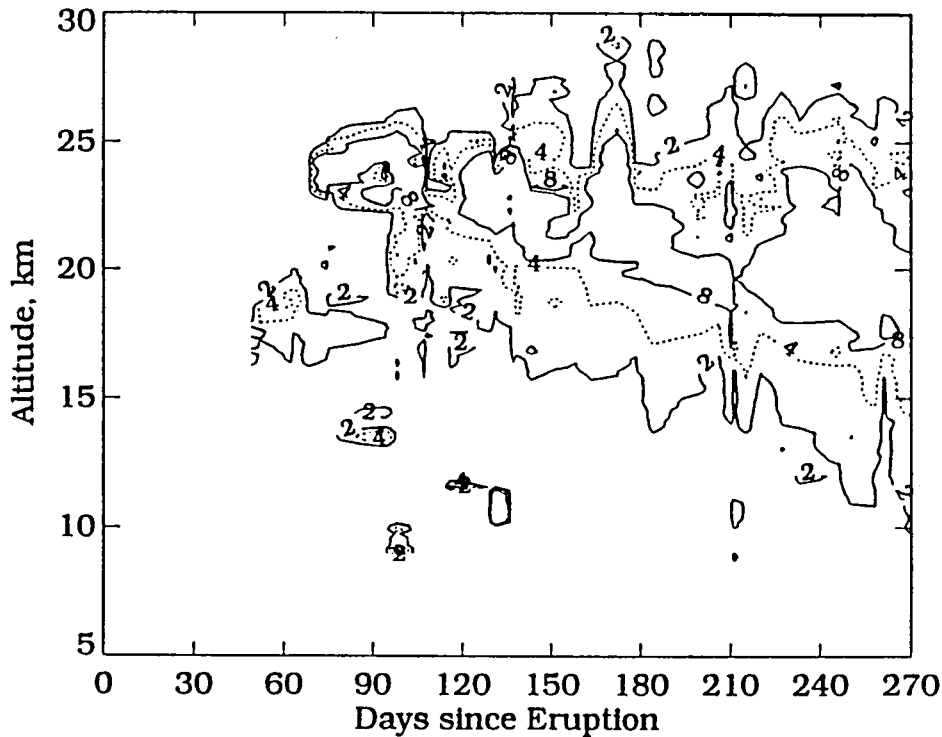


Figure 2. Contour plot of 48-inch lidar scattering ratio vs. altitude and days since eruption of Pinatubo on June 15.

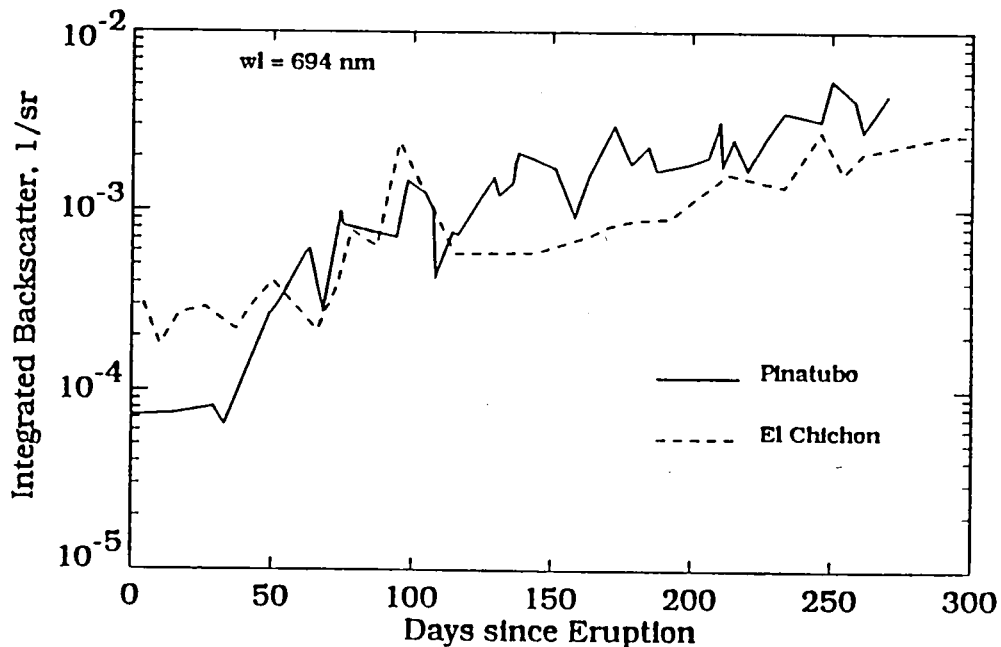


Figure 3. Time history of integrated stratospheric aerosol backscatter measured at LaRC following the eruptions of El Chichon and Pinatubo.

LaRC following the eruptions of both Pinatubo (15.1°N, 120.4°E) and El Chichon (17.3°N, 93.2°W). The increase seen is due to a combination of aerosol formation and growth via gas-to-particle conversion, and a general poleward transport of the aerosol from its initial concentration in the tropics. The background aerosol level preceding the eruption of El Chichon was higher than the

level preceding Pinatubo due to several smaller volcanic eruptions in 1980 and 1981. The first volcanic aerosol layer from El Chichon reached Hampton on May 10, 1982, approximately 42 days after the first major eruption on March 28, 1982, whereas the first volcanic aerosol layer from Pinatubo was measured 48 days after the eruption. These transport times are very similar, especially since the first Pinatubo aerosol layer may have arrived a few days earlier. The integrated backscatter measured for the first 100 days after each eruption is similar. However, after approximately 120 days, the Pinatubo integrated backscatter consistently exceeds the values measured after El Chichon. As of mid-March 1992, the largest Pinatubo integrated backscatter, .0053 1/sr, occurred on February 20, 1992, 250 days after the eruption. This is approximately twice the maximum loading due to El Chichon, which occurred 245 days after the eruption.

The lidar backscatter measurements at LaRC were compared with several overpasses of the SAGE II satellite instrument (McCormick, 1987). Figure 4 shows the comparisons obtained on October 24 and December 31, 1991. The lidar data were smoothed to match the 1 km vertical resolution of the satellite data and converted to aerosol extinction at 1020 nm, using an extinction-to-backscatter ratio of 36.8 sr, calculated directly from the integrated lidar backscatter and SAGE II extinction measurements obtained on October 24. The error bars reflect the 1- $\sigma$  uncertainties in the SAGE II and the lidar-converted extinction measurements. The comparison on October 24 is excellent at all altitudes above the tropopause (14 km), showing a similar sensitivity to size distribution for the two measurements (Wang et al., 1990). The SAGE II observation on December 31 represents a case when the SAGE II instrument was saturated due to the large Pinatubo aerosol layer. Nevertheless, the comparison is also excellent down to the saturation altitude and provides a means of estimating stratospheric aerosol loading when the satellite measurements saturate above the tropopause.

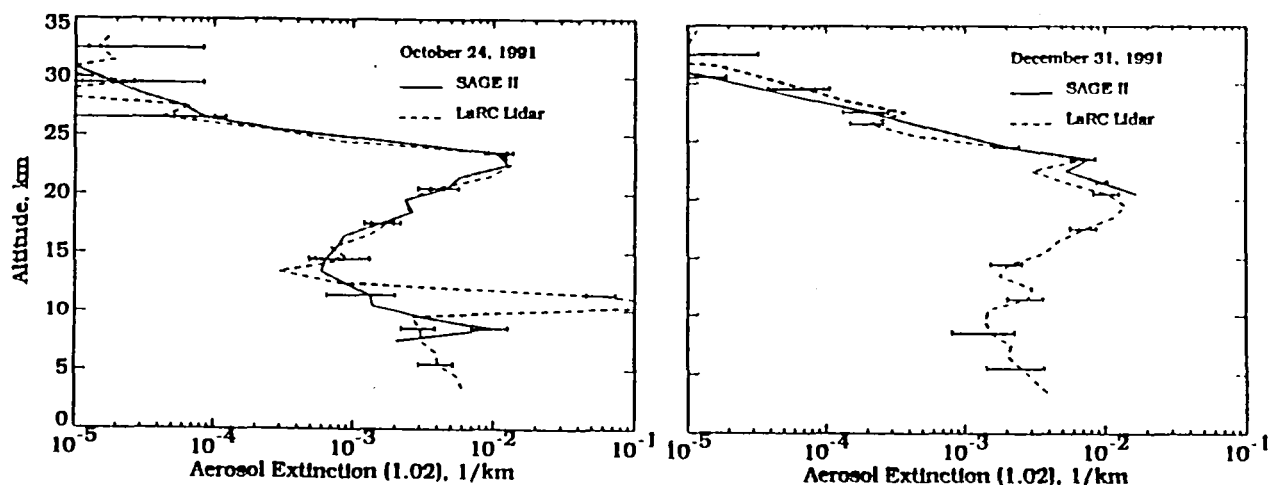


Figure 4. Comparison of profiles of lidar-derived extinction with SAGE II 1.02- $\mu$ m extinction.

#### References

- Bluth, Gregg J. S., Scott D. Doiron, Charles C. Schnetzler, Arlin J. Krueger, and Louis S. Walter, Global tracking of the SO<sub>2</sub> clouds from the June 1991 Mount Pinatubo eruptions, *Geophys. Res. Letts.*, **19**, 151-154, 1992.
- Fuller, W. H., Jr., M. T. Osborn, and W. H. Hunt, 48-inch lidar aerosol measurements taken at the Langley Research Center: May 1974 to December 1987, NASA RP 1209, October 1988.
- McCormick, M. P., SAGE II: An Overview, *Adv. Space Res.*, **7**, 219-226, 1987.
- Wang, Pi-Huan, M. P. McCormick, and M. T. Osborn, Conversion of SAGE II aerosol extinction-to-backscatter, Abstracts for Fifteenth International Laser Radar Conference, Tomsk, USSR, 15-18, 1990.

## Ozone Measurements with the U.S. EPA UV-DIAL: Preliminary Results

H. Moosmüller,\* D. Diebel,<sup>†</sup> D. H. Bundy,<sup>‡</sup> M. P. Bristow,<sup>‡</sup> R. J. Alvarez II,<sup>‡</sup>  
V. A. Kovalev,<sup>°</sup> C. M. Edmonds,<sup>‡</sup> R. M. Turner,<sup>†</sup> and J. L. McElroy<sup>‡</sup>

\* Desert Research Institute, University of Nevada, P.O. Box 19040, Las Vegas, Nevada 89193

<sup>†</sup> Environmental Research Center, University of Nevada, 4505 Maryland Parkway, Las Vegas, Nevada 89154

<sup>‡</sup> U.S. Environmental Protection Agency, P.O. Box 93478, Las Vegas, Nevada 89193

<sup>°</sup> Permanent address: Main Geophysical Observatory, Karbysheva St. 7, 194018 St. Petersburg, Russian Federation

A compact airborne down-looking lidar system has been developed at the Environmental Protection Agency in Las Vegas.<sup>1</sup> This differential absorption lidar (DIAL) has been designed to simultaneously measure range-resolved concentrations of ozone (O<sub>3</sub>) and sulfur dioxide (SO<sub>2</sub>) in the lower troposphere, together with an indication of the aerosol distribution. The five laser wavelengths (i. e.,  $\lambda_1 = 277$  nm,  $\lambda_2 = 292$  nm,  $\lambda_3 = 313$  nm,  $\lambda_4 = 319$  nm,  $\lambda_5 = 369$  nm) have been generated via Raman conversion of a focused KrF excimer laser.<sup>2</sup> The system is currently installed in a truck-based mobile laboratory. For the ground testing, an opening in the truck floor together with a folding mirror under the truck makes a horizontal, or upwardly inclined direction of measurement possible.

Initial ground testing has been performed in the vicinity of a Desert Research Institute (DRI) ambient air monitoring site, located at Cottonwood Cove (latitude 35° 29' N, longitude 114° 42' W) approximately 85 km south east of Las Vegas, Nevada. At this site O<sub>3</sub> and SO<sub>2</sub> concentrations are continuously monitored with an average accuracy better than  $\pm 10\%$ .<sup>3</sup> A temporary ozone measurement station with identical accuracy was set up at a distance to get a second point of comparison for the range-resolved DIAL measurements.

The lidar return signal  $S$  as a function of distance  $r$  is described by the lidar equation

$$S(r, \lambda) = A(r, \lambda) C(\lambda) \frac{\beta(r, \lambda)}{r^2} e^{-2 \int_0^r \sigma(x, \lambda) dx}, \quad (1)$$

where  $A$  is the overlap integral between laser beam and field of view of the telescope,  $C$  the system constant,  $\beta$  the backscattering coefficient,  $\sigma$  the extinction coefficient, and  $\lambda$  the respective wavelength. Actual lidar return signals graphed as  $\ln(r^2 S)$

$$\ln(r^2 S) = \ln(AC\beta) - 2 \int_0^r \sigma dx \quad (2)$$

with a range resolution of  $\Delta r = 30$  m are shown as a function of  $r$  in Fig. 1.

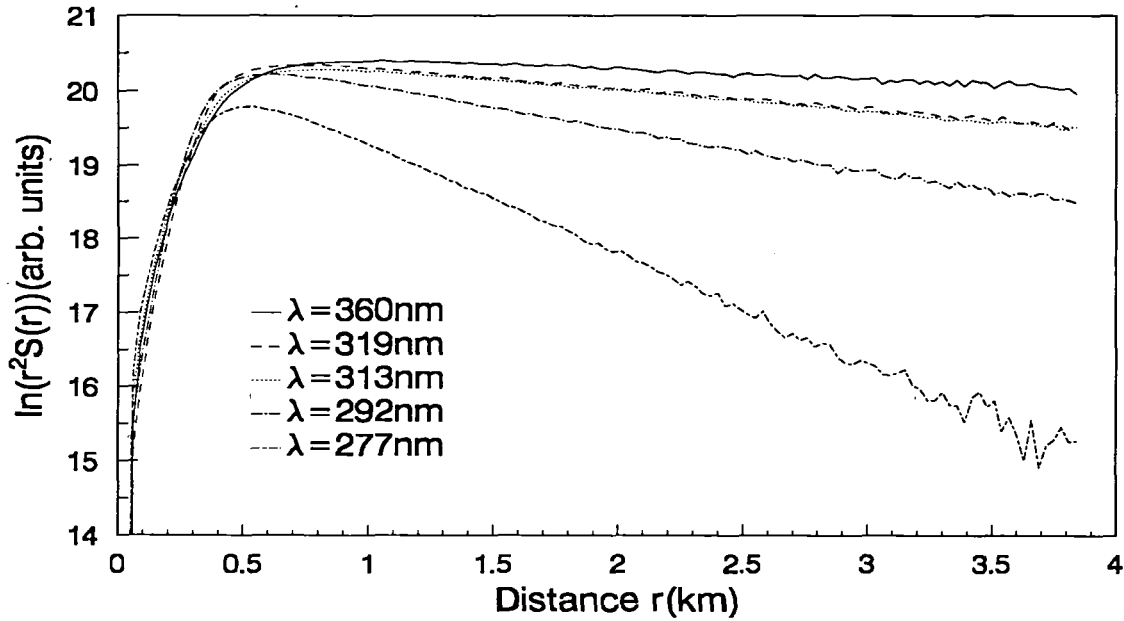


**Fig. 1:** Lidar Return Signals  $S(r)$  Graphed as  $\ln(r^2 S(r))$

For distances smaller than about 0.8 km the overlap integral  $A$  is a function of distance  $r$ , making  $\ln(r^2 S)$  a nonlinear function of  $r$ . For larger distances,  $\ln(r^2 S)$  is linear, indicating a homogeneous atmosphere. In this case the extinction coefficient  $\sigma$  may be calculated with the slope method,<sup>4</sup> resulting in  $\sigma(277 \text{ nm}) = 0.748 \text{ km}^{-1}$ ,  $\sigma(292 \text{ nm}) = 0.295 \text{ km}^{-1}$ ,  $\sigma(313 \text{ nm}) = 0.139 \text{ km}^{-1}$ ,  $\sigma(319 \text{ nm}) = 0.138 \text{ km}^{-1}$ , and  $\sigma(360 \text{ nm}) = 0.068 \text{ km}^{-1}$ , from a linear fit for  $\ln(r^2 S)$  between 1.5 km and 3.5 km. At  $\lambda_5 = 360$  nm, where the laser radiation is absorbed by neither  $\text{O}_3$  nor  $\text{SO}_2$ , the extinction coefficient is only about 10% larger than the Rayleigh extinction coefficient  $\sigma_R(360 \text{ nm}) = 0.0593 \text{ km}^{-1}$  at ambient conditions ( $p = 980$  mb,  $T = 25$  °C).<sup>4</sup> This Rayleigh scattering dominated homogeneous atmosphere was typical for all of our ground tests.

The extinction coefficient  $\sigma$  at a distance  $x$  and wavelength  $\lambda_i$  may be written as

$$\sigma(x, \lambda_i) = \sigma_s(x) + \alpha_i n(x), \quad (3)$$

where  $\sigma_s$  is the extinction due to scattering at  $\lambda_i$ ,  $\alpha_i$  denotes the absorption coefficient at  $\lambda_i$  and  $n$  the concentration of the absorbing gas. If Eq. 1 is applied at two different wavelengths  $\lambda_i$  and  $\lambda_j$ , the concentration  $n$  can be calculated from the resulting equations as

$$n(r) = \frac{1}{2\Delta\alpha_{ij}} \frac{d}{dr} \left( \ln \frac{S(\lambda)}{S(\lambda')} \right) - \frac{\Delta\sigma_{ij}(\lambda)}{\Delta\alpha_{ij}} + \frac{1}{2\Delta\alpha_{ij}} \frac{d}{dr} \left( \ln \frac{\beta(\lambda)}{\beta(\lambda')} \right) + \frac{1}{2\Delta\alpha_{ij}} \frac{d}{dr} \left( \ln \frac{A(\lambda)}{A(\lambda')} \right), \quad (4)$$

where  $\Delta\alpha_{ij} := \alpha_i - \alpha_j$  and  $\Delta\sigma_{ij} := \sigma_i - \sigma_j$ . The first term in Eq. 4 is the main term, the second term the extinction correction  $[E_{ij}]$ , the third term the backscatter correction  $[B_{ij}]$ , and the fourth term the overlap correction  $[O_{ij}]$ . For  $O_3$  measurements, the differential absorption coefficients  $\Delta\alpha_{ij}$  (at  $p = 980$  mb,  $T = 25^\circ\text{C}$ ) for the most important wavelength pairs are  $\Delta\alpha_{1,2} = 0.00932 \text{ ppb}^{-1}\text{km}^{-1}$ ,  $\Delta\alpha_{1,3} = 0.01195 \text{ ppb}^{-1}\text{km}^{-1}$ , and  $\Delta\alpha_{2,3} = 0.00263 \text{ ppb}^{-1}\text{km}^{-1}$ . The resulting Rayleigh extinction correction is  $[E_{1,2}] = 3.6 \text{ ppb}$ ,  $[E_{1,3}] = 5.7 \text{ ppb}$ , and  $[E_{2,3}] = 13.1 \text{ ppb}$ . This correction is in first order approximation independent of atmospheric density. For a homogeneous atmosphere the backscatter correction  $[B_{ij}]$  can be taken as zero. The overlap correction  $[O_{ij}]$  can improve the results in the near field, but it has not been included in this brief description. A calculation of  $O_3$  concentrations corresponding to the extinction coefficients derived from Fig. 1 yields:  $O_3(\lambda_1, \lambda_2) = 45.0 \text{ ppb}$ ,  $O_3(\lambda_1, \lambda_3) = 45.3 \text{ ppb}$ , and  $O_3(\lambda_2, \lambda_3) = 46.4 \text{ ppb}$ , in agreement with the *in situ* measurement ( $45.6 \text{ ppb} \pm 10\%$ ). The precision at  $(\lambda_2, \lambda_3)$  is expected to be worse, as this wavelength pair is better suited for higher  $O_3$  concentrations.<sup>1</sup> The  $O_3$  concentrations from the wavelength pairs  $(\lambda_1, \lambda_3)$  and  $(\lambda_2, \lambda_3)$  are susceptible to a weak  $\text{SO}_2$  interference. However corrections have not been made as the ambient  $\text{SO}_2$  concentration was below 1 ppb.

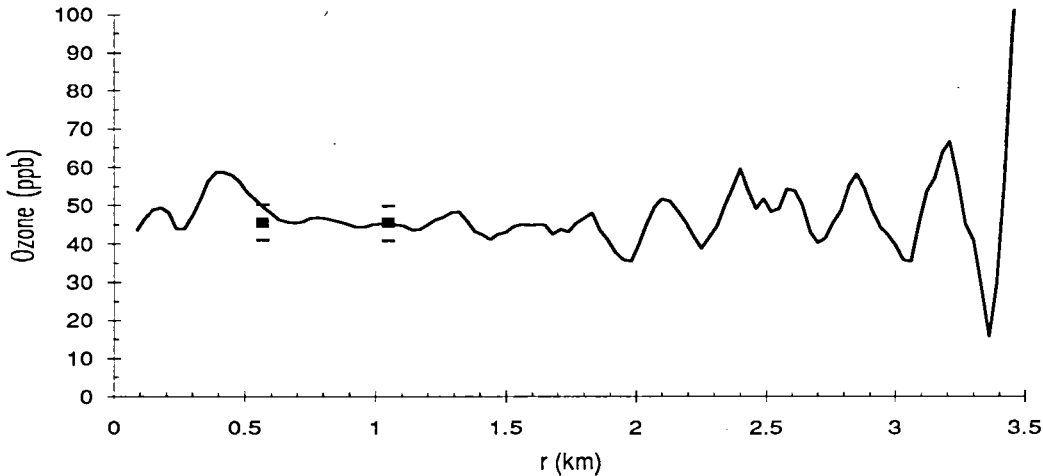


**Fig. 2:** UV-DIAL Ozone Concentrations (Solid Line) in Comparison with *In Situ* Measurements

A range-resolved analysis of the same data set is obtained by 9-point linear regressions of the log-ratio in Eq. 4. The results are shown in Fig. 2, together with the simultaneous

results from the DRI stations at 0.57 km and 1.05 km. The variations of the DIAL data in the near field ( $r \leq 0.6$  km) are due to the variation of the overlap term  $[O_{i,j}]$  as a function of  $r$ . For larger distances the fluctuations are ascribed mainly to photomultiplier nonlinearities. Beyond about 2 km, the decreasing signal to noise ratio increases the error of the DIAL measurements drastically. It is planned to reduce this problem by  $r^2$ -modulating the photomultiplier gain, and thereby increasing the useful range of the system.

Ozone concentrations as a function of time are presented in Fig. 3. UV-DIAL data at  $r = 1.05$  km have been compared with *in situ* ozone measurements of the second station. The comparison generally shows good agreement within the accuracy of the *in situ* measurement.

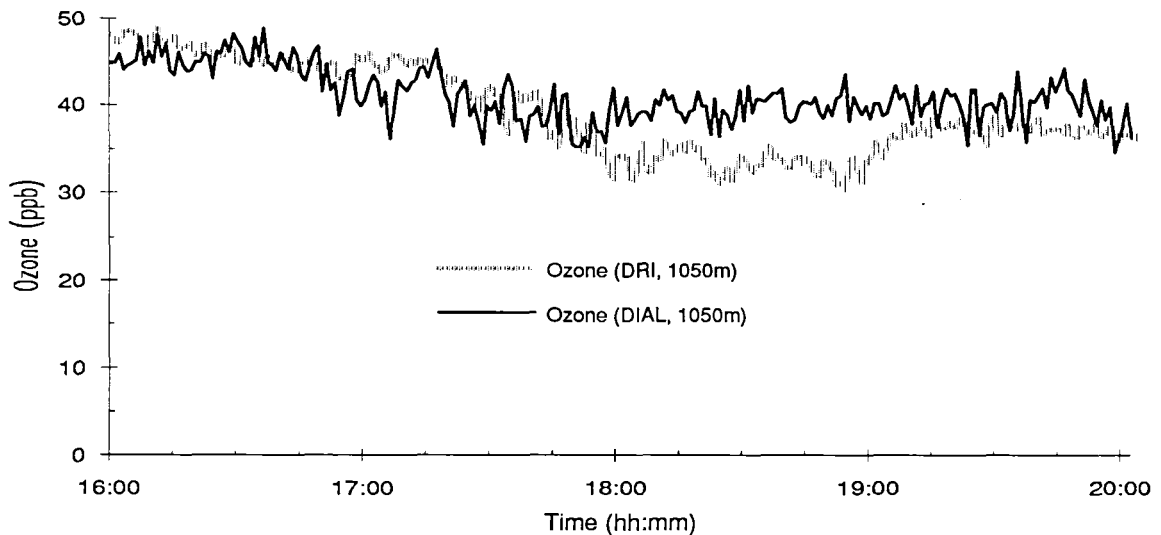


**Fig. 3:** Ozone Concentrations at  $r = 1.05$  km as a Function of Time

Initial flight testing of the UV-DIAL system is planned for May 1992 in the Western Great Lakes area. Results will be reported at the conference.

**References:**

1. H. Moosmüller, D. Diebel, D. H. Bundy, M. P. Bristow, C. M. Edmonds, R. M. Turner, V. A. Kovalev, R. P. Haas, and J. L. McElroy, "The U.S. EPA airborne UV-DIAL system," *Technical Digest on Optical Remote Sensing of the Atmosphere*, volume 18, Optical Society of America (Washington, D.C., 1991), p. 253-255.
2. D. Diebel, M. P. Bristow, and R. Zimmermann, "Stokes shifted laser lines in KrF-pumped hydrogen: reduction of beam divergence by addition of helium," *Appl. Opt.* **30**, 626-628 (1991).
3. W. G. Coulombe, A. W. Gertler, and T. E. Hoffer, "Ozone concentrations in two rural southwest desert areas," In *Tropospheric Ozone and the Environment*, R. L. Berglund, D. R. Lawson, and D. J. McKee, eds., Air & Waste Management Association (Pittsburgh, PA, 1991), p. 704-716.
4. R. M. Measures, *Laser Remote Sensing* (Wiley, New York, 1984).

## **Lidar Development for the Atmospheric Radiation Measurement (ARM) Program**

**J. Griffin**  
Applied Physics Center  
Pacific Northwest Laboratory  
Richland, WA 99352

**M. Lapp**  
Sandia National Laboratories  
Livermore, CA 94551

The Atmospheric Radiation Measurement (ARM) Program<sup>1</sup> was initiated by the Department of Energy's Atmospheric and Climate Research Division (DOE/ACRD) to improve parameterizations of cloud radiative effects in general circulation models of the Earth's climate. The Instrument Development Program (IDP), a major component of ARM, is directed toward the improvement of radiometric and remote sensing instrumentation pertinent to near real-time characterizations of atmospheric parameters. The ultimate goal of this program is to provide state-of-the-art instruments suitable for installation and extended use in ARM's field measurement component, the Cloud and Radiation Testbed (CART).

Remote sensing instrumentation is particularly important to CART measurement activities, supporting the evaluation and improvement of computer codes for the quantification of instantaneous radiative fluxes. For these activities, it is important to measure, in near real-time, all atmospheric parameters pertinent to the transport of solar, atmospheric, and terrestrial radiative fluxes and the deposition of energy into the Earth's troposphere. Radiatively important parameters include: vertical distributions of water vapor and other "greenhouse" gases, vertical distributions of solid and liquid aerosols, and physical and optical properties of clouds (cloud morphology, base height, phase, optical scattering and extinction cross sections).

The ARM IDP component is presently supporting the development of four laser remote sensing systems appropriate for characterization of all these atmospheric variables. A Polarization Diversity Lidar (PDL) is being developed at the University of Utah for real-time monitoring of cloud altitude and hydrometeor phase (liquid and/or ice). At the University of Wisconsin, a High Spectral Resolution Lidar (HSRL) is being assembled for the measurement of vertical aerosol distributions, aerosol scattering cross sections and backscatter-to-extinction ratios. Instrument development activities at NASA

Goddard Space Flight Center include the design of an eye-safe, solid-state laser ceilometer for measurement of cloud base height. Finally, a collaborative effort between Sandia National Laboratories and NASA/Goddard Space Flight Center is aimed at development of a field-hardened Raman lidar system for daytime and nighttime measurements of vertical water vapor distribution, possibly including scanning.

Plans are being evolved presently to combine data from the constituent laser remote sensing and radiometric measurement systems at the CART sites — a "sensor/data" fusion activity that offers a unique challenge to the ARM Program. For example, in order to conduct studies of cloud formation, maintenance, and dissipation it is desirable to track the fate of water vapor from near ground level up to the altitudes where condensation, nucleation, coalescence, and ice formation occur. To achieve this microphysical time history, it will be extremely important to insure that the lidar systems are: (1) illuminating the same or physically equivalent atmosphere/cloud coordinates; (2) sampling comparable volumes; (3) acquiring data at similar bandwidths (i.e., comparable time responses for the different remote sensing systems); and (4) acquiring and processing data of similar "quality." In the process envisioned, "data quality" is particularly important since, for example, verification of lidar-derived aerosol parameters (particulate number densities, optical properties, and moments of the size distribution) is extremely difficult. Of advantage is the fact that the different lidar techniques to be utilized in acquiring aerosol data for CART activities provide some key *complementary* information, so that the ensemble of instrumentation is far more powerful than simply the sum of the individual components in determining a useful physical picture of the aerosol field.

Since the ultimate objective of the ARM Program is to provide a better understanding of cloud radiative effects, it also will be necessary to correlate these laser remote sensing measurements of water vapor and cloud/aerosol parameters with ground-based radiometric observations of visible and infrared fluxes. These radiometric observations will nearly always be acquired with different measurement parameters (e.g., field-of-view, measurement bandwidth,...) than those associated with the remote sensing systems, thus compounding the difficulty of the "sensor/data" fusion problem. This paper will describe problems involved in the fusion of CART laser remote sensing data as well as fusion of this data with coincidentally-acquired ground-based short- and long-wave radiometric observations. We use as baseline inputs to the discussion descriptions of the IDP lidars, as well as data acquired with them during field campaigns conducted in

November-December 1991 in Coffeyville, Kansas — the NASA-led FIRE Cirrus (First ISCCP Regional Experiment) and the joint NASA/DOE SPECTRE (Spectral Radiance Experiment) campaigns.

#### References

1. Atmospheric Radiation Measurement Program Plan, February 1990, DOE/ER-0441. (Available from the National Technical Information Service, U. S. Department of Commerce, Springfield, Virginia 22161.)



# LIDAR MEASUREMENTS OF STRATOSPHERIC OZONE, TEMPERATURE AND AEROSOL DURING 1992 UARS CORRELATIVE MEASUREMENT CAMPAIGN

Thomas J. McGee<sup>1</sup>, Upendra N. Singh<sup>2</sup>, Michael Gross<sup>2</sup>, William S. Heaps<sup>1</sup>,  
and Richard Ferrare<sup>3</sup>

1. Environmental Sensor Branch, Code 917  
NASA/Goddard Space Flight Center  
Greenbelt, MD 20771

2. Hughes STX Corporation,  
4400 Forbes Blvd.  
Lanham, MD 20706

3. Universities Space Research Association  
Laboratory for Atmospheres, Code 917  
NASA/Goddard Space Flight Center  
Greenbelt, MD 20771

Measurements of stratospheric ozone, temperature and aerosols were made by the NASA/GSFC mobile stratospheric lidar during the UARS (Upper Atmospheric Research Satellite) Correlative Measurement Campaign at the JPL-Table Mountain Facility (34.4 °N, 117.7 °W) in February and March 1992. Due to the presence of substantial amounts of residual volcanic aerosol from the eruption of Mt. Pinatubo, the GSFC lidar system (*McGee et al., 1991*) was modified (*Singh et al., 1992*) for an accurate measurement of ozone concentration in the stratosphere. While designed primarily for the measurement of stratospheric ozone, this lidar system has also been used to measure middle atmosphere temperature and density from 30 to 65 km (*McGee et al., 1991*) and stratospheric aerosol from 15 to 35 km (*McGee et al., 1991A*). In the following sections, we will briefly describe and present some typical measurements made during this campaign. Stratospheric ozone, temperature, and aerosols profiles derived from data taken between February 15 and March 20, 1992 will be presented at the conference.

## STRATOSPHERIC OZONE

A new Raman Differential Absorption Lidar (DIAL) technique has been employed to derive the continuous ozone profile from 15 to 50 km (*Singh et al., 1992*) in the presence of heavy aerosol loading due to the eruption of Mt. Pinatubo. Prior to this new scheme, no lidar ozone measurements were possible below about 30 km. Using this technique, we were able to retrieve the only lidar ozone data in the lower stratosphere. This is particularly important since previously there had been no ground truth available for the UARS instruments in this altitude region.

Data taken during February 1992 at JPL-Table Mountain Facility has been analyzed and Figure 1 shows three complete vertical profiles of ozone from 15 to 50 km along with the appropriate MAP and US Standard models. Agreement can be seen to be quite good.

## STRATOSPHERIC TEMPERATURE

We use the off-line wavelength (351 nm) of the GSFC DIAL system to derive the temperature profiles between 30-75 km altitude range. The XeF laser emits about 150 mJ/pulse and operates at 70 Hz. During a typical night of operation, 600,000 shots are accumulated, from which the temperature profile is derived. A more complete description of the system and the technique is described by *McGee et al., 1991*.

The relative atmospheric density is obtained from the 351 nm lidar return using the method described in *Ferrare et al., 1992*. The temperature profile is computed for the derived relative density profile using the hydrostatic equation and the ideal gas law (*Chanin and Hauchecorne, 1984*). Figure 2 shows the vertical temperature profiles for the same three nights in February for which ozone profiles are shown (Figure 1). The temperature retrieval is not valid below 30 km, because of the presence of aerosols.

## STRATOSPHERIC AEROSOLS

Using the Rayleigh/Raman lidar technique one can directly measure both the aerosol scattering ratio and extinction. Raman measurements of aerosol extinction and Pinatubo stratospheric aerosols have been recently discussed in detail (*Ansmann et al., 1990, 1991*). We have utilized this technique to derive an average profile of aerosol extinction (Figure 3) in the stratosphere. These measurements were used to correct the low altitudes ozone profiles. Profiles of aerosol scattering ratio were also obtained by inverting the returns from 351 channel (*Fernald, 1984*) and are shown in Figure 4. The measurements at the lower altitude is limited to 24 km due to saturation in that channel. Modifications to the GSFC lidar to include a low altitude Rayleigh channel at 308 and 351 nm are now underway. We will provide at the conference, the information regarding the vertical distribution of the Pinatubo aerosol and indicate how this distribution varies with time.

## ACKNOWLEDGEMENTS

The authors wish to thank S.H. Melfi and D. Whiteman for helpful discussions in the design and development of this experiment. We also wish to thank them for the loan of several optics necessary to the design. The research has been supported by the NASA Upper Atmosphere Program. Thanks also to the staff of the JPL Table Mountain Facility where the data were taken.

## REFERENCES

Ansmann, A., M. Riebesell, and C. Weitkamp, "Measurement of atmospheric aerosol extinction profiles with a Raman lidar," *Optics Letters*, 15, No. 3, 746-748, 1990.

- Ansmann, A., U. Wandinger, C. Schulze, C. Weitkamp, and W. Michaelis, "Stratospheric aerosol measurements with a combined Raman elastic-backscatter lidar," in *Proceedings of Optical Remote Sensing of the Atmosphere*, November 1991, Williamsburg, VA. 1991.
- Chanin, M.L. and A. Hauchecorne, "Lidar studies of temperature and density using Rayleigh scattering," Handbook for MAP, SCOTSEP 13, 87-99, 1984.
- Fernald, F.G., "Analysis of atmospheric lidar observations: some comments," *Appl. Opt.* **23**, 652-653, 1984.
- Ferrare, R.A., T.J. McGee, D. Whiteman, J. Burris, M. Owens, and J. Butler, "Lidar Measurements of stratospheric Temperature during STOIC," to be submitted to *J. Geophys. Res.*, 1992
- McGee, T.J., D. Whiteman, R. Ferrare, J.J. Butler, and J. Burris, "STROZ-LITE: Stratospheric Ozone Lidar Trailer Experiment," *Opt. Eng.* **30**, 31-39, 1991.
- McGee, T.J., M. Gross, U. Singh, "353 nm lidar measurements of the Mt. Pinatubo aerosol cloud," postdeadline paper in *Proceedings of Optical Remote Sensing of the Atmosphere*, November 1991, Williamsburg, VA. 1991A.
- Singh, U.N., T.J. McGee, M. Gross, W.S. Heaps, and R. Ferrare, "A new Raman DIAL technique for measuring stratospheric ozone in the presence of volcanic aerosols", in *Proceedings of 16th International Laser Radar Conference*, Cambridge, MA., 20-24 July 1992.

Fig. 1: STROZ-LITE Ozone Concentration Profiles from the UARS  
Correlative Measurement Campaign at JPL-TMO 1992.

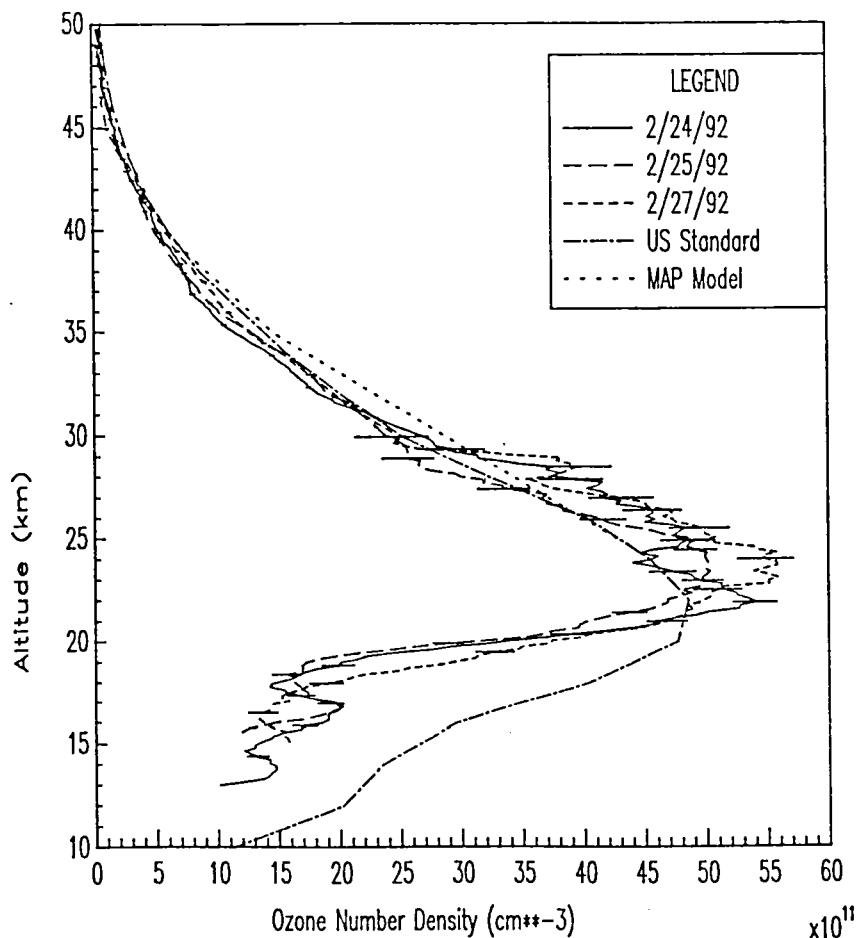


Fig. 2: STROZ-LITE Temperature Profiles from the UARS Correlative Measurement Campaign at JPL-TMO 1992.

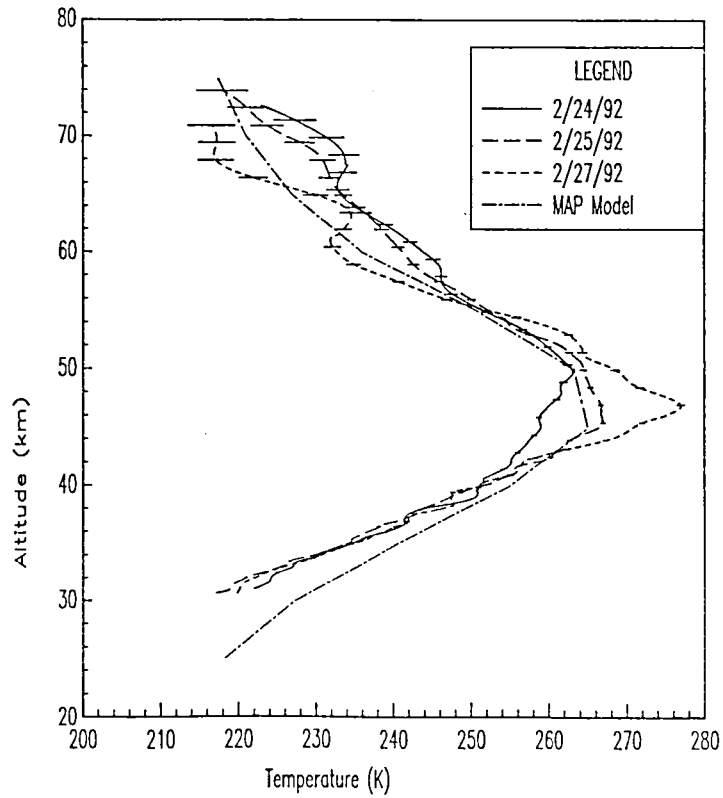


Fig. 3: STROZ-LITE Aerosol Extinction Profiles at 382nm from the UARS Correlative Measurement Campaign at JPL-TMO 1992.

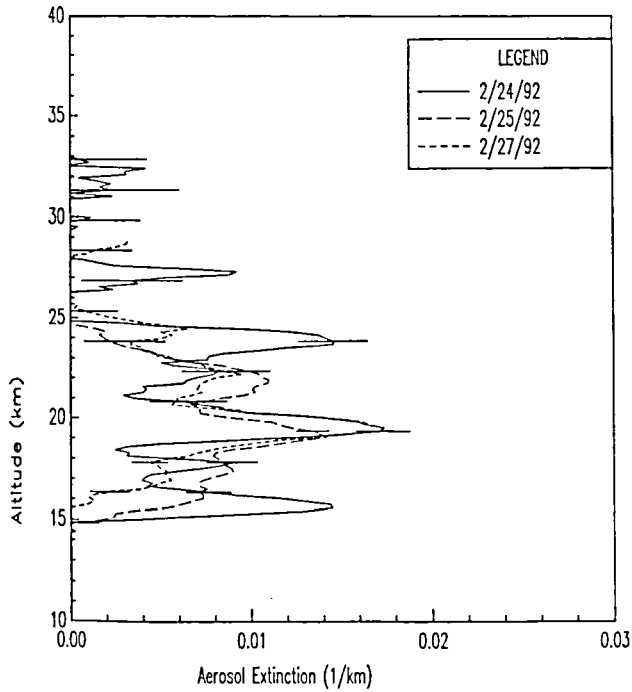
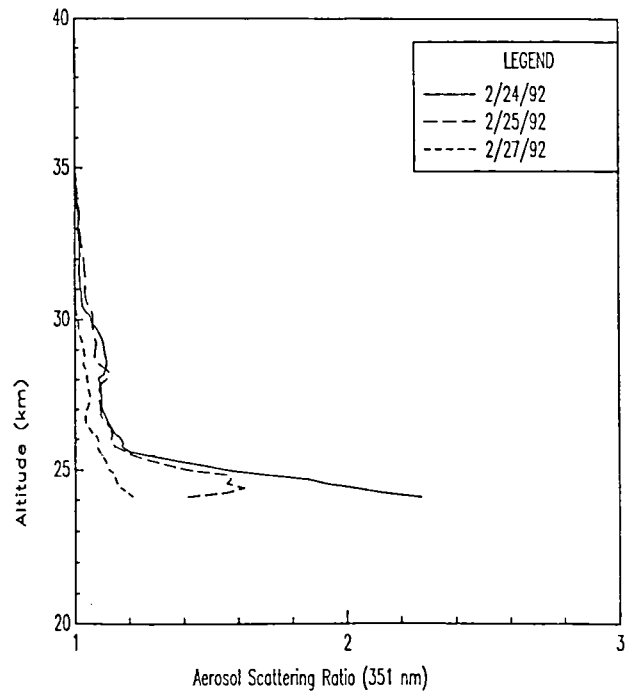


Fig. 4: STROZ-LITE Aerosol Scattering Ratio Profiles at 351nm from the UARS Correlative Measurement Campaign at JPL-TMO 1992.



# Airborne Dial Remote Sensing of the Arctic Ozone Layer

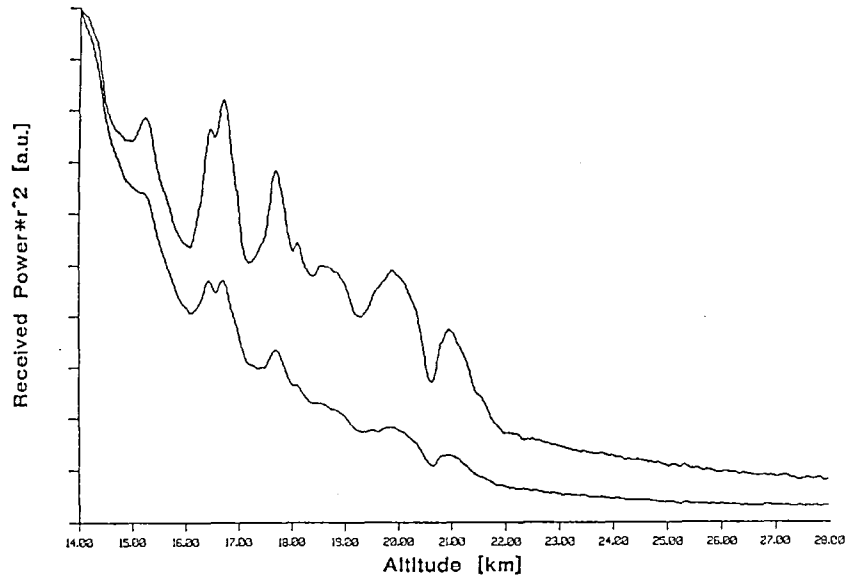
*Martin Wirth, Wolfgang Renger, Gerhard Ehret  
DLR - Institut für Physik der Atmosphäre  
8031 Oberpfaffenhofen / Germany*

A combined ozone and aerosol LIDAR has been developed at the Institute of Physics of the Atmosphere at the DLR in Oberpfaffenhofen. It is an airborne version, that, based on the DIAL-principle, permits the recording of two-dimensional ozone profiles. In this talk we will focus on the ozone-part, the aerosol subsection will be treated by another contribution.

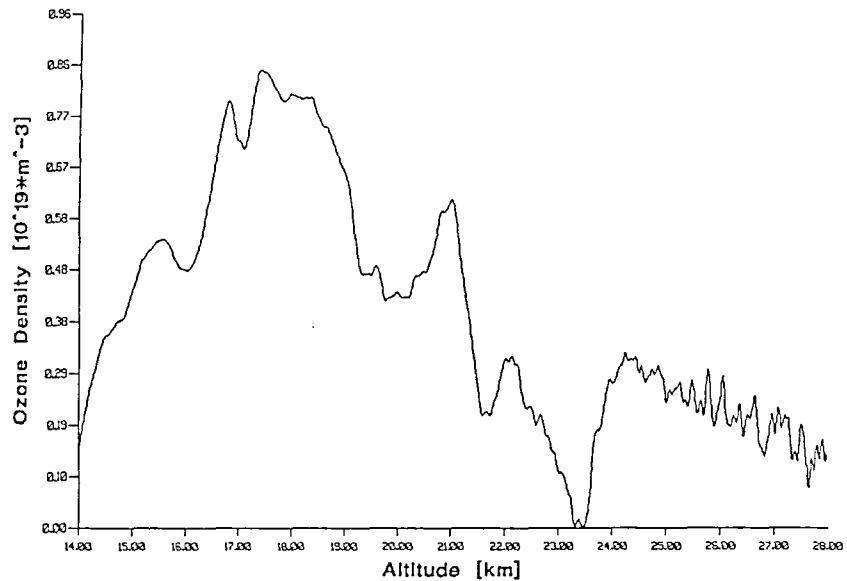
Based on the absorption spectrum of O<sub>3</sub> and the availability of powerful pulsed lasers we decided to use an online wavelength of 308nm generated by an XeCl excimer laser and an offline wavelength of 354nm produced by tripling the groundwave of a NdYAG laser. We were able to achieve pulse energies of 250mJ on the online wavelength and 50mJ offline. The maximum repetition rate for a pair of laser-pulses is 5Hz, mainly limited by the data rate of the storage medium. The receiver optics consists of a 35cm Cassegrain-telescope and a three channel optical filter bank based on dielectrical beamsplitters and bandpasses. Photomultiplier tubes operated in current-mode are used as detectors. The analog signals are digitized by a quad-channel oscilloscope and stored on an optical disk for later analysis.

The system was tested for the first time last winter in the EASOE/Astor campaign funded by the EG and the german BMFT. The ozone-DIAL (named OLEX for Ozone Lidar EXperiment) was, among various other experiments, mounted in a C160-Transall aircraft. Based in Kiruna (northern Sweden), a total of 46 flights with almost 300 flight hours were performed in four two-week campaigns from December to March. The observed area extended westwards to the westcoast of Greenland (50°W), to Novaja Semlja in the east (60°E) and up to 85°N. At the end of the March campaign we undertook a north-south section starting from 68°N down to 17°N.

The aerosol section of our system was operated almost all the time, only the occurrence of high clouds forced us to stop the data acquisition. Ozone could only be measured under nighttime conditions, due to a relatively broad (5nm) filter for the offline wavelength at 354nm. The obtained vertical resolution was 1000m, in an altitude range from about 13km up to 25km. These values depend of course on the flightlevel of the aircraft, which was typically around 7km. The horizontal resolution ranges from 50km to 200 km, depending on accuracy and range requirements.



*This figure shows the  $r^2$ -corrected backscattering signals of our lidar system for the online wavelength at 308nm and the offline wavelength at 354nm. They are averages of 1000 shots taken over the North Atlantic ( $5^\circ\text{O}$ ,  $75^\circ\text{N}$ ) at Feb .3 , 92. (1000 shots correspond to a distance of 30km).*



*This graph shows the ozone density calculated from the two signals above with a vertical resolution of 1.5km. A correction was only made for the Rayleigh extinction. The errors due to inhomogenous aerosol backscattering showing up at the edges of the various thin Pinatubo layers were not considered yet. Also the ozone values above 24km should be taken with care, because they are very sensitive to offset problems encountered in our electrical signal processing.*

Lidar Measurement of Stratospheric Ozone at Hohenpeissenberg  
- An Improved Evaluation Method -

W. Vandersee, F. Schönenborn, H. Claude

Deutscher Wetterdienst  
Meteorologisches Observatorium  
Hohenpeissenberg

In 1987, the schedule of long-term ozone monitoring at the Meteorological Observatory Hohenpeissenberg was extended by operational DIAL measurements. A detailed description of the system is given by Claude et al. (1989).

An improved evaluation method will be described, which allows the calculation of stratospheric ozone distribution up to 50 km. A good balance between precision and range resolution is achieved.

The evaluation begins with the calculation of the relative error for each channel in accordance with the Poisson distribution. During the following evaluation an error calculation is performed according to the Gaussian error propagation.

After normalization of the backscatter profiles to count per shot and kilometer an empirical function is applied to correct non-linearities of the photomultipliers:

$$S^*(I) = S(I) \cdot (a \cdot \exp(g \cdot (I - NMIN + 1)) + 1) \quad (1)$$

where  $S^*$  is the true number of counts,  $S$  is the measured number of counts at channel  $I$ ,  $NMIN$  is the lowest evaluable channel,  $a$  is a constant factor, and  $g$  is the following equation:

$$g = b \cdot f(NMIN)^c \quad (2)$$

where  $b$  and  $c$  are constants, and  $f$  is the PMT load at  $NMIN$  given in MHz, i. e. the maximum load, that is received by the photomultipliers.  $a$ ,  $b$ , and  $c$  are found to be 0.5085, -0.61274, and -0.47471 respectively. Both equations are valid for the used Thorn Emi 9893QB/350 tubes up to a maximum load of 12 MHz. They base on test measurements made under running conditions. A spectral dependency was not detected.

Equations 1 and 2 show that the severity of non-linearity at consecutive channels depends on the PMT maximum load received at  $NMIN$ , which means that the effect of non-linearity increases with increasing maximum load. Non-linearity effectuates with respect to its severity a diminution of the gradient along the backscatter profiles. Figure 1 shows the corrected and uncorrected normalized backscatter profiles of a lower range measurement, which was performed on March 1st in 1991.

The stronger the non-linearity is the stronger the diminution becomes. A significant difference between the diminutions of the "on" and "off" wavelengths leads to

serious consequences to the differentiation of the logarithmic backscatter ratio. Because the ozone concentration is determined by the difference of the logarithmic gradients of the backscatter profile, the relative increase/decrease of the "on" line's gradient against the "off" line's gradient increases/decreases the estimated ozone concentration.

If this correction is not applied, an underestimation of the ozone concentration of more than 30% within the first kilometers will result. The difference between correction and omission of the non-linearity is shown in figure 2. The dotted curve denotes the above mentioned lower range measurement, which is evaluated without the correction. The corrected profile is displayed by the solid curve. This profile is a combination of the lower and upper range measurements. The fit point is marked with inverted ticks at the ordinates. The Brewer-Mast profile (dashed curve), obtained 13 hours before, validates the correction.

In the next evaluation step the logarithmic backscatter profiles are filtered by a Gaussian lowpass filter. This filter is symmetric and guarantees high fidelity. The filter weights are calculated from the following equation, which is given by Panofsky and Brier (1958):

$$w_k = 1 / \sqrt{2\pi} \cdot \exp(-k/2 \cdot (6/T^*)^2) \quad \text{with } k = 1, 2, \dots, +\infty \quad (3)$$

Because it is not useful to calculate with an infinite number of filter weights, the series is truncated, when  $w_{k=n} < 0.1 w_{k=1}$ , where  $w_{k=1}$  is the central weight. The filter weights are normalized according to

$$\sum_{k=-n}^{+n} w_k = 1 \quad (4)$$

$T^*$  gives the desired filter strength. It is the maximum period of fluctuations along the backscatter profiles, that should be removed.

$$T^* = A \cdot \exp(B \cdot (1 - NMIN + 1) - C \cdot (1 - NMIN + 1)^4) \quad (5)$$

where A is a constant and

$$B = \ln(T^*_{\max}/A) \cdot 4 / (3 \cdot I^*_{\max}) \quad (6)$$

$$C = B / (I^*_{\max}{}^3 \cdot 4) \quad (7)$$

Equation 5 describes  $T^*$  as a function of height relative to NMIN.  $T^*$  increases exponentially with height whereas the error of the ozone estimation remains nearly constant. On the other hand the height resolution becomes worse. In order to save a reasonable height resolution in the upper altitude range  $T^*$  is limited by  $T^*_{\max}$ , which is attained at channel  $I^*_{\max}$ . Standard measurements with an integration time between one and eight hours are evaluated with  $T^*_{\max} = 70$ , which corresponds to a height resolution of  $\pm 3.7$  km, and  $I^*_{\max} = 70$ . Above  $I^*_{\max}$

$T^*$  equals  $T^*_{max}$ , approving the increase of the error.  $A$  equals 1.

After filtering the logarithmic backscatter ratio  $\ln(S_{off}/S_{on})$  is calculated. If the lower and upper range measurements should be fitted together, the described procedure has to be performed for each measurement. The combination of lower and upper range measurement results from a simple parallel shift of both logarithmic backscatter ratio profiles. The fit point is located at the lower end of the upper range measurement. The combined profile is smoothed by a very weak Gaussian lowpass filter,  $T^* = 5$ . Since the individual peculiarities of the lower and upper range measurement were taken into account by the first filtering, the filter weights now remain constant with height.

The ozone profile is now obtained by differentiating the logarithmic backscatter ratio profile with respect to height. The temperature dependency of the absorption cross section and the Rayleigh correction are considered by averaged seasonal temperature and air density profiles, which were obtained by the soundings from 1967 to 1986 and which are extrapolated with the standard atmosphere above 32 km.

Except of an aerosol correction after the eruption of Mt. Pinatubo no further correction is necessary. Instead of "range gating" a mechanical chopper has been used to protect the photomultipliers against overload since the very beginning of the regular DIAL measurements. In addition the photomultipliers work far below the saturation limit so that all measurements are free of signal induced noise. In consequence a high-quality data set is available, spanning a period of more than four years.

#### References:

Claude, H., B. Geh, R. Hartmannsgruber, T. Hohmann, K. W. Rothe, F. Schönnenborn, H. Walther, K. Wege, (1989). Weiterentwicklung, Bau und Betrieb eines Lidars zur Bestimmung des atmosphärischen Ozonprofils, Ber. d. DWD No. 179.

Panofsky, H. A., G. W. Brier, (1958). Some Applications of Statistics to Meteorology, Pennsylvania State Univ., University Park (USA).

MET. OBS. HP LIDAR  
 NORMALIZED BACKSCATTER PROFILES

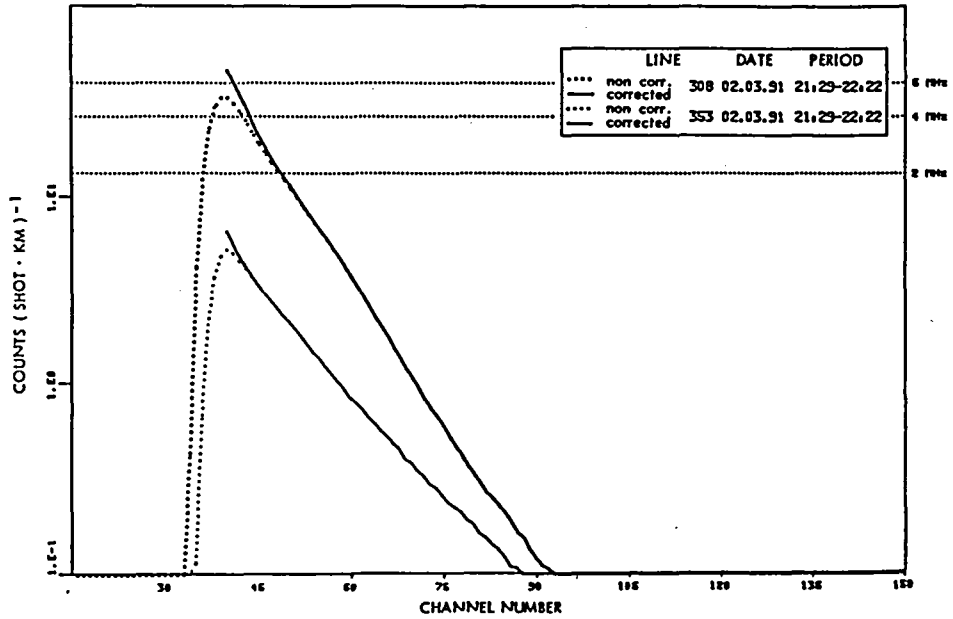


Fig.1. Correction of the PMT-non-linearity. Lower range measurement recorded on March 1st, 1991.

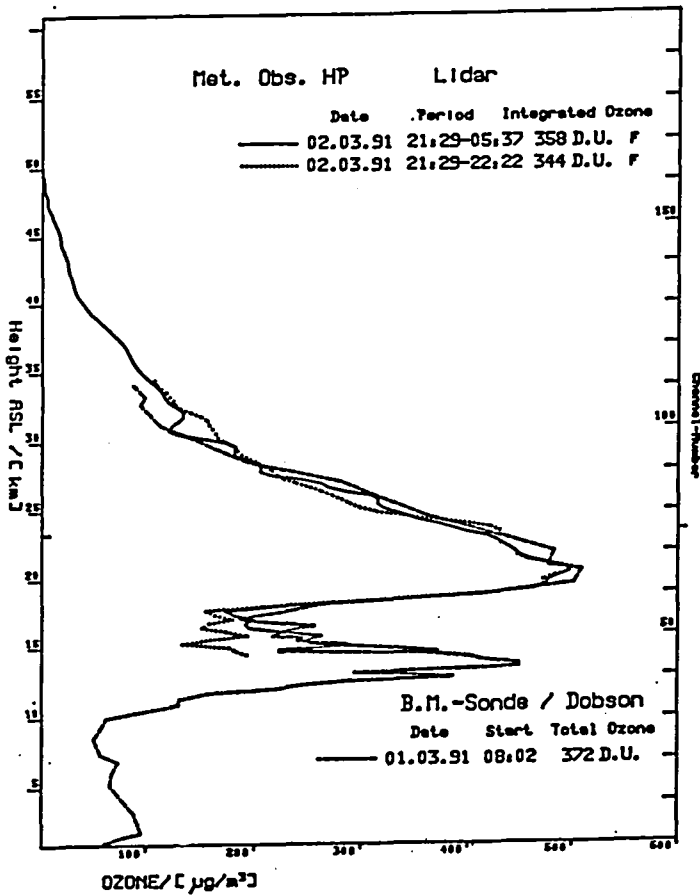


Fig.2. Vertical ozone distribution measured by Lidar and Brewer-Mast sonde on March 1st, 1991.

# A MULTI-WAVELENGTH OZONE LIDAR FOR THE EASOE EXPERIMENT

S. Godin, G. Ancellet, C. David  
J. Porteneuve, C. Leroy  
Service d'Aéronomie du CNRS (Fr.)

V. Mitev, Y. Emery, C. Flesia  
Observatoire de Neuchatel (CH)

V. Rizi, G. Visconti  
Universita de l'Aquila (It.)

L. Stefanutti  
I.R.O.E. (It.)

## 1. Introduction

The study of the ozone layer during winter and springtime in high latitude regions has now become a major issue in atmospheric research. For a better understanding of these problems, an important experimental campaign called EASOE (European Arctic Stratospheric Ozone Experiment) was organized by the European Community during the winter 1991-1992. Its main objective was to establish a budget of the ozone destruction processes on the whole northern hemisphere. This implied the simultaneous operation of different types of instruments located in both high and mid-latitude regions in order to study the destruction processes as well as the evolution of the ozone layer during the period of the campaign. A description will be given here of a mobile ozone lidar instrument specially designed for operation during the EASOE campaign. This system, which performs ozone measurements in the 5 to 40 km altitude range was located in Sodankyla, Finland (67°N, 27°E) as part of the ELSA experiment (Expérience Lidar dans la Stratosphère Arctique), which also includes operation of another multi-wavelength lidar designed for polar stratospheric clouds measurements, developed jointly by the IROE in Florence and the FREIE Universität in Berlin.

## 2. Experimental system

### *a) transmitter*

For the emitting part, the ELSA ozone lidar is a combination of the two lidar systems which are presently operating at the Observatoire de Haute-Provence (Godin et al., 1987, Ancellet et al., 1989). The "tropospheric" part of the experimental set up consists of two Spectra-Physics Nd:Yag lasers (model DCR11 and GCR 11) emitting respectively 40 mJ and 60 mJ per pulse in the fourth harmonic (266nm) at 10 HZ. The 289 and 299 nm wavelengths are generated by Stimulated Raman Scattering in D<sub>2</sub> and H<sub>2</sub> respectively. Optimization of the first Stokes is

obtained using Helium as a buffer medium and a slow focusing configuration with 1.5 meter long Raman cells. Energy obtained at 289 nm and 299 nm are respectively around 8 mJ and 10 mJ . For each wavelength a beam expander of magnification 2.5 is used. The 355 nm wavelength is generated by the Nd:Yag GCR-11 with a third harmonic generator located after the FHG (figure 1). The emitted energy is 40 mJ per pulse when the FHG is left on the optical path and 80 mJ when it is removed. The 308 nm is obtained by an XeCl Lambda Physik exciplex laser (model LPX 200) located under the Nd:Yag laser. Unstable resonator optics are used to limit the divergence to 0.5 mrad. The emitted energy is 200 mJ per pulse and the laser repetition rate can go up to 80 HZ. As for the tropospheric system, further reduction of the beam divergence is obtained by means of two beam expanders (magnification 2.5 for the Nd:Yag laser wavelength and 3 for the XeCl laser)

#### *b) Optical receiver*

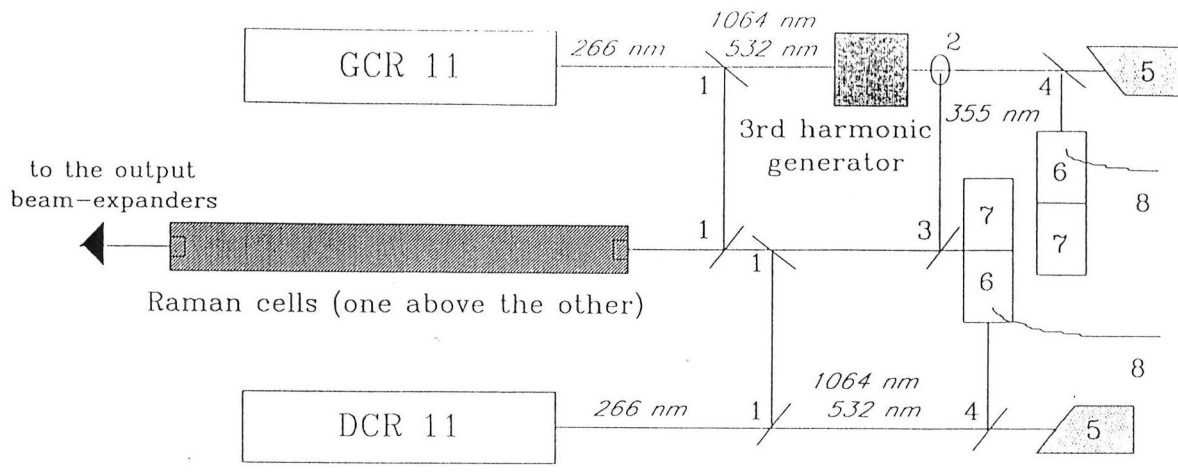
The optical receiving system consists of four similar F3 mirrors of 50 cm diameter, which corresponds to an equivalent receiving surface of 1 meter diameter (figure 2). The light is collected by four optical fibers of 1 mm diameter mounted in the focal plane of each mirror. The fiber mounts are motorized in the X-Y directions for the alignment of each mirror with respect to the different laser beams. The optical fibers transmit the backscattered light to the optical analysing device which includes imaging optics, a mechanical chopper used only for stratospheric measurements and a multichannel monochromator designed for the wavelength separation (figure 3)

#### *c) Electronic synchronization and acquisition system*

The whole experiment is driven by a Compaq 386 PC computer which allows the simultaneous operation of two lasers and the acquisition of 2 counting channels and 4 analogical channels. The data acquisition system, entirely built at CNRS, includes four 10 MHz 12 bits waveform recorder for analog detection and two 200 MHz photocounting units. Both detection mode can work simultaneously. During the acquisition, the computer provides real time plots as well as ozone profiles calculated on a limited number of shots in order to check the validity of the experiment.

#### **References**

- Ancellet G., A. Papayannis, J. Pelon and G. Mégie: "DIAL Tropospheric Ozone Measurement Using a Nd:Yag Laser and the Raman Shifting Technique", J. Atmos. and Ocean. Technol., Vol 6, No. 5, 832, 1989
- Godin S., G. Megie and J.Pelon : " Systematic lidar measurements of the stratospheric ozone vertical distribution", Geophys. Res. Lett., 16, 547-550, 1989
- Pelon J., S. Godin and G. Megie : "Upper Stratospheric Lidar Observation of the Ozone Vertical Distribution", J. Geophys. Res., 91(D8), 8667-8671, 1986



- 1 – Dichroic mirrors (Rmax for 4th harmonic at 45°)
- 2 – 3rd harmonic periscope, consisted of dichroic mirrors (Rmax for 355nm at 45°)
- 3 – Dichroic mirrors (Rmax for 355 nm at 45°)
- 4 – Dichroic mirrors (Rmax for 532 nm at 45°)
- 5 – Beam-stops
- 6 – Attenuator for 532 nm
- 7 – Photodiodes for the laser 4th harmonic feedback
- 8 – Optical fibers for synchronization

fig. 1: plan view of the transmitter

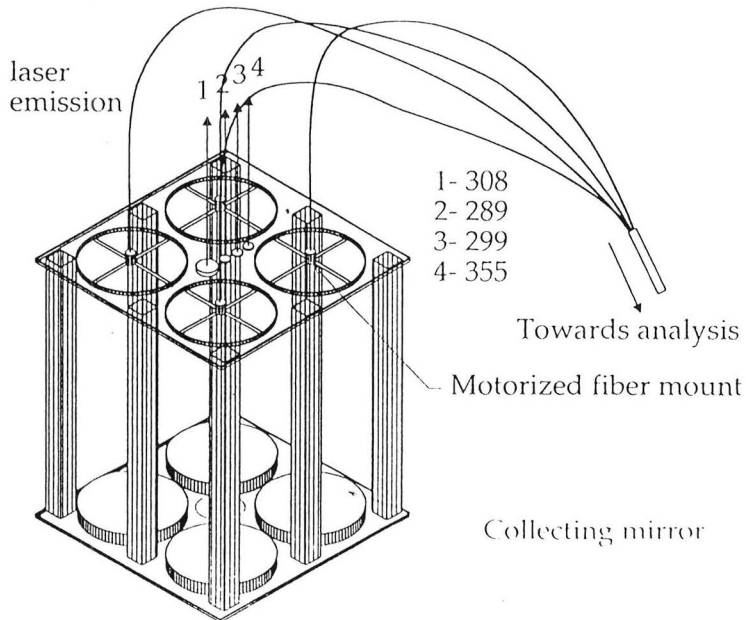


fig 2: Optical receiving system



## Correction of DIAL Stratospheric Ozone Measurements in the Presence of Pinatubo Aerosols

Marta A. Fenn<sup>1</sup>, Syed Ismail<sup>2</sup>, Edward V. Browell<sup>2</sup>, Carolyn F. Butler<sup>1</sup>

<sup>1</sup>Hughes ST Systems Corp., 28 Research Drive, Hampton, VA 23666

<sup>2</sup>NASA Langley Research Center, Atmospheric Sciences Division, MS 401A, Hampton, VA 23665.

NASA Langley's airborne lidar system measured aerosol and ozone distributions in the stratosphere from January through March 1992 as part of the Airborne Arctic Stratospheric Expedition (AASE-II) (Browell et al., 1992). The eruption of Mount Pinatubo in June 1991 has increased the aerosol burden of the stratosphere and thereby increased the importance of applying an aerosol correction to the ozone measurements. The correction relies on a Bernoulli solution to derive a backscatter correction to the differential absorption lidar (DIAL) returns at two wavelengths in the ultraviolet spectral region ( $\lambda_{on} = 301.5$  nm,  $\lambda_{off} = 310.87$  nm) as described in Browell et al. (1985). This paper discusses how the parameters for the correction were optimized for application to the AASE-II data set.

The backscatter correction to the ozone calculation is required because the backscatter characteristics at  $\lambda_{on}$  may be different from those of  $\lambda_{off}$ . It is especially important in regions of strong vertical gradients in existing aerosol layers. The backscatter correction requires knowledge of the normalized aerosol backscattering phase function ( $P\pi$ ) and the aerosol backscatter wavelength dependence ( $\alpha$ ) at the measurement wavelengths. The parameter  $\alpha$  can be measured directly from lidar returns in the infrared (IR=1064 nm) and visible (VIS=603 nm) which are transmitted simultaneously with the ultraviolet (UV) returns. The value for  $\alpha$  can also be measured between the visible and  $\lambda_{off}$  after correcting the  $\lambda_{off}$  scattering ratio for ozone extinction. The value of  $\alpha$  between  $\lambda_{off} - \lambda_{on}$  cannot be calculated directly from the lidar returns because of the strong absorption of  $\lambda_{on}$  by ozone, but it is estimated from the measured  $\alpha$ 's to be 0.7. The sensitivity of the correction to various values of  $\alpha$  is discussed in this paper. The value of  $P\pi$  is not known a priori, but the sensitivity of the correction to changes of  $P\pi$  is shown in this paper to be quite small. A nominal value of  $0.028$  sr<sup>-1</sup> has been used extensively in DIAL backscatter correction calculations.

The sensitivity of the aerosol correction to these parameters is demonstrated using lidar returns at two adjacent locations on the AASE-II flight of Jan. 30, 1992 at 20° N latitude, and 120° E longitude. The first profile is obtained over a 5 minute period centered at 4:50 UT ("inside the layer") with a strong Pinatubo aerosol layer at about 23 km altitude. Five minutes later, this layer is no longer observed, and a second 5 minute average is collected centered at 5:00 UT ("outside the layer"). Figure 1 shows the total scattering ratio for each of these 5 minute averages. For the sensitivity analysis, the range cell size is set to 525 m, which is half that used in the normal analysis. By comparing the ozone measured without a backscatter correction at these two times, Figure 2, it is clear that the swing in ozone at altitudes 22-24 km from

greater than 4000 ppbv to less than 2000 ppbv is a measurement anomaly caused by the sharp aerosol gradient at around 23 km; the anomaly is present "in the layer" but not "outside the layer". Figure 3 shows the results of applying  $\alpha = 0.7$  and  $P\pi = 0.028 \text{ sr}^{-1}$  to the ozone measurement within and without the 23 km aerosol layer. The corrected ozone within the layer comes very close to the corrected ozone outside the layer at both 22.5 km and 24 km (i.e., below and above the aerosol layer). But between those altitudes the profile within the layer is about 25 % lower than the profile outside the layer. This is interpreted to be a real difference in the air sampled, rather than an measurement error; a single DIAL calculation between the aerosol free altitudes of 22.3 km and 24 km compares with the average corrected ozone between those altitudes.

The AASE-II DIAL data set was reduced using the Bernoulli solution with the parameters optimized as described. Both the altitude at which to stop the correction and the final scattering ratio for the inverse solution were determined on a flight by flight basis. The goal is to stop the calculation in a "clean" region above the aerosol layer and set the final scattering ratio there to 1.0. Since this data set covered latitudes from the pole to south of the equator, the  $\alpha$  parameter was also tuned for different flights. Once the correction scheme removed anomalous features, the remaining differences in the ozone measurements between aerosol rich and aerosol free regions are interpreted to be real. The interpretation of these differences is addressed in another paper (Grant et al, 1992).

#### References:

E.V. Browell, S. Ismail and S.T. Shipley, "Ultraviolet measurements of  $O^3$  profiles in regions of spatially inhomogeneous aerosols," *Appl. Opt.* 24, 2827-2836, 1985.

E.V. Browell, C.F. Butler, M.A. Fenn, W.B. Grant, and A.F. Carter, "Lidar measurements of aerosol and ozone distributions during the 1992 Airborne Arctic Stratospheric Expedition," paper presented at 16 ILRC (1992).

W.B. Grant, E.V. Browell, M.A. Fenn, C.F. Butler, W.G. Brackett, R.E. Veiga, S.D. Mayor, J. Fishman, D. Nganga, A. Minga, B. Cros, L.L. Stowe, "Interpretation of DIAL measurements of lower stratospheric ozone in regions with Pinatubo aerosol clouds," paper presented at 16 ILRC (1992).

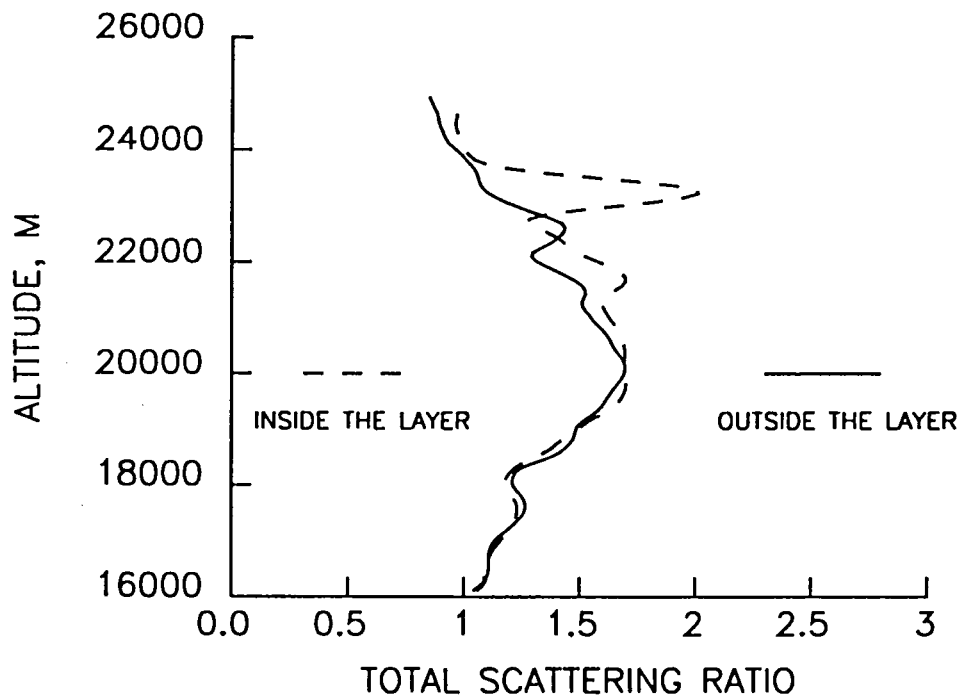


Figure 1.  $\lambda_{off}$  total scattering ratio derived from the Bernoulli solution. Each profile is a 5 minute horizontal average about the time indicated. A vertical smooth of 525 m has been applied.

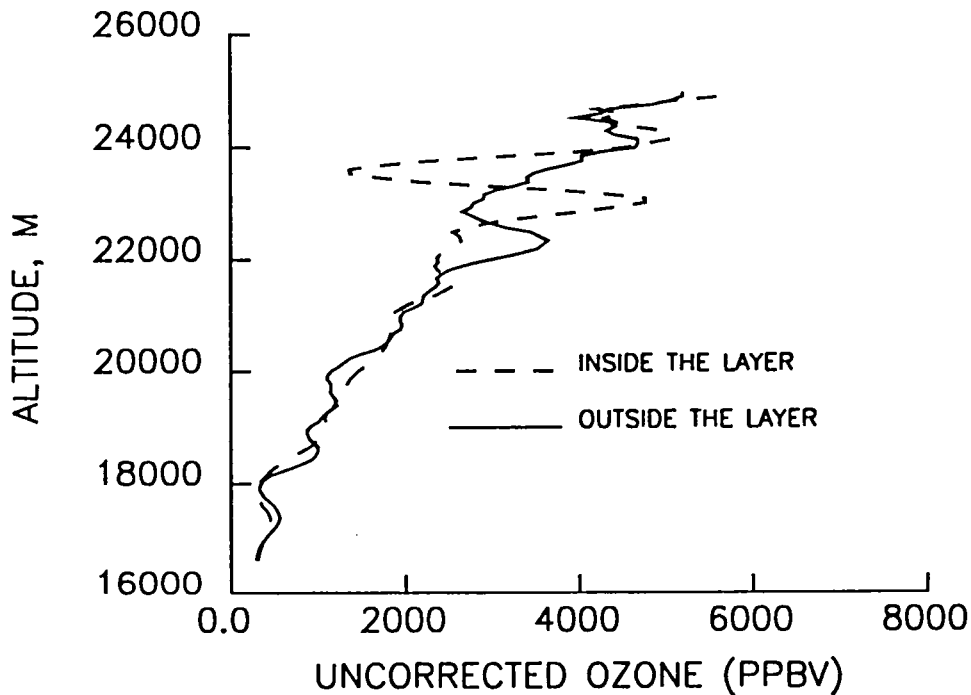


Figure 2. Measured ozone mixing ratio without a backscatter correction. The resolution is the same as Figure 1.

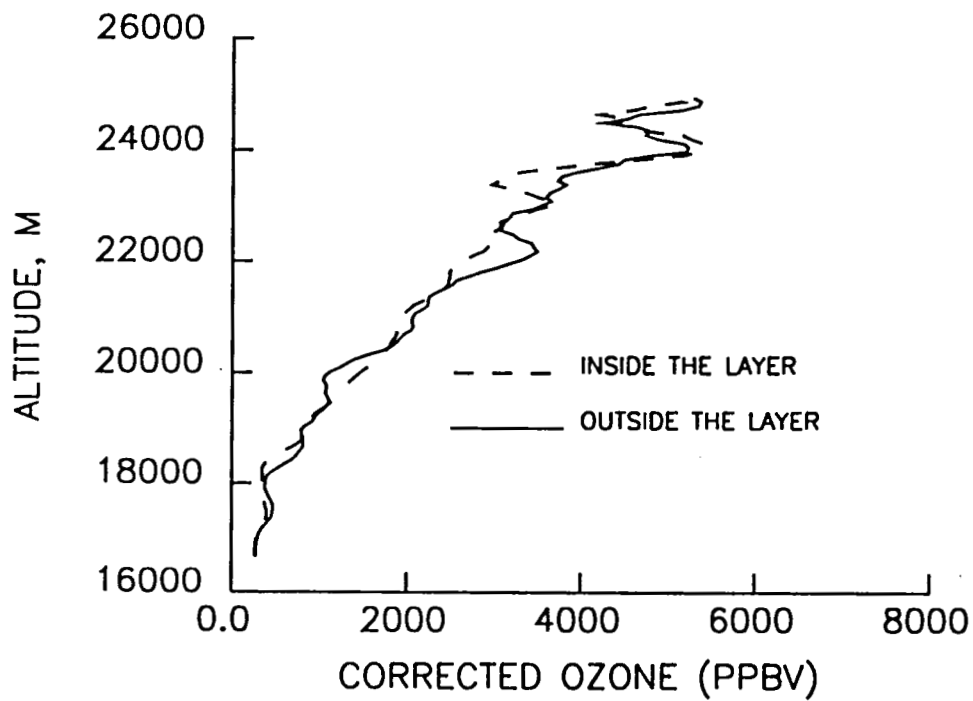


Figure 3. Measured ozone mixing ratio with a backscatter correction. The resolution is the same as Figure 1.

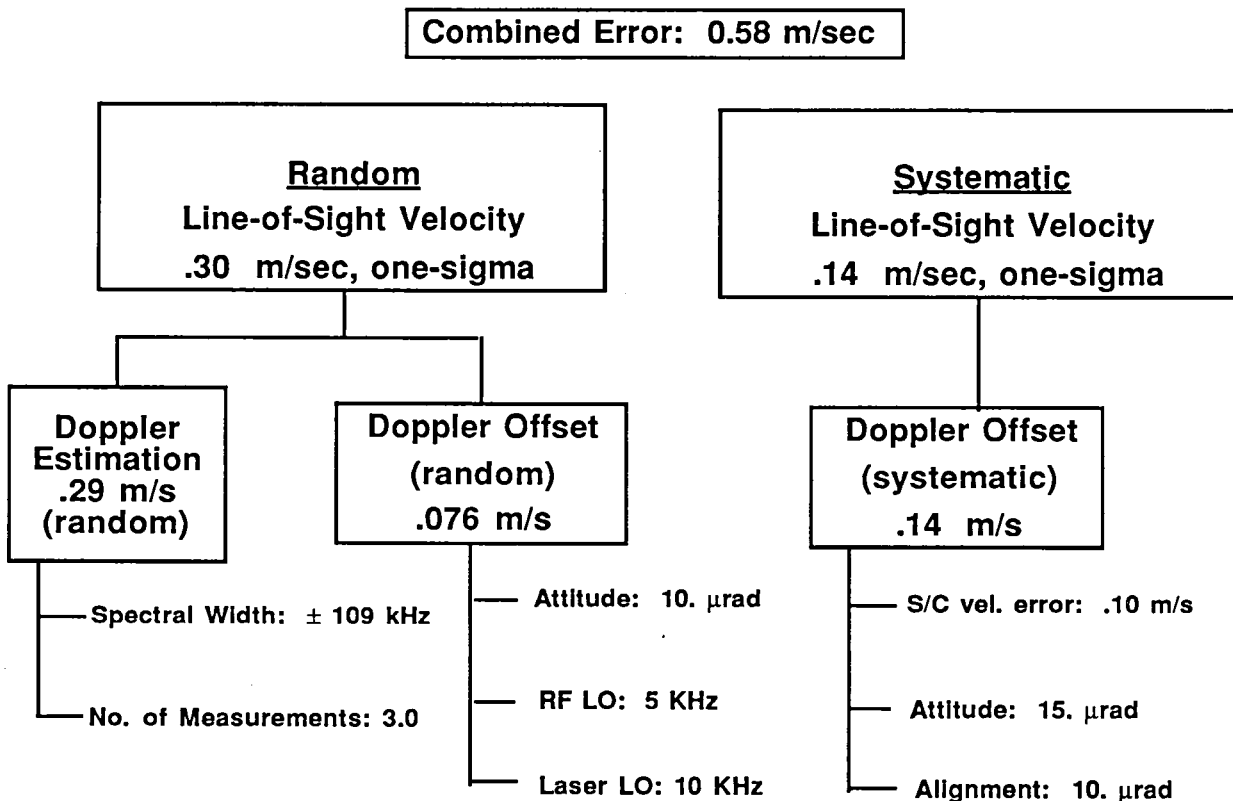
# THE LASER ATMOSPHERIC WIND SOUNDER (LAWS) PRELIMINARY ERROR BUDGET AND PERFORMANCE ESTIMATE

David L. Kenyon, Kent Anderson  
General Electric Company  
Astro Space Division  
P.O. Box 800, Princeton, NJ 08543-800

The Laser Atmospheric Wind Sounder (LAWS) study phase has resulted in a preliminary error budget and an estimate of the instrument performance. This paper will present the line-of-sight (LOS) Velocity Measurement Error Budget, the instrument Boresight Error Budget and the predicted signal-to-noise ratio (SNR) performance. The measurement requirements and a preliminary design for the LAWS instrument are presented in a companion paper (The Laser Atmospheric Wind Sounder (LAWS) Phase II Preliminary Design, Petheram, et. al.).

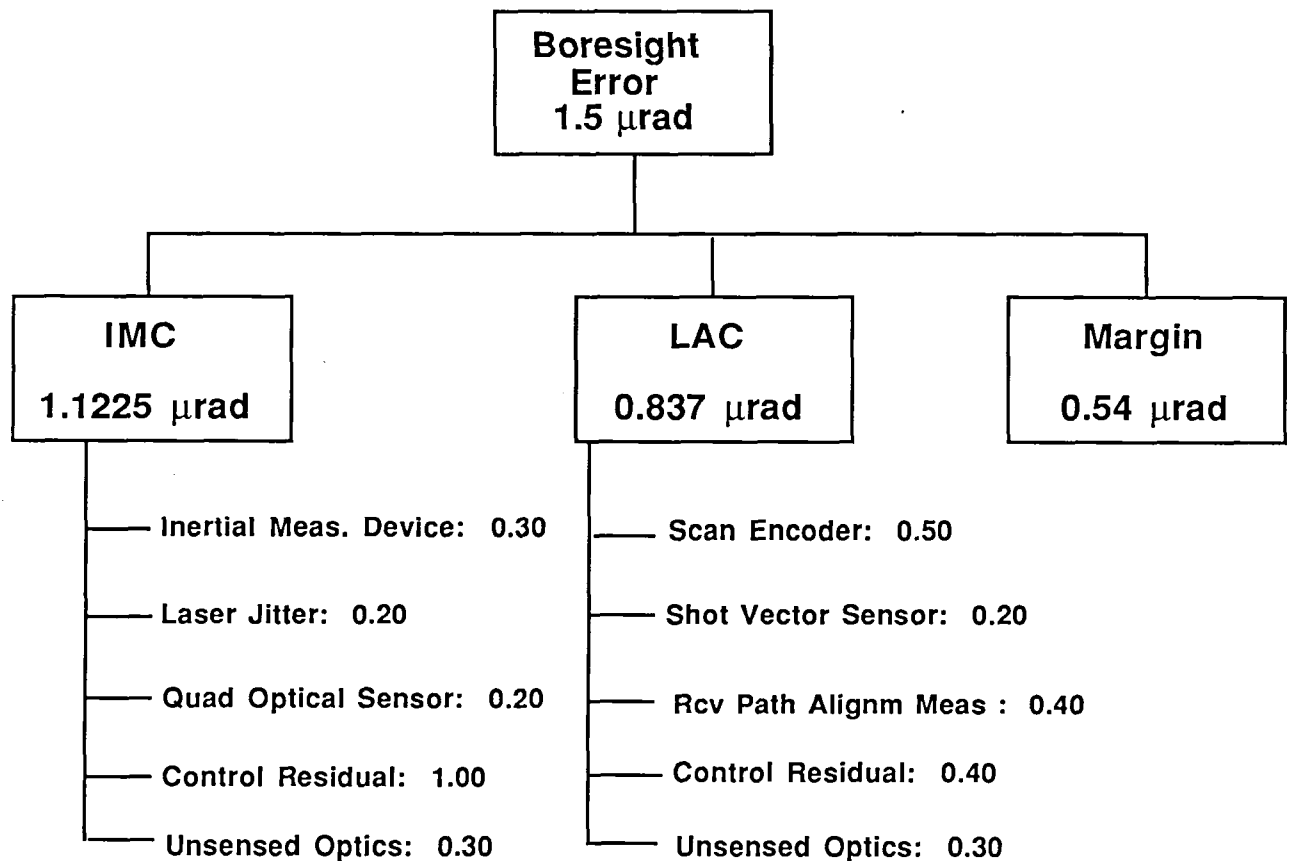
Figure 1 is the LOS Velocity Measurement Error Budget prediction for the LAWS instrument. This shows a predicted LOS error of 0.58 meters/sec and consists of the sum of the random component and twice the systematic component. The random component is made up of errors which vary from one laser pulse to the next while the systematic component remains constant over the 5 second scan period. Notice that this error budget prediction consists only of instrument errors and does not include atmospheric error sources which would increase the Doppler Estimation Error.

Figure 1. Error Budget Estimates



The other major LAWS error budget is the Boresight Error Budget presented in Figure 2. This predicted error of 1.5  $\mu$ radians consists of a lag angle compensation (LAC) term, an image motion compensation (IMC) residual and a reserve of .54  $\mu$ rad. All of the numbers presented are one-sigma, per axis and the total of 1.5  $\mu$ rad results in a 1 dB loss in system SNR. The IMC consists of a high bandwidth steering mirror which compensates for errors between the transmit and receive LOS over the pulse round trip time, about 5 msec. The LAC is a feed-forward control loop which corrects for the telescope motion during the pulse receive time. Another companion paper (Lag Angle Compensation in a Space borne Scanning Lidar, Wissinger) details the LAC subsystem.

Figure 2. Predicted Boresight Errors



The photon noise limited signal-to-noise ratio for a telescope focused at the far field and in the absence of atmospheric turbulence may be expressed as:

$$\text{SNR} = \eta P_S / (h\nu B)$$

$$P_S = \pi c E_t \beta D^2 e^{-(2kR)} / (8 R^2)$$

where:  $E_t$  = transmitted pulse energy  
 $\beta$  = atmospheric backscatter ( $\text{m}^{-1}\text{sr}^{-1}$ )  
 $k$  = atmospheric extinction coefficient ( $\text{m}^{-1}$ )  
 $D$  = receive aperture diameter  
 $R$  = slant range  
 $\eta$  = receiver efficiency  
 $h\nu$  = photon energy ( $2.182 \cdot 10^{-20}$  J)  
 $B$  = noise equivalent bandwidth.

The computed wide-band SNR is -14.9 dB, for the parameters listed below:

$B = 10$  MHz  
 $\beta = 10^{-11}$  /m-sr  
 $R = 752.6$  km (for 525 km orbit and 15 km sensed altitude)  
 $E_t = 17.5$  J  
 $D = 1.5$  m  
 $\eta = 0.0862$ .

Details of the error budgets and the system SNR estimates will be given in the presented paper.



Lag Angle Compensation in a Space borne Scanning Lidar  
A. B. Wissinger  
Hughes Danbury Optical Systems, Inc.

---

The so-called "lag angle" is inherent in any spaceborne scanning lidar system. It is also important in systems where the scanning causes a significant pointing error during the laser interrogating pulse echo time. In a heterodyne lidar system, the lag angle, if uncompensated, will significantly reduce the signal-to-noise ratio.

What is "Lag Angle"?

Lag angle is the apparent change in direction to the laser-illuminated spot in the atmosphere relative to the transmitted line of sight angle during the laser pulse round trip time. It occurs in all nadir-oriented, orbiting systems whether fixed or scanning. Let's take the case of a non-scanning lidar first.

Why should there be any lag angle when the system is not scanning?

It occurs as the space-borne lidar system rotates continuously to remain aligned with the Earth, as in a nadir-oriented system. The spacecraft and lidar must pitch in order to remain oriented to nadir; therefore the line of sight rotates during the laser pulse round-trip time and during the pulse reception time. A numerical example will make this effect clear.

During a single orbital revolution, the spacecraft rotates  $2\pi$  radians. The rotation rate is  $2\pi$  radian per orbital period. For an altitude of 525 km, the orbital period will be about 88 minutes. The pitch rate is then 1190  $\mu$ radians per second. During a pulse round trip time of  $\sim 5$  milliseconds, the spacecraft will rotate 6  $\mu$ radians. This is equal to the lag angle. For a system whose beam spread is 15  $\mu$ radian, an uncorrected lag angle of this magnitude is unacceptable. Note that the lag angle change during pulse reception (stretched due to reflection from the layers of the atmosphere) may be as high as 0.23  $\mu$ radians. If we budget a total error of 1.5  $\mu$ radians (10% of the beam spread) to the lag angle, the 0.23  $\mu$ radians lag angle error is comparable to other error contributors in the error budget.

The lag angle due to pitching is separable into a fixed component and a time-varying component. The fixed component can be compensated in the optical design since it's

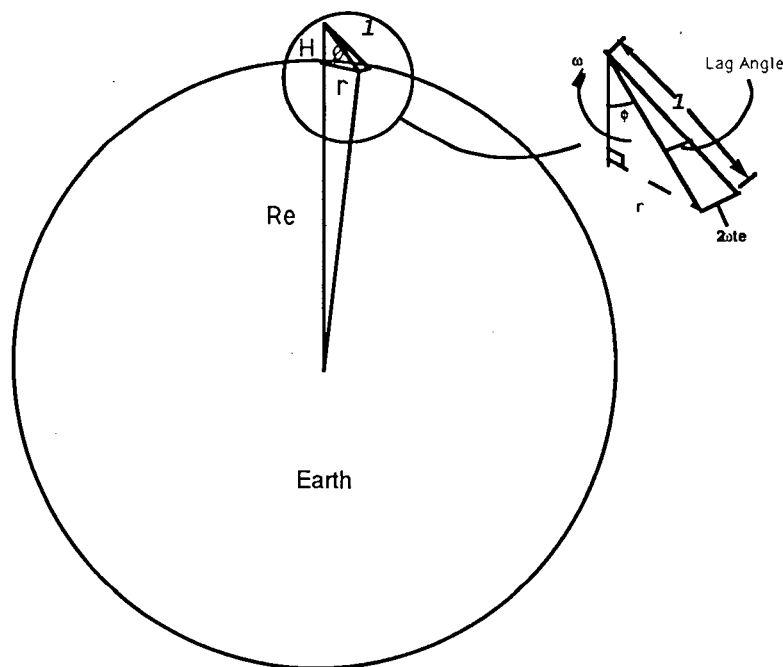
merely the equivalent to a fixed position in the field of the telescope. The dynamic correction is required to compensate for the variation in field angle during the time the stretched pulse is being received. Note that the lag angle due to pitching will occur only in the plane of the orbit, which is not the case in a scanning system.

Let us now go on to the case of a scanning lidar system in Earth orbit.

The angular scan rate, given by  $\omega$ , in radians per second, is defined as the rotation rate around the scan axis (not necessarily about nadir). Since light propagates in inertial space (not affected by transmitter motions after pulse transmission), the source of the backscattered light is the part of the atmosphere that is illuminated by the pulse. As seen from the reference frame of the transmitter telescope, this point will move continuously in the field of view in the direction tangentially away from the direction of the scan.

Figure 1 illustrates the geometry during the scan. In this example, the scan axis coincides with nadir, but the lag angle geometry is not affected if there is an angle between the two. However, the placement of the laser shots on the atmosphere (or ground) will be a function of the magnitude of the angle between the scan axis and nadir.

**Figure 1**  
**Computation of Lag Angle for Scanning System**



The lag angle is the angle subtended by  $r(t) \cdot \omega \cdot t_e$  at the slant range  $L(t)$ ,

where  $\omega$  is the scan rate

(radians per second)

$t_e$  is the echo time

(seconds) corresponding to

the slant range  $L(t)$

$r(t)$  is the instantaneous perpendicular radius from the scan axis to the range-

gated scatterer

Defining the lag angle explicitly, we have

$$\text{Lag Angle} = r(t) \cdot \omega \cdot t_e / L(t)$$

$r(t)$  is simply the sine component of the slant range:  $r(t) = L(t) \sin \phi$ . Substituting for  $r(t)$  and simplifying, we have

$$\text{Lag Angle} = \sin \phi \cdot \omega \cdot t_e$$

Note that the lag angle is only a function of time (given a fixed angle relative to nadir and a constant scan rate); it is a *not* a function of altitude, although the echo time corresponding to an echo from a ground *will* be a function of altitude, H. If there is a variation in altitude, the *range* of the lag angle compensation must be large enough to accommodate the maximum variation in echo time. We can accomplish this by increasing the size of the fixed lag angle mirrors, and designing the lag angle compensation control to have sufficient range to cover all possible values of lag angle, to  $3\sigma$  or maybe even to  $5\sigma$ .

How can we compute the echo time and its variation as a function of altitude?

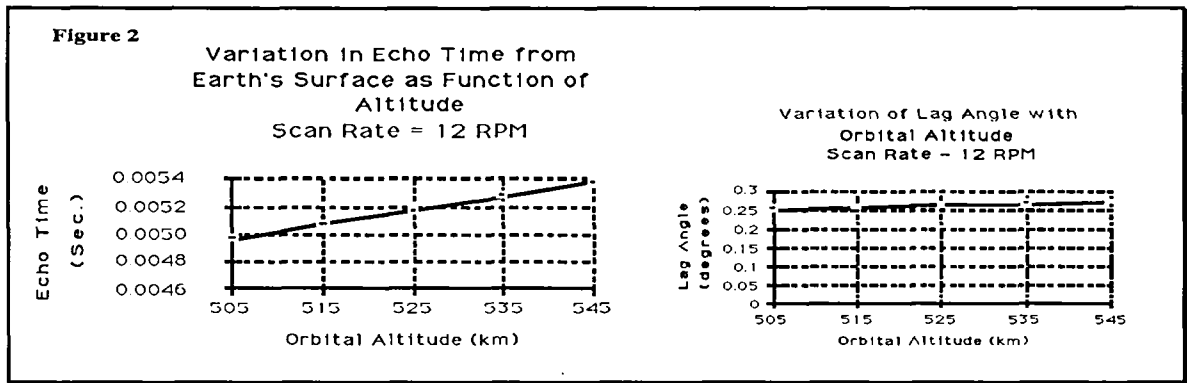
The echo time,  $t_e$ , is merely the slant range to the target of interest (a layer of the atmosphere or the ground) divided by the speed of light,  $c$ . Referring again to Figure 1 and for the moment assuming that the scan axis is coincident with nadir, we can write the expression for the slant range,  $L(t)$ , as

$$L(t) = (H(t) + R_e) \cos \phi - \sqrt{(H(t) + R_e)^2 \cos^2 \phi - H(t)(H(t) + 2R_e)}$$

Dividing by the speed of light,  $c$ , we have

$$t_e = L(t) / c$$

As an example, let us compute the variation in lag angle for an oblate Earth, where the altitude may vary by 40 km. Taking a nominal altitude of 525 km and allowing a variation due to oblateness of  $\pm 20$ km, we obtain the graphs shown in Figure 2.



These curves are essentially linear for the cases considered. The variation in both lag angle and echo time when compared to the nominal altitude is about  $\pm 4\%$ . By extending the range of our lag angle compensator by  $\sim 10\%$ , we can readily cover the range of variation cause by the Earth's oblateness.

There is, however, another effect that can cause a variation of the lag angle. If the scan axis does not coincide with the nadir axis, the line of sight will describe an ellipse on the Earth's surface (neglecting the spacecraft motion). The slant range and lag angle will vary around each scan.

The geometry and mathematics for this situation is not straight-forward, but through a series of approximations, we derived a relationship between the angle between the spin axis and nadir,  $\epsilon$ , and the total variation in lag angle,  $\Delta LA$ , over a single scan revolution. The relationship is (good for small  $\epsilon$ )

$$\Delta LA = LA(\phi_o + \epsilon) - LA(\phi_o - \epsilon) = 4 \times LA(\phi_o) \cdot \epsilon$$

where  $\phi_o$  is the nominal scan angle relative to nadir.

Expressing  $\Delta LA/LA(\phi_o)$  as a fraction and evaluating for  $\epsilon = 1$  milliradian, we compute

$$\Delta LA/LA(\phi_o) = 0.0017 \%$$

The ranging to the ground will vary by about 0.3 Km for every milliradian error between the spin axis and nadir. The corresponding echo time will vary by 1  $\mu$ second. We expect the nadir error to be less than a milliradian, and conclude that a few percent of added lag angle compensation will be adequate to provide margin for both of the effects discussed in this paper.

# LIDAR IN-SPACE TECHNOLOGY EXPERIMENT (LITE) ELECTRONICS OVERVIEW

Michael P. Blythe, Richard H. Couch, Carroll W. Rowland  
Wayne L. Kitchen, Curtis P. Regan, Michael R. Koch  
Charles W. Antill, William T. Stevens, Courtney H. Rollins  
Edward H. Kist, David M. Rosenbaum, Ruben W. Remus  
Clayton P. Turner

NASA/Langley Research Center  
Hampton, Virginia 23665-5225

## 1. INTRODUCTION

The LITE electronics consists of the following seven subsystems (refer to Figure 1): Laser Transmitter Module (LTM), Boresight Assembly (BA), Aft-Optics Electronics (AOE), Digital Data Handling Unit (DDHU), Engineering Data System (EDS), Instrument Controller (IC), and the Ground Support Equipment (GSE). Each of these subsystems is explained below.

## 2. LTM

The LTM fires laser pulses into the atmosphere ten times per second at the 1064, 532, and 355 nanometer wavelengths. The pulsewidth is approximately 20 ns and the beam divergence is about one milliradian. The output energy is approximately 500 millijoules for the 1064 and 532 nanometer wavelengths and 200 millijoules for the 355 nanometer wavelength. The LTM is controlled by discrete interfaces with the orbiter and also by the IC via ground commands. LTM parameters are monitored by the IC and EDS.

## 3. BA

The Boresight Assembly insures that the laser beam is aligned with the axis of the receiving telescope. Five percent of the received light signal is directed to a quad detector (micro-channel plate) in the AOE. The four outputs of the quad detector are conditioned and sent to the BA where they are integrated and digitized to produce an error signal. This error signal is processed by an 8097 microprocessor to determine how much motion if any is required to align the laser output to the center of the quad detector. The steering of the laser beam is accomplished via a two-axis gimballed turning prism which has a range of one degree in each axis.

## 4. AOE

The Aft-Optics Electronics is housed in the base of the telescope. The received light signal is optically separated into the three wavelengths of 355, 532, and 1064 nanometers after being focused at the aperture wheel. This wheel has four positions: closed, large aperture, annular aperture, and small aperture. The closed aperture is used anytime that a datatake is not taking place. The

large aperture is used during boresighting and multiscatter operations. The annular aperture is used during multiscatter operations. The small aperture is used during day, night, and multiscatter operations. Each of the above three light sources are directed to detectors optimized for that wavelength. The 355 and 532 channels utilize Photo-Multiplier Tubes (PMT) and the 1064 channel utilizes an Avalanche Photo-Diode (APD). At the input to each detector is a moveable interference filter which is inserted into the light path during daylight measurements to minimize unwanted background from reaching the detector. The filter is removed from the light path for night measurements. The output of each detector is amplified and conditioned and then sent to the DDHU to be digitized.

The AOE uses an 8751 microcontroller to accept commands from and to send status to the IC. The commands control such things as interference filter motion, detector channel gains and offsets, detector high voltage, and background subtraction enable.

## 5. DDHU

The Digital Data Handling Unit receives from the AOE the analog data from each of the three science channels and digitizes this data at 10 Mhz into 12 bits and formats it for transmission to the ground. The DDHU also generates a ten second average (100 laser shots) for the 355 and 532 science channels. This data is called the Quick Look Science Data (QLSD) and is also formatted for transmission to the ground. The QLSD is sent to the IC once every ten seconds over one of the two 1553 serial channels. The other 1553 channel is used by the EDS. Each second the IC sends the Instrument Status Data Block (ISDB) to the DDHU which is incorporated with the QLSD and the raw science data. This data is sent to the ground via the orbiter Ku Signal Processor (KuSP) interface at 4 Mbps and is also recorded on the High Data Rate Recorder (HRR) in the aft flight deck at 2 Mbps.

The DDHU also generates a 10 Hz and a 1 Mhz clock from which all other system timing is derived.

## 6. EDS

The Engineering Data System monitors the majority of the housekeeping measurements for the LITE instrument (over 200). These measurements include temperatures, pressures, voltages, and currents. The signals from the transducers are conditioned and digitized. Then this digitized data is formatted and once per second is sent over the 1553 interface to the IC to be included in the ISDB.

## 7. IC

The Instrument Controller is the heart of the system and is based on an 80186 microprocessor. It interfaces to all the subsystems internal to the instrument and externally it interfaces to the

orbiter via two Serial Digital Input/Output (SDIO) channels on the Smart Flexible Multiplexer/DeMultiplexer (SFMDM) on the pallet.

The IC receives commands from the ground on SDIO channel 0 and executes them accordingly by issuing the appropriate commands to the subsystems. The commands to the subsystems may be serial commands to the AOE and BA or they may be discrettes (lines set high or low) such as the ones that go to the LTM or DDHU. The commands may also be of the type in which parameters inside the IC are updated.

When no commanding is in progress, the IC is building the ISDB once per second. Recall the ISDB contains all the EDS parameters and other parameters deemed necessary for ground inspection. The IC sends the ISDB to the ground approximately once per second over SDIO channel 0 to the Payload Data Interleaver (PDI) interface via the SFMDM. Once every ten seconds the DDHU sends the QLSD to the IC. One tenth of this data is transmitted over SDIO channel 1 each second to the PDI interface via the SFMDM also.

## 8. GSE

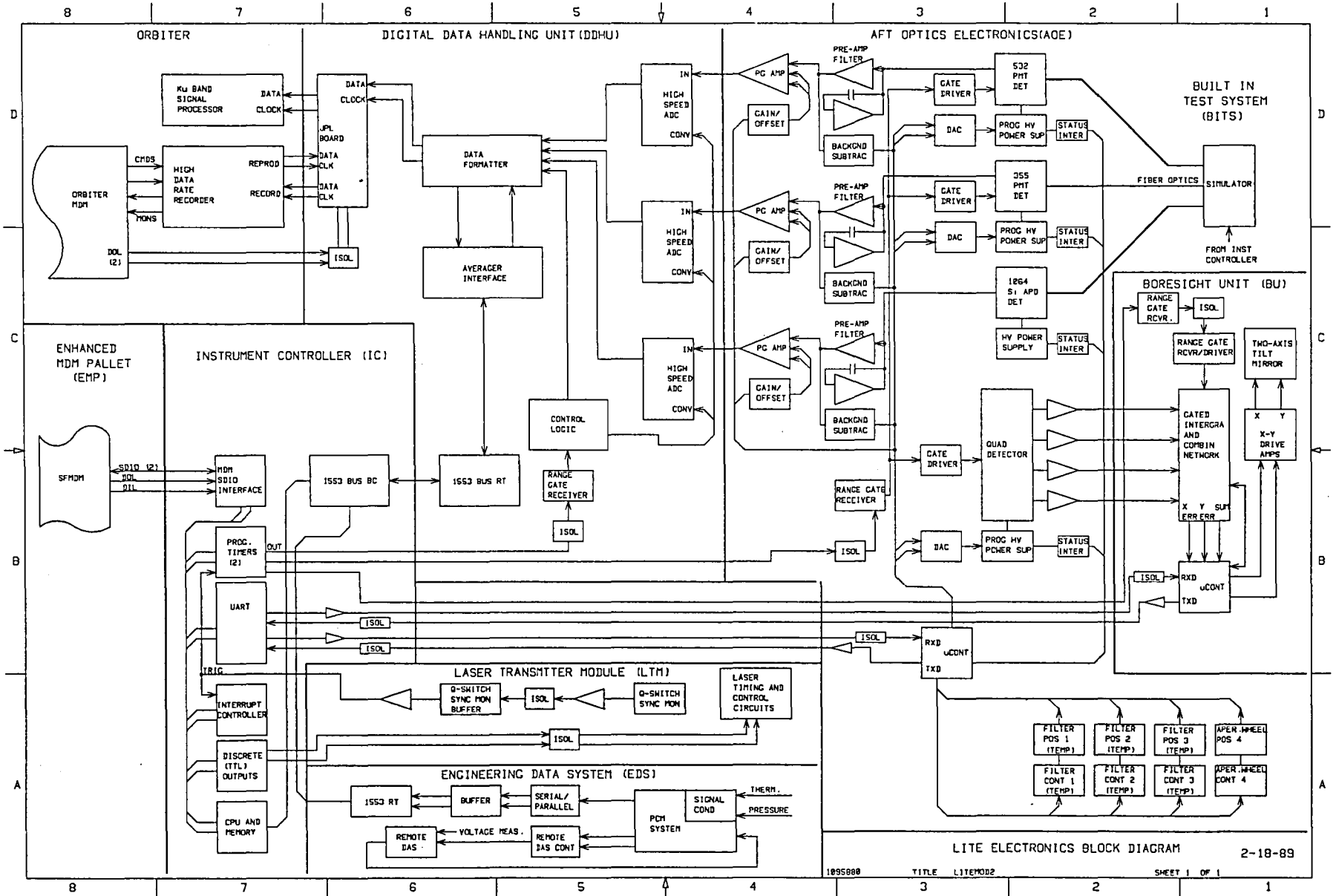
The Ground Support Equipment is a very important part of LITE. Even though it will not fly, it is still built to flight standards. This is necessary because it simulates external interfaces to the instrument which are flight. The GSE must match as closely as possible these external interfaces so that testing is as realistic as possible. The GSE will travel with the instrument wherever it goes.

The GSE consists of two major subsystems which are the pallet and orbiter simulators. The pallet simulator simulates the interface with the SFMDM which allows commands to be sent to and status to be received from the instrument. The orbiter simulator simulates the interfaces with the orbiter. The orbiter interfaces are the HDRR and the KuSP downlink. These two interfaces receive the high rate (raw science) data from the DDHU.

## 9. CONCLUSION

The design requirements for the electronics was to use existing designs and off the shelf components. These requirements have been met except for the use of the high speed 10 Mhz twelve bit digitizers in the DDHU and the extensive use of electrically programmable logic devices (EPLD) throughout the electronics for space savings.

The electronics has been built and is being integrated and tested at this time.



# LASER TRANSMITTER MODULE (LTM) FOR LITE

John Chang<sup>1</sup>, Marc Cimolino<sup>2</sup>, Edmond Joe<sup>3</sup>, Mulgeta Petros<sup>2</sup>, Karl Reithmaier<sup>4</sup>,  
Ray Thompson, Ron Villane

TITAN SPECTRON DIVISION  
Costa Mesa, CA 92626

## 1. Introduction

In December 1991 TITAN SPECTRON successfully completed its six year effort to design build, space qualify, test and deliver the Laser Transmitter Module (LTM) for NASA Langley Research Center's LITE Program. The delivered LTM is a three color Q-switched flashlamp pumped Nd:YAG laser that is described by Dr. Pat McCormick, LITE Project Scientist, to be " the first true world-class lidar in space ". The preliminary design and verification tests results were first presented at the 14th ILRC in 1988. This paper describes not only the delivered product but also the verification and space qualification processes that resulted in the world's first space qualified high powered laser system for environmental exploration from space. Video of the laser operating in a Class 100 clean room and subsystems undergoing 10G vibration tests will provide a vivid illustration of the key elements that separate a space qualified system from its laboratory counterpart. Flight laser performance measurements form the baseline in post-delivery test results to be presented at this conference.

## 2. Laser Design and Performance Verification

The optical, structural and thermo-mechanical design ( Figures 1 and 2 ) remain the same as presented at the 14th ILRC. The laser output is required to exceed 200MJ of IR, 400MJ of green and 150MJ of UV at 10HZ. This was accomplished by doubling and tripling the fundamental 1.06 radiation through CD\*A and KD\*P harmonic generators respectively. The fact that the LITE experiment is designated a primary shuttle payload translates to benign power, weight and volume requirements that were readily accommodated. The delivered LTM system is in an aluminum canister with dimensions of 2ft in diameter and 5ft in length. The system weighs 500lbs and consumes 1500 Watts of power.

In addition to survival of the launch loads the fundamental design goal was to make it possible for the laser to operate in space as it does on the ground. This was accomplished by placing the flight LTM in the canister slightly above atmospheric pressure and design the system to maintain temperature and optical alignment in flight. The similarity in operation conditions makes laboratory verification tests directly relevant for space. An engineering verification laser (EVL) of identical architecture to the flight system ( Figure 1 ) was utilized to A) verify laser performance and architecture, B) provide baseline test results for the flight LTM and C) be used as a test bed for prototype components and mounts. Selected results from the EVL will be shown.

---

<sup>1</sup> Gemstar Development Corporation, Pasadena, CA

<sup>2</sup> Science and Technology Corporation, Hampton, VA

<sup>3</sup> A, E & M, Hampton, VA

<sup>4</sup>California Institute of Technology, Pasadena, CA

The EVL performance data serve as both a design verification and a baseline for measured performance of the delivered system. Systematic performance measurements at component, subsystem and system levels with the space qualified system ( Figure 3 ) were conducted as part of the integration and test tasks. Selected test results verifying system performance will be presented along with requirements. These results form the baseline in the post-delivery measurements to be presented at ILRC16.

### 3. Space Qualification

Space qualification of the laser system with demonstrated laboratory performance is under taken by the combination of analysis, tests, and disciplined process with appropriate documentation and traceability. An invaluable tool used for the development and verification of the LTM system design is an intergated use of analytical models. The mathematical models were used as a system tool to determine and quantify the thermal, structural and optical characteristics of the LTM under varying environmental conditions in space. Three stages of analytical modeling were used. The first stage began with the thermal model. MINI-MITAS was used to characterize the thermal behavior of the LTM design. The sensitivity of the LTM to various ambient conditions was also quantified. The results from this model were used as inputs to the structural model.

The structural analysis, through the use of PATRAN, determined the safety margins of the LTM design. Optical bench deformation caused by the varying temperature distribution and by flight loads was also quantified. This information was fed into the optical model.

The optical model, through the use of CODE V , verified the ray trace of the LTM given the worst case scenarios of the optical element displacement caused by both thermal and structural stress.

The linked models were utilized to generate extensive calculations over a broad range of environments, load conditions and operating conditions to verify the robustness of the design for space operation. Selected illustrative results will be shown.

A successful test program is vital to producing a space qualified laser system. It is only through testing that confidence can be gained on the performance and reliability of components during the environmental stresses experienced in the space shuttle and in space. This test program is especially important to the LTM since many components are first of its kind in space application, some without applicable military specifications.

The LTM test program is comprised of three levels of testing: component level testing, subsystem level testing and system level testing. All the component and subsystem level testing were performed by either TITAN SPECTRON or by the component manufactures. The components and subsystems chosen for environmental testing all had one common denominator: they have never before been flown in space. Each of these components and subsystems were subject to a random vibration test, a sine sweep test ( 10G max ) and a thermal cycle test. Where applicable, the EVL was used as the test bed in order to obtain the measurements before and after each environmental test. Selected segment of video recording of component or subsystem testing at 10G vibration will be shown.

Upon completion of the design verification phase, the program progressed into a system fabrication, integration and test phase. The implementation and verification of the design dictates disciplines associated with space qualified hardware both within TITAN SPECTRON and with vendors and subcontractors. Documentation, procedures and integration plans are integral parts of the hardware building process. Product Assurance was a major element of

the system, with a successful NASA audit and approved Product Assurance plan initiating the formal acceptance.

Contamination control was a critical element in the assembly and testing of the LTM. Three clean facilities were utilized at TITAN SPECTRON. A Class 100,000 Assembly lab was the site for mechanical inspections and for cleaning operations. Within the assembly lab are Class 100 laminar flow hoods. This is the area that the optics were inspected and the optical subassemblies assembled. System integration and system level testing were done in a separate Class 100 clean room.

The delivered system included Ground Support Equipment (GSE) to power up the LTM. This GSE is comprised of three sections: the electrical GSE, thermal GSE and optical GSE. The electrical GSE simulated all the electrical signals going into and out of the LTM from the LITE pallet. The operator of the electrical GSE has access to all command lines through the use of switches on the front panel of the electrical GSE. All monitoring signals are accessed by an off-the-shelf data acquisition program for the PC computer.

In addition, all monitoring signals can be accessed through an array of BNC connections on the front panel should the need to see the signal on an oscilloscope arise. During its test on the ground or during its mission in space, the LTM will not notice any differences in the command and monitor signals. This will eliminate any surprises while the LTM is in space.

#### 4. Conclusion

A system approach to the design, fabrication and testing of the LTM resulted in the successful completion of the world's first space qualified high power laser system. Tools, procedures and risk reduction approaches were developed to address first of a kind issues. The LTM was delivered on December 12, 1991 to Langley Research Center for integration into the LITE pallet and additional system tests. The LTM process and the lessons learned form an unique data base that will serve as the foundation for future lidars in space.

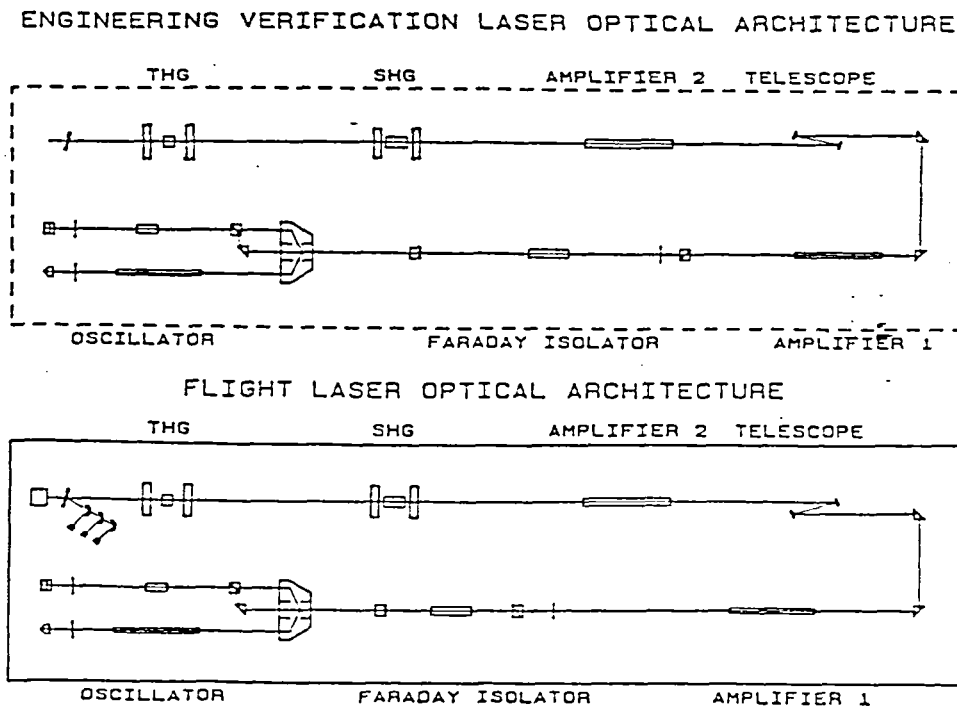


Figure 1. LTM Optical Architecture

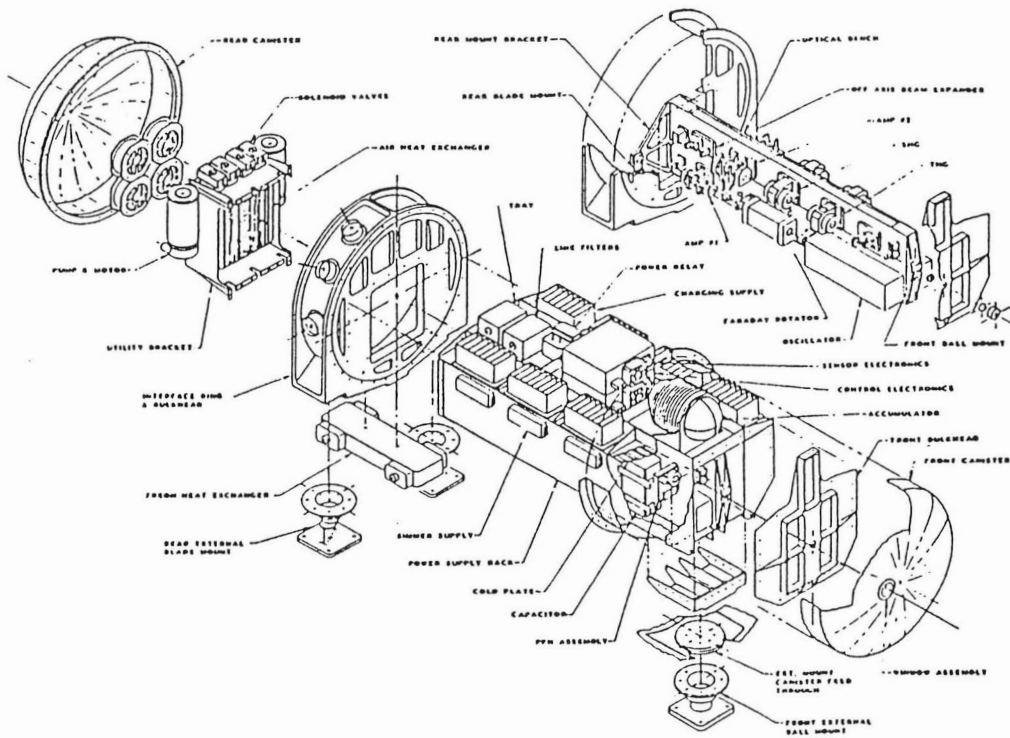


Figure 2, LTM Isometric

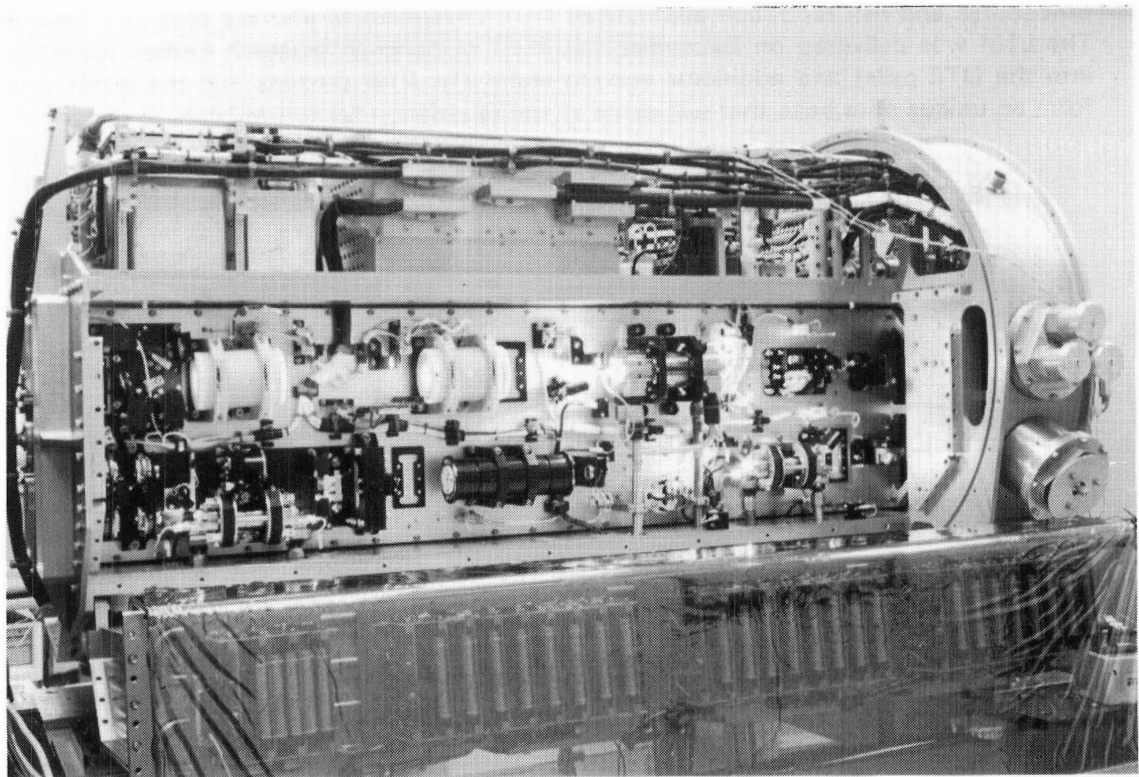


Figure 3, LTM Lasing/Performance Test

## INTERCOMPARISONS OF LIDAR BACKSCATTER MEASUREMENTS AND IN-SITU DATA FROM GLOBE

S. Chudamani\* and James D. Spinhirne  
Laboratory for Atmospheres  
NASA Goddard Space Flight Center  
Greenbelt, MD 20769 USA

The Global Backscatter Experiment (GLOBE) took place during November 1989 and May-June 1990 and involved flight surveys of the Pacific region by the NASA DC-8 aircraft. The experimental instruments were lidars operating at wavelengths ranging from the visible to the thermal infrared and various optical particle counters for in-situ measurements. The primary motivation for GLOBE was the development of spaceborne wind sensing lidar. This paper will concern a comparison of direct backscatter measurements and backscatter calculated from particle counter data. Of special interest is that the particle measurements provided data on composition, and thus refractive index variation may be included in the analysis.

Visible and near IR backscatter measurements were obtained by a lidar system that operated at 1.064, 0.532, and 1.54  $\mu\text{m}$  and was driven by a Nd:YAG laser. A Raman cell containing about 300 psi of methane was used to generate the 1.54  $\mu\text{m}$  transmission by Raman shifting of the 1.064  $\mu\text{m}$  pulse passed through it. The instrument operated at 50 pulses per second and had the flexibility of nadir or zenith viewing. A hard target measurement was applied for backscatter calibration.

The aircraft optical particle counters obtained in-situ measurements of particle size distributions and composition. The information has been applied in Mie calculations of purposes of intercomparison with the lidar data. The results allow the importance for lidar backscatter cross section for various aerosol particle types to be judged. Another interest in the particle data was to validate the lidar calibration for regions of very low backscatter and to extend results to regions where the backscatter was below the accuracy of the lidar measurement. A third application is extrapolation of backscatter measurements to other wavelengths. By comparing the MIE calculations to measured backscatter cross-sections at 0.532, 1.064, and 1.54  $\mu\text{m}$  and verifying accuracy we can extrapolate to other wavelengths with some confidence. Backscatter for 2.1  $\mu\text{m}$  is especially of interest due to the development of 2.1  $\mu\text{m}$  laser technology for coherent wind measurements.

MIE calculations were performed primarily from the particle size-distribution and composition data from the University of Hawaii optical particle counter system (Clarke and Porter, 1991). The University of Hawaii Laser Optical Particle Counter (LOPC) was designed to provide particle size distributions ranging in diameter from 0.15  $\mu\text{m}$  to 7.0  $\mu\text{m}$ . Furthermore it could separate out constituents from their volatility by heating to various temperatures. The distribution measured at 40° C represents the total aerosol content. When heated to 150° C the sulfuric acid content volatilizes, and a new distribution is obtained. Upon further heating to 300° C the sulfate content volatilizes as well and dust-like, crustal or refractory components are left. The sulfuric acid distribution is obtained by taking the difference between the distributions at 40° C and 150° C. The ammonium sulfate distribution is obtained by performing the same arithmetic on 150° C

and 300° C distributions. Mie scattering was calculated with an appropriate refractive index for each component of the particle size distribution.

An illustration of data is shown in Fig. 1 and 2. The case is from a local flight on June 3, 1990 over the Pacific Ocean South East of Japan. During the course of the flight the DC-8 overflew the same track at different altitudes, thus providing in-situ measurements from various levels for intercomparison with the lidar data. Using the size distribution from the LOPC, Mie calculations were performed at 0.532, 1.064, 1.54, 2.1 and 9.25  $\mu\text{m}$ . Appropriate refractive indices were chosen for sulfuric acid, sulfate, and dust for the relevant wavelengths. Fig.1 shows the comparison between our LIDAR data and the MIE calculations from particle measurements at an altitude of 6.2 km. Although the magnitude of cross sections differ the wavelength dependence is consistent. The lidar profile was obtained from a higher altitude an hour earlier. The fact that the backscatter cross-section ratios does not vary with height in Fig.1 would suggest that the particle size distribution is constant with height.

From the LOPC data it is possible to examine the contribution of the particle components to the total backscatter cross-section and also the importance of the different size ranges. A stacked bar chart format illustrates these factors in Fig. 2. The particle size contributions have been grouped in 0.5  $\mu\text{m}$  wide bins. For each bin the contributions of the three components are identified. In this example sulfate is the biggest contributor to the total backscatter cross-section ranging from about 65% at 1.064  $\mu\text{m}$  to about 85 % at 9.25  $\mu\text{m}$ . For 1.064  $\mu\text{m}$  the contribution of the smallest size bin is as much as 35% in a region of moderately high backscatter cross-section. In regions of low backscatter the small particle contribution was even more significant. In the case of 9.25  $\mu\text{m}$  the situation is just the opposite due to the significant contributions of the large size ranges. As a result the large particle statistics are important especially when their count is low. For the intermediate wavelengths of 1.54 and 2.1  $\mu\text{m}$  the contributions of the various size ranges do not vary as significantly and possible errors from the integration procedure should be less significant.

Results from different data sets of the GLOBE Pacific surveys have been studied. The errors arising from the integration scheme, the extrapolation of the size distributions to small particles, and the coarse particle statistics especially in low backscatter regions will be presented. Also the uncertainties in backscatter cross-section associated with the relative humidity variations which affect both the refractive index and the size shifting correction factor applied to the measured size distribution will be examined.

#### Acknowledgements

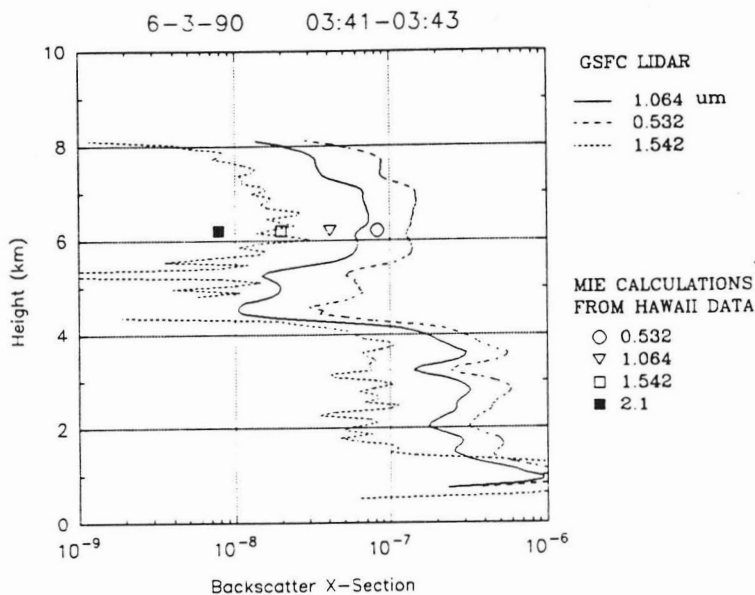
The authors wish to acknowledge Dr. Anthony D. Clarke from the University of Hawaii for providing us with his LOPC size distribution data used in the MIE calculations. They also wish to acknowledge the support of Dr. Ramesh Kakar, NASA Headquarters.

#### References

Clarke, A.D., and J.N. Porter, 1991: Aerosol Size Distribution, Composition, and CO<sub>2</sub> Backscatter at Mauna Loa Observatory. *J. Geophys. Res.* 96, 5237-5247.

\* Science Systems Applications Inc., Lanham Maryland

Fig. 1 Corrected aerosol backscatter cross-section profiles at 1.064, 0.532, and 1.542  $\mu\text{m}$ . Symbols represent MIE calculations at the same 3 wavelengths and 2.1  $\mu\text{m}$  and are from a dataset collected between 04:39-04:48 over the same flight track.



June 3, 1990 04:39-04:48

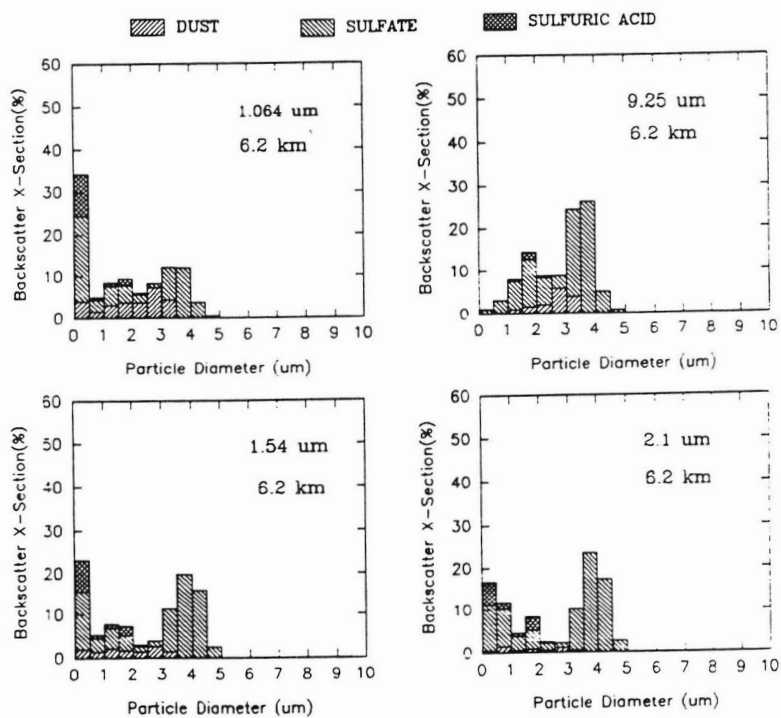


Fig. 2 Stacked bar chart showing percentage contributions of the various size ranges to the total backscatter cross-section. Each bin is broken up to show contributions from sulfuric acid, sulfate and dust. The dataset used is the same as in the MIE calculations in Fig.1.



## **Simulation of the performances of WIND an airborne CO<sub>2</sub> lidar**

D. Oh, A. Dabas, F. Lieutaud, C. Loth, P.H. Flamant

*Laboratoire de Météorologie Dynamique, Ecole Polytechnique, 91128 Palaiseau*

An airborne Doppler coherent lidar is under development as a joint project between France (CNRS/CNES/Météo France) and Germany (DLR). The instrument is designed around the CO<sub>2</sub> laser technology, a heterodyne detection and a conical scanning of the line-of-sight. The 10  $\mu\text{m}$  domain is suitable for long range measurements due to the maturity of the technology and for it corresponds to an atmospheric window. The objectives of WIND are twofold : a) to conduct mesoscale scientific studies in particular over oceanic and inhomogeneous terrain areas; b) to support the Earth-orbiting wind lidar projects (ALADIN, LAWS and BEST). The measurement objectives are a 1 to 3  $\text{m s}^{-1}$  accuracy for the horizontal wind velocity and a 300 m vertical resolution in the lower atmosphere (0-10 km). The first flights are scheduled late 1994 on board a Falcon 20 operated by DLR. The aircraft maximum cruising level is around 11 km. The sampling pattern depends on the flight altitude, aircraft speed, scan angle and revolution period, laser transmitter pulse repetition frequency. A combination of all these parameters result in a several hundred meter size grid at the ground. The vertical resolution is a combination of several factors which include the transmitter pulse length and the signal processor. The accuracy on radial velocity depends on Signal to Noise Ratio (SNR) and frequency estimator. The SNR is determined by the transmitted energy, the receiver collecting area and other instrumental parameters as well as the atmospheric backscatter coefficient and transmission. An efficient heterodyne detection requires a coherent illumination of the receiver by the scattering volume and results into the so-called speckles effect. The heterodyne efficiency depends on instrumental parameters, misalignment and atmospheric index structure function ( $C_n^2$ ). Signal processing is a critical area and various frequency estimators are considered in the study : Fast Fourier Transform, autocovariance (pulse-pair, poly-pulse-pair), auto regressive mean average (ARMA). In order to design an optimized instrument and work out the various trade-offs among the sub-systems a numerical simulation of the performance of WIND has been undertaken. It is done in two steps : it starts with a multi-purpose physical model, and then a dedicated instrumental model for WIND is built. The outputs of the model are used to derive the overall performance of various lidar configurations with respect to the transmitter laser, receiver and scanning characteristics, and frequency estimator. A special attention has been paid to the lag-angle effect due to scan motion and any additional misalignment between the backscattered power and local oscillator.

**Outputs of the model.** The objective of the study is a parametric analysis of an airborne coherent Doppler lidar working at  $10,6 \mu\text{m}$ . The main output of the model is a radial wind velocity error along a line-of-sight. The atmospheric section in the model extends from 0 to 20 km. It includes a standard vertical profile for clear-air backscatter, extinction and absorption coefficients, cirrus cloud between 8 and 10 km, refractive index structure function  $C_n^2$  with two strongly turbulent layers in the planetary boundary layer (from 0 to 1.2 km), plus a CAT layer (10 to 11 km). The computations are conducted on a single shot basis for a 300 m range gate. An average over several successive ranges or shots can be done. The lidar performance is also described in terms of SNR and heterodyne efficiency.

Figure 1 displays the SNR vs altitude for two different scan angles ( $30^\circ$  and  $45^\circ$ ). An improvement of 6 dB is observed in the planetary boundary layer and of about 4 dB in the free troposphere for  $30^\circ$ . The scanning angle results of a compromise between horizontal velocity error and sampling. Figure 2 shows the impact of the transmitter laser energy, pulselength, and chirp on the radial velocity error for a pulse-pair estimator with : a) 0.3 J,  $3 \mu\text{s}$ , 1 MHz; b) 0.15 J,  $2 \mu\text{s}$ , 2 MHz. The maximum error varies from 0.9 to  $2.1 \text{ ms}^{-1}$  around 6 km, while it varies from 0.5 to  $0.8 \text{ m s}^{-1}$  in the PBL and cirrus. A crucial parameter for heterodyne efficiency and SNR is a misalignment between the backscattered signal and the local oscillator onto the photomixer. A conical scan results of in a lag-angle which depends on the looking angle with respect to nadir, scanning period, aircraft altitude. In addition to it a misalignment can result of mechanical vibrations which could offset the transmitted or LO beams. Figure 3 shows the impact on heterodyne efficiency of a  $10 \mu\text{rad}$  static misalignment on top the lag-angle effect for a 30 cm diameter telescope. The dynamic lag-angle due to scanning is plotted in figure 4.

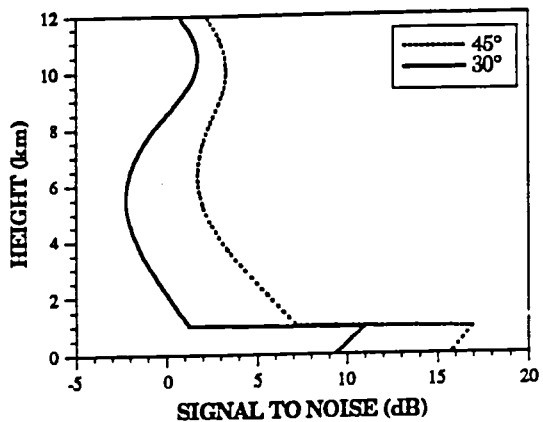


Figure 1. Signal to noise vs. altitude for two different scan angle.  
 Lidar parameters:  $\lambda = 10,6 \mu\text{m}$ ,  $E = 0,3 \text{ J}$ ,  $\tau = 3 \mu\text{s}$ , PBL  $C_n^2 = 10^{-14} \text{ m}^{-2/3}$ , CAT  $C_n^2 = 10^{-15} \text{ m}^{-2/3}$ , telescope diameter = 30 cm.

Figure 2. Radial velocity error vs. altitude for two different configurations of the transmitter.

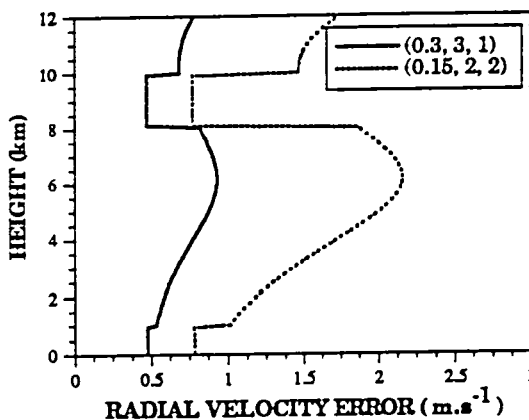


Figure 3. Heterodyne efficiency vs altitude Impact of the static misalignment

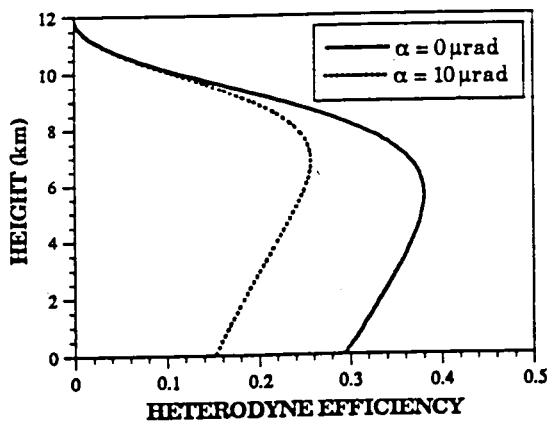
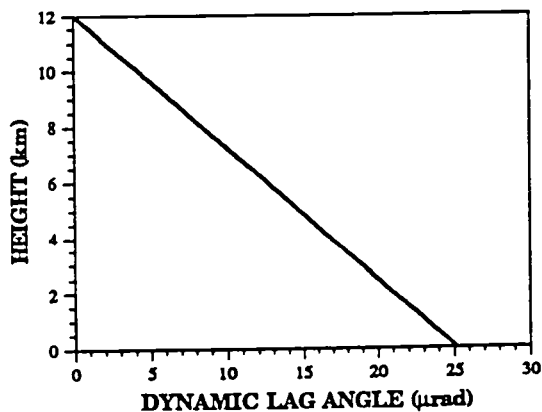


Figure 4. Dynamic lag angle vs. altitude





# Sampling & representativeness for a spaceborne wind lidar

\*F. Lieutaud, A. Dabas, P.H. Flamant, G. Sèze, \*\*Ph. Courtier

\*Laboratoire de Météorologie Dynamique, Ecole Polytechnique, 91128 Palaiseau

\*\* CNRM, Météo-France, 77 rue de Sevres, 92104 Boulogne Cedex

The capability of an Earth-orbiting lidar to produce a reliable windfield sampling with an error of 1-3 m s<sup>-1</sup> relevant to numerical forecasting and climate studies relies on the orbital and instrumental parameters. The spatial and temporal resolutions range from 100 km to 1000 km and 3 hr to 1 month respectively. In this respect cloud obstruction is of great concern, as it can prevent the lidar probing whole parts of the atmosphere, for both short and long periods of time. A worldwide analysis of cloudiness from either visual observations made from the ground or else from the SAGE instrument, has shown that the average cloud cover is 60%. This analysis is however only valid at large scales (time and space) compatible with the currently operating satellites. However, a lidar footprint is only about a hundred meters or less, and it has been observed from ground based lidars that, even when the cloudiness is "100%", some lidar shots get through. A complete analysis of the probability of probing through clouds by a spaceborne lidar is presently beyond our capacities for no small scale cloudiness data set is yet available representing all kinds of meteorological situation at all latitudes.

In order to answer some of the most urgent questions regarding the scientific pay-off of a wind lidar some low resolution cloudiness data set can be used. These can either be derived from satellite observations (ISCCP C1 data) or numerical model outputs (ARPEGE/IFS model). A satellite orbital simulation program gives the lidar shot location on the earth, for given orbital (satellite altitude, orbit inclination), and instrumental parameters (transmitter pulse-repetition frequency PRF, scan rotation time period, nadir angle). For every lidar shot, the cloudiness is used to determine its penetration depth in the atmosphere. The lidar shot density available at given altitude levels can then be derived. Four different orbital scenarios are tested

	Satellite altitude (km)	Orbit Inclination (deg)
orbit 1	450	55
orbit 2	450	90
orbit 3	800	55
orbit 4	800	90

The lidar parameters used for the sampling studies are a 10 s scanning period, a 10Hz PRF and a 45° nadir angle.

**ISCCP C1 data.** The basic information are derived from geostationary satellites (GOESs, METEOSAT, INSAT). The cloud classification and ISCCP C1 data analysis are carried out at LMD. We used the July 1986 data. For each pixel (2.5° by 2.5° at equator) the analysis provides the cloudiness integrated over the atmospheric depth. This cloudiness is then broken down among several layers corresponding to 7 altitude levels. The contribution from various types of clouds is identified using a cloud top temperature criteria based on IR-radiances. Each IR-channel is sampled eight times a day. For each lidar shot the corresponding pixel at ground is identified (and the useful part of the line-of-sight is assumed to be included in this pixel), then it is randomly decided whether there is obstruction or not, and if yes,

which particular layer is responsible for obstruction. A uniform random generator is used providing with a figure  $x$  in the  $[0,1]$  interval. Starting from the top of the atmosphere, if  $x$  is lower than layer 1 cloudiness, then obstruction by layer 1 is assumed. Else, if  $x$  is greater than layer 1 cloudiness, but lower than layer 1 cloudiness + layer 2 cloudiness, obstruction by layer 2 is assumed, and so on. For every level (out of the 8 levels defined by the 7 layers) the total number of shots available for every pixel and for a 24 hrs simulation, was counted. This number was transformed into a shot density per 100 km x 100 km boxes, over 24 hours. Figure 1 shows the maximum shot density at the upper level (25 km) for orbit 1 and orbit 2. Holes appear between swaths, which is not the case for 800 km orbits, so there exists a difference between 450km and 800km satellite altitudes when considering global coverage on a 24 hr period of time.

**ARPEGE/IFS GCM.** The "numerical atmosphere" used here is a T21L15 run output. The global cloudiness is given for 5 days (14<sup>th</sup> to 19<sup>th</sup> July 1989), every 6 hours, and for the 15 model levels. The model mesh is regular with longitude (64 longitude steps) and almost regular with latitude (32 latitude steps). The cloudiness is assumed to be decorrelated from one level to the other, so that the probability of cloud obstruction only depends on the level's cloudiness over the full range. During the 5 day simulation, the total number of shots available in every model mesh and level is counted. It is then transformed into a lidar shot density per 100 km x 100 km boxes, over 24 hours. Figure 2 displays the shot densities for the cirrus (13 km) and lower levels (at ground) for a 450 km orbit and 90° inclination. The various isolines represent : 0 shot, 10 shots and 50 shots. The upper level indicates the maximum shot density, for no cloud obstruction has occurred yet. The coverage is almost uniform for the four different orbits. Minor holes appear only for orbit 4 near the equator. The 55° orbits (orbit 1 and 3) do not allow measurements above about 65° latitude. The maximum shot density is to be found near the poles with a 90° orbit. Lower level shows areas with densities lower than 10 shots or even no shot at all. Those regions are mainly in the ITCZ and the southern hemisphere (south pole excepted). Cloud obstruction in the ITCZ is due to a large extent to cirrus type clouds.

**Wind speed error.** Considerations on single shot signal to noise ratio (SNR) are required to fully assess the unusefulness of wind measurement from space in addition to the spatial coverage presented above. At low SNR the horizontal wind speed error can be large. A separate numerical model was built to compute the radial (along a line-of-sight) and horizontal wind speed error in order to work out the trade-off between those two requirements on SNR and coverage. Considering the horizontal velocity the numerical results for a 9.1  $\mu\text{m}$  lidar show the scan angle with respect to nadir can varies at least from about 30° to 50° depending on the atmospheric target (aerosols, clouds) and the altitude range of interest. Figure 3 shows the vertical profile of horizontal velocity error for a 9.1  $\mu\text{m}$  lidar at an altitude of 400 km. The lidar parameters are : a 30 and 45° nadir angle, a 5 J transmitter energy, and a 1 m-diameter telescope. The PBL height is 1 km, and a cirrus is present at 8-10 km. The vertical resolution is 0.3 km below 2 km, and 1 km above.

*This work is supported by CNES and ESA.*

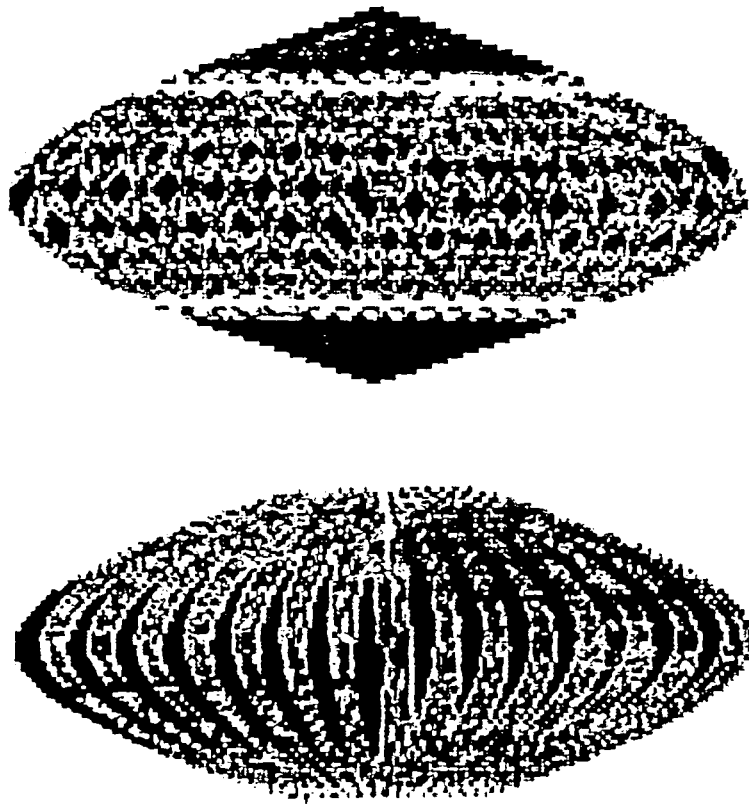


Figure 1

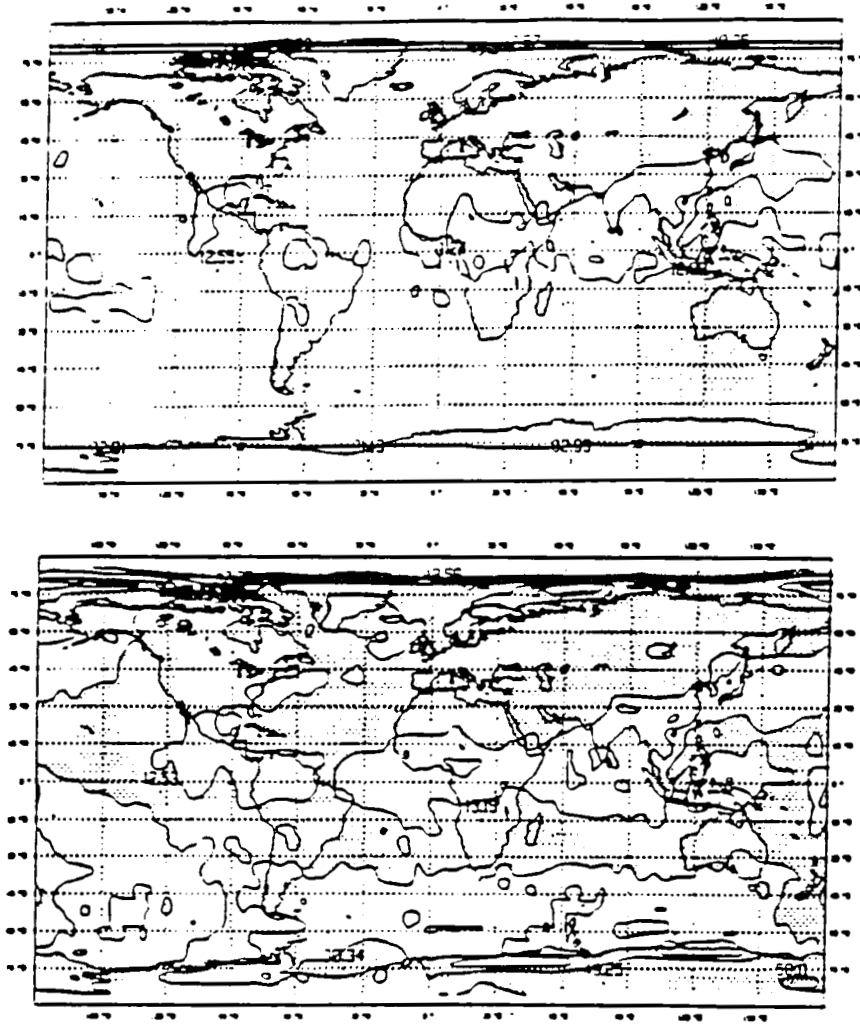


Figure 2

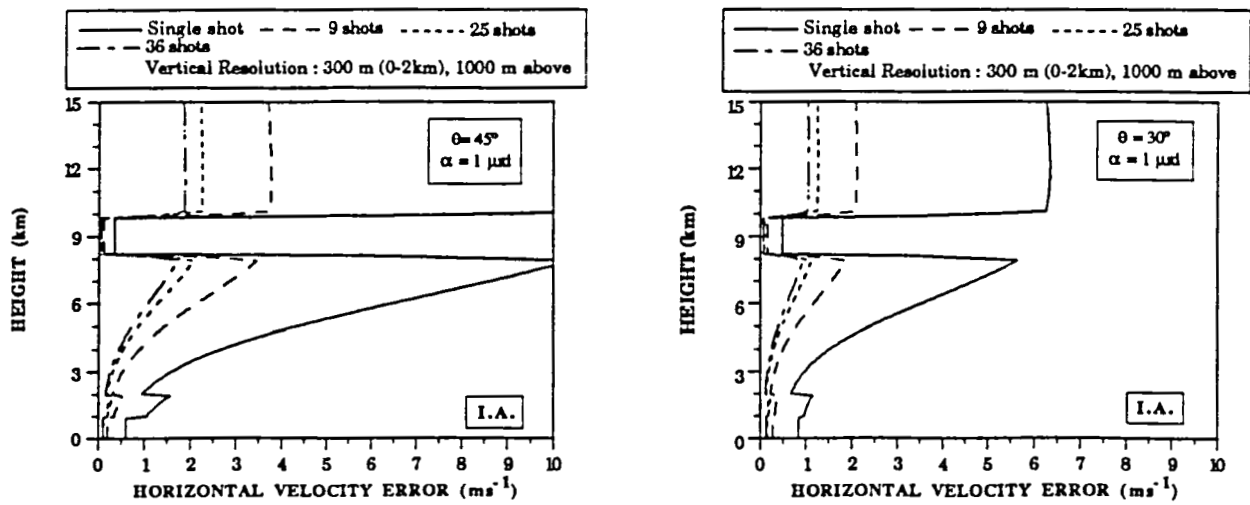


Figure 3

# Laboratory Velocimeter Measurements Using the Edge Technique

Bruce M. Gentry and C. Laurence Korb

NASA/Goddard Space Flight Center  
Laboratory for Atmospheres  
Code 917  
Greenbelt, MD 20771

(301) 286-6842  
(301) 286-6233

We have developed a simple but powerful measurement methodology using the edge technique to measure the Doppler shift of backscattered laser radiation <sup>1</sup>. With this method instantaneous velocity information, including wind measurements, can be obtained with sub-meter-per-second accuracy and with high range resolution using a pulsed lidar system.

This paper describes laboratory experiments which we have recently conducted which demonstrate the basic principles of the edge technique. These experiments demonstrate the sensitivity of the technique and the high velocity accuracy which can be obtained. In addition, many of the characteristics which make the edge technique a powerful method for use in lidar wind applications were verified. These include the insensitivity of the measurement to laser and/or edge filter frequency jitter and drift, and the ability to make Doppler shift measurements which are of the order of 100 times better than the spectral bandwidth of the measurement (the combined spectral width of the laser and edge filter).

A schematic of the optical setup which was used to measure target velocity is shown in Figure 1. A HeNe laser beam is expanded and transmitted via beam steering mirrors to a beamsplitter (BS1). The transmitted portion of the beam goes to a target which is moved along a linear rail at known velocities in the range 0 to  $\pm 1$  m/sec. The beam reflected from the beamsplitter provides the reference from which the unshifted laser frequency is determined. The target and reference beams are recombined by a second beamsplitter. The Doppler shift is determined by making a differential measurement between these two beams. The two beams are distinguished using a chopper which alternately passes either the target or reference beam while simultaneously blocking the other beam. The chopped beams are sent to the edge detection setup. This consists of a collimator and a beamsplitter to split the incoming signal into an energy monitor and an edge channel. The edge channel contains a high resolution edge filter. The edge and energy monitor channel signals are detected by silicon PIN photodiode detectors. The detector signals are digitized by a Tektronix 2430A digital oscilloscope and collected by an IBM compatible computer for processing. The signal detected by the energy monitor

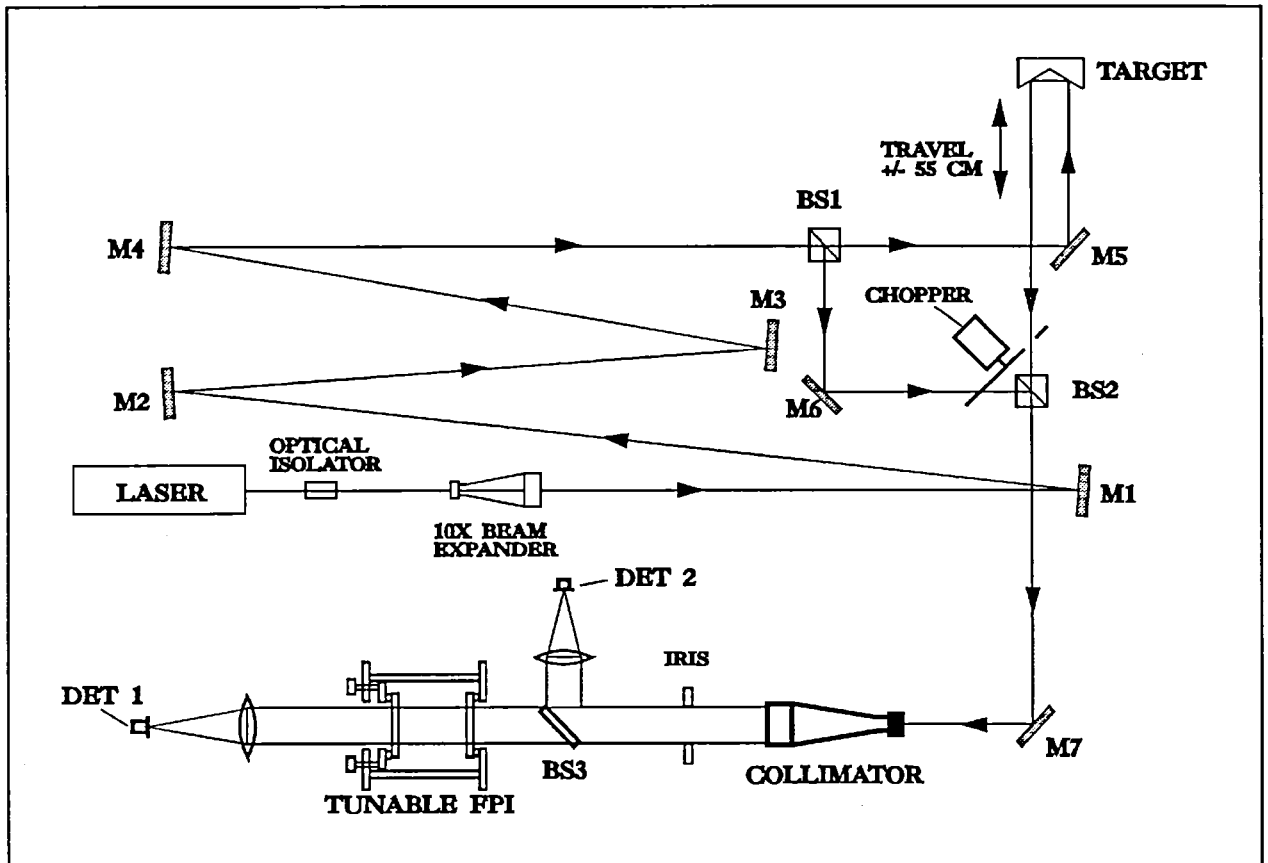


Figure 1 - Optical diagram of experimental setup.

detector (DET2) is used to normalize the edge filter detector signal (DET1) for signal magnitude. A differential measurement between the normalized edge filter signal for the target beam and the reference beam is made once per cycle of the chopper. This desensitizes the resultant differential measurement to frequency jitter and drift for timescales greater than one chopper cycle (2 msec). The Doppler shift is determined from this differential normalized edge filter measurement and a knowledge of the slope of the etalon response function in the region of the measurement.

The edge filter is, in this case, a piezoelectrically tunable Fabry-Perot etalon (Burleigh Model RC 110) with a plate separation of 8 cm and a measured finesse of 35. We note that various filters with sharp spectral edges could also be used. The etalon was temperature stabilized to about 0.75 K but still exhibited large frequency drifts, both long and short term, as shown in Figure 2. The short term frequency jitter observed in the experiment is representative of the magnitude of pulse-to-pulse jitter and frequency drift which might occur in a lidar measurement. We note that the short term frequency jitter is equivalent to Doppler shifts of  $\approx \pm 5$  m/sec which is large compared to the velocity

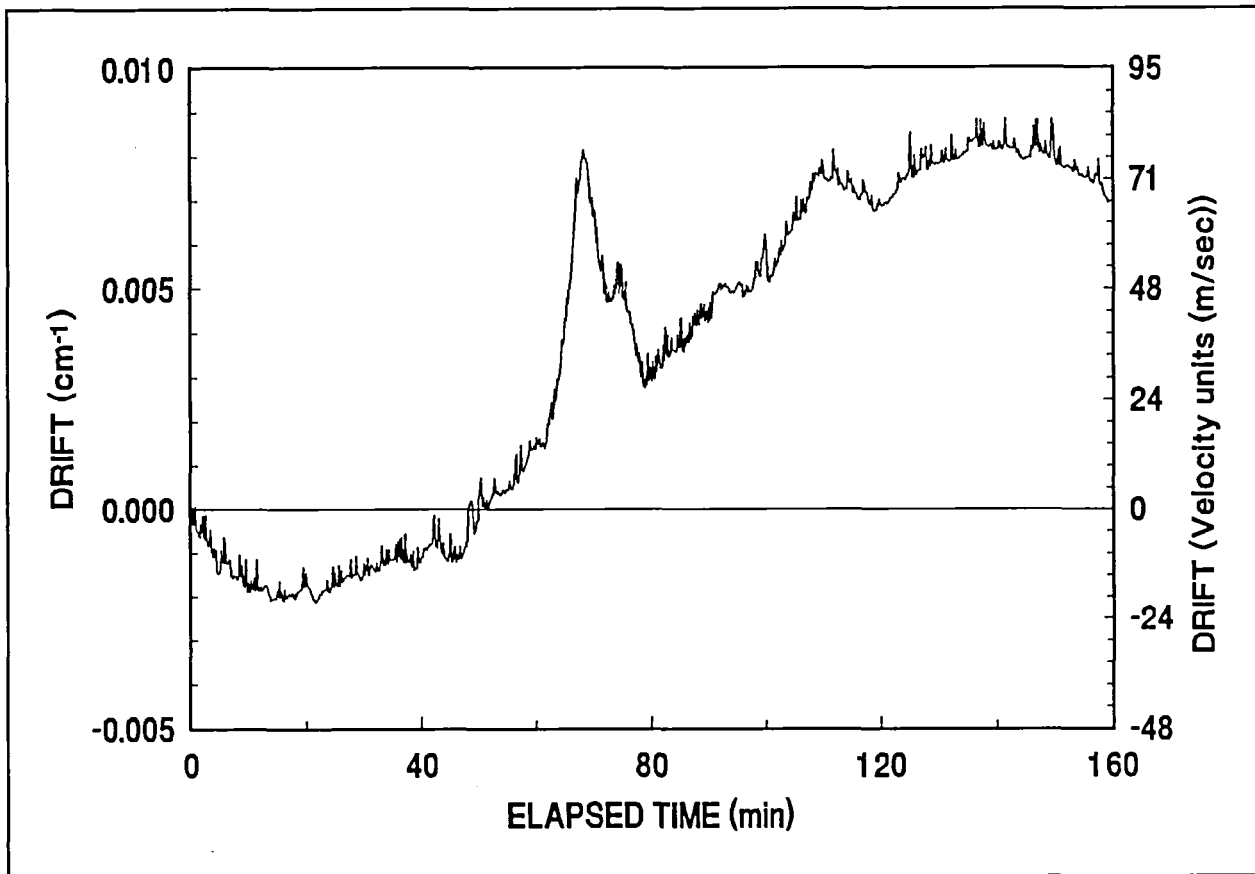


Figure 2 - Frequency drift of the etalon as a function of elapsed time in frequency units (right axis) and equivalent velocity units (left axis).

of the target which we measured. The short term frequency jitter was removed to a level of  $< 10$  cm/sec by the differential frequency measurement employed in the edge technique. The long term drift of the etalon was compensated for by piezoelectrically tuning the etalon to maintain the coincidence of the laser frequency with the edge of the etalon fringe.

Typical velocity measurements are given in Figure 3. This shows a comparison of the laser measured and known target velocity. The slope of a best fit line, in a least squares sense, is 0.99. The rms deviation of the 110 measured values from the line is 0.19 m/sec. As noted above, the high accuracy of these measurements was obtained despite the severe short term frequency jitter shown in Figure 2. This demonstrates the validity of the differential frequency measurement technique which we use in the edge technique measurements. Furthermore, the accuracy of the measurements obtained is nearly 100 times better than the spectral bandwidth of the measurement, the combined laser and filter widths.

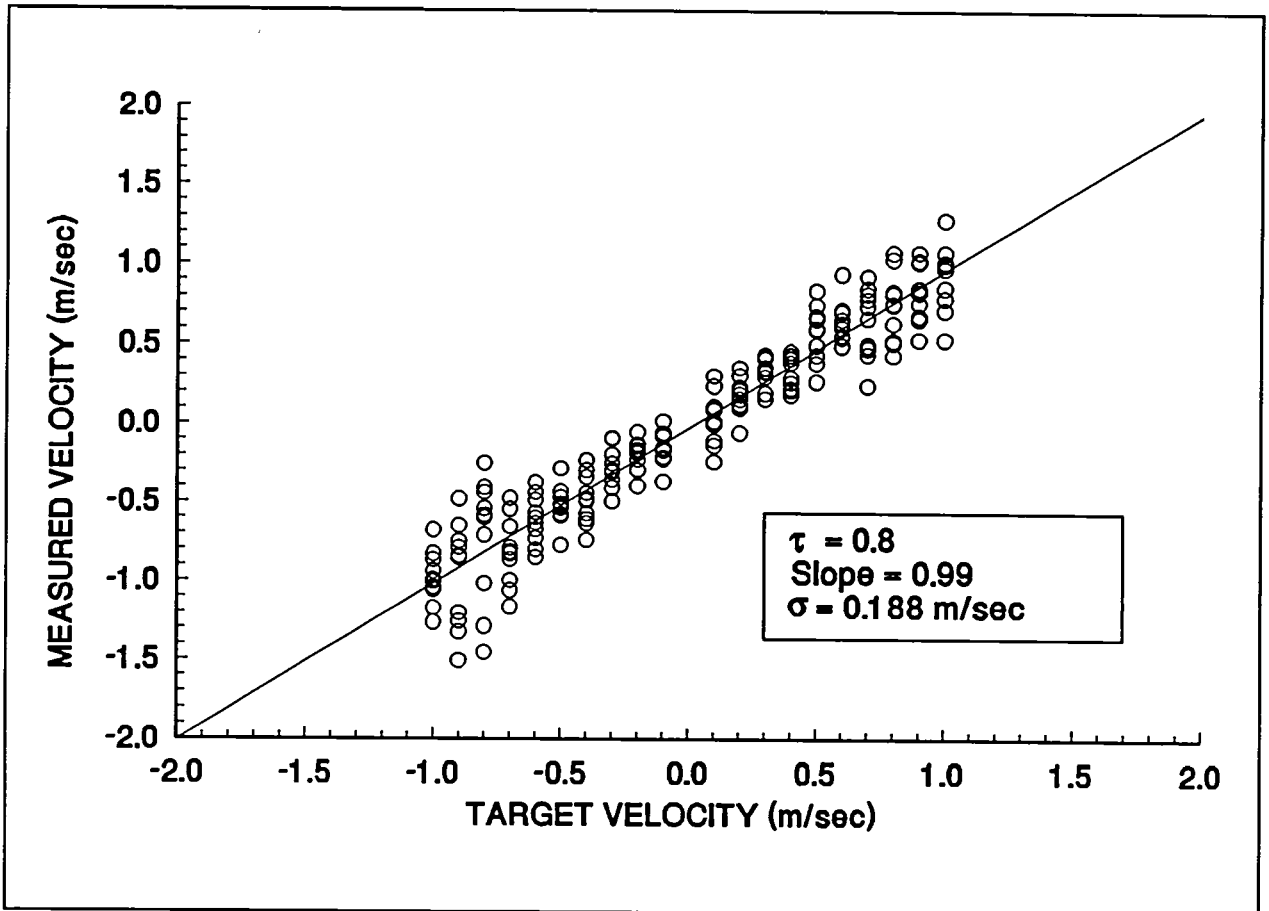


Figure 3 - Laboratory measurements of the velocity of a moving target measured by a laser velocimeter using the edge technique versus the actual target velocity. The best fit least squares line is also shown.

## REFERENCES

1. Korb, C. L., B. M. Gentry, and C. Y. Weng, "The Edge Technique - Theory and application to the lidar measurement of atmospheric winds", accepted for publication in *Appl. Opt.*.

IDENTIFICATION OF CRITICAL DESIGN POINTS  
FOR THE EAP OF A SPACE-BASED DOPPLER LIDAR  
WIND SOUNDER

G.D. Emmitt and S.A. Wood  
Simpson Weather Associates, Inc.  
Charlottesville, VA 22902

The feasibility of making tropospheric wind measurements with a space-based Doppler lidar has been studied by a number of agencies over the past 10-15 years. Currently NASA has a plan to launch such an instrument, the Laser Atmospheric Wind Sounder (LAWS), within the next decade.

The design of the LAWS continues to undergo a series of iterations common to most instruments targeted for a space platform. In general, the constraints of available platform power, weight allowance and project funds continue to change. With these changes the performance and design specifications also must change.

One of the most basic design considerations is the Energy Aperture Product (EAP) which is directly related to the weight and power constraints. The power requirements are scaled to the energy of the laser pulse and its average pulse repetition frequency (prf). The weight of the instrument is determined in part by the energy of the laser and its prf and in part by the size (aperture) of the optics. While not linearly, costs also scale to both the laser energy and telescope diameter.

One of the more critical trades being performed is that of the observations (number and accuracy) returned as a function of EAP. Lidar returns are obtained from aerosols, transparent cirrus, and the tops of opaque clouds. The accuracy of the line-of-sight (LOS) measurement is dependent upon the signal-to-noise ratio (SNR). The accuracy or representativeness of the wind information within a specific volume containing several LOS samples depends upon both the SNR and the number of samples.

The distribution of the observational opportunities can be described in terms of a log-normal distribution of aerosol backscatter with a median near  $3\text{-}5 \times 10^{-11} \text{ m}^{-1} \text{ sr}^{-1}$  for  $9.11 \mu\text{m}$  plus a broad distribution of high backscatter from clouds, desert dusts and

PBL aerosols with a median around  $10^{-7} \text{ m}^{-1} \text{ sr}^{-1}$  (see Figure 1).

Our ability to detect useful information (sufficient SNR and number of samples) can be expressed in terms of a consensus algorithm which is shown schematically in Figure 1b. Note that approximately 8 dB spans the gap between  $< 5\%$  useful returns to  $> 95\%$  useful returns. Overlaying Figure 1b on Figure 1a presents a clear picture of several of the critical regions for performance - one in the region less than  $10^{-10}$  and the other greater than  $10^{-8}$ .

In our presentation we will explore the sensitivity of the performance of a space-based Doppler lidar to a range of EAPs given a realistic distribution of observation opportunities around the globe. A GCM will be used in a simulation experiment to produce performance profiles in terms of the source of backscattered information (see Figures 2 and 3 for examples). Critical design points for the EAP vs backscatter will be identified in terms of marginal performance.

#### Acknowledgement

This work has been supported under NASA contract NAS8-38559.

#### Figure Captions

Figure 1: (a) Schematic distribution of backscatter opportunities for a space-based lidar wind sounder. (b) Schematic of a signal processing algorithm based upon the consensus of 8 independent observations along the LOS.

Figure 2: Summary plot of the distribution of backscatter returns from the equator to  $10^{\circ}\text{N}$  band for a 20 joule laser with a 1.45 meter diameter telescope and in a 500 km orbit during a 12 hour period simulated with a global general circulation model (GCM). This summary indicates the percentage of time the lidar system can make a useful wind measurement in terms of the backscatter conditions - clouds, thin cirrus, aerosols or no returns due to obscuration by higher clouds.

In the GCM based simulation experiment opaque cloud returns are derived from Nimbus 7 climatology and the GCM. Upper tropospheric thin cirrus are obtained from SAGE statistics. The aerosol returns are based upon a  $9.11 \mu\text{m}$

backscatter profile derived from recent GLOBE data and the LAWS baseline 9.11  $\mu\text{m}$  backscatter profile. The usefulness of a measurement is judged in terms of the SNR, the number of shots into a 200x200 km area and the resulting observational uncertainty,  $\sigma_o$ . A threshold value of  $\sigma_o = 5 \text{ m s}^{-1}$  is used above 300 mb while a value between 1 and 5  $\text{m s}^{-1}$  is used below that level. Fractional cloud coverage is used to calculate the number of shots (out of 26) that succeed in passing through to lower layers.

Figure 3: Same as Figure 2 except for a 4 joule .75 meter telescope system.

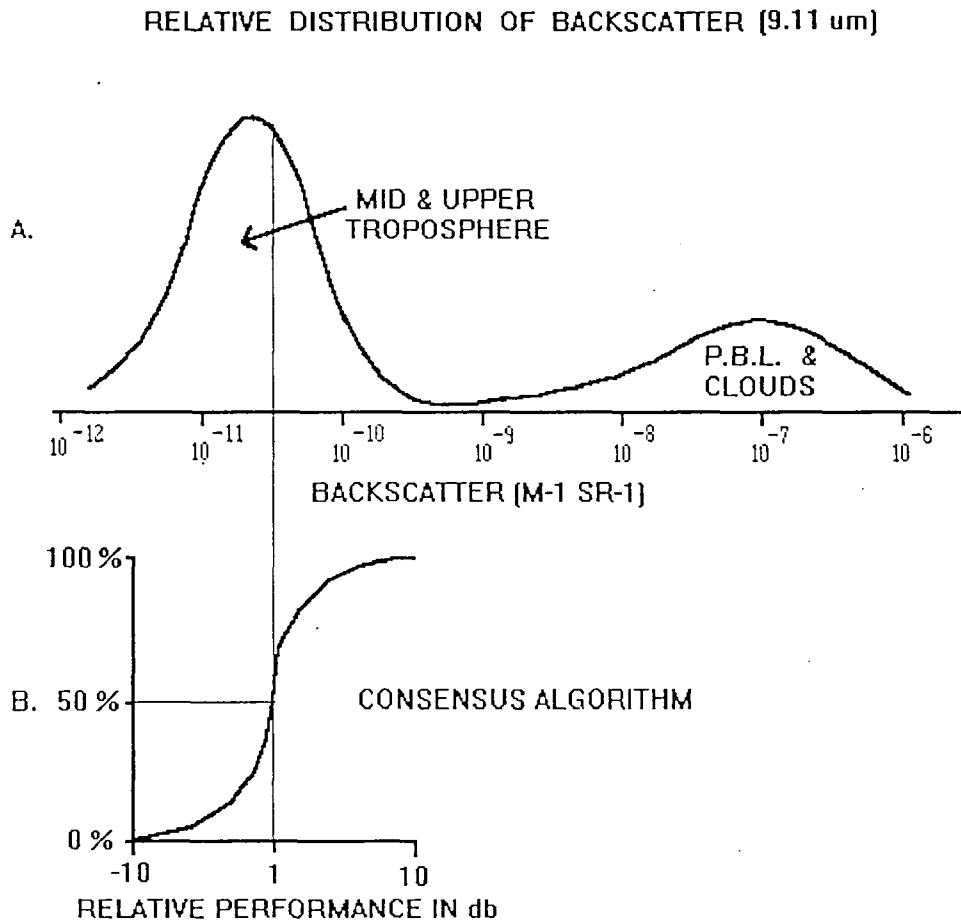


FIGURE 1

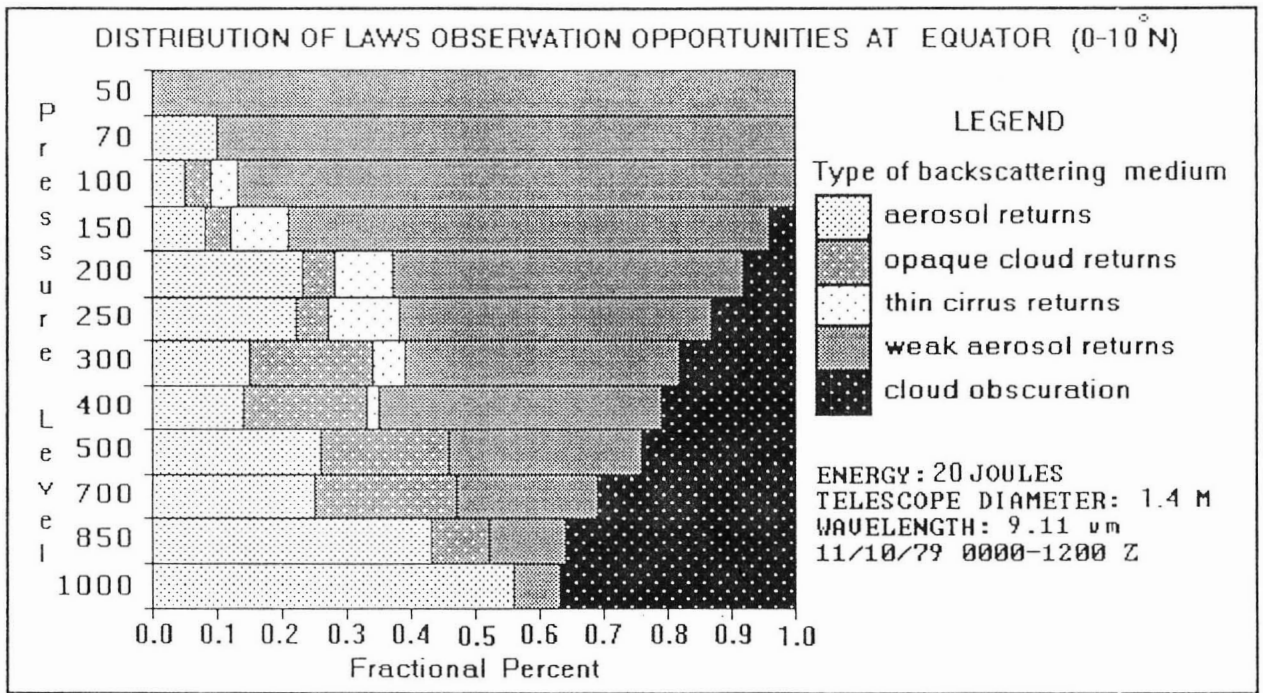


FIGURE 2

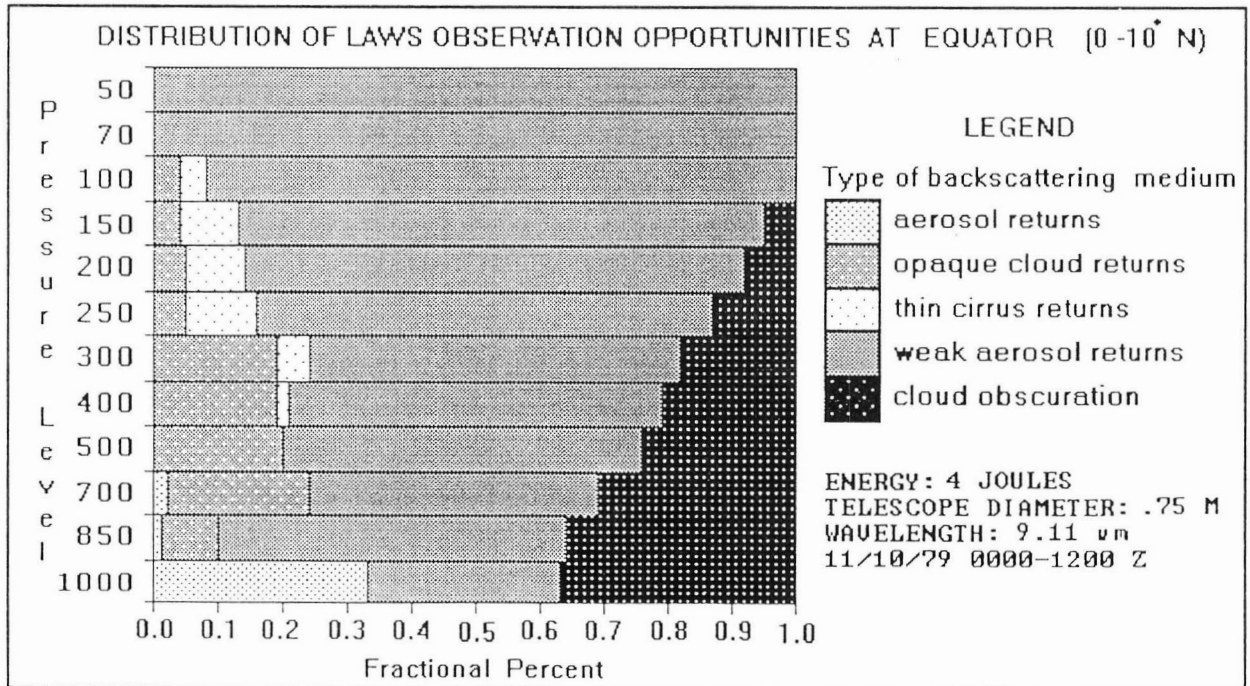


FIGURE 3

# Wind Profiles Derived from Volume Imaging Lidar Data: Enhancements to the Algorithm and Comparisons with Insitu Observations

Piironen, A.K., Eloranta, E.W., University of Wisconsin-Madison

This paper presents wind measurements made with the University of Wisconsin Volume Imaging Lidar (VIL) during August of 1989 as part of the First ISLSCP Field Experiment (FIFE). Enhancements to the algorithm described by Schols and Eloranta<sup>1,2</sup> are described. Comparisons of these results to aircraft, balloon and surface based wind measurements are presented. Observations of the spatial variance of aerosol backscatter are also compared to measurements of the convective boundary layer depth.

Measurements are based on two-dimensional cross correlations between horizontal image planes showing the spatial distribution of aerosol scattering observed by the lidar at intervals of approximately 3 minutes. Each image plane covers an area of 50-100 km<sup>2</sup> and the winds calculated represent area averages.

The calculation of winds from the lidar data requires several steps. In order to suppress the signal decrease as a function of range caused by attenuation, the logarithm of the energy normalized and range square corrected profiles<sup>3</sup> are first filtered using a running high pass median filter. After prefiltering, CAPPI planes are formed from the spherical coordinate VIL data. Scanning a single volume takes approximately three minutes so that image distortion caused by wind motion during the scan time must be corrected. The position of each lidar profile is adjusted by an upwind vector displacement equal to the estimated wind motion occurring in the time since the start of the scan.

A priori wind information is not necessary for this, since the correction is small and the wind calculation can be repeated by using the previous wind results as an estimated wind. Stationary aerosol sources produce fixed spatial patterns, which generate a large CCF peak at zero lag. To prevent on this, the data planes are filtered with a temporal high pass median filter.

There are often intense cloud echos in the CAPPI planes. When one of these moves in or out of the scan region between scans, the cross correlation function between planes is likely to show a strong peak due to correlation between the strong peak and a random structure in the other plane. To avoid this and to prevent correlations between single intense echos from dominating the CCF, the CAPPI planes are 'flattened' by using histogram normalization before the CCF calculation.

The cross correlation function is calculated using a Fast Fourier Transformation (FFT) on zero padded data to avoid overlaps caused by the periodicity of the Fourier

---

<sup>1</sup> Schols, J.L., Eloranta, E.W. (1990): 'The Calculation of the Horizontal Wind Velocity from Volume Imaging Lidar Data'. *Accepted for publication J. Geophysical Research*.

<sup>2</sup> Eloranta, E.W., Schols, J.L. : 'The Measurement of Spatially averaged Wind Profiles with a Volume Imaging Lidar'. *Abstracts 15th International Laser Radar Conference July 1990 Tomsk, USSR*.

<sup>3</sup> Hooper, W.P., Eloranta, E.W. (1986): 'Lidar Measurements of Wind in the Planetary Boundary Layer: The Method, Accuracy, and Results from Joint Measurements with Radiosonde and Kyttoon', *J. Climate Appl. Meteor*, 25, No 7.

Transform<sup>4</sup>. After calculation the CCF is scaled by variances of the data, giving a correlation coefficient function. The position of the CCF maximum gives the average movement of aerosols between the two scans. The CCF mass center is fitted with a quadratic polynomial surface and the maximum point of the fitted function is used to estimate the wind. This interpolates between pixel position and uses information from several pixels to improve the statistical reliability of the position estimate.

Longer time averages of the wind profiles can be done by simply averaging CCFs together. This improves the signal to noise ratio, since the random correlations average towards zero. It typically takes more than three scans for aerosol structures to move across the scan area and therefore at least two CCFs can be averaged together without significant loss in time resolution. If winds are low, we can also improve results by increasing the time separation between the scans used to calculate the CCF. If vertical resolution is not critical, vertical averaging of CCFs can also be used to increase the accuracy of the wind measurements.

Fig. 1. represents half an hour average wind profiles during  $4\frac{1}{2}$  hour measurement session on Aug 8, 1989. Much of this day exhibited very diffuse aerosol structure and thus provides a test of the wind algorithms under difficult conditions. Wind speeds and directions have been marked as • or ◦ depending whether the correlation coefficients were larger or smaller than 0.1, respectively. Larger correlation coefficients correspond to more reliable results. The upper part of the mixed layer typically produces high contrast CAPPI images as a result of intrusions of clear air from above the mixed layer into the more turbid mixed layer: in this region correlations are almost always high. By referring to figure 3 we see that regions of low correlation and therefore less reliable results occur above the mixed layer and in the very well mixed lower middle altitudes of the afternoon profile. In regions with low correlation we still often get good answers, however, occasional spurious values appear (see for example the wind direction at 700 m in 9:30-10:00 profile).

Fig. 2. compares the VIL wind profiles to aircraft, balloon, and surface measurements. Surface measurements were generated from the average of 8 National Center for Atmospheric Studies PAM stations using anemometers on 10 meter surface towers. The aircraft measurements are Canadian NAE Twin Otter flight path averaged measurements using a Rosemount 858 gust probe to sense relative air motion and LORAN-C to provide average aircraft velocity<sup>5</sup>. We see that the results are very close to the aircraft based wind measurement. The VIL wind profiles show less noise than the optically tracked balloon based measurements; they also show a significantly different profile. This is because the balloon samples a single line through the atmosphere while the VIL provides an area average. The balloon is sensitive to individual gusts in addition to the mean wind. Comparison with PAM data shows that, as expected, the surface winds speeds are slower and the directions backed with respect to the wind aloft. Even one hour averages of the surface winds show large fluctuations between stations; the standard deviation of the 8 station averages is shown by the error bars on the surface winds.

---

<sup>4</sup> Press, W.H., Flannery, B.P., Teukolsy, S.A., Vetterling, W.T. (1988): 'Numerical Recipes in C, The Art of Scientific Computing', Cambridge Univ. Press, ISBN 0-521-3546-X

<sup>5</sup> MacPherson, J.I., 'NAE Twin Otter Operations in FIFE 1989', National Aeronautical Establishment of Canada, Laboratory Report LTR-FR-113

We also calculate the variance of the backscattered prefiltered lidar data displayed in each CAPPI. Fig. 3. presents the logarithmic variance of the backscatter as a function of time and altitude. For comparison we also show mean boundary layer height, cloud base, and plume tops determined by visual inspection of VIL RHI images. Convective plumes produce enhanced variance inside the mixed layer and the plume top measurements correlate very well with the boundary of this enhanced region. Another region of enhanced variance is seen before 11 am and near 2 km; this corresponds to the top of a residual aerosol layer left from the previous day's convective boundary layer. In a previous study<sup>3</sup> visual estimates of the mean boundary layer depth were found to correspond to the altitude of the lowest variance maximum. In this case the variance maximum is quite weak and appears at a slightly lower altitude than the visual estimates.

If the internal scatter in the wind profiles are used to judge the probable errors in the VIL wind determinations, we estimate accuracies of about 0.15 m/s and 2° in these profiles. The single aircraft flight leg average wind provides remarkable agreement with the VIL area average wind determination(0.2 m/s and 1 deg).

Acknowledgements: We would like to thank Finnish Academy, University of Joensuu, Finland, and Suomen Kulttuurin Edistämmissäätiö Foundation for financial support to Antti Piironen, which made it possible for him to make research work in University of Wisconsin-Madison. Also NASA Grant NAG-5-902 and ARMY Research Office Grant DAAL03-86-K-0024 and DAAL03-91-C-0222 are acknowledged.

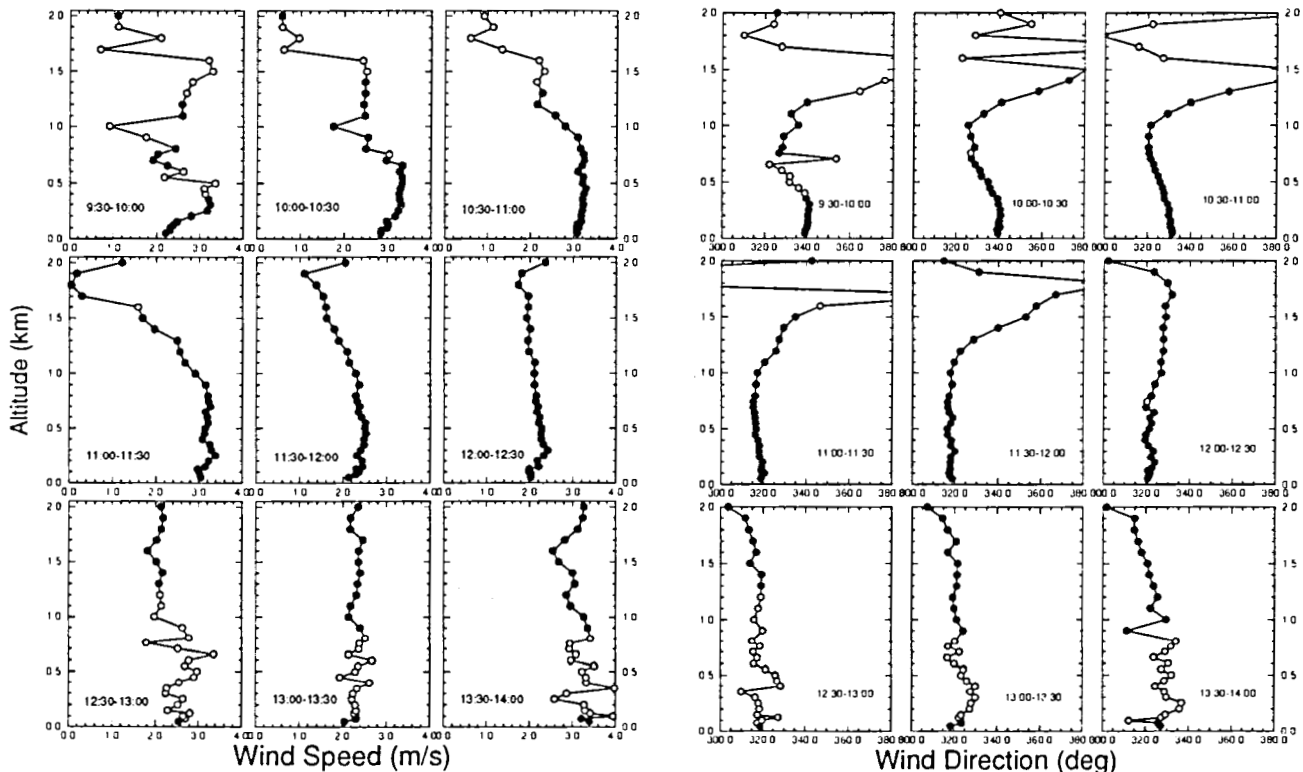
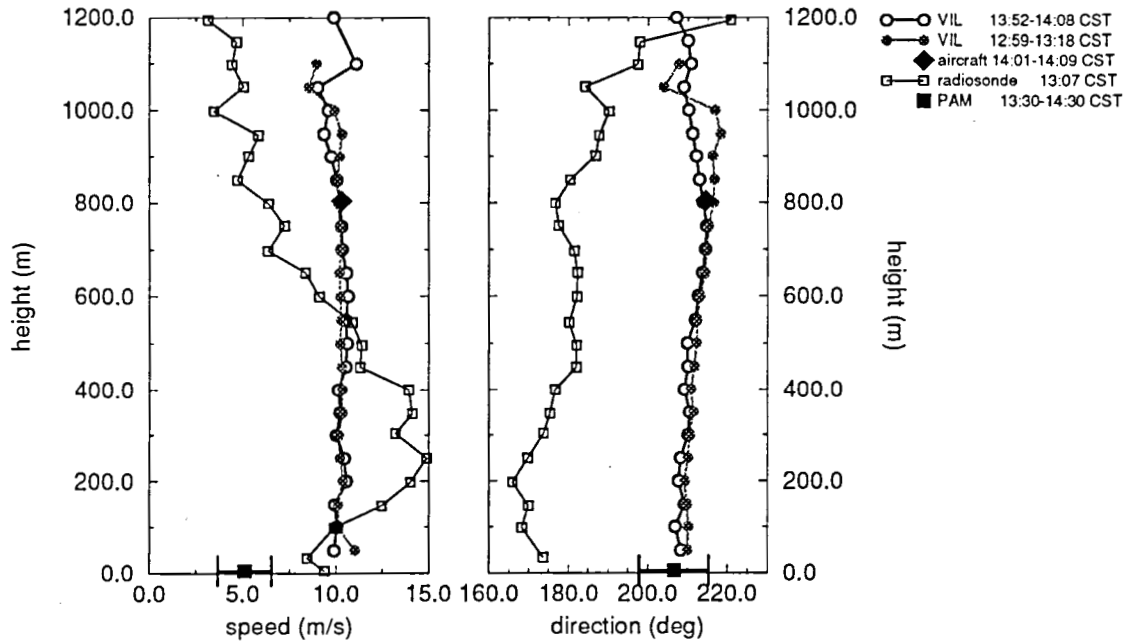
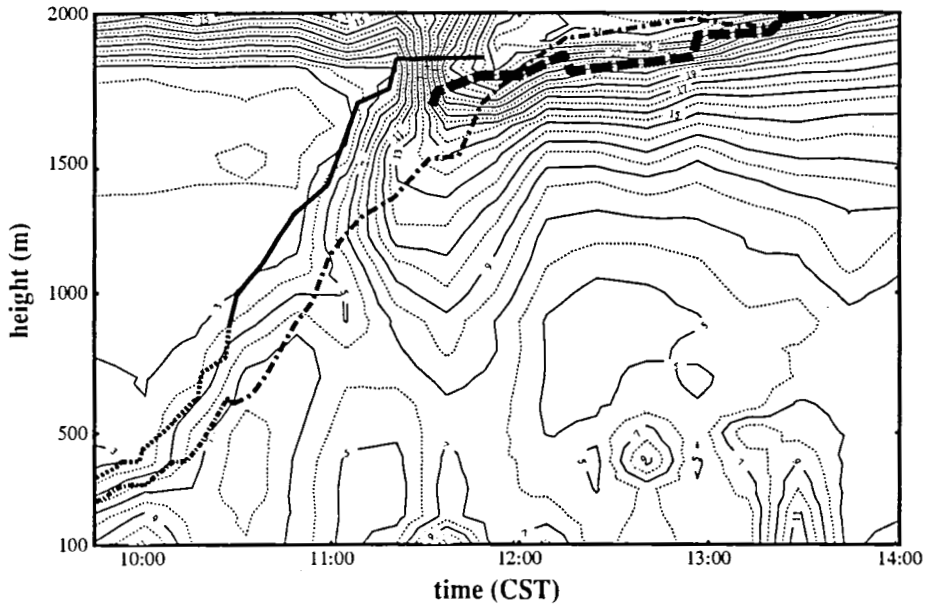


Fig. 1. VIL wind profiles between 9:30 and 14:00 on Aug 8, 1989. Open symbols indicate measurements where the correlation coefficient was smaller than 0.1.



**Fig. 2.** Wind speed and direction measured with VIL compared to measurements made by 1) an optically tracked radiosonde, 2) aircraft instruments, and 3) anemometers on 10 meter surface towers. One hour averages of results of eight NCAR PAM stations have been used for the 10 meter measurements. Data was acquired in clear weather conditions on Aug 3, 1989.



**Fig. 3.** Logarithmic variance of VIL CAPPI planes as a function of time at Aug 8, 1989. Plume tops are shown as continuous line. The altitude at which plumes from the mixed layer occupy 50 % of the area is shown as a dot-dashed line. Cloud base is shown as a dashed-bold line. Plume tops, mean mixed layer depth, and cloud base altitude were measured by visual inspection of VIL RHI images. The determination of boundary layer depth was difficult because of poor contrast between plumes and background before 10:30; these values are shown as shaded lines.

# MEASUREMENTS OF WIND DIVERGENCE WITH VOLUME IMAGING LIDAR

P.W. Young

Department of Physics  
University of Wisconsin - Platteville  
Platteville, WI 53818 USA

E.W. Eloranta

Department of Meteorology  
University of Wisconsin  
Madison, WI 53706 USA

Mesoscale horizontal divergence and vertical motion in the boundary layer are key ingredients in atmospheric and climate modeling. These quantities are very difficult to measure. This paper presents a technique for determining the divergence over a 10 km x 5 km area from lidar images depicting the spatial distribution of the naturally occurring atmospheric aerosols.

In the absence of sources, the temporal evolution of the spatial inhomogeneities in the atmospheric aerosol distribution is due predominantly to the wind. The mean wind translates the pattern; the spatial variations in the wind, including divergence, alter the pattern of the inhomogeneities. The University of Wisconsin Volume Imaging Lidar (VIL) produces a time sequence of three-dimensional maps of the aerosol content, thus showing the evolution of the inhomogeneities. The original line-of-sight data are first processed into horizontal sectors (typically 30° in azimuth) every 50 m in altitude. The data in each horizontal sector is then reprocessed to produce uniform, rectangular grids. These rectangular maps are then used for the divergence calculations.

The divergence is determined using the two-dimensional spatial cross correlation between successive maps in the same horizontal plane. Calculations of the mean wind from cross correlations of VIL data were first performed by Eloranta and Schols.<sup>1,2</sup> In those calculations the aerosol maps from the VIL were corrected for shape distortion caused by the mean wind over the scan time, but the effects of spatial wind variations were ignored. By taking into account at least some part of

those variations, the wind divergence can be determined from the correlation calculations along with the mean wind.

Divergence in the horizontal components of the wind velocity stretches (or compresses) the inhomogeneities in the aerosol distribution. The aerosol content in an area  $L_x \times L_y$  at the time  $t_1$  is spread into the area

$$L_x \left( 1 + \frac{\partial u}{\partial x} \Delta t \right) \times L_y \left( 1 + \frac{\partial v}{\partial y} \Delta t \right)$$

at time  $t_2$ . This spreading can be removed from the VIL map at time  $t_2$  by recalculating the horizontal data array at time  $t_2$  using this enlarged area instead of the actual area. This effectively compresses the inhomogeneities in the map back into their original shapes. The cross correlation between the actual map at  $t_1$  and the properly stretched map at  $t_2$  is greater than without this correction.

To determine the horizontal divergence, the above procedure is performed for different assumed values of  $\partial u/\partial x$  and  $\partial v/\partial y$  until the correlation is maximized. The original 10 x 5 km area, represented by a 200 x 100 array, is stretched in increments of 100 m (+50 m and -50 m) in both x and y. The VIL images are separated by approximately 3 minutes, so a 100-m stretch increment corresponds to increments of approximately  $5 \times 10^{-5} \text{ s}^{-1}$  and  $10 \times 10^{-5} \text{ s}^{-1}$  in  $\partial u/\partial x$  and  $\partial v/\partial y$ , respectively. Figure 1 shows the effects of this process on the cross correlation peak. The values for  $\partial u/\partial x$  and  $\partial v/\partial y$  are interpolated by fitting the correlation data around the maximum with a two-dimensional, second-order polynomial.

The results of this procedure for a half hour sequence at a single altitude are shown in figure 2. These data were determined from time-averaged correlation calculations, where a sequence of 5 correlations were averaged together to find the maximum. It is encouraging that the values obtained are of realistic magnitude and consistent over time, but much work remains to refine the method and verify the results.

Partial support for this work has been provided under NASA Goddard Grant NAG 5-902 and ARO Grants DAAL03-86-K-0024 and DAAL03-91-G-0222 and by a SAIF grant from UW - Platteville.

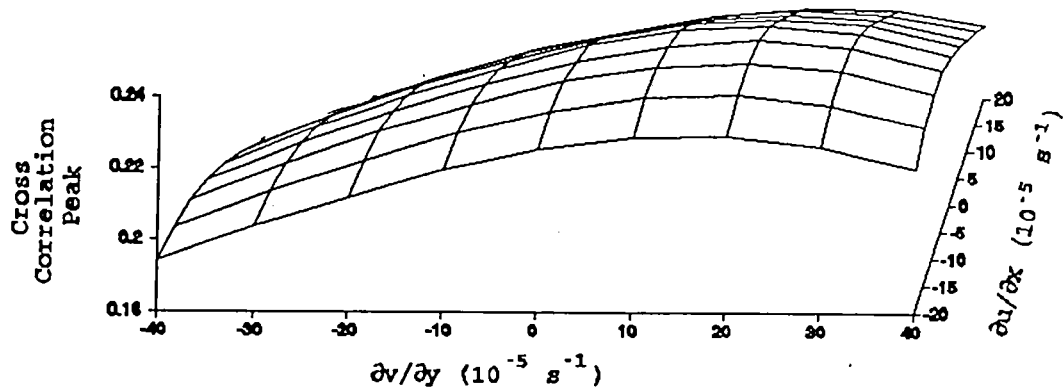


Figure 1. Cross correlation peak as a function of assumed horizontal divergence for data taken at 12:16 CDT on 8 August 1989 as part of the First ISLSCP Field Experiment (FIFE).

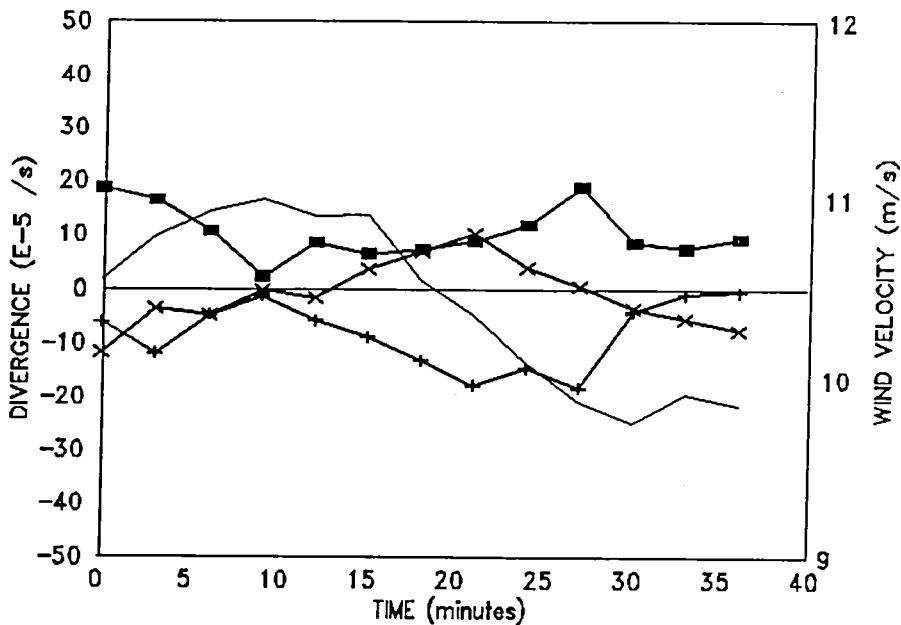


Figure 2. Divergence measurements at an altitude of 300 m starting at 11:33 CDT. Data were acquired during clear weather on 8 August 1989 as part of FIFE.   
 ..... velocity; --X--  $\partial u/\partial x$ ; --+--  $\partial v/\partial y$ ; —■— divergence =  $-(\partial u/\partial x + \partial v/\partial y)$

## References

1. J.L. Schols and E.W. Eloranta, "Calculation of Area-Averaged Vertical Profiles of Horizontal Wind Velocity using the University of Wisconsin Volume Imaging Lidar Data," accepted for publication, *J. Geophys. Res.*
2. E.W. Eloranta and J.L. Schols, "Measurements of Spatially Averaged Wind Profiles with Volume Imaging Lidar," *Abstracts, 15th International Laser Radar Conference*, Tomsk, USSR, 23-27 July 1990, 227-229.

## DIAL MAPPING OF ATMOSPHERIC ATOMIC MERCURY OF GEOPHYSICAL ORIGIN

H. EDNER, P. RAGNARSON, S. SVANBERG AND E. WALLINDER  
Department of Physics, Lund Institute of Technology  
P.O. Box 118, S-221 00 Lund, Sweden

### ABSTRACT

The atmospheric distribution of atomic mercury is studied with the differential absorption lidar technique using the 253.6 nm Hg resonance line. Using a mobile lidar system employing a Nd:YAG-pumped dye laser studies were performed in Italian geothermal and mining areas. Concentrations ranging from the background value  $2 \text{ ng/m}^3$  to several  $\mu\text{g/m}^3$  were measured.

- \* -

Mercury is the only atmospheric pollution gas occurring as free atoms. Mercury is released from chlorine-alkali and coal-fired power plants, refuse incineration plants and from crematories. Mineralizations, geothermal reservoirs and volcanism are also known to be associated with elevated atomic mercury concentrations. Mercury constitutes a considerable environmental problem that has received considerable attention. It has also been suggested that geothermal energy and ore deposits might be located focusing on associated atmospheric mercury anomalies.

Recently, we have demonstrated a differential absorption lidar technique for measurements of mercury down to the background concentration value of about  $2 \text{ ng/m}^3$  [1]. A compact Nd:YAG-pumped dye laser with subsequent doubling in BBO was used at the mercury resonance line at 254 nm. Range resolved measurements of Hg up till a range of about 1 km were possible employing a mobile system. Apart from studies of industrial pollution we have performed extensive measurements of atomic mercury in Icelandic and Italian geothermal fields [2,3]. Very high concentrations (up to  $1000 \text{ ng/m}^3$ ) were found in Italy, while in Iceland mercury seems to be present as molecular compounds. Studies were also made in the Mt. Amiata mercury mining area (Tuscany) revealing strong emissions from the distillation plant and from banks of roasted cinnabar (HgS) ore [4]. The present paper describes our recent lidar mappings of geophysically related mercury.

The basic description of the mobile lidar system used in the present measurements is given in Ref. 5. The mobile system is housed in the  $6 \times 2.3 \text{ m}^2$  laboratory area of a Volvo F610 truck, and electric power for field work is supplied from a 20 kVA diesel generator installed in a trailer towed by the truck. The laser source is a Continuum Model YG 692 frequency-tripled Nd:YAG system pumping a Continuum Model TDL-60 tunable dye laser. The dye laser is operated at wavelengths around 507 nm with Coumarine 500 dye. The pulse energies are 25-30 mJ and the repetition rate is 10 Hz. The dye laser output is frequency-doubled to the UV region by using a beta barium borate (BBO) crystal yielding pulse energies up to 5 mJ at the Hg resonance line at 253.6 nm. The linewidth of the radiation is 0.001 nm well matching the atomic line, which has a pressure- and isotope broadened width of about 0.005 nm. The dye laser wavelength is calibrated by separating 10% of the frequency-doubled beam and by monitoring the absorption of this beam in a cell of mercury vapour. In the differential absorption measurements the laser is tuned on and off resonance with the mercury line every second laser shot. The UV beam is directed into the atmosphere via right-angle quartz prisms and the large

beam-directing mirror placed in a dome on top of the lidar van. The mirror can be rotated under computer control around the horizontal and vertical axes to determine the direction of the output beam. Back-scattered radiation is received by the same mirror and directed into a vertical 40 cm diameter Newtonian telescope. An interference filter selects the appropriate wavelength range and a photomultiplier detects the radiation. In order to reduce the dynamic range in the detection electronics, the photomultiplier gain is ramped up to reach its full value at a range of about 300 m. A transient recorder performs A/D conversion of the signal with a time resolution of 10 ns. The digital signals are separately averaged for on and off-resonance laser shots in a computer that subsequently stores the data on floppy disks. During a measurement the computer controls laser firing, dye laser wavelength setting, beam direction, and data acquisition. In comparisons between the lidar recordings and the result from gold amalgamation point mercury monitors a good agreement was established [6].

Fig. 1 shows the result from a vertical scan close to the cooling tower at the geothermal power station at Larderello (Tuscany). Included in the picture are the results from point monitors showing values in good agreement with the lidar data. Measurements of the total mercury flux from the geothermal power station at Piancastagnaio (Tuscany) yielded an emission value of about 20 g/h; a vertical scan is shown in Fig. 2. Mercury concentration values at the now abandoned mercury mine at Abbadia S. Salvatore (Tuscany) are shown in Fig. 3. Especially high atmospheric concentrations were found close to the mercury roasting and distilling plant. There is also a considerable outgassing of mercury from the banks of roasted cinnaber (HgS) ore. The vertical concentration profile over such a bank as assessed by lidar is shown in Fig. 4.

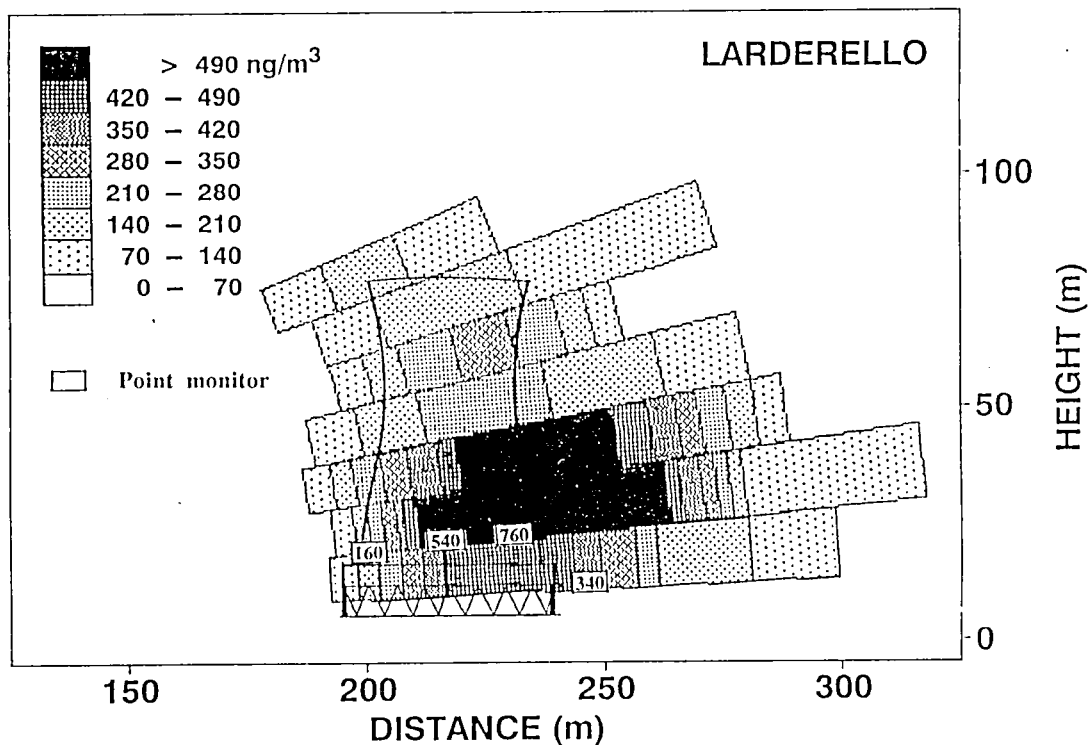


Fig. 1. Vertical scan close to the cooling towers at the geothermal power plant (120 MW) at Lardarelo (Italy)

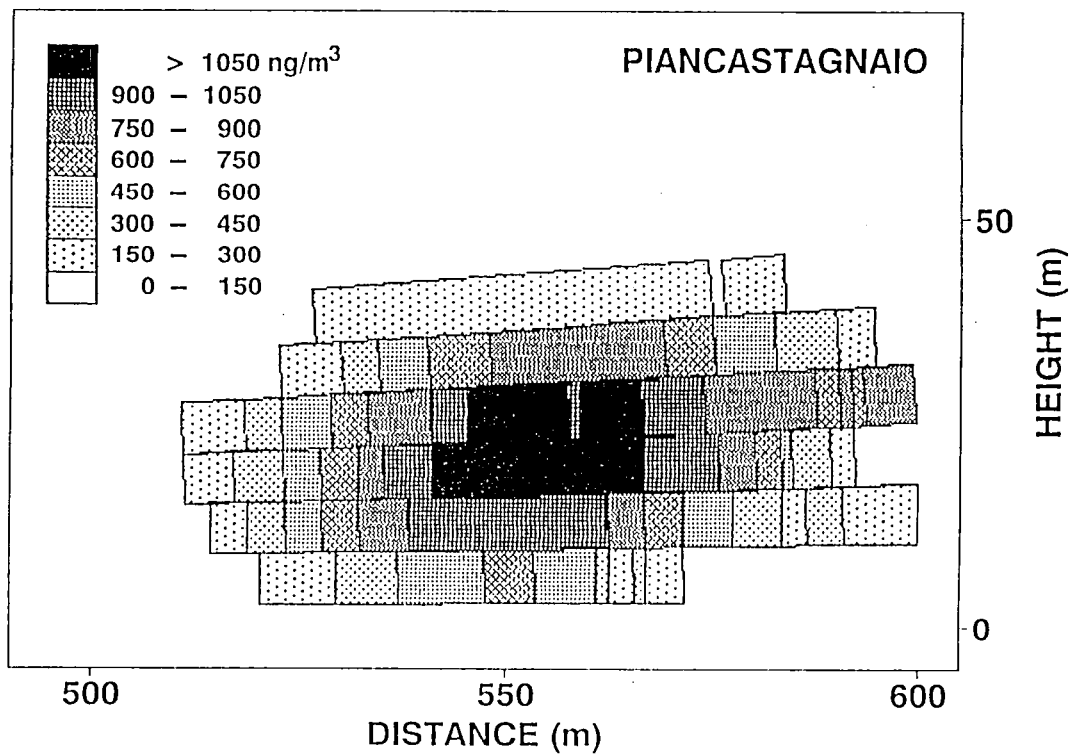


Fig. 2. Vertical scan through the plume from the geothermal power plant (20 MW) at Piancastagnaio (Italy)

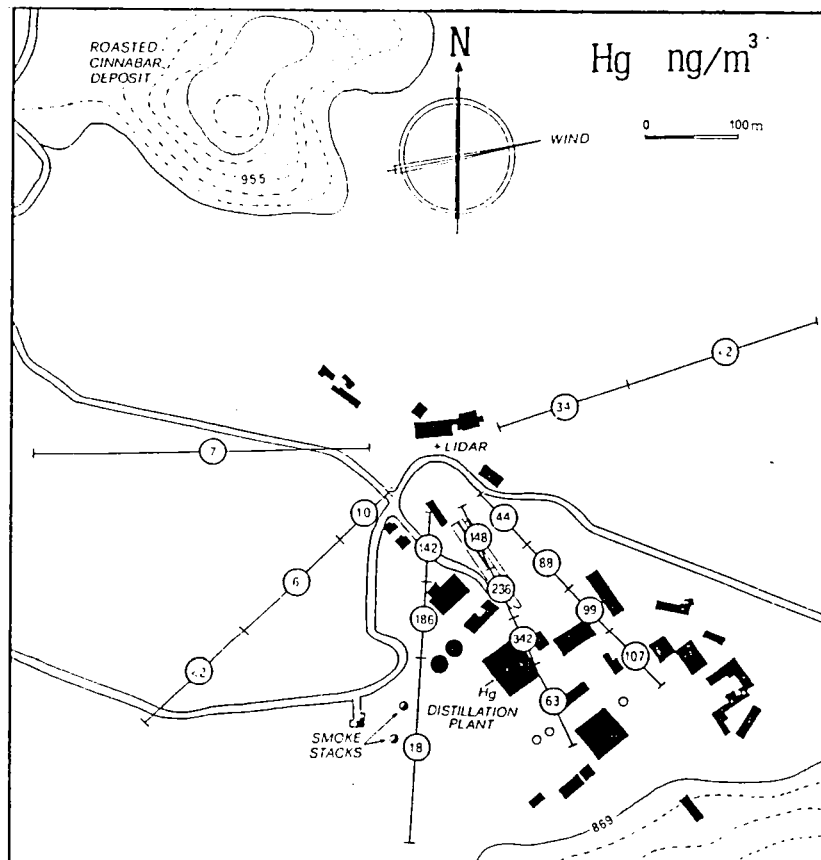


Fig. 3. Concentrations of atmospheric mercury at the mercury mine at Abbadia S. Salvatore (Italy)

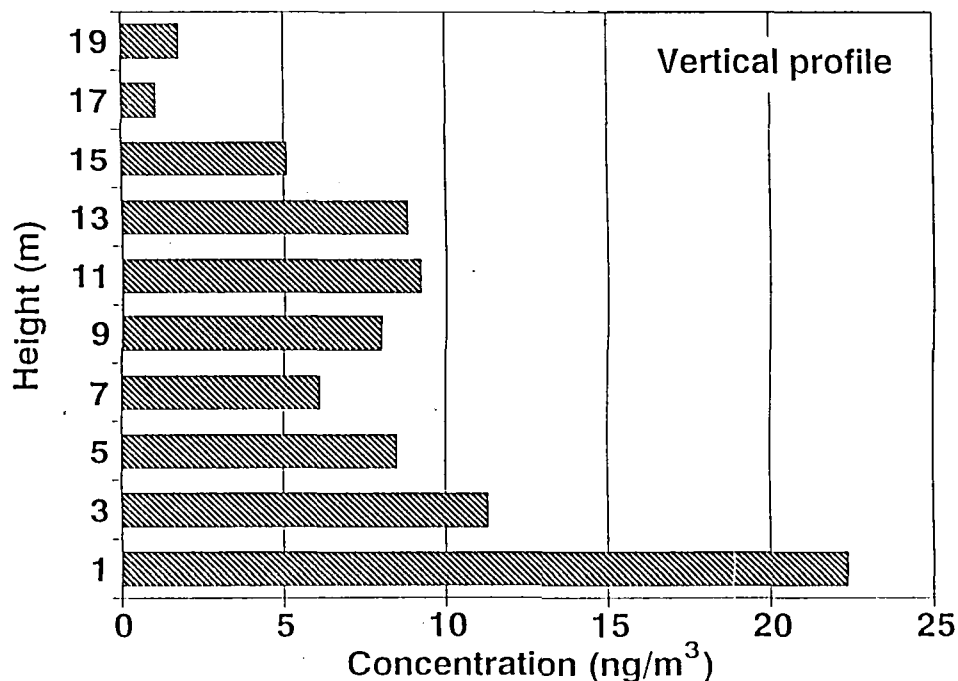


Fig. 4. Vertical profile of atmospheric atomic mercury above a roasted cinnabar ore deposit at Abbadia S. Salvatore (Italy)

As demonstrated by the examples chosen the differential absorption lidar method is a powerful technique for mapping of atmospheric atomic mercury. For the future we plan to extent our investigations to seismic and vulcanological processes, which are also known to produce mercury anomalies.

#### ACKNOWLEDGEMENTS

The authors would like to thank R. Ferrara and E. B. Maserti (CNR-IBF, Pisa) for collaboration in the project and thank P. Olsson and M. Morelli for assistance in the measurements. This work was supported by the Swedish Natural Science Research Council and the Swedish Board for Space Activities.

#### REFERENCES

1. H. Edner, G.W. Faris, A. Sunesson and S. Svanberg, *Appl. Opt.* **28**, (1989) 921.
2. H. Edner, G.W. Faris, A. Sunesson S. Svanberg, J.Ö. Bjarnason, H. Kristmannsdóttir and H.K. Sigurdsson, *J. Geophys. Res.* **96** (1991) 2977.
3. H. Edner, P. Ragnarson, S. Svanberg, E. Wallinder, A. DeLiso, R. Ferrara and B.E. Maserti, *J. Geophys. Res.* in press.
4. H. Edner, P. Ragnarson, S. Svanberg, E. Wallinder, R. Ferrara, B.E. Maserti and R. Bargagli, *Sci. Total Env.* in press.
5. H. Edner, K. Fredriksson, A. Sunesson, S. Svanberg, L. Unéus and W. Wendt, *Appl. Opt.* **26** (1987) 4330.
6. R. Ferrara, B.E. Maserti, H. Edner, P. Ragnarson, S. Svanberg and E. Wallinder, *Environmental Geochemistry and Health*, in press.

# Lidar Tracking of Multiple Fluorescent Tracers: Method and Field Test

Wynn L. Eberhard  
NOAA Wave Propagation Laboratory  
Boulder, Colorado

Ron J. Willis  
Cooperative Institute for Research  
in Environmental Sciences  
Boulder, Colorado

## INTRODUCTION

Past research (Rowland and Konrad, 1979; Schuster and Kyle, 1980; and Kyle et al., 1982) and applications (Uthe et al., 1985) have demonstrated the advantages and usefulness of lidar detection of a single fluorescent tracer to track air motions. Eberhard and Chen (1989a,b) performed an analytical study that showed good potential for lidar discrimination and tracking of two or three different fluorescent tracers at the same time. The present paper summarizes the multiple fluorescent tracer method, discusses its expected advantages and problems, and describes our field test of this new technique.

## SINGLE FLUORESCENT TRACER METHOD

In a conventional elastic-scatter lidar, the system detects the backscatter from particles in the air at the same wavelength as that transmitted by the laser. A plume or cloud of light-scattering particles can be used as a tracer of air motions tracked by a pulsed lidar. The fluorescent-tracer lidar excites the fluorophore placed in a tracer and detects the fluorescence using an optical filter with passband matched to the tracer's fluorescence spectrum. The fluorescent method overcomes a major limitation of the elastic method. Atmospheric dispersion rapidly dilutes a tracer, and the density of "natural" particles is quite variable, so the tracer signal soon can't be distinguished from that of particles from other sources. The fluorescence of "natural" particles in the air is small, so the fluorescent lidar can detect the tracer in very low concentrations. The fluorescent technique works best at night. During the day, the wide optical passband (~50 nm) passes so much background light that shot noise strongly limits the sensitivity. Uthe et al. (1985) reported field measurements in which an airborne lidar tracked a fluorescent tracer much longer after release than would have been possible for an elastic tracer.

## MULTIPLE FLUORESCENT TRACER METHOD

The method can be extended to multiple tracers, because fluorescent tracers with sufficiently different spectral characteristics are available. We have elected to use commercially available particles designed as pigments for dyes to make brilliant colors in fabrics, plastics, paints, etc. The particles are composed of a resin carrier mixed with a proprietary combination of fluorescent materials. The mode radius (by volume) for the tracers we use is typically 6  $\mu\text{m}$ , according to manufacturer specifications. Fluorescence emission is essentially instantaneous, so range resolution is determined mainly by laser pulse length and receiver response time. The particles are good atmospheric tracers, because they

are environmentally safe, small enough to follow air motions well, adequately resistant to bleaching in sunlight, and reasonably priced.

Figure 1 shows one example of an attractive two-tracer scheme evaluated by Eberhard and Chen (1989a,b). A Nd:YAG laser is frequency-multiplied to transmit simultaneously at 355- and 532-nm wavelengths. The shorter wavelength excites the Horizon Blue tracer. The Fire Orange tracer is principally excited by the 532-nm wavelength, but also slightly by 355 m. Raman scatter from O<sub>2</sub> or N<sub>2</sub> will add significant signal if the Fire Orange passband encompasses their wavelengths (shown in Fig. 1) and the tracer concentration is less than about 1 μg m<sup>-3</sup>. This could hinder detection of extremely low concentrations of Fire Orange, but it also would be helpful for calibrating the lidar. We expect very little receiver cross-talk between this pair of tracers. They will act as independent tracers (or nearly so), because the passband matched to the Fire Orange spectrum will detect very little or no signal from the Horizon Blue tracer, and *vice versa*.

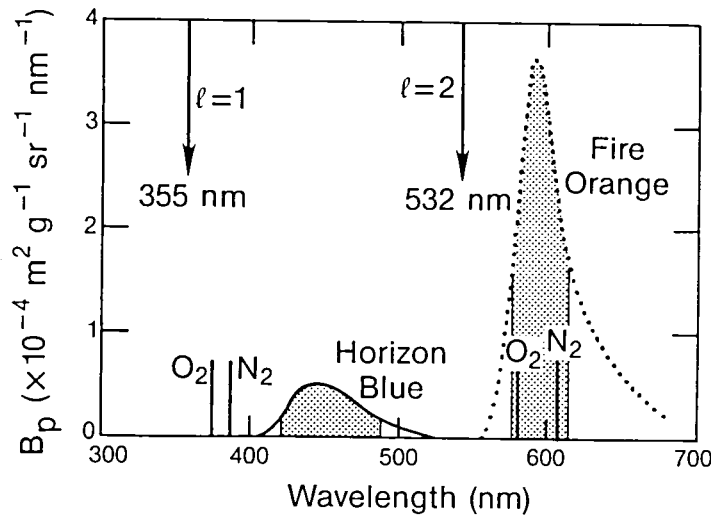


Fig. 1. Spectral relationships of laser excitation, fluorescent emission, and Raman scattering from O<sub>2</sub> and N<sub>2</sub> for a potential two-tracer system.  $B_p$  is the spectral fluorescence in the back direction based on laboratory measurements by Rowland and Konrad (1979). Possible receiver passbands are shaded.

Some other tracer combinations may have considerable cross-talk, and the signals in the various receiver channels must be solved simultaneously to obtain the tracer concentrations. If the number of detector channels is equal to the number of tracers, the solutions will have the form

$$\mathbf{C} = \mathbf{G}^{-1}\mathbf{M} , \quad (1)$$

where the elements of  $\mathbf{C}$  are the tracer concentrations,  $\mathbf{M}$  contains the measurements at each range gate, and  $\mathbf{G}$  is a gain matrix, including lidar sensitivity factors, pulse energy, range dependence of the signal, and fluorescent efficiency of the particles. Eberhard and Chen (1989a; and, with more detail, 1989b) calculate signal-to-noise ratios, estimate errors in concentrations for various operating conditions, and discuss calibration methods.

Potential applications of the multiple-tracer technique are numerous. One is study of the dependence of dispersion on release height. Multiple tracers could reveal the structure of complicated flows, such as in complex terrain, in the lee of hills or buildings, and near water-land interfaces. Source-receptor relationships could be investigated using multiple fluorescent tracers.

## FIELD TEST

We are conducting the first field trial of multiple fluorescent tracers mapped by lidar. The objectives of the project are as follows:

- (1) Modify an existing lidar (Eberhard and McNice, 1986) and processing software (Eberhard et al., 1987) for multiple fluorescent tracers,
- (2) Confirm predictions of sensitivity for detecting Fire Orange (used by previous researchers) and the other tracers listed in Table 1.
- (3) Demonstrate simultaneous detection of multiple fluorescent tracers and determine how well the lidar can discriminate between them, and
- (3) Recommend design factors for an airborne fluorescent lidar for detecting multiple tracers.

For the field test, tracers are released steadily from elevated platforms on the Boulder Atmospheric Observatory tower to form a plume. The lidar, located 1.2 km NNW of the tower, repeatedly performs scans vertically through the plumes to map out cross sections of the tracers. The frequency-multiplied Nd:YAG laser emits up to 15 mJ at 355 nm and up to

Table 1. Tracers and spectral characteristics for field tests

Tracer	Spectral peak (nm)	Primary optical passband (nm)
Invisible Blue	445	417-480
elastic green	532	531.5-532.5
Arc Yellow	567	550-570
Fire Orange	590	575-617
Corona Magenta	598	590-630

50 mJ at 532 nm. We had also planned to try Horizon Blue, whose spectral properties are similar to Invisible Blue, but this product was not in stock when the tracers were ordered. The lidar will be converted to three different configurations to detect tracers in three combinations:

- (a) Invisible Blue, elastic green (i.e. elastic backscatter at 532 nm), and Fire Orange, which are two nearly independent fluorescent tracers excited by two wavelengths.
- (b) Elastic green, Arc Yellow, and Corona Magenta, which is an example of two fluorescent tracers excited by only one wavelength, but with considerable receiver cross-talk.
- (c) Invisible Blue, Arc Yellow, and Corona Magenta, which are three fluorescent tracers excited by two laser wavelengths.

The plume flux technique will be used to calibrate the lidar-tracer system, with one tracer released at a time. The corresponding elements of  $G$  can be found by measuring the release rate of the tracer  $Q$ , the speed  $U$  at which the wind transports the tracer, and the signal (corrected for range) integrated over a cross section (and projected onto a plane normal to the plume axis)  $M_t$ , giving

$$G = M_t U / Q . \quad (2)$$

These results will be compared with Raman scatter measurements and our standard elastic calibrations of the lidar from a hard target and aerosol-free layers to determine the back-

fluorescent efficiency of the tracers.

At this writing, some data are in hand, and analysis in progress. Preliminary results will be presented at the conference.

*Acknowledgments* -- The encouragement of J.L. McElroy is appreciated. Z.-Z. Chen, K.R. Healy, and J. Wolta contributed greatly to the analytical studies and development of processing software. The excellent cooperation of R.E. Cupp, B. Gordon, M. Doran, D. Shalvi, and the staff of the Boulder Atmospheric Observatory during the field tests is gratefully acknowledged. This work was funded by the U.S. Environmental Protection Agency and the National Oceanic and Atmospheric Administration through Interagency Agreement DW13932524-01. It has not been subjected to EPA policy review and therefore does not necessarily reflect the views of EPA. Mention of a commercial product does not constitute any endorsement by NOAA or EPA.

## REFERENCES

- Eberhard, W.L., and G.T. McNice, 1986: Versatile lidar for atmospheric studies, including plume dispersion, clouds, and stratospheric aerosol. J. Atmos. Oceanic Technol., 3, 614-622.
- Eberhard, W.L., G.T. McNice and S.W. Troxel, 1987: Lidar sensing of plume dispersion: Analysis methods and product quality for light-scattering tracer particles. J. Atmos. Oceanic Technol., 4, 674-689.
- Eberhard, W.L., and Z.-Z. Chen, 1989a: Lidar discrimination of multiple fluorescent tracers of atmospheric motions. Appl. Opt., 28, 2996-3007.
- Eberhard, W.L., and Z.-Z. Chen, 1989b: Lidar technique for measuring multiple fluorescent tracers of atmospheric motions. NOAA Technical Memorandum ERL WPL-171, Environmental Research Laboratories, Boulder, Colorado, 60 pp.
- Kyle, T.G., S. Barr, and W.E. Clements, 1982: Fluorescent particle lidar. Appl. Opt., 21, 14-15.
- Rowland, J.R., and T.G. Konrad, 1979: A new lidar-fluorescent tracer technique for atmospheric research and pollution studies. Report #S1R 79U-036, Appl. Physics Lab., John Hopkins Univ., Laurel, MD, 55 pp.
- Schuster, B.G., and T.G. Kyle, 1980: Pollution plume transport and diffusion studies using fluorescence lidar. Appl. Opt., 19, 2524-2528.
- Uthe, E.E., W. Viezee, B.M. Morley and J.K.S. Ching, 1985: Airborne lidar tracking of fluorescent tracers for atmospheric transport and diffusion studies. Bull. Amer. Meteor. Soc., 66, 1255-1262.

# **Lidar Monitoring of Mexico City's Atmosphere During High Air Pollution Episodes##**

C. R. Quick, Jr., F. L. Archuleta, D. E. Hof, R. R. Karl, Jr., J. J. Tiee  
CLS-4, MS-J567

Los Alamos National Laboratory  
Los Alamos, New Mexico 87545

W. E. Eichinger, D. B. Holtkamp, L. Tellier  
P-3, MS-D449

Los Alamos National Laboratory  
Los Alamos, New Mexico 87545

Over the last two decades, Mexico City, like many large industrial and populous urban areas, has developed a serious air pollution problem, especially during the winter months when there are frequent temperature inversions and weak winds. The deteriorating air quality is the result of several factors. The basin within which Mexico City lies is Mexico's center of political, administrative and economic activity, generating 34% of the gross domestic product and 42% of the industrial revenue, and supporting a population which is rapidly approaching the 20 million mark. The basin is surrounded by mountains on three sides which end up preventing rapid dispersal of pollutants. Emissions from the transportation fleet (more than 3 million vehicles) are one of the primary pollution sources, and are mostly uncontrolled. Catalytic converters are just now working their way into the fleet.

The Mexico City Air Quality Research Initiative is an international collaboration project between the Los Alamos National Laboratory and the Mexican Petroleum Institute dedicated to the investigation of the air quality problem in Mexico City. The main objective of the project is to identify and assess the cost and benefits of major options being proposed to improve the air quality. The project is organized into three main activity areas:

Task 1 : Modeling and simulation

Task 2 : Characterization and Measurements

Task 3 : Strategic Evaluation

Task 1 is concerned with the adaptation of computer codes that will model : the basic meteorology of the Mexico City basin (3-dimensional, time-dependent calculations of the wind and temperature fields), the pollutant transport and dispersion over and beyond the urban terrain, and the photochemistry. Ultimately, the models will make predictions of the effect that various mitigation strategies would have on the spatial and temporal

variations of selected air quality parameters, such as ozone, carbon monoxide, nitrogen oxides, and visibility levels.

Task 2 is charged with characterizing the meteorology and ambient air quality with appropriate measurement and data gathering efforts. The data obtained will be used to validate the performance of the atmospheric models being developed.

Task 3 will provide socioeconomic analyses of proposed air quality improvement strategies using atmospheric model predictions of the effect on selected air quality parameters.

In February of 1991, a major measurements campaign was carried out in an attempt to gather sufficient information to allow a basic understanding of the meteorological processes that dominate the behavior of the atmosphere above the valley in which Mexico City is located. The campaign involved approximately 100 investigators from Mexico and the US over a three week period. In addition to standard EPA ground based instrumentation designed to measure the concentration of major pollutants, numerous advanced measurement techniques were utilized including : a fully instrumented aircraft laboratory , a real-time infrared vehicle emission monitor, a mobile lidar system for aerosol characterization, a mobile lidar for SO<sub>2</sub> measurements, tethered sonde instrumentation, time lapse photography, satellite imagery, rawinsonde monitoring, solar radiation monitors, particle-induced x-ray elemental analysis of aerosol particles, a cloud ceilometer, and GC/MS analysis of hydrocarbon samples.

The focus of this report is on the data obtained with the Los Alamos lidar system designed to examine the spatial and temporal distribution of aerosol particles present during high air pollution periods. A Nd:YAG elastic scattering lidar was deployed at three different locations within the valley, where fast elevation and azimuth angle scans were conducted around-the-clock, over several diurnal cycles at each location. The main lidar objective was to characterize the mix-layer, its height, texture and breakup, the manner in which plumes are transported and dispersed, and to obtain information regarding the atmospheric opacity.

February 22, 1991 was one of several days selected for detailed analysis and comparison between the measurements and meteorological models. The 22<sup>nd</sup> was a "typical" bad pollution day where ozone levels reached 288 on the local air quality index scale (over 300 ppb). One of the many factors that influence the occurrence of a high pollution episode is the height of the mix-layer. The lidar elevation angle scans (typically 0.5-1.0° increments) taken throughout the previous night and into the early morning hours show an aerosol layer confined to the first 200-300 m of altitude. As the sun rises and the level of activity in the city starts to pick up, the aerosol layer boundary starts to move

upwards and becomes more dense close to the ground. Fig. 1 shows an interpolated image obtained by extracting single angle data ( $50^\circ$  in this example) from a time sequence of elevation angle scans. The data shown has been corrected for  $1/r^2$  fall-off but not for atmospheric extinction. By early afternoon, other lidar elevation scans show that aerosols produced near the ground can be transported up to elevations of 2-3 km.

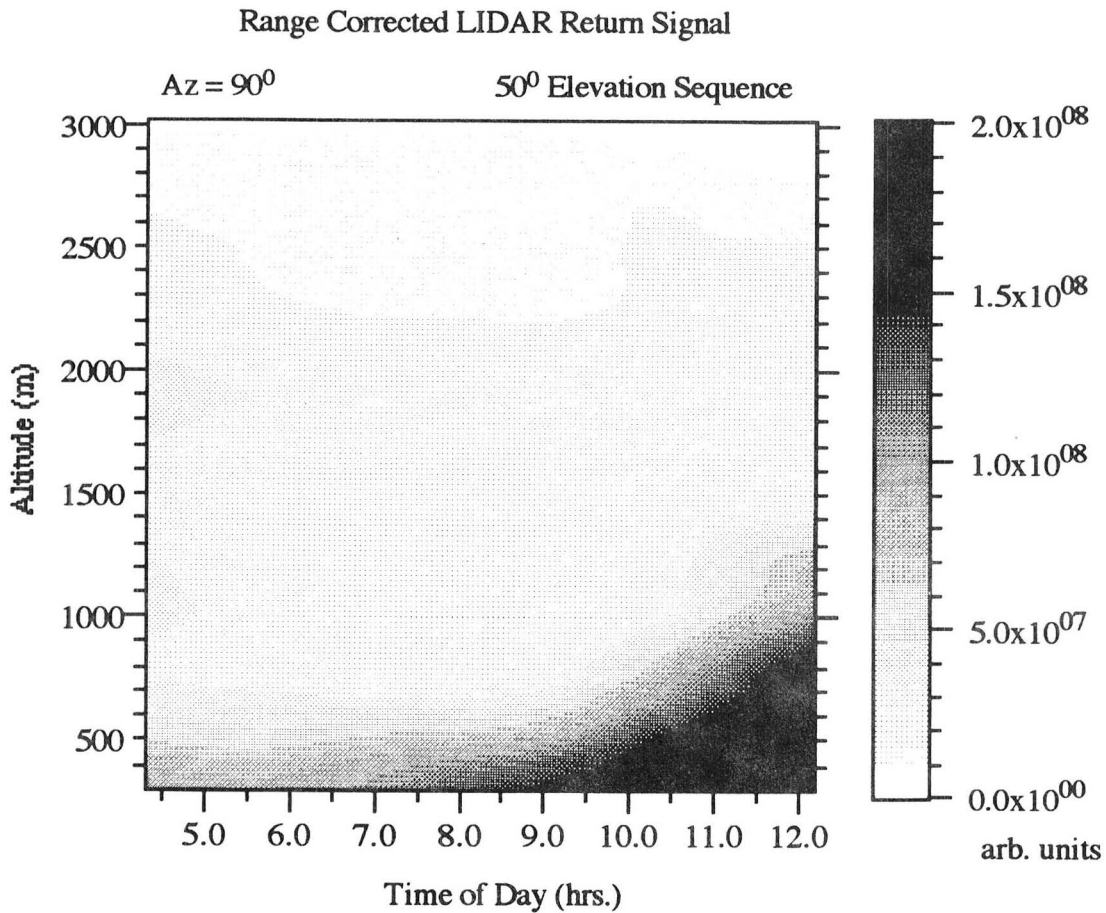


Fig. 1

The lidar data is currently being compared to other instrumentation as well as to meteorological model predictions. Examples will be presented and discussed.

## Work carried out under the auspices of the US Department of Energy in support of the Mexico City Air Quality Research Initiative, which is a joint project between the Los Alamos National Laboratory and the Mexican Petroleum Institute (IMP). The lidar operation was conducted with the assistance of IMP personnel primarily, and other local organizations.



A. Borghese , Istituto Motori, C.N.R., Napoli, Italy

## Introduction

Combustion technology and its environmental concerns are being considered with increasing attention, not only for global-scale effects, but also for toxicological implications, particularly in the life conditions of traffic-congested areas and industrial sites /Ref.1/.

Majority combustion by-products, e.g. CO, NO<sub>x</sub>, unburned hydrocarbons (HC), are already subject to increasingly severe regulations; however other, non-regulated minority species, mainly soot and heavy aromatic molecules, involve higher health risks, as they are suspected to be agents of serious pathologies and even muthagenic effects. This is but one of the reasons why much research work is being carried out worldwide on the physical properties of these substances.

Correspondingly, the need arises to detect their presence in lived environments, with as high sensitivity as required by their low concentrations, proper time- and space-resolutions and 'real-time' capabilities.

Lidar techniques are excellent candidates to this purpose, although severe constraints limit their applicability, eye-safety problems and aerosol Mie scattering uncertainties above all.

At CNR's Istituto Motori in Naples, a Lidar-like diagnostic system is being developed, aimed primarily at monitoring the dynamic behaviour of internal combustion engines, particularly Diesel exhausts, and at exploring the feasibility of a so-called 'Downtown Lidar'.

## Principle of operation

The operating principle of the system reflects combinedly those of a multi-wavelength Lidar and of a fluorosensor, as specified below. The relevant interactions involve back-scattering and extinction of U.V., visible and I.R. laser light by soot particles, emitted by Diesel engines and steady-state combustors as well; in addition, U.V. wavelengths induce broad-band fluorescence of heavy organic compounds, adsorbed onto soot particles, in the range 300-500 nm, as observed in sooty flames /Ref.2/. In the lab-scale configuration, which will be described here, the laser beam explores the axis of a 70m-long pipeline, where the exhaust gases are entered at  $r=r_0$  and are flown toward increasing  $r$ 's with a flow speed  $v_f$ , as shown in Fig. 1. The Lidar equation can be expressed as :

$$(1) I(r, t, \lambda, \lambda') = K(\lambda, \lambda') * A(r) * T(r, t, \lambda, \lambda') * \beta(r, t, \lambda, \lambda') * Dr$$

where the dependence on  $t$  accounts for the unsteady flow and  $I, K, A, T, \beta \cdot Dr$  account for i) received signal, ii) transmitter and receiver efficiencies, iii) range effects, iv) extinction between 0 and  $r$  of the transmitted ( $\lambda$ ) and received ( $\lambda'$ ) wavelengths and v) light-matter interactions at  $r$ , respectively.

Under the 'confined-flow' conditions (see Fig.1) :

$$(2) \quad \beta(r,t) = \beta(r_0,t-Dt) \quad , \quad \text{where } Dt = (r-r_0)/v_f$$

$$(3) \quad \partial T(r_0,t)/\partial t = \partial \beta(r,0)/\partial r = 0$$

and considering only elastic interactions, the system of Eq.(1) for  $r=r_0$  and  $r=r_1$  can be solved , yielding :

$$(4) \quad \int_{r_0}^{r_1} \alpha(r,t) dr = \frac{1}{2} \text{Log} [I(r_0,t-Dt) \cdot I(r_0,0) / I(r_0,t) \cdot I(r_1,0)]$$

$$(5) \quad \beta(r_0,t) = \beta_{\text{ref}} \cdot I(r_0,t) / I_{\text{ref}}(r_0)$$

where  $\alpha(r,t)$  is the extinction coefficient at  $r$  and  $t$  ;  $\beta_{\text{ref}}$  and  $I_{\text{ref}}$  are the backscattering coefficient and the signal intensity from a known species, entered at  $r=r_0$ .

Operation of the system as a fluorosensor, which is presently being carried out, will be treated elsewhere; at the moment, it is worth noting its potentialities, namely that combined evaluation of fluorescence and elastic signals can help detecting the relative amounts of soot particles, when mixed to non-absorbing aerosols.

The 'confined-flow' conditions turn out to be a powerful tool, enabling also more general and fundamental studies on scattering properties of relevant classes of aerosols, once they are injected individually or controlledly into the pipeline.

### Experimental set-up

A Nd-YAG laser (Quanta System S.r.l.), purposely modified to operate simultaneously on its harmonics at 532nm (SH), 355nm (TH) and 266nm (FH), transmits at 8 pps the three collinear beams along the pipeline axis.

The system is provided with diagnostic capabilities for future investigations on depolarized effects; this is obtained by aligning the polarization planes of the three beams via a first dispersing prism, a  $\lambda/2$  retarder on the SH and a final recombining prism.

The Lidar returns are collected by a 160mm dia., 1m f.l. off-axis paraboloid and focused onto the entrance slit of a flat-field polychromator (J.Y. Mod.CP200).

The backscattered light is detected on a 'continuous-wavelength, discrete-time' basis. A 'gated' optical multichannel analyzer (P.A.R.Co, Mod.1421, gate width=10ns), driven by a delay generator (Stanford, Mod.DG535), acquires and stores spectral data in the range 250-820nm. Data acquisition is carried out by interlacing the gate delays between  $2r_0/c$  (odd pulses) and  $2r_1/c$  (even pulses), so that each position is sensed four times a second.

## Short-range application and results

As an example of application, data acquired as described above are shown in Figg.2-4, which refer to the real-time monitoring of the exhausts of a Diesel car, run at the chassis dynamometer. Here, the car wheels roll 'surplace' over two spinning cylinders, thus simulating real driving conditions, as well as allowing ordinary sampling and chemical analysis of the exhausts: this joint facility supports and enhances the features of the Lidar probe, providing checks and references to optical measurements.

Figure 2 shows the car speed vs. time of the standard Extra-urban driving cycle (EUDC), used in the experiment.

Figures 3.A,B show the corresponding backscattered signals at 532nm from the positions  $r_0 = 15\text{m}$  and  $r_1 = 25\text{m}$  in the pipeline, respectively. Data in Fig.3.A reflect the behaviour of  $B(r_0, t)$ , since the extinction between 0 and  $r_0$  doesn't depend on time, whereas Fig.3.B shows additionally the effect of extinction between  $r_0$  and  $r_1$ .

The extinction coefficient  $\alpha$  in absolute units ( $\text{cm}^{-1}$ ), averaged in  $r_1 - r_0 = 10\text{m}$ , as function of time is reported in Fig.4.A, as evaluated from Eq.(4). It is worth noting that its behaviour should be attributed to time variations of both total number concentration and extinction cross section of the soot particles, as they occur in the different engine operation regimes of the driving cycle.

Furthermore, the ratio of  $\alpha$ 's at two different wavelengths does not depend on total number concentration.

Fig.4.B shows the ratio  $\alpha(266\text{nm})/\alpha(532\text{nm})$ , which accounts for the behaviour of physical properties of the soot particles, namely their size, shape and complex refractive index. Next work will deal with more detailed interpretation of the experimental results.

## Acknowledgements

The present paper has been partially supported by National Research Council (C.N.R.) of Italy, under the "Progetto Finalizzato" on Electro-optical Technologies.

The author thanks the whole staff of Standards, Quality and Reliability Division of Istituto Motori, for their skillful management of the chassis dynamometer.

## References

- /1/ Di Lorenzo, A. "Some important gaps in present knowledge which could be filled by future research to reduce vehicle exhausts", World Health Organization, Int'l Programme on Chemical Safety, Int'l Workshop on Human Health effects of motor vehicles and exhaust emissions, Sidney, Australia, 6-10 April '92
- /2/ D'Orsi, A. "Kinetics of soot formation in premixed flames", Ph.D. Thesis, 1991, Dept. Chemical Engineering, University of Naples "Federico II".

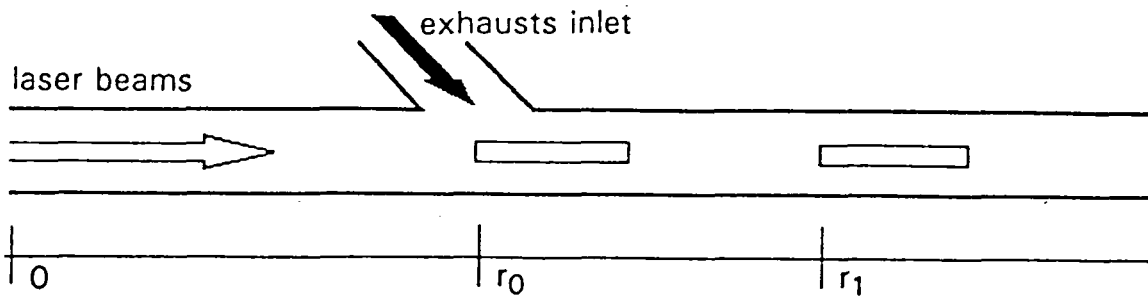
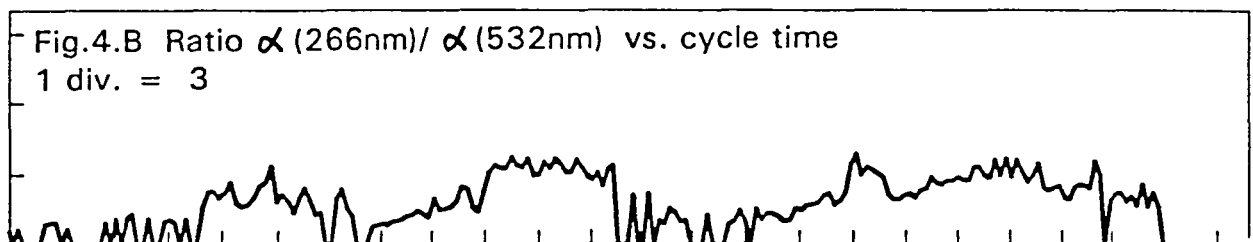
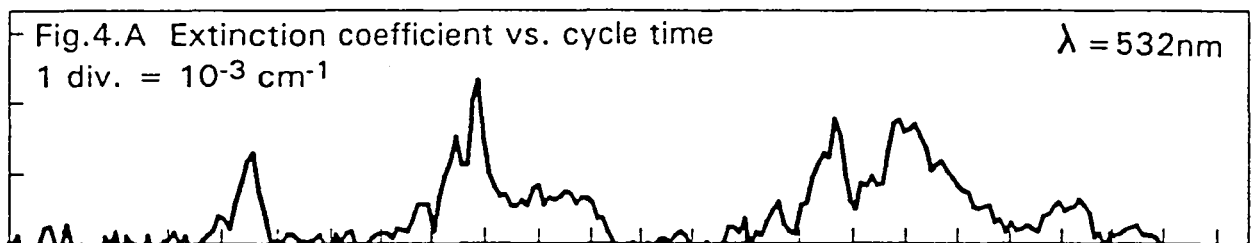
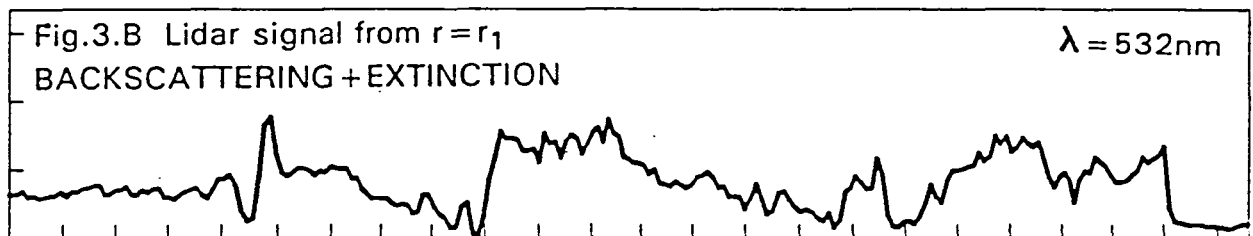
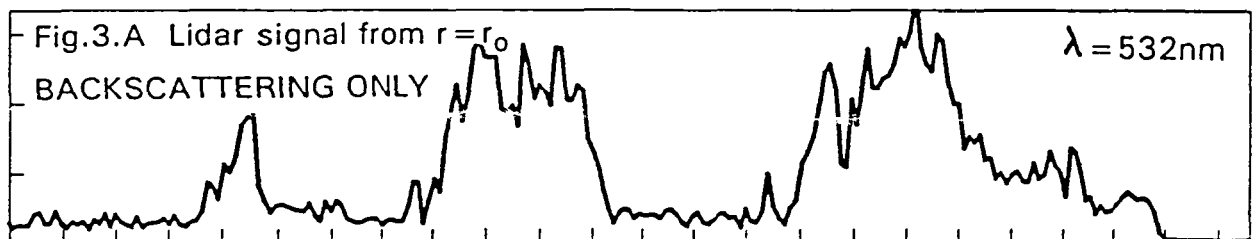
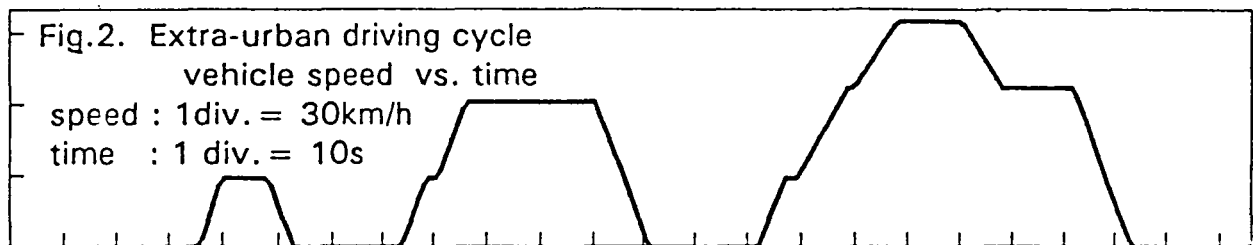


Fig. 1 Lay-out of the 'Confined-flow' . Flow speed  $v_f = 4.9$  m/s  
 $r_0 = 15$  m ;  $r_1 = 25$  m ; laser pulse width = 20 ns ; 'gate' = 10 ns



# Infrared Pulse-Laser Long-Path Absorption Measurement of Carbon Dioxide Using a Raman-Shifted Dye Laser

Atsushi Minato, Nobuo Sugimoto and Yasuhiro Sasano  
The National Institute for Environmental Studies  
16-2 OnogawaTsukuba, Ibaraki 305 Japan

Use of pulsed laser source is effective in infrared laser long-path absorption measurements when the optical path length is very long or the reflection from a hard target is utilized, because higher signal-to-noise ratio is obtained in the detection of weak return signals. We have investigated the performance of a pulse-laser long-path absorption system using a hydrogen Raman shifter and a tunable dye laser pumped by a Nd:YAG laser, which generates second Stokes radiation in the 2- $\mu\text{m}$  region. Figure 1 shows a schematic diagram of the system.

We measured the absorption spectrum of carbon dioxide in the 2- $\mu\text{m}$  region in an open path with a round-trip path length of 1 km using a retroreflector. The energy of return pulse from the retroreflector was normalized by the transmitted energy and averaged over 4 shots. Approximately 200 data were recorded in a spectrum measurement with scanning the laser wavelength. The spectral width of the laser was  $0.05\text{ cm}^{-1}$ . Figure 2 shows an example of the measured transmission spectrum. We determined the concentration of carbon dioxide by fitting a theoretical spectrum to the logarithm of the measured spectrum using the linear least square method. The absolute wavenumber was also determined in the fitting. We used the temperature and pressure data measured at a location close to the optical path. The theoretical spectrum and the residual are also shown in Fig.2.

We investigated theoretically the relation between errors in the concentration determined by the least square fitting and errors contained in the measured spectrum. The result shows that the error in the concentration can be estimated analytically, if the standard deviation of the noise in the measured spectrum is expressed as a function of the transmittance or the signal intensity. We can utilize this relation in optimizing measurement conditions such as absorption line intensity of target molecules and the wavelength region to be measured.

There are two dominant types of noise in an infrared pulse-laser long-path absorption system. One is the noise such as background noise and Johnson noise, whose standard deviation does not depend on the signal intensity. The other is the noise whose standard deviation is proportional to the signal intensity. Noise caused by the fluctuation of laser beam is a typical example of the latter. Noise in an actual system can be expressed as a combination of these two types.

We analyzed the standard deviation of the noise as a function of signal intensity using the measurement data. Fluctuation in the output beam pattern of the laser was found a dominant source of the noise in our system when the signal intensity was large. Detector noise became dominant when the signal was small. The measurement condition was optimized in our system when an absorption line with a transmittance of 0.1 at the absorption peak was used.

In the example shown in Fig.2, the signal-to-noise ratio of the measured spectrum was approximately 17 at the wing of the absorption line. The error in the concentration determined from the measured spectrum was estimated to be 0.6 percent or 2 ppm. The concentration obtained was 357 ppm and agreed very well with the NDIR (Non-Dispersive InfraRed gas analyzer) data measured at the same time.

We compared the error expected in the differential absorption method with that in the present wavelength scan method. The error in a measurement of concentration in the same measurement time is smaller in the differential absorption method by a factor of approximately 1/2. Even with a little bit larger error expected, the scan method is useful in such a system where control of absolute wavenumber is difficult.

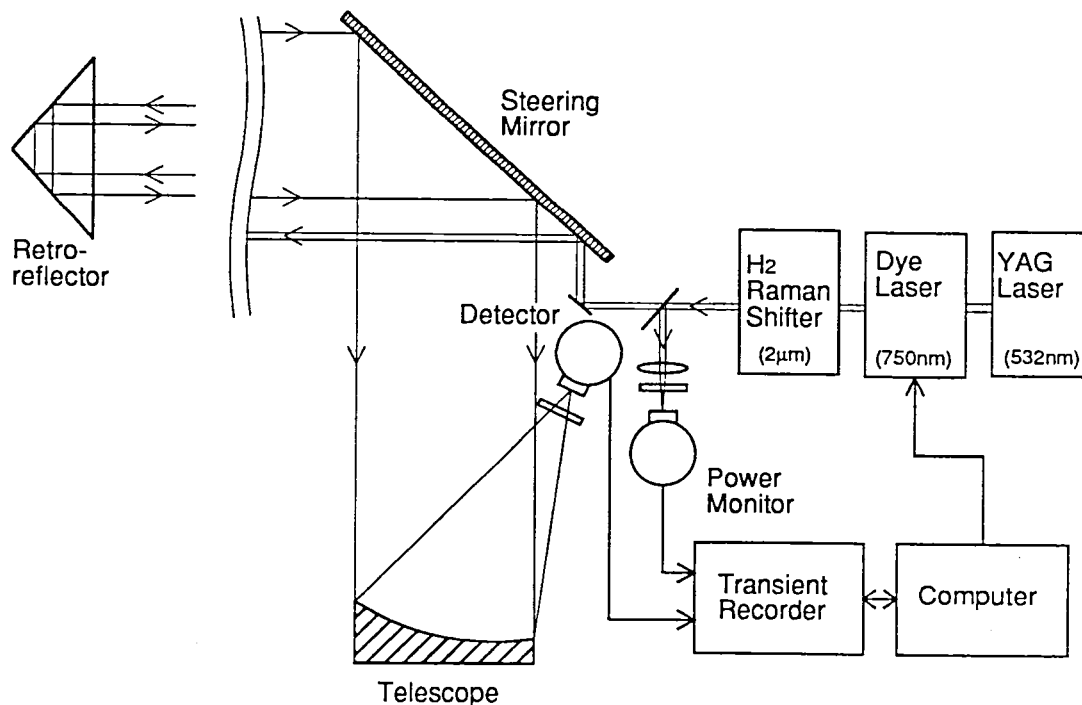


Fig.1 Schematic diagram of the system

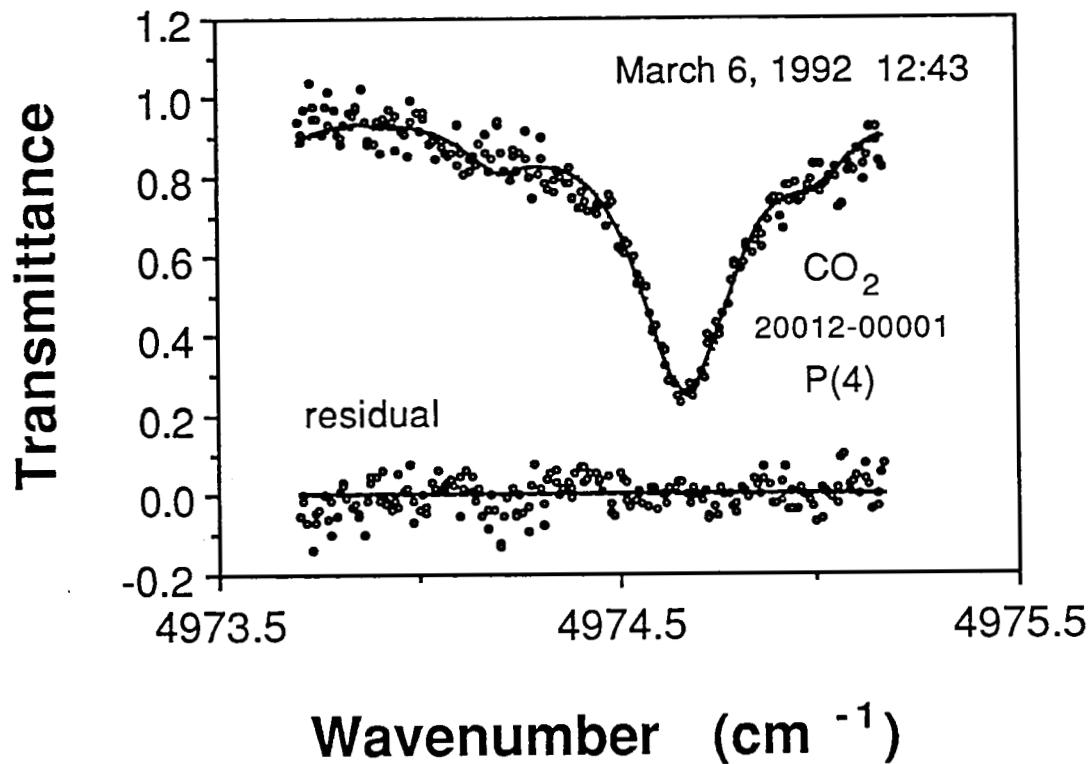


Fig.2 Measured atmospheric transmission spectrum in an open-path with a path length of 1km. The concentration of carbon dioxide was determined by fitting a theoretical spectrum indicated in the figure. The lower trace shows the residual of the fitting.



# **TRANSPORTABLE LIDAR FOR THE MEASUREMENT OF OZONE CONCENTRATION AND FLUX PROFILES IN THE LOWER TROPOSPHERE**

**Yanzeng Zhao  
and  
James N. Howell**

**CIRES, University of Colorado/NOAA**

**R. Michael Hardesty  
NOAA/ERL/WPL**

## **I. INTRODUCTION**

The importance of tropospheric ozone has been well recognized in recent years. Ozone is a greenhouse gas which contributes to global warming and climate change. Its concentration is also a key factor in the control of atmospheric oxidation since the photolysis of ozone initiates most reactions in tropospheric photochemistry, which in turn influence the concentrations of other radiatively important gas species, including ozone itself. In addition, ozone is a pollutant which affects crop production, forest growth, and human health.

In many areas of the United States, as well as in other industrial areas (such as Europe), elevated and potentially harmful levels of ozone are being measured during summer. Most of this ozone is photochemically produced. The relatively long lifetime of ozone allows industrially produced ozone to be transported on a hemispheric scale. Since the trends of tropospheric ozone are very likely dependent on the source strengths and distributions of the pollutants and the chemical/ transport processes involved, a predictive understanding of tropospheric ozone climatology requires a focus on the chemical and transport processes that link regional emissions to hemispheric ozone trends and distributions.

Of critical importance to these studies is a satisfactory data base of tropospheric ozone distribution from which global and regional tropospheric ozone climatology can be derived, and the processes controlling tropospheric ozone can be better understood. A transportable lidar for measuring ozone concentration and flux profiles in the lower troposphere is greatly needed, and one such system is nearly developed at the NOAA/ERL Wave Propagation Laboratory (WPL).

## **II. SYSTEM HARDWARE**

In WPL's ozone DIAL system, an Nd:YAG laser (with a repetition rate of 10 Hz) is used for the lidar's transmitter. Wavelength pair 266/289 nm has been chosen to obtain the high differential absorption coefficient needed for high spatial and temporal resolution of the measurement. The online wavelength (266 nm) is obtained by frequency-quadrupling the

fundamental wavelength of the YAG laser. The offline wavelength (289 nm) is produced by Raman shifting 532 nm to 632.5 nm and subsequently sum-frequency-mixing the above two wavelengths. The large separation of online and offline wavelengths also introduces errors due to a weak wavelength dependence of aerosol extinction and backscattering coefficients. To correct these errors, aerosol backscattering coefficient profiles at 1.06  $\mu\text{m}$  and/or 532 nm will be measured simultaneously.

A multibeam transmitter (Zhao and Hardesty, 1991) is designed to reduce the large dynamic range of the lidar signals (a typical problem for incoherent lidar systems), provide good near-range coverage, and eliminate quantization error at far ranges. The receiver will include an off-axis Newtonian telescope employing an 8" parabola mirror with surface accuracy of  $\lambda/10$  and UV-enhanced coating. An optical filter system has been designed for rejecting the daytime background radiation while maintaining a relatively high receiving throughput. A fast, multi-channel data acquisition and processing system is under development which will allow the display of ozone profiles and aerosol backscatter profiles in real time.

### III. SIGNAL PROCESSING

An improved numerical differentiation method (Zhao, 1990) has been designed to increase the accuracy, range resolution, and temporal resolution in estimating ozone concentrations from lidar signals. It consists of two steps: (1) a least-square polynomial fit to the slowly varying part of the differential absorption optical depth, and (2) a subsequent non-stationary Wiener filter for the fluctuation components. Numerical simulations have shown that the new technique produces high-resolution ozone profiles with better accuracy than the conventional numerical differentiation method for a given transmitter average power and diameter of receiver. As a result, the lidar system can be less expensive and more compact.

Also, a technique (Zhao, 1991) for correcting the effects of differential backscatter on retrieved ozone concentrations has been developed.

Because of the hardware design and data processing techniques, the WPL ozone lidar will have high range resolution and high temporal resolution. Numerical simulations show that if only the shot noise effect is considered, ozone profiles below 3-4 km can be measured in a few seconds with an accuracy better than 5% and a range resolution of 30-150 m below 1.5 km. Thus, once a high range resolution and high accuracy Doppler lidar system for wind measurement is available (one such system is under development in WPL), vertical profiles of ozone flux can be readily measured, using the eddy-correlation method. If only ozone profiles are desired, higher accuracy and/or higher range resolution can be obtained with a slightly longer measurement time (a few minutes). Ozone fluxes can still be derived from the gradient of the concentration profiles together with standard wind measurements.

## REFERENCES

Y. Zhao and R. M. Hardesty, SPIE's OE/Aerospace Sensing, April 1-5, 1991, Orlando, Florida, Proceedings, Vol. 1492, No. 10, pp. 85-90.

Y. Zhao, "Numerical Differentiation Methods for Estimating Ozone Concentration in DIAL Measurements," *1990 Technical Digest Series*, Volume 4, pp. 388-391, Optical Remote Sensing of the Atmosphere, February 12-15, 1990, Incline Village, Nevada.

Y. Zhao, "Simplified Correction Techniques for Backscatter Errors in Differential Absorption Lidar Measurements of Ozone," *1991 Technical Digest Series*, Volume 18, pp. 275-277, Optical Remote Sensing of the Atmosphere, November 18-21, 1991, Williamsburg, Virginia.



# Remote Detection of Biological Particles and Chemical Plumes Using UV Fluorescence Lidar\*\*

J. J. Tiee, D. E. Hof, R. R. Karl, R. J. Martinez, and C. R. Quick, Chemical and Laser Sciences  
Division, Los Alamos National Laboratory, MS-J567, Los Alamos, NM 87545 (505) 667-6137

and

D. I. Cooper, W. E. Eichinger, and D. B. Holtkamp  
Physics Division, Los Alamos National Laboratory, MS-D449, Los Alamos, NM 87545

\*\*Funding to this work is provided by U. S. Army CRDEC and Los Alamos National Laboratory LDRD program.

## ABSTRACT

A lidar system based on ultraviolet (UV) laser induced fluorescence (LIF) has been developed for the remote detection of atmospherically dispersed biological particles and chemical vapors. This UV fluorescence lidar has many potential applications for monitoring environmental pollution, industrial waste emission, agricultural insect control, illicit chemical processing, and military defense operations. The general goal of this work is to investigate the research issues associated with the long range detection and identification of chemicals, e.g. aromatic solvents and chemical precursors, and biological materials, e.g. bacillus thuringiensis (BT) and bacillus globiggi (BG). In the detection of biological particulates, we are particularly interested in extending the detection range of an existing solar-blind 248-nm lidar system. We are investigating the use of longer excitation laser wavelengths (i.e.  $\lambda > 280$ -nm to have more favorable atmospheric light transmission characteristics) for improving detection range to better than 10 km. In the detection of chemical plumes, our main research objectives are to determine how accurately and sensitively a chemical plume can be located at range, and how well spectrally the chemical species can be measured to allow their identification.

The research program is implemented basically in two fronts: (1) LIF experiments in laboratory to provide essential spectroscopic/optical detection parameters; and (2) field tests using an UV fluorescence lidar system to evaluate remote detection performance and capabilities. In the laboratory work, an experimental apparatus was set up to examine the laser induced fluorescence of several biological compounds in solution and volatile chemical substances in a gas chamber. The excitation laser used was either a fixed wavelength (UV excimer laser, e.g. KrF or XeCl) or a tunable wavelength (doubled dye laser pumped by a Nd:YAG laser covering the spectral region of

220 - 350 nm ) variety. Detection of the excitation fluorescence was accomplished using either a photomultiplier tube (PMT) or an optical multichannel analyzer (OMA) used in conjunction with a 1/4-m monochromator for spectral analysis. A commercial excimer laser capable of 100-W/ 250-Hz output at either 248-nm or 308-nm was installed in a lidar truck along with appropriate UV high power optics. The detection system included a 16" telescope, PMT's, optical filters, and a monochromator/OMA system. An 80486 computer was interfaced to the data acquisition (CAMAC driven dual 100-MHz digitizing channels) and reduction apparatus to allow high speed operation (at a repetition rate up to 90 Hz). An upgraded version of computer software was installed to provide enhanced graphics and color visualization in 2-D and 3-D scans to allow volumetric imaging. A scanning periscope mirror assembly allowed the laser/telescope optical system to cover a field of view of approximately 75 degrees horizontally and 30 degrees vertically with an angular resolution of 0.03 degrees. Because much of the species fluorescence occurred below 300-nm region with the 248-nm excitation, detection of these materials could be achieved with a solar-blind PMT. Gateable PMT's were also used for fluorescence at wavelengths longer than 300-nm. Detection of several substances in the day time was deemed possible.

In the interest of characterizing several excitation wavelengths for the lidar system, calibrated fluorescence measurements on BT, BG, and l-tryptophan in water solutions were conducted using 248-nm, 266-nm, 308-nm, and 355-nm laser excitation in laboratory experiments. The strong fluorescence near 350-nm attributed to tryptophan was observed only with the shorter excitation wavelengths (i.e. 248- and 308-nm, but not at 355-nm). At 355-nm excitation, strong emission in the visible region was attributed mostly to an interfering fluorescence from sugars or other inert ingredients in the BT solutions. A detailed comparison of the spectroscopic data (e.g. fluorescence spectrum and relative fluorescence quantum yield) has been obtained at different excitation wavelengths (see Fig.1) and will be presented. We detected very slight spectral differences due to different sources of BT's (concentrated powder or liquid). We have observed that an aging of the samples caused the fluorescence spectra to be significantly blue-shifted. LIF studies of several representative chemical species, such as precursors, reagents, or solvents for illicit chemical agents, have been conducted in controlled laboratory experiments. The list of volatile chemicals included species such as acetic acids, benzene, benzoyl chloride, bromobenzene, chlorobenzene, eperdine, ether, methylamine, piperdine, toluene, and xylene. As expected, we were able to obtain strong fluorescence from nearly all of the cyclic aromatic hydrocarbon derivatives (see some examples in Fig.2). Observable spectral shifts and features were noted and could be used for their identification. The fluorescence quenching under atmospheric conditions was also quantified empirically by introducing room air into the fluorescence chamber. Fluorescence spectra of several species were obtained with/without room air. For example, in the case of toluene, it was observed

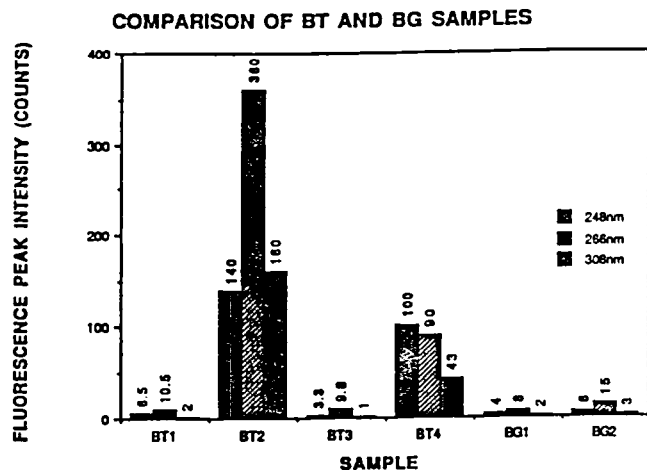


Fig. 1

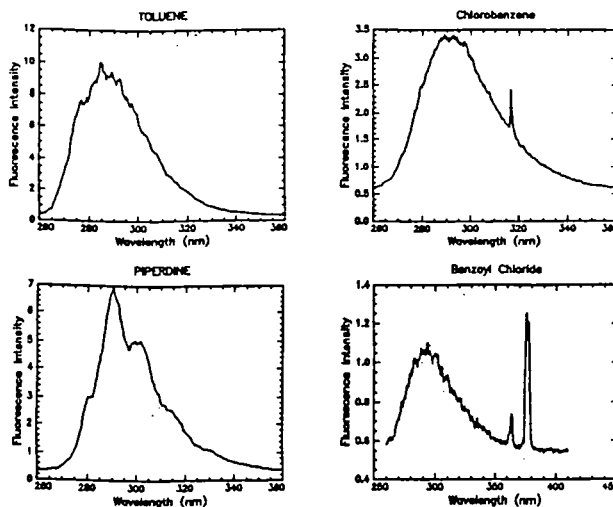


Fig.2

that under the test conditions fluorescence quenching reduces the fluorescence intensity by a factor 2 to 3. Since the fluorescence quenching cross section is a function of the particular excited state of the test molecule in question, its effect could only be determined by a case-to-case study. The fluorescence quantum yield of several of these species has been determined under collisionless conditions using the toluene fluorescence intensity as a calibration standard. Using known absorption cross sections, the detection sensitivity of these species was estimated. We believe that under ideal conditions detection of these species in the ppb levels at km ranges is attainable. We also were able to obtain strong fluorescence from one important methamphetamine precursor materials namely, methylamine, with detection sensitivity comparable to that of toluene.

Several local field experiments on BT and our fluorescence standard (a detergent. i.e. Tide) were conducted to evaluate the performance of the lidar detection system using the 308-nm laser at Los Alamos and Albuquerque (Phillips Laboratories). Optical alignment and detection system response were initially checked out and quantified by examining the strong elastic and Raman signal returns from N<sub>2</sub> (332-nm) and H<sub>2</sub>O (347-nm). A commercial fruit tree sprayer was used to disperse the materials and to create aerosol plumes of interest. The field tests were implemented in a progressive manner to cover distances from hundreds of meters to several kilometers. To date, UV fluorescence measurements were successfully performed at a distance varied from approximately 0.2 to 12.6-km. Figure 3 shows a typical UV fluorescence lidar "hit" at an approximate range of 12.6-km. In Figure 4, a 2-D fluorescence lidar horizontal scan of the sprayer dissemination located at approximately 1.5-km is displayed. We are currently analyzing these data

to assess the fluorescence lidar detection performance (i.e. range, sensitivity, species specificity, and so on). Detailed results and fluorescence detection sensitivity quantified using the N<sub>2</sub>/H<sub>2</sub>O Raman signal returns as calibration will be discussed. Additional field test measurements on BG samples have been conducted and will be presented as well.

Similarly, the fluorescence lidar system for detecting chemicals was evaluated in local field tests. This was accomplished by placing chemical species of interest in a chemical exhaust hood of a building and scanning the laser and the detection mirror to the exhaust stack above the building with the lidar truck situated some distance away. Detection sensitivity with this particular arrangement was estimated to be on the order of ppm at the kilometer distance. Because only a small fraction of the effective volume was being sampled in this particular arrangement, we believe much higher detection sensitivity can be achieved. We are currently conducting additional field tests to determine if better detection sensitivity can be obtained. This result will also be presented.

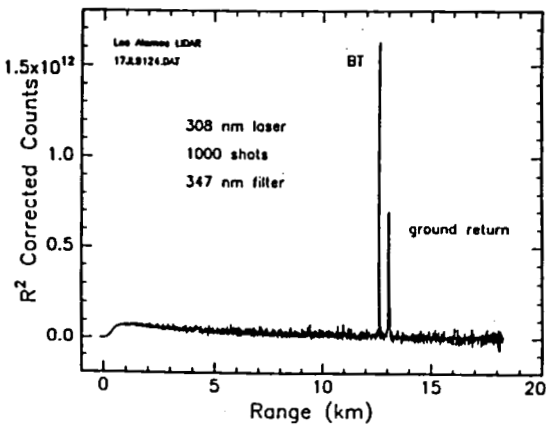
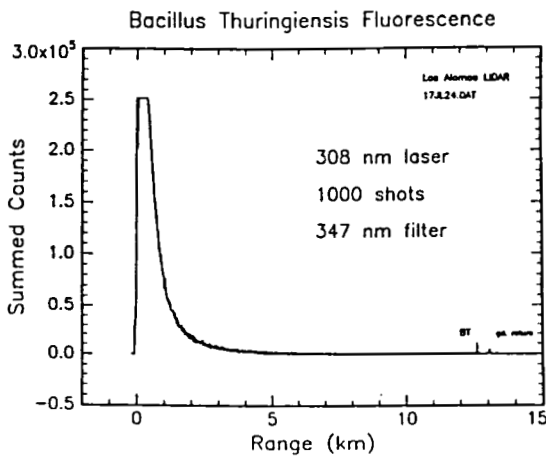


Fig. 3

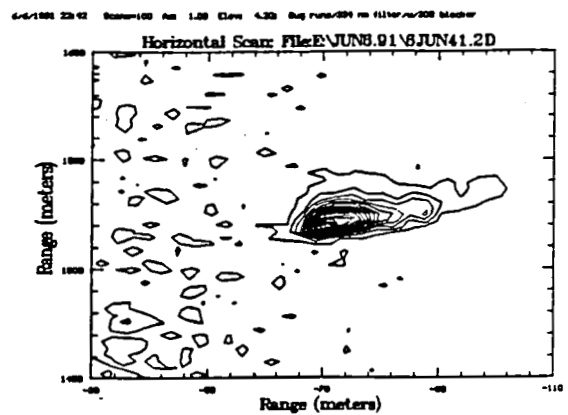
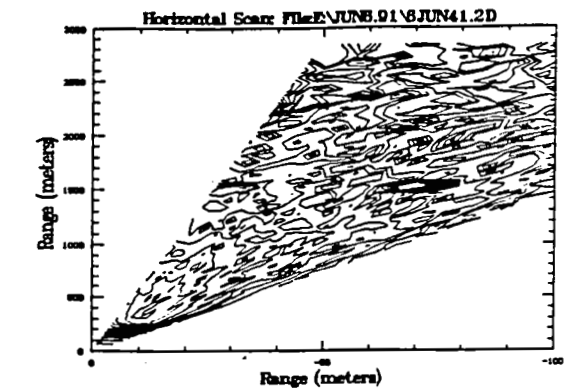


Fig. 4

# SIGNAL QUALITY INFLUENCE ON AVERAGING PROCEDURE FOR DIAL POLLUTION MONITORING

S. Egert and D. Peri  
Israel Institute for Biological Research  
P.O.Box 19, Ness-Ziona 70450, Israel  
L. Berg  
Laser Science Inc.  
75 Chapel Str. Newton, MA 02195, USA

Averaging process is usually necessary to increase the signal to noise ratio, and hence the resulted accuracy of LIDAR measurements. The averaging process relays on a proper statistical treatment of the different stochastic phenomena that influence the signal quality. The returned signals of a LIDAR system are degraded by the following factors: (a) Transmitted power irregularities, (b) Atmospheric turbulence and receiver-transmitter misalignment, (c) Receiver noise. When DIAL method is considered, a division of pairs of signals, different both in wavelength and in transmitting time, is performed. The averaging process can be applied either prior or after the division operation. Furthermore, a normalization relative to the transmitted energy is also involved, which in itself can include an averaging process. Some aspects related to the averaging procedure (like pulse pair correlation) were previously discussed by Menyuk et al.

We present here an analysis of the relative effect of each phenomenon on measurements accuracy and point out the preferred averaging procedure to be applied. The analysis takes into account the temporal correlation of the transmitted power variations which are associated to laser modal noise, short term temporal correlation of atmospheric turbulence and 'white' additive receiver noise. A distinction is made between two types of systems, one that transmits a sequence of pulses tuned into two wavelengths but with a relatively large time separation, and another that transmits pulses in two wavelengths almost

coincidentally. This distinction is important because the effect of speckle noise can be minimized when the pulses at two wavelengths are sent within the correlation time of the atmospheric turbulence.

The received signals  $P_{ri}$  are modeled as  $P_{ri} = \beta_i v_i P_{ti} + n_i$ . The index  $i=1,2$  represents the two different wavelengths employed.  $P_{ti}$  represent the transmitted power which may have a fluctuating component that accounts for laser modal noise. The term  $\beta$  is a loss factor which represents several factors such as atmospheric attenuation, target backscatter coefficient, aperture loss and light collection efficiency. To take atmospheric turbulence into consideration,  $\beta$  is multiplied by a random variable  $v$  of a unity mean and a standard deviation  $\sigma_v$ . This multiplicative noise factor accounts for speckles noise due to propagation through a turbulent atmosphere. The noise term  $n$  represents a zero-mean 'white' random process which accounts for electronic noise in the detection stage.

The presented analysis compares the signal to noise ratio in the calculation of the ratio  $\beta_1/\beta_2$ , as achieved by using two methods of calculations: (a) First averaging the data related to each wavelength and then taking the ratio. (b) First taking the ratio and then averaging. For both methods, normalization with respect to the transmitted power is considered either prior or after the averaging of the signals in each wavelength.

# EXTRACTION OF AEROSOL AND RAYLEIGH COMPONENTS FROM DOPPLER LIDAR RETURN SIGNAL

John E. Barnes, Ken W. Fischer, Vincent J. Abreu, Wilbert R. Skinner

Department of Atmospheric, Oceanic and Space Sciences  
Space Physics Research Laboratory  
The University of Michigan  
Ann Arbor, Michigan 48109-2143

One of the most significant physical problems which limits the applicability of lidar systems for pressure and density profile measurements below 30 km altitude is the presence of atmospheric aerosols which contaminate the molecular or Rayleigh return signal. A new technique is described which allows for the separation of return signal into aerosol and molecular scattered components. The technique is applied to data from the University of Michigan's High Resolution Doppler Lidar (HRDL) described by Abreu and co-workers (Abreu et al., 1992).

Transmitted light from the laser source for a seeded Nd:YAG laser is very narrow spectrally, approximately 134.5 MHz ( $0.0045 \text{ cm}^{-1}$ ). Light scattered by molecules is broadened spectrally due to pressure and Doppler broadening, to a spectral width of approximately 1060 MHz ( $0.035 \text{ cm}^{-1}$ ) at sea level pressure. Light scattered by aerosols, which are much heavier, is not broadened significantly. This physical process makes it possible to distinguish between Rayleigh scattered light from molecules and light scattered from aerosols. Figure 1a) is an example of how modeled Rayleigh scattered light appears to the detector system of the HRDL. Figure 1b) shows how modeled aerosol scattered light appears to the system. Figure 1c) illustrates the two spectra combined. The image plane detector used in HRDL records all twelve channels simultaneously.

Two techniques have been developed to separate the aerosol and Rayleigh components of the return signal. The first and simpler of the two techniques involves doing a one step least squares fit of the data to idealized aerosol and Rayleigh spectra. This method simply solves for the best fit of the linear superposition of the two types of return signal. This technique has

the advantages of being simple to implement and requires very little computation time to achieve results. The main disadvantage is that this method has difficulty compensating for variations in the data introduced by the instrument which is not-ideal.

The second and more sophisticated of the two techniques, known as beta-analysis, does an iterated least squares fit to the data for three parameters: aerosol and Rayleigh components of the signal and Doppler shift of the signal or wind. The technique uses a Fourier series representation of each channel of the detection system to account for variations in sensitivity and finesse across the detector. The program iterates to achieve a satisfactory fit to the data. This program is also used to determine Doppler wind velocities used to create wind profiles with the HRDL. Both techniques have been implemented. Recovered aerosol and Rayleigh profiles will be shown for the boundary layer, free troposphere and stratosphere.

### References

Abreu, V. J., J. E. Barnes, and P. B. Hays, Observations of Winds with an Incoherent Lidar Detector. *Applied Optics*, accepted for publication, 1992.

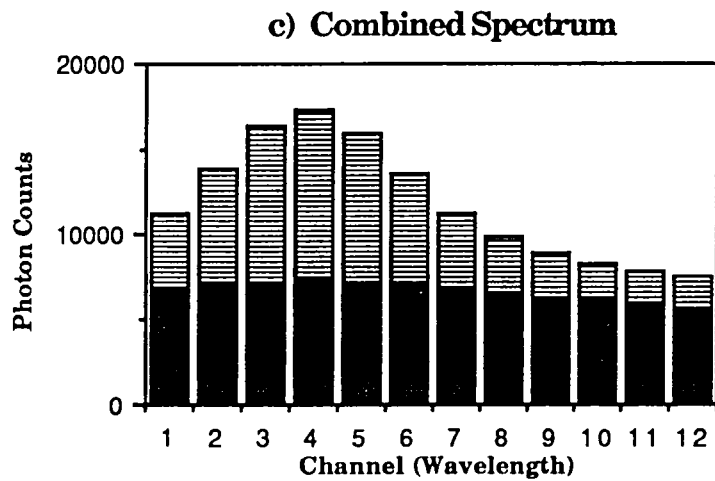
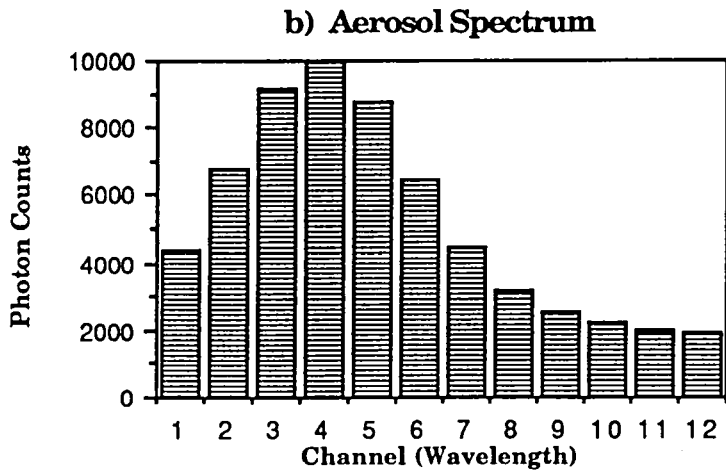
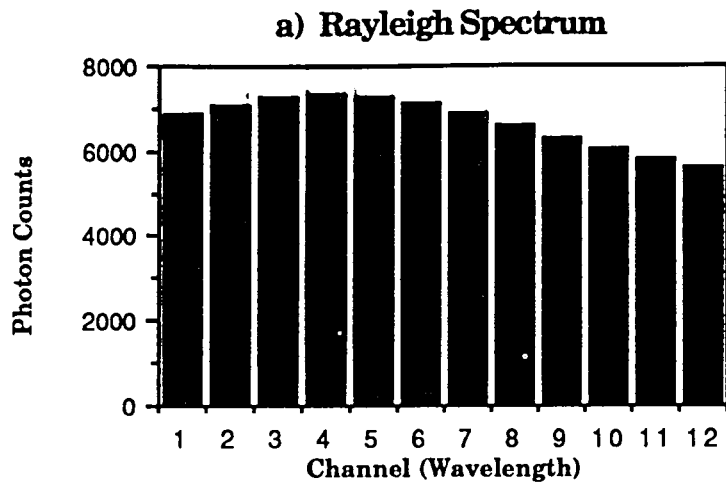


FIGURE 1. Rayleigh, aerosol, and combined spectra for University of Michigan High Resolution Doppler Lidar



## APPLICATION OF LASER IMAGING FOR BIO/GEOPHYSICAL STUDIES

J.R. Hummel, S.M. Goltz, N.L. DePiero, D.P. De Gloria,  
and F.M. Pagliughi  
SPARTA, Inc.  
24 Hartwell Avenue  
Lexington, MA 02173

Laser imagery provides a valuable tool for locating and quantifying the positions of objects. In programs requiring information about geophysical and biophysical backgrounds, laser imagery provides a quick and efficient method of obtaining information from complex scenes. As an example, laser imagery can obtain information about the positions of elements in a background. This information can be used to describe the physical structure of the objects making up the background. With laser imagery, one can also construct the 3-D objects in a format for use in physics models, such as energy budget models.

SPARTA has developed a low-cost, portable laser imager that, among other applications, can be used in bio/geophysical applications. In the application to be discussed here, the system was utilized as an imaging system for background features in a forested locale.

The SPARTA mini-ladar system was used at the International Paper Northern Experimental Forest near Howland, Maine to assist in a project designed to study the thermal and radiometric phenomenology at forest edges. The imager was used to obtain data from three complex sites, a "seed" orchard, a forest edge, and a building. The goal of the study was to demonstrate the usefulness of the laser imager as a tool to obtain geometric and internal structure data about complex 3-D objects in a natural background.

The data from these laser images have been analyzed to obtain information about the distributions of the objects in a scene. A range detection algorithm has been used to identify individual objects in a laser image and an edge detection algorithm then applied to highlight the outlines of discrete objects. An example of an image processed in such a manner is shown in Figure 1.

This paper will describe the results from the study. In addition, results will also be presented outlining how the laser imaging system could be used to obtain other important information about bio/geophysical systems, such as the distribution of woody material in forests.

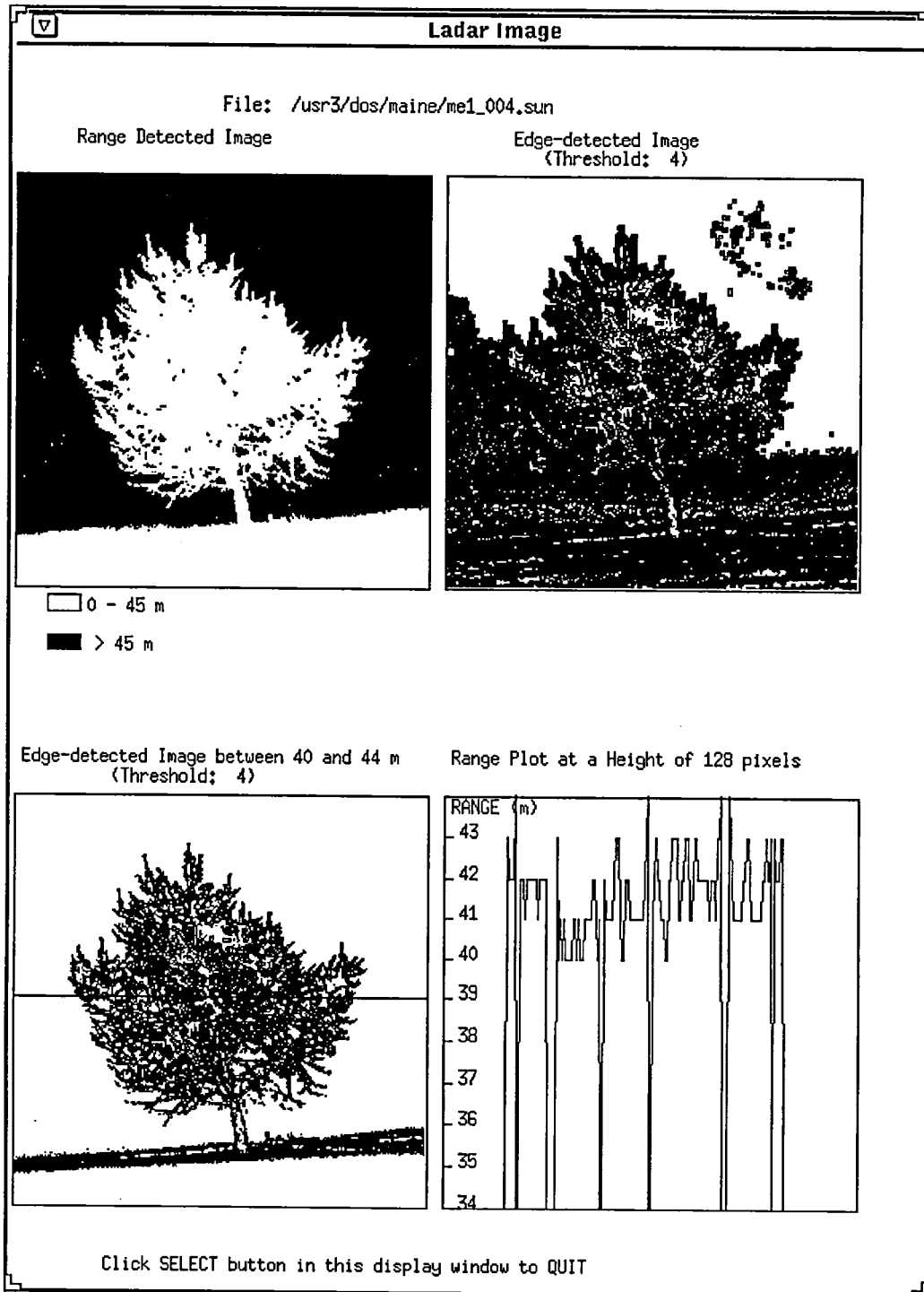


Figure 1. Example of Laser Images of a Single Tree That Have Been Processed to Identify Internal Structure

**ARCLITE: The Arctic Lidar Technology Facility  
at Søndre Strømfjord, Greenland**

J. P. Thayer

Geoscience and Engineering Center, SRI International,  
333 Ravenswood Ave.,  
Menlo Park, CA 94025, USA

SRI International is presently developing an Arctic lidar (ARCLITE) facility at the incoherent-scatter radar site in Søndre Strømfjord, Greenland (67.0° N, 309.2° W). The project, funded by NSF through the CEDAR (Coupling Energetics and Dynamics of Atmospheric Regions) initiative, is to perform high-altitude molecular/aerosol backscatter measurements in the Arctic covering the stratosphere/mesosphere region during nighttime and daytime conditions. The lidar system employs an injection seeded, high-energy GCR-5 Spectra Physics Nd:YAG laser for primary operation at 532 nm (550 mJ per pulse at 30 Hz). The receiver system is designed around a 36-inch Cassegrainian telescope of astronomical quality with receiver components and photon-counting electronics for day and night operations. The Rayleigh backscatter measurements will conduct investigations concerning:

- Long-term studies of the basic density and temperature structure of the Arctic stratosphere/mesosphere region.
- Effects of stratospheric warming on the structure of the stratosphere/mesosphere region.
- Occurrence and properties of polar stratospheric clouds.
- Occurrence of noctilucent clouds and their properties at high latitudes.
- Dynamic and thermodynamic coupling between the stratosphere/mesosphere region and the lower thermosphere.

The measurement accuracy, and consequently the performance, of the lidar system is largely determined by the product of the laser power and the telescope area. This power-aperture product may be used to compare the performance between lidar systems. A factor of 10 improvement in the power-aperture product increases the measurement altitude, for a fixed accuracy, by about two scale heights (Gardner, 1989).

Power-aperture products for the ARCLITE Rayleigh lidar system and the mobile Philips Lab Rayleigh lidar system operating an Nd:YAG laser at 532 nm are given in Table 1.

**Table 1**  
**Power-Aperture Products of ARCLITE and Philips Lab**  
**Rayleigh Lidar Systems at 532 nm**

<u>Facility</u>	<u>Laser Power (W)</u>	<u>Telescope Area (m<sup>2</sup>)</u>	<u>P · A (Wm<sup>2</sup>)</u>
ARCLITE	16.5	0.66	10.90
Philips Lab*	3.0	0.29	0.88

\*J. W. Meriwether, private communication—Sondrestrom performance

The significant laser power and large telescope area of the ARCLITE facility provide a performance factor that is high compared with the Philips Laboratory mobile Rayleigh lidar system placed temporarily at the Sondrestrom radar site during the fall/winter period of 1990-91. Density and temperature profiles were obtained up to 85 km (10% error) with a vertical resolution of 300 m and an integration time of three hours (J. W. Meriwether, private communication). From Table 1, the ARCLITE system is a factor of more than 12 more sensitive than the Philips Lab system and, thus, should obtain density profiles up to ~ 95 km with the same temporal and spatial resolution.

The motivation to install a lidar system at the Sondrestrom site includes (i) the scientific return, owing to the lack of middle-atmosphere Rayleigh lidar observations at high latitudes, (ii) the unique assemblage of optical and RF instrumentation at or near the radar facility, and (iii) existing logistic support (i.e., shelter, electrical power, personnel). The scientific potential for coordinated experiments with the lidar and existing instrumentation at the site is impressive; performing coincident lidar measurements with other mobile lidar systems is also possible.

Installation of the system at the site will begin in September 1992 with nighttime operations starting that winter. Daytime observations will be evaluated in the Spring of 1993 using a Fabry-Perot interferometer and polarization techniques. Once operational,

the facility will be maintained and operated by SRI for use by the general scientific community.

### Reference

Gardner, C. S., Sodium resonance fluorescence lidar applications in atmospheric science and astronomy, *Proceedings of the IEEE*, 77, 408-418, 1989.



# Rotational Raman Lidar for Lower Tropospheric Temperature Profiling

Takao KOBAYASHI , Takunori TAIRA , Takanobu YAMAMOTO

Faculty of Engineering, Fukui University, 3-9-1 Bunkyo, Fukui 910, JAPAN

Akihiro HORI , and Toshinobu KITADA

R & D center, Kansai EPCO, 3-11-20 Wakaouji, Amagasaki 661, JAPAN

## 1. Introduction

Accurate sensing of the tropospheric temperature profile is basically needed in meteorology and 3D mapping of the boundary layer atmospheric temperature over urban and industrial area is interesting in the environmental research. Several temperature lidar techniques have been investigated including DIAL, rotational and vibrational Raman, Rayleigh and high resolution Rayleigh schemes. For the tropospheric applications, the rotational Raman scheme looks potentially advantageous but several stringent technical problems still remain to be solved<sup>1,2</sup>.

This paper reports continuing efforts of the system development of the rotational Raman lidar<sup>3</sup>.

## 2. Basic Conditions

Practical advantage of the rotational Raman lidar over other schemes is the simplicity of applicable high power and fixed wavelength laser transmitters. In the receiving section, however, several sophisticated techniques are needed; (1) simultaneous two rotational Raman line measurements for the atmospheric transmittance correction and for increasing the temperature coefficient, (2) a high resolution spectral filter with large rejection ratio of the Mie backscatter ( $>10^6$ ), (3) a high sensitive and high SNR (signal-to-noise ratio) detection technique for the relatively small cross-section of the rotational Raman lines. (the temperature accuracy  $\Delta T[K]=210/SNR$ ), and (4) high stability of the system sensitivity.

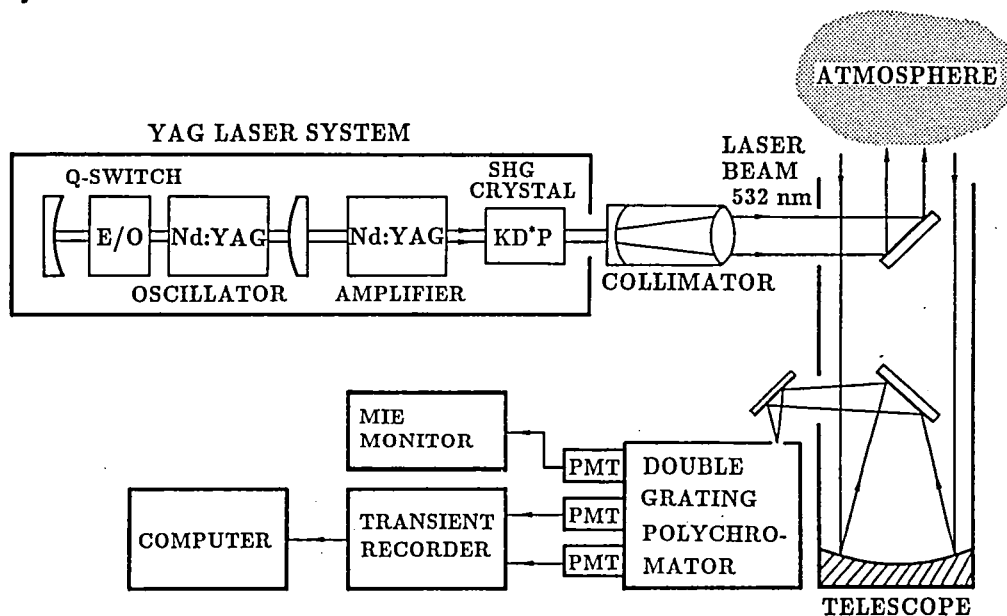


Fig.1 Block diagram of the rotational Raman lidar system.

### 3. System Improvement

The block diagram of the rotational Raman lidar system is shown in Fig.1. The Q-switched Nd:YAG laser oscillator-amplifier is used and the 100 mJ energy second harmonic green beam is vertically transmitted in the atmosphere with narrow beam divergence of 0.2 mrad. The backscatter is collected by the 46 cm diameter receiving mirror.

A major system improvement has been made in the high resolution filter by designing a double grating polychromator in place of the double interference filter (IF) polychromator<sup>3</sup>. Basic arrangement of the compact double grating polychromator-detector system is shown in Fig.2. High efficiency holographic gratings are used. The optical characteristics are compared with the IF polychromator in Table 1. A high Mie rejection ratio over  $3 \times 10^6$  is obtained for the nearest S(4) line and an overall transmittance is increased up to 38%. High blocking and high throughput characteristics are essential in this Raman lidar scheme.

Three photomultilines are used; two channels for the rotational lines and one for the Mie backscatter for checking intense clouds. A large number of signal pulses ( $10^3$ - $10^4$ ) are averaged in the transient recorder and the data is processed by the micro-computer.

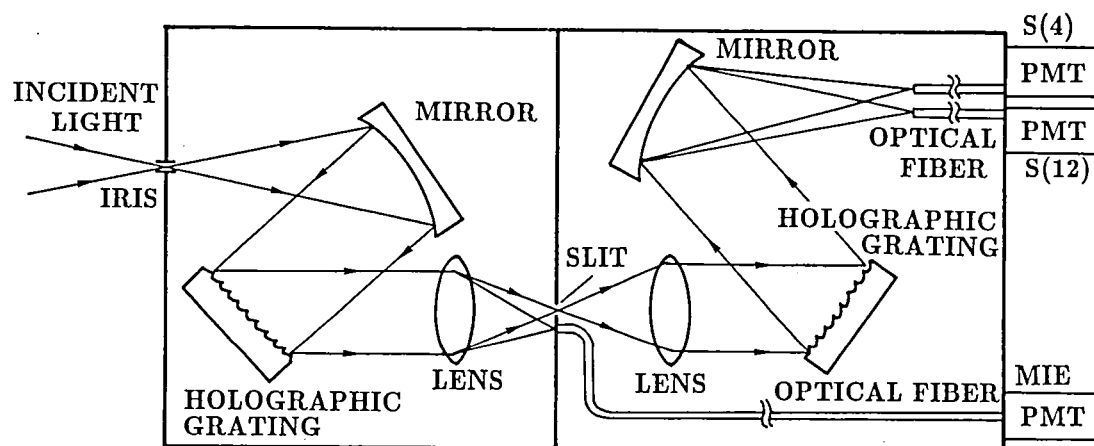


Fig.2 Schematic of the compact double grating polychromator-detector system.

Table 1 Comparison of Mie rejection and transmittance of the two polychromators; the double grating system and the double interference filter system.

Raman Line	Wavelength $\lambda$ (nm)	Mie Rejection		Transmittance		Bandwidth	
		$\gamma$		T (%)		$\Delta \lambda$ (nm)	
		Grating	Filter	Grating	Filter	Grating	Filter
S(4)	533.27	$3 \times 10^6$	$2 \times 10^5$	38	8.7	0.39	0.18
S(12)	535.11	$3 \times 10^7$	$4 \times 10^6$	38	3.5	0.40	0.38

#### 4. Experimental Results and Discussion

After an laboratory test of the system, atmospheric temperature measurements was performed. As an example, Fig.3 shows the experimental data of vertical profiles of the S(4) and S(12) rotational Raman line intensities with range correction, the ratio S(4)/S(12) and the derived atmospheric temperature. The range resolution is about 50 m. Absolute temperature value was calibrated by the ground data and the balloon data. In this experiment, the random error of the temperature  $\Delta T$  due to SNR was reduced to 0.7 K at 1 km height.

On the other hand, larger systematic error was sometimes observed. The origin of this error was checked carefully and resulted in the fluctuation of the laser beam pointing direction and hence a receiver system efficiency instability of the order of 1 %. This problem will be solved after minor modification.

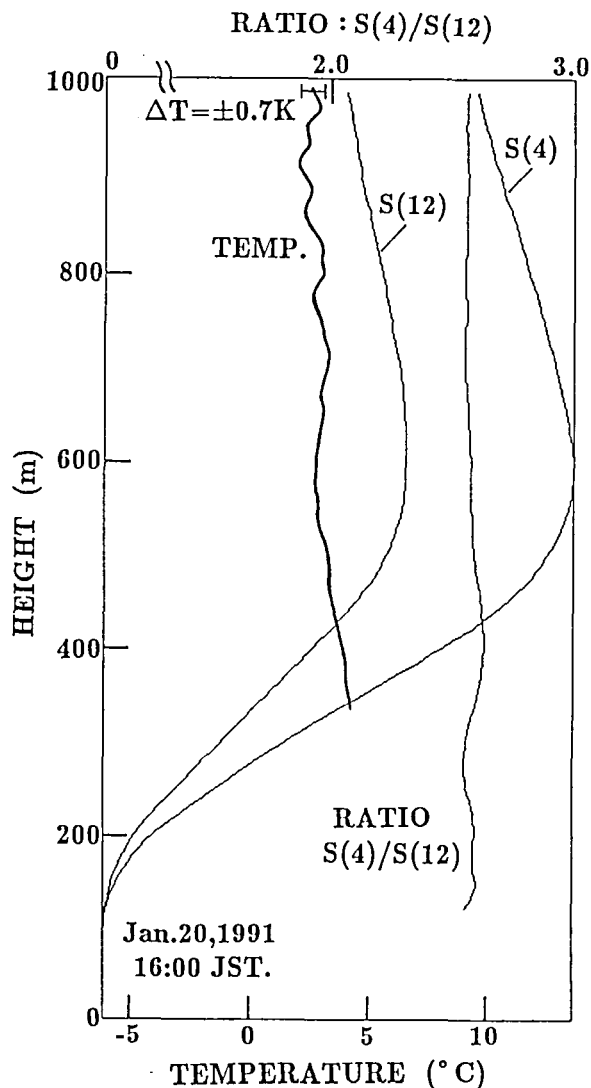


Fig.3 Experimental data of vertical profiles for the S(4) and S(12) rotational Raman line intensities, the ratio S(4)/S(12) and the derived atmospheric temperature.

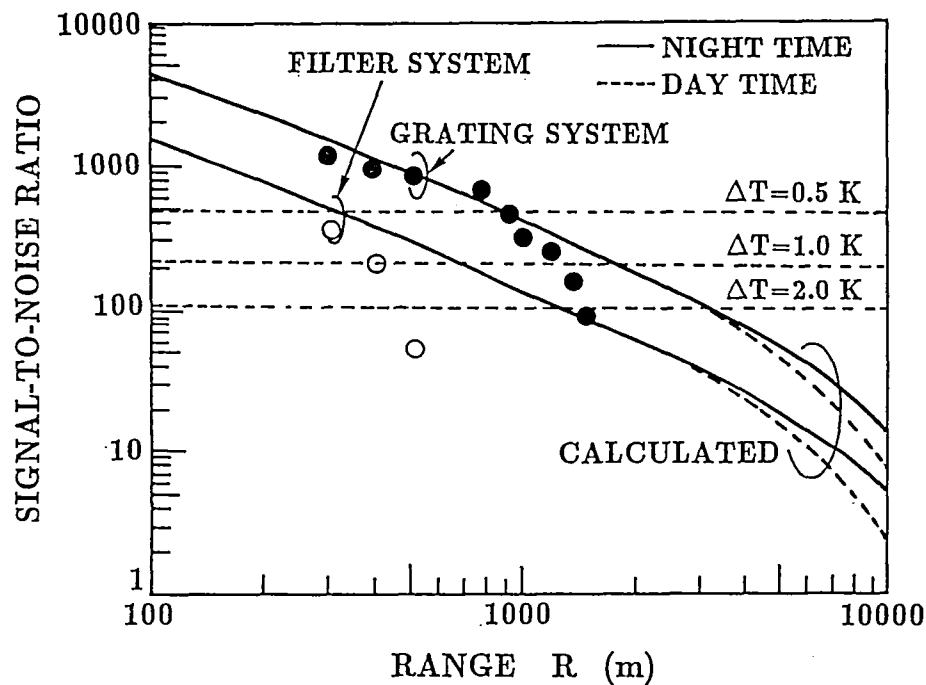


Fig. 4 Range dependence of the experimental and calculated SNR and the temperature accuracy  $\Delta T$  due to SNR of the present system.

Fig. 4 shows the range dependence of the experimental and calculated SNR and the temperature accuracy  $\Delta T$  due to SNR of the present system. By increasing the laser beam energy and the telescope size, the rotational Raman lidar will be possible to increase the maximum range around 5-10 km with temperature accuracy  $\Delta T=1K$ .

#### References

- 1) T. Kobayashi, H. Shimizu and H. Inaba; "Laser radar technique for remote measurement of atmospheric temperature", 6th ILRC Abstracts, 49, Japan (1974).
- 2) Y. F. Ashinov, S. M. Bobrovnikov, V. E. Zuev and V. M. Mitev; "Atmospheric temperature measurements using a pure rotational Raman lidar", *Appl. Opt.*, 22, 2984 (1983).
- 3) T. Kobayashi and T. Taira; "Development of a rotational Raman lidar for practical tropospheric temperature sensing", 15th ILRC Abstracts, USSR 290 (1990).

## One Year of Rayleigh Lidar Measurements at Toronto

James A. Whiteway and Allan I. Carswell

Institute for Space and Terrestrial Science and  
Department of Physics and Astronomy, York University  
4700 Keele Street, North York, Ontario, Canada, M3J 1P3  
Tel: (416) 736-2100 Fax: (416) 736-5516

The Rayleigh lidar technique is being used at York University to study middle atmospheric thermal structure with particular emphasis on the properties and influence of internal gravity waves [1]. These measurements are now carried out on a routine basis (every clear night) in order to determine seasonal variability and eventually long term trends.

The transmitter consists of a doubled Nd:YAG laser with an output of 0.4 Joules per pulse at 20Hz (8 Watts) which is expanded to obtain a divergence of 0.4 milliradians. Backscattered photons are collected by a half meter cassegrain telescope, filtered to a bandwidth of 1nm, detected by a PMT and counted with a multi-channel scaling averager. Strong backscatter from lower altitudes is blocked using a rotating chopper (25000rpm) which triggers the laser. The range gate and hardware averaging interval are variable but typically 300m and 5 minutes.

Relative density profiles are obtained by simply normalizing to a model (eg. CIRA) at some altitude. Absolute temperature is derived using the hydrostatic equation, ideal gas law and a model pressure value at the altitude where the photocount statistical uncertainty is about 15% [2] - typically 90km for the entire night's average. The lower limit is currently about 30-35km due the presence aerosol from the volcanic eruption of Mt. Pinatubo.

Figure 1 illustrates time series of nightly mean temperature profiles for September, 1991, and March, 1992. The most interesting features are the mesospheric temperature inversions which persist for consecutive nights at altitudes of 70km in September and 60km in March. From the seasonal variation of height and probability of occurrence of inversions Hauchecorne et. al. [3] concluded they are likely a result of turbulence generated by gravity wave breaking. We often observe the temperature gradient to be adiabatic (or nearly) in the region of enhanced temperature above an inversion. If one considers the elimination of potential temperature gradient due to turbulent diffusion in a sharply defined well mixed layer the corresponding absolute temperature profile consists of an inversion and overlying adiabatic lapse. There may be another inversion at the top of the mixed layer depending on the magnitude of turbulent dissipation. A one-dimensional numerical model of middle atmospheric thermal structure has been developed to apply this concept. Using fabricated profiles of eddy diffusion coefficient, we are able to obtain excellent agreement with our measured temperature profiles containing inversions. Such an example is shown in Fig. 2. The model is similar to that of Chandra [4] who also used turbulent diffusion and dissipation to simulated a measured mesospheric temperature inversion. Although dynamical effects other than turbulence have been neglected, we find that well defined turbulent layers will result in mesospheric temperature structure similar to that observed.

Temperature fluctuations, interpreted as being a result of internal gravity waves, are

observed in the difference between half hour average profiles and a cubic polynomial fit which approximates the unperturbed state. The fluctuation profiles of September 26/27 (Fig. 3) exhibit an apparently stationary wave pattern. These have been smoothed with a 1.5km running mean and high pass filtered to remove wavelengths longer than 15km - possibly introduced by the fitting process. The temperature profiles of Fig. 4, corresponding to the last three in Fig. 3, have not been smoothed (300m resolution) and show regions of near convective instability associated with the wave perturbations. The variation of rms wave amplitude with altitude for all measurements in September and March is shown in Fig. 5 with the same filtering as applied to the profiles of Fig. 3. The long dashed line represents the amplitude growth rate for energy conserving propagation of internal gravity waves. There appears to be significant dissipation in the 30km to 50km altitude region. Note that measurements below 35km are suspect due to the possible presence of stratospheric aerosol.

Since June, 1991, we have been able to observe for an average of about 10 nights per month. The findings from one year of routine observations will be presented.

## References

1. Whiteway, J.A. and A.I. Carswell, "Rayleigh lidar measurements at Toronto," in Technical Digest on Optical Remote Sensing of the Atmosphere, 1991 (Optical Society of America, Washington, D.C., 1991), Vol. 18, pp. 244-246.
2. Hauchecorne, A. and M.L. Chanin, Density and temperature profiles obtained by lidar between 30 and 80km, *Geophys. Res. Lett.*, 7, 565-568, 1980.
3. Hauchecorne, A., M.L. Chanin and R. Wilson, Mesospheric temperature inversion and gravity wave breaking, *Geophys. Res. Lett.*, 14, 933-936, 1987.
4. Chandra, S., Energetics and thermal structure of the middle atmosphere, *Planet Space Sci*, 28, 585-593, 1980.

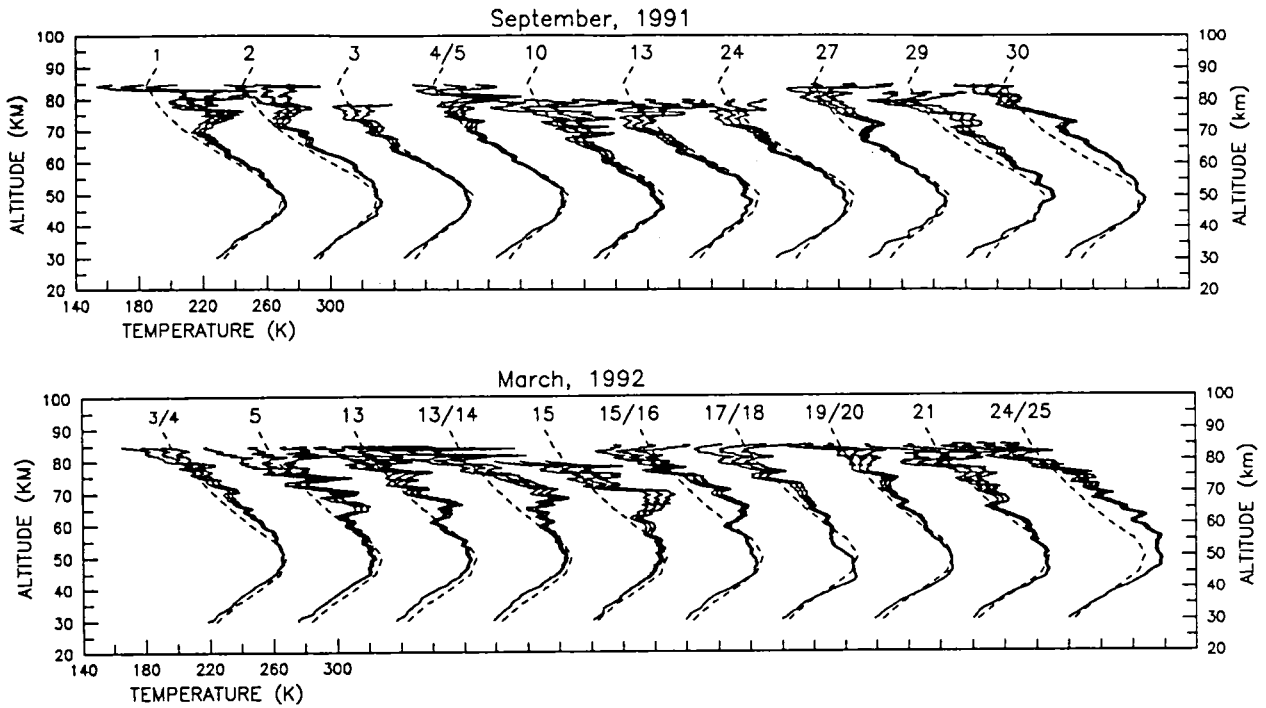


Fig. 1. Nightly mean temperature profiles obtained in September, 1991, and March, 1992. All profiles have been smoothed with a 5- point (1.5km) running mean. Dashed lines represent the CIRA (1972) reference for each month.

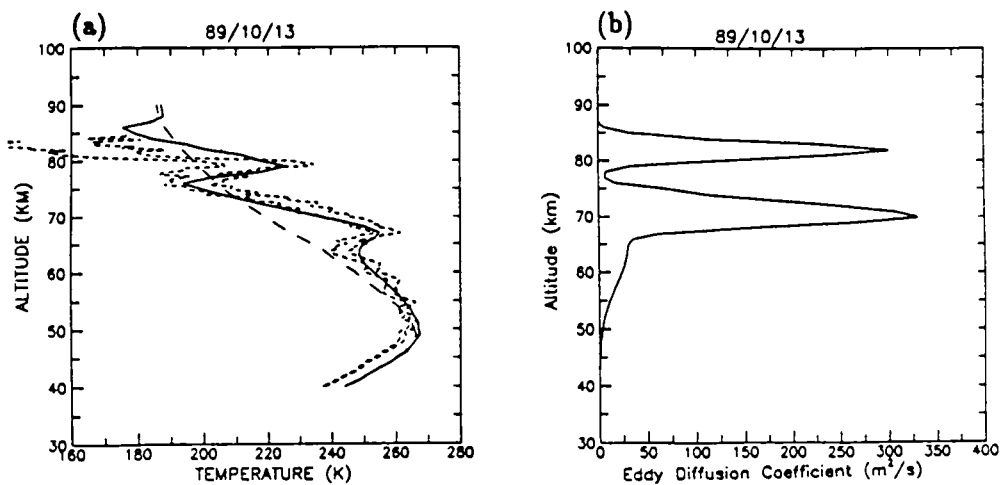


Fig. 2. (a) Limits of uncertainty for the measured average (7 hours) temperature profile (short dash) of Oct. 13, 1989, compared with calculated results (solid) using the eddy diffusion coefficient profile of (b). The long dashed line represents the calculated radiative equilibrium temperature (no turbulence).

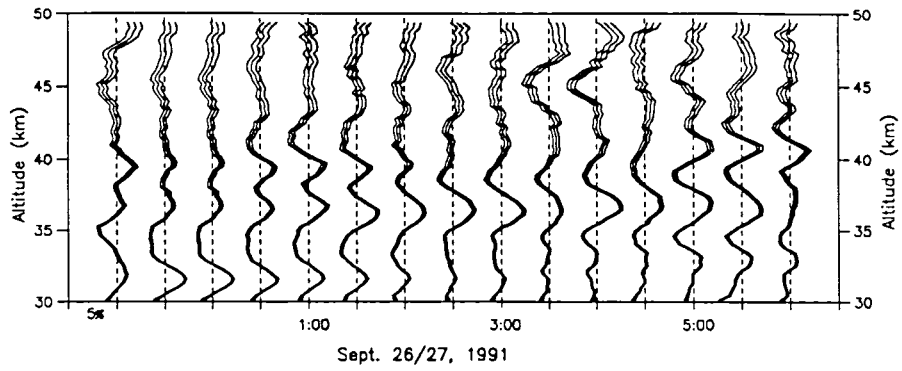


Fig. 3. Temperature fluctuation profiles for the night of Sept. 26/27, 1991. Separation of the dashed lines represents 5% deviation and a half hour in time.

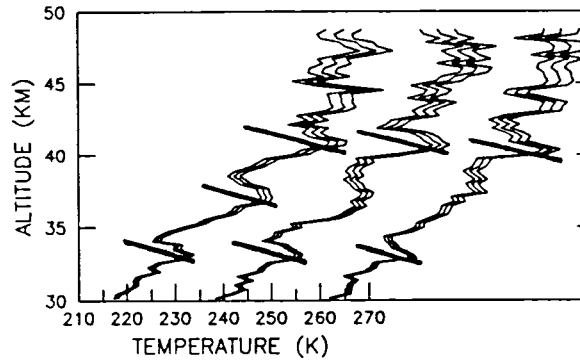


Fig. 4. Half hour average temperature profiles corresponding to the last three of Fig. 3. The temperature scale corresponds to the first. Thick lines indicate an adiabatic lapse rate (-9.8 deg/km).

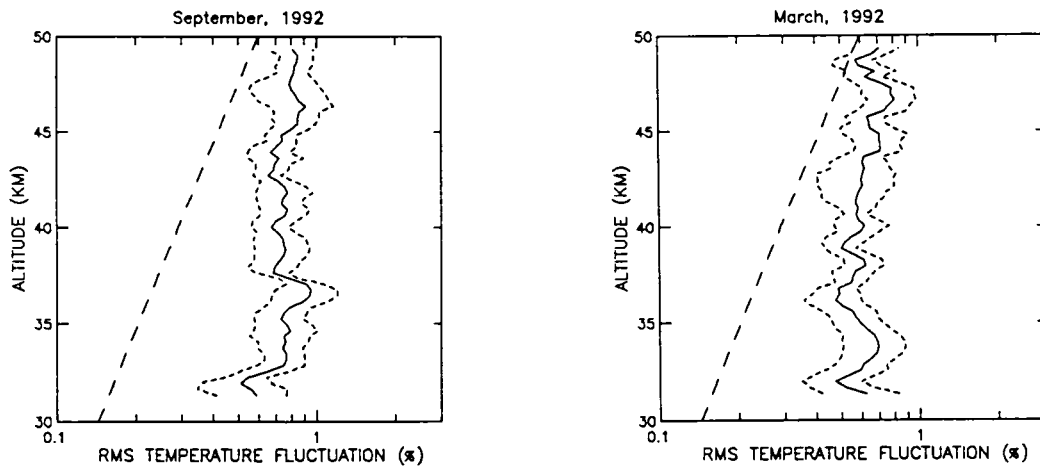


Fig. 5. RMS temperature fluctuation profiles for the entire months of September and March. The short dashed lines represent standard deviation of individual nights from the mean and the long dash shows the growth rate for linear conservative propagation.

# LIDAR OBSERVATION OF AEROSOL AND TEMPERATURE STRATIFICATION OVER URBAN AREA DURING THE FORMATION OF A STABLE ATMOSPHERIC PBL

I.Kolev, O.Parvanov, B.Kaprielov, V.Mitev, V.Simeonov, I.Grigorov

Institute of Electronics of Bulgarian Academy of Sciences  
72 blvd. Trakia, Sofia 1784, Bulgaria

## INTRODUCTION

In the recent years the processes in the atmospheric planetary boundary layer (PBL) over urban areas were intensely investigated [1,2], due to ecological problems related to the air, soil and water pollution. New pollution sources in the new residential districts, transportation, etc., when contradicting to the microclimate (and the topography resp.) requirements of the particular region create a number of considerable hazards and problems [3,4].

The present study is a continuation of our preceding investigations [5] and aims at revealing of aerosol structure and temperature stratification during the transition after the sunset by two lidars. Such observation of the nocturnal stable PBL formation over an urban area in Bulgaria are not reported so far.

The lidars' high time and spatial resolutions allow the changes of the internal structure of the PBL's part located above the surface layer to be observed [1].

## APPARATUS

Fig. 1 shows the general arrangement of the experiment.

The triple-beam near-vertically sounding aerosol meteorological lidar (TBAML) (30 mJ YAG-Nd, ADC of 10 bits, 20 Msamples) and the used correlation technique are described in detail [5].

The Raman lidar (RL) (2 W Cu-Br, photon accumulation - by 256 channels 100 ns each) for temperature measurement and the used methods for its profile obtaining are presented in [6,7].

## EXPERIMENTAL RESULTS

Results of more systematic investigations of the aerosol structure in the PBL over this part of Sofia city (residential district of Mladost) were presented by us in a series of papers [8,9]. The lidar data were compared with profiles of the atmospheric thermodynamic parameters determined by conventional means.

For the present study the synoptic situation (anticyclonic) and the meteorological conditions (clear and calm weather) were chosen to favour an undisturbed formation of stable stratification. So transition process from convective to stable PBL between 18:30 and 22:00 on Oct. 10, 11 and 16, 1990 was traced.

An attempt is made to determine on the basis of lidar data only (TBAML and RL): retentive and mixed layers height, relationship between the time variation of aerosol layer parameters and temperature stratification of the entire PBL. TBAML took 8 spatial series at 15-30 min intervals and 2 time series 10 min each. The RL took 3 time series 18 min each.

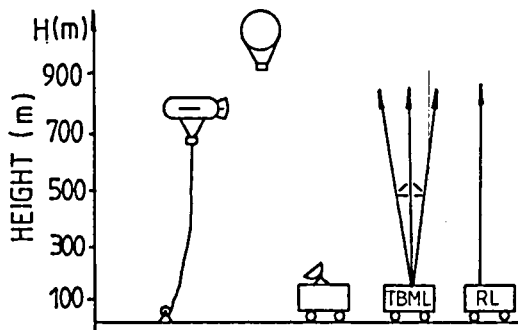


FIG.1

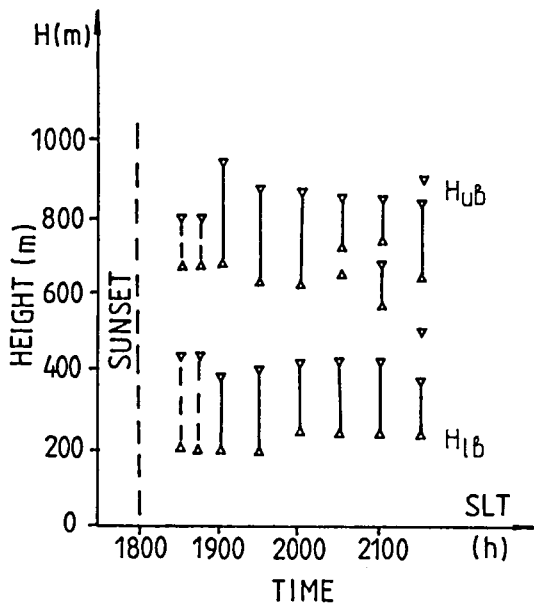
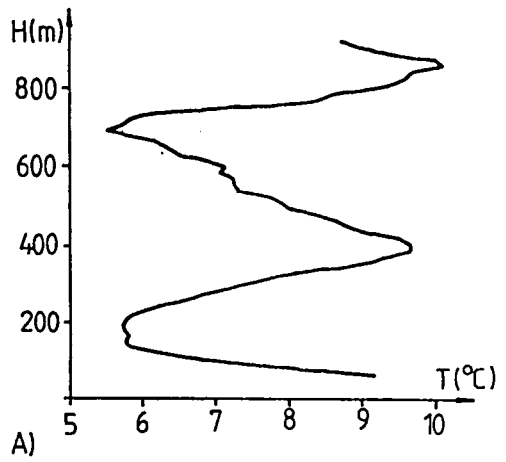
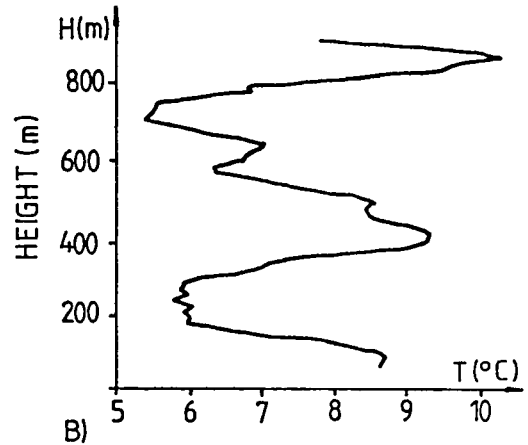


FIG.2

16 OCT. 1990 20:15-20:34 h



21:00-21:13 h



21:22-21:40 h

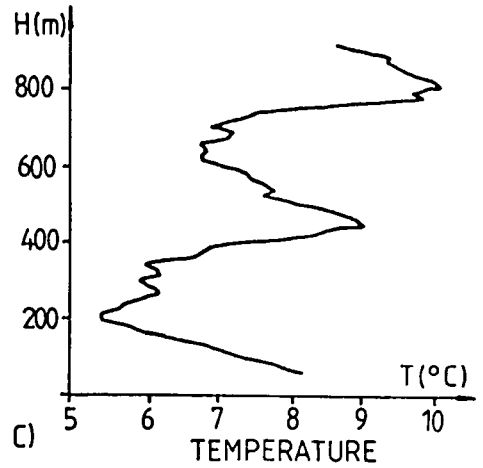


FIG.3

Fig. 2 shows the time variation of the aerosol layer height on Oct. 16, its lower ( $H_{lb}=225$  m) and upper ( $H_{ub}=938$  m) boundaries. The lidar data show that the prevailing aerosol loading is located between 225 and 563 m. Autocorrelation functions of lidar returns (not shown here) indicate that the aerosol field is homogeneous between 225 and 375 m.

Fig. 3 shows the temperature profiles obtained by the RL on Oct. 16 between 20:15 and 20:34-(a), 21:00 and 21:13-(b), 21:22 and 21:40-(c). In Fig. 3a the following can be seen:

- in the layer 0-150 m the temperature decreases; this is the mixing layer where turbulent and radiation processes play substantial role;
- from 150 to 400 m a retentive layer, i.e. temperature inversion (TI) follows;
- up to 700 m a layer of decreasing temperature is located;
- in the layer 700-900 m a second TI is observed;
- the free atmosphere follows above.

Comparison (Fig. 2 and 3a) of the aerosol stratification with the retentive layer (i.e. TIs) heights shows a good coincidence.

## DISCUSSION

As we mentioned above, in this experiment TBAML data confirm the results from 1984 [10] and 1988 [9], namely that there is a structure in the urban PBL connected with the topography.

Here an attempt is made to emphasize on the physical interpretation of this structure. Heights from 100 to 900 m are observed. Four layers are found within the aerosol stratification.

Our hypothesis for the aerosol structure in the layer from 200(180) to 900 m is: the aerosol in daytime at a developed convection is mixed in the entire PBL (1500-2000 m thick). After the sunset it is kept by the elevated TIs which form in this period. After the sunset the convective boundary layer is being destroyed and as no buoyancy forces exist to lift the aerosol upwards, it should descend to the ground, which is the case. However, on the other hand the second effect, namely the influence of the thermal island appears.

The presence of the Vitoshka and Losenska mountains causes the appearance of several more TIs. We shall limit ourselves to heights up to 700-900 m, where aerosol is retained.

The hypothesis build up on the basis of the aerosol structure obtained by TBAML is confirmed by the data about the temperature from the RL and corresponds to the kytoon data as well.

From Fig. 3 a-c some coinciding zones are apparent: kytoon data show isothermal layers between 200-400 m and 700-800 m on Oct. 10 and 11 (not shown here), and on Oct. 16 RL data reveal TIs at the same heights. It should be also emphasized that the layer up to 100-150 m is substantially affected by radiation and turbulent processes near the ground which is evidenced by the consecutive RL measurement at 15 min intervals. Sounding from 21:00 to 21:13 on Oct. 16 (Fig. 3b) registers the beginning of surface inversion and rising of the lifted inversion, i.e. radiation processes lead to the TI elevation. Temperatures in Figs. 3a and 3b differ only at lower heights, showing that the depth of the mixing

layer (where temperature drops with height) increased, i.e. radiation and turbulent processes in it continue. Our suggestion is that this is due to the heat released by the buildings. Fig. 3c shows that the processes at low heights have completed; height of the separate layers are preserved. The temperature change is at higher elevations - in the zone of the second TI between 600 and 800 m, i.e. moved 100 m downwards.

In the end we can definitely say that both lidars reveal a structure in the PBL (which is confirmed by the kytoon as well), corresponding to the general model [3]. Here it should be noted that the RL obtains the temperature profiles at once which corresponds to the TBAML technique while the kytoon measures each value at different times which impedes the consideration of rapid changes. At the same time some deviations from the model, i.e. certain dynamics was found within the so-defined zone, namely an ascending of the lifted inversion during the night. This effect has been predicted and also observed [11].

### CONCLUSIONS

In conclusion we shall note that, besides its scientific significance for the more detailed investigation of the processes in the entire PBL, lidar technique (use of aerosol and Raman lidars in the case) can substantially contribute to concrete studies of the microclimate over built-up areas, being harmless to the inhabitants, as well as when choosing the situation of future industrial pollution sources in the vicinity of populated areas.

A part of these experiments and the overall data processing are financed under Contract No 200302 with the Presidium of the Bulgarian Academy of Sciences.

### REFERENCES

1. Sasano Y., I.Matsui, N.Sugimoto, 15th Int. Laser Radar Conf., July 23-27, 1990, Tomsk, USSR, Abstracts, p. II, 77-79.
2. Wakimoto R.M., J.L.McElroy, 1986, J. Cl. Appl. Meteor., 25, 1583-1599.
3. Nieuwstadt F.F.M., H.Van Dop, Atmospheric Turbulence and Air Pollution Modeling, Riedel Dordrecht, 1982.
4. Hooper W., E.Eloranta, 1986, J. Climate Appl. Meteor., 25, 990-1001.
5. Kolev I., O.Parvanov, B.Kaprielov, 1988, Appl. Opt., 27, 2524-2531.
6. V.M.Mitev, V.Simeonov, L.M.Ivanov, Yu.Arshinov, S.Bodorovnikov, 1985, Bulg. J. of Phys., 12, 429.
7. V.Mitev, I.Grigorov, V.Simeonov, P.Tomov, P.Georgiev, 14th Int. Laser Radar Conf., June 20-24, 1988, Innichen San Candido, Italy, Proceedings, 157-158.
8. Kolev I., O.Parvanov, V.Polianov, Y.Paneva, 1988, Atmospheric Optics, 1 (2), 100-103, (in Russian).
9. O.Parvanov et al., Atmospheric Optics, (in press), (in Russian).
10. Kolev I., L.Yordanova, V.Polianov, O.Parvanov, C. R. Acad. Bulg. Sci., 1988, 41 (3), 37-40.
11. Whiteman C.D., 1986, Meteor. Atmos. Phys., 35, No 3, 220-226.

# A COMPARISON BETWEEN RAMAN LIDAR AND CONVENTIONAL CONTACT MEASUREMENTS OF ATMOSPHERIC TEMPERATURE

V. M. MITEV, V. B. SIMEONOV, I. V. GRIGOROV  
INSTITUTE OF ELECTRONICS, BULG. ACAD. OF SCI.  
BUL. TRAKIA 72, SOFIA 1784, BULGARIA

THIS PAPER DESCRIBES THE RESULTS OF COMPARISON BETWEEN LIDAR AND CONVENTIONAL CONTACT MEASUREMENTS OF THE VERTICAL TEMPERATURE PROFILE OF THE ATMOSPHERE. THE LIDAR MEASUREMENTS ARE BASED ON THE METHOD OF TEMPERATURE DEPENDENCE OF PURE ROTATIONAL RAMAN SCATTERING OF NITROGEN AND OXIGEN MOLECULES AS DESCRIBED IN [1,2].

THE RAMAN LIDAR CONSISTS OF: CuBr-VAPOUR LASER, 40 CM CASSEGRIAN TELESCOPE, DOUBLE POLYCHROMATOR FOR SPECTRAL SELECTION, PHOTON-COUNTING SYSTEM AND PERSONAL COMPUTER EQUIPPED WITH A BUFFER MEMORY FOR DATA ACQUISITION WITH 256 INTERVALS IN THE PROFILE, 100 NS EACH INTERVAL [3]. THE CONTACT MEASUREMENTS WERE PERFORMED BY INDUSTRIAL RADIOSONDE MODEL "MAP3-2-2" USED IN REGULAR MEASUREMENTS WITH FREE FLYING BALLOONS PERFORMED BY INSTITUTE OF HYDROLOGY AND METEOROLOGY IN SOFIA [4] AND A THERMORESISTIVE METER PLACED ON A TIED BALLOON.

THE MEASUREMENTS WERE PROCEEDED AT NIGHT. THE ACQUISITION TIME WAS UP TO 40 MIN. IT WAS SELECTED IN SUCH A WAY THAT THE STATISTICAL ERROR IN DETERMINING TEMPERATURE DUE TO QUANTUM NOISE OF THE ACCUMULATED SIGNAL SHOULD NOT EXCEED  $\pm 1$  K AT MAXIMUM HEIGHT OF SONDING. AT THE BOTTOM PART OF THE PROFILE THIS ERROR IS ESTIMATED TO  $\pm 0.3$  K. UNDER THESE CONDITIONS THE MAXIMUM HEIGHT OF SONDING WAS LIMITED TO 800-900M. THE REGULAR AEROGICAL MEASUREMENTS ARE PROCEEDED FROM A STATION SITUATED AT ABOUT 150 M FROM THE LIDAR. THE TIED BALLOON WAS LAUNCHED NEAR THE LIDAR. IN BOTH CASES OUR AIM WAS THE COINCIDENCE OF THE LIDAR AND CONTACT MEASUREMENTS.

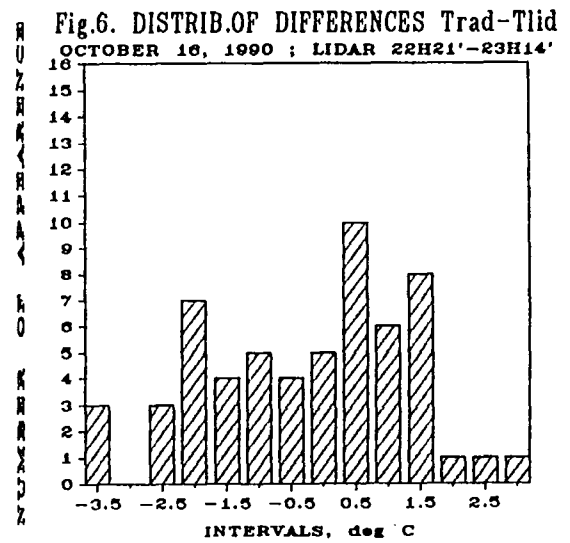
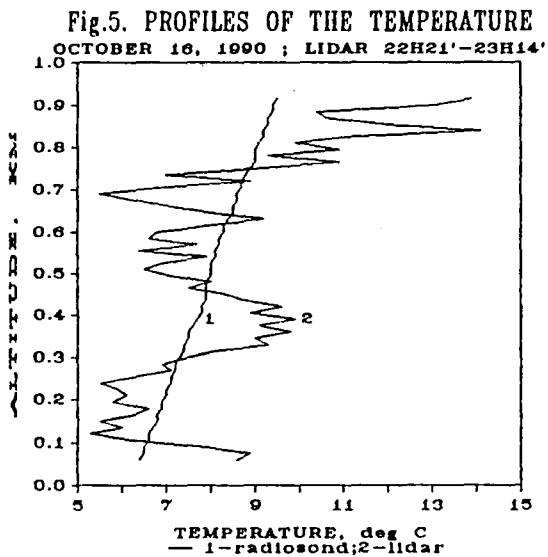
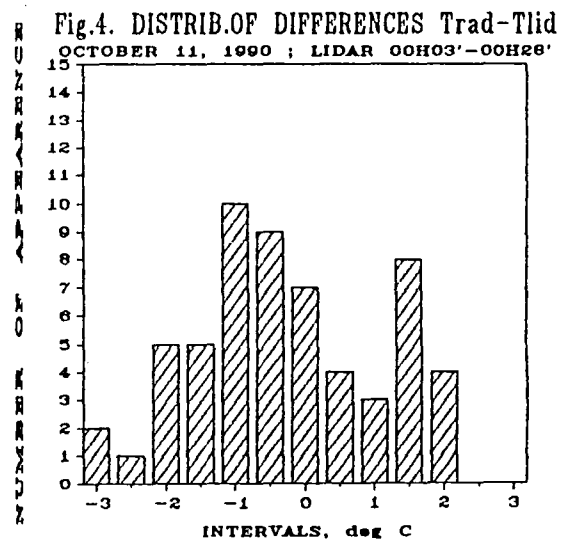
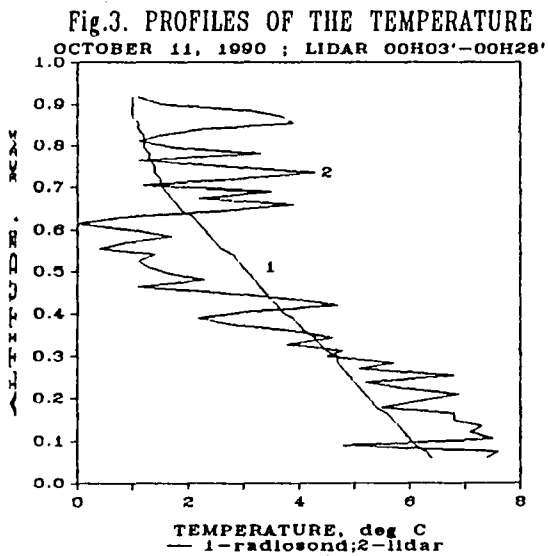
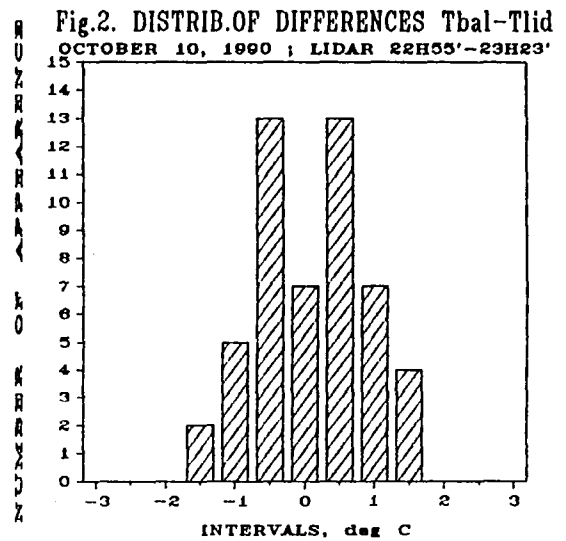
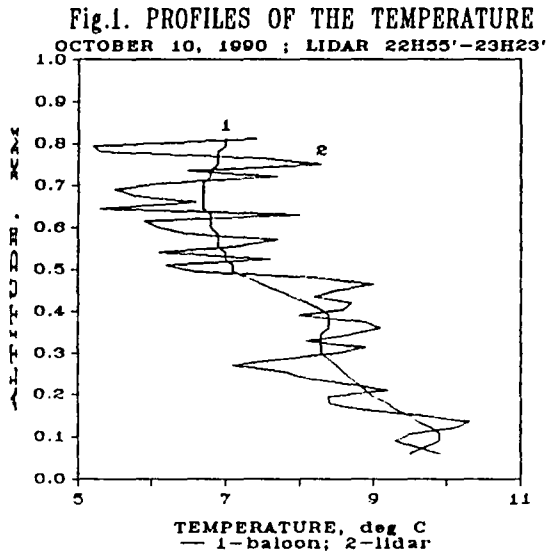
ON FIG.1, 3 AND 5 EXAMPLES OF VERTICAL TEMPERATURE PROFILE OF THE ATMOSPHERE OBTAINED BY LIDAR AND CONTACT METERS ARE PRESENTED. ON THE SAME FIGURES THE MEASURING TIME OF THE LIDAR AND THE TYPE OF THE CONTACT METER ARE ALSO GIVEN. THE DISTRIBUTION OF THE DIFFERENCES BETWEEN CONVENTIONAL CONTACT METERS AND LIDAR MEASUREMENTS ARE GIVEN ON FIG.2, 4 AND 6.

THE PRESENTED RESULTS SHOW, THAT AS A WHOLE THE MOTION OF THE LIDAR AND CONVENTIONAL PROFILES COINCIDES IN THE CONFIDENCE INTERVALS. STIL THERE ARE DISTRICTS IN WHICH THE DIFFERENCES LAY OUT OF THE CONFIDENCE INTERVALS. IN ANALYSIS AND ESTIMATION OF THE COINCIDENCE AND THE DISTINCTION IN MOVING OF THE PROFILES WE MUST TAKE IN ACCOUNT THE DIFFERENCES BETWEEN THE METHODS FOR MEASURING THE TEMPERATURE PROFILES BY LIDAR AND CONTACT METHODS, I.E. THE NEXT ADDITIONAL FACTORS. THE TIED BALOON METER GIVES THE MOMENTARY VALUES OF THE TEMPERATURE IN PARTICULAR POINTS OF THE PROFILE ,AS THIS MOMENTARY VALUES ARE THE RESULTS OF CONSEQUENT BUT NOT SIMULTANEOUS MEASUREMENTS. IN THE CASE OF FREE FLYING BALOON,- THE TIME OF MEASURING THE LOWER SEVERAL HUNDRED METERS IS LITTLE BECAUSE OF HIGH VERTICAL VELOCITY (ABOUT 300 M/MIN). THIS LEADS TO AN INDEFINITE INCREASEMENT OF THE MEASURING ERROR. THE COMPLETE SPACE COINCIDENCE BETWEEN THE LIDAR'S AND CONVENTIONAL PROFILES ISN'T POSSIBLE. THE CONTRIBUTION OF THE FACTORS MENTIONED ABOVE ABOUT THE ERROR OF COMPARISON COULD INCREASE BECAUSE OF NONSTABLE LAYERS IN THE PLANETARY BOUNDARY LAYER OF THE ATMOSPHERE AS WELL AS BY THE INFLUENCE OF THE MOUNTAINS AND THE CITY SITUATED NEAR BY. THE LARGE BASE AND ASYMETRY OBSERVED IN FIG.4 AND 6, OF THE DISTRIBUTIONS OF DIFFERENCES BETWEEN RADIOSONDE AND LIDAR DATA, COULD BE EXPLAINED BY THE LACK OF COINCEDENCE IN TIME AND SPACE OF THE MEASUREMENTS USING BOTH METERS. CONVERSELY, THE SYMETRY AND NARROW BASE OF DIFFERENCES BETWEEN THE DATA OF THE METER PLACED ON A TIED BALOON AND THE LIDAR, IN FIG.2, WOULD BE DUE OF THE COINCIDENCE IN TIME AND PRACTICALLY IN

SPACE OF THESE MEASUREMENTS.

REFERENCES:

1. ARSHINOV YU.F., S.M.BOBROVNIKOV, V.E.ZUEV, V.M.MITEV, APPL.OPT., v.22, 2984 (1982).
2. MITEV V.M, V.SIMEONOV, L.IVANOV, YU.ARSHINOV, S.BOBROVNIKOV, BULG. J. PHYS., v.12, 429 (1985).
3. MITEV V.M, I.V.GRIGOROV, V.B.SIMEONOV, YU.F.ARSHINOV, S.M.BOBROVNIKOV, BULG. J. PHYS., v.17, 67 (1990).
4. GORODETZKI O.A., I.I.GURALNIK, V.V.LARIN, METEOROLOGY, METHODS AND TECHNICAL INSTRUMENTS OF THE OBSERVATIONS, GYDROMETEOIZDAT, PETROGRAD, 1984 (IN RUSSIAN).



# EFFICIENCIES OF ROTATIONAL RAMAN, AND RAYLEIGH TECHNIQUES FOR LASER REMOTE SENSING OF THE ATMOSPHERIC TEMPERATURE

I. D. Ivanova, L. L. Gurdev, V. M. Mitev

*Institute of Electronics, boul. Tzarigradsko shose 72, Sofia 1784, Bulgaria*

## I. INTRODUCTION

Various lidar methods have been developed [1-5] for measuring the atmospheric temperature, making use of the temperature dependant characteristics of rotational Raman scattering (RRS) from nitrogen and oxygen, and Rayleigh or Rayleigh-Brillouin scattering (RS or RBS). These methods have various advantages and disadvantages as compared to each other but their potential accuracies are principal characteristics of their efficiency. Except [5,6], no systematic attempt has been undertaken so far to compare the efficiencies, in the above meaning, of different temperature lidar methods. In [6], two RRS techniques have been compared. In this presentation, we involve in such comparison and two methods based on the detection and analysis of RS (RBS) spectra [4,5]. So, four methods are considered here for measuring the atmospheric temperature. One of them (Schwiesow and Lading, 1981) is based on an analysis of the RS linewidth with two Michelson interferometers (MI) in parallel. The second method (Shimisu et al., 1986) employs a high-resolution analysis of the RBS line shape. The third method (Cooney, 1972) employs the temperature dependance of the RRS spectrum envelope. The fourth method (Armsrong, 1974) makes use of scanning Fabry-Perot interferometer (FPI) as a comb filter for processing the periodic RRS spectrum of the nitrogen. Let us denote the corresponding errors in measuring the temperature by  $\sigma_{MI}$ ,  $\sigma_{HR}$ ,  $\sigma_{ENV}$ , and  $\sigma_{FPI}$ . Let us also define the ratios  $\chi_1 = \sigma_{MI}/\sigma_{ENV}$ ,  $\chi_2 = \sigma_{HR}/\sigma_{ENV}$ , and  $\chi_3 = \sigma_{FPI}/\sigma_{ENV}$  interpreted as relative errors with respect to  $\sigma_{ENV}$ .

## II. EVALUATION OF THE ERRORS $\sigma_{MI}$ , $\sigma_{HR}$ , $\sigma_{ENV}$ , AND $\sigma_{FPI}$ .

A feature of all methods considered here consists in the following. Namely, two appropriately extracted portions  $P_i$  ( $i=1,2$ ) of the RRS- or RS (RBS)-spectrum powers are used such that the ratio  $R = P_1/P_2$  to be an unambiguous function  $R = f(T)$  of the temperature  $T$ . Then, the temperature is determined on the basis of the inverse dependence  $T = f^{-1}(R)$ . The error in the measurement of  $T$  can be evaluated as

$$\sigma = \left( \frac{d \ln R}{dt} \right)^{-1} \left[ \frac{Q_1 + 2Q_{1N}}{Q_1^2} + \frac{Q_2 + 2Q_{2N}}{Q_2^2} \right]^{1/2}, \quad (1)$$

where a Poassonian photon-counting regime is assumed for measuring  $P_1, P_2$ , and the respective noise powers  $P_{1N}$  and  $P_{2N}$ . The quantities  $Q_1 = \alpha P_1$ ,  $Q_2 = \alpha P_2$ ,  $Q_{1N} = \alpha P_{1N}$ , and  $Q_{2N} = \alpha P_{2N}$  are the corresponding mean photon-counting rates, and  $\alpha$  is the photodetector quantum efficiency. Thus, in order to evaluate the different errors  $\sigma_{MI}$ ,  $\sigma_{HR}$ ,  $\sigma_{ENV}$ , and  $\sigma_{FPI}$ , we have to know the dependences  $Q_i = Q_i(T) = \alpha P_i(T)$ , and the noise sources. Let us introduce additional subscripts to  $P_i$  in order to denote the different methods, i.e.  $P_{i,MI}$ ,  $P_{i,HR}$ ,  $P_{i,ENV}$ , and  $P_{i,FPI}$ .

### 1. Expression for $P_{i,MI}$

In [4], the following analytical expression is derived:

$$P_{i,MI}(T) = (P_0/2)[1 - \exp(-d_i^2 M)], \quad (2)$$

where  $P_0$  is the input power;  $2d_i$  is the optical path difference between delayed and undelayed signal parts in the *MI* at some minimum of the oscillatory factor of the interferometric output;  $M = (4\omega_0^2 b/c^4)T = \gamma^2/c^2$ ,  $\omega_0$  is the transmitted light angular frequency,  $b$  is a constant in the troposphere equal to  $5,74 \cdot 10^2 \text{ m}^2 \cdot \text{sec}^{-2} \cdot \text{k}^{-1}$ ,  $c$  is the speed of light,  $\gamma$  is the RS linewidth. The value of  $P_0$  is given by the corresponding lidar equation [4] where the RS differential cross section is of importance. The aerosol-scattering noise is assumed to be fully rejected. The presence of a background is only supposed with a constant spectral density within the prefilter-transmittance band. The later is assumed to have a Gaussian shape with bandwidth equal to  $4\gamma$ .

#### 2. Expression for $P_{i,HR}$

In this case we have [5]

$$P_i(T) = \int B_i(\omega)I(\omega)d\omega, \quad (3)$$

where  $B_i(\omega)$  are the transmittance-band shapes of the narrow-band absorbing block filters used for rejection of the aerosol-backscatterind radiation and forming of the powers  $P_1$  and  $P_2$ ;  $I(\omega)$  is the RRS spectrum. We also assume the same prefilter and background characteristics as in the preceding case. Moreover, we use two approximations which simplify the analysis and would not change essentially the real value of the error. Namely, we assume that

$$I(\omega) = P_0(\pi\gamma^2)^{-1/2} \exp[-(\omega - \omega_0)^2/\gamma^2], \quad (4)$$

and

$$B_i(\omega) = 1 - \exp[-(\omega - \omega_0)^2/\gamma_i^2], \quad (5)$$

where  $P_0$  and  $\gamma$  are the same as in the preceding method, and  $\gamma_i$  is the absorption bandwidth.

#### 3. Expression for $P_{i,ENV}$

The expression has the form

$$P_{i,ENV}(T) = \sum_{i,j} \Gamma_i(\omega_{i,j})P_{i,j}(T), \quad (j = 1, 2), \quad (6)$$

where  $\Gamma_i(\omega)$  is the spectral contour of an optical filter centered at some appropriately chosen frequency  $\omega_i$ ;  $P_{j,1}$  and  $P_{j,2}$  are Stokes and anti-Stokes Raman powers from  $N_2$  and  $O_2$ , respectively, at frequencies  $\omega_{j,1}$  and  $\omega_{j,2}$ ;  $j$  is rotational quantum number. The Raman powers are given by the corresponding lidar equation [1,2] which takes into account the RRS differential cross section. The contour  $\Gamma(\omega)$  is assumed to be Gaussian one with bandwidth  $\gamma_0$ .

#### 4. Expression for $P_{i,FPI}$

The form of this expression is extremely complicated and is derived in detail in [2]. Here  $P_1 = P(\Delta_n)$ , and  $P_2 = P(\Delta_0)$ , where  $P(\Delta_k)$  is the total transmitted Raman power from  $N_2$  at the  $k$ -th order interferogram maximum,  $\Delta_k$  is the corresponding free spectral range,  $\Delta_0 = 4B_0$  is the free spectral range at the matched condition,  $B_0$  is the rotational constant for nitrogen. The instrumental width of FPI is  $\Delta\omega_{FPI} = \Delta_k/F$ , where  $F$  is the finesse of the interferometer. The RRS line in the troposphere is assumed to have Lorentzian shape with width  $\gamma_R = 1,59p/\sqrt{T}$  ( $\text{cm}^{-1}$ ), where  $p$  is the pressure measured in atmospheres.

### III. COMPARISON OF THE EFFICIENCIES AND CONCLUSION

The values of the ratios  $\chi_1, \chi_2$ , and  $\chi_3$  characterize the efficiencies of the considered methods with respect to each other. The comparison is performed on the basis of eqs. (1)—(6) and expressions for  $P(\Delta k)$ , at identical experimental conditions such as the power and the wavelength of the exciting radiation, the state of the atmosphere, the transmittance of the receiving optics, the noise level, the photodetectors etc. Therefore, the parameters characterizing these conditions are not specified. The other parameters are chosen in an

optimum way so that  $\sigma_{MI}, \sigma_{HR}, \sigma_{FPI}$ , and  $\sigma_{ENV}$  to have minimum values when  $P_{1N} = P_{2N} = 0$ . So, for  $\lambda_0 = 2\pi c/\omega_0 = 510,6$  nm, we have obtained  $\lambda_1 = 2\pi c/\omega_1 = 510,9$  nm, and  $\lambda_2 = 2\pi c/\omega_2 = 514,8$  nm for temperatures from 220 K to 320 K. The optical filter bandwidth  $\gamma_0$  corresponds to 10 Å.

For the FPI method, optimal interferometric order is  $k = 5$  for temperatures from 220 to 320 K, pressures from 0,6 to 1 atm, and finesse  $F = 70$ .

For the RS-bandwidth method an optimum pair is  $d_1 = 3.28$ cm, and  $d_2 = 6.56$ cm.

For the high-resolution method an optimum combination is  $\gamma_1 \rightarrow 0, \gamma_2 \approx \gamma$ .

The noise is considered as an effective background specified by its spectral density. The latter is determined in relative units with respect to the spectral density at the peak of the most intensive RRS line ( $j = 8$ ), at temperature  $T = 273$  K, and pressure  $p = 1$  atm.

The ratios  $\chi_1, \chi_2$ , and  $\chi_3$  vs  $T$  are shown in Figs. 1,2, and 3, respectively for different background levels proportional to  $l = 10, 5, 2, 1, 0.5, 0.1, 0$ . The analysis of the results shows that at low noise levels  $\chi_1 \sim \chi_2 \ll \chi_3 \sim 1$ , i.e. the total selected signal powers and the sensitivities of all methods are combined so that the RS (RBS) methods are more efficient than the RRS methods. The main reason for this is the lower signal power of the RRS methods. When the noise level increases, the values  $\chi_1, \chi_2$ , and  $\chi_3$  decrease, so that  $\chi_1 \sim \chi_2 \ll \chi_3 \ll 1$ . Consequently, the RRS methods are more sensitive to noise due to the lower signal power and/or the higher noise admittance. At extremely high noise levels the ratios  $\chi_1, \chi_2$ , and  $\chi_3$  tend to constant values determined by the selected signal powers, the sensitivities, and the noise admittances of the corresponding methods (See Eq. (1)). The RS methods have comparable efficiencies at arbitrary noise intensity. In the presence of intensive background, the FPI method has considerably higher potential accuracy than the envelope method due to the lower noise admittance.

## REFERENCES

1. J.A. Cooney, J Appl. Meteorol., vol. 11, p. 108 (1972).
2. R.L. Armstrong, JOSA, vol. 64, p. 871 (1974).
3. G. Fiocco, G. Benedetti-Michelanqeli, K. Maischberger, and E. Madonna, Natur. Phys. Sci., vol. 229, p. 78 (1971).
4. R.L. Schwiesow and L. Lading, Appl. Opt., vol. 20, p. 1972 (1981).
5. H. Shimisu, K. Noguchi, and Chiao-Yao She, Appl. Opt., vol. 5, p. 1460 (1986).
6. I. Ivanova, L. Gurdev, V. Mitev, Proc. of IGARSS, Espoo, Finland, 1991, p. 923.

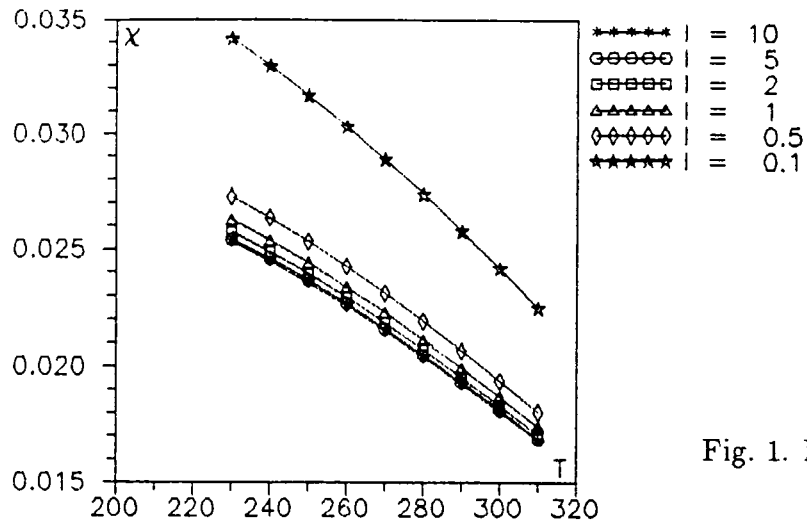


Fig. 1. Ratio of errors  $\chi_1$ .

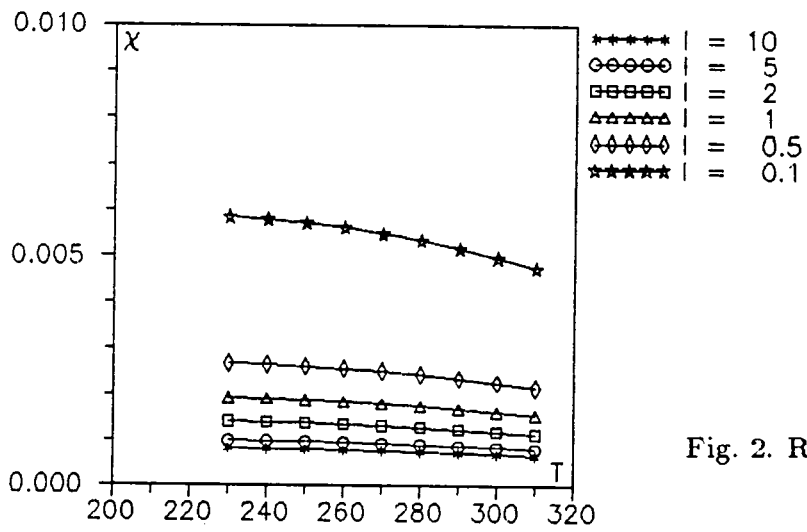


Fig. 2. Ratio of errors  $\chi_2$ .

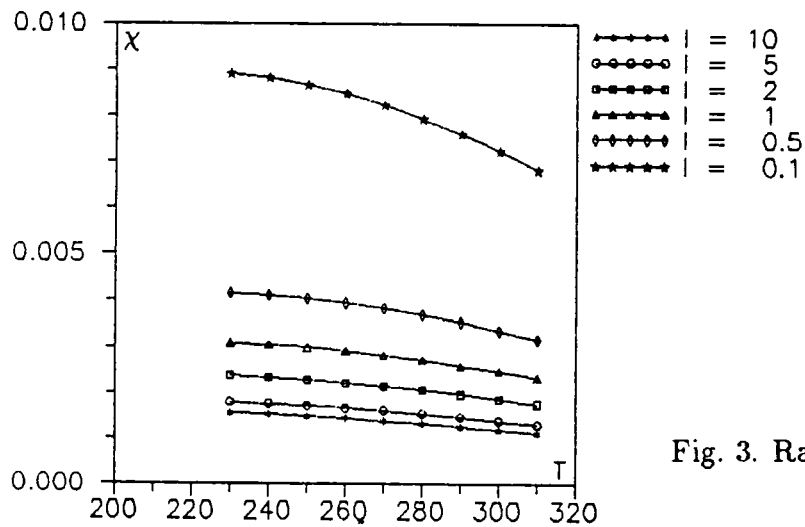


Fig. 3. Ratio of errors  $\chi_3$ .

# LIDAR INVESTIGATION OF AEROSOL POLLUTION DISTRIBUTION NEAR A COAL POWER PLANT

Ts. Mitsev, G. Kolarov

Institute of Electronics, Bulgarian Academy of Sciences  
72, Blvd. Tsarigradsko Shose, 1784 Sofia, Bulgaria

## INTRODUCTION

Using aerosol lidars with high spatial and temporal resolution with the possibility of real-time data interpretation [1] can solve a large number of ecological problems related to the aerosol-field distribution and variation and the structure of convective flows. Significantly less expensive specialized lidars are used in studying anthropogenic aerosols in the planetary boundary layer.

In this paper we present results of lidar measurements of the mass-concentration field around a coal-fired power plant with intensive local aerosol sources. We studied the pollution evolution as a function of the emission dynamics and the presence of retaining layers. The technique used incorporates complex analysis of three types of lidar mapping: horizontal map of the aerosol field, vertical cross-section map, and a series of profiles along a selected path. The lidar-soundings cycle was performed for the time of atmosphere's quasi-stationarity.

## SYSTEM DESCRIPTION AND DATA PROCESSING

The scanning lidar used a copper-vapor laser with repetition rate of 10 kHz and low pulse energy [2]. The receiving system comprised a Cassegrainian telescope with diameter of 20 cm and focal length of 1 m, an interference filter ( $\Delta\lambda = 0.3$  nm), and a photon-counting photo multiplier type EMI 9863QB100. The lidar range was up to 5 km, the spatial resolution, 20 - 50 m, and the temporal resolution, 10 sec. The incoming data was recorded on a virtual disk of a PC/AT-compatible computer. The lidar response was processed using Klett's method [3]. The transition from extinction coefficient to mass concentration was carried out by

binding the data of a conventional dust-probing device.

## RESULTS

The Varna coal-fired power plant is located in the vicinity of the Black Sea coastline. The lidar was placed at forty-meter altitude and distances 600 m and 720 m from the two plant's smokestacks. In the period 14 - 17 June, 1991, we carried out systematic observations of the aerosol field within the lidar range. The lidar maps presented were taken during the night of 17 June in stationary atmosphere. The horizontal path was sounded every minute from 02:00 to 3:00 hours local time. Thus, we established the intervals of smoke eruptions from the smokestacks (fig.1). The horizontal map of the aerosol mass-concentration (fig.2) was taken at 03:12 hours and is superimposed with region's topographic map; it shows the zones of increased aerosol concentration. In the rail-road station area, the sounding plane crosses the smoke plume, while smoke from barges was detected above the lake. The vertical aerosol-field cross-section, taken at 03:38 hours along a path between the smokestacks (fig.3), forms a better picture of its spatial distribution. The retaining inverse layer, present at an altitude of 100 - 150 m, held the aerosol cloud down to the earth's surface. The zone of high near-ground concentration extended in this direction to a distance of 700 - 800 m from the smokestacks.

## CONCLUSION

The aerosol mass-concentration maps, obtained by means of a scanning lidar, contain large amount of information which can be used to assess the aerosol pollution near industrial sites. Adequate interpretation of the lidar data can be achieved by combining horizontal and vertical aerosol concentration maps with time-evolution registering of the local sources emissions. The time of implementing a measurement cycle depends on the time during which the atmosphere can be considered quasi-stationary.

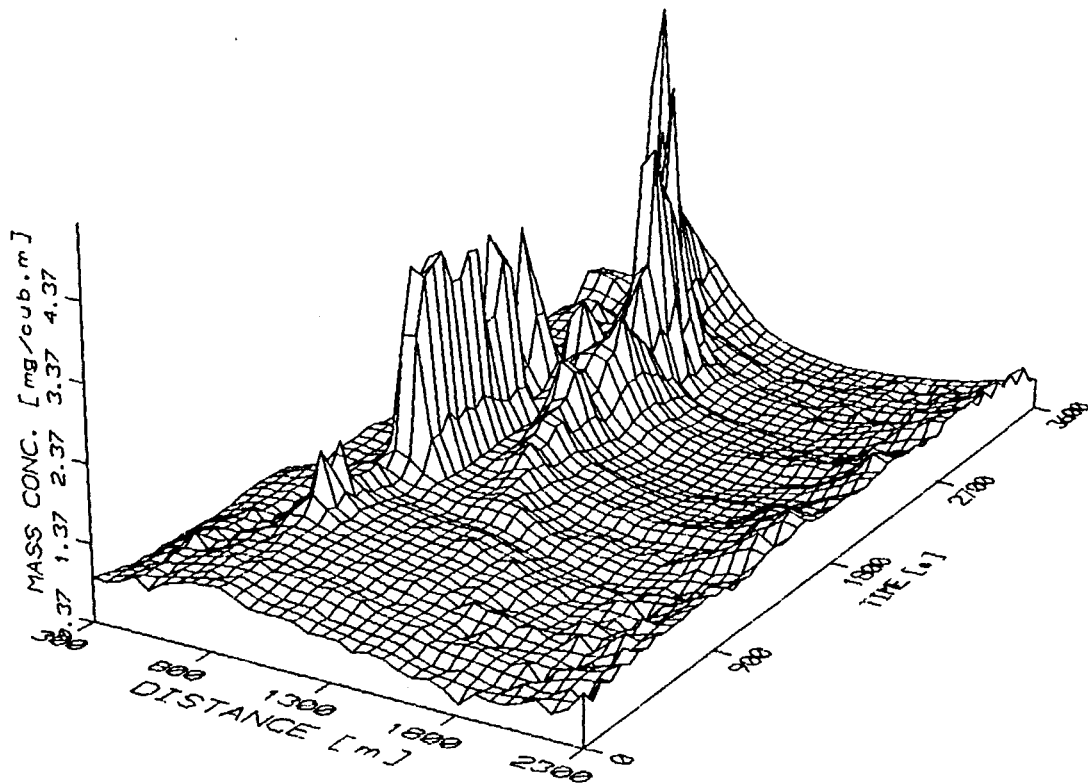


Fig.1. Lidar observation of smoke eruption from the power plant's chimneys: sounding along horizontal path in direction A from 02:00 to 03:00 h every 60 s on June 17, 1991.

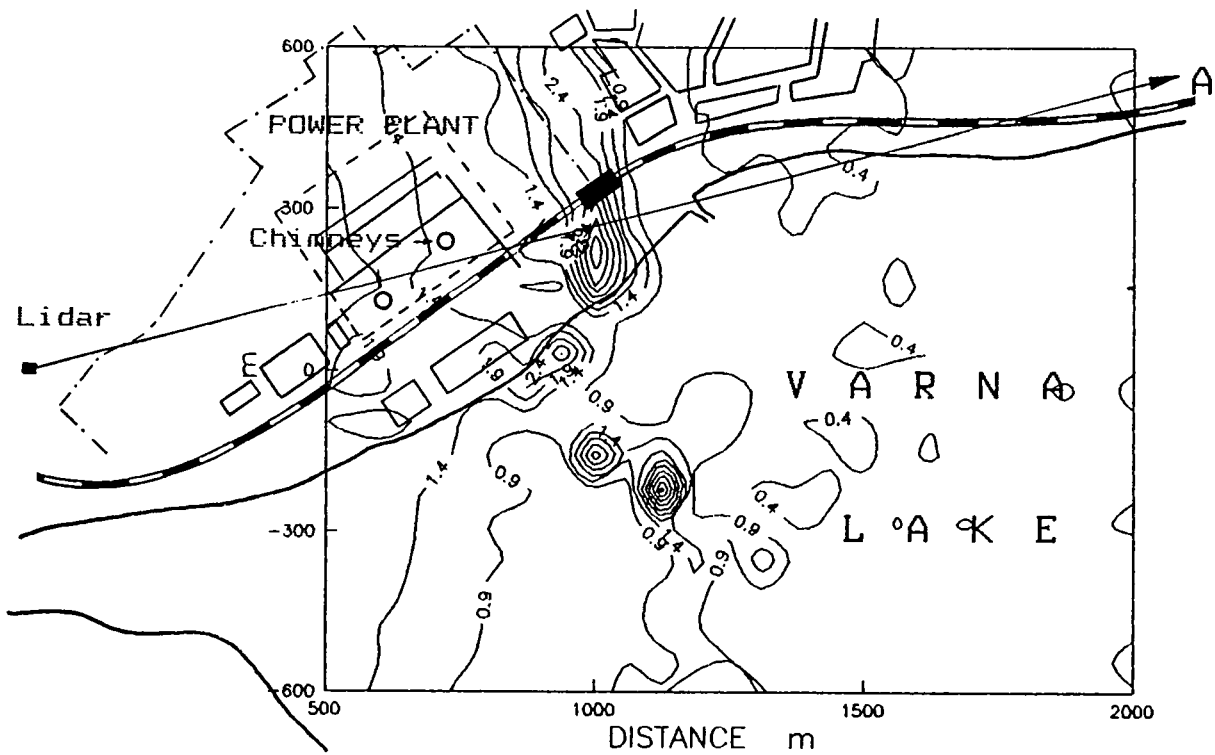


Fig.2. Mass-concentration ( $\text{mg}/\text{m}^3$ ) lidar map in a horizontal plane at altitude of 40 m; 03:12 h on June 17, 1991.

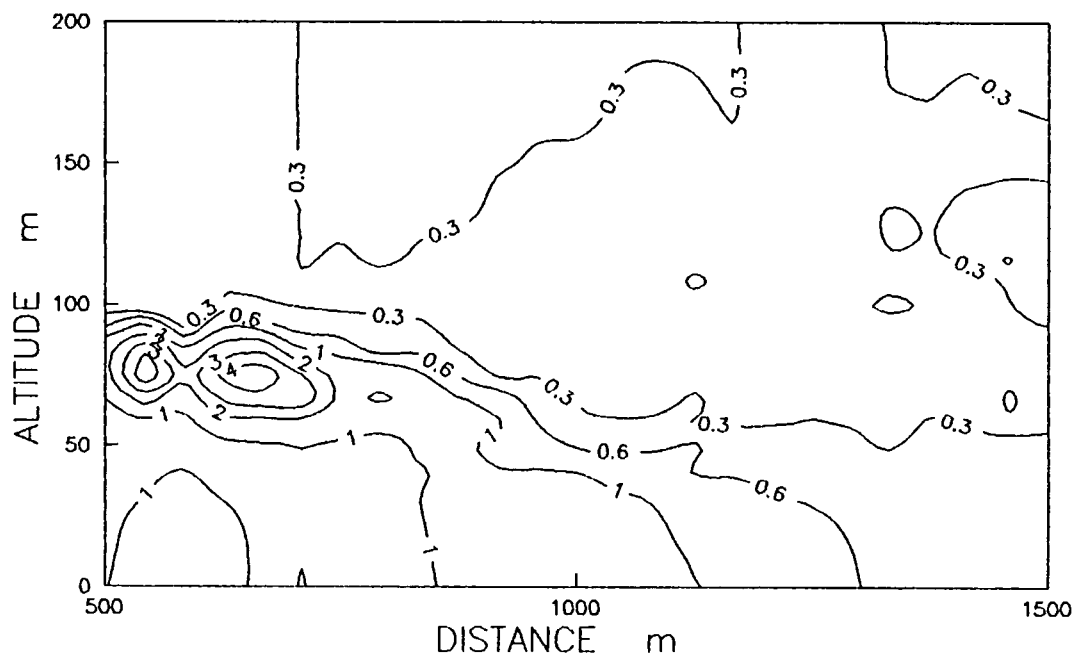


Fig.3. Mass-concentration ( $\text{mg}/\text{m}^3$ ) lidar map in a vertical plane in direction A; 03:38 h on June 17, 1991.

#### References

1. E.W.Eloranta, D.K.Forrest, S.Kohn, The Display of Volume Imaging Lidar Data, 16 International Laser Radar Conference, Abstracts of papers, Tomsk, USSR, 304, July 1990.
2. Ts.Mitsev, G.Kolarov, D.Stoyanov, Lidar Mapping of Aerosol Field above the City of Velingrad, The Third Bulgarian-Russian Conference, Conference Abstracts, 163, Oct. 1989.
3. J.D.Klett, Stable Analytical Inversion Solution for Processing Lidar Returns, Appl.Opt.,20, 211, 1981.

# LASER REMOTE SENSING OF POLLUTION ON WATER SURFACES

A.F.Bunkin, A.L.Surovegin\*

Institute of General Physics, Russian Academy of Sciences,  
Vavilova 38, 117942, Moscow, Russia.

\*R&D center RADIANT ,p.o. box 1929, 129010, Moscow, Russia.

One of the most important problems of the modern environmental science is detection and identification of various impurities in the ocean. Sources of impurities in sea water are diverse, the most common of them are transport, agriculture, oil industry and accidental spills. Once ecological balance is disturbed, biological processes in sea water become affected, the result being altered chlorophyll concentrations, water turbidity and temperature changes etc.

During the last few years we have created new types of lidars and arranged nearly ten aircraft and shipboard expeditions. Some aircraft expeditions deal with terrestrial investigations. Others were devoted to oceanological research and results of which are the subject of this paper.

## INSTRUMENTATION

Figure 1 shows a simplified scheme of the optical train of our lidar, which are designed for chlorophyll and oil slick detection and for studying underwater scattering layers.

A high-power Nd:YAP laser (modified laser LTI-207) with the second and fourth harmonic generators was used as a transmitter in the experiments (for depth sounding, only the second harmonic is used). The frequency-doubled laser output provides pulse duration 8ns with energy of 300-500mJ and repetition rate 10-30Hz. The beam diameter (at  $1/e^2$  level) just after laser is 8mm and at the telescope output (after beam expansion) is 4cm. The beam divergence at different experiments was 0.2-1mrad. The receiving telescope is of Newtonian type, the diameter being 40 or 20cm for airborne or shipborne lidars, respectively. At the

focal point, the light is collected on the entrance slit of a polychromator (for the fluorescence lidar) or streak camera (for the depth sounder). The polychromator provides two bandwidths of 250nm and 500nm that can be shifted, if desired. The depth sounder streak camera is triggered by a laser pulse and an optical pulse coming from the sea surface. Then, after the delay automatic measurement, a high voltage pulse and sweep pulse are generated and sent to the streak camera. The resulting temporal image is read by a CCD array, individually for each laser pulse, into an IBM PC microcomputer or Apple II in some examples and stored. The spectral image is then read by an O.M.A. detector with an MCP and a CCD-array receiver.

#### DETECTION OF PHYTOPLANKTON CHLOROPHYLL AND HYDROCARBON IN THE SEA WATER

Phytoplankton sensing is carried out primarily with the object of determining concentration, functional condition as well as species composition of algae. In our field experiments, we studied the former topic using sounding technique to estimate temporal and spatial distributions of chlorophyll "a" in the Mediterranean, Baltic, Caspian, Black seas. The technique is based on measurement and mapping of the K parameter of chl"a",  $K = [I(f)/I(r)]$ , where  $I(f)$  is chl"a" or oil fluorescence intensity in non-saturation conditions and  $I(r)$  is water Raman scattering intensity taken as a reference signal.

The data were acquired during 6 shipboard and 4 aircraft expeditions. The sounding distances were 20-30m in shipboard and 500-800m in airborne measurements. The most interest was to determine oil pollution sites and by distinguishing spectra of oil and gelbstoff containing waters. Our experience suggested that the simplest method to solve these problems is by means of remote sensing employing the fourth harmonic of the Nd:YAP laser as excitation source. Figure 2 shows chl"a" and hydrocarbons distribution in coastal waters nearby the Novorossyisk harbour in the Black sea. Chl"a" concentration varies around 0.3mg/l ( $k=0.4$ ), while that of hydrocarbons varies from 0.2 to 0.6 mg/l.

## SUMMARY AND CONCLUSIONS

A number of lidar systems for chlorophyll "a" and hydrocarbons monitoring and depth sounding were created and tested during several years of field experiments. Backscattered laser light from underwater layers and sea bottom was captured from down to 100m.

Work on further modification of lidar systems is currently underway. Instruments under development are expected to reduce signal of Fresnel reflection from sea surface and to improve the S/N ratio.

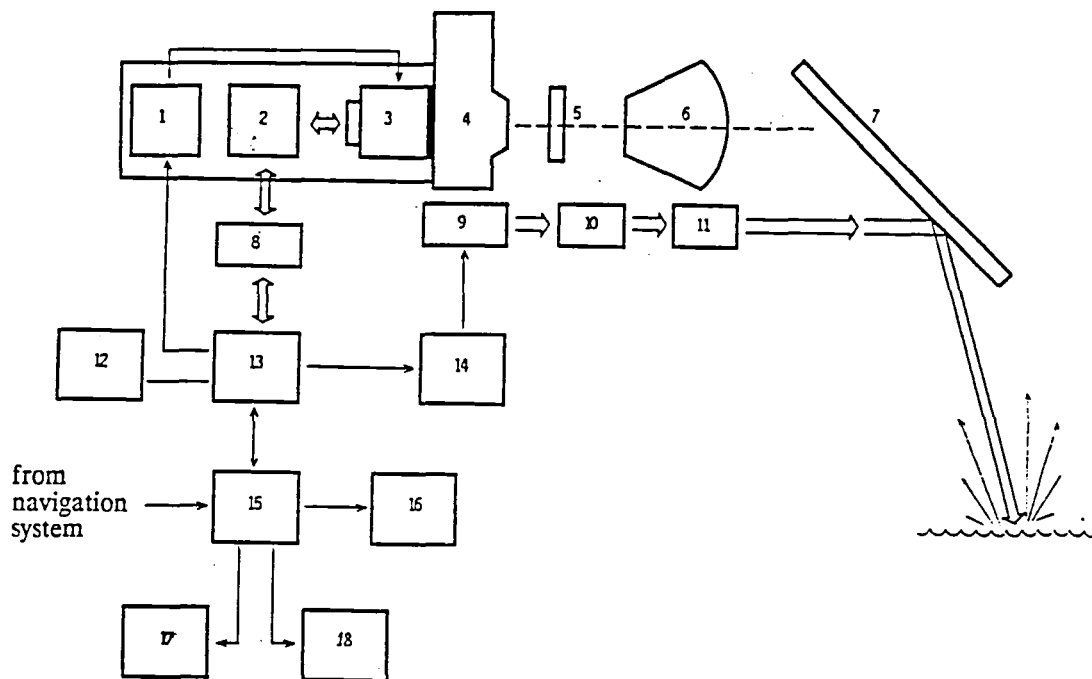


Fig.1 Lidar Fluorosensor. 1 - high voltage strobe pulse forming, 2 - CCD array electronic support, 3 - image intensifier, 4 - polychromator, 8 - glass filter, 6 - collecting objective, 7 - folding mirror, 8 - interface, 9 - laser, 10 - second harmonic generator, 11 - third or fourth harmonic generator, 12,16 - hard and floppy disk memory, 13,15 - personal computers, 14 - laser power supply, 17 - data bank, 18 - hard copy.

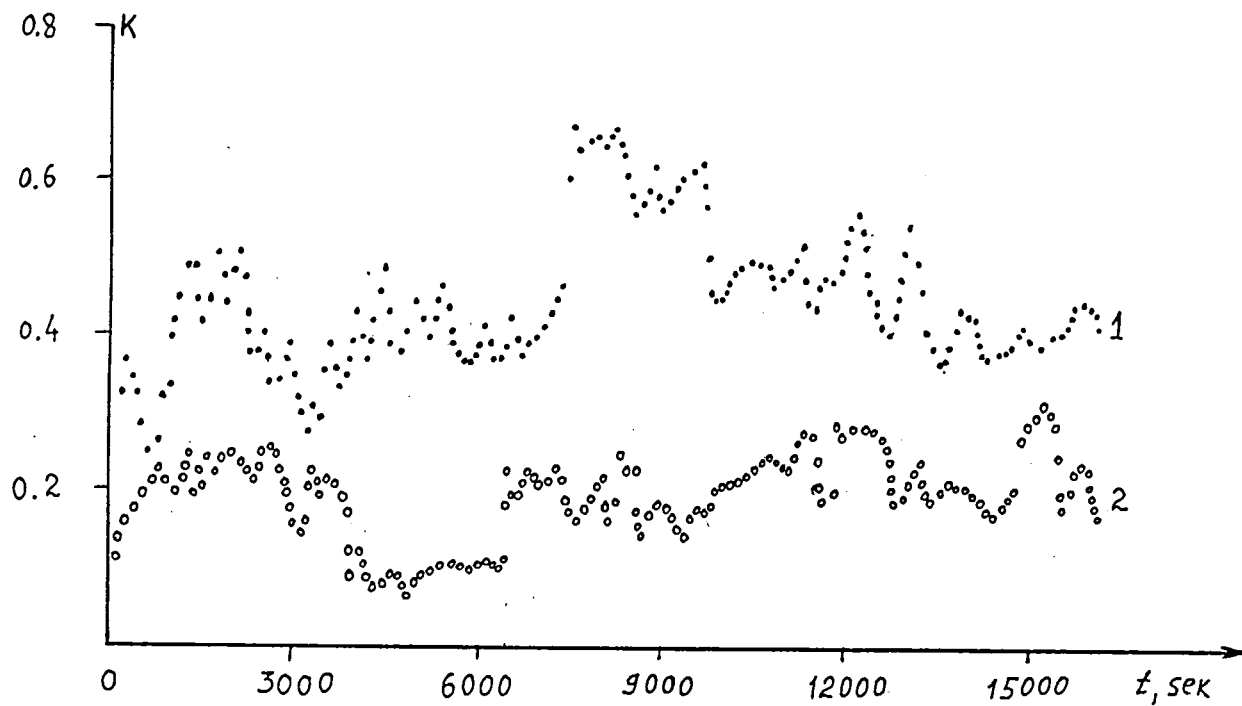


Fig.2 Chlorophyll "a" (1) and hydrocarbons (2) distribution at the coastal zone of Black Sea near Gelenjik and Novorosiisk. Start point is  $44.5^{\circ}\text{N}$ ,  $37.6^{\circ}\text{O}$ ; finish point is  $44.6^{\circ}\text{N}$ ,  $38.2^{\circ}\text{O}$ .

# CORRELATION ANALYSIS OF WIND LIDAR DATA

R.P.Avramova

Institute of Electronics,  
Bulgarian Academy of Sciences, Sofia 1784, Bulgaria

The proposed correlation analysis represents an analysis of time sequences of lidar returns from observing points, situated at corners of a right angle triangle in horizontal planes, spaced by altitude.

The purpose of the present paper is the choice of an optimal correlation techniques for the lidar data to increase the number of the successful measurements of the wind velocity, in a wide range of meteorological situations.

The main tasks, solved by the suggested correlation analysis are:

1. A choice of an optimal model of the space-time correlation function for a correlation analysis of the lidar data by means of the criteria [1] developed in terms of the "apparent velocity", requiring a pilot lidar experiment at a variable spacing between the observation pair points.
2. The algorithm of the required digital time series analysis incorporates Rader's algorithm for high speed correlation [2] and Hermitian and "half-zero" procedures [6] in order to reduce the required memory and operations. The algorithm is applicable to real-time processing.
3. Detrending and the noise reduction is performed on the correlation functions [3].
4. The estimation of the statistical errors of the quantities, derived by FCA (full correlation analysis) [4].
5. The interpretation of the lidar measured parameters includes a check for an artificial anisotropy [5], using a velocity diagram (fig.1) and velocity dispersion and determining their physical meaning [1].

The algorithm 2) for high sped correlations of overlapped sections is developed by the following basic relations:

$$z_i^J(n) = X_i^J(n) + jX_i^{J+1}(n)$$

$$(1) X_i^J(n) = X(n + J \cdot M/2) \quad n = 0, 1, \dots, M/2 - 1; \quad J = 1, 3, \dots, \frac{2N}{M} - 2$$

$$(2) Z_i^{e(J)}(r) = \mathcal{F}\{z_i^J(n)\} \quad n, r = 0, 1, \dots, M/2 - 1$$

$$\text{where } Z_i^{e(J)}(r) = Z_i^{(J)}(2r)$$

$Z_i^{(J)}(2r)$  is DFT of the augmented with  $M/2$  zeros sequence  $z_i^{(J)}(n)$ .

$$(3) X_i^{e(J)}(r) = \frac{Z_i^{e(J)}(r) + Z_i^{e(J)}(M/2 - r)}{2} \quad r = 0, 1, \dots, M/4$$

$$X_i^{e(J+1)}(r) = \frac{Z_i^{e(J)}(r) + Z_i^{e(J)*}(M/2 - r)}{2j}$$

$$(4) S_{ik}^{e(J)}(r) = S_{ik}^{e(J-1)}(r) + X_i^{e(J)*}(r) (X_k^{e(J)}(r) + (-1)^r X_k^{e(J+1)}(r))$$

$$S_{ki}^{e(J)}(r) = S_{ki}^{e(J-1)}(r) + X_i^{e(J+1)*}(r) (X_k^{e(J)}(r) + (-1)^r X_k^{e(J+1)}(r)),$$

$$r = 0, 1, \dots, M/4 \quad i, k = 1, 2, 3$$

$$\text{where } S_{ik}^{e(J)}(r) = S_{ik}(2r)$$

$$(5) Z_i^{\alpha(J)}(r) = \mathcal{F}\left\{z_i^J(n) \cdot W_{M/2}^{n/2}\right\}, \quad n, r = 0, 1, \dots, M/2 - 1$$

$$\text{where } Z_i^{\alpha(J)}(r) = Z_i^J(2r+1)$$

$Z_i^{\alpha(J)}(2r+1)$  is DFT of the augmented with  $M/2$  zeros sequence  $z_i^{\alpha(J)}(n)$ .

(6) Repeat computations in steps (3) and (4) for  $X_i^c(r), S_{ik}^c(r), S_{ki}^o(r)$  respectively.

$$\text{Computing noncircular correlation } R_{ik}(m) = \frac{1}{N} \sum_{n=0}^{N-1} x_i(n) x_j(n+m):$$

$$R_{ik}(m) = \begin{cases} 1/2N R_{ik}^{\cdot}(m) & m = 0, 1, \dots, M/2 \\ 1/2N R_{ki}^{\cdot}(M+m) & m = -1, \dots, -M/2 \end{cases}$$

$$\text{where } R_{ik}^{\cdot}(2m) = \frac{1}{N} \text{Re } \mathcal{F}^{-1}\{S_{ik}^{\cdot}(r)\} \quad r = 0, 1, \dots, M/2 - 1$$

$$R_{ik}^{\cdot}(2m+1) = \frac{1}{N} \text{Re } \mathcal{F}^{-1}\{S_{ik}^{\cdot}(r)\} \quad m = 0, 1, \dots, M/2 - 1$$

$$\text{where } S_{ik}^{\cdot}(r) = S_{ik}(r) + S_{ik}^*(M/2 - r) + j[S_{ik}(r) - S_{ik}^*(M/2 - r)]W_{M/2}^{-r/2}$$

Similar computations is performed for the beginning and the ending sections. The algorithm is realized at Microsoft FORTRAN.

The estimating of the correlation functions by means of this algorithm yields an arithmetically identical results to those of an ordinary estimation over all length of the sequence.

#### REFERENCES

1. Avramova R.P. XV th International Laser Radar Conference, 1990, Tomsk, USSR
2. Rader Ch.M. IEEE Transaction on Audio and Electroacoustics, v. AU-18, No. 4. 1970
3. Matvienko G.G., Zadne G.O., Ferdinandov E.S., Kolev I.N., Avramova R.P. Correlation Techniques of Lidar Measurements of the Wind Speed, Novosibirsk, Nauka, 1985
4. Briggs B.H. MAP Handbook, vol. 13, 1984
5. Meek C.E. Radio Science, vol. 25, No. 4, 641, 1990
6. Otnes R.K., Enochson L Digital Time Series Analysis, John Wiley, 1972

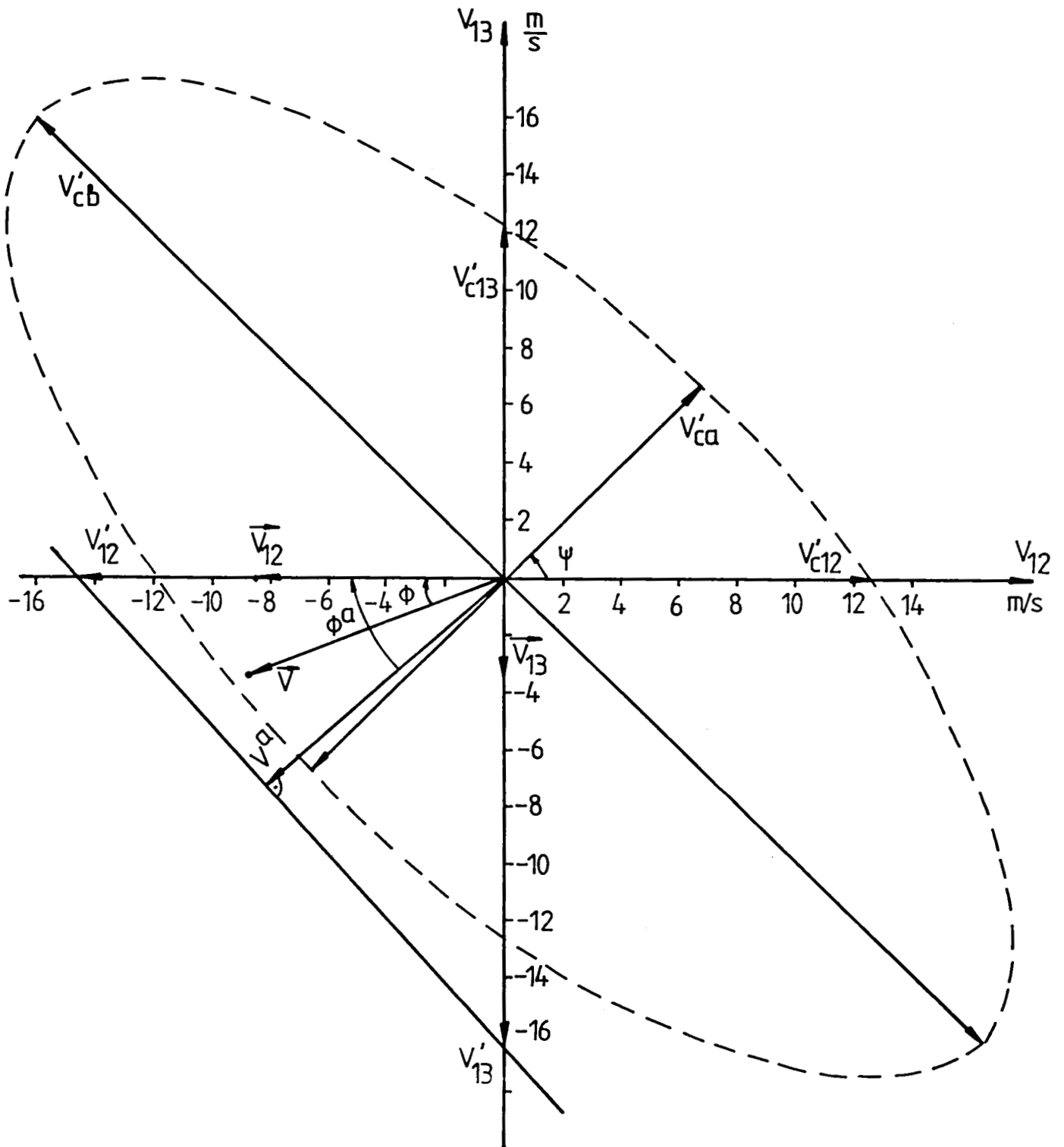


Fig.1 A velocity diagram observed by means of FCA

# A DEVELOPING MULTIPLE-WAVELENGTH LIDAR FOR DETECTING MAINLY OZONE AND AEROSOL DISTRIBUTIONS IN THE STRATOSPHERE

*Zheng Siping, Qiu Jinhuan, Wang Shufang, Huang Qirong  
Wang Wenming and Wu Shaoming*

*Institute of Atmospheric Physics  
Chinese Academy of Sciences, Beijing 100029, China*

A multiple-wavelength lidar is being developed in our Institute for measuring mainly ozone and aerosol distributions in the stratosphere.

The system is based on a XeCl excimer laser operating at 308nm and a Nd-YAG laser with three wavelengths of 1060nm, 532nm and 355nm. Specification of the Lidar System is listed in Table 1. Some further details of the lidar will be given here.

The system is designed to measure the following parameters:

- |                                 |         |
|---------------------------------|---------|
| (1) Ozone vertical distribution | 15-45km |
| (2) Aerosol distribution        | 6-35km  |
| (3) Atmospheric temperature     | 30-70km |
| (4) High cloud                  |         |

The expected performances of the lidar system are simulated. According to simulated three-wavelength (532nm, 355nm and 308nm) return signals and signal to noise ratios, retrieving simultaneously ozone and aerosol distributions in the stratosphere is made, and the inversion errors are analyzed.

**Table 1 Specification of the Lidar System**

<b>Transmitter</b>				
Laser		Nd: YAG		XeCl
Wavelength(nm)	255	532	1060	308
Output Energy(mJ)	80	250	600	150
Repetition rate(Hz)	10	10	10	60
Beam divergence(mrad)	0.5	0.5	0.5	1
<b>Receiver</b>				
Telescope diameter	1m			
Field of view(mrad)	1-3			
<b>Detector</b>				
Photomultiplier	R331 for 308nm and 355nm			
Pre-AMP(MHz)	100			
<b>Signal Processor</b>				
Photoelectron counter	2 channels for 308nm and 355nm			
Transient recorder	2 channels for 532nm (polarizations)			
	1 channel for 1060nm			



An Extension of the Raman-Lidar Technique to  
Measure the Velocity and Temperature of the  
Atmospheric Emission Jets from Stacks

Yu.F.Arshinov, S.M.Bobrovnikov, V.K.Shumskii,  
A.G.Popov, I.B.Serikov

Institute of Atmospheric Optics, Siberian Branch  
of the Academy of Sciences of Russia, Tomsk, Russia

In the problem of air quality control over industrial areas it is implied that the parameters of atmospheric emissions from plants' stacks are measured. In earlier lidar studies devoted to the development of Raman-lidar techniques the main attention was paid to the gas analysis of the emissions from stacks. Normally, such techniques were aimed only at measuring the number densities of molecular species in the emissions. At the same time it is quite clear that the ecological load on the environment depends not only on the concentration of pollutants but on their gross yields as well.

To estimate the gross yield of a specie from a stack one needs to measure, in addition to its number density, the velocity of the emission outflow from a stack and to know the sizes of the emission jet. The exhaust products of many technological processes, as for example in steel production, are hot. Taking this into account one can assume that only the Archimedes force makes the hot gaseous mixture to ascend in a stack. It is also clear from general considerations that at the stack mouth the pressure inside the emission jet is equal to the pressure of ambient air, while its temperature is still higher than the temperature of ambient air. As a result the density of the gaseous mixture inside the emission jet should be lower than that of the atmosphere. Assuming also that the mixing ratio of nitrogen in the emission is the same as in the atmosphere one can readily obtain a simple formula for the velocity of the emission outflow from a stack

$$v = \sqrt{2gH(1 - n_1/n_2)} \quad (1)$$

where  $g$  is the acceleration of gravity,  $H$  is the height of a stack  $n_1$  and  $n_2$  are the number densities of nitrogen molecules within the emission jet and in the atmosphere, respectively. It is understandable from this expression that a Raman-lidar technique for gaseous analysis of the emissions from stacks is readily applicable to simultaneous measurements of the emission outflow velocity since, normally, the Raman-lidar return from nitrogen molecules of the atmosphere and the emission jet is used as an internal standard in Raman-lidar measurements of pollutions concentrations [1], and because its intensity profile is proportional to the profile of the nitrogen number density.

If a Raman lidar possesses a proper spatial resolution sufficient for acquiring profiles of return signals across an

emission jet, then the difference in number densities of nitrogen molecules within the jet and outside it will cause a dip in the lidar return signal from nitrogen, as shown in Fig.1. This figure presents Raman-lidar returns from nitrogen and CO molecules recorded with a Raman lidar [2] in the atmospheric volume that involved an emission jet from a stack of a battery of coke ovens at a steel production plant. Spatial resolution of the lidar returns presented in this figure is about 12 m. The recording system of our lidar provides a possibility of acquiring a 96 m long portion of a lidar return centered at a desired range with the spatial resolution of 1.5 m. Such portions of the return signals shown in Fig.1 are presented in Fig.2. A more detailed records of return signals from an emission jet enable one to perform a Raman-lidar technique of measuring number densities of the emission components more correctly, since in this case a scattering volume can be chosen exactly within the jet.

Assuming the gaseous components of the emission to be mixed uniformly over the jet's cross section and neglecting the values of their concentrations out of the jet one can schematically present the spatial distributions of nitrogen and pollutants molecules along the sounding beam as shown in Fig.3. It is also important, for the further discussion, to note that we assume that the spatial distribution of the aerosol extinction coefficient within the emission jet is narrower than that of gaseous species, as shown in Fig.4. Such a model seems to be realistic since the diffusion of hot gases from the jet is more rapid than the diffusion of heavier aerosol particles, at least in the region just above the stack mouth. Based on these assumptions one can present Raman-lidar returns as follows

$$P_{N_2}(R) \sim \sigma_{N_2} n_2 (1 + Af(R)) T^2(R_2) \exp\left(-2 \int_{R_2}^R \alpha(R') dR'\right) \quad (2)$$

$$P_i(R) \sim \sigma_{N_i} n_2 G_i f(R) T^2(R_2) \exp\left(-2 \int_{R_2}^R \alpha(R') dR'\right) \quad (3)$$

where  $\sigma_{N_{2,i}}$  are the cross-sections of Raman scattering by  $N_2$  and  $i$ -th molecular component, respectively; The number density of nitrogen molecules in the atmosphere is assumed to be constant everywhere in the atmosphere excluding the emission jet;  $T(R)$  is the transmission of the atmosphere along the sounding path interval  $[\emptyset, R]$ ;

$$f(R) = \begin{cases} \emptyset & R < R_2 \text{ U } R > R_3 ; \\ f(R_m) = 1; & \\ f(R) & R \in [R'_2, R'_3] ; \end{cases} \quad (4)$$

$$A = (n_1 / n_2) - 1; \quad G_i = n_i / n_2 ;$$

$n_i$  is the number density of the  $i$ -th molecular component of the emission,  $\alpha$  is the extinction coefficient.

Assuming the extinction of the laser beam by the emission jet to be caused mainly by aerosols one can neglect the spectral behavior of the jet's transmission. As a result the ratios of Raman returns can be written as follows

$$F_i(R) = (P_i(R)/P_{N_2}(R)) = \sigma_{n_i} G_i(R) / \sigma_{T_{N_2}} (1 + Af(R)), \quad (5)$$

$$R \in [R'_2, R'_3]$$

From this expression it follows that

$$f(R) = c_i F_i(R) / A (G_i A^{-1} - c_i \bar{F}_i(R)) \quad (6)$$

where  $c_i = \sigma_{n_i} / \sigma_{T_{N_2}}$ . It is quite clear from the Expr. (6) that the derivative  $f'(R) = 0$  at the same point  $R$ , where the derivative  $F'(R) = 0$ . Then one obtains the following formula for  $A$

$$A = G_i / c_i F_i(R_m) - 1 \quad (7)$$

Using also the combinations of return signals at  $R'_2$  and  $R'_3$  (see figures)

$$S = R_3^2 P_{N_2}(R_3) / R_2^2 P_{N_2}(R'_2); \quad S_i = R_3^2 P_i(R_3) c_i / R_2^2 P_{N_2}(R'_2)$$

and

$$Q = P_3 R_3' R'_2 / P_1 R_1' R'_2 = \exp(-2 \int_{R'_2}^{R'_3} \alpha(R') dR')$$

where  $P_1 = \int_{R'_1}^{R'_2} P_{N_2}(R) dR$  and  $P_3 = \int_{R'_3}^{R'_4} P_{N_2}(R) dR$

one obtains that

$$(A/G_i) = (S-Q) / S_i \quad (8)$$

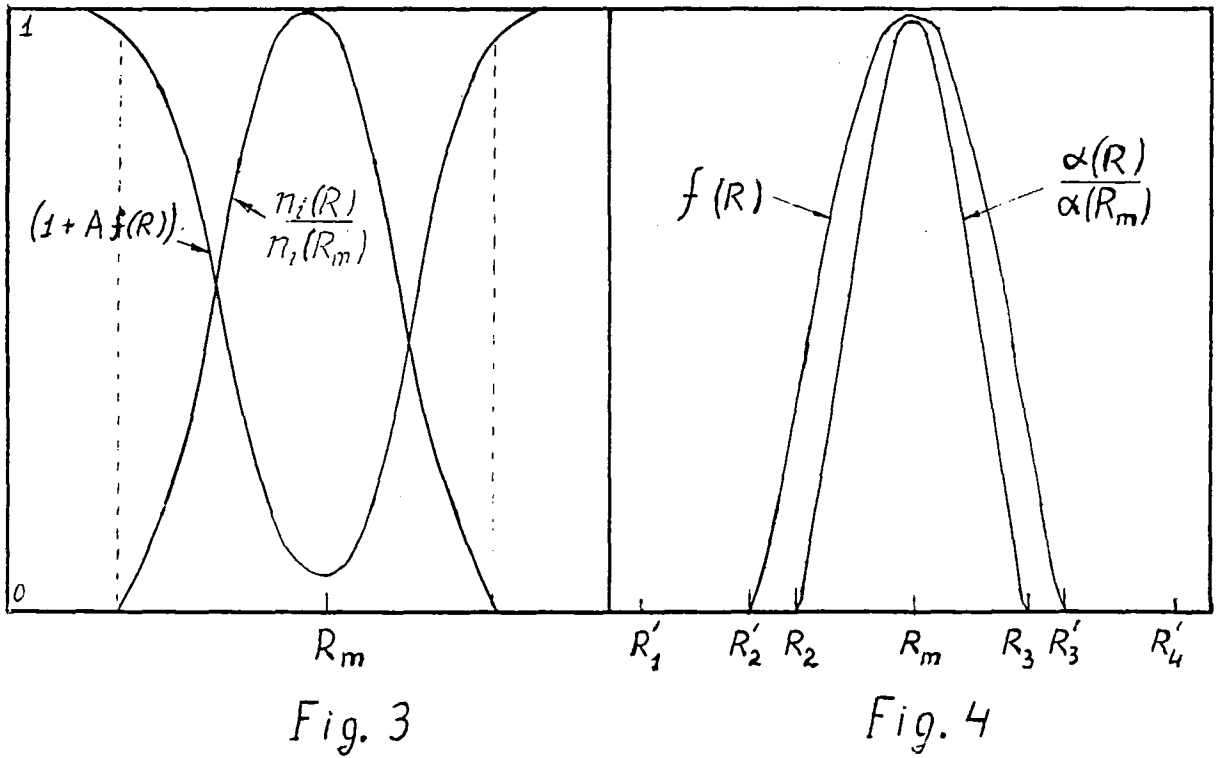
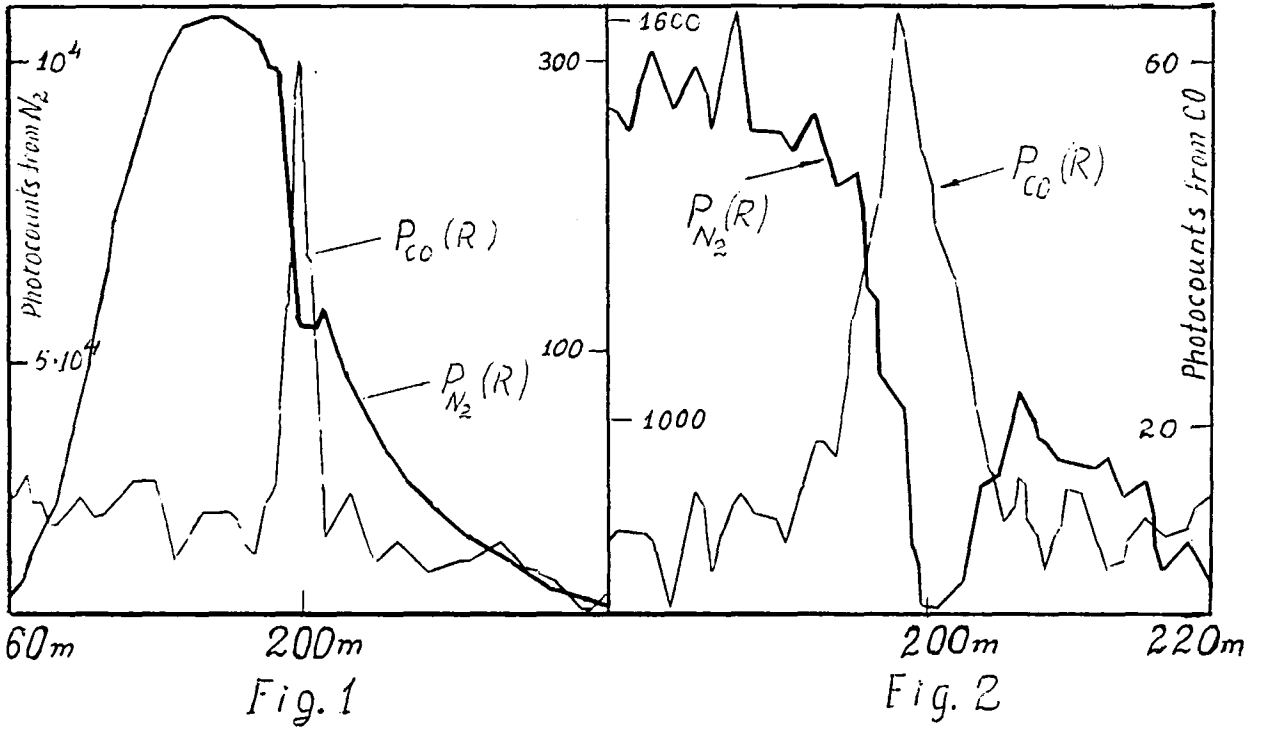
From this expression and Expr. (6) we have

$$G_i = (n_i / n_2) = c_i F_i(R_m) \cdot S_i / (S_i - c_i \bar{F}_i(R_m)(S-Q)) \quad (9)$$

So, one can see from the Exprs. (1), (8), and (9) that the above combinations of experimentally measured Raman-lidar returns from the molecular nitrogen and pollutants, in the atmospheric region involving the emission jet from a stack, allow one to determine, in addition to number densities of pollutants, the velocity of the emission jet outflow. Moreover, since the value  $(n_1 / n_2) = A+1$  is also known, one can easily estimate the temperature of the emission according to the ideal gas law as  $T_{st} = T_{atm}(A+1)$ . Of course, in this case the atmospheric temperature  $T$  must be measured independently. Thus the values of temperature and velocity of the emission jet estimated from the return signals shown in Figs. 2 and 3 are 462 K and 21.2 m/s, respectively. The error of temperature estimation is about 10 K, while the error of the velocity estimate is below 1 m/s.

#### REFERENCES :

1. Laser Monitoring of the Atmosphere. Ed by E.D.Hinkley, Springer-Verlag, Berlin, Heidelberg, New York, 1976.
2. Yu.F.Arshinov et al, Atmospheric Optics, 2, No.9, p.963, 1989.



LIDAR OBSERVATIONS OF STRATOSPHERIC CLOUDS  
AFTER VOLCANIC ERUPTION OF PINATUBO

Sun jinhui, Qiu jinhuan, Xia qilin, Zhang jinding

Institute of Atmospheric Physics  
Academia Sinica

Abstract

Enormous increase of backscattered light from stratospheric aerosol layer was observed by using a ruby lidar in Beijing (39°54'N, 116°27'E) during the period from end of July 1991 to March 1992. On the basis of much information, this is almost certainly due to the volcanic eruption of Pinatubo in the Philippines, in June 1991.

The laser radar system used here consists of Q-switched ruby laser ( $\lambda=0.6943 \mu\text{m}$ ) which produces an output of 0.5~1.0 J/pulse and a 40cm Cassegrain type telescope. A photomultiplier gain switching circuit is used to switch the gain of PMT to eliminate signal-induced noise. The profile of backscattering ratio is obtained from the average value of the return signals of numerous laser pulse firings. The sample rate of ADC used here is 20MHz. The height resolution of the data is 0.3km. The so-called "matching method" was used to distinguish the backscattered light due to particulate matter from the total backscattered light including both the components due to air molecules and due to particles (Russell et al., 1976).

The backscattering ratio  $R(z)$  is defined by following relation:

$$R(z) = [B_M(z) + B_R(z)] / B_R(z) \text{-----(1)}$$

Where:  $B_M(z)$ ---backscattering coefficient due to Mie scattering of aerosols  
 $B_R(z)$ ---backscattering coefficient due to Rayleigh scattering of atmospheric molecules.

Figure 1 shows vertical profiles of  $R(z)$  measured in Beijing during the period from July 22 1991 to March 7 1992.

The increase of backscattering ratio was measured at the height range 15~20km ( $R \approx 2.5 \sim 6$ ) from July 22 to Sept. 18, but there is small variation of backscattering ratio above 20km. From Sept. 27 the profiles of backscattering ratio began to show a double-layer structure having a peak ( $R \approx 2.7$ ) at 25~27 km and a second peak ( $R \approx 2.7$ ) at 16~17km. On Oct. 16 1991 a sudden increase of backscattering ratio at the height range 20~25km ( $R \approx 37$ ).

Figure 2. shows a fluctuation of the maximum backscattering ratio above 20km during the nine month period.

Figure 3. shows the time variation of the integrated backscattering coefficient in the height region from 15km to 30km. There is a maximum integrated backscattering coefficient about  $4.2 \times 10^{-3} \text{Sr}^{-1}$  on Oct. 16 1991.

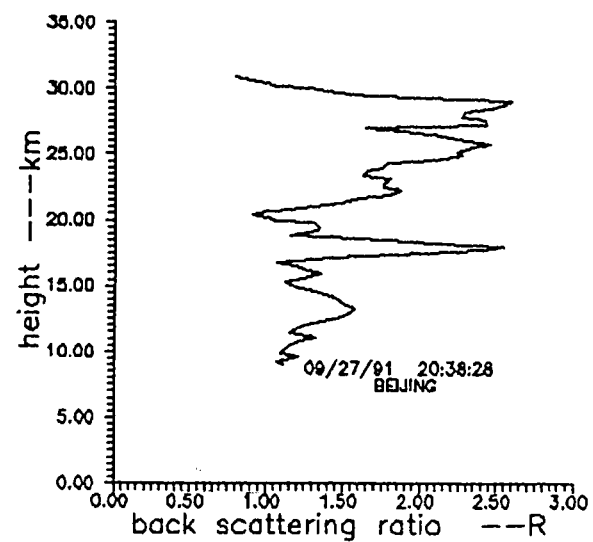
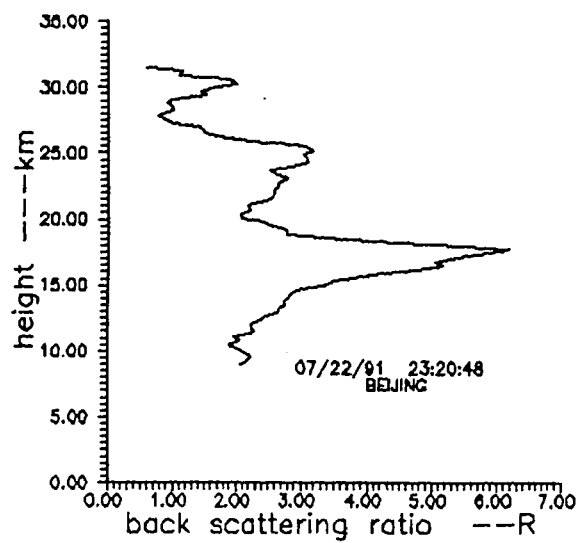
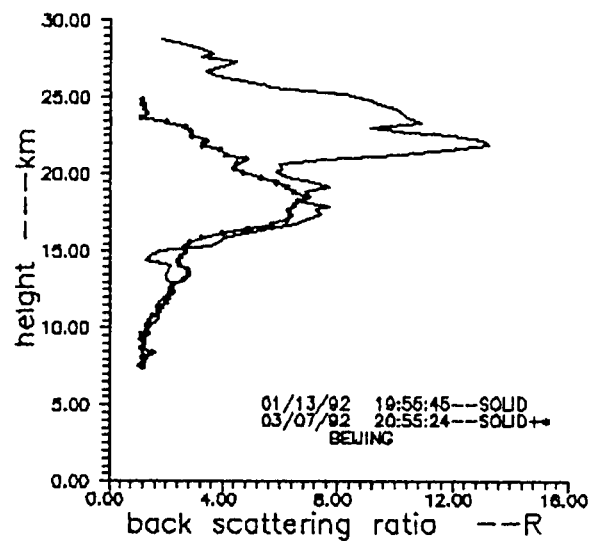
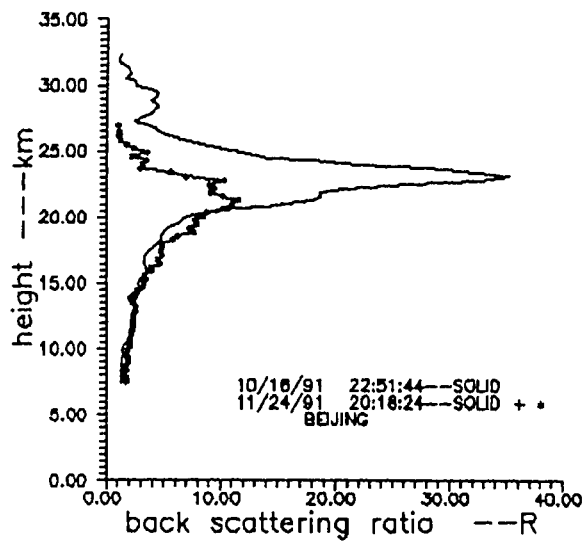


Fig. 1

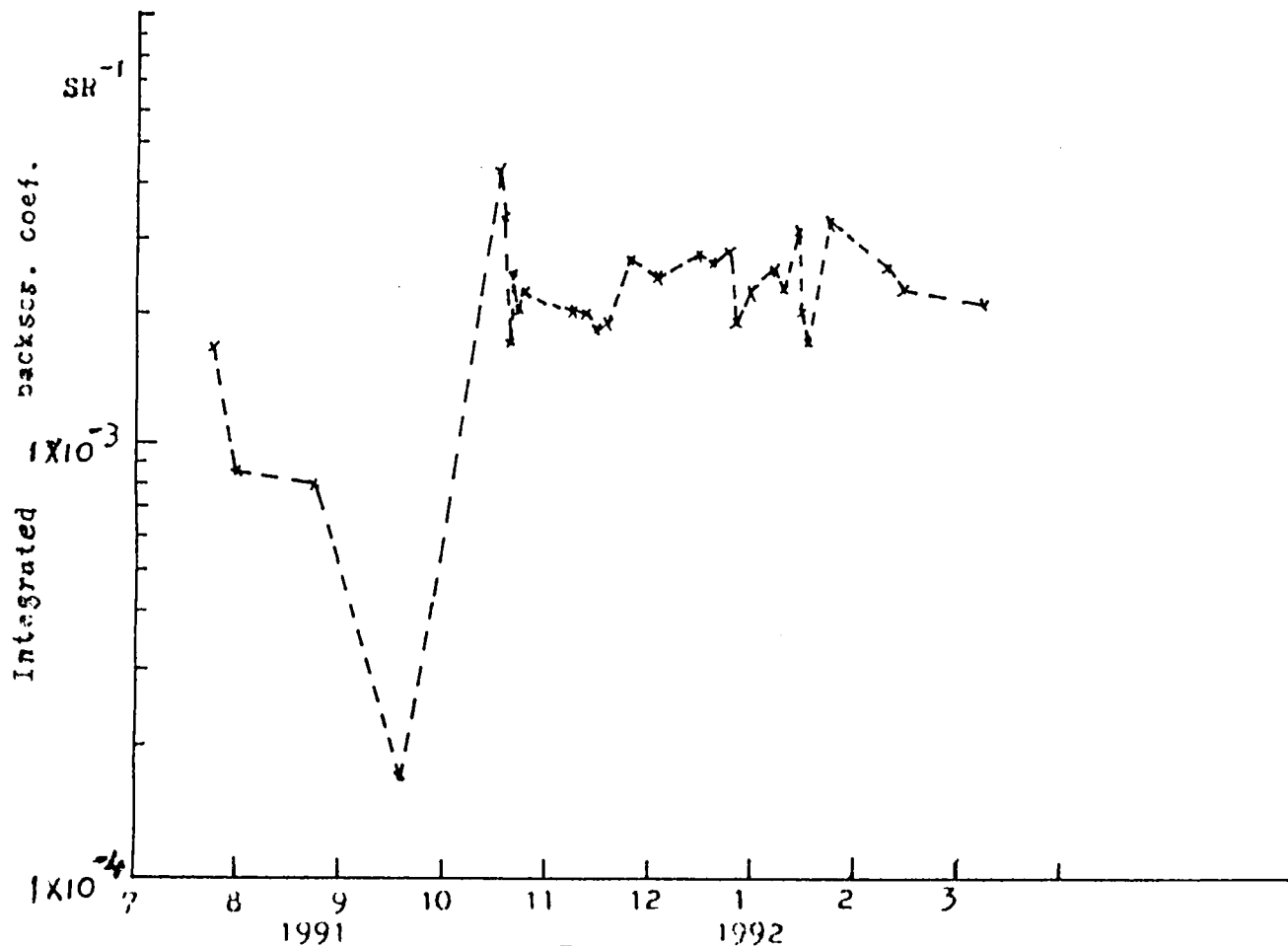


Fig. 3

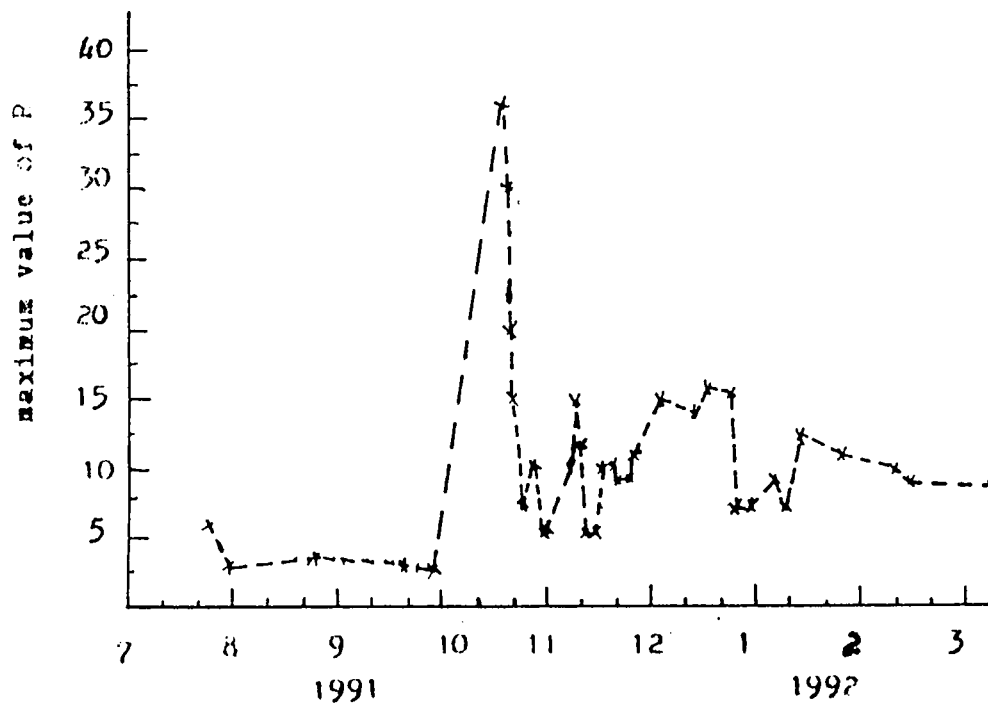


Fig. 2



# In Vivo and In Vitro Chlorophyll-a and Pheophytin-a Concentration Measurements by Laser Fluorometry

Demidov A.A., E.V.Baulin and E.A.Chernyavskaya

Physics Department of Moscow State University  
119899 Moscow, Russia

## INTRODUCTION

Presented paper is devoted to application of laser fluorescent technique in *in vivo* and *in vitro* phyto- and zooplankton analysis involving popular lasers: (a) impulse YAG laser ( $\lambda=532$  nm) and (b) steady state He-Cd laser ( $\lambda=440$  nm).

The YAG laser is widely used in laser remote sensing of seawater phytoplankton [1-4,8] *in situ* mode, but here we do a special attention to its exploration in the probe analysis (*in vivo* and *in vitro*) for a precise estimation of phytoplankton pigments using their laser induced fluorescence. The He-Cd laser is a novice one in this field [7,9] and, we believe, a very promising.

Now our methods enable one: (*in vivo*) to detect chlorophyll-a (*Chl-a*) concentration in water probe **up to 10 nanogram/liter** without its concentration, and (*in vitro*) to measure *Chl-a* and pheophytin-a (*Ph-a*) concentrations in acetone extracts of phyto- and zooplankton **up to 1 nanogram/liter**.

## YAG LASER FLUOROMETRY

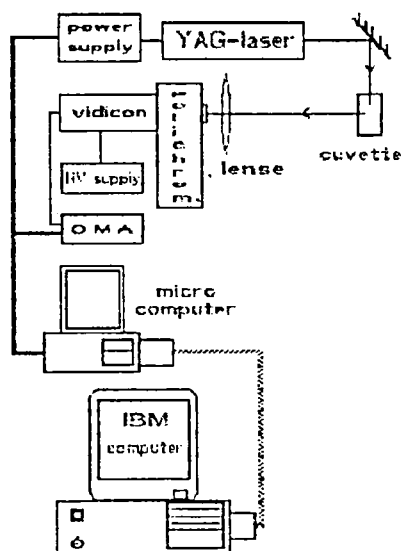


Fig.1

On the Fig.1 there is presented the block-scheme of YAG laser fluorometer. It is a modification of a common YAG Lidar for remote sensing [3-5]. Laser generates light pulses of 532 nm wavelength, 10 ns pulse duration and 0.5 MWt pulse power. Detection system is based on the Optical Multichannel Analyzer (OMA). Water probe or acetone extract of pigments are placed in cuvette.

IN VIVO.

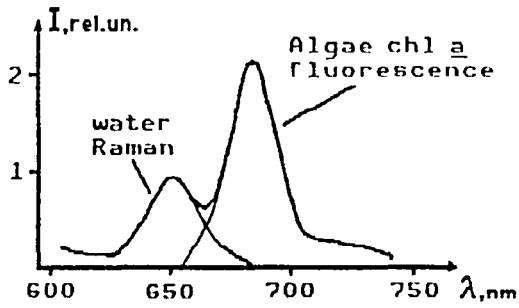


Fig. 2

In Fig. 2 there is presented the spectrum of response signal detected in 1986 near Namibia (South Atlantic). This spectrum contains two specific signals: (1) Raman scattering of laser light by water molecules ( $I_R$ ,  $\lambda_R=651$  nm) and (2) phytoplankton *Chl-a* fluorescence ( $I_{fl}$ ,  $\lambda_{fl} \approx 685$  nm). Their ratio  $\Phi = I_{fl}/I_R$  [2-4] is linearly connected with *Chl-a* concentration ( $C_a$ ) and may be used for its evaluation. We have to say, that there are some effects which complicates  $C_a$  estimation (singlet-singlet annihilation etc.), but carrying out measurements at a special conditions of probe excitation it is possible to do these measurements precisely.

During our scientific shipboard trips in Pacific, Indian, Atlantic oceans and Black sea we have obtained:  $C_a [\mu\text{g}/\text{l}] = (2.6 \pm 0.3)\Phi$  with correlation coefficient  $R(C_a, \Phi) = 0.85$ . Theoretical evaluation gave us  $C_a [\mu\text{g}/\text{l}] \approx 3\Phi$ . Sensitivity of this approach is about  $0.1 \mu\text{g}/\text{l}$ .

IN VITRO. In Fig. 3 there are presented the spectra of response signals from phytoplankton acetone extracts before (a) and after (b) its acidification by HCl acid. The classical acidification technique [4-6,10] is involved in our method.

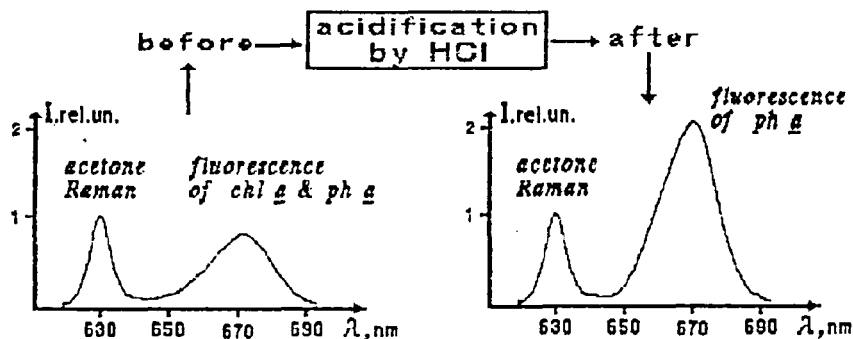


Fig. 3

Here, instead of water Raman we use the acetone Raman signal ( $\lambda_R=632$  nm). Parameters  $\Phi$  (before acidification) and  $\Phi_a$  (after acidification) allowed us to estimate both *Chl-a* and *Ph-a*

concentrations:

Theory:  $C_a [\mu\text{g/l}] = 3 (\Phi - \Phi^a)/(1 - \xi)$   
 $C_p [\mu\text{g/l}] = 1.5 (\Phi - \xi\Phi^a)/(1 - \xi), \quad \xi = 2$

Experiment:  $C_a [\mu\text{g/l}] = (2.7 \pm 0.6)(\Phi - \Phi^a)/(1 - \xi^{\text{exp}})$   
 $C_p [\mu\text{g/l}] = (1.4 \pm 0.2)(\Phi - \xi^{\text{exp}}\Phi^a)/(1 - \xi^{\text{exp}}),$   
 $\xi^{\text{exp}} = 2.0 \pm 0.15$

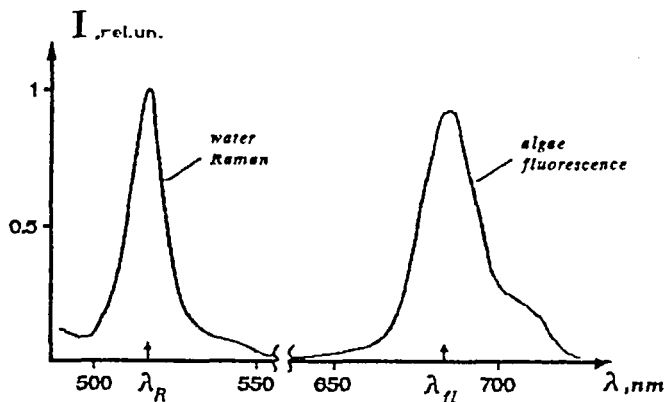
Sensitivity:  $10^{-8}$  gram/liter.

Here  $\xi$  is the "acidification parameter". This method can be used for analyzing of feed processes of individual sample of zooplankton as well [6].

He-Cd LASER FLUOROMETRY

Steady state He-Cd laser fluorometer is a modification of fluorometer described above, where YAG laser is replaced by He-Cd laser (power ~ 20 mWt).

IN VIVO.



In Fig.4 there is presented the typical spectrum of response signal of phytoplankton probe (South Atlantic). Here, the Raman signal has the wavelength  $\lambda_R = 518$  nm.

Fig.4

Our estimations gave [7,9]:

Theory:  $C_a [\mu\text{g/liter}] = 1.8 \Phi$   
 Experiment:  $C_a [\mu\text{g/liter}] = (1.73 \pm 0.13) \Phi$   
 Correlation coefficient:  $R(\Phi, C_{chl}) = 0.93$   
 Sensitivity:  $10^{-8}$  gram/liter .

Sensitivity of this magnitude allowed one to conduct measurements in ocean waters with extremely low phytoplankton content (oligotrophic areas) without concentration a probe.

IN VITRO. The approach is the same as in the case of YAG laser, but extract spectra are more complicated. Besides

fluorescence of *Chl-a* and *Ph-a*, these spectra contain fluorescence of chlorophylls-b,c and their pheophytins. In our method it decreases the accuracy of *Chl-a* and *Ph-a* measurements, but, in principle, it increases the analytical potentiality of this approach, because these spectra are very informative. Now we are going to develop method for simultaneous estimation not only *Chl-a* and *Ph-a*, but also other chlorophylls and pheophytins.

Just now, our estimations gave [7,9]:

$$\begin{aligned} \text{Theory: } C_a [\mu\text{g/l}] &= 0.4 (\Phi - \Phi^a)/(1 - \xi) \\ C_p [\mu\text{g/l}] &= 5.4 (\Phi - \xi\Phi^a)/(1 - \xi), \quad \xi = 0.078 \end{aligned}$$

$$\begin{aligned} \text{Experiment: } C_a [\mu\text{g/l}] &= (0.38 \pm 0.12)(\Phi - \Phi^a)/(1 - \xi^{\text{exp}}) \\ C_p [\mu\text{g/l}] &= (5 \pm 2)(\Phi - \xi^{\text{exp}}\Phi^a)/(1 - \xi^{\text{exp}}), \\ &\xi^{\text{exp}} = 0.076 \end{aligned}$$

Sensitivity:  $10^{-9}$  gram/liter.

One can see that it is the most sensitive method that allowed to measure *Chl-a* concentration as low as 1 nanogram/liter.

#### REFERENCES

1. Measures R.M. (1984) Laser Remote Sensing. Ed. John Wiley & Sons.
2. Hoge F.E. and R.M. Swift (1989) Remote Sens. Environ., v.30, pp.67-76.
3. Demidov A.A., A.M. Chekalyuk, T.V. Lapshenkova and V.V. Fadeev (1988) Meteorologiya i Gydrologiya (USSR), N 6, pp.62-70.
4. Demidov A.A., E.V. Baulin, V.V. Fadeev and L.A. Shur (1981) Okeanologiya (USSR), v.21, pp.174-179.
5. Demidov A.A. and I.G. Ivanov (1989) Izvestiya Akademii Nauk SSSR, seriya biologicheskaya (USSR), v.3, pp.378-385.
6. Pasternak A.F., A.A. Demidov, A.V. Dritz and V.V. Fadeev (1987) Okeanologiya (USSR), v.27, pp.852-856.
7. Demidov A.A. and E.A. Chernyavskaya (1991) Biofizika (USSR), v.36, pp.982-986.
8. Fadeev V.V., A.A. Demidov and A.M. Chekalyuk (1991) Proceedings of the 12th Asian Conference on Remote Sensing, Singapore, F-3-1 - F-3-6.
9. Demidov A.A. and E.A. Chernyavskaya (1991) Proceedings of the 12th Asian Conference on Remote Sensing, Singapore, Q-11-1 - Q-11-6.
10. Water. Spectrophotometric method of a chlorophyll a determination. - GOST SSSR 17.1.04.02-90, Moscow. - 14 p.

# SCIENCE GOALS AND MISSION OBJECTIVES OF NASA'S LASER ATMOSPHERIC WIND SOUNDER PROGRAM

Wayman E. Baker

Development Division  
National Meteorological Center  
Washington, D. C. 20233

## 1. INTRODUCTION

Knowledge of the global wind field is widely recognized as fundamental to advancing our understanding and prediction of the total Earth system. Yet, because wind profiles are primarily measured by land-based rawinsondes, the oceanic areas (covering roughly three quarters of the Earth's surface) and many regions of the less-developed southern hemisphere land areas are poorly observed. The gap between our requirements for wind data and their availability continues to widen. For example, as faster computers become available to model the atmosphere with ever increasing resolution and sophistication, our ability to do so will be hampered because of the lack of data, particularly wind profiles.

In order to address this important deficiency in wind observations, NASA plans to construct the Laser Atmospheric Wind Sounder (LAWS) instrument, with deployment tentatively scheduled between 2002 and 2005 as part of NASA's Earth Observing System (EOS) mission.

This article addresses the importance of wind measurements for advancing our understanding and prediction of the total Earth System. The current characteristics of the LAWS instrument under study are also summarized.

## 2. IMPORTANCE OF WIND DATA FOR EARTH SYSTEM SCIENCE

The fundamental importance of wind observations for advancing our understanding and prediction of the total Earth System may be seen in Fig. 1 (reproduced from Fig. 11 in a report by the Committee on Earth and Environmental Sciences, 1989).

The original figure has been modified to show critical (denoted by a \*) and secondary (denoted by \*\*) anticipated contributions of LAWS to the U.S. Global Change Program science priorities. An additional entry ("Aerosols and Sub-Visible Cirrus") has also been added under "Climate and Hydrologic Systems", because of the expected contribution of the LAWS measurements there.

The LAWS data products that are expected to provide contributions to the science priorities in Fig. 1 are listed in Table 1 along with the expected resolution and accuracy. In addition to horizontal winds, LAWS will provide the distribution of aerosols (sampled at 9.11

µm wavelength) and cirrus clouds, and the height of cirrus and stratiform clouds. These measurements will be extremely important for a variety of climate studies (i.e., cloud-radiation interaction).

U. S. Global Change Science Priorities

Climate and Hydrologic Systems	Biogeochemical Dynamics	Ecological Systems and Dynamics	Earth System History	Human Interactions	Solid Earth Processes	Solar Influences
Role of Clouds ** Ocean Circulation and Heat Flux * Land/Atm/Ocean Water & Energy Fluxes * Coupled Climate System & Quantitative Links * Ocean/Atm/ Cryosphere Interactions * Aerosols and sub-visible Cirrus*	Bio/Atm/Ocean Fluxes of Trace Species * Air Processing of Trace Species Surface/Deep Water Biogeochemistry Terrestrial Biosphere Nutrient and Carbon Cycling Terrestrial Inputs to Marine Ecosystems	Long-Term Measurements of Structure/Function ** Response to Climate and Other Stresses ** Interactions between Physical and Biological Processes ** Models of Interactions, Feedbacks, and Responses Productivity/Resource Models	Pleistocene Paleoclimatology Atmospheric Composition Ocean Circulation and Composition Ocean Productivity Sea Level Change Paleohydrology	Data Base Development Models Linking: Population Growth and Distribution Energy Demands Changes in Land Use Industrial Production	Coastal Erosion Volcanic Processes ** Permafrost and Marine Gas Hydrates Ocean/Sea-floor Heat and Energy Fluxes Surface Processes Crustal Motions and Sea Level	ELV/AV Monitoring Air/Solar Energy Coupling Irradiance (Measure/Model) Climate/Solar Record Proxy Measurements and Long-Term Data base

← Increasing Priority

Fig 1 Anticipated contributions of the LAWS measurements to the U.S Global Change Science Priorities. Reproduced from Fig. 11 of a report by the Committee on Earth and Environmental Sciences, 1989. See text for more details. Critical and secondary anticipated LAWS contributions are denoted by a \*\*\* or a \*\*\*, respectively.

LAWS will have the capability of providing winds in the troposphere from cloud returns and from aerosols in the lowest 2 km. Typically, the spacing between line-of-sight (LOS) samples will be on the order of 50-75 km with roughly 6 shots being combined to produce horizontal vector winds on a 100 km grid. Any given grid area will be overflowed once every 12 hours at the Equator (assuming a platform in polar orbit) with increasing frequency as one goes poleward. When there are sufficient aerosols (including thin cirrus), it may be possible to use single shots and pairs of shots to achieve ≈60 km resolution with temporal resolution remaining at 12 hours near the Equator. With some form of shot management it may be possible to further increase the resolution to 25-30 km in regions of interesting meso-α phenomena without impacting laser lifetime or jeopardizing the system performance for global scale applications.

2.1 Improved Numerical Weather Prediction

The relatively advanced state of atmospheric general circulation models (GCM's) now available for coupling with those of the ocean and biosphere, in order to model the Earth system, is due in large part to the advances in numerical weather prediction (NWP) for which atmospheric GCM's are now widely used.

The first NWP models were designed to use only mass (height) data. Winds were derived from the mass observations using the geostrophic relationship. This relationship assumes that the latitudinally dependent Coriolis force is balanced by the pressure gradient force. This was a natural choice because pressure observations were more abundant and more accurate than wind observations. With the advent of global primitive equation models, however, the need for accurate wind profile data has become increasingly clear. There are two independent reasons for this (Kalnay et al., 1985).

The first reason is derived from the concept of geostrophic adjustment (Rossby, 1938; Washington, 1964; Daley, 1980). On the scales measured by a data swath of a low Earth-orbiting satellite, variations in mass data are quickly rejected by the model. This rejection process is consistent with atmospheric behavior. Specifically, small-scale pressure-height variations do not result in small-scale changes in the wind field; instead they are rapidly dispersed as gravity waves. Simply posed, models accept the wind data more readily than mass data for scales which can be observed. Pressure or height data are not retained as well unless they are forced a priori to be in geostrophic balance with the winds.

The second reason for the importance of wind data is that differentiation enhances the effect of noisy observations, whereas integration reduces the effect of noise. The geostrophic relationship relates the wind to the horizontal pressure gradient; at increasingly smaller scales, the geostrophic relationship is often invalid so that winds become an increasingly more important measure of the atmospheric state than pressure or height measurements.

Table 1. The data products expected from LAWS and corresponding resolution and accuracy.

LAWS Data Products, Expected Resolution and Accuracy		
Product	Expected Resolution	Expected Accuracy
1. Horizontal Vector Wind	100 km - Horiz; 1 km - Vert. (300 m in high aerosol regions (e.g., PBL) or cirrus)	$\pm 1$ to $5 \text{ m s}^{-1}$ depending on aerosol amount with quality flags
2. Line of Sight Wind	6 per $100^2 \text{ km}^2$ - Horiz; 1 km - Vert. (300 m in high aerosol regions (e.g., PBL) or cirrus)	$\pm 1$ to $5 \text{ m s}^{-1}$ depending on aerosol amount with quality flags
3. Aerosol <sup>A</sup> Distribution	100 km - Horiz; 1 km - Vert. (300 m in high aerosol regions (e.g., PBL). Temporally averaged (e.g., daily)	TBD
4. Cirrus <sup>B</sup> Distribution	100 km - Horiz; 300 m - Vert. Temporally averaged (e.g., daily)	TBD
5. Cirrus Cloud Top Height	50 km - Horiz.	$\pm 20$ - $50 \text{ m}^C$
6. Stratiform Cloud Top Height	50 km - Horiz.	$\pm 50 \text{ m}$
<small>NOTES: A. Wavelength dependent (currently <math>9.11 \mu\text{m}</math>)            B. Cirrus not detectable by passive techniques (i.e., sub-visible)            C. Height determination for thin cirrus will be significantly more accurate with LAWS than current passive techniques</small>		

## 2.2 More Accurate Diagnostics of Large-Scale Circulation and Climate Dynamics

Fluctuations in the climate system over one part of the globe are capable of being communicated great distances to other parts. The remarkable weather experienced in many areas of the world during the tropical Pacific El Niño event of 1982-83 (Rasmusson, 1984) is a dramatic case in point.

The degree to which behavior in one part of the globe can be communicated elsewhere by the atmosphere appears to depend subtly on the background atmospheric state (Branstator, 1983). For instance, one such teleconnection, namely the one between the tropical Pacific and northern hemisphere extratropics, may be sensitive to the structure of the wind field in the exit region of the subtropical east Asian jet that lies between the two regions. Indications are, however, that the currently available data base is not able to depict the structure of the east Asian jet exit region sufficiently well. For example, Rosen *et al.*, (1985) found large differences between two different analyses of the zonal wind field in the area of the east Asian jet based on the data collected during the Global Weather Experiment despite the

apparent extensive nature of these observations. Data from the LAWS instrument should significantly improve the quality of the wind analyses in such critical regions as the subtropical Pacific.

### 2.3 Improved Surface/Atmospheric Fluxes

Fluxes of momentum, heat, moisture, CO<sub>2</sub>, and other constituents are important to a large number of interdisciplinary studies. Under cloud-free conditions, and, perhaps under some cloudy conditions, LAWS winds will uniquely contribute to the study of low-level tropospheric dynamics. The lowest level LAWS winds will be averaged over a height of only a few hundred meters in the planetary boundary layer. This mean velocity can be used in traditional parameterizations of air-surface fluxes, which are crucial to studies of the energetics of storms, regional weather analyses and global climate modelling.

### 2.4 Improved Understanding of Global Biogeochemical and Hydrologic Cycles

The wind data set obtainable from the LAWS system will form a significant component of the temporally continuous global data base required for studies of coupled climate systems. This data base is needed to: (1) describe the atmospheric general circulation including annual and interannual changes and the transport of energy, momentum, moisture, trace gases, and aerosols; (2) quantify the cycles of atmospheric variables that are key ingredients of climate change; and (3) test and verify existing coupled climate models and develop new and improved ones.

Wind observations obtained from LAWS will contribute in two very important ways toward an improved understanding of global and regional hydrologic cycles. First, they will provide a more accurate estimate of the horizontal transport of water vapor. Second, their use in global models in a data assimilation cycle will contribute toward improved analysis and prediction of vertical motion (and vertical transport of water vapor) and precipitation.

Two important components of biogeochemical cycles and budgets of aerosols are the horizontal and vertical transport of trace gases and aerosols, and their interactions with cloud and precipitation systems. The latter are important through their role in chemical transformations and in removal through wet scavenging. The same wind observations and models that will better define the hydrologic cycle will also be useful in estimating the long-range transport of trace gases and aerosols and in establishing better estimates of precipitation systems over the oceans.

## 3. SUMMARY

In summary, LAWS will provide a significant improvement in our ability to observe the global wind field. This will directly lead to an improvement in numerical weather forecasts and will fundamentally advance our understanding of the atmospheric circulation and dynamics and the biogeochemical and hydrologic cycles.

#### 4. ACKNOWLEDGMENTS

The contributions of the LAWS Science Team Members in defining the science requirements and in guiding the instrument development are sincerely acknowledged.

Much of the information for this article has been taken from the NASA EOS LAWS Instrument Panel Report, Volume IIg, Section II - Science Objectives. The report was one of the documents released as part of the NASA EOS Announcement of Opportunity in February 1988. The contributions to the LAWS Instrument Panel Report by the Members of LAWS Instrument Panel are sincerely acknowledged.

The author also benefited from discussions with R. Atlas, D. Johnson, E. Kalnay, H. Melfi, and R. Rosen.

#### 5. REFERENCES

Branstator, G., Horizontal energy propagation in a barotropic atmosphere with meridional and zonal structure, J. Atmos.Sci., 40, 1689-1708. Committee on Earth and Environmental Sciences, 1989: Our changing planet: The FY90 Research Plan, Executive Summary, The U.S. Global Change Research Program. Available from the Office of Science and Technology Policy Coordinating Council on Science, Engineering, and Technology, Washington, D. C., 43 pp.

Daley, R., 1980: On the optimal specification of the initial state for deterministic forecasting, Mon. Wea.Rev., 108, 1719-1755.

Kalnay, E., J. C. Jusem, and J. Pfaendtner, 1985: The relative importance of mass and wind data in the present observing system, Report of the NASA Workshop on Global Wind Measurements, edited by W. E. Baker and R. J. Curran, STC 2081, A. Deepak Publishing, Hampton, VA, 1-5.

Rasmusson, E. M., 1984: El Niño: The ocean/atmosphere connection, Oceanus, 27, 5-12.

Rosen, R. D., D. A. Salstein, J. P. Peixoto, A. H. Oort, and N.-C. Lau, 1985: Circulation statistics derived from level III-b and station-based analyses during FGGE, Mon. Wea. Rev., 113, 65-88.

Rossby, C. G. 1938: On the mutual adjustment of pressure and velocity distribution in certain simple current systems, J. Mar. Res., 1, 239-263.

Washington, W., 1964: A note on the adjustment towards geostrophic equilibrium in a simple fluid system, Tellus, 16, 530-534.



**THE LASER ATMOSPHERIC WIND SOUNDER (LAWS)  
PHASE II PRELIMINARY SYSTEM DESIGN**

John C. Petheram, David L. Kenyon  
General Electric Company  
Astro Space Division  
P.O. Box 800, Princeton, NJ 08543-800

Alan. B. Wissinger  
Hughes Danbury Optical Systems  
100 Wooster Heights Road  
Danbury, CT 06810

T. Rhidian Lawrence  
STI Optronics  
2755 Northup Way  
Bellevue, WA 98004-1495

The Laser Atmospheric Wind Sounder (LAWS) is intended to measure global wind profiles in the lower and upper troposphere as part of the Earth Observing System (EOS). Global scale wind profiles will lead to a better understanding of large scale circulation processes and climate dynamics, an understanding of mesoscale phenomena, improved numerical weather prediction, and further insights into the coupling of the atmosphere/oceans/biosphere system. The LAWS Phase I/II Study which ran for 33 months concluded in June 1992. This paper will present details of the Phase II preliminary design.

The measurement requirements for the Phase II LAWS instrument are given in Table 1.

Velocity Accuracy	$\pm 1$ m/s Lower Troposphere $\pm 5$ m/s Upper Troposphere
Vertical Resolution	1 km
Spatial Resolution	100 km x 100 km, 6 shots per box
Vertical Range	0 - 20 km

Table 1. LAWS Measurement Requirements

The instrument developed to meet these requirements consists of 3 major subsystems: a 9.1- $\mu\text{m}$   $^{12}\text{C}^{18}\text{O}_2$  laser transmitter; an optical system conically scanning about nadir, which acts both as transmitter and receiver; and a HgCdTe detector in the focal plane of the optical system. The top-level instrument specifications are given in Table 2 and the functional block diagram for the instrument given in Figure 1.

Far-Field Pulse Energy	17.5 Joules
Optics Aperture	1.5 m
Laser Pulse Length	3 $\mu\text{sec}$
Scan Rotation Rate	12 rpm
Scan Nadir Angle	45°
Laser Repetition Rate	Asynchronous up to 20 Hz, 5 Hz average

Table 2. Top-Level Instrument Specifications

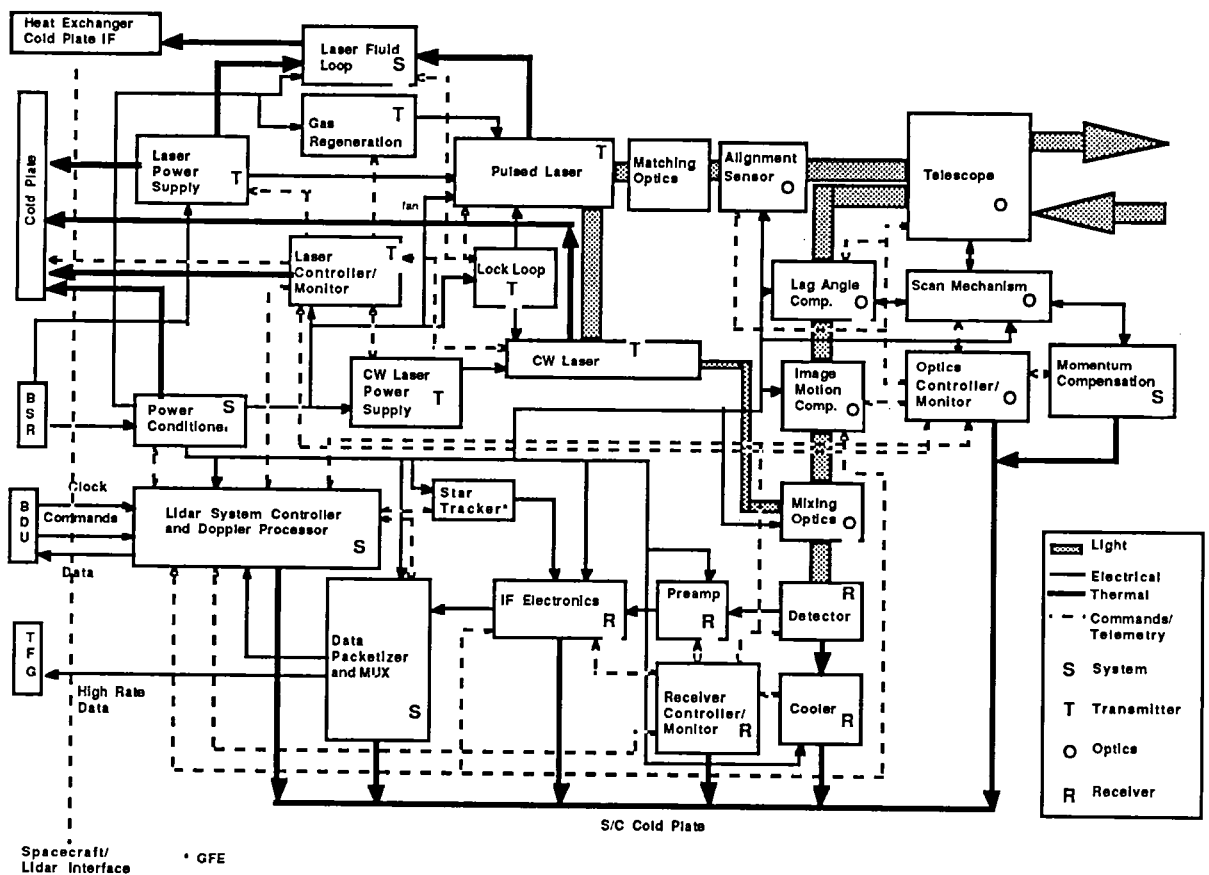


Figure 1. System Functional Block Diagram

The preliminary LAWS configuration is shown in Figure 2. The laser and telescope are mounted to a planar optical bench made of 2.5 inch thick aluminum honeycomb with graphite-epoxy face sheets. Heat from the laser is rejected to 3 EOS cold plates mounted underneath the optical bench. Sundry electronics boxes and support subsystems are shown mounted separately on cold plates to the side of the main instrument structure. The total instrument weight is 800 kg and the average power required, for a nominal 5 Hz laser repetition rate, is 2200 Watts. The instrument was configured to fit a generic Atlas IIAS spacecraft bus supplied to the contractors by NASA Marshall Space Flight Center. Details of the mechanical configuration, the optical subsystem and the receiver subsystem will be addressed in the presented paper. Details of the predicted performance of the instrument and the laser subsystem will be given in companion papers.

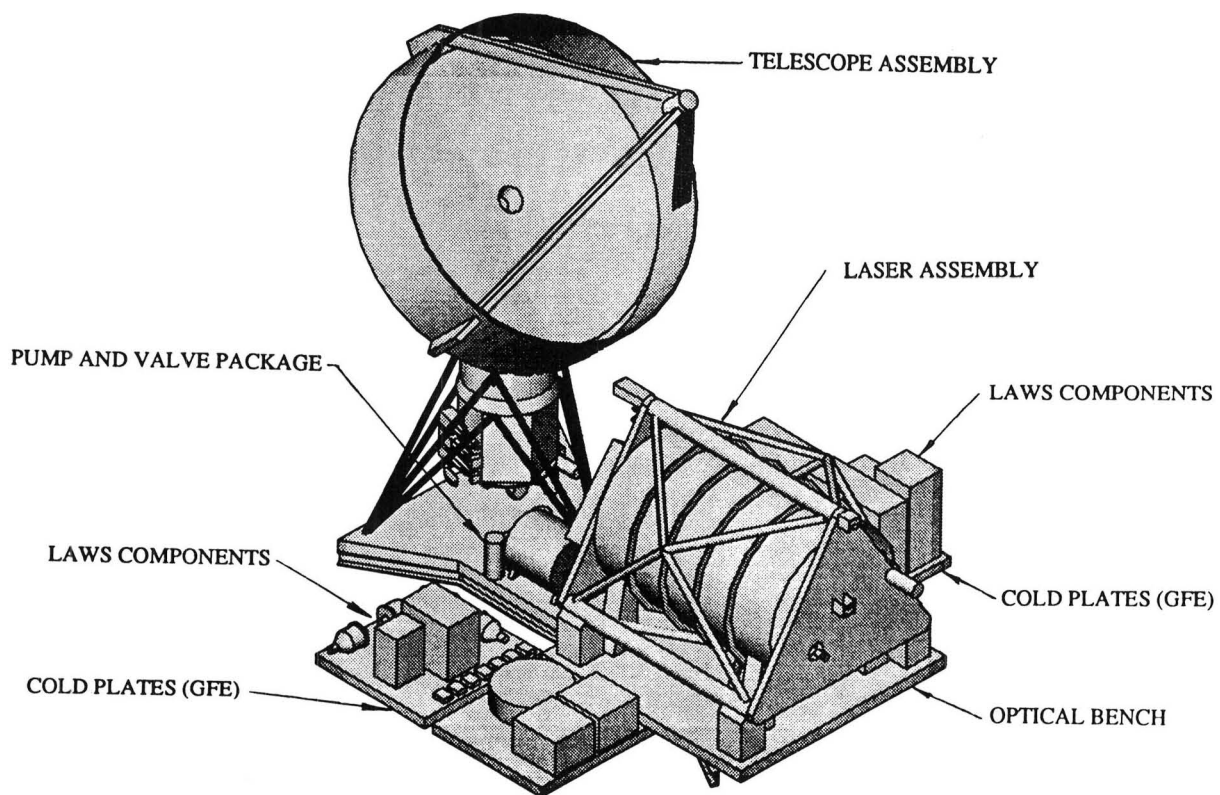


Figure 2. LAWS Mechanical Configuration



**THE LASER ATMOSPHERIC WIND SOUNDER (LAWS)  
PHASE II PRELIMINARY LASER DESIGN\***

T. Rhidian Lawrence, Albert L. Pindroh, Mark S. Bowers, Terence E. DeHart,  
Kenneth F. McDonald, Ananda Cousins and Stephen E. Moody.

STI Optronics  
2755 Northup Way  
Bellevue, WA 98004-1495

The requirements for a Laser Atmospheric Wind Sounder (LAWS) laser have been determined from system considerations and are summarized in Table 1.

**TABLE 1  
LAWS LASER SUBSYSTEM REQUIREMENTS**

Requirement	Value	Comment
Pulse Energy	15 J	Useable in far field
Pulse Repetition Rate	10-Hz average, 20-Hz max.	Asynchronous
Pulse Length	3 $\mu$ s	FWHM
Wavelength	9.11 $\mu$ m	Maximize scattering
Chirp (temporal coherence)	200 kHz	Velocity resolution
Spatial Coherence	B.Q. <1.1, Strehl >0.85	Maximize SNR
Beam Jitter	<25 $\mu$ r	Maximize SNR
Weight	< 165 kG	Platform constraint
Wall Plug Efficiency	> 6%	Platform constraint
Lifetime	>10 <sup>9</sup> shots	5-year life

The Laser Subsystem provides for the generation and frequency control of two beams, the transmit high power and local oscillator beams, which are delivered to the Optical and Receiver Subsystems, respectively. In our baseline approach, the excitation of the gain section is achieved by a self-sustaining uv-(corona) preionized discharge. Gas is recirculated within the laser flow loop using a transverse flow fan. An intra-flow-loop heat exchanger, catalyst monolith

\*Work supported by NASA Marshall Contract No. NAS8-37589 through GE/Astro-Space Subcontract No. A28-W20233 .

and acoustic attenuators condition the gas to ensure uniform energy output and high-beam quality during high-pulse repetition-rate operation. The baseline frequency control scheme consists of injection of radiation from a low-power line-center-locked CW RF-pumped laser into the power oscillator cavity via the zeroth order of a Littrow grating. A sample of this same laser is provided the receiver to fulfill the function of the local oscillator reference. The injected beam is used as a probe beam to tune the power oscillator to resonance at the injected frequency during the interpulse period and as a seed frequency during the power pulse build-up. An electro-optic modulator in the injection beam path effects isolation between the injection and power oscillators. The resonator incorporates a graded reflectivity feedback/output coupler, so chosen because of the superior far-field properties of the output mode. A lens in the cavity is used as an alternative for a concave grating to minimize astigmatism.

Major laser parameter selections are summarized in Table 2.

**TABLE 2**  
**PARAMETER SELECTIONS FOR LASER SUBSYSTEM**

Parameter	Value
Gain Section Length	75 cm
Gain Region Cross Section	5 x 5 cm
Resonator Length	3 m
Cavity Pressure	0.5 atm
Discharge Loading	200 J/liter-atm
Pump Pulse Duration	4 $\mu$ sec
Gas Mix - He/N <sub>2</sub> /CO <sub>2</sub>	3/2/1

A perspective view of the baseline laser configuration is shown in Figure 1. The gain module is contained in a cylinder supported by the system platform and is vibrationally isolated from it. The line pulser is an integral part of the gain module. The resonator components, auxiliary optics, injection optics, injection/local oscillator lasers and detectors are attached to triangular end plates, which are supported by a truss structure mounted directly to the system optical bench. Various power supplies and electronic units are located on a central system bench. The baseline line pulser design consists of two "type E" pulse forming networks (PFN's) connected in series through the laser head in a bi-polar arrangement. Ten-section matched impedance PFN's provide 60 kV to initiate and 30 kV to sustain the required flat-topped discharge pulse profile, while simultaneously minimizing undesirable reflections, and optimizing the the energy transfer efficiency.

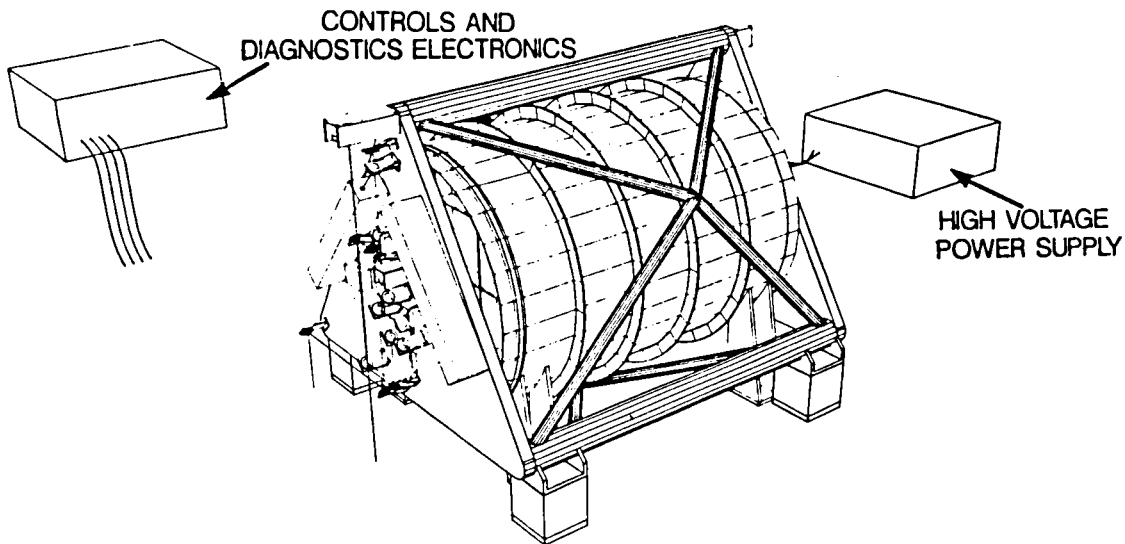


Figure 1. Perspective View of Laser Subsystem

The baseline LAWS laser pulse temporal profile as calculated by in-house laser codes is shown in Figure 2. Also shown is the integrated pulse energy temporal profile. The useful energy within the pulse is defined as the contribution that emerges in the time interval between the decay of the gain-switch spike and the 50% decay level of the pulse tail. The chirp profile has been estimated using a coupled kinetics-fluid dynamics-optics numerical simulation, and the results are shown in Figure 3 and are predicted to be within the 200-kHz requirement. Figure 4 shows the power spectral density of the outgoing pulse. The calculated far-field encircled energy distribution is shown in Figure 5 and illustrates the excellent energy conversion into the central lobe possible using the graded reflectivity coupler resonator approach.

The design features of and performance predictions for our baseline LAWS laser will be evaluated using a breadboard version of the laser subsystem that is currently being fabricated.

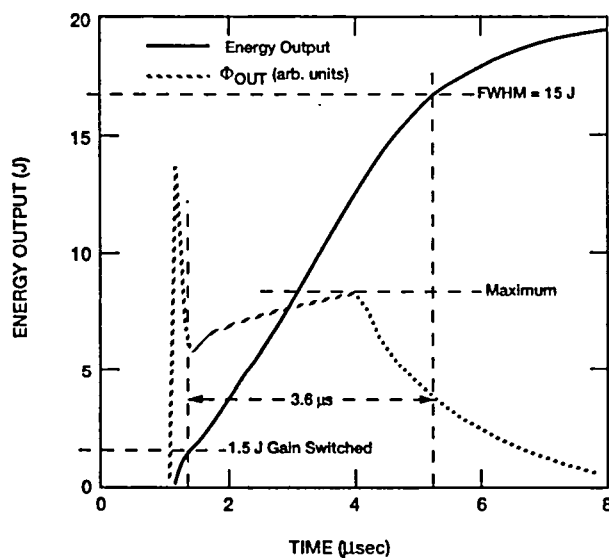


Figure 2. Baseline LAWS Pulse Temporal Profile

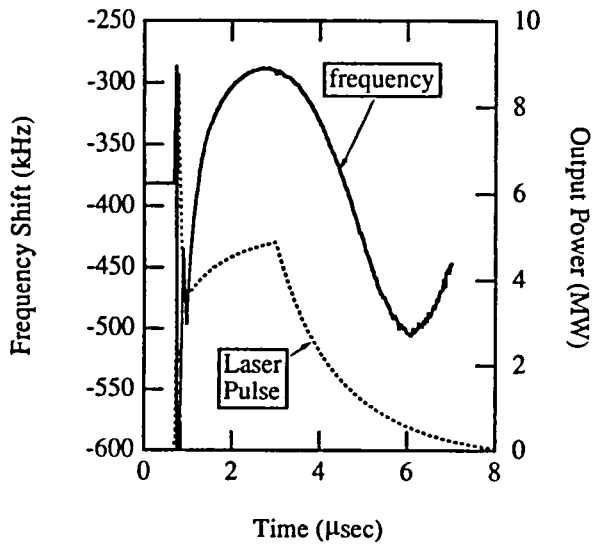


Figure 3. Estimates of Gasdynamic Chirp in Baseline LAWS Laser

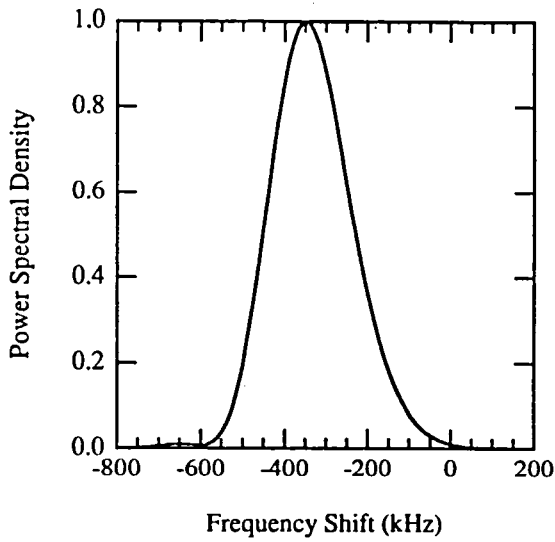


Figure 4. Estimate of Spectral Power Density of Baseline LAWS Laser Pulse

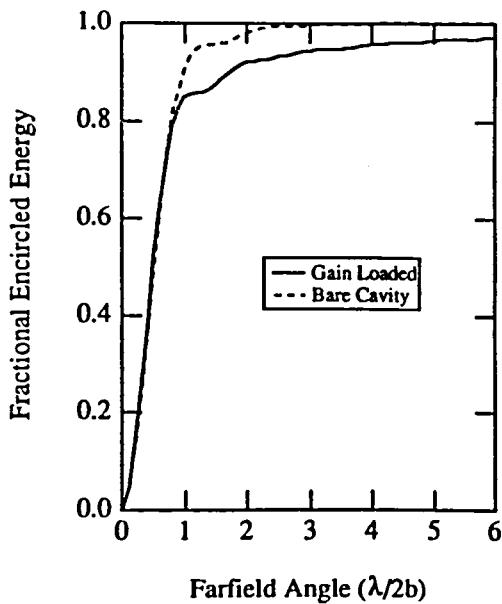


Figure 5. Far-Field Encircled Energy Profile of Baseline LAWS Laser Beam

$M = 1.25$	$R = R_o[1-(ra)^2]$
$L = 310 \text{ cm}$	$R_o = 0.8$
$\lambda = 9.11 \text{ } \mu\text{m}$	$a = 1.87 \text{ cm}$
$g_o L = 2.6$	$b = Ma$

## **G.E's Mobile, Coherent Doppler Lidar Test/Evaluation Facilities**

J.T. Sroga, J. W. Scott, S.C. Kiernan,  
F.J. Weaver, J.E. Trotta, J.C. Petheram

General Electric Company  
Astro Space Division  
P.O. Box 8555  
Philadelphia, PA 19101

GE Astro Space Division, as part of an IR&D effort, has invested significant funding in support of the Laser Atmospheric Wind Sounder (LAWS) program over the last four years. The primary objective of this IR&D program is twofold: 1) to develop and evaluate technologies with direct applications to spaceborne laser wind sensing; 2) develop system level engineering experience (both analytical and hardware) in designing, operating and modelling a coherent Doppler lidar. As part of this IR&D effort, GE is developing a mobile, ground based coherent Doppler lidar as an end-to-end system level test facility to evaluate applicable technologies, verify system level performance issues, perform instrument calibration and validate end-to-end system performance model predictions. This paper will primarily focus on a description of the ground based lidar system and the performance during the initial shakedown operation after system integration.

A block diagram of the system is shown in Figure 1 with a list of the top level system design parameters given in Table 1. The transmitter (manufactured by STI Optronics, a GE teammate on LAWS) is an injection seeded, TEA laser similar to one described in Post and Cupp (1990) with significant modifications to pulse power, injection seeding source, TEA flow loop and the corona bar design to improve laser performance. The transceiver optical subsystem has been designed to include diagnostics to monitor the laser pulse (energy, pulse shape, frequency content), and to provide system capabilities to use single and multiple element detectors in the receive path simultaneously. The transceiver subsystems (laser and optics) are mounted to a vibration isolated, optical table. The lidar system is housed in a 40'x8.5' semitractor trailer for mobility. A two axis (azimuth-elevation) optical scanner is mounted to the roof of the trailer to provide hemispheric pointing coverage for the lidar. The scanner motors are individually microprocessor controlled and interfaced to the data acquisition system.

The data acquisition system is based on the SUNrise Weather Processing System developed by Lassen Research. The SUNrise system utilizes multiprocessor architecture (Sun 68020 host, 6830 product generator, 4 Doppler processor computational boards) in a VME bus structure to acquire, store, process and display the Doppler lidar data in real time. The data are displayed on an 8 bit, 19" color monitor in various formats depending upon the scan pattern (RHI, PPI, RTI, etc.). The SUNrise data system is interfaced to a custom 16 channel IF electronics chassis (manufactured by Lassen Research) with digital I and Q sampling (20MHz, 8 bit, 8K words/sample) required for the 4 Doppler processor boards. Amplification (~80dB), bandwidth filtering ( $\pm 10$ MHz) and programmable gain control (0-70dB in 10dB increments) are incorporated into the IF electronics front end to improve the dynamic range of the system. The data is archived to hard disk or tape for post processing.

The mobile, CO<sub>2</sub> Doppler lidar system is currently under final assembly and testing. The major transceiver components (laser transmitter, transmit/receive optics, telescope and detectors) have been installed and aligned in the trailer. Heterodyne return signals have been observed from clouds with the system pointed vertically. The data acquisition and two axis scanner subsystem are currently being integrated. Performance results from tests on the laser transmitter spectral characteristics (frequency stability, pulse chirp) along with system level performance will be presented at the conference.

Reference:

Post, M.J. and R. E. Cupp (1990) "Optimizing a Pulse Coherent Doppler Lidar" Appl. Opt., v 29, pp4145-4158.

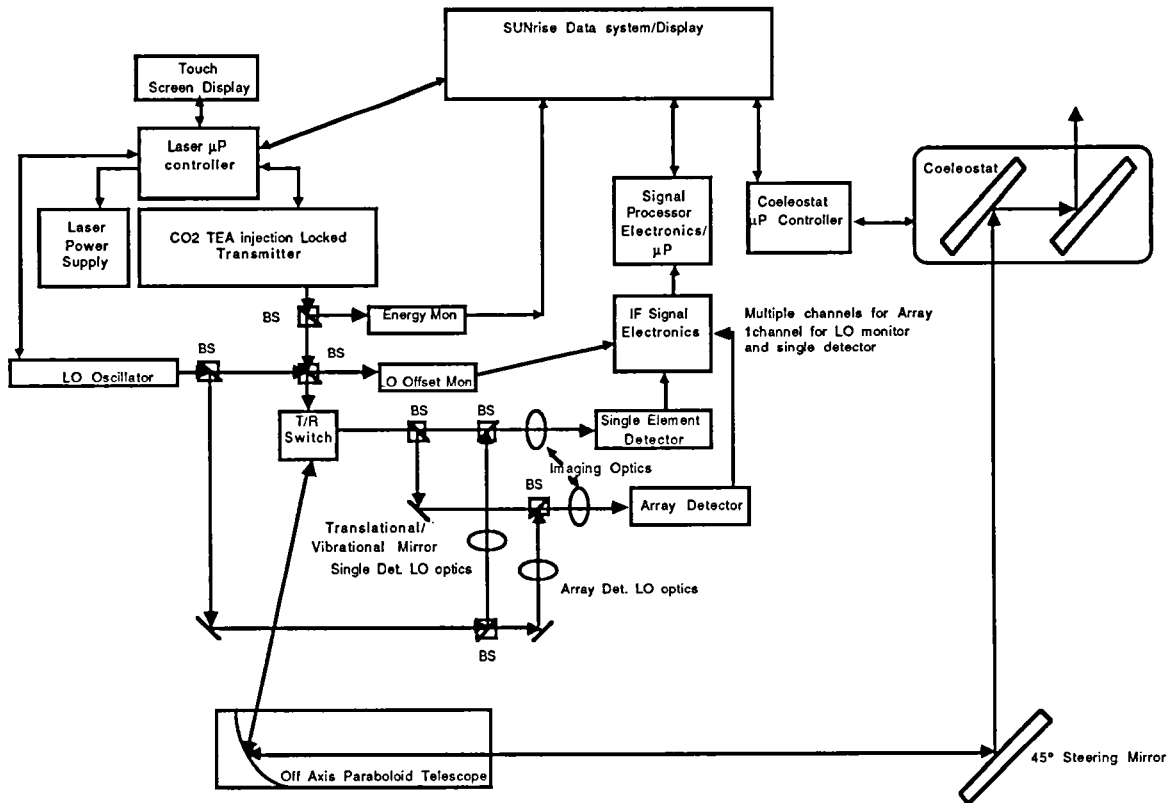


**Figure 1: Doppler Lidar Block Diagram**

**Table 1. CO<sub>2</sub> Coherent Doppler Lidar Design Parameters:**

Laser Transmitter:

Type	TEA pulsed CO <sub>2</sub> laser (STI Optronics manufacturer)
Wavelength	10.6μm (tuning range 9.2-10.9μm with grating)
Energy:	1-2J/pulse
PRF	50Hz (max)

Transceiver Optics:

Telescope-30cm dia off axis, parabolic  
 T/R- thin film polarizer and Fresnel Rhomb

Detection channels: Laser pulse diagnostics  
 single element atmospheric channel  
 multi-element atmospheric channel

Scanner:

2-axis hemispheric coverage, 30cm dia clear aperture

Data Acquisition:

SUNrise Weather Processing System (Lassen Research)  
 16 separate IF channels  
 Programmable gain control  
 Digital sampling  
 Multiprocessor architecture  
 9-track tape archive  
 Realtime data acquisition, process, display (16 channels @ 10Hz)



## e-Beam Sustained Laser Technology for

### Space-based Doppler Wind Lidar

M.J. Brown, W. Holman, R.J. Robinson, P.M. Schwarzenberger, I.M. Smith and S. Wallace

Applied Physics Division, GEC Avionics Limited, Elstree Way,  
Borehamwood, Hertfordshire, WD6 1RX, United Kingdom

M.R. Harris and D.V. Willetts

Defence Research Agency,  
RSRE, St. Andrew's Road, Malvern,  
Worcestershire, WR14 3PS, United Kingdom

S.C. Kurzius

Lockheed Missiles & Space Co. Inc.  
4800 Bradford Drive, Huntsville, Alabama, USA

#### Introduction

This paper presents an overview of GEC Avionics activities relating to Spaceborne Doppler Wind Lidar. In particular, the results of design studies into the use of an e-beam sustained CO<sub>2</sub> laser for spaceborne applications, and experimental work on a test-bed system will be discussed.

#### LAWS Laser Transmitter Phase One Study

GEC Avionics has carried out the Phase One Laser Transmitter Study for the Laser Atmospheric Wind Sounder (LAWS), under contract to Lockheed Missiles and Space Company, prime contractor for LAWS under contract to NASA. (Reference 1). Dr. D.V. Willetts and Mr. M.R. Harris of the Defence Research Agency (DRA) were consultants for the study, and Mr. I. McMillan of Matra Marconi Space (UK) acted as specialist on space aspects.

The laser requirement was originally for a 10 Joule, 10 Hertz laser with a 3 microsecond pulse width, a frequency stability of better than 200 kHz, an efficiency of 5% and a lifetime of 10<sup>9</sup> pulses. Trade studies were carried out to determine the optimum discharge technology for LAWS. Efficiency, pulse shape, gas/catalyst lifetime, and anticipated weight, size and power requirements were compared for self-sustained, pulser-sustainer, and e-beam sustained laser technology.

The study led to the selection of an e-beam sustained laser for high efficiency, good frequency control, low CO<sub>2</sub> dissociation and a top hat pulse shape. All of NASA's requirements were met with a compact lightweight design. The lifetime of the electron transmitting foil was identified as a risk area which required further study and testing.

#### Foil Lifetime Studies

A programme of work has recently been undertaken to identify the optimum foil material and foil support structure for a space-based e-beam sustained laser, and carry out accelerated foil lifetests. The work was undertaken by GEC Avionics, with DRA as consultants, under contract to Lockheed Missiles and Space Company.

In an e-beam sustained laser, the electron gun operates at near vacuum, and the laser at between half and one bar. The laser and gun are separated by a metal foil strong enough to maintain a gas seal but sufficiently thin to permit electron transmission. As each laser discharge produces a pressure pulse, it is possible for the foil to become fatigued with repeated laser pulsing, and then break, which would result in a failure of the entire laser.

A simulator has been designed and built to mimic the pressure pulse generated by the laser but operate at much greater pulse repetition frequencies. The electron transmissions of materials investigated in the simulator have also been determined in an e-beam sustained laser, over a range of operating voltages.

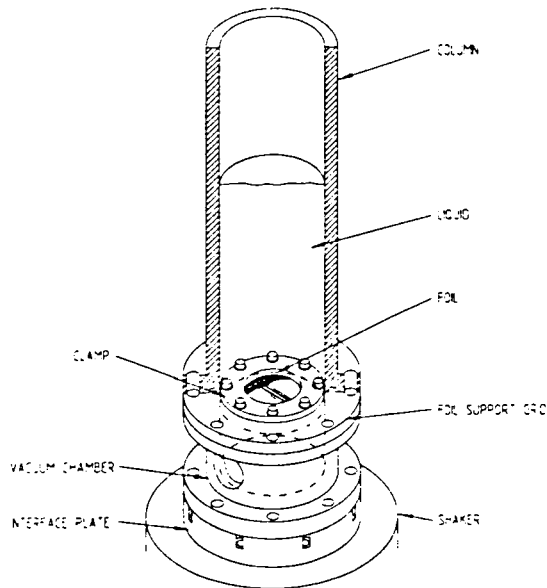


Figure 1

The equipment built is shown in Figure 1.

The simulator is mounted on a powerful vibration testing machine or "shaker", which vibrates it in a vertical direction at frequencies of up to four kilohertz. As the equipment moves upwards, so does the column of liquid contained in the upper section.

The force required to move the liquid is provided by the foil which is thus subjected to an equal and opposite reaction. This reaction constitutes the pressure pulse.

Changing the height of the liquid column or the density of the liquid changes the amplitude of the pressure pulse applied to the foil.

Initially, a very careful calibration procedure was undertaken to provide confidence in the representativeness of the simulation tests. It was found that the required pressure pulse could be accurately simulated up to a frequency of four kilohertz, which allows  $10^9$  pulse lifetests to be completed in just a few days.

Aluminium, titanium and titanium alloy foils of appropriate thicknesses for use in a laser were all lifetested using the simulator. A permanent pressure differential of one bar was maintained and pressure pulses of 0.7, 1.4 and 2.1 bar applied. These test conditions represent one, two and three times the real laser pressure pulse respectively

Aluminium foils behaved variably, some foils lasting  $10^9$  pulses, others failing at  $10^6$  pulses (Figure 2). The variation in aluminium foil lifetime, and the failures observed, are to be expected as the material is being used above its elastic limit. The titanium and titanium alloy foils, being used well below their elastic limits, both survived  $10^9$  pulses at all three test pressures, with no failures whatsoever.

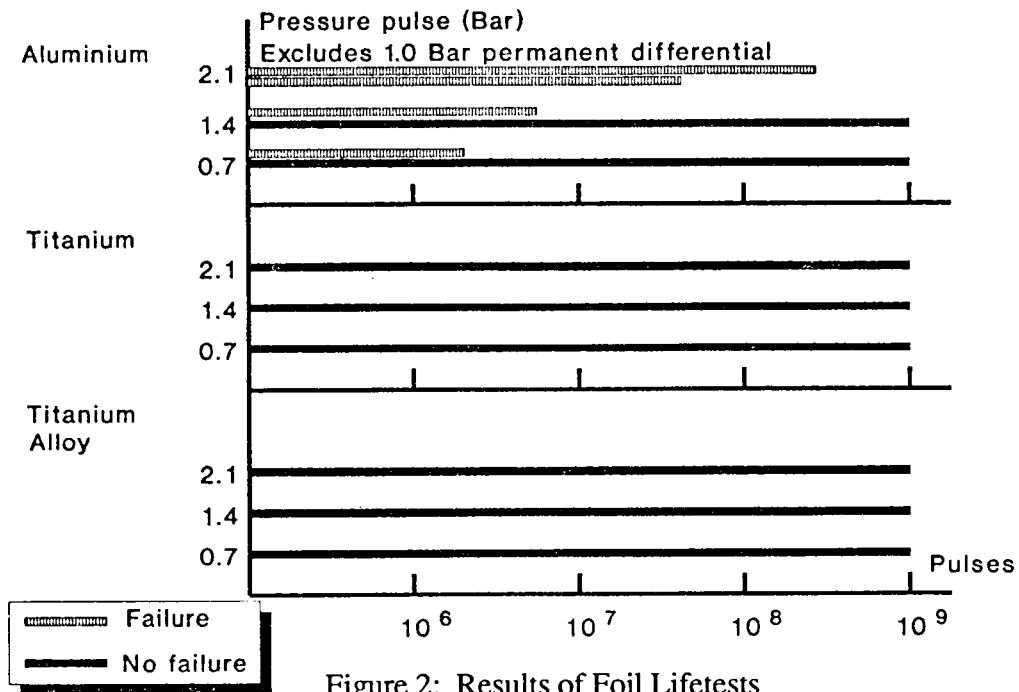


Figure 2: Results of Foil Lifetests

The fact that  $10^9$  pulse lifetimes have been routinely demonstrated, even at much higher pressure pulse levels than on the real laser, provide a high degree of confidence in designing an electron-beam sustained laser with a  $10^9$  pulse life.

#### Development of CO<sub>2</sub> Laser for Spaceborne Doppler Wind Lidar

GEC Avionics is a member of an international team carrying out a significant part of the European Space Agency programme for development of a CO<sub>2</sub> laser for Spaceborne Doppler Wind Lidar, with DRA as prime contractor, and CISE Spa and Dornier GmbH as the other sub-contractors.

The system requirements for velocity accuracy, data coverage and instrument lifetime, lead to a laser specification of 10 Joules, 10 Hertz, a 5 microsecond pulse width, frequency stability of 200 kHz, an efficiency of 5% and a lifetime of  $10^9$  pulses. The eventual wavelength will be 9.11 μm, obtained with <sup>12</sup>C <sup>18</sup>O<sub>2</sub> but during the current programme, a wavelength of 9.25 μm will be demonstrated using <sup>12</sup>C <sup>16</sup>O<sub>2</sub>.

During earlier phases of the project, an e-beam sustained laser concept was selected, with a novel DRA designed compact electron gun. The present programme is of three years' duration, starting in July 1991. Experiments with existing equipment, critical component analysis, and the laser, electron gun and resonator design, are being carried out in the first year, construction of equipment in the second year, and test in the third year.

GEC Avionics' role is to undertake validation experiments using an existing e-beam sustained laser, and to design a compact breadboard laser, working closely with DRA who are also designing the electron gun, and CISE, who are designing the optical resonator. GEC Avionics will then procure components and assemble the laser, integrate with the DRA built electron gun, and carry out test and analysis, including frequency stability measurements and monitoring of output characteristics over a period of extended operation.

One particularly promising area being explored is that of homogeneous catalysis (Reference 2). DRA have recently discovered an effect present in e-beam sustained lasers in which the primary electron beam from the electron gun directly oxidises CO to CO<sub>2</sub>, under correct conditions. It may therefore be possible to dispense with a solid catalyst altogether, with significant advantages of no flow impedance, no particulate shedding, no additional mass, lower cost, and elimination of isotopic scrambling. Even if solid catalyst is required, it will be a very much smaller quantity than that needed for an equivalent self-sustained laser.

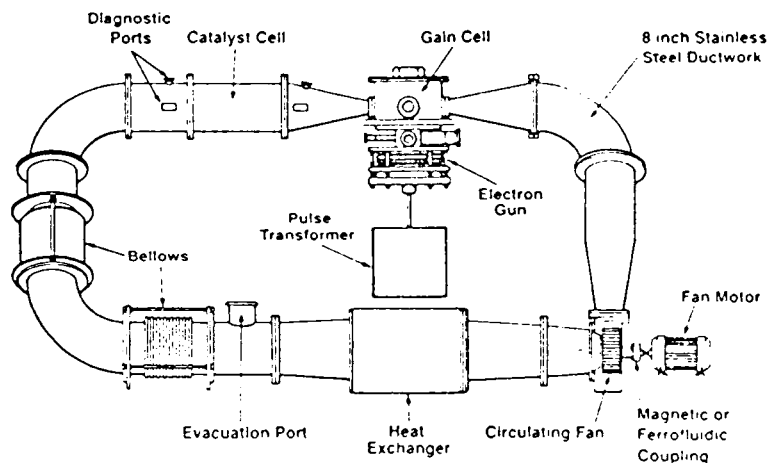


Figure 3: Test Bed Schematic

The experimental work GEC Avionics is undertaking includes using an existing sealed e-beam sustained test bed (Figure 3) and carrying out long sealed lifetests to determine the effectiveness of gas phase catalysis over periods of 10<sup>7</sup> pulses. Work to date has included modification of the system to provide a 5 microsecond pulse and the installation of optics mounts for resonator experiments. Initial sealed runs have also been undertaken.

GEC Avionics has now completed a compact laser design, working closely with DRA. As well as laser performance, particular attention has been paid to the severe vibration requirements, thermal and gas flow aspects.

### Conclusion

In the LAWS Phase One Study, it has been shown that the e-beam sustained laser has many advantages for Spaceborne Doppler Wind Lidar, but foil lifetime was identified as a risk area. The Lockheed funded programme addressed this risk area and foil lifetimes of 10<sup>9</sup> pulses were routinely demonstrated. In the European Space Agency programme, the potential for gas phase catalysis is being explored and GEC Avionics' experimental programme is well under way.

Finally, a compact, rugged, e-beam sustained laser breadboard has been designed, which will soon be constructed and tested.

### References

1. Lockheed Phase One LAWS Study, Contract NAS 8-37590, DR-19, Final Study Report, April 1990
2. Homogeneous Catalysis for CO<sub>2</sub> Lasers, D.V. Willetts and M.R. Harris OSA 1991 Technical Digest Series Volume 12

## The Lidar In-Space Technology Experiment (LITE)

M. Patrick McCormick  
Atmospheric Sciences Division  
NASA Langley Research Center  
Hampton, Virginia

The Lidar In-Space Technology Experiment (LITE) is being developed by NASA Langley Research Center for a series of flights on the Space Shuttle. Using a doubled and tripled Nd:YAG laser, an approximately 1-meter diameter telescope, and a modular design, the system will be used to study clouds, tropospheric and stratospheric aerosols, characteristics of the planetary boundary layer, stratospheric density and temperature perturbations, and to some degree, surface albedo and topography. The greatly improved resolution of LITE with respect to passive sensors is expected to provide a new and unique data set on the global distribution and optical properties of clouds and aerosols and, therefore, their radiative and chemical effects. In addition, this data set will be useful in validating and improving retrieval algorithms currently in use. Similarly, the ability to accurately locate the top of the planetary boundary layer will aid in global climate model (GCM) parameterizations of flux transport between the oceans and the atmosphere. Measurements of density perturbations in the middle stratosphere will provide a greatly improved glimpse of the global dynamics of this region compared to that given by current spaceborne sensors. A science steering group has been formed (Table 1) which is directing the scientific applications of the experiment.

The primary goals of LITE are to demonstrate the maturity of space-based lidar technology, to provide some unique measurements, and to provide a platform for the development of technology for future space-based systems. LITE is currently scheduled to fly on the Shuttle in early 1994. Approval has recently been given for the first of several planned follow-on missions at 2-year intervals. The first mission will be used to develop experience in operating a lidar system in a space environment and to evaluate the sensitivity of the instrument for performing scientific studies. The second mission will focus on scientific studies of clouds, aerosols, and the middle atmosphere. On subsequent follow-on missions LITE will be used as a test bed for demonstrating more advanced measurement capabilities.

### Instrument Description and Operational Scenario

The LITE instrument has been discussed in detail by Couch et al. [1991] and Winker [1992]. The LITE system consists of a laser transmitter module, a receiving telescope, receiving optics and electronics, and associated control electronics. A time lapse camera will be used to make a visual record of the Shuttle ground track over the sunlit side of the Earth. These sub-assemblies are all mounted to a spacelab pallet which will be carried in the cargo bay of the Space Shuttle.

The transmitter consists of two identical flashlamp-pumped Q-switched Neodymium-YAG lasers. Each laser generates greater than 1.0 J per pulse at the fundamental wavelength of 1064 nm at a 10-Hz rate although power limitations prevent simultaneous operation of both lasers. Doubling and tripling crystals are used to provide 0.46 J and 0.20 J energy at 532 nm and 355 nm, respectively. Approximately 0.49 J remains at the fundamental wavelength. This laser was developed specifically for the LITE experiment and will represent the first time such a powerful laser has been operated in a space environment. These and other instrument parameters are shown in Table 2.

The receiving telescope was originally built for the NASA Orbiting Astronomical Observatory (OAO) spacecraft and was the prototype for the Goddard Experiment Package of the OAO. The refurbished telescope is a Ritchey-Chretien Cassegrain design with a 38-inch diameter primary mirror. Laser light backscattered by the atmosphere is collected by the telescope and focused through a variable field stop onto two photomultipliers for the 532-nm and 355-nm channels and

an avalanche photodiode for the 1064-nm channel. A portion of the return is reflected to a quadrant detector, allowing transmitter boresight alignment to be done in orbit using a gimballed steering mirror. The lidar return signals are amplified, digitized, stored on tape, and sent to the ground using a high-speed data link. The instrument is commanded from the ground over a low-rate data link.

The first flight of LITE is scheduled for a standard  $28.5^\circ$ , 160 nautical mile (296 km) orbit taking data for 40 hours during a 7-day mission. After verifying nominal system operations, nighttime observations will be conducted in conjunction with correlative measurements. This will be followed by daytime operations and performance verification, and then routine observations.

#### Science Investigations and Simulations

LITE has been designed to study species and phenomena of the lower and middle atmosphere. Additionally, returns from the land and ocean surfaces will be recorded and evaluated for use in determining atmospheric column optical depth and sea surface wind speed. Future missions will address additional objectives such as measurements of mesospheric dynamics or tropospheric water vapor. The science steering group is involved in developing retrieval techniques and operational modes for the various LITE measurements. In addition, they are developing the correlative measurements program for validating the LITE data products, and performing sensitivity analyses for these products. A representative set of simulated signal profiles shown as a function of altitude above the Earth's surface is given in Figure 1. In the absence of clouds, the backscattered signal amplitude will generally increase down to the surface of the Earth, from which a very strong return will be received. The stratospheric aerosol model used in this simulation is an estimate of the state of the stratosphere in 1994. The range of surface return strengths is indicated, as well as the effect of a layer representing the optical characteristics of Saharan dust in the mid-troposphere. The pulse will penetrate most cirrus clouds allowing the atmosphere and other cloud layers beneath to be probed.

The signal-to-noise ratio of the return varies by many orders of magnitude between the stratosphere and the Earth's surface, and will cause the error in the determination of the scientific parameters from a single lidar profile to vary from a few percent to hundreds of percent. Clouds can be detected with a single lidar return, while the measurement of stratospheric aerosol requires averaging several hundred shots to achieve the required accuracy. The inherent high vertical and spatial resolution of the lidar technique provides higher resolution data than available from current passive techniques in nearly all cases. As an example, Table 3 shows the number of laser shots required to detect and determine the altitude of subvisible cirrus, dense cirrus, Saharan dust, and the top of the planetary boundary layer. Multiplying the number of shots by 0.8 km gives the horizontal resolution obtainable. These simulations indicate LITE will be capable of sensing most cirrus on a single-shot basis, allowing the location of even subvisible cirrus to 40 m in the vertical with horizontal resolution of 1 km at night and 5 km during the day.

#### Future

A  $57^\circ$  inclination orbit is planned for the first LITE reflight which will provide mid-latitude coverage and allow study of the transport of aerosol from the Tropics to mid-latitudes and of the differences in radiative characteristics of tropical and mid-latitude clouds. The modular design approach of LITE allows individual components to be upgraded as desired. Present capabilities may be enhanced and additional capabilities added by upgrading one or more modules. For example, the receiver could be modified to provide better daytime performance or allow depolarization measurements of cloud returns. New laser sources can be added to address new science objectives. A tunable laser based on Alexandrite or Ti-Sapphire would allow LITE to perform DIAL measurements of water vapor or other trace species. Incorporation of a source at 589 nm would allow resonance fluorescence measurements of mesospheric atomic sodium, which is an excellent tracer of wave effects in the mesopause region. LITE will provide a test bed for

development of the technology necessary for the ultimate goal of a free-flying lidar system in polar orbit, able to measure clouds, aerosols, gases, and temperature on a global basis.

References

Couch, R. H., C. W. Rowland, K. S. Ellis, M. P. Blythe, C. R. Regan, M. R. Koch, C. W. Antill, J. W. Cox, J. F. DeLorme, S. K. Crockett, R. W. Remus, J. C. Casas, and W. H. Hunt, Lidar In-Space Technology Experiment: NASA's First In-Space Lidar System for Atmospheric Research, *Opt. Engin.*, **30**, 88-95, 1991.  
 Winker, D. M., Atmospheric Sounding With the Lidar In-Space Technology Experiment (LITE), Proceedings of Lasers '91, December 9-13, 1991, San Diego, CA, 1992.

<i>TABLE 1. Science Steering Group Membership</i>	
Dr. John Theon, Chairman	NASA Headquarters
Dr. M. P. McCormick, Project Scientist	NASA Langley Research Center
Dr. D. M. Winker, Deputy Project Scientist	NASA Langley Research Center
Dr. Edward V. Browell	NASA Langley Research Center
Dr. James Coakley	Oregon State University
Dr. C. S. Gardner	University of Illinois
Dr. R. M. Hoff	Atmospheric Environment Service (Canada)
Dr. G. S. Kent	Science and Technology Corporation
Dr. S. H. Melfi	NASA Goddard Space Flight Center
Dr. R. T. Menzies	Jet Propulsion Laboratory
Dr. C. M. R. Platt	CSIRO (Australia)
Dr. David Randall	Colorado State University
Dr. John Reagan	University of Arizona

<i>TABLE 2. LITE Instrument Parameters</i>			
Output wavelength (nm)	1064	532	355
Output energy (mJ)	486	460	196
Laser pulse length (ns)	27	27	31
Beam divergence (mr)	0.9	0.6	0.6
Detector QE	33	14	21
Field-of-view	Selectable: 1.1 mr, 3.5 mr, and opaque		
Sampling interval (m)	15		
Primary mirror diameter (m)	0.985		

**TABLE 3. Aerosol detectability - number of shots required for 95% detection probability with 40-meter vertical resolution. Surface albedo = 0.1 except for dense cirrus, where albedo = 0.8.**

	Top Height (km)	Layer Thickness (km)	1.064 $\mu\text{m}$		0.532 $\mu\text{m}$		0.355 $\mu\text{m}$	
			night	day	night	day	night	day
Boundary Layer	0.6	0.6	1	6	1	55	224	>1000
Saharan Dust	6	2	1	1	1	3	5	>1000
Subvisible Cirrus	10	.03	1	1	1	4	1	286
Dense Cirrus	10	.03	1	1	1	1	1	3

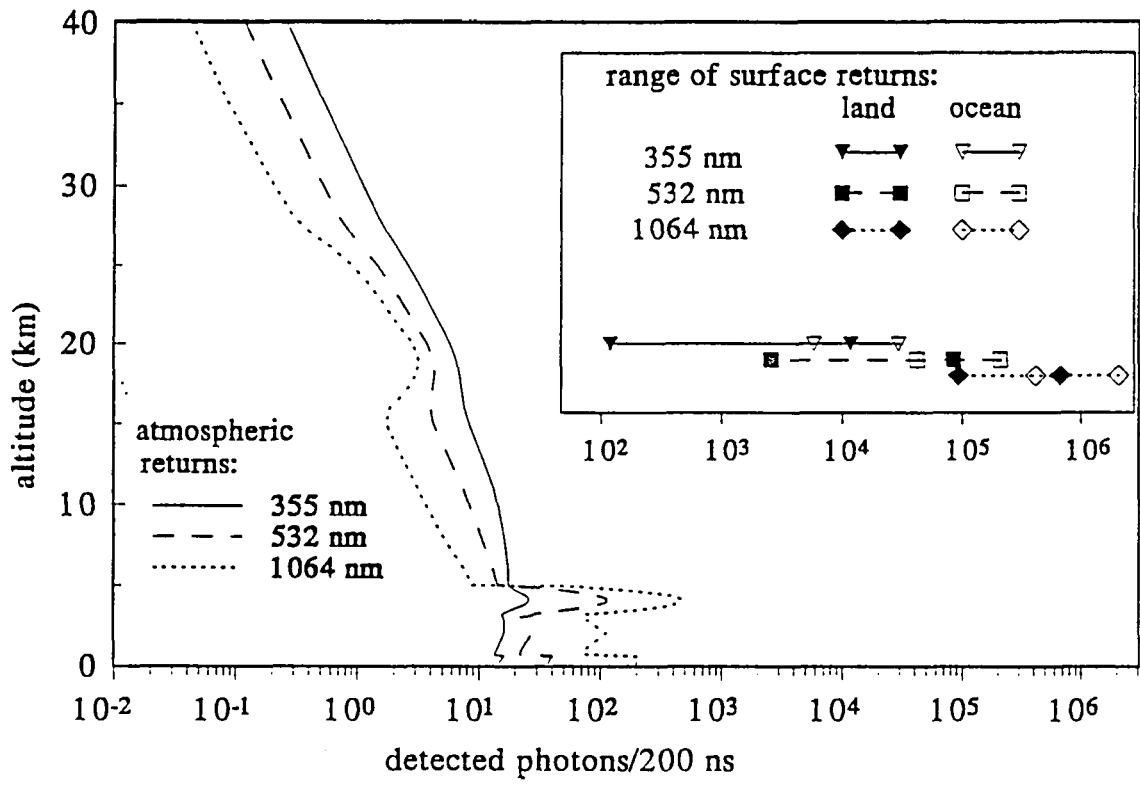


**FIGURE 1. Simulation showing the LITE atmospheric return signal and the range of returns expected from land and ocean surfaces in terms of the number of photons detected per system time constant.**

## System Testing and Performance Characterization of the LITE Laser Transmitter Module at NASA

Marc C. Cimolino, Mulugeta Petros  
Science and Technology Corporation  
Hampton, VA 23666

The Laser Transmitter Module (LTM) is a three-color Q-switched flashlamp-pumped Nd:YAG laser. The original design concept was to package commercially available optics and flashlamp electronics for space flight with a power consumption goal of 2200W and a weight goal of 600 lbs. The optical output was to exceed 200 mJ of IR, 400 mJ of green and 150 mJ of UV per pulse at 10Hz. Although a laboratory test laser which implemented the flight architecture exceeded the optical output requirements, space qualification required: extensive new design of optical hardware mounts, optical bench, structural frames and a canister; and thermo-mechano-optical analysis for the space shuttle environment presented by Joe et al. [1992]. The commercial electronics are space qualified by upgrading components to high reliability levels that meet stringent shuttle flight requirements. The new space qualified laser (see Figure 1) exceeds the optical output requirements by 188%, 50%, 13% in the IR, green and UV respectively (see Table 1). This output needs only 1500W at a weight of only 500 lbs.

Optical, electrical, and thermal systems are all integrated inside the canister. Only the Freon heat exchanger is external (Figure 1). There is a forced air flow common to the optics and electronics. This will thermally equilibrate the structure in space as well as on earth. This approach required careful attention to contamination control. A space qualified conformal coating was used on all circuit boards only after testing with the optics.

The successful integration and testing of the LTM optical system was facilitated by the grouping of optical functions into discrete subassemblies as illustrated in Figure 2.

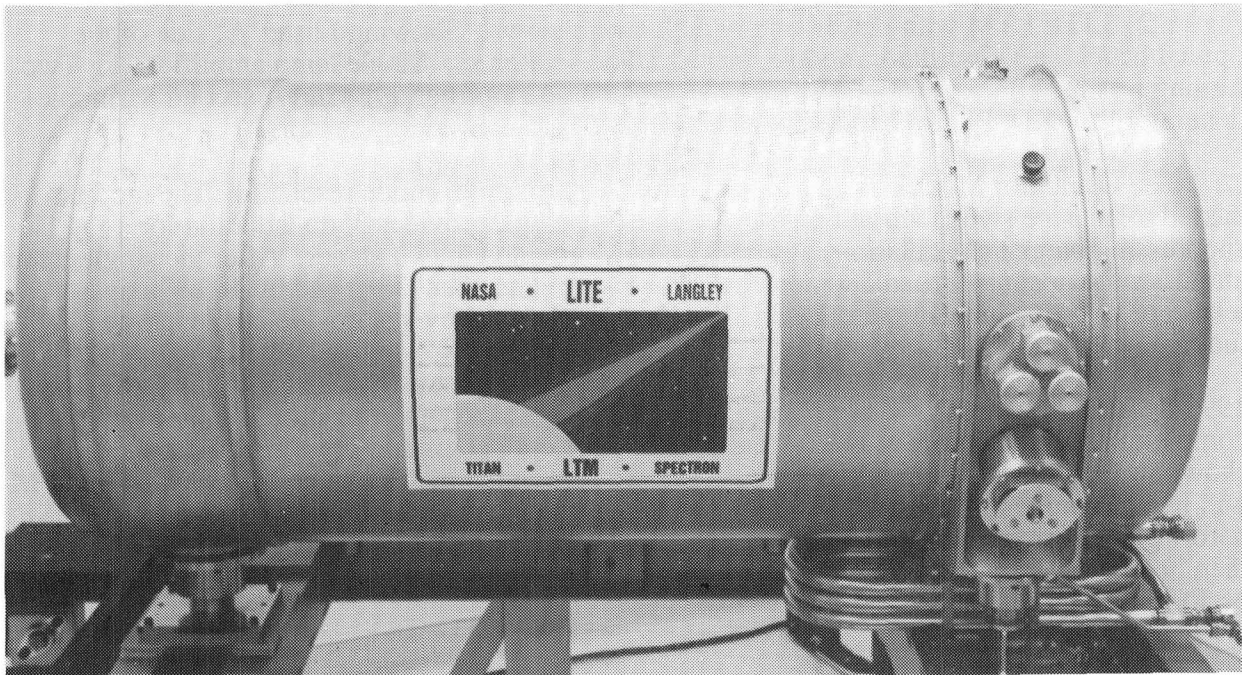


Figure 1. The LITE LTM in the cleanroom at Titan/Spectron Division. The water/Freon 114 heat exchanger is coiled beneath the interface ring and between the rear blade mounts. The triply redundant pressure relief and vacuum breaker valves are seen attached to the interface ring. The front (left) and rear welded aluminum canisters are bolted to the interface ring and o-ring sealed.

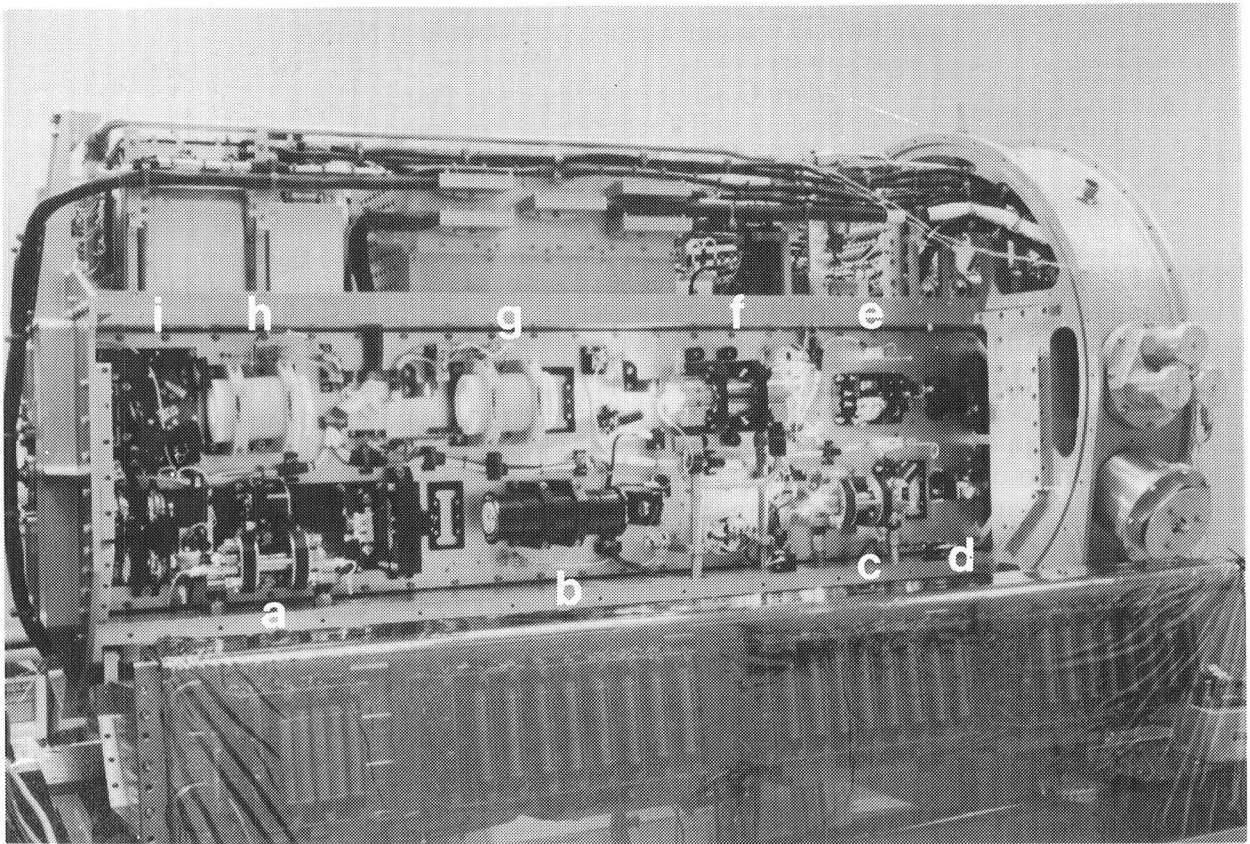


Figure 2. LITE LTM with power supply rack swung down. Showing Laser 'A' side of the optical bench: a.) Oscillator module, b.) Faraday isolator, c.) Single lamp amplifier, d.) Two turning prisms, e.) expansion telescope, f.) Dual lamp amplifier, g.) CD\*A second harmonic generator, h.) KD\*P third harmonic generator, and i.) Laser energy sensors.

The Oscillator Module is an efficient crossed-porro multi-mode resonator. The module passed a 10g sine sweep vibration test. A Faraday isolator provides 35db isolation for suppressing parasitic oscillation. Amplification is provided in two stages. After the single lamp amplifier the beam is turned 180 degrees using two prisms, then expanded by an off-axis telescope into the dual lamp amplifier. The harmonic crystal ovens provide stable harmonic tuning.

The LTM was delivered to NASA Langley Research Center (NASA LaRC) in December 1991 by Titan/Spectron Division, Costa Mesa, CA. Optical characterization is now being completed in a clean room at NASA LaRC, using the optical ground support equipment (GSE) shown in Figure 3. Design of the optical GSE was presented by Chang et al. [1991]. The LTM will be environmentally tested as required for shuttle launch as a module, using the optical GSE before and after vibration and thermal tests to evaluate any performance changes. The LTM will then be integrated with the instrument for full scale system tests, using only internal sensors as performance monitors.

The baseline optical performance, on arrival at NASA is summarized in Table 1 for the primary 'A' laser.

Table 1: LTM Baseline Optical Performance vs. Design						
		Output Energy (mJ)	Energy Stability	Pulse Width (W)	Beam Divergence	Pointing Stability
Design	1064	>200	>90%	<100ns	.5 to 1.5mrad	<+/- .25mrad all three colors
	532	>400	within 5%	<100ns	.5 to 1.5mrad	
	355	>150	of average	<100ns	.5 to 1.5mrad	
Baseline	1064	550	>99%	30ns	1.7mrad	<+/- .05mrad each color <.1mrad/532
	532	600	within 5%	20ns	1.0mrad	
	355	170	of average	16ns	.9mrad	

The pointing stability of each color is well below the specification of <+/- .25 mrad. The energy centroid offset of 1064 and 355nm beams are each less than .1mrad from 532nm, allowing for a smaller field stop aperture to be implemented for daytime operation. The performance for the final settings of laser 'A' and 'B' will be presented along with the results of completed environmental tests. The output energy, energy stability, beam divergence, and pointing stability, all interact to establish the lidar signal level and statistical fluctuations given a particular field stop aperture in the receiver.

Three color encircled energy data from the far field imaging CCD camera is analyzed using a synthetic aperture centered on the 532nm beam since this is the wavelength used by the boresight mechanism to aim the laser in the telescope field of view.

References:

Joe, E. J.; Chang, J. H. "Space Qualified Three Color Solid State Lidar", Proceedings SPIE No. 1633, Los Angeles, CA, January 19-25, 1992.

Chang, J.; Cimolino, M.; Petros, M. "Characterization of the Shuttle Flight Qualified NASA LITE LTM Three Color Nd:YAG Output Beams", IEEE/Summer Topicals, Newport Beach, CA, July 1991.

Acknowledgements:

The authors were with Titan/Spectron Division through shipment of the LTM. We would like to acknowledge the essential contributions of each member of the team which created the LTM: John Chang, Karl Reithmaier, Edmond Joe, Suzanne Lenahan, Joan Smith, Ray Thompson, Ron Villane, David Rothman, Pravin Mehta, Ray Hayashi, and Art Kittle.

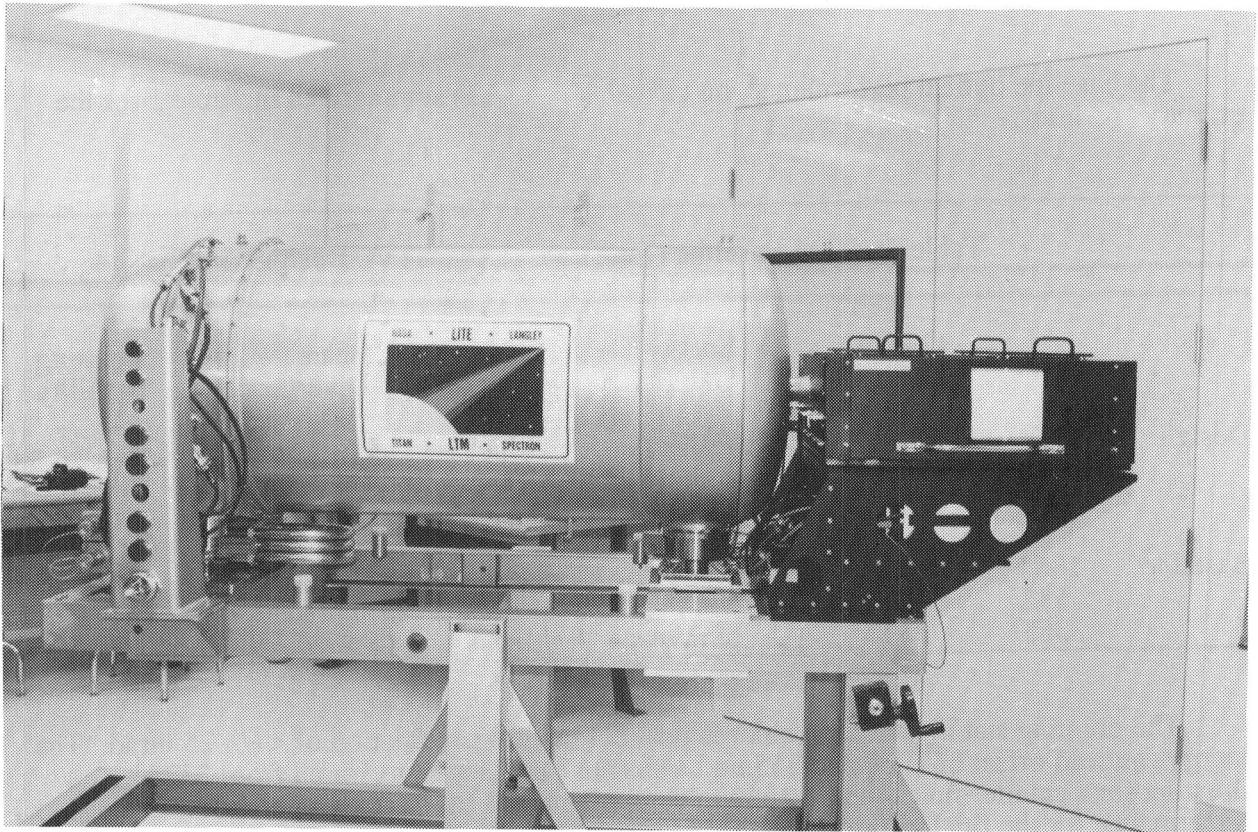


Figure 3. The LITE LTM on the assembly jig, which will be used during environmental testing. The optical GSE housed in the black enclosure to the right contains the power meters and CCD camera diagnostics mounted to a 2 foot square breadboard.

# Mechanical and Thermal Issues in the Development of a Spaceborne Lidar System

Joseph F. DeLorme  
LITE Technical Project Engineer  
NASA Langley Research Center

The Lidar In-space Technology Experiment (LITE) is being developed by NASA's Langley Research Center (LaRC) to conduct spaceborne remote sensing of the Earth's atmosphere from the Space Shuttle. LITE is currently manifested as the primary payload on STS-63 to be launched in February 1994. This paper will address some of the key mechanical and thermal issues in the design and development of this spaceborne lidar system.

LITE (figure 1) incorporates a modular design capable of multiple flights, and is intended to serve as a testbed for evolving lidar technologies. The instrument consists of 8 major subsystems; Receiver System; Laser Transmitter Module; Boresight System; System Electronics; Camera System; Orthogrid System; Active Thermal Control System; and OASIS-I. To reduce cost and maximize reliability, proven technology and "off-the-shelf" components are used wherever possible. A good example of this is the Receiver System which consists of a one-meter diameter Cassegrain telescope, telescope support structure, and aft optics assembly (figures 2 & 3). The telescope was originally built as the engineering prototype for the Orbiting Astronomical Observatory in the mid 1960's. It has been completely disassembled, refurbished and reassembled for flight at a cost of approximately \$500,000. The cost of developing a new telescope of this size has been estimated at over \$6 million.

The Laser Transmitter Module (LTM) consists of two, flashlamp-pumped, Q-switched Nd:YAG lasers with a fundamental output at 1064 nm. Each laser is frequency doubled and tripled to provide energies per pulse of 200 mJ at 1064 nm, 400 mJ at 532 nm, and 150 mJ at 1064 nm, with a pulse width of 20 ns and pulse repetition rate of 10 Hz. The LTM was designed and built by Titan-Spectron Development Laboratories, in Costa Mesa, CA.

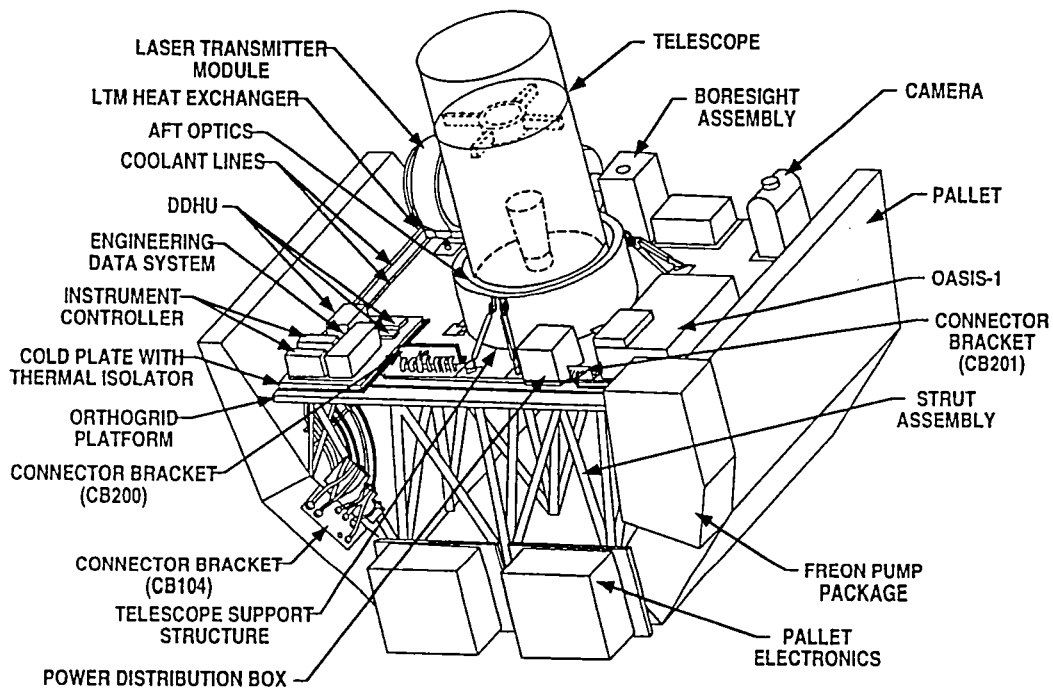


Figure 1: Lidar In-space Technology Experiment (LITE)

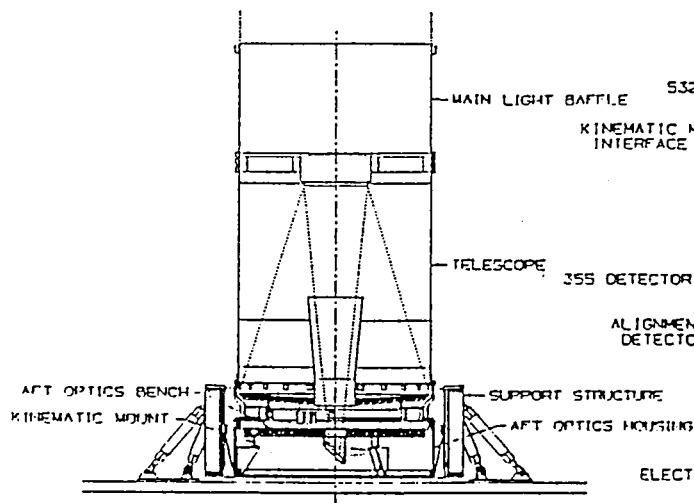


Figure 2: Receiver System

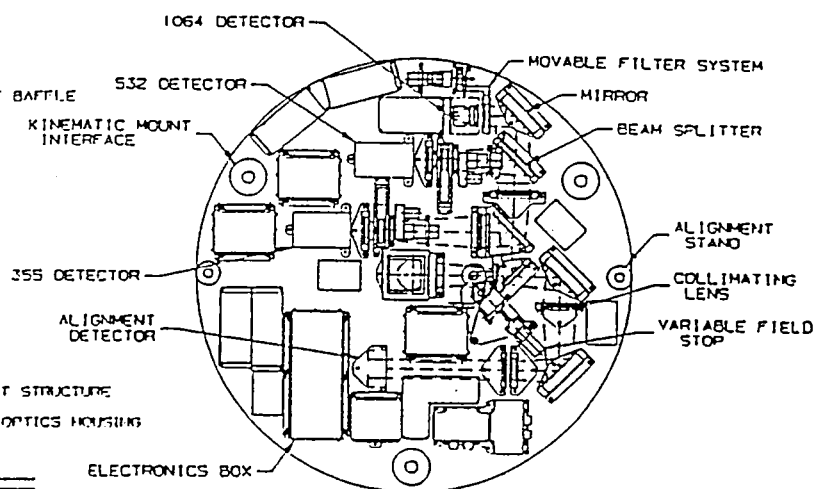


Figure 3: Aft Optics Layout

The Boresight System is a two-axis gimballed system that redirects the LTM beam 90° from the output axis and maintains alignment, within 50 microradians, with the Receiver System optical axis by steering the redirected beam. The Boresight System utilizes a closed-loop feedback control system to maintain alignment based on the location of the backscattered signal as measured by a quadrant detector located in the aft optics.

The System Electronics provide the command, control and data handling capability for the instrument. The Camera System will provide daytime correlative photographs of cloud cover and ground tracks for science data analysis. The Active Thermal Control System (ATCS) provides Freon coolant to the LTM and the cold plate-mounted System Electronics.

The Orthogrid System is the main support structure for the instrument and is the mounting platform for all other subsystems. The orthogrid is a flight-proven design developed by Marshall Space Flight Center (MSFC) and consists of a 110 x 132 x 2.1 inch thick aluminum plate in which 480 square cells have been machined to form a grid pattern. This orthogrid platform is supported by 52 struts, which are hollow aluminum tubes with clevises at each end. The struts attach to the orthogrid platform and pallet through hardpoints. Each of the hardpoints, 20 on the pallet and 25 on the orthogrid, are machined aluminum and are unique to their location. The orthogrid system provides the maximum amount of area to locate subsystems while reducing weight and evenly distributing loads to the pallet. The pallet is the Enhanced Multiplexer-Demultiplexer Pallet (EMP). It is a general purpose experiment carrier developed and flown for the Spacelab Program and is being provided by MSFC as flight certified hardware. The pallet is a U-shaped aluminum shell, four meters wide by three meters long, and is attached to the STS through four titanium trunnions and one keel fitting. The EMP provides avionics and Freon cooling capabilities to the instrument.

The first flight of LITE is intended primarily as a technology demonstration of lidar operations in space, and to that end, a significant amount of engineering data is to be obtained. Two systems are to be utilized to collect this data. The Orbiter experiments Autonomous Supporting Instrumentation System I (OASIS-I) is a stand-alone payload bay environmental data acquisition and storage device provided by NASA Johnson Space Center (JSC). OASIS-I collects data from 99 sensors distributed among the LITE subsystems, getting information on accelerations, temperatures, pressures, strains, acoustic levels, and solar flux levels. OASIS-I operates continuously during STS launch, ascent to orbit, descent from orbit, and landing. The system operates periodically on orbit as well. The Engineering Data System, part of the System Electronics, collects engineering data continuously on orbit, monitoring instrument health and status from 205 different sensor locations.

Future reflights of LITE will incorporate technology upgrades, possibly including photon

counting detectors, diode pumped lasers, or a Differential Absorption Lidar (DIAL) System utilizing a Ti:Sapphire laser.

The single most important mechanical/thermal issue in the design of LITE is the survivability and alignment stability of the optical systems, specifically the LTM and Receiver. Rugged, adjustable and lockable optical mounts are used in both the LTM and Receiver Aft Optics. All laser and aft optics components are mounted to aluminum, honeycomb-cored optical benches. Both benches are kinematically mounted to their respective support structures. The kinematic mounts allow the benches to expand or contract due to temperature changes without inducing significant thermal deformations in the bench mounting plane which could degrade alignment. Kinematic mounts are also used to mount the entire LTM to the Orthogrid in order to keep thermal deformation of the orthogrid mounting plane from affecting laser alignment. Flexible tangent bars are used to attach the telescope's 38 inch beryllium primary mirror to its support ring, allowing the support ring to thermally expand and contract without inducing significant stresses into the primary mirror that could affect its optical figure. Flexbeams are also used in the Receiver to attach the telescope/aft optics to the telescope support structure (ref. fig. 2). The flexbeams are like kinematic mounts in that they allow the telescope to expand or contract without inducing thermal deformations that could affect aft optics alignment, as well as distributing launch loads evenly around the telescope shell.

To further reduce the potential for misalignment of the instrument on orbit, both active and passive thermal control are utilized. The LTM lasers are enclosed within a pressurized canister filled with nitrogen at 16 psia. Nitrogen is used instead of air to eliminate the possibility of combustion, a manned space flight safety concern. Fans circulate the nitrogen to provide convection cooling of electronics and to form an evenly distributed temperature profile within the system. Two heat exchangers are used in the LTM. An external heat exchanger ties into the LITE ATCS Freon loop to cool deionized water that is, in turn, used to cool the laser oscillator, amplifiers, and cold plate mounted electronics. This water also ties into an internal water-to-air heat exchanger to cool the nitrogen that is circulated by the fans. An annular strip heater is used on the back of the aft optics bench to stabilize the bench temperature during operation and to provide survival heating during periods of non-operational orbiter deep space attitudes. Passive thermal control is achieved through the use of thermal blankets over all subsystems and thermal isolators between each subsystem and the orthogrid.

Another factor to be considered in addressing the issue of alignment stability is the effect of zero gravity. Alignment of optical components has been done on the ground with both the LTM and Receiver optical benches oriented vertically, along each bench's stiff axis, to minimize 1-g sag. Alignment of the telescope mirrors to each other and to the aft optics bench was done with the Receiver in the horizontal orientation due to facility limitations at LaRC. A V-block fixture was utilized to support the telescope during these alignments, and an analysis was performed that predicted secondary mirror decenter due to gravity effects to be on the order of .001 inches, which is acceptable.

Deflection of the entire orthogrid due to thermal changes and zero gravity effects is compensated through the passive thermal control methods mentioned previously and actively through the operation of the Boresight System, which steers the outgoing laser beam to maintain alignment of the beam with the Receiver optical axis.

The second essential mechanical/thermal issue in the development of LITE is space qualification. In order to assure mission success, i.e., the successful operation of a lidar system in space, as well as to assure safe operation as part of a manned space system, an extensive space qualification program has been developed for LITE. Proper selection of materials, contamination control, static and dynamic structural analyses, fracture analysis, hardware screening, and safety analyses and reviews are all ongoing to assure system safety and reliability.

The most important phase of space qualification is the hardware testing program. The LITE project is currently in the subsystem testing and integration phase at LaRC. Static load testing has been conducted on all 52 Orthogrid struts, 2 hardpoints and a representative Orthogrid

panel section, and is being conducted on the Receiver telescope support structure. Environmental testing on components and subsystems is ongoing. Random and sinusoidal vibration tests are being performed to simulate STS launch and landing environments. Thermal/vacuum testing is being conducted to simulate the space environment. Electromagnetic Interference and Electromagnetic compatibility (EMI/EMC) tests are also being performed. Instrument level thermal/vacuum and EMI/EMC testing is to be conducted at Goddard Space Flight Center, utilizing their capabilities to test large spacecraft, prior to delivery of the instrument to Kennedy Space Center for integration with the Shuttle.

All analytical computer models are required by JSC to be test verified. To comply with this requirement a Load Path Verification Test was conducted on the complete Orthogrid system to test verify the static math model of the Orthogrid System. A number of modal surveys are being performed on flight hardware to measure vibrational natural frequencies and mode shapes and then to correlate the analytical dynamic math models to the test results. A modal survey has been conducted on the entire instrument (figure 4) including the flight Orthogrid System and Pallet and flight telescope support structure with mass simulators of the Telescope/Aft Optics and LTM that duplicate the weight, center of gravity, and dynamics of those subsystems. Simple boxes simulating the weight, center of gravity and mounting footprint were used for the Boresight, Camera, OASIS and Electronics. The entire pallet was suspended from its 4 trunnions through airbags to an overhead A-frame support to simulate a free boundary condition for the modal test. A clean tent was constructed to maintain cleanliness of the flight hardware. This test was performed at MSFC utilizing their capabilities to perform large scale modal testing.

In summary, key mechanical and thermal issues in the development of the LITE instrument, including alignment stability and space qualification, are being addressed at LaRC, with the support of four other NASA centers, and the project is on schedule for a 1994 first flight.

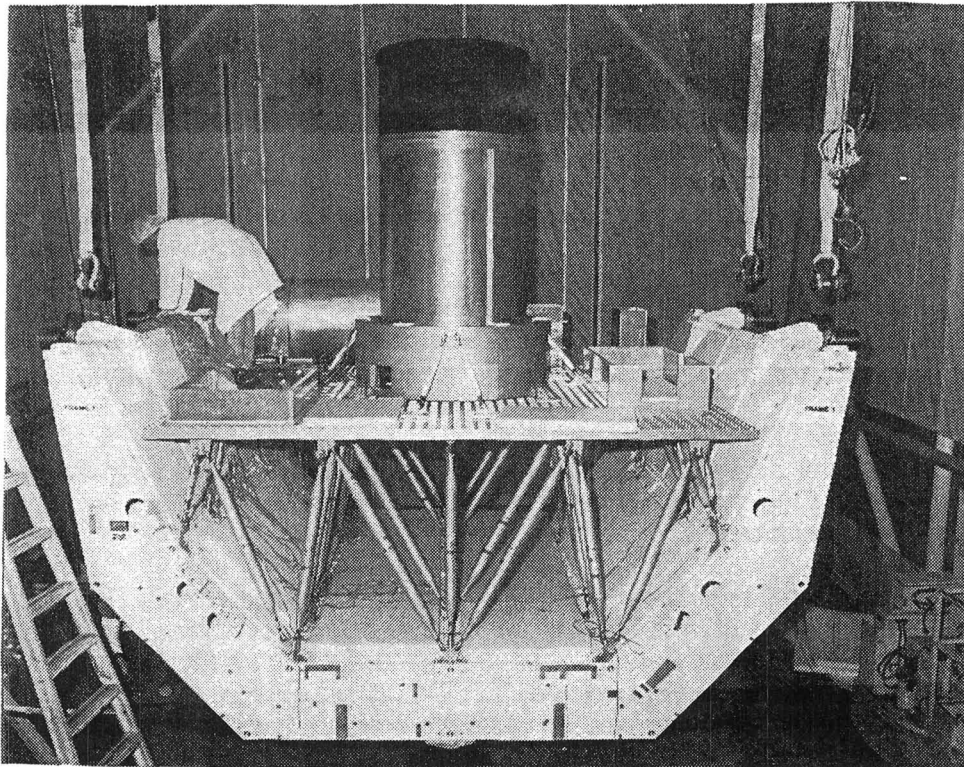


**Figure 4: Instrument Modal Testing**

# LIDAR MEASUREMENTS OF AEROSOL AND OZONE DISTRIBUTIONS DURING THE 1992 AIRBORNE ARCTIC STRATOSPHERIC EXPEDITION

E. V. Browell, C. F. Butler<sup>1</sup>, M. A. Fenn<sup>1</sup>, W. B. Grant, and A. F. Carter

Atmospheric Sciences Division  
NASA Langley Research Center  
Hampton, Virginia 23665-5225  
U. S. A.

The NASA Langley airborne lidar system was operated from the NASA Ames DC-8 aircraft during the 1992 Airborne Arctic Stratospheric Expedition (AASE-II) to investigate the distribution of stratospheric aerosols and ozone (O<sub>3</sub>) across the Arctic vortex from January to March 1992. Monthly flights were made across the Arctic vortex from Anchorage, Alaska, to Stavanger, Norway, and then back to Bangor, Maine, and additional round-trip flights north into the vortex were made each month from either Stavanger or Bangor depending on the location of the vortex that month.

The airborne lidar system uses the differential absorption lidar (DIAL) technique at laser wavelengths of 301.5 and 310.8 nm to measure O<sub>3</sub> profiles above the DC-8 over the 12-25 km altitude range. Lidar measurements of aerosol backscatter and depolarization profiles over the 12-30 km altitude range are made simultaneously with the O<sub>3</sub> measurements using infrared (IR) and visible (VIS) laser wavelengths of 603 and 1064 nm, respectively. This paper discusses the measurements of Pinatubo aerosols, polar stratospheric clouds, and ozone made with the airborne DIAL system during the AASE-II, and these results are related to the measurements made during the 1989 AASE-I expedition (Browell et al., 1990a, 1990b) and to chemical and dynamical process that contribute to O<sub>3</sub> depletion in the wintertime Arctic stratosphere.

---

<sup>1</sup>Hughes-ST Systems Corporation, 28 Research Drive, Hampton, Virginia 23666

## Pinatubo Aerosols

Aerosols from the Mount Pinatubo eruption in July 1991 were observed across the entire Arctic region throughout the AASE-II field expedition. Outside the Arctic vortex the Pinatubo aerosols were found to extend over the 12-26 km altitude range with an aerosol peak near 20 km. The maximum IR and VIS atmospheric scattering ratios at the peak were about 12 and 6, respectively. These values are about half of the values observed for the Pinatubo aerosols at low latitudes (5-20°N) during the NASA Pacific Exploratory Mission (PEM-West) conducted in September-October 1991. The ratio of the IR to VIS aerosol scattering ratios was found to be about 2.2 for the peak Pinatubo layer in both the low latitudes and outside the Arctic vortex. This ratio represents an aerosol backscatter wavelength dependence ( $\alpha$  in  $\lambda^{-\alpha}$ ) of 2.6. This generally indicates an abundance of small size aerosols (of order 1  $\mu\text{m}$  in diameter).

The Pinatubo aerosol distribution at the center of the Arctic vortex extended from the tropopause to about 17 km in January and to about 18-18.5 km in February and March. The center of the Pinatubo layer in the vortex remained at about 15 km for the entire period. The average IR and VIS atmospheric scattering ratios at the peak of the layer were estimated to be about 5 and 3, respectively. The ratio of the IR and VIS aerosol scattering ratios inside the vortex was also found to be about 2 with the same resulting backscatter wavelength dependence that was found outside the vortex. The distribution and scattering properties of the Pinatubo aerosols were significantly different across the vortex edge during January; however, in February and March, aerosol layers outside the vortex in the 18-24-km range began to be slowly transported toward the center of the vortex. The start of the aerosol transition region coincided with the location of the vortex edge predicted by the potential vorticity (PV) distribution on the 440 K potential temperature surface.

Low depolarization (<2%) was measured across the main portion of the Pinatubo layer both outside and inside the vortex, and this did not change over the field experiment. This low depolarization is consistent with the small size and nearly spherical nature of the sulfuric acid aerosols that dominate the composition of the Pinatubo layer. Frequent enhancements in the aerosol depolarization of 5-20% were found at the bottom of the Pinatubo layer (generally below 15 km) where the aerosol scattering ratios were low (<2). These are thought to be caused by a low density of larger nonspherical aerosols resulting from the subsidence of large crustal particles.

## Polar Stratospheric Clouds

Polar stratospheric clouds (PSC's) were observed on only one mission during the AASE-II. On January 19, 1992, PSC's were observed near the top of the Pinatubo layer (near 22 km) in a cold region (<195 K) just outside the vortex between Norway and Iceland. A tropospheric high-pressure system created a dome of cold temperatures which forced the air in the lower stratosphere to rise by several kilometers. Cirrus clouds were observed as high as 14 km in the center of this region. The PSC's exhibited enhanced depolarizations (>25%) and large peak IR and VIS atmospheric scattering ratios of about 50 and 9.5, respectively. These characteristics are similar to the Type II water ice PSC's observed during the AASE-I field experiment in January-February 1989. The backscatter wavelength dependence of the aerosols was about 0.9, and this indicates that the aerosols were generally greater than 2  $\mu\text{m}$  in diameter. There was also a general low-level increase in aerosol depolarization across the entire Pinatubo aerosol layer between 14-22 km in this cold region. This may have resulted from the deposition of nitric acid onto the aerosols and the formation of larger nonspherical ice crystals.

## Ozone

The O<sub>3</sub> distribution observed over the altitude range from 12-25 km with the lidar system showed a clear transition across the Arctic vortex edge with the O<sub>3</sub> profile generally decreasing in altitude by about 1.5 km upon going from outside to inside the vortex. The location of the vortex edge determined from the O<sub>3</sub> distribution corresponded closely with the location of the edge derived from the potential vorticity analysis on the 440 K potential temperature surface. There was general correlation between the lidar O<sub>3</sub> and aerosol distributions near the edge; however, the O<sub>3</sub> distribution did not show the small-scale structure observed in the aerosol data.

There was only a minor influence of the presence of the Pinatubo aerosols on the O<sub>3</sub> distribution derived from the lidar measurements. The vertical O<sub>3</sub> distribution outside the vortex showed an increase in the O<sub>3</sub> mixing ratio from about 0.4 ppmv (parts per million by volume) at 14 km to about 4.8 ppmv at 23 km with an apparent depression in the O<sub>3</sub> distribution across the Pinatubo aerosol layer. This low level of decrease is difficult to quantify because there was no clean region observed for comparison. Inside the vortex in the region of the lowest potential vorticity, the O<sub>3</sub>

distribution was found to have a constant increase from about 0.8 ppmv at 14 km to about 4.2 ppmv at 23 km. There was no apparent trend in the O<sub>3</sub> data associated with the low level of Pinatubo aerosols inside the vortex.

Between January and March, the only change in the O<sub>3</sub> profile was a slight decrease in O<sub>3</sub> in the region between about 16-18 km. The maximum decrease was less than 20% at the center of this layer. No other obvious O<sub>3</sub> changes were observed inside the vortex over the period of the AASE-II.

## Acknowledgements

The authors would like to thank N. S. Higdon, M. L. Jones, M. N. Mayo, , W. J. McCabe, B. L. Meadows, and J. A. Williams of the Lidar Applications Group in the Atmospheric Sciences Division at the NASA Langley Research Center for their assistance in developing the comprehensive measurement capabilities of the airborne DIAL system, integrating the system into the DC-8, and operating the lidar system in the field, and we would also like to thank S. Ismail, S. A. Kooi, S. D. Mayor, and G. D. Nowicki for their help in reducing the lidar data and producing the color data plots. This research was supported by NASA's Upper Atmospheric Research Program.

## References

- Browell, E. V., C. F. Butler, S. Ismail, P. A. Robinette, A. F. Carter, N. S. Higdon, O. B. Toon, M. R. Schoeberl, and A. F. Tuck, Airborne lidar observations in the wintertime Arctic stratosphere: Polar stratosphere clouds, Geophys. Res. Lett., 17, 385-388, 1990a.
- Browell, E. V., C. F. Butler, S. Ismail, M. A. Fenn, S. A. Kooi, A. F. Carter, A. F. Tuck, O. B. Toon, M. H. Proffitt, M. Loewenstein, M. R. Schoeberl, I. Isaksen, and G. Braathen, Airborne lidar observations in the wintertime Arctic stratosphere: Ozone, Geophys. Res. Lett., 17, 325-328, 1990b.

## **Airborne Lidar Measurements of Stratospheric Aerosols during the European Arctic Stratospheric Ozone Experiment (EASOE)**

*Wolfgang Renger, Gerhard Ehret, Peter Moerl, Martin Wirth  
DLR - Institute of Atmospheric Physics  
D-8031 Oberpfaffenhofen / Germany*

The European Arctic Stratospheric Ozone Experiment was performed during winter 1991 /1992 to study processes in the Arctic Stratosphere, which possibly might result in an ozone depletion similar to what has been found in the Antarctic. Besides a number of ground observations at several locations and numerous balloon borne in situ and remote sensing experiments, three aircrafts were operating from the airport of Kiruna /Sweden, two of them equipped with LIDARs.

The DLR LIDAR, mounted on a Transall type aircraft consists of a 35 cm cassegranian, a XeCl excimer laser (308nm) and a Nd:YAG laser (532 nm, 355 nm) to measure ozone profiles, polar stratospheric clouds and profiles of stratospheric aerosols. The Transall aircraft is a twin prop engined transport system. Typical cruising altitude is 7 km, the maximum flight time is around 10 flight hours.

After a short testing phase in January 1991, during last winter a total of more than 40 flights were performed. Main operation area was the Northatlantic between western Greenland and the Baltic sea and between Iceland and 80 degrees latitude. But also one flight via UK , Gran Canaria down to the Cape Verdes at 15 ° N could be performed to study the latitudonal variation of the stratospheric pinatubo cloud.

A general not unexpected result is the rapid decrease of aerosol concentration together with a decreasing upper boundary with increasing latitude. The maximum upper boundary, detected during these campaigns, was around 24 km altitude. The backscatter cross sections in form of color coded plots show multilayers quasi stable over some 100 or even 1000 km, but also clearly remarkable changes in concentration when crossing the polar vortex, especially at levels above 16 km when passing from areas of cold stratospheric air parcels to warmer regions. .

Downwind of the mountains east of Greenland and northern Scandinavia lee waves can be seen at levels from 12 km to about 26 km. First the wave structure is found in the ondulation of cirrus layers at 10 to 12 km altitude with a typical wavelength of 12 to 14 km. The same wave structure with the same wavelength and nearly identical amplitude can be found at different higher levels marked by Pinatubo layers and in the few cases where polar stratospheric clouds were present in the vertical pattern of these clouds.

Lidar data will be shown in comparison to some balloon borne in-situ samplers and a balloon borne backscatter sonde.

## References

Renger, W., Ehret, G., Moerl, P., Airborne Lidar for Atmospheric Research in the Arctic, 15th ILRC Conference, Tomsk, p74-76, (1990)

Renger, W., Moerl, P., Detetction of Polar Stratospheric Clouds by Airborne LIDAR ALEX-F, BMFT Workshop 12 - 13 June 1989. Die nordpolare Stratosphäre im Winter 1988/89, IX/1-IX/6

**Aerosols and polar stratospheric clouds  
measurements during the EASOE campaign**

*D. Haner, S. Godin, G. Mégie, C. David, V. Mitev,  
Service d'Aéronomie CNRS, Université Pierre et Marie Curie  
B 102 - 4, Place Jussieu - 75252 Paris Cedex 05, France*

Preliminary results will be presented of observations performed using two different lidar systems during the EASOE (European Arctic Stratospheric Ozone Experiment), which has taken place in the winter of 1991-1992 in the northern hemisphere high latitude regions. The first system is a ground based multi-wavelength lidar intended to perform measurements of the ozone vertical distribution in the 5 km to 40 km altitude range. It was located in Sodankyla (67°N, 27°E) as part of the Elsa experiment (Expérience Lidar dans la Stratosphere Arctique). The objectives of the Elsa cooperative project is to study the relation between polar stratospheric clouds events and ozone depletion with high vertical resolution and temporal continuity, and the evolution of the ozone distribution in relation with the position of the polar vortex.

The second system is an airborne backscatter lidar (Leandre) which allows to study the three dimensional structure and the optical properties of polar stratospheric clouds. The Leandre instrument is a dual-polarization lidar system, emitting at 532 nm, which allows to determine the type of clouds observed, according to the usual classification of polar stratospheric clouds (type Ia, Ib or II). More than 60 hours of flight have been performed in December 1991, January and February 1992 in Kiruna (Sweden). The operation of the Leandre instrument has led to the observation of the short scale variability of the Pinatubo volcanic cloud in the high latitude regions and to several episodes of polar stratospheric clouds. Preliminary analysis of the data will be presented.



# LIDAR OBSERVATIONS OF POLAR STRATOSPHERIC CLOUDS AND STRATOSPHERIC TEMPERATURES AT THE SOUTH POLE

Richard L. Collins, Kenneth P. Bowman, and Chester S. Gardner

*University of Illinois at Urbana-Champaign*

Polar stratospheric clouds (PSCs) play a crucial role in the ozone chemistry of the polar regions. Current chemical models rely on the presence of these clouds to explain the rapid destruction of ozone observed each spring in Antarctica. We present lidar observations of PSCs and stratospheric temperatures at the South Pole throughout the Antarctic winter and spring of 1990.

The University of Illinois Na lidar system was installed at the Amundsen-Scott South Pole Station (90°S) in December 1989. The lidar was operated, weather permitting, from 17 December 1989 until 28 October 1990.

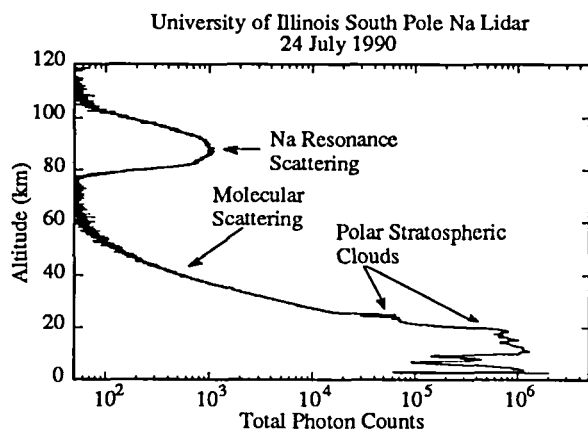


Figure 1. Integrated photon count for 0243-1034 24 July 1990 at the South Pole.

Temperatures are derived from the Rayleigh signal above the cloud layers.

The backscatter ratio,  $R(z)$ , is defined as

$$R(z) = \frac{N(z)}{M(z)} \quad (1)$$

where  $N(z)$  is the total (aerosol plus molecular) photon count signal backscattered from altitude  $z$  and  $M(z)$  is the expected molecular photon count signal backscattered from altitude  $z$ . The backscatter ratio is calculated by normalizing the lidar signal to the atmospheric molecular density profile at an altitude of 30 km above the highest clouds. Radiosondes are launched daily at the South Pole. Where the radiosondes do not reach 30 km the density profile is approximated

---

K. P. Bowman, Department of Atmospheric Sciences,,  
University of Illinois, 105 S. Gregory, Urbana, IL 61801  
R. L. Collins and C. S. Gardner, Department of Electrical and Computer Engineering,  
University of Illinois, 1406 W. Green, Urbana, IL 61801 (217) 333-4232

by an exponential fit from the top of the balloon flight to 30 km. The hydrostatic equation can be combined with the ideal gas law and integrated to yield a temperature profile

$$T(z) = T(z_1) \frac{\rho_a(z_1)}{\rho_a(z)} + \frac{M}{R} \int_z^{z_1} g(r) \frac{\rho_a(r)}{\rho_a(z)} dr \quad (2)$$

The density profile is integrated downwards using an estimated value of  $T(z_1)$ , the upper level temperature. Because the atmospheric density appears as a ratio of densities in (2) the relative density profile measured by the lidar can be used to determine  $T(z)$ .

Figure 2 provides an overview of the evolution of PSCs and temperature in the stratosphere at the South Pole in 1990. The temperature contours in the 25-40 km altitude region from April through early September are derived from lidar data, while the rest of the temperature data is from radiosondes.

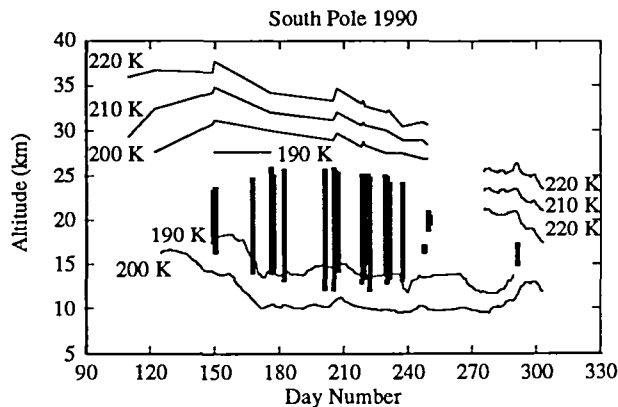


Figure 2. Evolution of PSCs and temperatures in the stratosphere at the South Pole in 1990.

The altitude regions with backscatter ratio greater than 1.1 are denoted by solid vertical bars. PSCs are clearly observed for about 100 days. PSCs begin to form in late May at about 20 km. By mid-June clouds exist from 14 to 26 km as the lower stratosphere continues to cool. This broad band of clouds persists until late August. In September clouds are not observed above 21 km as the stratosphere warms from the top down. An isolated cloud is observed in mid-October.

The backscatter ratio profiles of the PSCs show considerable vertical structure throughout the winter. Profiles for the, 25 June, 24 July, 6 August and 19 August are shown in Figure 3. After mid-June PSCs tend to exist in two broad layers, a lower layer between 15 and 20 km and a separate layer above it.

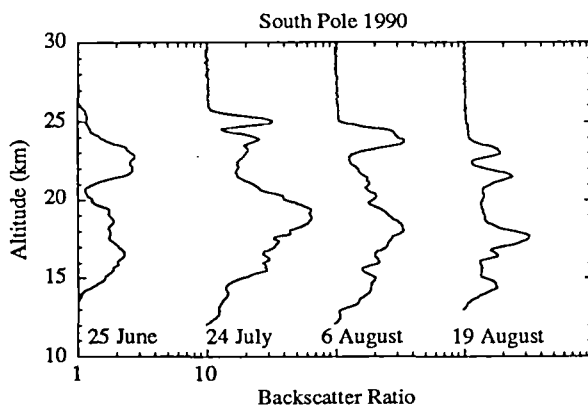


Figure 3. Average PSC backscatter ratio profiles at South Pole in 1990. Profiles are plotted on log scale.

Variations in the PSCs over periods of several days are associated with changes in the 15-20 km region rather than the higher altitude cloud layers. Balloonborne frostpoint measurements suggest that the lower altitude PSCs are composed predominately of water ice particles (Type II PSC) while the higher altitude clouds are nitric acid trihydrate particles (Type I PSC).

Several long duration observations (>12h) were made during the winter at the South Pole. Figure 4 shows the sequence of backscatter ratio profiles observed on 25 June plotted at 30 minute intervals. The PSCs are stratified in two broad layers

with little variation over the 14 h observing period. The relative constancy of the backscatter ratio profiles indicates the relatively stable conditions inside the polar stratospheric vortex at mid-winter. A radiosonde reported wind speeds of approximately 4.5 m/s in the lower stratosphere during this period, suggesting that these PSCs extend over 200 km. There are several downward moving features in the sequence of profiles. These motions are suggestive of the downward phase progressions associated with upward propagating gravity waves in the middle atmosphere. Thus, these fine scale structures may be maintained by gravity waves propagating through the clouds.

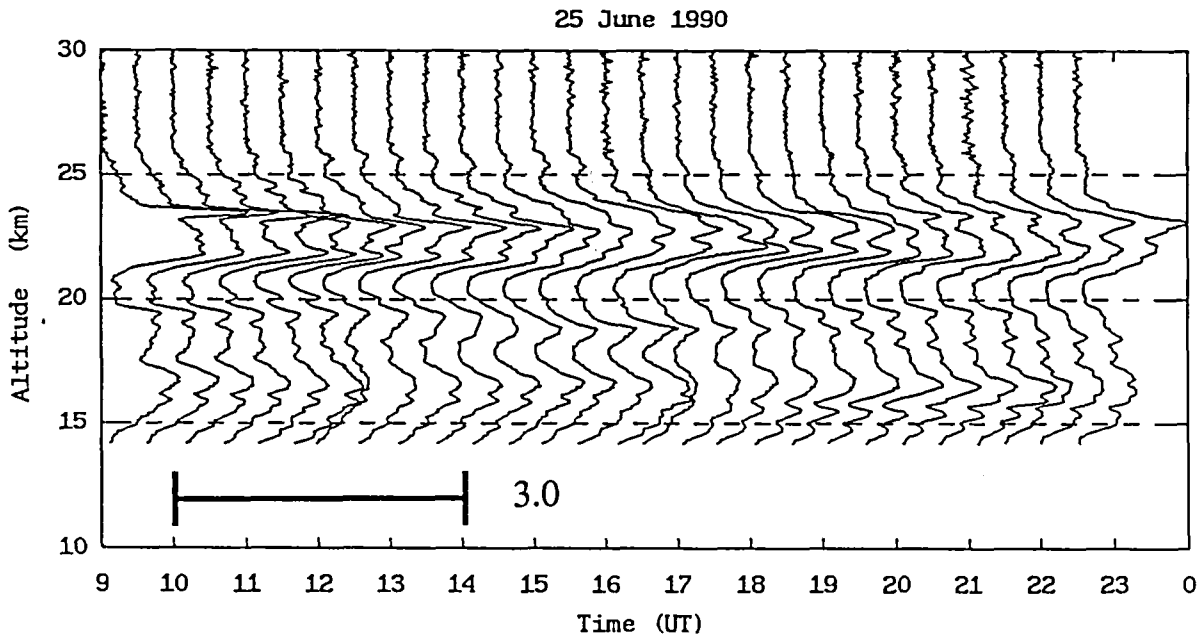


Fig 4. Sequence of PSC backscatter ratio profiles plotted at 30 minute intervals on 25 June 1990 at the South Pole. Profiles are plotted on a linear scale.

PSCs in the Antarctic interior show variations on several time scales. The seasonal variation of the clouds follows the variations in the temperature of the lower stratosphere during the winter and spring. During the winter the PSCs are stratified in two broad layers. These distinct layers may represent different cloud particle types. Fine scale variations are visible over periods of hours at scales of a kilometer. These are suggestive of gravity waves propagating through the clouds. A more complete discussion of the observations, methods and analysis will be presented at the conference.



# DEVELOPMENT OF MESOSPHERIC SODIUM LASER BEACON FOR ATMOSPHERIC ADAPTIVE OPTICS\*

T.H. Jeys

Lincoln Laboratory, Massachusetts Institute of Technology  
244 Wood Street, Lexington, Massachusetts 02173-9108  
(617) 276-6739

Adaptive optics can reduce atmospheric distortion effects in astronomical imaging, if a bright light source is available in the area of the sky under study. Although bright stars are an obvious source of light for astronomical studies<sup>1</sup>, most of the sky does not contain stars with the requisite brightness for near infrared or visible wavelength adaptive optics.<sup>2</sup> Alternatively, it has been suggested that laser backscattering from molecules in the earth's atmosphere (Rayleigh scattering) or from the earth's mesospheric atomic sodium layer (resonance scattering) can provide the beacon for the adaptive-optics compensation of atmospheric distortion.<sup>3,4,5,6</sup> In fact, such compensation has been demonstrated with low-altitude Rayleigh scattering of laser light.<sup>7,8,9</sup> Although low-altitude Rayleigh scattering can provide much more backscattered signal to an adaptive optics system, the higher altitude (90 km) of the mesospheric sodium layer reduces the beam divergence of backscattered radiation and makes the light source more star-like; this makes sodium fluorescence the preferred method of producing an artificial beacon.<sup>10</sup> Because of saturation of the sodium excitation, the laser energy must be delivered in a relatively long pulse and the spectral characteristics of the laser must be tailored so as to maximize the fluorescence signal. In addition, optical pumping and radiation pressure can dramatically affect the amount of signal from the mesospheric sodium beacon and must be accounted for in the maximization process.

A solid-state source of long pulse length, sodium-resonance radiation has been developed for the purpose of generating an artificial star in the earth's mesospheric sodium layer. This radiation is generated by sum-frequency mixing the output of a 1.064- $\mu\text{m}$  Nd:YAG laser with the output of a 1.319- $\mu\text{m}$  Nd:YAG laser (Figure 1). By operating these lasers at wavelengths very close to the peak of their tuning curves as shown by the arrows in Figure 2, it is possible to match the wavelength of the sum-frequency radiation to that of the sodium D<sub>2</sub> absorption wavelength.<sup>11</sup> Two pulsed laser systems have been constructed<sup>12</sup>, one producing as much as 0.6 J of sodium resonance radiation at a 10-Hz repetition rate and another producing as much as 24 mJ at a 840-Hz repetition rate. In both laser systems, the 1.06- $\mu\text{m}$  and 1.32- $\mu\text{m}$  Nd:YAG lasers are configured as mode-locked master oscillators followed by power amplifiers. An intracavity aperture restricts laser oscillation to the TEM<sub>00</sub> cavity mode for both oscillators, and an intracavity nonlinear crystal serves to suppress laser spiking in each oscillator through second harmonic generation.<sup>13</sup> After passing through the amplifiers, the 1.06- $\mu\text{m}$  and 1.32- $\mu\text{m}$  radiations are combined onto a common beam path by a dichroic mirror and focused into either a lithium iodate (10-Hz system) or lithium triborate (840-Hz system) crystal for sum-frequency generation of sodium resonance radiation. The 10-Hz and 840-Hz laser systems produce sodium resonance radiation with macro-pulse lengths of 80- $\mu\text{s}$  and 60- $\mu\text{s}$ , respectively, which each consist of a train of mode-locked micro-pulses which are 0.7-ns and 0.35-ns long, respectively, and are spaced at intervals of 10 ns (Figure 3). The 10-Hz laser source is being used to investigate the effects of laser polarization and optical pumping

on the backscattered intensity from the mesospheric sodium layer. The first observations of optical pumping in a remote sensing application have been accomplished using this laser system (Figure 4).<sup>14</sup>

---

\* This work was supported by the Air Force Phillips Laboratory and the Army Strategic Defense Command.

#### References

1. F. Merkle, G. Rousset, P. Kern, and J. P. Gaffard, *Proc. SPIE* **1236**, 193-202 (1990).
2. J. M. Beckers, F. J. Roddier, P. R. Eisenhart, L. E. Goad, and K-L Shu, *Proc. SPIE* **628**, 290-297 (1986).
3. R. Foy and A. Labeyrie, *Astron. Astrophys.* **152**, L29-L31 (1985).
4. L. A. Thompson and C. S. Gardner, *Nature* **328**, 229-231 (1987).
5. B. M. Welsh and C. S. Gardner, *Applied Optics* **28**, 4141-4153 (1989).
6. G. P. Collins, *Physics Today* **45**, 17-21 (1992).
7. C. A. Primmerman, D. V. Murphy, D. A. Page, B. G. Zollars, and H. T. Barclay, *Nature* **353**, 141-143 (1991).
8. R. Q. Fugate, D. L. Fried, G. A. Ameer, B. R. Boeke, S. L. Browne, P. H. Roberts, R. E. Ruane, G. A. Tyler, and L. M. Wopat, *Nature* **353**, 144-146 (1991).
9. D. V. Murphy, C. A. Primmerman, B. G. Zollars, and H. T. Barclay, *Optics Letters* **16**, 1797-1799 (1991).
10. R. A. Humphreys, C. A. Primmerman, L. C. Bradley, and J. Herrman, *Optics Letters* **16**, 1367-1369 (1991).
11. T. H. Jeys, A. A. Brailove, and A. Mooradian, *Applied Optics* **28**, 2588-2591 (1989).
12. T. H. Jeys, *The Lincoln Laboratory Journal* **4**, 133-150 (1991).
13. T. H. Jeys, *Applied Optics* **30**, 1011-1013 (1991).
14. T. H. Jeys, R. M. Heinrichs, K. F. Wall, J. Korn, T. C. Hotaling, and E. Kibblewhite, submitted to *Opt. Lett.*

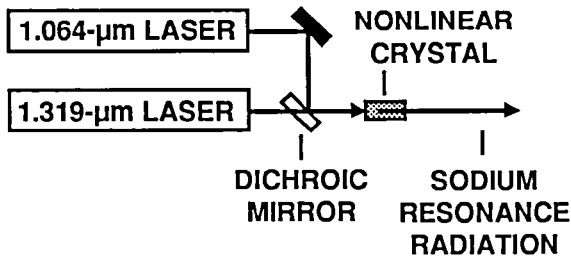
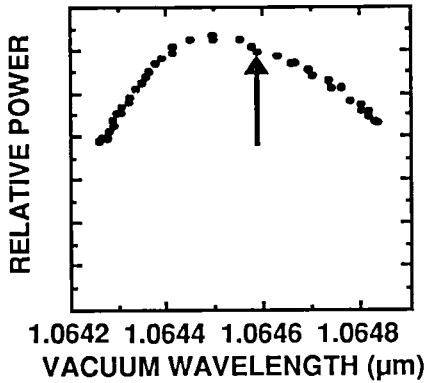
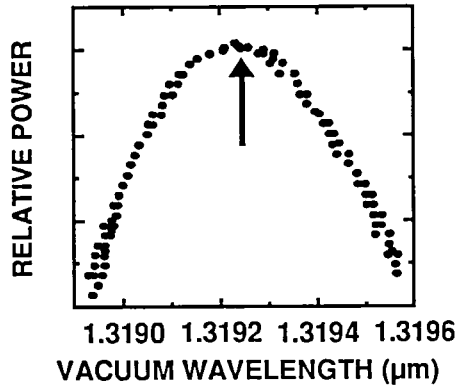


Figure 1. Schematic of Nd:YAG laser sum frequency generation of sodium resonance radiation.

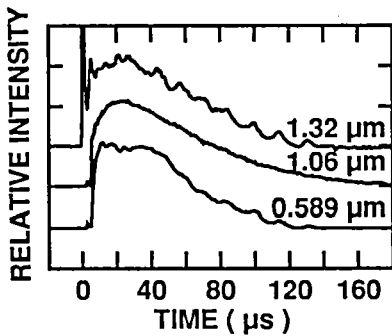


(a)

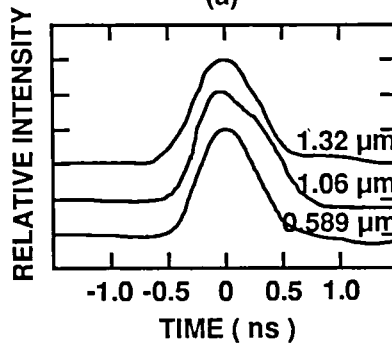


(b)

Figure 2. Tuning curves of 1.06- $\mu\text{m}$  (a) and 1.32- $\mu\text{m}$  (b) Nd:YAG lasers. Sodium resonance radiation may be generated by sum frequency mixing the wavelengths indicated by the arrows.



(a)



(b)

Figure 3. Temporal profiles of 10-Hz laser system macropulses (a) and micropulses (b).

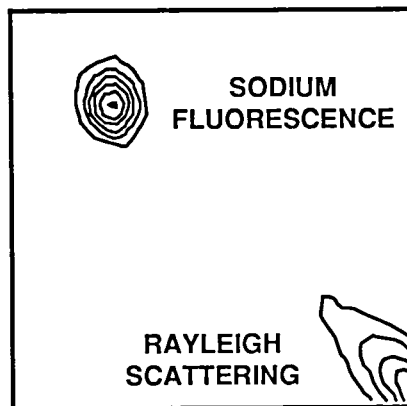


Figure 4. CCD image of laser induced Rayleigh scattering and mesospheric sodium fluorescence. The field of view of the image is  $484 \mu\text{r} \times 484 \mu\text{r}$ . The contours are drawn every 40 CCD counts per pixel beginning at 40 counts above zero.



# Characterization of Artificial Guidestars Generated in the Mesospheric Sodium Layer

M.P. Jelonek\*, R.Q. Fugate\*, W.J. Lange\*, A.C. Slavin\*,

R.E. Ruane†, R.A. Cleis††

\*Starfire Optical Range, Phillips Laboratory, Propagation Branch, Kirtland AFB, NM 87117

†Rockwell Power Systems, Albuquerque, NM 87117

†† the Optical Sciences Company, PO Box 1329, Placentia, CA 92670

Using a 10 W average power sum-frequency laser, we have generated resonant fluorescence beacons in the mesospheric sodium layer and are currently evaluating them for use as an artificial guidestar for atmospheric compensation using adaptive optics. Two flashlamp-pumped Nd:YAG lasers operating at 1.064  $\mu\text{m}$  and 1.319  $\mu\text{m}$  are mixed in a lithium triborate crystal to produce 589 nm light at 840 Hz. The laser emits 47.5  $\mu\text{s}$  mode-locked pulse trains at 11-14 mJ per pulse and is tuned to the sodium resonance transition with intracavity etalons.

We expanded the laser beam to approximately 5 cm in diameter and propagated it vertically, offset 8.8 m from a 1.5 m aperture imaging telescope and 17.7 m from a 14-inch telescope equipped with a photomultiplier tube. We alternately used two cameras on the 1.5 m aperture -- an intensified CID video camera operating at 30 frames per second and a low noise, high resolution CCD camera. Images from both cameras show Rayleigh scatter where the upper end of the laser beam enters the field of view of the telescope, a bright spot at 23 km from a localized layer of volcanic ash from the Mt. Pinatubo eruption, a dark gap between 36 and 90 km, and the resonant return from the mesospheric sodium layer at 93 km (see Figure 1). By calibrating against binary stars of known separation, we measure the image size of the sodium guidestar from this image data to be on the order of 32 microradians (6.6 arcseconds) full-width-at-half-maximum which is  $2.76 \lambda/D$  for a 5 cm beam. Our most recent experiments have generated spots of 19  $\mu\text{rad}$  (3.92 arcseconds) or 1.64 times  $\lambda/D$ . Based on the total counts in the CCD camera images, we estimate

the signal return collected by the 1.5 meter aperture to be 5200 photons per 47.5 microsecond pulse. This is equivalent to the signal from a star of magnitude +9.02. These characteristics of the sodium guidestar make it suitable for use in a planned hybrid Rayleigh-sodium beacon adaptive optics experiment at a compensation wavelength of 0.88  $\mu\text{m}$  or a single sodium beacon compensation experiment with four subapertures at 2.2  $\mu\text{m}$ .

We collected temporally resolved fluorescence signals using the photomultiplier tube and 14-inch telescope (Figure 2). The signals were stored on a multichannel scaler/averager for processing. From this data, we calculated the number of photons collected per laser pulse and predicted the number available for specific configurations of an adaptive optics experiment. Despite the long pulse of the laser, we use this data to estimate the column density of the sodium layer using the field of view of the telescope as a range gate. With this method, our column density measurements are lower than the actual value but in the range expected for our latitude. Measured values of column density are in the range of  $2\text{-}3 \times 10^{13} /\text{m}^2$ . From the temporal data, the average altitude of peak sodium density was 94.2 km above sea level with layer widths varying from 15.8 to 23.6 km.

We have also conducted polarization studies of the resonant fluorescent return by inserting a quarter-wave plate in the transmitted beam and analyzing the return signal with different combinations of wave plates and polarizers. We have verified the phenomenon of optical pumping in which the resonant fluorescent return signal is enhanced by exciting the sodium layer with circularly polarized light instead of linearly polarized light. At transmitted peak power densities of approximately  $1.003 \text{ mW}/\text{cm}^2$  incident on the sodium layer, we measured a 41-48% increase in return signal for circularly polarized light over linearly polarized light.

11 October 1991

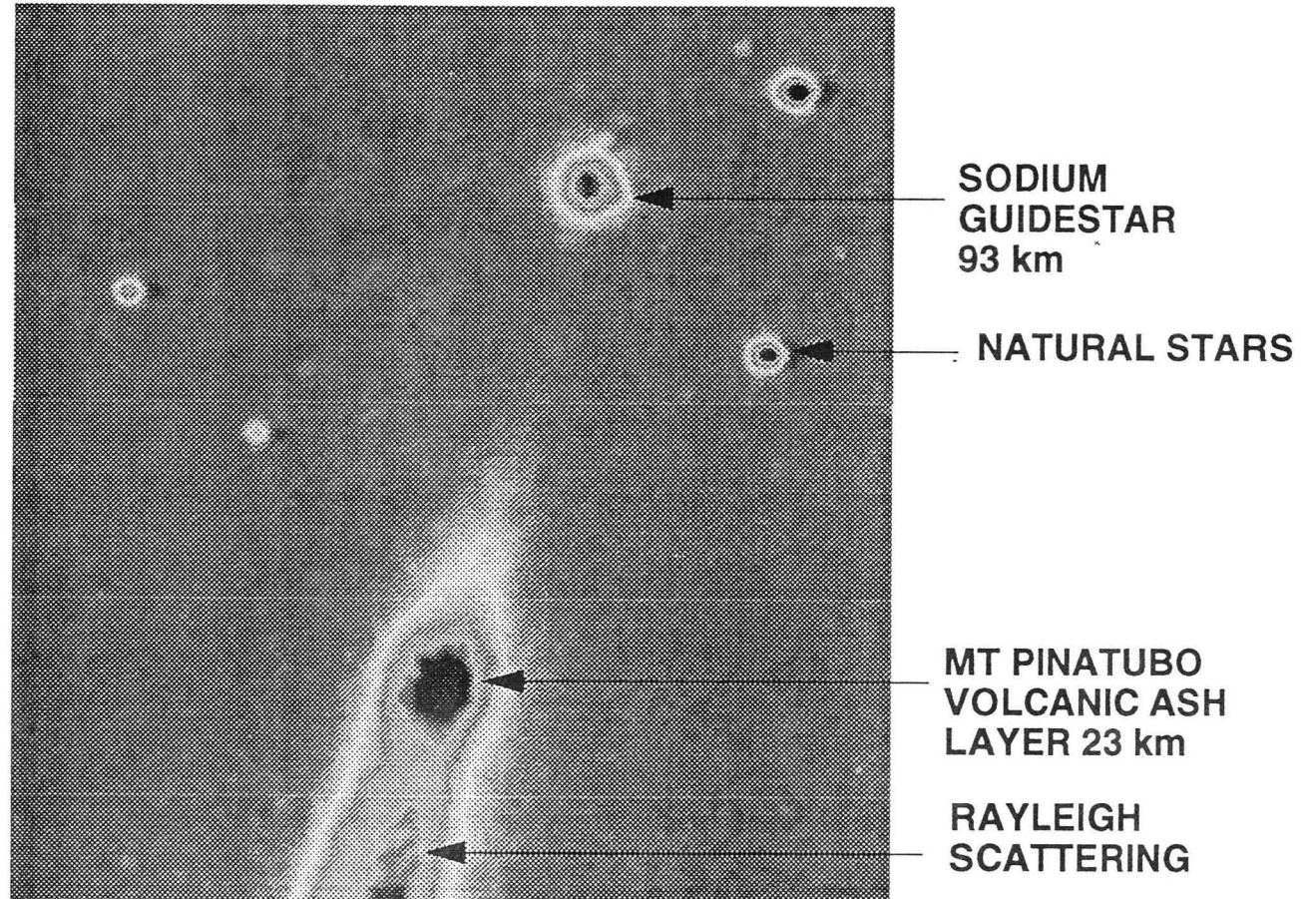


Figure 1. Single frame of digitized video from an intensified CID camera showing a 1/30 second exposure from a 1.5 m aperture. The laser was emitting 6.5 W at 840 Hz with a 5 cm diameter output beam. The field is approximately 125 arcseconds square.

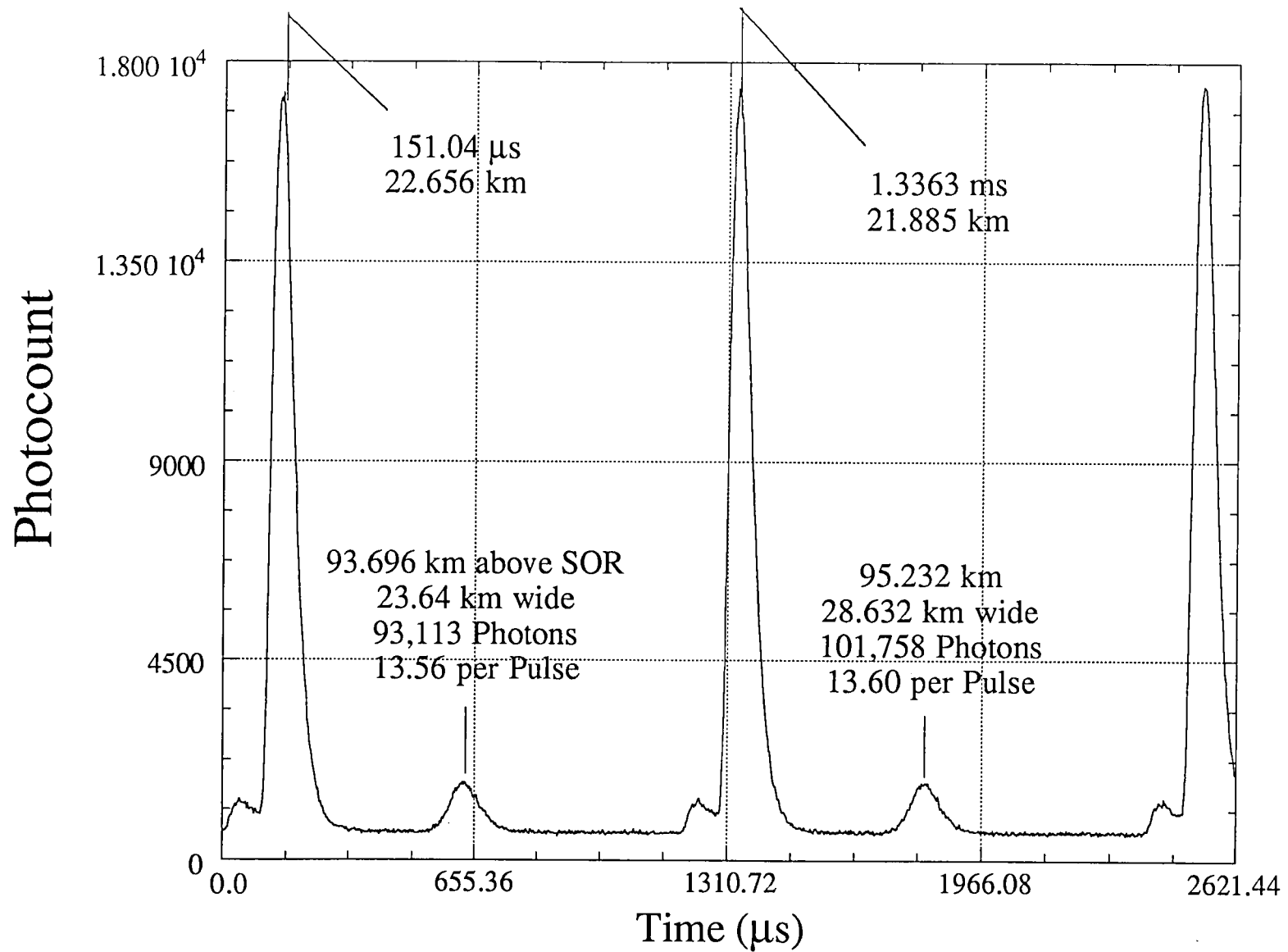


Figure 2. Temporal trace from the 14" telescope showing the resonant fluorescent return from the mesospheric sodium layer with the upper altitude Rayleigh backscatter. The laser power was 9 W with a quarter wave plate adjusted for circularly polarized light. The plot is a sum of 3000 pulses.

## Optical Pumping of Mesospheric Sodium: A New Measurement Capability

R.M. Heinrichs, T.H. Jeys, K.F. Wall, J. Korn, and T.C. Hotaling

Lincoln Laboratory, Massachusetts Institute of Technology  
244 Wood Street, Lexington, Massachusetts 02173-9108  
(617)981-4141

### Abstract

The first observation of laser-induced optical pumping in a remote sensing application is reported. We have observed a large variation in the amount of laser light resonantly backscattered from the earth's mesospheric sodium layer depending on the laser polarization. This is consistent with optical pumping of the mesospheric sodium atoms. A new lidar capability is being developed based on measurements of the rethermalization rate of the optically pumped sodium atoms. These measurements have potential applications in the fields of global warming research, spacecraft re-entry, and upper atmospheric dynamics.

### Introduction

Lidar measurements of the mesospheric sodium density, temperature, and wind speeds have produced valuable information on the geophysics of the upper atmosphere.<sup>1-3</sup> Recently, the potential use of the sodium layer for adaptive optics compensation has generated additional interest in mesospheric sodium.<sup>4-6</sup> We report measurements of mesospheric sodium fluorescence produced by a solid state laser system developed for adaptive optics<sup>7</sup> which provides the first known demonstration of optical pumping in a remote sensing experiment.<sup>8</sup> We are developing a new upper atmospheric measurements capability with the addition of a probe laser which will measure the optical pumping rethermalization rate, thus providing information about several upper atmospheric parameters including the background gas density in the 85-100-km altitude range. Densities above 70 km presently can only be obtained with large aperture, long integration period, Rayleigh backscattering measurements<sup>9</sup> or by inference from sodium measurements.<sup>2,3</sup> Applications of density measurements in the 85-100-km altitude regime include research into global warming, spacecraft re-entry, and upper atmosphere dynamics.

### First observation of optical pumping

The Doppler broadened absorption spectra of atomic sodium (Figure 1) is dominated by the 1.8-GHz hyperfine splitting of the ground state. Long pulse radiation, resonant with the  $F=2$  transition, can result in many excitation-decay cycles. During each cycle an atom may decay to either ground state level, so each atom will continue to absorb and re-emit radiation until it has decayed into the nonresonant  $F=1$  ground state. After decaying to the  $F=1$  ground state the atoms are no longer resonant with the incident radiation and have been optically pumped to transparency. The process of optical pumping can be more readily accomplished if the incident

radiation has linear rather than circular polarization since the angular momentum imparted to the atom by circularly polarized light inhibits decay to the  $F=1$  level.

In the present experiment the 300-mJ, 589-nm output of a mode-locked laser<sup>7</sup> with a pulse length of 80  $\mu\text{s}$  and 10-Hz repetition rate is directed to a 5-m-diameter spot in the mesospheric sodium layer. The backscattered radiation is detected as a function of time by a photomultiplier tube mounted on a 14" aperture telescope and is detected spatially by imaging the fluorescence spot on a CCD camera with an 8" aperture telescope. The measured backscatter efficiency of the laser pulse is greatly increased when the transmitted radiation is circularly polarized as compared to linearly polarized, as shown in Figure 2. The ratio of the backscattered signal for circular versus linear laser polarization increases monotonically during the pulse. The fluorescence images for circular laser polarization show a factor of 3 increase in signal as compared to linear polarization at the center of the image, as shown by the radial averages in Figure 3. These observations demonstrate optical pumping of the mesospheric sodium atoms.

### Rethermalization measurements

We are developing a new capability for measuring the rethermalization of the optically pumped sodium atoms by adding a temporally short probe pulse, transmitted with a set delay after the 80- $\mu\text{s}$  pump pulse and tuned to the same wavelength as the pump laser. The change in the probe pulse backscattered signal with increasing pump-probe delay time will provide a direct measurement of the rethermalization rate. This measurement can be performed with the pump pulse either pumping a few of the sodium velocity groups, which is the case for the mode-locked laser spectrum, or all the velocity groups, which is the case with a filled in laser spectrum obtained by phase modulating the laser output at 30 MHz. Both measurements are planned. In the former case, relaxation is due to a combination of velocity changing collisions with background gas molecules and spin-flip collisions with molecular oxygen (Figure 4a). In the latter case, relaxation is due only to spin-flip collisions (Figure 4b). The cross section for velocity changing collisions is about  $5 \times 10^{-15} \text{ cm}^2$  resulting in a mean time between velocity changing collisions which varies from 10 to 300  $\mu\text{s}$  through the sodium layer. The cross section for spin-flip collisions with  $\text{O}_2$  is unmeasured but is estimated to be near  $10^{-17} \text{ cm}^2$  from measurements of the electron- $\text{O}_2$  spin-flip collision cross section.<sup>10</sup> Since the contribution due to spin-flip collisions can be determined by measuring the rethermalization rate when all the velocity groups are pumped, the mean time between collisions can also be determined by relating these two measurements which, in turn, can be related to the background gas density at 85-100 km. The collision rate for a given process is proportional to  $\sigma \rho v$ , where  $\sigma$  is the collision cross section,  $\rho$  is the gas density and  $v$  is the mean relative velocity of the collision species. Since the velocity varies as the one-half power of the temperature, an expected 10% variation of the temperature through the sodium layer<sup>2</sup> will thus contribute about a 5% uncertainty in the value of the density. This inaccuracy can be overcome by combining measurements of the temperature and background gas collision rates. Even with the uncertainty in temperature, these measurements should provide much more precise values of the density near 100 km than otherwise possible.

### Acknowledgments

This work was supported by the National Science Foundation under Grant #AST89-21756, the University of Chicago, and the Army Strategic Defense Command.

### References

1. Gardner, C.S., D.G. Voelz, C.F. Sechrist, and A.C. Segal, *J. Geophys. Res.* **91**, 13659 (1986).
2. Bills, R.E. and C.S. Gardner, *Opt. Eng.* **30**, 13 (1991).
3. Fricke, K.H. and U. von Zahn, *J. Atmos. Terr. Phys.* **47**, 499 (1985).
4. Foy, R. and A. Labeyrie, *Astron. Astrophys.* **152**, L29 (1985).
5. Thompson, L.A. and C.S. Gardner, *Nature* **328**, 229 (1987).
6. Humphreys, R.A., C.A. Primmerman, L.C. Bradley, and J. Hermann, *Opt. Lett.* **16**, 1367 (1991).
7. Jeys, T.H., *The Lincoln Laboratory Journal*, **4**, 133 (1991).
8. Jeys, T.H., R.M. Heinrichs, K.F. Wall, J. Korn, T.C. Hotaling, and E. Kibblewhite, submitted to *Opt. Lett.*
9. Chenin, M.L. and A. Hauchecorne, *J. Geophys. Res.* **86**, 9715 (1981).
10. Ratliff, J.M., G.H. Rutherford, F.B. Dunning, and G.K. Walters, *Phys. Rev. A* **39**, 5584 (1989).

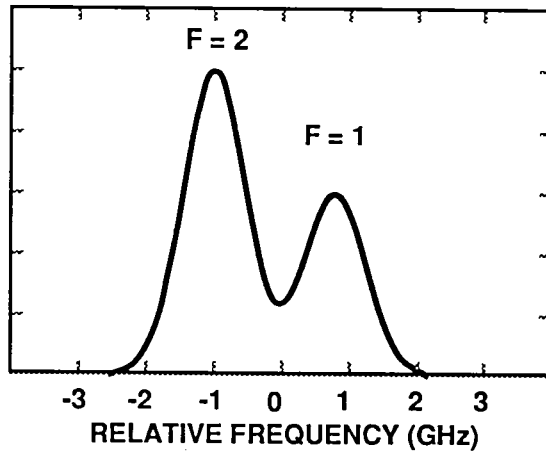


Figure 1. Doppler-broadened sodium absorption profile.

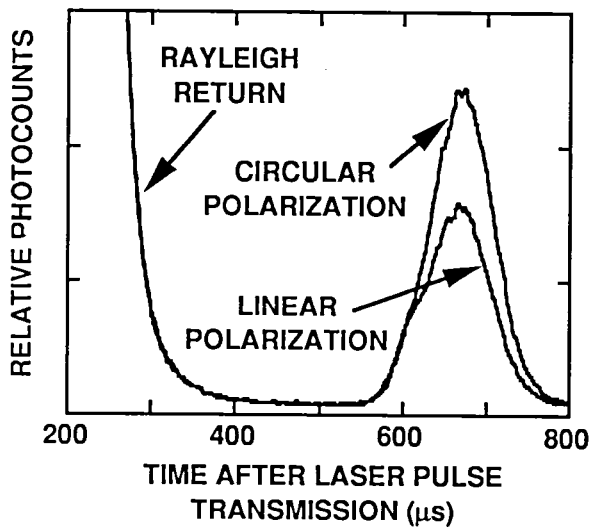


Figure 2. Measured backscatter for circularly and linearly polarized transmitted laser radiation.

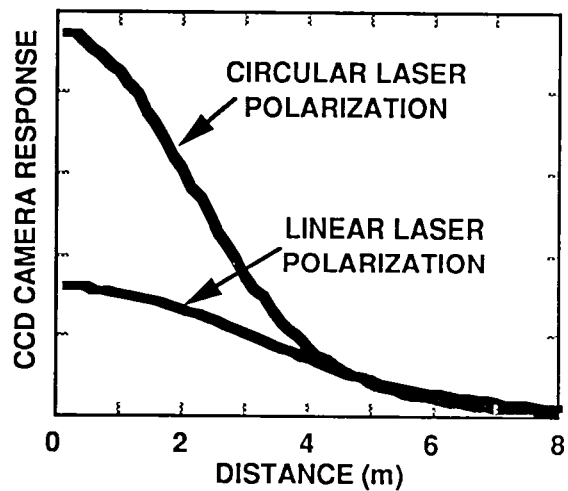


Figure 3. Radial averages of sodium fluorescence images.

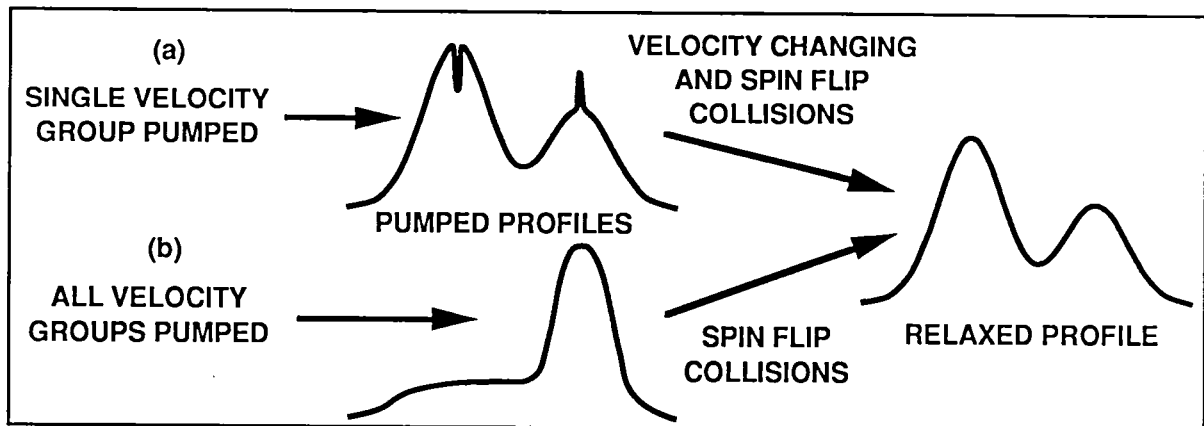


Figure 4. Rethermalization of optically pumped system is due primarily to velocity changing and spin-flip collisions when only a few velocity groups are pumped (a) and due only to spin-flip collisions when all velocity groups are pumped (b).

LIDAR PROBING OF THE MESOSPHERE:  
SIMULTANEOUS OBSERVATIONS OF SPORADIC SODIUM AND IRON FORMATIONS,  
CALCIUM ION LAYERS, NEUTRAL TEMPERATURE AND WINDS

Timothy J. Kane, Jun Qian, Daniel R. Scherrer, Daniel C. Senft, W. Matthew Pfenninger,  
George C. Papen and Chester S. Gardner

*Department of Electrical and Computer Engineering, University of Illinois at Urbana-Champaign*

Meteoric ablation in the upper atmosphere is the commonly accepted source of the mesospheric metals between about 80 and 105 km. The vertical and temporal behavior of some of these metals can be probed with high accuracy and resolution using resonance fluorescence lidar techniques. Of considerable interest in recent years has been the sporadic and rapid formation of thin, dense enhancements in these metallic layers. These sporadic layers, as they are referred to, have been observed for years in the Na layer and have recently been seen in Fe [Batista et al. 1989; Hansen and von Zahn, 1990; Kane et al., 1992]. The formation of these events have been linked conclusively with sporadic-E ( $E_S$ ) layers. In this paper, simultaneous resonance fluorescence lidar observations of sporadic Na ( $Na_S$ ), sporadic Fe ( $Fe_S$ ) and  $Ca^+$  (a component of  $E_S$  layers) are presented along with concurrent neutral temperatures and winds obtained with a Na Doppler/temperature lidar.

Since late March 1991 the UIUC CEDAR lidar system, located at the Urbana Atmospheric Observatory (40°N, 88°W), has been routinely operating at the Fe resonance line of 372 nm in order to probe the mesospheric Fe layer. In November 1991, the capability to investigate mesospheric  $Ca^+$  at the resonance line of 393.4 nm was added. The lidar's excimer-pumped dye laser uses Exciton QUI laser dye dissolved in p-dioxane, which can lase at both the Fe and  $Ca^+$  frequencies. By tuning the laser to the alternate line and changing the interference filter in the receiving system, Fe and  $Ca^+$  density profiles can be obtained within 10 minutes of each other. The laser produces 20 mJ pulses at 25 pps, yielding an average transmitted power of 0.5 W. The receiving telescope is a 1 m Cassegrain with a 3 mrad field-of-view (FOV) pointed to within 1 mrad of zenith. The profile integration time of this system is typically 3 min and the vertical range resolution is either 37.5 m or 48 m depending on computer configuration. The UIUC Na Doppler/temperature lidar has been in operation at the Urbana Atmospheric Observatory since January 1991. This system has the capabilities to measure Na densities and background temperature and winds in the region spanned by the mesospheric Na layer (roughly 80-105 km). The temperature and winds are obtained by examining the Doppler broadening and shifting, respectively, of the Na backscatter cross-section. The average transmitted power of this system is 0.8 W at 30 pps. The receiving telescope is either the same 1 m Cassegrain as for the Fe/ $Ca^+$

system or a 35 cm Schmidt-Cassegrain, both with a 3 mrad FOV. The smaller telescope is used for off-zenith measurements of wind. The profile integration time for the Na system is about 1 minute and the vertical range resolution is 48 m. This system is described in greater detail in the paper by Scherrer et al. presented elsewhere in this issue.

In Figure 1, both a Na density profile (a) and a Fe density profile (b) obtained simultaneously on the evening of 25 November 1991 exhibit an extremely dense and narrow ( $\sim 100$  m FWHM) enhancement at nearly identical altitudes lasting less than 1 min each.

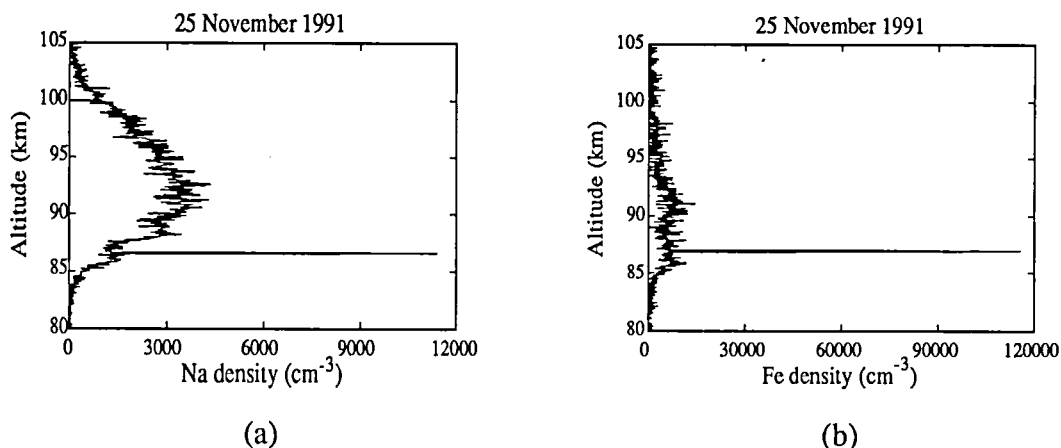


Figure 1. Simultaneous meteor trails observed in the mesospheric Na (a) and Fe (b) layers on 25 November 1991.

We believe that these enhancements are the result of the neutralization of ions released from an ablating meteor. The thin layering of the ions before they neutralize can be explained by the so called "windshear mechanism" which has been used for years to explain mid-latitude  $E_S$  layers. The Lorentz force imparts some vertical motion on ions blown by a horizontal wind across the earth's magnetic field lines. An east-west shear in the winds, possibly due to a gravity wave or tide, can thus cause these ions to collect near the null in the wind field. Further insight into our results will be gained upon investigation of the temperatures and winds measured by the Na lidar. We refer to the events shown in Figure 1 as "meteor trails" because of their apparent origin and brevity. We reserve the term "sporadic layer" to describe enhancements which last many minutes to hours and having typical widths  $\sim 1$  km FWHM.

The origin of sporadic layers has been a topic of much debate in recent years. Valuable insight can be gained, however, from simultaneous observations of these events and associated constituents and conditions. On the evening of 17-18 December 1991, sporadic layers appeared simultaneously in the Na and Fe layers. Single profiles depicting these sporadic layers near their peak densities are shown in Figure 2 along with a measurement of a Ca<sup>+</sup> layer taken about 15 minutes earlier.

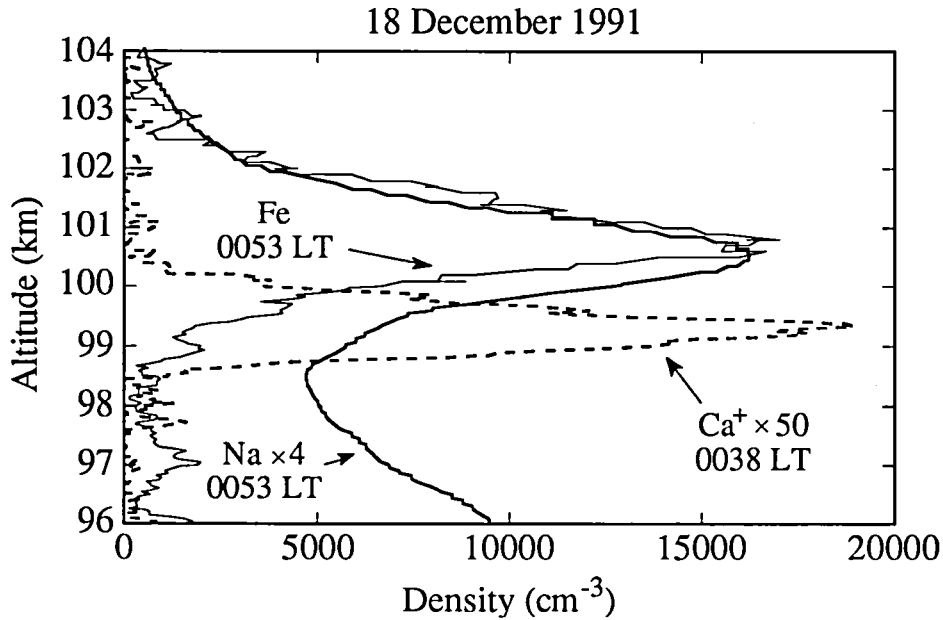


Figure 2. Superimposed density profiles of sporadic Na ( $Na_S$ ), sporadic Fe ( $Fe_S$ ) and  $Ca^+$  layers observed on 18 December 1991.

The influence of atmospheric dynamics on these events can be seen in Figure 3, which shows the peak altitude of both sporadic layers versus time as well as the altitude of the  $Ca^+$  layer, which was measured at two discrete points in time. Both the  $Fe_S$  and  $Ca^+$  layers showed a similar downward propagation of about -0.25 m/s, which is typical of tidal motion. The  $Na_S$  layer was absorbed by the background layer before it had time to move downward, but a node in the background layer near where the sporadic event disappeared follows a downward path similar to the other events.

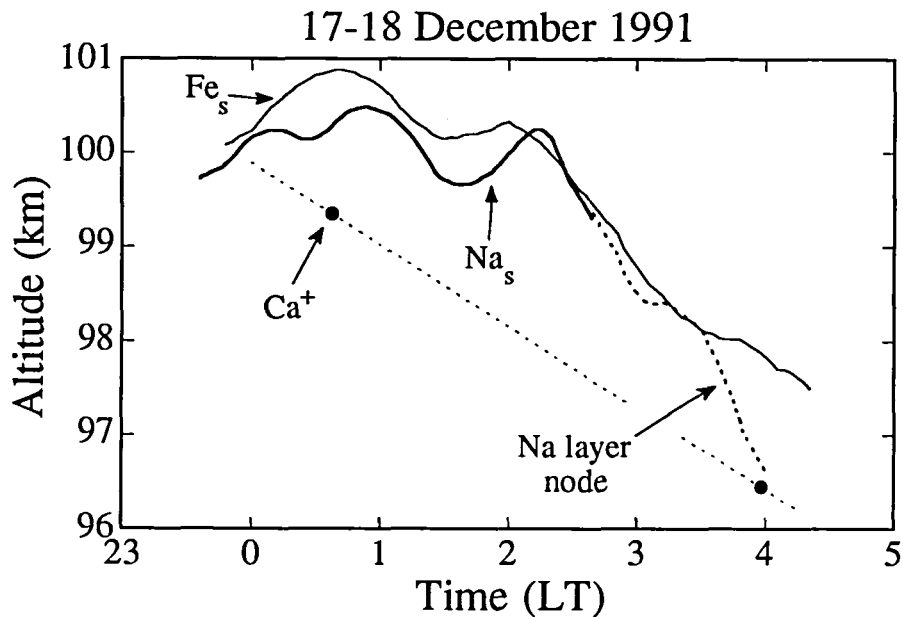


Figure 3. The altitude trajectories of the 17-18 December  $\text{Ca}^+$ ,  $\text{Fe}_s$  and  $\text{Na}_s$  layers. The altitude of the wave induced perturbation in the Na background layer which absorbed the  $\text{Na}_s$  layer is shown as a dashed line.

Note that although all the layers tend to move down at the same velocity, the  $\text{Ca}^+$  maintains about a 1 km separation below the  $\text{Na}_s$  and  $\text{Fe}_s$  layers. If the neutral atoms in these sporadic layers are related to their ions, the windshear theory presented earlier predicts such a separation based on the differences in ion mass. Increases in local temperature and wave/tidal activity associated with  $\text{Na}_s$  has been reported in the past, so the temperature and wind measurements will once again yield valuable information.

#### REFERENCES

- Batista, P.P., B.R. Clemesha, I.S. Batista and D.M. Simonich, Characteristics of the sporadic sodium layers observed at  $23^\circ$  S, *J. Geophys. Res.*, 94, 15,349-15,358, 1989.
- Hansen, G. and U. von Zahn, Sudden sodium layers in polar latitudes, *J. Atmos. Terr. Phys.*, 52, 585-608, 1990.
- Kane, T. J., P. Mui and C. S. Gardner, Evidence for substantial seasonal variations in the structure of the mesospheric iron layer, *Geophys. Res. Lett.*, 19, 405-408, 1992.

# Lidar Measurements of Metallic Species in Mesopause Region

Chikao NAGASAWA and Makoto ABO

Department of Electronics and Information Engineering,  
Tokyo Metropolitan University  
Minami-Osawa, Hachioji, Tokyo 192-03, Japan

Sodium density distributions have been measured over more than 20 nights since July 1991 at Tokyo Metropolitan University (35.6°N, 139.4°E). Our sodium lidar specifications are shown in Table 1. Figure 1 shows the block diagram of the sodium lidar system. The lidar consists of a dye laser that is pumped by a pulse Nd:YAG laser. The dye laser is tuned to the D<sub>2</sub> resonant absorption line of Na at the wavelength of 589 nm. A small fraction of the output beam is directed to a hollow-cathode lamp. The precise tuning of Na D<sub>2</sub> line is accomplished by monitoring signal obtained from the hollow-cathode lamp and controlling the grating in the dye laser oscillator cavity. The raw data for each profile were obtained by firing the laser 5000 times for approximately 8.5 minutes. After the data are saved into the micro-computer, the next observation starts. Therefore, each observation time established 10 minutes. An example of nocturnal variation of the observed sodium layer is shown in Figure 2. The data are smoothed to resolution of approximately 4km using a low-pass filter. Considerable gravity waves and tidal activities were observed in the Na profiles. According to Senft et al. (1989), the sporadic sodium layers have been observed mainly at low- and high-latitude sites and rarely observed at mid-latitude sites, however, we have observed three times the sporadic sodium layers during relative little opportunities of observation. The example of the sporadic sodium layer appeared on September 6, 1991 is shown in Figure 3. The duration of the layer was approximately 60 min. The ionosonde site of Communication Research Institute (Kokubunji) of Japan locates 13km nearly north-east of our lidar site. We could not recognize significant correlations between appearance of sporadic sodium layers and that of sporadic E layers in the Kokubunji ionosonde data observed at the same time.

Recently, lidar measurements of iron atoms have been also performed and measurements of sodium temperature and other species such as ionic calcium and potassium in the mesopause region are planned at Tokyo Metropolitan University.

## Reference

Senft, D.C., R.L. Collins and C.S. Gardner, Geophys. Res. Lett., Vol.16, No.7, 715-718, 1989.

Table I. Specifications of the sodium lidar

Transmitter		Receiver	
Laser	:Nd:YAG SHG pumped dye	Telescope aperture:	280mm
Peak energy	:100mJ(max.)	Field of view	:0.7mrad
Wavelength	:589nm	Filter bandwidth	:3.5nm
Beam divergence:	0.2mrad	PMT	:R1463-01
		Range resolution	:20m(min.)

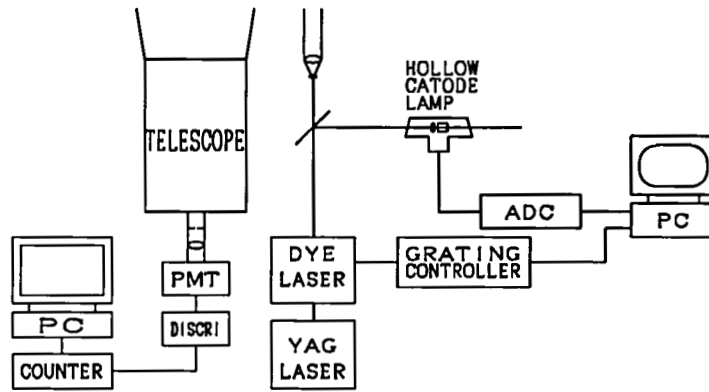


Figure 1 Block diagram of the sodium lidar and tuning system.

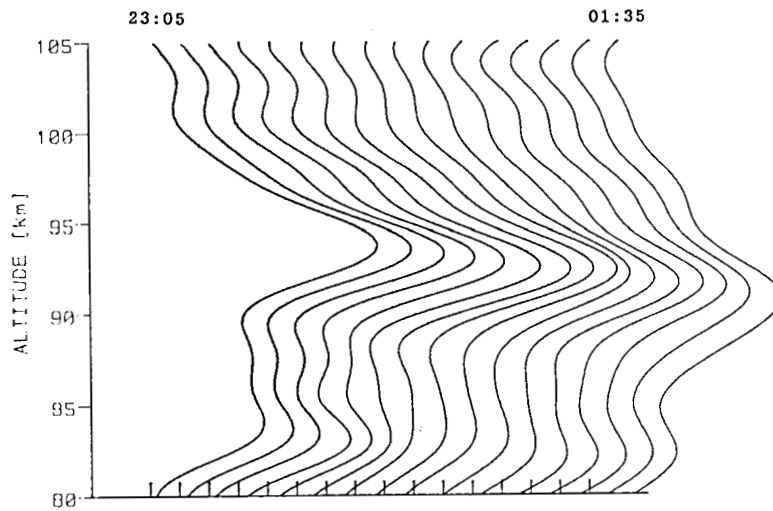


Figure 2 Na density profiles measured during the nighttime of January 14, 1992 at Tokyo. The profiles have been plotted on a linear scale at 10 min intervals.

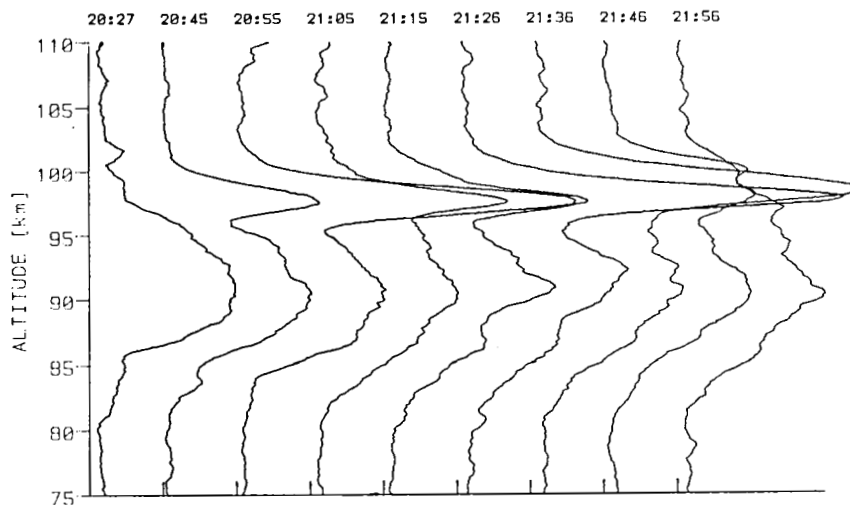


Figure 3 Sequence of Na density profiles of the sporadic Na layer observed from 20:45 LST to 21:45 LST on September 6, 1991.

# NARROWBAND NA LIDAR SYSTEM FOR MEASUREMENT OF UPPER MESOSPHERE TEMPERATURES AND WINDS

Daniel R. Scherrer, William M. Pfenninger, Daniel C. Senft,  
George C. Papen, Chester S. Gardner

Department of Electrical and Computer Engineering  
University of Illinois at Urbana-Champaign  
Urbana, IL 61801  
(217) 333-4303

In this paper we describe a four-frequency lidar technique to measure the vertically resolved temperature structure and wind field of the mesopause region (75 to 110 km). The technique uses a narrowband lidar to probe the resonance structure of the neutral sodium atoms which exist in the mesopause region. The vertically resolved sodium density, temperature structure, and wind field within the layer can be determined by examining the fluorescence scattering of light in the layer at four different frequencies within the sodium D<sub>2</sub> resonance line.

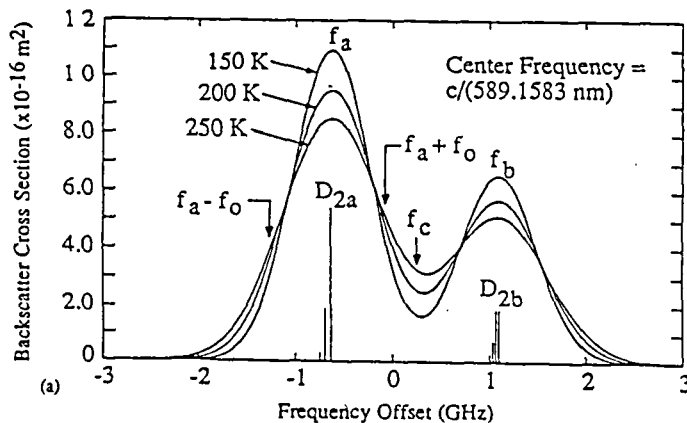


Figure 1. Na D<sub>2</sub> Backscatter Cross Section

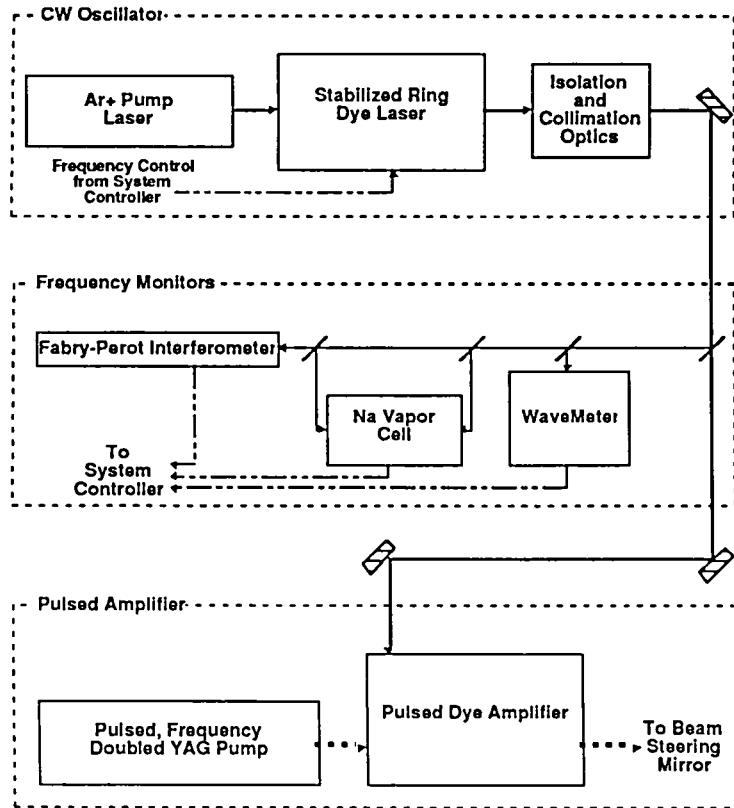
The backscatter cross section of the sodium D<sub>2</sub> resonance line at several different temperatures is given in Fig. 1. The shape of the spectrum is strongly influenced by Doppler broadening of the line due to thermal motion of the atoms thus making it a strong function of temperature. The spectrum is also sensitive to Doppler shifting by the wind field. By probing the D<sub>2</sub> resonance line of the atoms in the sodium layer at several frequencies, the vertically resolved temperature and wind field can be determined.

To measure temperatures within the sodium layer, profiles are taken at two different frequencies. These are labeled as  $f_a$  and  $f_c$  in Fig. 1. The ratio of the backscatter cross-section at these two frequencies is a strong function of temperature. The backscatter cross-section at these frequencies is also relatively insensitive to tuning errors, since the frequency derivative of the spectrum at these frequencies is very small.

During wind measurements the laser beam is split and two lidar channels are used, one vertical and the other tilted 15 to 30 degrees off zenith. Measurements of the backscatter are made at two additional frequencies  $f_a + f_0$  and  $f_a - f_0$  (see Fig. 1). The ratio of the backscattered signal at these two frequencies is dependent upon the Doppler shift caused by the background winds. The techniques for temperature and wind measurements are discussed in Bills et al. [1991].

To make these measurements a laser transmitter is needed that has a very narrow line width and is tunable throughout the D<sub>2</sub> resonance line. The absolute frequency of the system must also be accurately determined. In addition the line width must be highly reproducible.

The transmitter system diagram is seen in Fig 2. It can be divided into three major subsystems: the cw oscillator, the frequency measurement system, and the pulsed amplifier stage.



The cw oscillator system consists of a frequency stabilized, tunable ring dye laser which is pumped by an Argon ion laser. The oscillator beam is tunable throughout the Na D<sub>2</sub> line and has an rms frequency jitter of less than 1 MHz.

The frequency stability of the transmitter is a critical part of the experiment which is controlled by a PC compatible computer which actively tunes and stabilizes the ring dye laser. The frequency of the oscillator beam is monitored using 3 separate devices. The first is a wave meter which has a resolution of 1 picometer. After using the wave meter to tune the laser roughly to the Na D<sub>2</sub> line, the Doppler free fluorescence spectrum (see Fig. 3) created by counter propagating the oscillator beam through a sodium vapor cell is used to tune the laser accurately to  $f_a$  and  $f_c$ . The tuning for wind measurements is accomplished by tuning to  $f_a$  and then counting the fringes from a Fabry-Perot interferometer with a free spectral range of 150 MHz to tune the laser to  $f_a + f_0$  and  $f_a - f_0$  ( $f_0 = 600$  MHz).

The output stage consists of a 3 stage pulsed dye amplifier pumped by an injection locked Nd:YAG laser. The oscillator beam is pulse amplified with a pulse length of 4.2 nanoseconds. The resulting beam is nearly fourier transform limited with a line width less than 150 MHz (FWHM).

Figure 2. System Transmitter Diagram

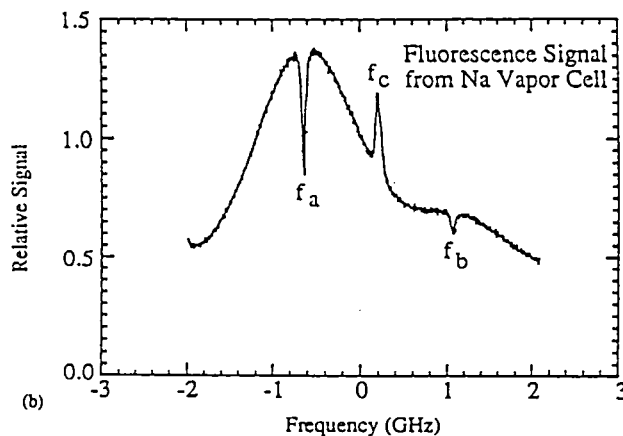


Figure 3. Na vapor cell resonance fluorescence spectrum

## REFERENCES

Bills, R.E. , C.S. Gardner, and C.Y. She, Narrowband lidar technique for sodium temperature and Doppler wind observations of the upper atmosphere, *Opt. Eng.*, **30**, 13-21, January 1991.

# Error Analysis of Wind Measurements for the University of Illinois Sodium Doppler Temperature System

W. Matthew Pfenninger and George C. Papen  
Department of Electrical and Computer Engineering  
University of Illinois at Urbana-Champaign  
1406 W. Green St.  
Urbana, IL 61801

Four-frequency lidar measurements of temperature and wind velocity require accurate frequency tuning to an absolute reference and long term frequency stability [Bills, et al., 1991]. In this paper, we quantify frequency tuning errors for the Illinois sodium system. The Illinois sodium lidar system contains two frequency references: a sodium vapor cell to measure absolute frequencies and a reference interferometer to measure relative frequencies. To determine laser tuning errors, we monitor the vapor cell and interferometer during lidar data acquisition and analyze the two signals for variations as functions of time. Both sodium cell and interferometer are the same as those used to frequency tune the laser. By quantifying the frequency variations of the laser during data acquisition, an error analysis of temperature and wind measurements can be calculated [Bills, et al., 1991]. These error bounds determine the confidence in the calculated temperatures and wind velocities.

## Frequency Tuning for Temperatures and Winds

The temperature and wind measurements of the University of Illinois' system are based on the doppler-broadened sodium  $D_2$  resonance line, shown in Figures 1 and 2. Temperatures are calculated from a ratio of returns from  $f_a$  and  $f_c$ . The temperature measurements are taken at frequencies where resonance is relatively insensitive to small variations in frequency. The change in temperature,  $\Delta T$ , as a function of frequency tuning error  $\Delta f$  is given by

$$\Delta T = 0.25 (\Delta f / \sigma_d)^2 \quad (1)$$

where  $\sigma_d$  is the sodium rms Doppler width [Bills, et al., 1991]. Using Eq. (1), temperature errors less than 1 K require laser tuning within 10 MHz of  $f_a$  and  $f_c$ .

Wind measurements are performed by acquiring returns with the laser tuned to two other frequencies on the sides of the  $D_{2a}$  resonance ( $f_a + f_0$ ,  $f_a - f_0$ ). These two frequencies were chosen as the locations on the resonance curve where backscatter cross-section varies strongly with frequency. As atoms move toward the receiver, the resonance returns shift to a higher frequency. This results in enhanced  $f_a + f_0$  returns while  $f_a - f_0$  is decreased.

Wind tuning is much more sensitive to frequency errors since the laser is tuned to the sides of the  $D_{2a}$  resonance where cross section varies more rapidly with frequency. Velocity error,  $\Delta v$ , as a function of frequency error,  $\Delta f$ , and wavelength,  $\lambda_0$ , is given by

$$\Delta v = 0.71 \lambda_0 \Delta f \quad (2)$$

[Bills, et al., 1991]. At  $\lambda_0 = 589 \text{ nm}$ , this corresponds to an allowed 2.4 MHz error in frequency tuning to maintain a 1 m/s error in radial velocity.

The Doppler free features of the temperature stabilized sodium vapor cell provide frequency markers (Fig. 2). These lines are stable and provide an absolute frequency reference. Tuning to  $f_a$  is achieved by adjusting the ring laser frequency until the cell output just begins increasing on the high frequency edge of the  $D_{2a}$  trough. Tuning to  $f_a -$

$f_0$  and  $f_a+f_0$  is accomplished by adjusting the laser frequency by four free spectral ranges of the reference interferometer corresponding to 600 MHz.

The interferometer is adjusted to match the sodium cell once for every four one-minute profiles. Thus it is important to calibrate the interferometer to determine how stable the interferometer is for the duration of each profile and throughout the series of four profiles that are required for a wind measurement. Once the interferometer is calibrated, the laser frequency errors can be used to calculate an error bar for the wind velocity measurements.

### Calibration of the Reference Interferometer

The transfer function ( $I_{out}/I_{in}$ ) of the reference interferometer is given by

$$I_O(f) = \frac{1}{1 + \left[ \frac{2F}{\pi} \sin\left(\frac{\pi f}{FSR}\right) \right]^2} \quad (3)$$

where  $F$  is the finesse and  $FSR$  is the free spectral range. The reference interferometer's stability is determined using a stabilized HeNe laser. The interferometer output is monitored with a computer controlled acquisition system with the stabilized HeNe laser as the source. The frequency error is determined by multiplying the output intensity of the interferometer by the inverse of the transfer function Eq. (3) centered at the maximum sensitivity ( $\approx 0.7 I_{max}$  where  $I_{max}$  is the maximum interferometer output).

Figure 3 shows experimental setup. An acousto-optic cell and iris are inserted to isolate the laser from the interferometer. Approximately 1-1/2 hours of interferometer output intensity measurements were taken at  $\approx 20$  Hz. The intensity data is then converted to frequency data using the inverse of Eq. (3). This frequency data is then processed into one-minute means. The variance of the histogram of the means over the 1-1/2 hour period provides a quantitative measure of the frequency variation in the reference interferometer.

### Calculation of Frequency Variation of the Na System

Once the interferometer is calibrated, frequency errors are monitored by computer during lidar data acquisition. The reference interferometer is repositioned as a frequency monitor for the sodium system. During each profile (one profile being 1 minute integration time during lidar acquisition), similar measurements of the interferometer output are acquired and converted to frequency measurements. This frequency data is then grouped into tuning frequencies ( $f_a$ ,  $f_a+f_0$ , and  $f_a-f_0$ ) to determine the frequency stability of the laser. These frequency errors are converted to temperature and wind velocity errors using Eqs. (1) and (2). The average variation in tuning frequency provides error bars to bound wind velocity and temperature measurements. During processing, lidar profiles with poor frequency stability can be marked and later removed if required.

## REFERENCES

Bills, R. E., and Chester S. Gardner, Narrowband Lidar Technique for Sodium Temperature and Doppler Wind Observations of the Upper Atmosphere, Opt. Eng., 30, 13-21, 1991.

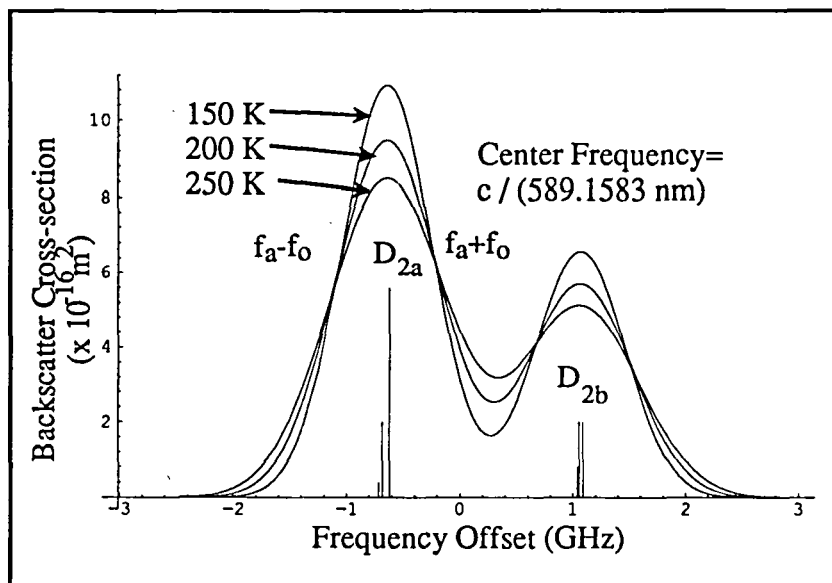


Figure 1. Na Doppler-broadened absorption spectrum plotted as a function of frequency for three temperatures

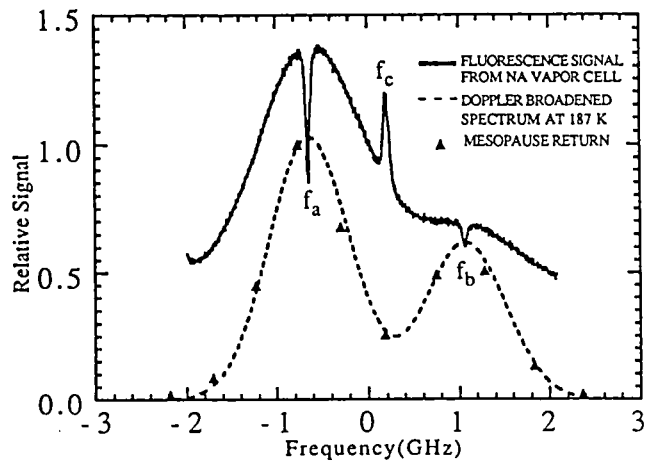


Figure 2. The solid curve is the measured Na vapor cell fluorescence spectrum. The labels denote the Doppler-free features at the D<sub>2a</sub> peak ( $f_a$ ), crossover resonance ( $f_c$ ), and D<sub>2b</sub> peak ( $f_b$ ). The triangles denote the measured mesospheric signal accumulated from  $92 \pm 0.5$  m averaged over 1200 laser shots at each frequency. The dotted curve is the theoretical Doppler-broadened spectrum for  $T=187$  K.

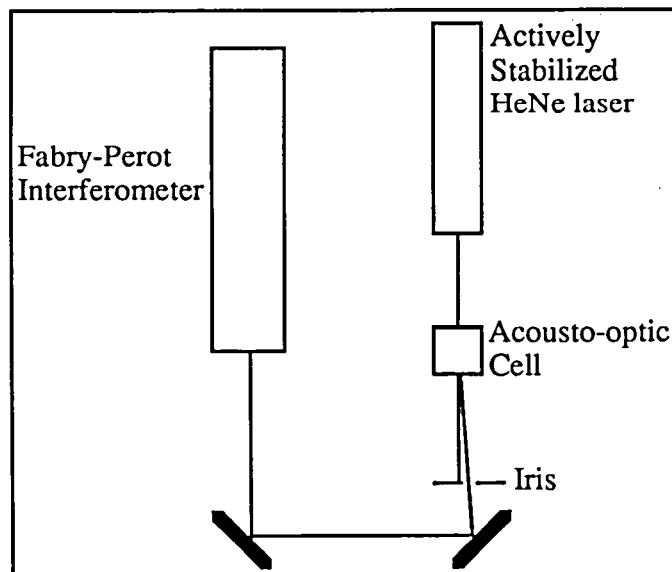


Figure 3. Table setup for reference interferometer stability test

# SODIUM DOPPLER TEMPERATURE LIDAR OBSERVATIONS OF THE MESOPAUSE REGION TEMPERATURE AND WIND STRUCTURE

Daniel C. Senft, Daniel R. Scherrer, and Chester S. Gardner

*Department of Electrical and Computer Engineering  
University of Illinois at Urbana-Champaign  
Urbana, IL 61801  
(217) 333-4155*

Measurements of the mesopause region (~ 80-105 km) temperature structure are being routinely conducted at Urbana, Illinois with the University of Illinois (UIUC) Sodium Doppler Temperature Lidar. The first measurements were taken with this system in January of 1991, and are now being performed on a weekly basis. Measurements of the mesopause wind structure have also been made, and will soon be done routinely in conjunction with the temperature measurements. This presentation will concentrate on results obtained with the UIUC Sodium Doppler Temperature Lidar (SDTL). A description of the system is given in the accompanying articles by Scherrer et al. and Pfenninger et al.

Sodium temperature data have been collected at the Urbana Atmospheric Observatory (40° N, 88° W) on 43 nights from January 1991 through March 1992. The temperature structure is highly variable on a daily basis, as well as seasonally. Figure 1 illustrates the lowest and highest measured mesopause region temperatures, with a 140 K temperature near 90 km on 28 May 1991 and 255 K near 90 km on 24 January 1991.

Long- and short-term variations are evident in the temperature contours for 5/6 February 1992 shown in Figure 2. The downward phase progression due to a tidal oscillation is evident throughout the night. Strong tidal effects are seen in almost all of the temperature results, as well as smaller scale structures due to atmospheric gravity waves. Randomly occurring events, such as sporadic Na layers ( $\text{Na}_g$ ) are also seen on some nights.

The vertical temperature structure on 9/10 December 1991 from 30 to 110 km is shown in Figure 3. Temperatures from 30 to 65 km were determined using the returns from Rayleigh backscattering to obtain relative atmospheric density, and then applying the hydrostatic equation and ideal gas law to deduce temperature. The temperatures from 75 to 110 km were determined directly from the SDTL data.

A current topic of interest is the occurrence of sporadic sodium ( $\text{Na}_g$ ) layers. At present there are a number of theories that attempt to explain the formation and structure of these layers. The SDTL and the UIUC CEDAR lidar (also located at Urbana) are providing joint information on temperature, wind, and Na/Fe/ $\text{Ca}^+$  densities when these layers occur. Figure 4 shows a substantial temperature enhancement at the time of occurrence of a  $\text{Na}_g$  layer. Further information on the correlation between Na, Fe, and  $\text{Ca}^+$  layering phenomenon is given in the paper by Kane et al., this issue.

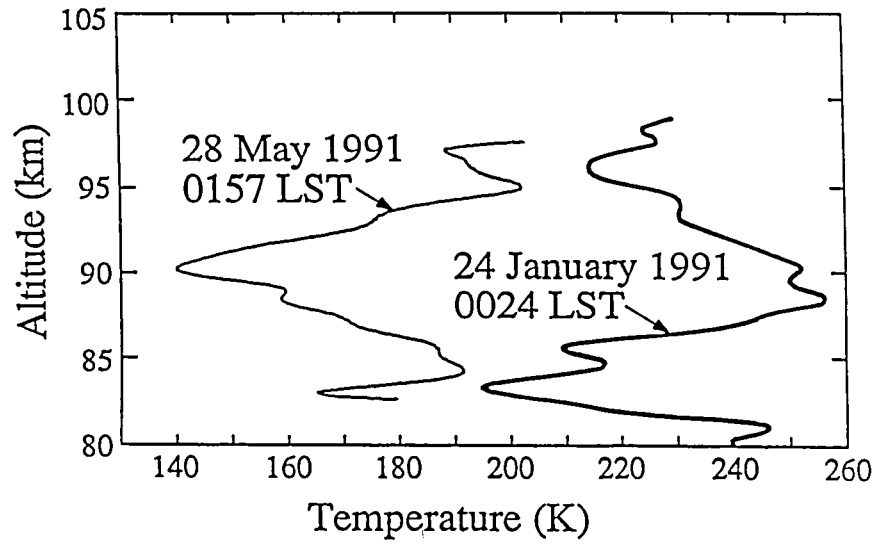


Figure 1. Temperature profiles demonstrating the coldest and warmest mesopause region temperatures measured over Urbana.

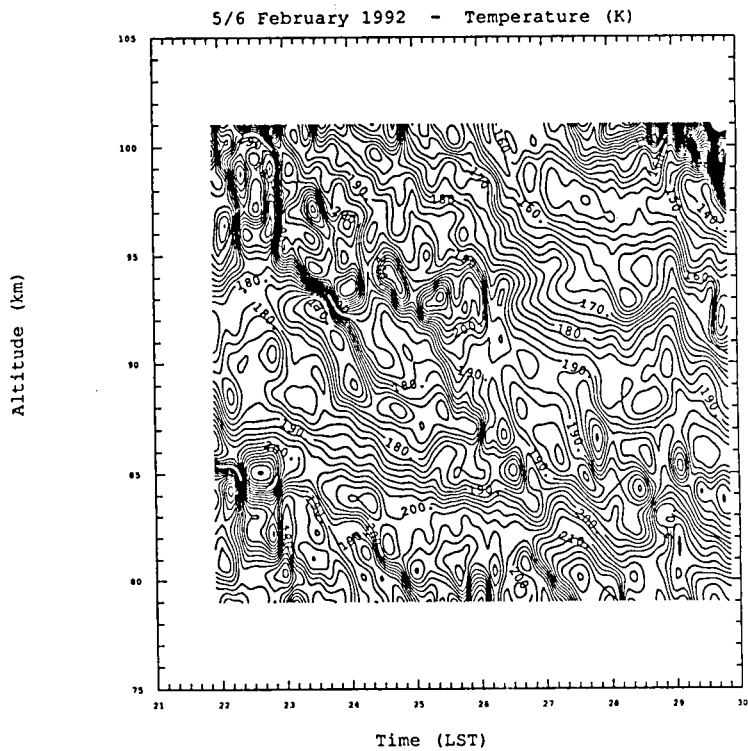


Figure 2. Temperature contours versus altitude/time for 5/6 February 1992. A downward tidal phase progression is evident throughout the night.

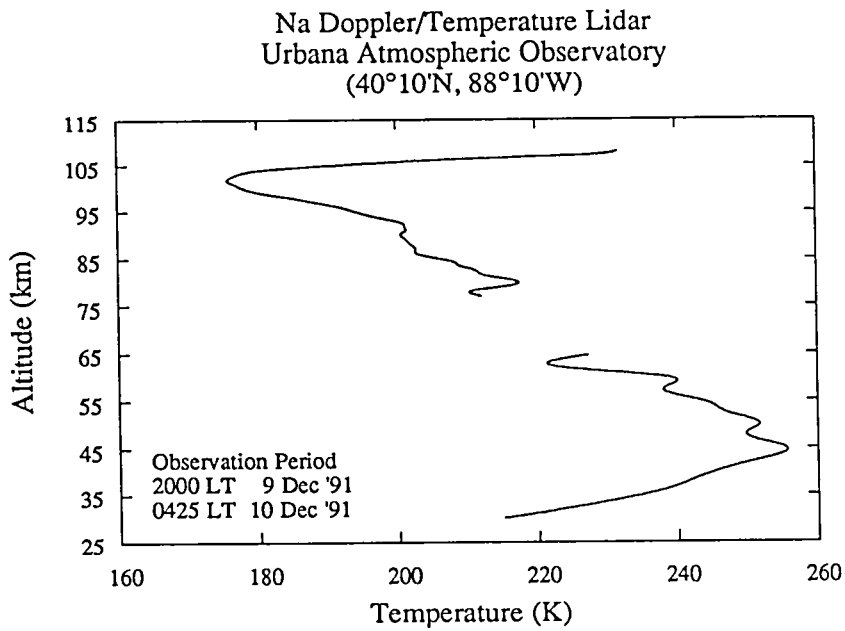


Figure 3. Vertical temperature structure over Urbana from 30 to 110 km on 9/10 December 1991.

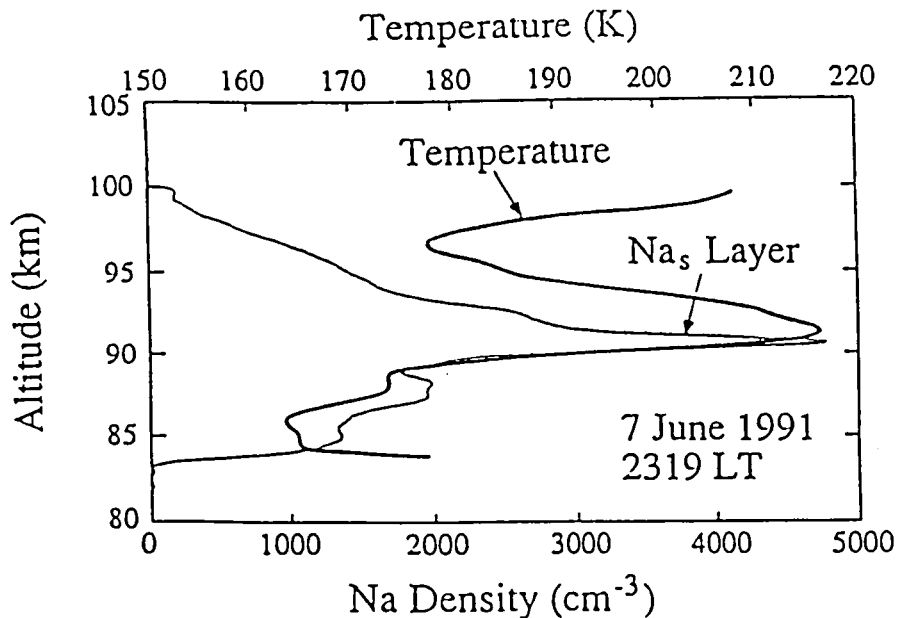


Figure 4. Temperature structure and Na density during a  $\text{Na}_s$  event on 7 June 1991. Further observations are being conducted to determine the temperature and wind structure of the mesopause region at the times these events occur, as well as the correlation with other minor atmospheric constituents (primarily Fe and  $\text{Ca}^+$ ).



# Airborne Sodium and Rayleigh Lidar Observations from ALOHA-90

by

Chris A. Hostetler and Chester S. Gardner  
Department of Electrical and Computer Engineering  
1406 W. Green Street, Everitt Laboratory  
University of Illinois at Urbana-Champaign  
Urbana, Illinois 61801  
(217) 333-4155

## Introduction

Many observations exist on wind and density fluctuations due to gravity waves in the stratosphere and mesosphere as well as the chemistry of atomic and ionic metal layers near the mesopause. Most of these observations provide information on the vertical and temporal variation of these phenomenon; however, very little information exists on their geographic variability and horizontal scales. The Airborne Lidar and Observations of Hawaiian Airglow Campaign (ALOHA-90) was conducted to address some of these observational deficiencies. Here we describe airborne Na and Rayleigh lidar observations from the ALOHA-90 campaign. We present gravity wave vertical and horizontal wave number spectra from the upper stratosphere and the upper mesosphere. Also, we document the occurrence of a large amplitude short horizontal scale ( $\lambda_h \sim 16$  km) quasi-monochromatic gravity wave event and discuss the implications of the event in light of recently developed gravity wave horizontal wave number spectra models [Gardner et al., 1992]. Finally, we discuss observations of sporadic Na layer events.

## Experimental Description

The NCAR Research Aviation Facility provided their Lockheed Electra 4-engine turbo-prop aircraft for the ALOHA campaign. The University of Illinois operated a Na/ Rayleigh lidar on board the Electra. This lidar measured

relative atmospheric density profiles in the stratosphere (25–45 km) and Na density profiles near the mesopause (80–105 km). Of the eleven flights undertaken during the ALOHA campaign, this paper concerns the five straight-line flights over the Pacific Ocean conducted on 22, 25, 27, 31, March and 3 April, 1990. These flights originated from Maui (20°N, 156°W) and followed predominately zonal or meridional paths to a turnaround point and then back. The average horizontal span of each flight leg was ~1800 km.

The CEDAR Na/Rayleigh lidar includes a 200 pps excimer laser, a tunable dye laser pumped by the excimer laser and a 35 cm diameter zenith-pointing telescope. The lidar relies on resonance fluorescence scattering from neutral sodium near the mesopause (85-105 km) and Rayleigh scattering in the upper stratosphere (20-50 km). The receiving system includes a PMT detector operating in photon counting mode and a range-gated data acquisition system. At the beginning of each mission the output powers of the excimer and dye lasers were approximately 90 W and 10 W, respectively. By the end of each mission, the powers typically dropped to about 70 W and 7 W as the excimer gas and laser dye aged. The nominal power-aperture product of the lidar is approximately 1 W m<sup>2</sup>. Lidar photon count profiles were acquired by integrating the detected backscattered signal from 2400 laser

shots over a period of 12 s. The ground speed of the aircraft averaged about 150 m/s so that the 12 s integration period corresponds to a horizontal resolution of approximately 1.8 km. The vertical resolution of the photon count profiles is 37.5 m.

### Gravity Wave Vertical and Horizontal Wave Number Spectra

Figure 1 shows the vertical and horizontal wavenumber spectra of atmospheric density fluctuations from both the mesopause and upper stratosphere. Several theories have been proposed to explain the magnitude and power law shape of the vertical wave number spectrum [Dewan and Good, 1986; Gage, 1979; Weinstock, 1990; Hines, 1991]. The linear instability model of Dewan and Good [1986] predicts that the saturated portion of the vertical wave number spectrum follows an  $m^{-3}$  power law dependence and that the saturation magnitude is independent of altitude. While the slope of the vertical wave number spectrum for the mesopause region is very near -3, the slope of the spectra from the upper stratosphere is closer to -2. Moreover, the magnitude of the spectrum in the mesopause region is 20 times greater than the magnitude in the upper stratosphere. Under the linear instability model, the disparity of the slopes and magnitudes between the two regions suggests that the gravity wave spectrum in the stratosphere is not saturated over the range of observed vertical wave numbers. The horizontal wave number spectrum in the mesopause region also exhibits a power law dependence with a slope near -2. Recent gravity wave spectra models developed by Gardner et al. [1992] suggest that the slope of the horizontal wave number spectrum should equal the slope of the temporal frequency spectrum in the horizontal wave number range between  $h_*$  and  $m_*$ . Indeed the slope of the

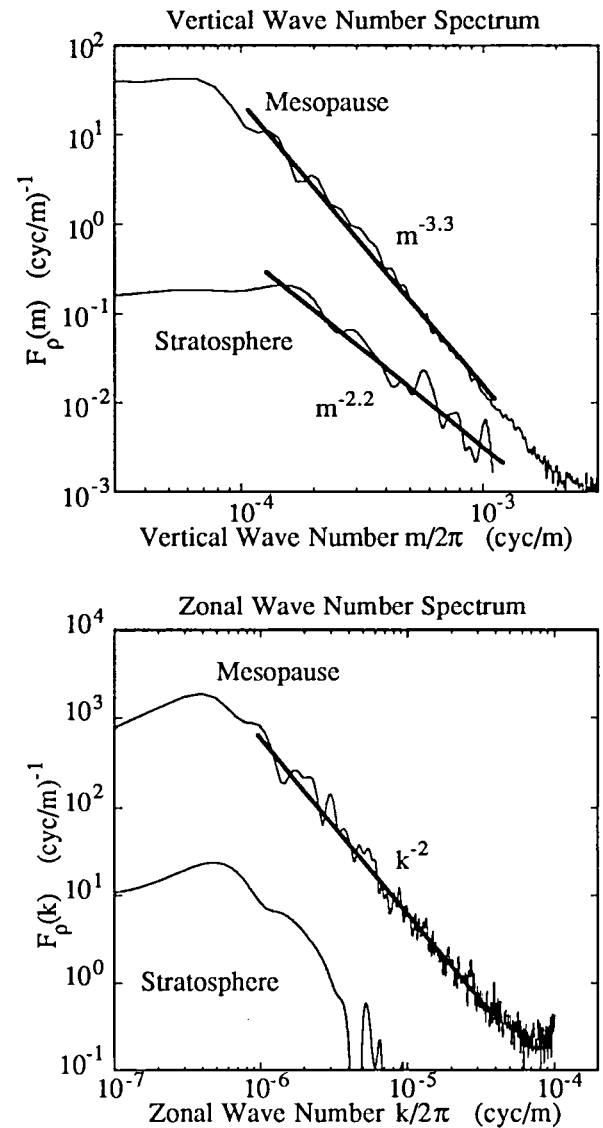


Fig. 1 Atmospheric density vertical and horizontal wave number spectra from the 31 March 1990 mission.

horizontal wave number spectrum is consistent with the slopes of the temporal frequency spectra observed at Urbana, IL, by Senft and Gardner [1991]. In the stratopause region the horizontal wave number spectrum was too corrupted by photon noise to allow a power law fit. However, it is quite clear that the magnitude of the horizontal spectrum in the

upper stratosphere is much lower than the magnitude in the mesopause region.

High Amplitude Short Horizontal Scale Gravity Wave Events

On the 22 March 1990 mission an extremely energetic, short horizontal scale, quasi-monochromatic gravity wave event was observed in the mesopause region on the return flight. Figure 2 shows Na density between 99 and 100 km plotted versus latitude. The Na density exhibits an oscillatory behavior over a horizontal span of ~225 km. The amplitude of the Na density oscillation is ~70% of the background density at the maximum and the wavelength of the oscillation is ~16 km. The quasi-monochromatic feature is easily seen in the horizontal wave number spectrum shown in Fig. 3. A model horizontal spectrum was computed for this flight following the approach of Gardner et al. [1992] and is shown as the darker line on the same plot. The quasi-monochromatic event exhibits a spectral energy that is 30 times higher than predicted by the model. The feature had a vertical wavelength that appeared to be comparable to or larger than the sodium layer thickness. Similar short horizontal wave length events ( $\lambda_h \sim 15$  to 25 km) were observed in the OH night glow by airglow imagers positioned at Haleakala, Maui [Taylor and Edwards, 1991]. In order to be observed by the airglow imagers, the vertical wavelength of these events had to be at least as large as the thickness of the OH layer (~10 km FWHM). The temporal period of the events varied between 5 and 13 min. Horizontal wavenumber spectra models developed by Gardner et al. [1992] suggest that these waves come from the unsaturated portion of the vertical wave number spectrum ( $\lambda \leq \lambda_z^* \cong 14\text{km}$ ) and have periods near the buoyancy period ( $T_B \cong 5$  min). The predictions of the

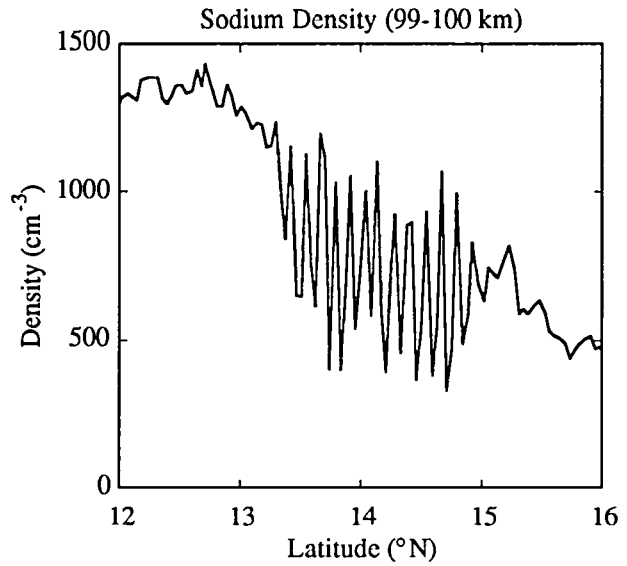


Fig. 2 Oscillations in Na density due to the quasi-monochromatic gravity wave event on 22 March 1990 ( $\lambda_h \sim 16$  km).

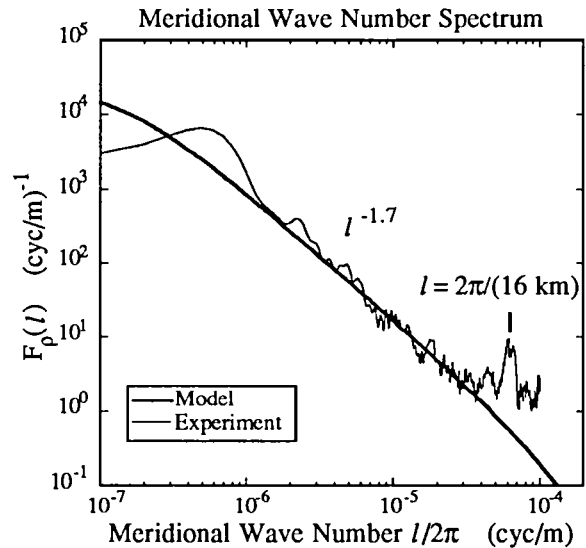


Fig. 3. Atmospheric density meridional wave number spectrum for 22 March 1990.

model are consistent with both lidar and airglow observations.

### Sporadic Sodium Layers

Sporadic sodium layers are very dense and very thin (~1 km FWHM) anomalies in the sodium layer that can form over periods ranging from a few minutes to several hours. Large sporadic sodium events were encountered on several flights during the ALOHA-90 campaign [Kane, et al., 1991]. Figure 4 shows a sodium density profile from the 22 March mission. The sporadic sodium layer at 94 km formed shortly after takeoff and was observed to have a meridional extent of at least 1800 km. Airglow measurements on Haleakala show enhancements in both OH and O<sub>2</sub> emissions as well as elevated temperatures during the same observation period, suggesting that the sporadic sodium layer formed within a very short time period over both the aircraft and Haleakala [Gardner et al., 1991].

Acknowledgments: The authors gratefully acknowledge Timothy J. Kane for his many contributions throughout this project.

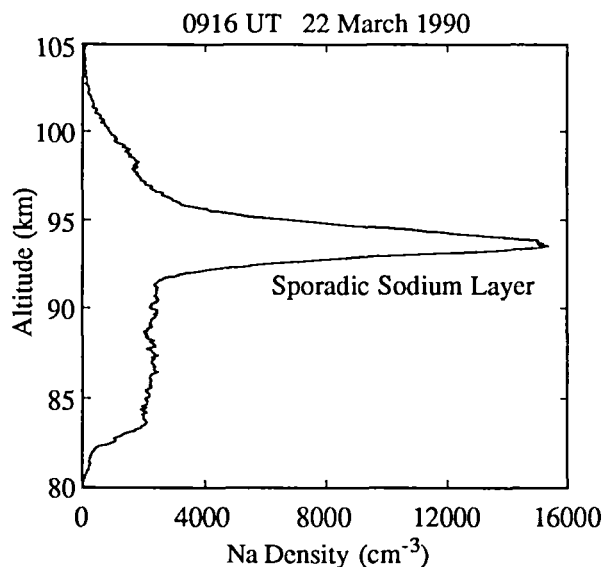


Fig. 4 Sporadic sodium event from the 22 March 1990 mission.

### References

- E. M., and R. E. Good, Saturation and the "universal" spectrum for vertical profiles of horizontal scalar winds in the atmosphere, *J. Geophys. Res.*, 91, 2742-2748, 1986.
- Gage, K. S., Evidence for a  $k^{-5/3}$  power law inertial range in mesoscale two-dimensional turbulence, *J. Atmos. Sci.*, 36, 1950-1954, 1979.
- Gardner, C. S., T. J. Kane, J. H. Yee, J. H. Hecht, D. N. Turnbull, and R. P. Lowe, Formation characteristics of sporadic Na layers observed simultaneously by lidar and airglow instruments during ALOHA-90, *Geophys. Res. Lett.*, 18, 1369-1372, 1991.
- Gardner, C. S., C. A. Hostetler, S. J. Franke, Gravity wave models for the horizontal wave number spectra of atmospheric velocity and density fluctuations, *J. Geophys. Res.*, submitted March 1992.
- Hines, C. O., The saturation of gravity wave in the middle atmosphere, Part II, Development of Doppler-spread theory, *J. Atmos. Sci.*, 48, 1360-1379, 1991.
- Kane, T. J., C. A. Hostetler, C. S. Gardner, Horizontal and vertical structure of the major sporadic sodium layer events observed during ALOHA-90, *Geophys. Res. Lett.*, 18, 1365-1368, 1991.
- Senft, D. C., and C. S. Gardner, Seasonal variability of gravity wave activity and spectra in the mesopause region at Urbana, *J. Atmos. Sci.*, 44, 1404-1410, 1987.
- Taylor, M. J., and R. Edwards, Observations of short period mesospheric wave patterns: *In situ* or tropospheric wave generation?, *Geophys. Res. Lett.*, 18, 1337-1340, 1991.
- Weinstock, J., Saturated and unsaturated spectra of gravity wave and scale-dependent diffusion, *J. Atmos. Sci.*, 2211-2225, 1990.

## Rayleigh/Raman Greenland lidar observations of atmospheric temperature during a major Arctic stratospheric warming event

John W. Meriwether, Robert Farley¶, Capt. R. McNutt, Phan D. Dao, Ionospheric Physics Division, Geophysics Directorate, Phillips Laboratory, Hanscom AFB, MA 01731  
¶Air Force Geophysics Scholar  
Warren P. Moskowicz, Gilbert Davidson, PhotoMetrics, Inc., 4 Arrow Drive, Woburn, MA 01801

Between 22 January 1991 to 5 February 1991, we made numerous observations of atmospheric temperature profiles between 10 and 70 km by using the combination of Rayleigh and Raman lidar systems contained in the PL mobile lidar facility located at the National Science Foundation incoherent radar facility of Sondrestrom in Greenland [67°N, 51°W]. The purpose of these measurements was to observe the dynamics of the winter Arctic stratosphere and mesosphere regions during a winter period from the succession of temperature profiles obtained in our campaign observations.

Figure 1 illustrates the optical configuration of our instrumentation. A XeF 351 nm excimer laser excited the N<sub>2</sub> Raman-shifted 382 nm backscattered signal to altitudes of 40 km. The Nd:YAG 532nm laser produced the high altitude Rayleigh backscattered signal profile from 20 km to 75 km. A shutter wheel protected the 532 nm phototube from the Rayleigh backscattered signal below 20 km. The inclusion of the Raman channel in our instrumental configuration avoids the aerosol contamination that exists for the lower stratosphere. The signals for both backscattered signals were received by a 0.6 m telescope, and a dichroic filter separated the two signals as illustrated. The 382 nm filter was constructed to include extra blocking at the Rayleigh excimer backscattered signal so that the intense 351 nm Rayleigh signal was excluded from the Raman channel with a blocking rejection factor of 10<sup>-10</sup>.

Figure 2 plots both the Raman and Rayleigh relative density profiles with the two curves normalized to unity at a tie point of 30 km. The integration time was one hour for each of the two profiles shown. The Rayleigh/Raman composite relative density curve between 10 and 80 km was used to compute a temperature profile from the scale height dependence of density upon temperature. Figure 3 presents a succession of one hour averaged temperature profiles for the night of 31 January, 1991. Dynamical activity is evident in these profiles, and the dashed line denotes the downward phase progression of a gravity wave event near the stratopause. Generally speaking, the activity in the lower mesosphere appears to have a vertical wavelength of about 5 to 10 km; a more quantitative study will require power spectral density analysis. Also shown with each temperature profile for the purpose of reference is the 76 atmosphere temperature model. One can see that the stratopause is significantly colder than this model in the region between 30 to 60 km. The Raman data below 10 km is not to be trusted as the analysis should include a more careful treatment of atmospheric extinction, which was not done. A LOWTRAN 7 model was used to compute atmospheric extinction profiles for the Raman region above 5 km.

Figure 4 illustrates a succession of one hour averaged temperature profiles selected from a series of 8 nights between 22 January 1991 to 5 February 1991. The total number of hours of observations collected during this clear period was about 105 hours. One can see that major changes were taking place throughout this period. Between 22 January to 28 January, the middle atmosphere became colder and then warmed while the lower stratosphere was initially hot and gradually became colder. Substantial dynamic activity can be seen in the lower mesosphere region between 50 and 70 km. From the 30 of January to the 5 February, 1991, the stratopause region became warmer, and reached a normal looking profile by the end of the observation period. However, the profile between 10 and 25 km showed a substantial cooling trend.

Figure 5 presents the potential vorticity maps that were generated by Dr. Ib Mikkelsen [courtesy of the Danish Meteorological Institute] for the period of our observations. We have included a selection of four that illustrates the breakup of the polar vortex during the progress of the major stratosphere warming event of late January, 1991. The x denoted in each of the four maps is the location of the Sondrestrom site. We have outlined the region of the boundary of the polar vortex denoted by multiple contours. At this point the potential vorticity exhibits a large gradient from the interior of the vortex to the outside region. It is clear that initially the Sondrestrom site was some distance removed from the central region of the polar vortex. Two days later, the vortex had started to bifurcate, and this division was completed by 2 February. The western cell had migrated south towards the Sondrestrom site, and on 5 February, the Sondrestrom site was within the cell interior.

Figure 6 illustrates in greater detail a selection of four one hour averaged temperature profiles between 29 January to 5 February. One can see that as the Sondrestrom site became immersed within the center of the polar cell that the temperature profile below 20 km became progressively cooler. The vertical dashed line denotes the temperature of 192 °K necessary for the formation of polar stratospheric clouds. Had the observations continued much longer, the temperatures may well have reached the lower levels required to support PSC formations. Unfortunately, the skies became overcast after 5 February, and further observations were not possible.

These observations illustrate the value of the Rayleigh/Raman lidar for monitoring the dynamic state of the atmosphere at high latitudes. The inclusion of a second 532 nm channel in our optical configuration for low altitude measurements would enable the determination of the extent of aerosol loading by comparison with the Raman profile.

#### PL/GD Raman lidar configuration

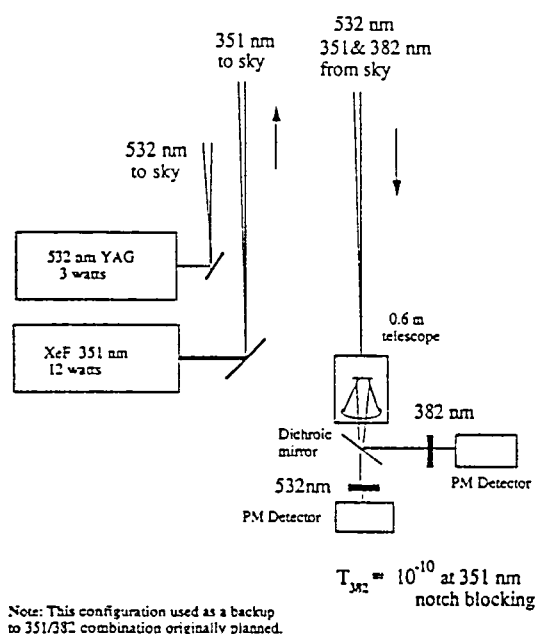


Figure 1: The optical configuration used for the Greenland Rayleigh/Raman measurements.

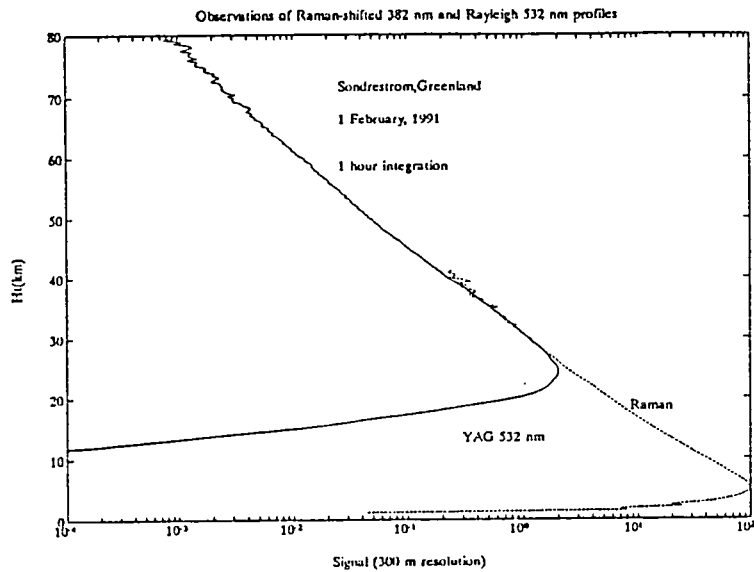


Figure 2: Lidar profiles of 532 nm YAG Rayleigh and 382 nm Raman profiles

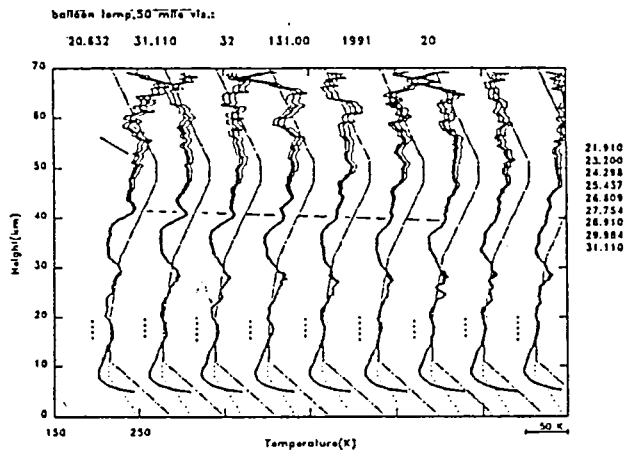


Figure 3: Succession of one hour averaged temperature profiles for 31 January 1991. Also shown are the  $\pm 1 \sigma$  error envelopes for each temperature profile.

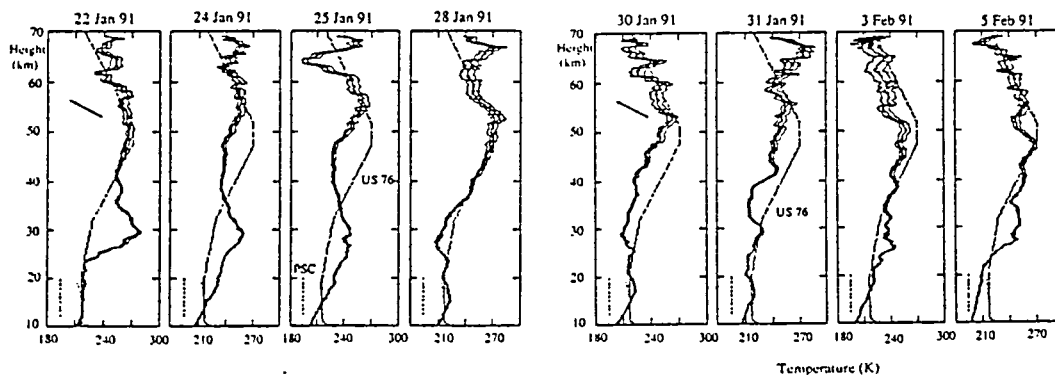


Figure 4. Series of one hour averaged temperature profiles selected from 8 nights in late January and early February, 1991.

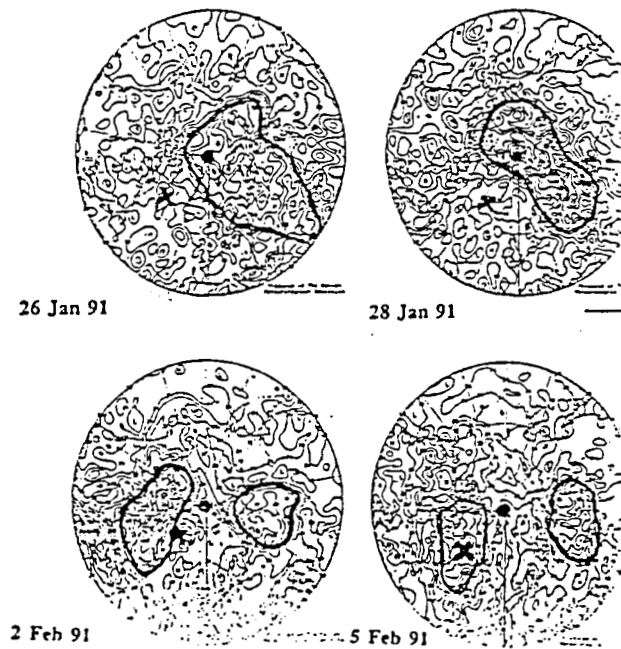


Figure 5. Four potential vorticity maps of the Arctic region for selected nights. The outline of the polar vortex is indicated, and the x denotes the location of the Sondrestrom lidar station in southern Greenland.

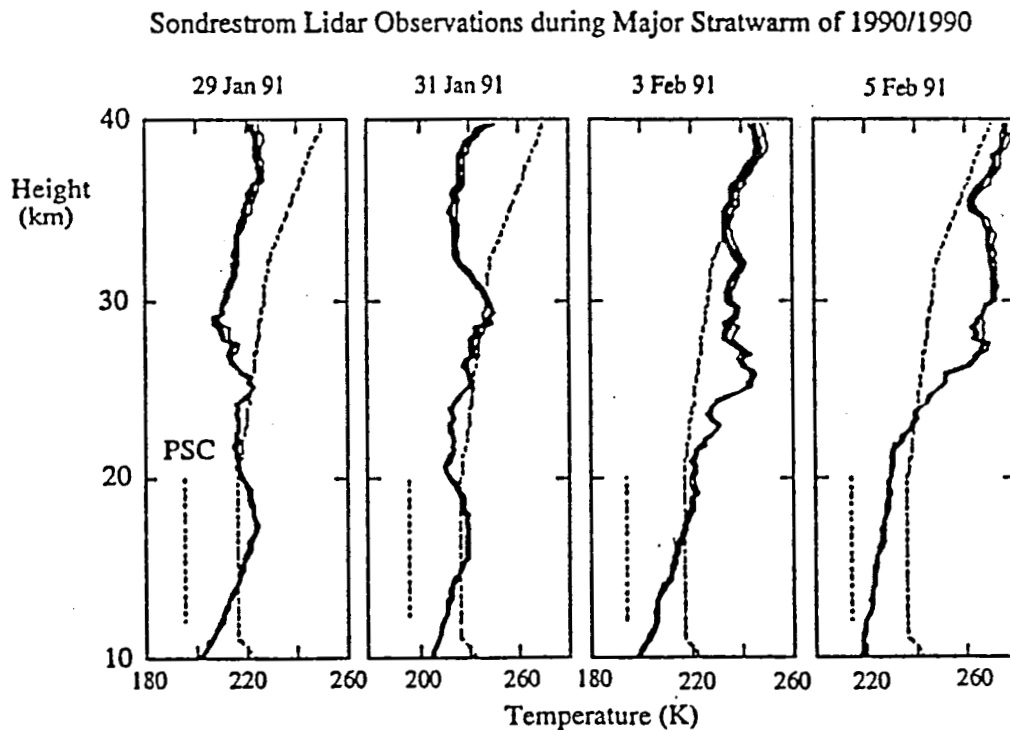


Figure 6. Four vertical profiles of temperatures between 10 and 40 km from selected nights in the last phase of the stratospheric warming event.

## Elastic and Raman lidar temperature measurements from Poker Flat, Alaska during February 1992.

Michael Burka<sup>1</sup>, Phan Dao<sup>2</sup>, Gilbert Davidson<sup>1</sup>, Robert Farley<sup>2</sup>  
John Meriwether<sup>2</sup>, Lt Alex Wilson<sup>2</sup>

<sup>1</sup>PhotoMetrics, Inc., 4 Arrow Rd, Woburn, MA 01801

<sup>2</sup>Ionospheric Physics Division, Geophysics Directorate, Phillips Laboratory  
Hanscom AFB, MA 01731

Ground-based lidar observations are increasingly used to elucidate the dynamical structure of the stratosphere and mesosphere. Here we report observations made from Poker Flat, Alaska (65.130° N, 147.483° W) during February, 1992 using the Phillips Laboratory Mobile Lidar Facility.

Table 1 gives the parameters of the lidar system used for these measurements. The transmitter consisted of a XeF excimer laser with a 351 nm wavelength. Average power ranged between 9W and 14W. The telescope had a 60 cm aperture for a power aperture product of 4 W-m<sup>2</sup> during the periods of optimal performance. The receiver contained two channels, one for elastic backscattering at 351 nm and a nitrogen Raman backscattering channel at 382 nm. The elastic channel contained a mechanical shutter to protect the photomultiplier from the intense, low altitude return. The Raman channel had no shutter, and a neutral density filter was introduced to prevent afterpulsing in the photomultiplier.

Figure 1 displays photocount profiles for the two channels. Each point represents the total number of photocounts collected from 216,000 laser shots (1 hour integration) in a 2 microsecond time bin. The 351 nm elastic channel peaks at about 20 km, the altitude at which the mechanical shutter is fully open. The 382 nm Raman channel peaks lower, with an apparent peak at 5 km, although that channel's photomultiplier may have been saturated by the return from lower altitudes. The small amount of structure seen in the elastic profile between about 18 and 30 km is real; it represents Mie scattering from aerosols deposited in the stratosphere by the Mt. Pinatubo eruption of last year.

Analysis of the data consisted of the following steps. First, the average background in each channel was estimated by averaging the photocounts in bins 330-399, corresponding to the altitude range of 99.4 to 120.1 km. These backgrounds, which consisted of sky background plus photomultiplier dark count, were subtracted from the photocount profiles. Second, the number of photocounts was corrected for atmospheric extinction as a function of altitude. Different extinction coefficients were used for the elastic and Raman channels, because atmospheric extinction is more severe at 351 nm than at 382 nm. Extinction coefficients were taken from a Lowtran model, but did not include volcanic aerosols. Next, the number of photocounts in each bin was multiplied by the square of the corresponding altitude, to compensate for the inverse square falloff of the signal. Then, the two profiles were normalized to the density of the US 76 Standard Atmosphere at an altitude of 30 km, and a composite density profile was created

using the Raman signal for altitudes below 30 km and the elastic signal for altitudes of 30 km and above. The reason for this composition is that above 30 km the atmosphere is relatively free of aerosols, and the elastic signal consists almost entirely of Rayleigh scattering from air molecules. However, at lower altitudes the elastic channel is contaminated by Mie backscatter from aerosols, and the signal overestimates the atmospheric density. The Raman channel is sensitive only to atmospheric nitrogen, so it should give a true measure of atmospheric density at lower altitudes. Figure 2 shows the density profile corresponding to the raw photocount profile in Figure 1. Subtracting the Raman channel density profile from the elastic channel density profile yields a measure of the aerosol content of the atmosphere. During the time of these measurements, the region between 20 and 30 km was dominated by aerosols deposited by the Mt. Pinatubo, and Figure 3 shows the vertical structure of this aerosol layer. This particular profile represents a one hour integration from 05:10 to 06:10 (UT) on 23 February, 1992. The vertical structure of the Pinatubo aerosols shows quite a bit of temporal variation on time scales of hours.

The temperature profile extracted from a measured density profile is given by

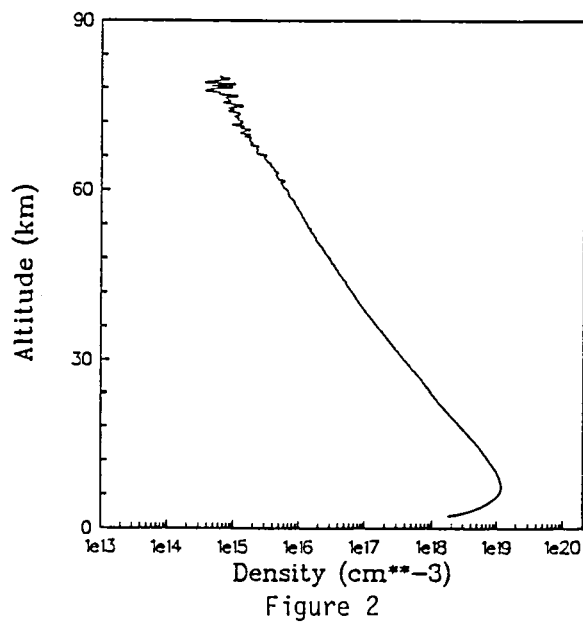
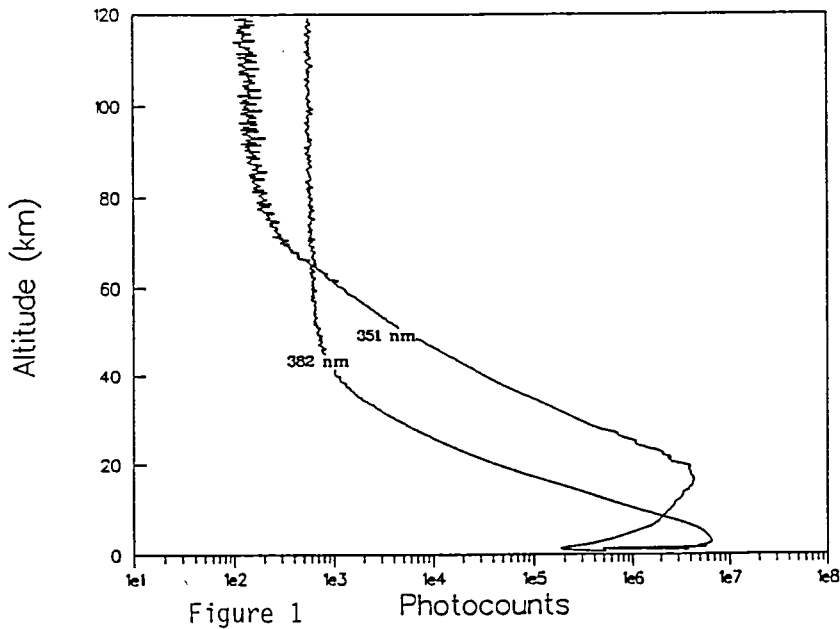
$$T(z) = \frac{T(z_0) n(z_0)}{n(z)} + \frac{m}{k n(z)} \int_z^{z_0} g(z') n(z') dz' \quad (1)$$

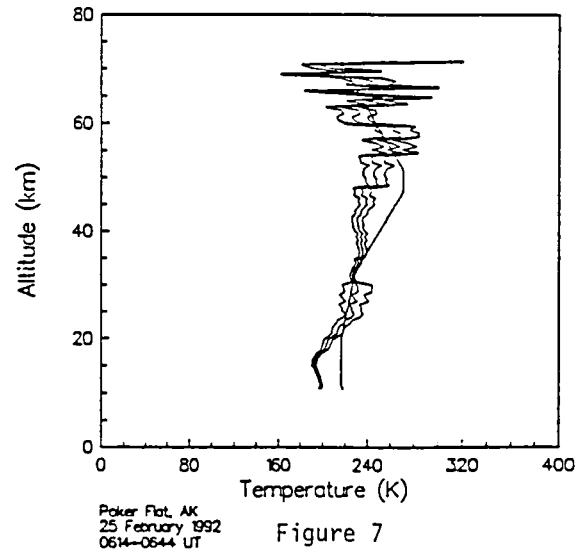
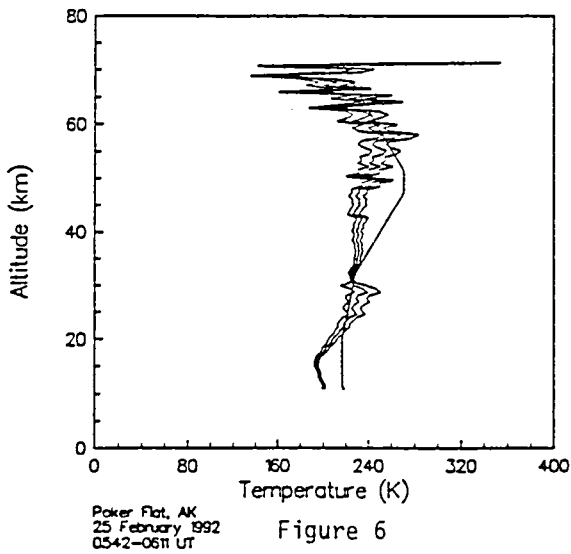
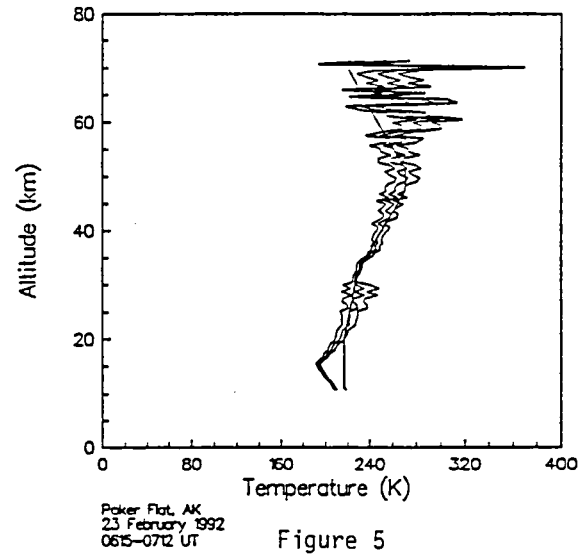
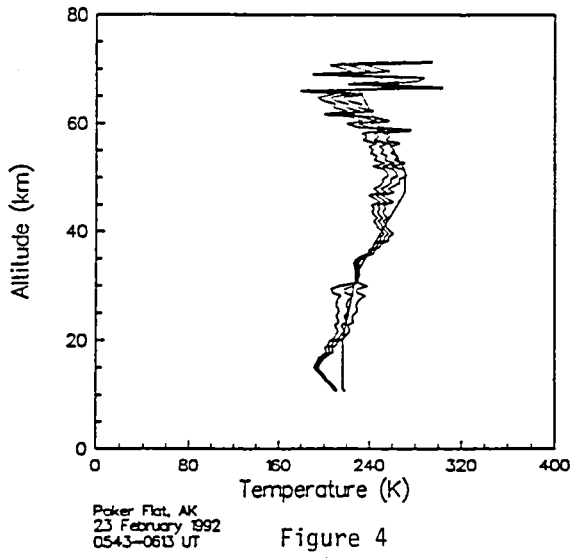
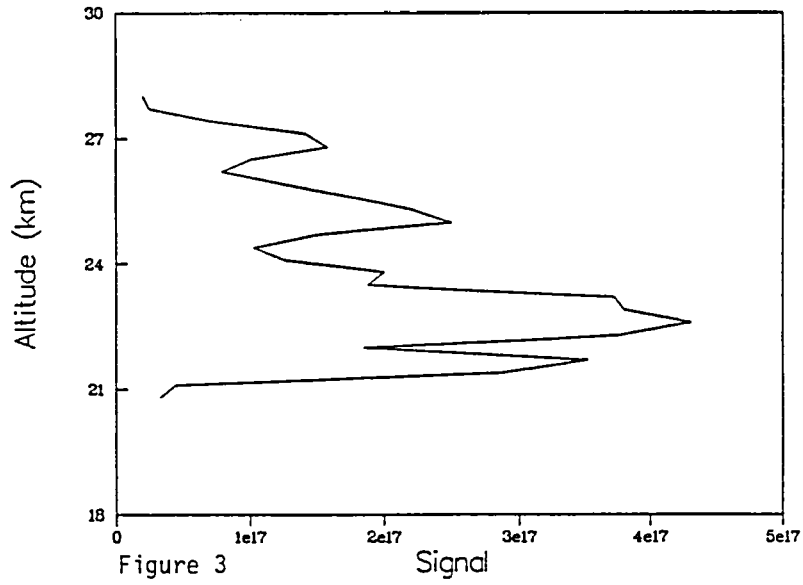
where  $T$  is temperature,  $n$  is density,  $z$  is altitude,  $m$  is the average molecular mass of air,  $k$  is Boltzmann's constant and  $g$  is the gravitational acceleration.  $T(z_0)$  and  $n(z_0)$  are the assumed temperature and density at a reference topside altitude  $z_0$ . In this analysis, these boundary values were taken from the US 76 Standard Atmosphere. Although they may vary from the true topside boundary conditions, any error becomes negligible at altitudes more than a scale length below the  $z_0$ . Equation 1 relies upon the assumptions that the atmosphere obeys the ideal gas law and the law of hydrostatic equilibrium, both good assumptions at the altitudes under study.

Figures 4 through 7 show temperature profiles from two of our nights of observation. In all four plots, the temperature profile is shown bounded by a plus or minus one standard deviation envelope. All four plots represent integration of 108,000 laser shots over one half hour, and a range resolution of 600 m was used in the data analysis. Also shown in each plot is the US 76 Standard temperature profile. The standard deviation is larger below 30 kilometers than above because the Raman channel signal is used at the lower altitudes, and both the Poisson noise and the dark count are larger in that channel. Figures 4 and 5 are from the morning of 23 February. They closely track the standard atmospheric model between 20 and 60 km, with Figure 4 showing a hint of possible gravity wave activity. Figures 6 and 7 are from the morning of 25 February. On this date the temperature profile is substantially cooler between 40 and 60 km. No gravity wave activity is visible to the eye. A statistical analysis of the data is underway. Its purpose is to quantify the amount of gravity wave activity throughout the data sample collected from 23 February to 26 February 1992.

Parameter	Value
Pulse energy	200 mJ
Pulse repetition rate	60 Hz
Atmospheric transmission at 351 nm	0.32
Atmospheric transmission at 382 nm	0.40
Range resolution	300 m
Telescope area	$2.9 \times 10^3 \text{ cm}^2$
Receiver optical efficiency	0.25
Photomultiplier quantum efficiency	0.3
Photomultiplier dark count	100 Hz

Table 1. Parameters of the PL/GPI Mobile Lidar System.





# RAYLEIGH/RAMAN LIDARS : INTERCOMPARISONS AND VALIDATION

*Marie-Lise CHANIN*  
Service d'Aéronomie du CNRS  
BP 3 - 91371 Verrières le Buisson CEDEX - France

## INTRODUCTION

Vertical sounding of the atmosphere by Rayleigh lidar has been extensively used in France to study the structure, the dynamics as well as the long term trend of the middle atmosphere. More recently the addition of a rotational-Raman mode fills the gap between the ground and 30 km in such a way that the whole altitude range from ground up to 90-100 km can be studied with a unique instrument. The growing need of absolute measurement of temperature with high precision for climatic purpose led us perform to a critical review of all the sources of errors which can occur in this type of measurement. This is the subject of a recent paper (Keckhut et al., 1992) which shows that the increase of the performances of the instrument in the last decade has been successfully obtained without compromising the accuracy. It will be briefly reviewed. This paper will be mainly concerned with the presentation of the recent improvements of the technique and of the results of intercomparisons and validation of new satellites data.

## THE NEW ROTATIONAL RAMAN LIDAR

The method uses the Antistokes rotational Raman lines of  $N_2$  and  $O_2$ . The fact that the envelop of the rotational Raman spectrum is temperature sensitive is used to deduce the temperature profile in the troposphere and low stratosphere up to 30 km - where the Rayleigh starts to be operationnal. Two major problems had to be solved : first the elimination of the contribution of the Mie backscattering. (A rejection factor of  $10^8$  was obtained by doubling the filters) and second the choice of the calibration function which can be expressed, for well defined experimental conditions, by an analytic expression with 2 constants. An intercomparison with a radiosonde profile is required once to choose the values of those constants (Nedeljkovic et al., 1992).

The results have shown to be very satisfactory, even in presence of a large aerosol backscattering, as it is observed since July 1991 at the Observatory of Haute Provence where the experiment was tested. Fig. 1 and 2 show respectively an example of such Raman profile compared with a radiosonde and the difference between the two measurements. Such a mode is now being implemented on the operational stations.

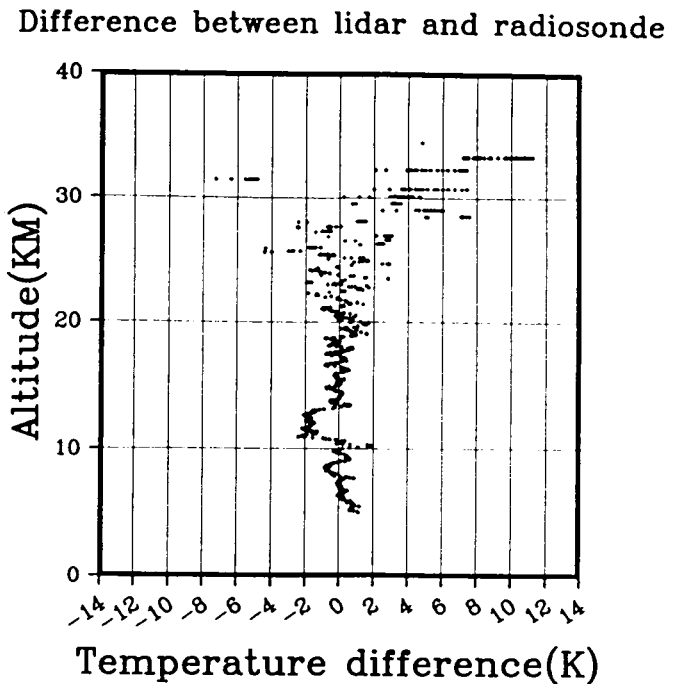
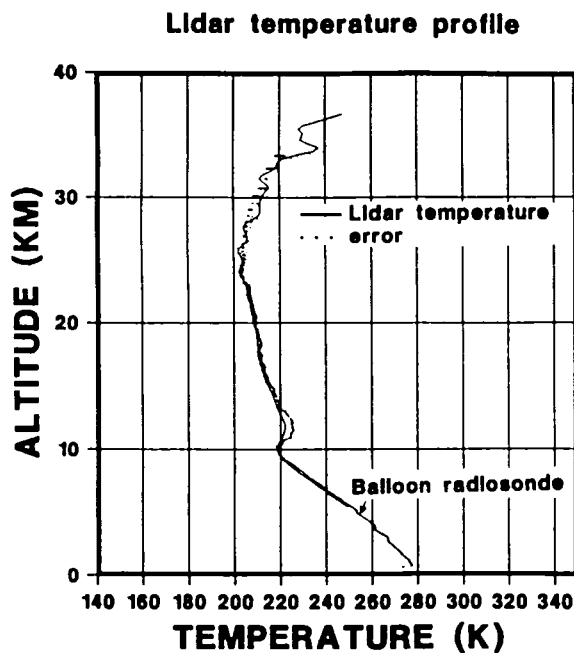


Fig. 1 - Vertical profiles of temperature obtained by radiosonde .... and by lidar – at OHP on 16 Dec. 1991. The error in the lidar measurement is shown a  $\pm 1\sigma$  (...)

Fig. 2 - Difference between the 2 profiles

## INTERCOMPARISONS

Comparisons were performed either with other instruments or with different lidars and some of the results will be presented

### Rocketsonde

Numerous comparisons have been made with datasondes since 1978. At the time they were considered as quite satisfactory up to 60 km, mainly if compared with the differences between different data sondes placed on the same rocket.

Recent comparisons with falling spheres during the DYANA campaign in 1990 were performed on 9 simultaneous opportunities. The statistical comparisons indicate a good agreement between 45 and 65 km with difference less than 2 K with a 3 K statistical dispersion. However a systematic difference of about 10 K was discovered at the altitude where the falling sphere goes through Mach 1 around 70 km, and could be taken into account in the analysis of the rocket data.

### Balloon radiosondes

The intercomparison with the Raman technique has been very satisfactory within  $\pm 1$  K as seen before. Unfortunately the common range between the radiosonde and the Rayleigh lidar is limited to low altitude, 30-35 km, but such a comparison is however very critical, as the major sources of errors in the Rayleigh lidar is situated in that altitude range. Comparison performed with radar tracked balloon have given excellent agreement with difference never

more than 1 K, if the measurements are made simultaneously and at the same site. When the balloon altitude is determined by pressure sensor, the error in the altitude determination can reach several hundred meters and therefore a difference of a few K at 30 Km is observed.

### Satellites

The main difficulty with nadir pointed radiometers, beside their low height resolution is the absolute calibration of the radiometer. It has anyway been possible to observe the same short and long time variability with instruments as SSU (Aikin et al., 1991). Comparisons make more sense with limb pointed instruments, as the instrument on board SME, SAGE II and more recently ISAMS on board UARS. Recent intercomparisons with SAGE II and ISAMS will be presented.

### Other lidars

In previous studies the lidars were too far apart to obtain more than a mean statistical difference. Recently with the help of either the movable lidar on board of a ship which was as close as 100 km from one of our site (CEL) or a mobile station placed at the same site, we obtained very interesting results : Any distance of the order of magnitude of a fraction of the horizontal wavelength of the gravity waves induces a difference which can be easily interpreted as due to the wave pattern (Fig. 3). But instruments placed at the same site even using very different configuration have led to an excellent agreement (Fig. 4). Such a comparison is the best way to evaluate the limit of precision of the technique.

## CONCLUSION

We are strongly confident that a world network of such lidars is the way to monitor the upper atmosphere in the next decade. But intercomparison campaigns between the lidars of different stations may be needed to detect the possible sources of errors which we have identified after more than a decade of continuous operation.

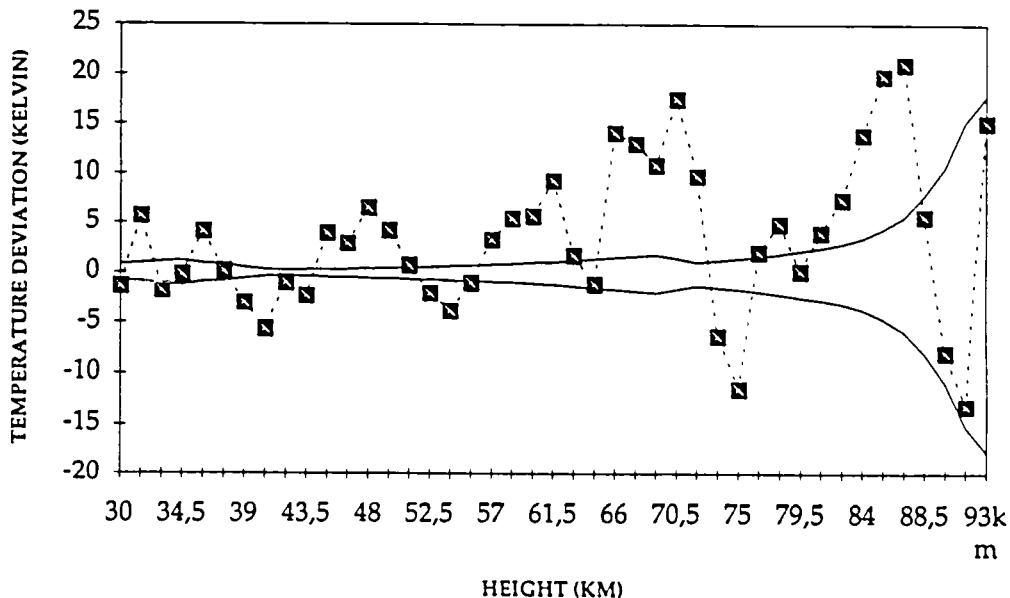


Fig. 3 - Difference between simultaneous vertical temperature profiles obtained at the CEL and with the lidar on board ship H. Poincaré located at Brest (500 km North of the CEL) on June 12, 1990 (black square). Full lines represent the  $\pm 1$  standard deviation

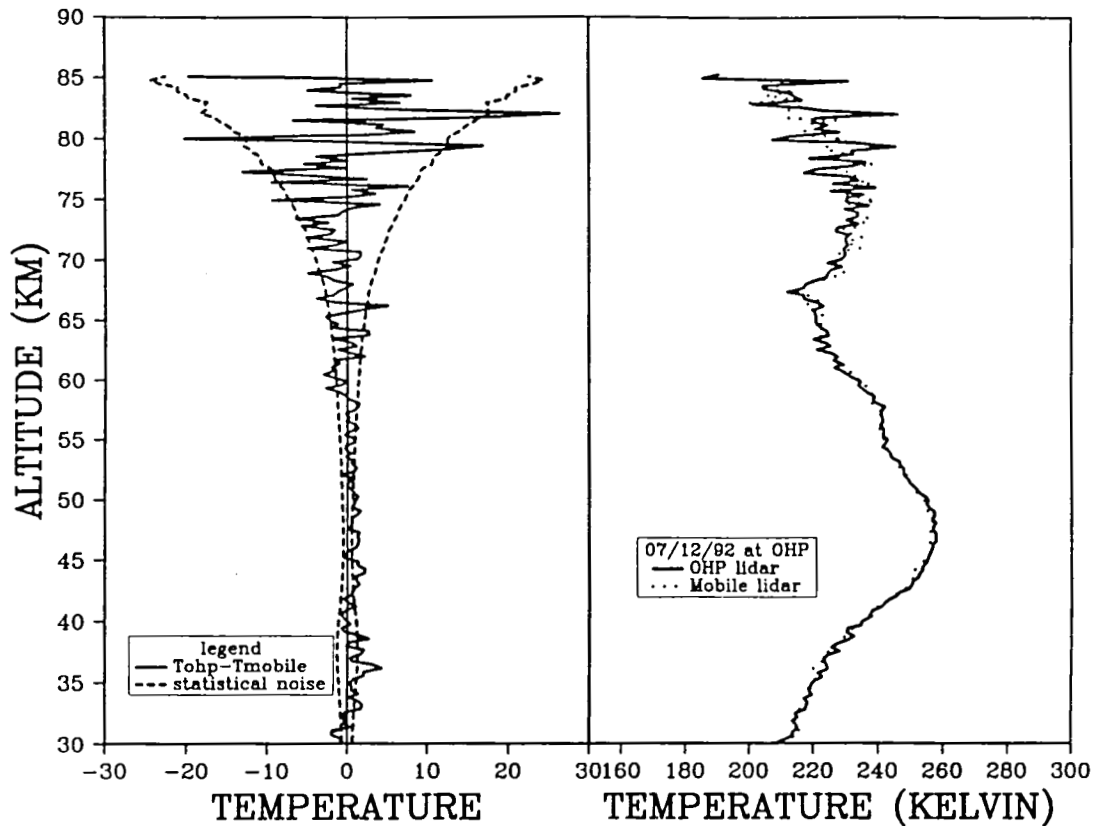


Fig. 4 - Comparison between simultaneous profiles obtained in the same site with the permanent OHP lidar and the mobile lidar. The difference between both measurements is represented in the left side compared with the total statistical noise

#### REFERENCES

- KECKHUT P., HAUCHECORNE A., M.L. CHANIN - A critical review of the data base acquired for the long term surveillance of the middle atmosphere by the french Rayleigh lidars, Submitted to J. Geophys. Res. (janvier 1992).
- NEDELJKOVIC D., A. HAUCHECORNE, M.L. CHANIN - Rotational Raman lidar to measure the atmospheric temperature from the ground to 30 km, To be submitted to IEEE Special Issue on Remote Sensing of the Atmosphere, 1992.
- AIKIN A.C., M.L. CHANIN, J. NASH and D.J. KENDIG - Temperature trends in the lower mesosphere, Geoph. Res. Lett., 18, 3, 416-419, 1991.

# WIND MEASUREMENTS FROM 15 TO 50 KM WITH A DOPPLER RAYLEIGH LIDAR

A. Garnier

Service d'Aéronomie du C.N.R.S. / S.E.S.O.  
Verrières le Buisson, France

M. L. Chanin

Service d'Aéronomie du C.N.R.S., France  
Verrières le Buisson, France

## Introduction

The possibility to measure the mean wind in the high stratosphere using a Doppler Rayleigh lidar was demonstrated in 1989, at the Observatory of Haute Provence (44°N, 6°E) (Chanin et al., 1989). It was originally developed to cover the height range 25 - 60 km, a region where the radars cannot operate and therefore the system was designed to cover altitudes where the signal is only due to the Rayleigh backscattering. The instrument is right now set up at the Centre d'Essais des Landes or C.E.L. (44°N, 1°W) where it operated during the DYANA (DYnamic Adapted Network for the Atmosphere) campaign in 1990. As the contribution of the Mie scattering was very low during this period above southern France, we have obtained vertical wind profiles in the stratosphere down to 15 km (Garnier and Chanin, 1992).

Since the eruption of the Pinatubo volcano in June 1991, the contribution of Mie scattering has increased between 15 and 30 km and it was very difficult with the original system to obtain wind measurements below 30 km. We will show in this paper that using the same method with slightly different characteristics of the system, it is possible to measure the wind in the presence of Mie scattering. The first experimental results will be presented.

## Method

We have limited our study to the determination of the main horizontal components of the wind. The experiment is up-to-now limited to night-time.

We use the second harmonic of a seeded pulsed Nd:YAG laser ( $\lambda = 532$  nm), which spectral line can be represented by a Gaussian distribution with a full width at half height (FWHH) of 0.14 pm. The Rayleigh backscattered line is Doppler broadened by a value depending upon the atmospheric temperature (typically 2.1 pm) but the Mie backscattered line has about the same width than the laser line. It appears that the spectral shape of the backscattered line depends upon the contribution of the Mie scattering. It is spectrally shifted by about 0.1 pm for an horizontal wind velocity of 40 m/s. The Doppler shift is measured through the analysis of the

backscattered line by a single dual Fabry Perot interferometer with two band-passes tuned on either side of the scattered line. The fluxes transmitted through these two "filters", A and B, are noted respectively NA and NB.

The altitude range of the measurements is divided into layers which thickness  $\Delta z$  is given by the height range of the electronic gate. For each layer centered at the height  $z$  ( $z-\Delta z/2$  ;  $z+\Delta z/2$ ), we measure the response  $R(z)$ , that we define as :

$$R(z) = \frac{NA(z) - NB(z)/C}{NA(z) + NB(z)/C}$$

where C is a corrective factor determined experimentally by taking into account an eventual imbalance between the two channels (for example different efficiency of the detectors).

These response profiles are measured successively for a tilted line of sight (we choose  $45^\circ$ ) and for the vertical one, corresponding to a null radial Doppler shift, and used therefore as a reference. Each altitude point of the two response profile  $R(z)$  ( $45^\circ$  and zénith) corresponds to the position of the center of the backscattered line compared to the one of the transmission peaks  $\lambda_A$  and  $\lambda_B$ . The difference between these two positions at each altitude gives the profile of the spectral shift,  $\Delta\lambda(z)$ , and then the wind velocity profile,  $v_h(z)$ , as :

$$v_h(z) = \frac{c \Delta\lambda(z)}{2 \lambda_0 \sin 45^\circ}$$

c being the velocity of light in the medium, and  $\lambda_0$  the mean wavelength.

Two such measurements in two orthogonal azimuths are necessary to determine completely the horizontal velocity component.

The calibration curve, giving the response  $R(z)$  of the device as a function of the position of the center of the backscattered line, is calculated knowing the spectral characteristics of the Fabry Perot interferometer - experimentally controlled - and knowing the spectral shape of the backscattered line for each height .

If it is aimed to cover high altitudes where Rayleigh scattering is the only contribution to the signal, the spectral shape of the backscattered line depends only upon the atmospheric temperature which is inferred from the temperature profile simultaneously obtained with the Rayleigh lidar or given by an atmospheric model. In this case, the spectral characteristics of the interferometer - FWHH of each band-pass (1.2 pm) and spectral spacing between the peaks of the band -passes (3.2 pm) - are chosen to minimize the statistical standard error on the wind velocity.

If the contribution of the Mie scattering cannot be neglected, the spectral shape of the backscattered line depends mainly upon the amplitude of this contribution, expressed in the following discussion using the definition of SR as :

$$SR = \frac{N_{RAY} + N_{MIE}}{N_{RAY}}$$

where  $N_{RAY}$  and  $N_{MIE}$  are the number of photoelectrons detected from Rayleigh and Mie scattering respectively.

If the spectral characteristics of the interferometer are chosen as said above, the calibration curve can be very different, depending upon the value of SR. If the contribution of Mie scattering is neglected, the error on the wind increases up to 33% of the velocity if SR reaches a value of 10. A correction of the calibration curve according to SR is possible, but requires accurate measurements of SR. We have calculated that it is possible to make the calibration curve insensitive to the value of SR (it means  $\partial(R)/\partial(SR) = 0$ ) by changing the spectral characteristics of the Fabry Perot interferometer ; one of the solutions obtained is FWHH = 2.3 pm and spectral spacing between the band-passes = 5.3 pm. If the contribution of Mie scattering is neglected, the error on the wind remains lower than 1% even if SR reaches values of 10.

### Experiment

Wind measurements with a new interferometer giving a calibration curve insensitive to Mie scattering has just been tested on the Doppler lidar installed at the C.E.L. The lidar has been recently made more powerful by increasing the power of the laser and improving the optical efficiency. Table I summarizes the characteristics of the system.

EMITTER		RECEIVER	
Wavelength :	532 nm	Telescopes :	f/4.5 0.155 m <sup>2</sup> (tilted)
Repetition rate :	30 Hz		f/4.5 0.070 m <sup>2</sup> (vertical)
Energy per pulse :	0.33 J	Field of view (full angle) :	2 10 <sup>-4</sup> rad (tilted)
Pulse duration :	6 ns		3 10 <sup>-4</sup> rad (vertical)
Divergence full angle after collimation :	7 10 <sup>-5</sup> rad	Interferential filter bandwidth :	1 nm
Laser bandwidth :	0.14 pm	Optical efficiency :	0.2
		Quantum efficiency of each detector :	0.17

Table I : Characteristics of the Doppler lidar system

We show on Figure 1 the zonal wind profile obtained at the C.E.L. during the night 21-22 February 1992. The  $\pm 1 \sigma$  error bar includes the statistical standard deviation and the calibration uncertainty. We see on the vertical profile of SR obtained simultaneously at the C.E.L. and plotted on Figure 2, that SR has a value between 1 and 7 in the 15-30 km height region. The integration time is about 2 hours for both profiles. The vertical resolution of the wind and SR profiles are 2 km and 0.3 km respectively.

The wind lidar profile has been corrected for the systematic uncertainty induced by the instrumental spectral drift using the wind profile obtained with a balloon sounding at Bordeaux (located 90 km northwards from the C.E.L.) the same night at midnight. This balloon profile is plotted on Figure 1 (dashed line). The lidar profile is limited downwards by the saturation of the detectors. The upper limit of the lidar profile is about 50 km, where the error on the wind is  $\pm 15$  m/s. We observe a satisfactory agreement between both wind profiles even at the altitudes where SR reaches a value of 7.

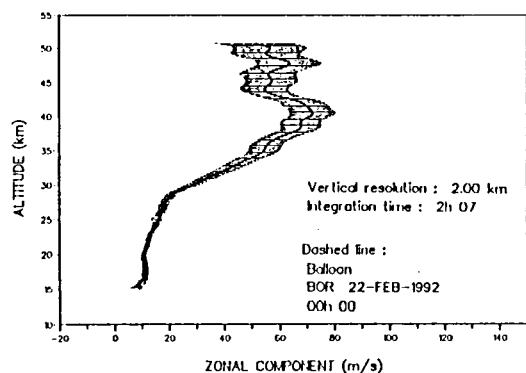


Figure 1 : Zonal wind profile obtained during the night 21-22 February 1992 at the C.E.L. with the Doppler Rayleigh lidar (see text).

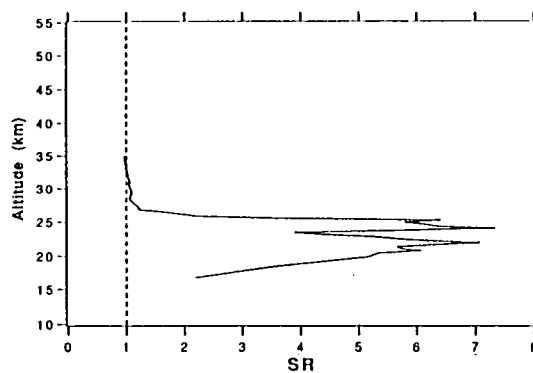


Figure 2 : Vertical profile of SR (see text) obtained during the night 21-22 February 1992 at the C.E.L. with the aerosols lidar.

### Conclusion

This first result obtained in February 1992 shows that it is possible to measure the mean wind in presence of aerosols with the recent new version of the Doppler Rayleigh lidar. We are now working to obtain more night measurements to confirm this result and to evaluate the possible residual error on the wind induced by Mie scattering. This Doppler lidar working from 15 to 50 km is presently used to validate the wind measurements provided by the experiment HRDI (in the stratosphere) on UARS.

### References

- Chanin M.L., A. Garnier, A. Hauchecorne and J. Porteneuve, A Doppler lidar for measuring winds in the middle atmosphere, *Geophys. Res. Lett.*, vol 16, n° 11, 1273-1276, 1989.  
 Garnier A. and M.L. Chanin, Description of a Doppler Rayleigh lidar for measuring winds in the middle atmosphere, to be published in *Applied Physics B - Special issue*, 1992.

# LIDAR STUDIES OF EXTINCTION IN CLOUDS IN THE ECLIPS PROJECT

C.Martin R. Platt, Stuart A. Young and Graeme P. Patterson  
CSIRO Division of Atmospheric Research  
Private Mail Bag 1, Mordialloc, Vic, 3195, Australia

## Introduction

The Experimental Cloud Lidar Pilot Study (ECLIPS) project has now had two active phases in 1989 and 1991. A number of laboratories around the world have taken part in the study. The observations have yielded new data on cloud height and structure, and have yielded some useful new information on the retrieval of cloud optical properties, together with the uncertainties involved.

Clouds have a major impact on the climate of the earth. They have the effect of reducing the mean surface temperature from 30°C for a cloudless planet to a value of about 15°C for present cloud conditions. However, it is not at all certain how clouds would react to a change in the planetary temperature in the event of climate change due to a radiative forcing from Greenhouse gases. Clouds both reflect out sunlight (negative feedback) and enhance the greenhouse effect (positive feedback), but the ultimate sign of cloud feedback is unknown. Because of these uncertainties, campaigns to study clouds intensely have been initiated. The International Satellite Cloud Climatology (ISCPP) and the FIRE Campaigns (cirrus and stratocumulus) are examples.

## The ECLIPS project

The ECLIPS was set up similarly to the above experiments to obtain information specifically on cloud base, but also cloud top (where possible), optical properties, and cloud structure. ECLIPS was designed to allow as many laboratories as possible globally to take part to get the largest range of clouds. It involves observations with elastic backscatter lidar, supported by infrared fluxes at the ground and radiosonde data, as basic instrumentation. More complex experiments using beam filter radiometers, solar pyranometers and satellite data and often associated with other campaigns were also encouraged to join ECLIPS.

Two periods for observations were chosen, September–December 1989 and April to July 1992, into which investigators were requested to fit 30 days of observations. These would be either continuous, or arranged to coincide with NOAA satellite overpasses to obtain AVHRR data. The distribution of the ECLIPS international effort as in 1991 is shown in Figure 1. The main gaps in the global distribution are in the tropics and in the Southern Hemisphere.

## Progress in ECLIPS - Extinction Coefficient

The results from ECLIPS I phase were discussed in the third ECLIPS workshop at Porano, Italy, October 1990 and ECLIPS II was discussed at the fourth ECLIPS workshop in

as pointed out by Platt et al (1987), the accuracy of  $\sigma(z)$  is reduced by the presence of a large number of multiple-scattered photons in the received signal. These photons have the effect of decreasing the  $\sigma$ 's by factors ( $\eta$ ), which vary between 0.7 for boundary-layer clouds to 0.2 to 0.4 for cirrus clouds, where  $\sigma(\text{correct}) = \sigma/\eta$ . Corresponding profiles of depolarisation ratio are shown in Figure 1b, and the build-up of multiple scattering with cloud penetration is evident.

It has been pointed out by Platt (1979) that an infrared absorption coefficient can be retrieved more accurately than the extinction coefficient at the lidar wavelength if a filter radiometer at 10-12 micron wavelength is also employed (the LIRAD method). Using the forward linear solution, Platt (Ibid) indicates about 30% error in  $\tau_c$  for a 10% error in backscatter to extinction ratio for  $\tau_c$  approximately 0.7, whereas this will give only an 8% error in the infrared optical depth  $\tau_a$ .

### Conclusion

Inversion methods are available which give an acceptably accurate value of  $\tau_c$  when  $\tau_c$  is very high. However, multiple scattering degrades this accuracy. Considerably more cloud data is needed before the full picture can be assessed.

**TABLE 1**

Errors in Klett solutions. X and R are defined in the text. (After Jinhuan, 1988)

FORWARD SOLUTION							BACK SOLUTION						
		$R_o$							$R_m$				
$X_o$	$\tau_c$	0.1	0.5	1.0	2.0	3.0	$X_m$	$\tau_c^*$	6	3	2	1	0.5
0.85		0.82	0.75	0.59	0.44	0.30	0.5		0.95	0.85	0.80	0.70	0.58
0.90		0.85	0.82	0.67	0.51	0.39	0.6		0.97	0.92	0.87	0.75	0.68
0.95		0.89	0.86	0.82	0.65	0.47	0.7		0.99	0.96	0.91	0.80	0.77
1.00		1.00	1.00	1.00	1.00	1.00	0.8		1.00	0.98	0.94	0.90	0.85
1.05		1.05	1.06	1.18	>4	>4	0.9		1.00	0.99	0.96	0.92	0.91
1.10		1.10	1.14	1.47			1.0		1.00	1.00	1.00	1.00	1.00
1.15		1.15	1.25	2.4			2.0		1.06	1.11	1.18	1.29	1.46
1.20		1.20	1.38	>4			3.0		1.10	1.18	1.27	1.49	1.80
							4.0		1.12	1.23	1.34	1.63	2.00

### References

Klett, J.D., 1981: Stable analytical inversion solution for processing lidar returns. *Appl. Opt.*, **20**, 211-220.

Toronto, Canada, in May 1992.

Problems in the retrieval of cloud base and cloud top by backscatter lidar have been discussed previously in the third ECLIPS workshop and by Platt (1991). Here, we consider the retrieval of extinction coefficient. The sensitivity of this retrieval accuracy to cloud optical depth and cloud backscatter to extinction ratio has been explored to some extent, and it is now agreed that retrieval of extinction coefficient from a single wavelength backscatter lidar can only be achieved to a good accuracy in the two extreme cases of very high extinction coefficient (e.g. stratocumulus) or very low extinction coefficient (e.g. thin cirrus).

The accuracy of a backscatter lidar retrieval can be examined through the well-known Klett solution of the logarithmic lidar equation (Klett, 1981). The logarithmic forward solution has the form:

$$\sigma(z) = \frac{\exp[S(z) - S(z_o)]}{1/\sigma(z_o) - 2 \int_{z_o}^z \exp[S(z'') - S(z_o)] dz''} \quad (1)$$

where  $\sigma(z)$  is the volume extinction coefficient,  $S(z) = \ln [P(z)z^2]$ , where  $P(z)$  is return power from range  $z$ , and  $z_o$  is the boundary value range at, or under the cloud base.

The corresponding back solution is:

$$\sigma(z) = \frac{\exp[S(z) - S(z_m)]}{1/\sigma(z_m) + 2 \int_z^{z_m} \exp[S(z'') - S(z_m)] dz''} \quad (2)$$

where  $z_m$  is now a "distant" range, from which the back, integration is performed. Following Jinhuan we can define  $X_o$ ,  $X_m$ ,  $R_o$ ,  $R_m$  as  $X_{o,m} = \sigma(z_{o,m})/\sigma(z_{o,m})^*$ , where the \* represents the correct value, and  $R_{o,m} = \tau_c(z_{o,m})/\tau_c(z_{o,m})^*$ , where the denominator is the "correct" value of cloud optical depth  $\tau_c$ .

Table 1 indicates that the forward solution is generally inaccurate ( $> 15\%$  error), if  $\sigma_o$  is more than 10% in error and  $\tau_c > 0.5$ , and that for higher values of  $\tau_c$  and a too-high value of  $\sigma_o$ , the solution rapidly becomes unstable. In the case of the back solution,  $R_m$  is seen to be extremely insensitive to  $\sigma_m$  when  $\tau_c$  is high, even when  $\sigma_m$  is in error by 200 to 300%. The errors increase with decreasing  $\tau_c$ , but are still reasonable for  $\sigma_m$  approximately 20% in error until  $\tau_c$  drops below 0.5. However, for thin clouds and a short-wavelength lidar, it is possible to assign a reasonable value to  $\sigma_m$  if there is sufficient backscatter signal from above the cloud, and the backscatter is assumed to be molecular.

We illustrate these problems in extinction retrieval by examples from ECLIPS observations at Aspendale, Australia. Profiles of extinction coefficient for stratocumulus are shown in Figure 2. The characteristic increase in  $\sigma(z)$  above cloud base as the cloud droplets grow is evident. As  $\tau$  is high (3 to 5) the Klett solution is accurate. However,

Platt, C.M.R., 1979: Remote sounding of clouds: I. Calculation of visible and infrared optical properties from lidar and radiometer measurements. J. Appl. Meteor., 18, 1130-1143.

Platt, C.M.R., 1991: The experimental cloud lidar pilot study (ECLIPS) program. OSA, Opt. Rem. Sensing of the Atmos. Nov 18 - 21, Williamsburg, VA 1991 Technical Digest Series 18, Opt. Soc. of Amer. pp. 163-165.

Platt, C.M.R., J.C. Scott and A.C. Dille, 1987: Remote sounding of high clouds: VI. Optical Properties of midlatitude and tropical cirrus. J. Atmos. Sci., 44, 729-747.

Qiu Jinhuan, 1988: Sensitivity of lidar equation solution to boundary values and determination of the values. Advances in Atmos. Sciences, 5, 229-241.

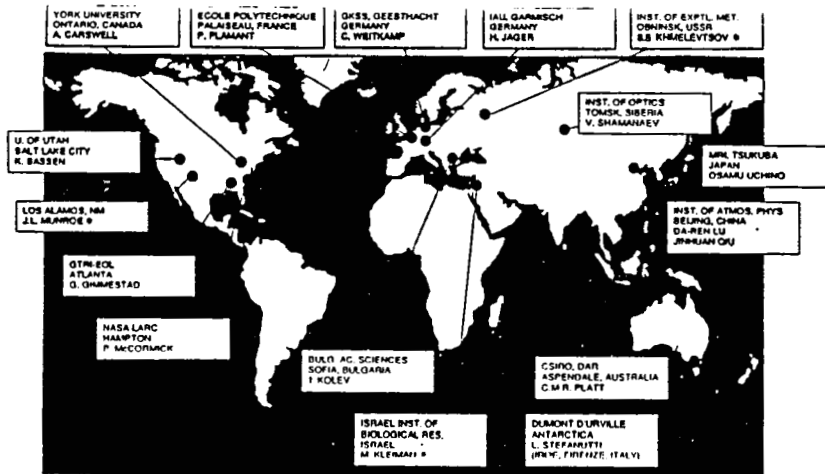


Figure 1. Participants in the ECLIPS project. The list of laboratories is not inclusive.

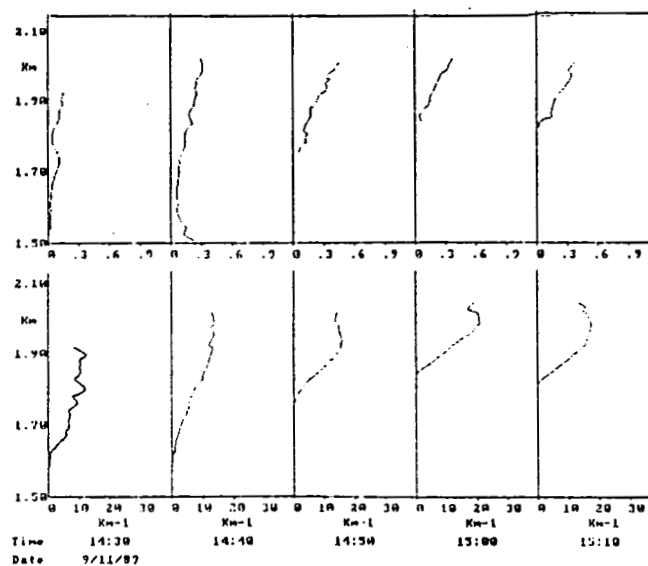


Figure 2. Top: Altitude profile of lidar depolarisation ratio. Bottom: Corresponding volume extinction coefficient. Ten-minute averages in a strato cumulus cloud. ECLIPS I at Aspendale, Australia

# Lidar Studies of Clouds at Toronto During the ECLIPS Program

S. R. Pal, A. I. Carswell, A. Y. Fong, I. Pribluda and W. Steinbrecht

Institute for Space and Terrestrial Science and  
Department of Physics and Astronomy, York University  
4700 Keele St., North York, Ontario, Canada, M3J 1P3  
Tel: 416-736-2100 Fax: 416-736-5516

The Experimental Cloud Lidar Pilot Study ( ECLIPS) [1] measurement program involves the measurement of cloud optical and physical parameters with a vertically pointing ground-based lidars simultaneously with satellites observing the same cloud system from above. A lidar measurement time- series of about 3 hours encompassing a satellite overpass provides statistical behaviour of cloud physical parameters such as the altitudes of cloud base, peak and top  $r_b, r_p, r_t$ . As well, the cloud optical parameters such as the attenuation coefficient,  $\sigma$ , optical depth,  $\tau$ , and linear depolarization ratio,  $\delta$  can be derived. The wavelength dependence of cloud parameters provides further insight into the size distribution and cloud reflectivity properties. A study of these cloud parameters at one or more wavelengths enables one to examine the assumptions implemented in GCM's and radiative transfer calculations in clouds. We have developed and utilized the methodologies to analyse Phase 1 and Phase 2 ECLIPS data which enable us to investigate the value of the results for cloud microphysical and GCM studies.

Our frequency doubled Nd:YAG lidar transmits about 500 mJ of linearly polarized radiation at each wavelength (532, 1064 nm) with a prf of 20 Hz. The 0.5 m diameter receiving telescope provides 4-channel polarization measurements of the backscatter [2]. The lidar cloud measurements are also augmented with the solar radiation flux data and radiosonde measurements of important meteorological parameters such as the profiles of pressure, temperature, relative humidity and wind.

This paper presents an overview of the statistical behaviour of cloud physical and the optical parameters. The wavelength dependence of these parameters is examined utilizing the measured time series at 532 and 1064 nm. The measurements are also correlated with the theoretical calculations of cloud models. In our measurements the cloud parameters, initially derived for an interval of 15 seconds by averaging about 300 lidar returns, are further averaged, for the ECLIPS format, over an interval of 10 minutes or less depending on the continuity in the cloud.

In Fig. 1 we give a sample of a data set showing the behaviour of the optical depth,  $\tau$ , for a multi-layer cirrus cloud system. The horizontal lines show the relative contributions of the various layers. In this cirrus cloud system the  $\tau$  values as high as 3 were encountered.

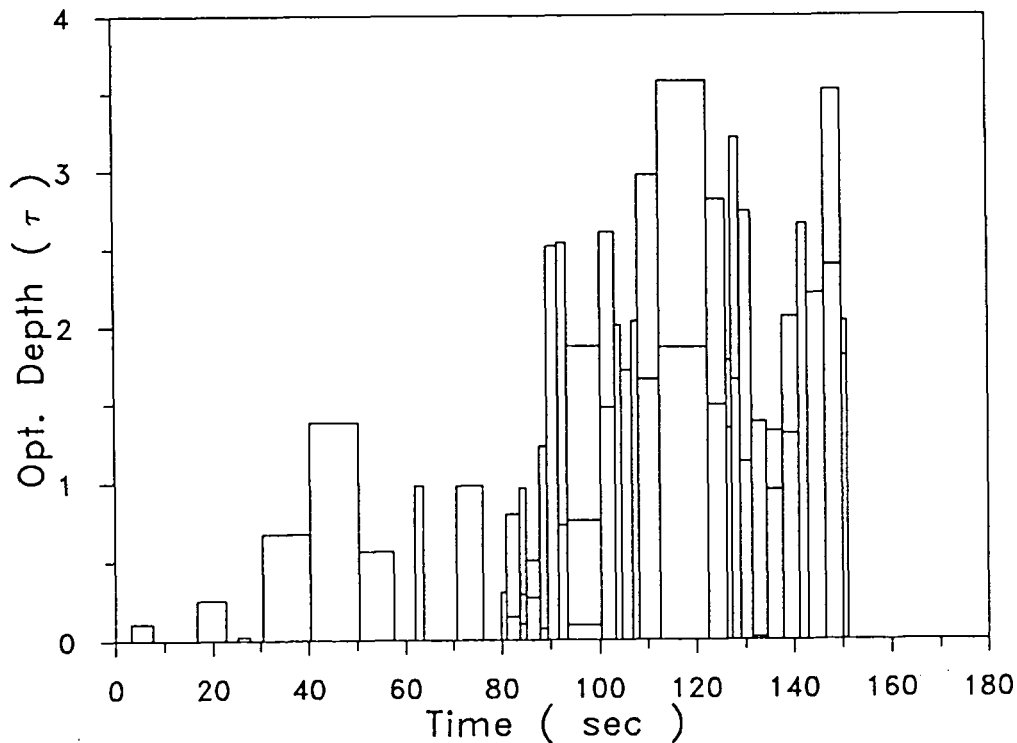


Figure 1. Time series of optical depth,  $\tau$ .

Another parameter of interest in radiative transfer calculations for modelling purposes is the probability density  $p(\tau)$  of  $\tau$  in clouds. From our data sets we can derive  $p(\tau)$  and a sample display is shown in Fig. 2 for a cirrus cloud system. For this cirrus system Fig. 2 shows that  $p(\tau)$  does not exhibit a random behaviour but displays a dual-peak distribution. The shape of these distributions depends on a number of parameters and to date no well-defined pattern has emerged, however, we are continuing the analysis of our large data set. Comparison of the lidar optical depth data with downward radiation flux data is also in progress.

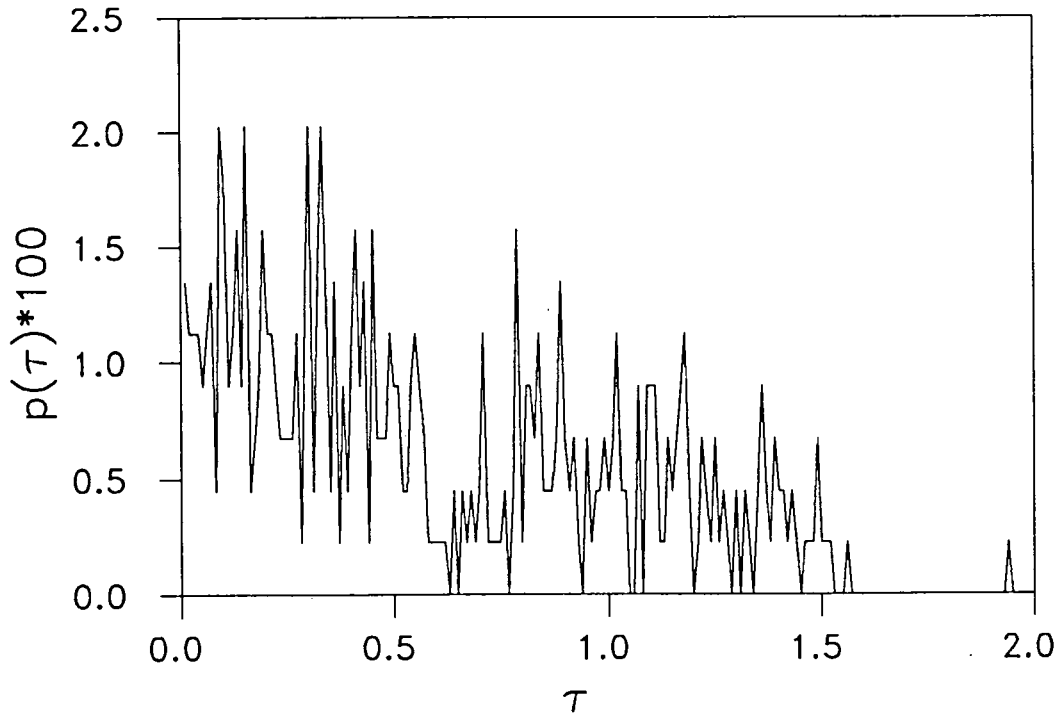


Figure 2. Probability density  $p(\tau)$  versus  $\tau$ .

Cloud temperature plays an important role in defining the ice crystal structure in clouds. In cirrus clouds, where multiple scattering is negligible, the polarization properties of the backscattered lidar are controlled by the ice particles in the cloud. We have been examining the polarization properties of the lidar returns and in Fig. 3 we show a data sample. In this figure we show the dependence of  $\delta$  on the mid-cloud temperature for all of the cirrus clouds observed in Phase 2 of ECLIPS ( June and July 1991 ). The  $\delta$  values were averaged over one degree temperature bins as determined from sonde data. In the figure it is apparent that there is a pronounced peak in the  $\delta$  distribution around -15 C. The high  $\delta$  in this temperature range could be associated with maximum in the diffusional ice crystal growth rate as suggested by Rogers and Yau [3]. Large regions in cirrus clouds with very low  $\delta$  values (  $\delta < 10^{-2}$  ) are frequently observed. These often have a vertical extent of several hundred meters. It is believed that these regions contain descending and growing ice crystals horizontally oriented to produce a strong specular reflection of the vertically pointing incident linearly polarized lidar beam.

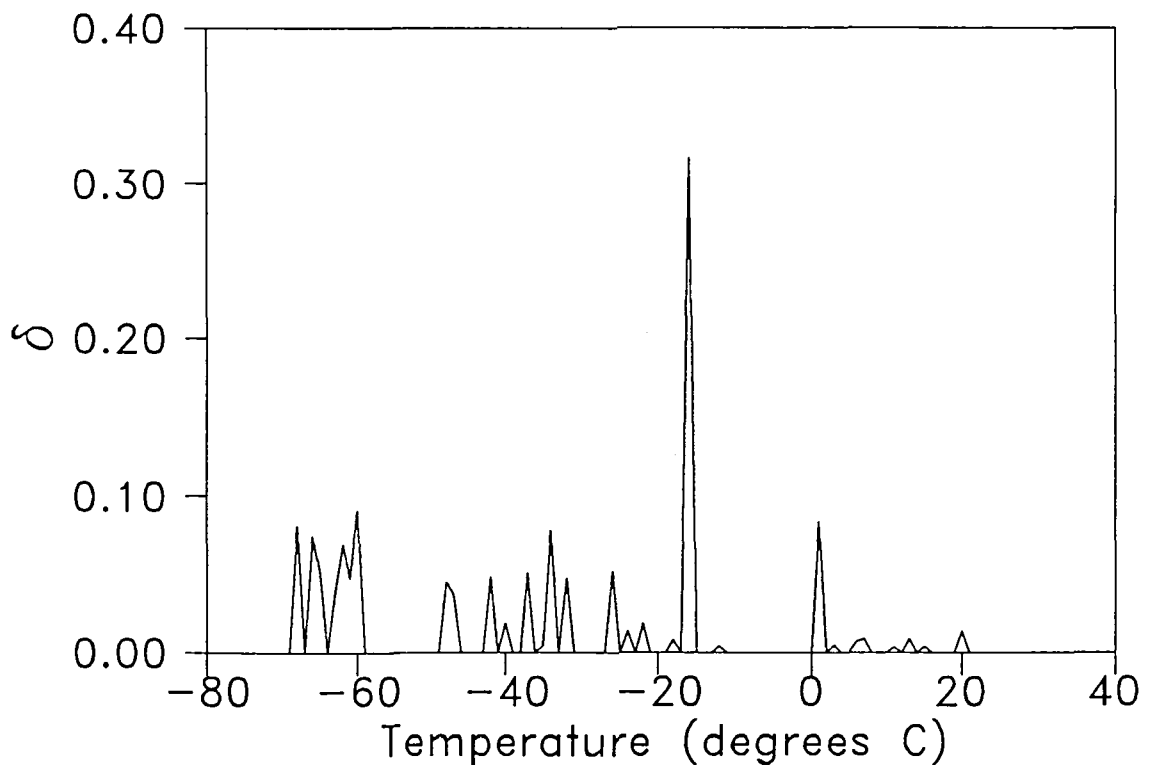


Figure 3. Linear depolarization ratio  $\delta$  versus mid-cloud temperature for cirrus clouds.

This paper will summarize the lidar measurements and their comparison with the observations of other meteorological sensors.

## References

- [1] "Experimental Cloud Lidar Pilot Study (ECLIPS)", Report of the WCRP/CSIRO, Cloud Base Measurement Workshop, CSIRO, Division of Atmospheric Research, Modilloc, Victoria, (Feb. 29- Mar. 3, 1988).
- [2] A.I. Carswell, S.R. Pal, W. Steinbrecht, J.A. Whiteway, A. Ulitsky and T-Y Wang, "Lidar measurements of the Middle Atmosphere", *Can. J. Phys.*, 69, 1076, 1991.
- [3] R.R. Rogers and M.K. Yau, "A Short Course in Cloud Physics", 3rd Ed, Pergamon Press, England, pp 160, 1989

# Adaptation of the University of Wisconsin High Spectral Resolution Lidar for Polarization and Multiple Scattering Measurements

E. W. Eloranta and P. K. Piironen

University of Wisconsin  
Dept. of Meteorology  
Madison, WI 53706

Quantitative lidar measurements of aerosol scattering are hampered by the need for calibrations and the problem of correcting observed backscatter profiles for the effects of attenuation. The University of Wisconsin High Spectral Resolution Lidar (HSRL) addresses these problems by separating molecular scattering contributions from the aerosol scattering; the molecular scattering is then used as a calibration target which is available at each point in the observed profiles (Shipley et al., Grund et al.). This approach does not require knowledge of the backscatter/extinction ratio to correct for attenuation and thus avoids the uncertainties and numeric instabilities of schemes for inversion of single channel lidar profiles. Because the molecular backscatter cross section is approximately one thousand times larger than the Raman scattering cross section, the HSRL also holds a significant signal strength advantage over the use of Raman scattering approaches for measurement of aerosol backscatter cross sections.

While the HSRL approach has intrinsic advantages over competing techniques, realization of these advantages requires implementation of a technically demanding system which is potentially very sensitive to changes in temperature and mechanical alignments. This paper describes a new implementation of the HSRL in an instrument van which allows measurements during field experiments. The instrument has been modified to provide measurements of depolarization. In addition, both the signal amplitude and depolarization variations with receiver field of view are simultaneously measured. These modifications allow discrimination of ice clouds from water clouds and observation of multiple scattering contributions to the lidar return. In the past it has been very difficult to verify models of the multiply scattered lidar return. The ability to measure calibrated backscatter cross sections and optical depths while simultaneously measuring depolarization and field-of-view variations make the HSRL a unique instrument for these investigations.

Figure 1 provides a block diagram of the new HSRL transmitter and receiver. The depolarization measurement capability is implemented so as to provide extremely precise measurements. The transmitted polarization is rotated 90 degrees between alternate laser pulses by a Pockels cell. Calibrations show that with proper alignment the residual cross polarization in the transmitted beam can be reduced to approximately 0.1% of the parallel component. Separate depolarization measurements can be made in both the "molecular" and "aerosol" channels of the HSRL while simultaneously observing the depolarization in the wide field of view channel. Because both polarization components are observed with the same detector and receiver optics, no calibration is required to make accurate measurements of the depolarization ratio. Photon counting detection also provides linear detector response over a very large dynamic range. The small time separation between laser pulses ( $250 \mu\text{s}$ ) insures that the both polarization components are measured from the same ensemble of scattering particles.

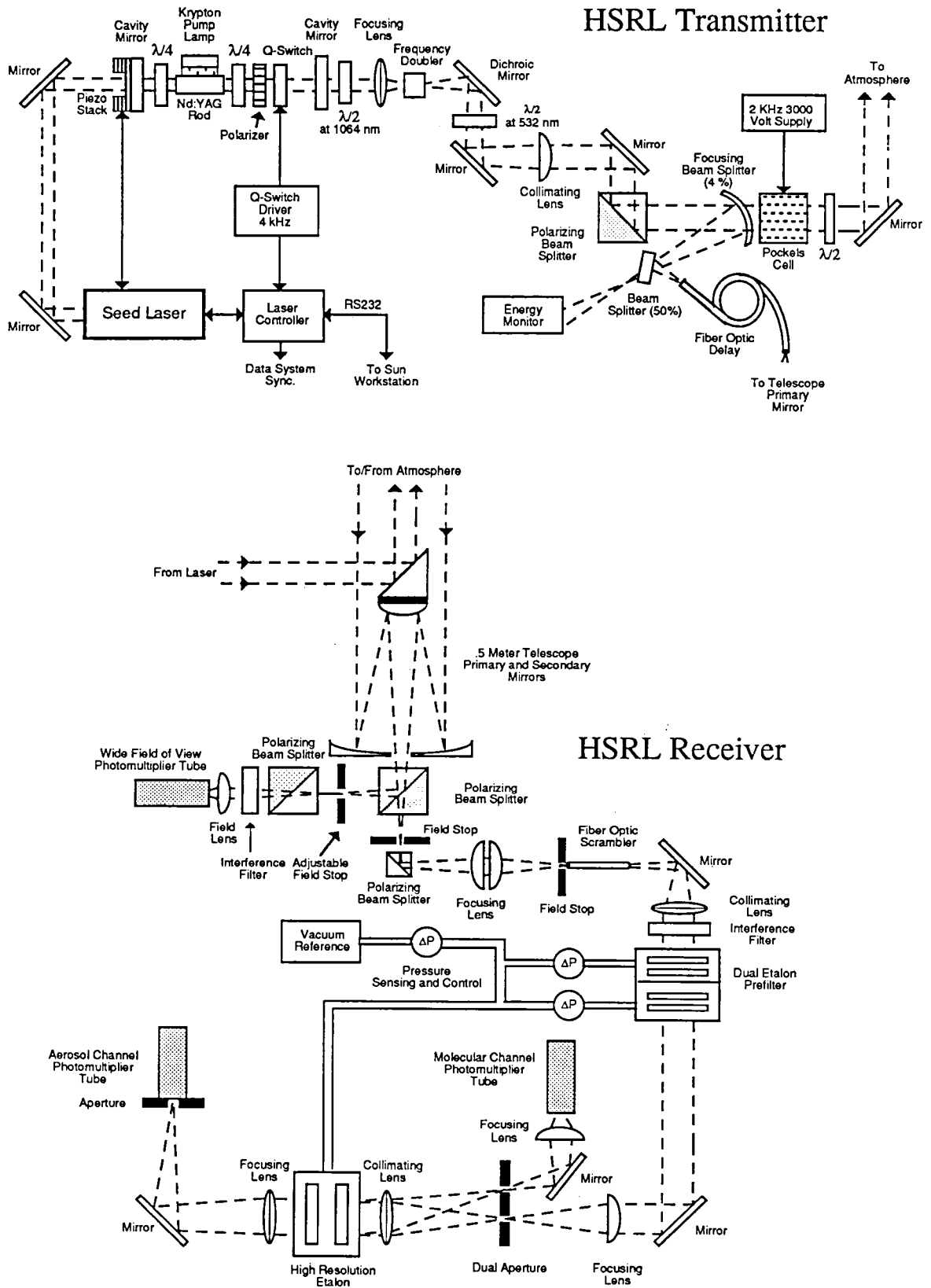
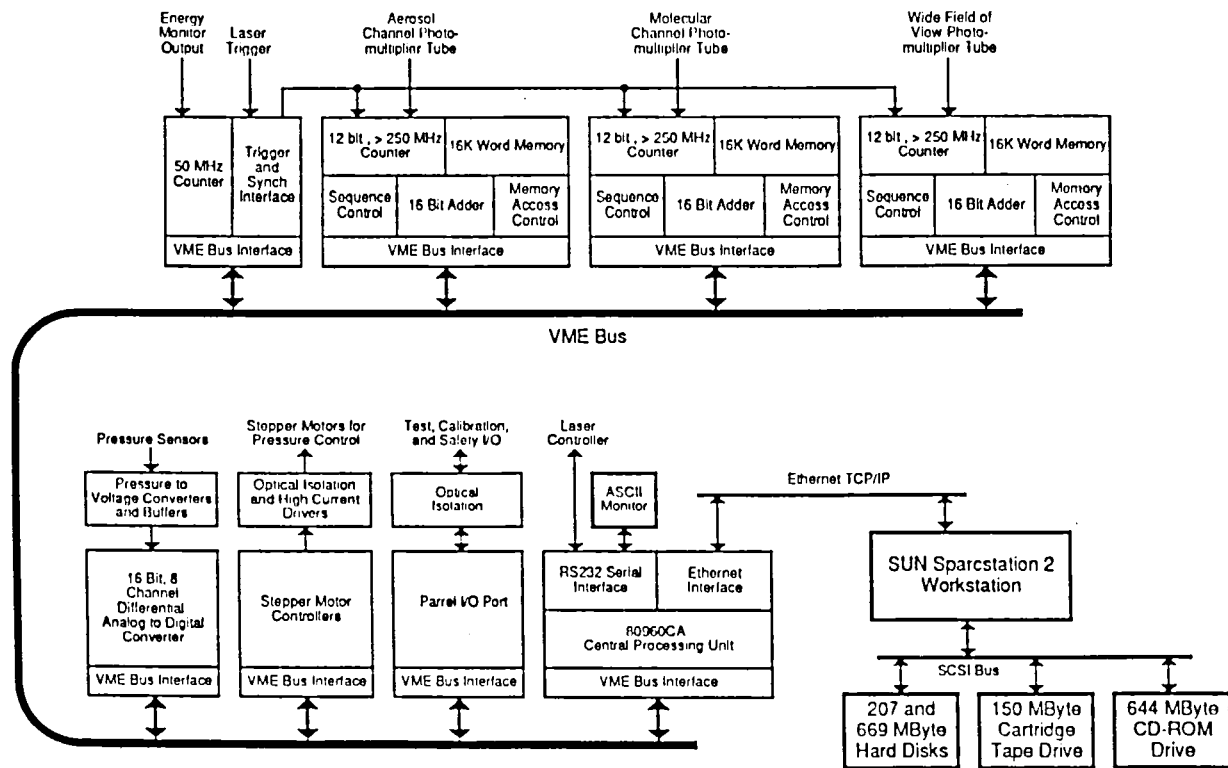


Figure 1.

In order to increase the dynamic range of the HSRL we have designed new photon counting electronics to enable count rates near 1 GHz while accumulating counts in up to 8,192 range bins of 100 ns each. These counters have thus far been tested to count rates of over 250 MHz. Full utilization of these counters awaits the installation of phototubes providing shorter single photon pulses than the EMI model 9860 currently employed. A schematic of the HSRL data system is shown in figure 2.



HSRL Data Acquisition System

Figure 2.

Figure 3 shows HSRL returns from a super-cooled water cloud (at an altitude of 5 km) and from ice crystal precipitation falling from this cloud (between altitudes of 3.3 and 4.8 km). The received signals polarized parallel and perpendicular to the transmitted polarization are shown along with the depolarization ratio. Notice that the depolarization observed in the clear air below the cloud is approximately 1% and thus very near the depolarization expected for molecular depolarization of the Cabannes line. Also note that the water cloud depolarization is approximately 2% indicating that for this cloud the 200 microradian field-of-view of the HSRL effectively suppresses depolarization caused by multiple scattering.

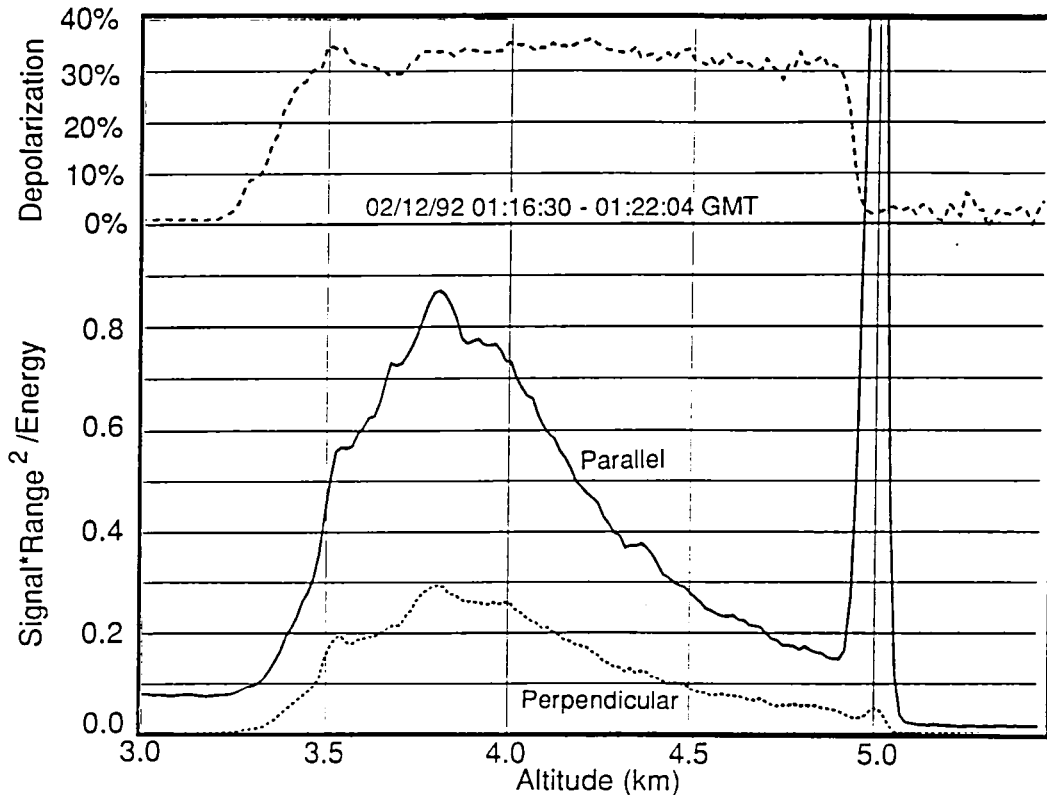


**Figure 3.**

#### Acknowledgements

This work was supported by grants from the Dept. of Energy (DE-FG01-90ER61058), the National Aeronautics and Space Administration (NAG-1-882) and the Office of Naval Research (N00014-91-J-1558). Support to P. K. Piironen was provided by Foundation of Maj and Tor Nessling, and University of Joensuu, Finland.

#### References

Shipley, S.T., D.H. Tracy, E.W. Eloranta, J.T. Sörga, F.L. Roeseler, and J.W. Weinman, "High spectral resolution lidar to measure optical scattering properties of atmospheric aerosols. 1: theory and instrumentation," *App. Optics*, 22, 1983, p3716-3724.

Grund, C.J. and E.W. Eloranta, "University of Wisconsin high spectral resolution lidar", *Optical Engineering*, Vol 30. #1, p6-12, Jan 1991.

Polarization Lidar Liquid Cloud Detection  
Algorithm for Winter Mountain Storms

Kenneth Sassen and Hongjie Zhao

Department of Meteorology  
University of Utah  
Salt Lake City, UT 84112

ABSTRACT

Lidar returned power profiles contain information on the height distribution of various atmospheric scatterers including air molecules, aerosols, and cloud particles in either the liquid or solid phase. Multi-channel polarization lidars provide unique information for discriminating these targets, but it should not be overlooked that simple one-channel data could be used to some degree to identify extramolecular scattering layers. A key ingredient in the ECLIPS program (WMO, 1988), e.g., is the generation of cloud base statistics in support of orbiting meteorological satellite observations on the basis of worldwide lidar observations. This is an ambitious goal in view of the various combinations of cloud types that can occur in the atmosphere. In reality, the determination of the lidar cloud base and top heights can prove essentially meaningless unless the radiative and/or microphysical importance of the various cloud components are considered, and the wavelength dependencies in cloud backscattering and attenuation are taken into consideration.

Under some conditions, however, simple criteria based on the change in the slope of the lidar return can be effective in identifying the cloud base altitude, and assuming weakly attenuating targets, cloud top height can be estimated from the attainment of noise-dominated signals aloft. These conditions apply to optically thin cirrus clouds, and physically thin cumulus or altocumulus clouds with most lidars. On the other hand, most cloud systems can not be so easily treated because they are of mixed phase composition and typically precipitate. The worst case scenario involves cloud systems producing precipitation reaching the surface -- simple methods cannot define a cloud base altitude under such conditions.

We have collected an extensive polarization lidar dataset from elevated sites in the Tushar Mountains of Utah in support of winter storm cloud seeding research and experiments. Our truck-mounted ruby ( $0.694 \mu\text{m}$ ) lidar, which was powered by field generators along with collocated microwave radiometers and

radars, collected zenith, dual-polarization lidar data through a roof window equipped with a wiper system to prevent snowfall accumulation. Lidar returns were collected at a rate of one shot every 1 to 5 min during declared STORM periods over the 1985 and 1987 mid-January to mid-March field seasons. The mid-barrier remote sensor field site was located at 2.57 km MSL.

Of chief interest to weather modification efforts are the heights of supercooled liquid water (SLW) clouds, which must be known to assess their "seedability" (i.e., temperature and height suitability for artificially increasing snowfall). Since radar measurements are generally insensitive to SLW clouds, dual-channel microwave radiometers detect but do not spatially locate SLW emissions, and instrumented aircraft usually are not permitted to fly at sufficiently low levels above the mountain barrier, only the polarization lidar technique can measure the heights of SLW clouds. Once identified, the SLW cloud base height is converted to temperature, and wind speed and direction on the basis of local radiosonde launches.

During several earlier case studies (see, e.g., Sassen et al. 1990) the identification of SLW clouds embedded in precipitating winter mountain storms was done manually on the basis of the visual appearance of height-versus-time displays of relative returned lidar power  $P$  (in the parallel polarization plane) and linear depolarization ratios  $\delta$ . The criterium was simply a concurrent rapid increase in  $P$  and rapid decrease in  $\delta$  (in comparison to the snowfall returns) at and above the SLW cloud base. Typically, if minimum  $\delta \leq 0.15$  were present just above cloud base the layer was termed water-dominated, although other obvious SLW layers contained somewhat higher minimum  $\delta$  (presumably due to a higher relative precipitating ice content).

We are currently reexamining our entire dataset to determine the climatological properties of SLW clouds in winter storms using an autonomous computer algorithm. The foundation of the approach comes from recent lidar return simulations of similar clouds, in which lidar backscattering, attenuation, and multiple-scattering depolarization are calculated from Mie theory for cloud droplet size distributions that evolve with height in updrafts (Sassen, 1991; Sassen et al. 1992). Preliminary results from a subset of the storm data have yielded somewhat surprising results, in that a simple slope ( $dP/dR$ ) criteria appears effective (in ~80% of the cases when SLW was concurrently detected radiometrically) in identifying the SLW base.

(Actually we determine the water cloud return peak height, which is generally within ~50 m above the cloud base and is less subject to uncertainties caused by snowfall variations at cloud base.) Minimum  $\delta$  value considerations indicate only about a 10% error in falsely identified SLW layers (attributable to rapid changes in the vertical distribution of snowfall) when  $\delta$  criteria are not also applied. In about another 10% of the cases the single slope method fails to detect SLW layers because of the strong parallel backscattering from horizontally oriented plate crystals falling through the cloud base, which can swamp the cloud droplet backscatter signal without significantly reducing the SLW content, as heavy snowfall would do. However, these cases are identified by the very low  $\delta$  values in the snow and the droplet multiple scattering-induced  $\delta$  value increasing trend above the slight cloud base peak. A further algorithm iteration effective in the remaining cases (where SLW should have been detected within the available attenuation-limited cloud depth) identifies very low level SLW clouds by applying our criteria below the 200 m height limit usually applied to the data to avoid problems sometimes caused by snowfall in the lidar cross-over region. The details of our algorithm and typical results will be presented.

#### References

- Sassen, K., A.W. Huggins, A.B. Long, J.B. Snider and R.J. Meitin, 1990: Investigations of a winter mountain storm in Utah. Part II: Mesoscale structure, supercooled liquid cloud development, and precipitation processes. *J. Atmos. Sci.*, 47, 1323-1350.
- Sassen, K., 1991: The polarization lidar technique for cloud research: A review and current assessment. *Bull. Amer. Meteor. Soc.*, 72, 1848-1866.
- Sassen, K., H. Zhao and G.C. Dodd, 1992: Simulated polarization diversity lidar returns from water and precipitating mixed phase clouds. *Appl. Opt.*, 31 (in press).
- WMO, 1988: An Experimental Cloud Lidar Pilot Study (ECLIPS), Report of the WCRP/CSIRO Workshop on Cloud Base Measurements (CSIRO, Mordialloc, Victoria, Australia, February 29-March 3, 1988). Report No. WCRP-14, Sept. 1988, WMO/TD-NO.251, WMO, Geneva.



# Measurement of Mean or Effective Radius of Cloud Drop Size Distributions with a 10.6- $\mu\text{m}$ Wavelength Lidar

Wynn L. Eberhard

NOAA Wave Propagation Laboratory  
Boulder, Colorado

Platt and Takashima (1987) proposed and analytically evaluated a technique to observe the mode radius  $r_p$  of drop size distributions in clouds using the backscatter detected by a CO<sub>2</sub> lidar. The scheme depends on fortuitous relationships between the backscatter and extinction properties of common drop size distributions when probed with wavelengths between about 9 and 11  $\mu\text{m}$ , which is the range of CO<sub>2</sub> laser transitions. This study extends their work to measurement of mean and effective radius and presents experimental results that demonstrate the technique is practical.

The lidar measures the cloud's extinction-to-backscatter ratio

$$S = \sigma/\beta , \quad (1)$$

where  $\sigma$  is the volumetric extinction cross section and  $\beta$  is the volumetric backscatter cross section. The range-resolved lidar signal is processed for calibration, geometrical range, and molecular absorption factors to obtain the apparent backscatter coefficient

$$\beta'(R) = \beta(R) \exp\{-2 \int_0^R [\eta(R') \sigma(R')] dR'\}, \quad (2)$$

where  $R$  is range,  $\eta$  is a multiple scattering correction, and the contribution of dust particles to the backscatter is negligible or has been subtracted.  $\beta'$  is the measured backscatter coefficient without correction for attenuation by the cloud. The measured  $\beta'$  is integrated through the penetration depth of the pulse to obtain  $\gamma'$ . Neglecting multiple scatter (discussed below) and assuming  $S$  is constant with range, it can be shown that (Platt and Takashima, 1987)

$$S = [1 - \exp(-2\tau)] / 2\gamma' , \quad (3)$$

where  $\tau$  is the optical depth of the cloud along the beam. When  $S$  changes with range, the result from (3) is actually a weighted average over the penetration depth of the pulse, with weight decreasing with optical depth into the cloud. When the cloud is optically thick (a common case), the exponential term becomes negligible, and

$$S = (2\gamma')^{-1}. \quad (4)$$

When a cloud is optically thin it is sometimes possible to determine  $\tau$  if an unchanging cooperative target is available on the side of the cloud opposite the lidar, such as stratospheric aerosol (Hall et al., 1988) when viewing upward or the surface when viewing downward.

This study evaluated the method's potential for measuring the mean radius

$$r_m = \int r n(r) dr / [ \int n(r) dr ] \quad (5)$$

and the effective radius

$$r_e = \int r^3 n(r) dr / [ \int r^2 n(r) dr ] \quad (6)$$

where  $n(r)$  is the size distribution, as well as revisiting  $r_p$ .

The relationship between  $S$  and each of these radius parameters is determined by comparison with these quantities calculated for a variety of typical size distributions using Mie theory. We found, in agreement with Platt and Takashima (1987), a useful relationship between  $S$  and  $r_p$  for idealized, unimodal size distributions represented by a modified gamma distribution. Unfortunately, when we used the 156 measured size distributions compiled by Pinnick et al. (1983), some of which are bimodal, the relationship between  $S$  and  $r_p$  was too scattered to be very useful. However, the relationships between  $S$  and the integral quantities  $r_m$  (Fig. 1) and  $r_e$  (Fig. 2) are quite useful. The solid curves in these two figures are fourth-order polynomial fits to the measured size distributions were used as the algorithms in our initial application of the method.

Potential sources of error are discussed in Eberhard (1993). Accurate calibration of the lidar and proper correction of the signal for molecular absorption along the path are necessary for accurate results. Possible errors in the published values of refractive index of water are unlikely to cause more than 10% error in  $S$ . Correction for multiple scattering for a lidar with a 5-mr receiver field of view was shown by Platt and Takashima (1987) to be manageable. However, multiple scatter is negligible at this wavelength for a diffraction-limited lidar like the one operated by Wave Propagation Laboratory.

Our coherent CO<sub>2</sub> lidar (Post and Cupp, 1990) measured the backscatter from fair weather cumulus at Kennedy Space Center (KSC) in Florida as a preliminary test of this new technique. The system had been calibrated as normal (Post and Cupp, 1990). Data were acquired between 1130 and 1137 LST. The lidar operated at 10.591- $\mu$ m wavelength, 10-Hz pulse repetition rate, and 0.77-J pulse energy. The lidar first pointed in one direction at a constant elevation angle  $\epsilon$  of 23.2° while a cloud advected past the beam and two data files, each of 50-s duration, were recorded. Then the lidar was aimed at a different cloud using  $\epsilon=10.9^\circ$  while two additional files were recorded. The data were divided into 20 periods, each having little change in the structure of  $\beta'(R)$ , and the pulses were averaged within each period. The range to the cloud changed as it advected with the wind, and the height where the lidar beam intercepted the cloud changed in proportion. This height was specified as

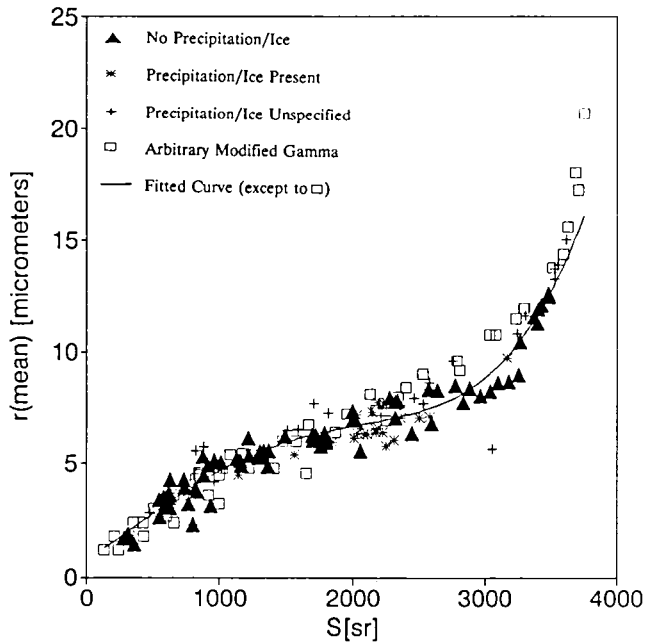


Fig. 1. Calculated relationship at 10.59- $\mu\text{m}$  wavelength between extinction-to-backscatter ratio  $S$  and mean radius  $r_m$  for 156 measured (triangles, stars, and pluses) and 50 idealized (squares) cloud drop size distributions. The solid curve is a fourth-order polynomial fit to the points only from the measured size distributions.

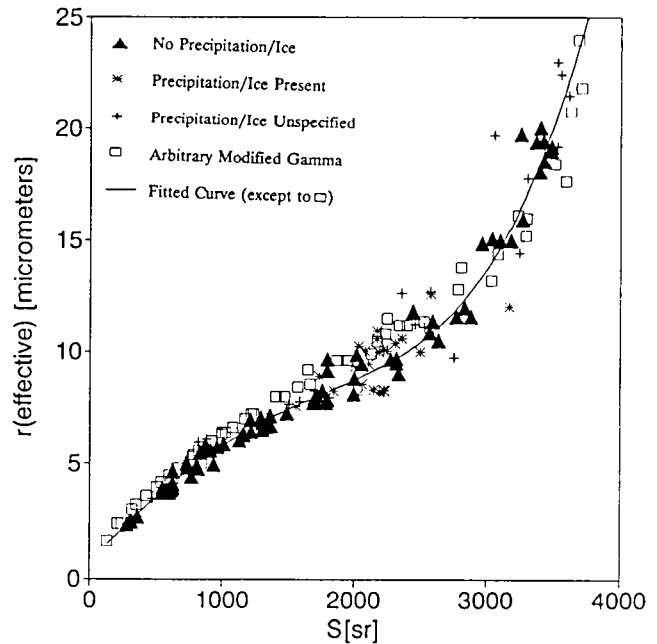


Fig. 2. As in Fig. 1 except for effective radius  $r_e$ .

$h = R_m \sin \epsilon$ , where  $R_m$  was the range to the median in  $\beta'$ . The magnitudes (Fig. 3) of  $r_m$  are reasonable for this type of cloud. The most interesting feature is the increase of  $r_m$  with height, which is expected to occur in cumulus that are convectively active like these. The larger  $r_m$  for the second cloud indicates differences in the development of the two clouds.

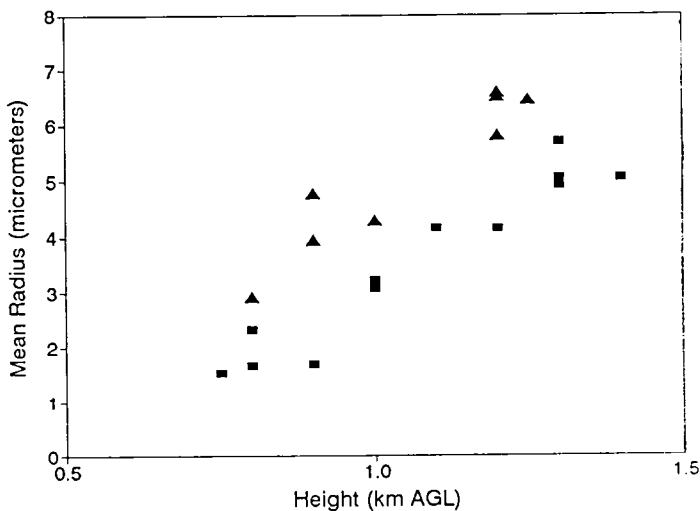


Fig. 3.  $\text{CO}_2$  lidar measurements of  $r_m$  on the sides of fair weather cumulus clouds: (squares) first cloud observed at  $23.2^\circ$  elevation angle, and (triangles) second cloud observed at  $10.9^\circ$ .

Unfortunately, we do not yet have independent size measurements for substantiation. Although this technique has a solid analytical foundation, comparison with other methods is needed to establish the practical accuracy of the lidar method. We plan extensive application in field programs studying clouds, including comparisons with *in situ* drop size measurements by aircraft.

This example shows how a pulsed, range-gated CO<sub>2</sub> lidar operating from the surface can apply the method. The method could also be applied by similar lidar systems operating from an airplane or satellite. Scanning lidars could quickly interrogate many parts of a cloud or multiple clouds. An airborne system could also probe the interior of clouds, but the minimum range of the lidar should be kept very small or else some assumptions must be made about the backscatter and extinction within the minimum range. If the lidar can probe a much larger volume than an aircraft using conventional *in situ* drop size measuring systems, the lidar could obtain a representative measurement more quickly.

*Acknowledgments.* The author thanks M.J. Post and R.E. Cupp, who obtained the lidar measurements in Florida. R.G. Pinnick kindly shared his tabulations of 156 measured size distributions. Mike Jardon performed the calculations and graphics leading to Figs. 1-2. This work was funded through the Climate and Global Change Program Office of the National Oceanic and Atmospheric Administration and Grant # DE-FG02-90ER61059 from the Department of Energy's Atmospheric Radiation Measurements program.

## REFERENCES

- Eberhard, W.L., 1993: CO<sub>2</sub> lidar technique for observing characteristic drop size in water clouds. Submitted to *IEEE Trans. Geosci. Remote Sensing*, 31, January special issue on remote sensing at optical and infrared wavelengths.
- Hall, F.F., Jr., R.E. Cupp and S.W. Troxel, 1988: Cirrus cloud transmittance and backscatter in the infrared measured with a CO<sub>2</sub> lidar. *Appl. Opt.*, 27, 2510-2616.
- Pinnick, R.G., S.G. Jennings, P. Chylek, C. Ham and W.T. Grandy, Jr., 1983: Backscatter and extinction in water clouds. *J. Geophys. Res.*, 88, 6787-6796.
- Platt, C.M.R., and T. Takashima, 1987: Retrieval of water cloud properties from carbon dioxide laser soundings. *Appl. Opt.*, 26, 1257-1263.
- Post, M.J., and R.E. Cupp, 1990: Optimizing a pulsed Doppler lidar. *Appl. Opt.*, 29, 4145-4158.

# OBSERVATIONS OF CIRRUS CLOUDS OVER THE PACIFIC REGION BY THE NASA MULTIWAVELENGTH LIDAR SYSTEM

Syed Ismail<sup>1</sup>, Edward V. Browell<sup>1</sup>, Marta A. Fenn<sup>2</sup>, and Greg D. Nowicki<sup>2</sup>

<sup>1</sup>Atmospheric Sciences Division, NASA Langley Research Center  
Hampton, VA 23665-5225

<sup>2</sup>Hughes STX Corporation, 28 Research Drive  
Hampton, VA 23666

Cirrus clouds have a significant influence on the Earth's radiation budget. The role of cirrus clouds on climate is being studied by several major experimental projects including the First International Satellite Climatology Project Regional Experiment (FIRE), the Experimental Cloud Lidar Pilot Study (ECLIPS), and Atmospheric Radiation Measurement (ARM). Lidar measurements by Platt [1971] and Platt et al. [1987] from the ground have demonstrated the capability of making high resolution measurements of cirrus cloud base, height, and optical thickness. Sassen [1991a] has recently reviewed the advantages of using the polarization lidar technique to monitor the variation in cirrus cloud characteristics. NASA Langley Research Center's airborne Differential Absorption Lidar (DIAL) system transmits in the UV (300-nm), visible (600-nm), and IR (1064-nm) spectral region for the measurement of tropospheric and/or stratospheric ozone and aerosols [Browell, 1989]. This DIAL system has participated in a large number of major field experiments. During these campaigns, a large number of cirrus cloud observations have been made. Most recently, as part of the Pacific Exploratory Mission - West campaign that took place during September 16 to October 21, 1991, lidar measurements were made from the NASA Ames DC-8 aircraft at an altitude of approximately 9 km. This mission provided a unique opportunity to make cirrus cloud observations around the Pacific region covering the latitude range from 5 to 55°N and the longitude range from -114 to 120°E. Cirrus clouds were observed on most of these flights providing a unique data base. The latitudinal coverage of cirrus observations was further extended to -5°S from observations on January 30, 1992, as part of the Airborne Arctic Stratospheric Expedition II [Browell et al., 1992]. During this latter mission, aerosol depolarizations at 622 and 1064 nm were also measured. This paper summarizes the optical characteristics and statistics related to these cirrus cloud observations.

A segment of the data illustrating cirrus cloud observations of enhanced relative aerosol scattering derived from visible lidar signals is shown in Figure 1. The cirrus cloud tops are located below 16 km, and the Pinatubo aerosols are seen in the 19- to 21-km altitude region. The top of the cirrus cloud appears to change gradually from left to right, and the bottom is highly structured. The left side of Figure 1 shows optically thin cirrus clouds with optical thickness ( $\tau$ ) < 0.1, and the right side shows two layers of cirrus with higher optical depth as can be seen by modulations in lidar backscatter signals above the cloud and a general fading of signals across the Pinatubo aerosols. The differences in the total atmospheric scattering ratio (aerosol backscatter ratio +1) profiles from the visible and IR channels is shown in Figure 2. The vertical resolution is 60 m, and lidar signals have been averaged over a horizontal distance of about 200 m (15 shots, 2 s). The scattering ratio normalization was done at 16 km, and a tropical atmospheric model

was used to determine the molecular scattering profile. Due to the small amount of signal attenuation ( $\tau < 0.1$ ) observed during 20:26 to 20:48 UT (Figure 1), this portion of the cloud can be classified as a weak cirrus. In the case of weak cirrus, the cloud top was generally well defined. The average altitude of the bottom of the cloud can be identified by using a statistical criteria. There is considerable structure in the aerosol scattering between the top and bottom altitude regions of the cirrus cloud (Figure 2). The aerosol scattering structure is similar in the IR, visible, and UV scattering profiles. The aerosol scattering wavelength dependence parameter [ $\alpha$ , Browell, 1989] profile derived from a combination of the visible and IR scattering is given in Figure 3 (for the data presented in Figure 2). The average  $\alpha$  value for most of the cloud is  $\sim 0.5$  which is consistent with large particles ( $> 1 \mu\text{m}$ ) associated with cirrus clouds [Dowling and Radke, 1990], and an  $\alpha \approx 0.06$  at 16.7 km coincided with a strong peak in the scattering near the top of the cloud. This very low  $\alpha$  value indicates near-absence of aerosol scattering wavelength dependence which is caused by either very large-size ice crystals and/or by a small number of horizontally oriented ice crystals causing specular reflections which result in very high backscatter, low signal attenuation, and no wavelength dependence.

A systematic decrease in the altitude of the cirrus cloud-top heights with increasing latitude was observed. This general trend can be seen in Figure 4 with the scatter in the data points reflecting the natural variability of the clouds. Highest cloud tops were seen near the Equator and reached altitudes near 17 km, and lowest cloud tops ( $< 7$  km) were observed in the range 50-55°N latitude. The data could be roughly classified into low (0-25°N), mid ( $> 25$ -45°N), and high ( $> 45$ °N) latitudes with typical cloud height altitudes of 16, 12, and  $< 10$  km, respectively. Considerable altitude variation was seen in the 20-30°N latitude range. Cirrus top heights near the Equator (-5 to 12°N) were measured on January 30, 1992. These data show a slight dip at the Equator and a near symmetry about the Equator. Observations made by Sassen [1991b] show that cirrus cloud tops occur near the tropopause, and other observations indicate that the centers of cirrus cloud altitude occur at about three-quarters of the local tropopause heights [Dowling and Radke, 1990]. The relationship between cirrus cloud top and the tropopause height will be further investigated in conjunction with the airborne lidar O<sub>3</sub> data which clearly show the location of the tropopause. On some occasions (as seen in Figure 1), the lidar data indicate that the cirrus top heights remain steady and change only gradually during a flight, and at other times the cirrus top heights vary widely along the flight track. The spatial variability of the cirrus clouds and their optical characteristics are discussed in this paper. During the course of these field experiments, two storm systems (or typhoons) and a tropopause folding event were observed. The characteristics of the cirrus clouds observed during these events are also presented.

#### References

- Browell, E. V., Proc. IEEE, **77**, 419, 1989.  
Browell, E. V et al., Conf. Digest 16th ILRC, 1992.  
Dowling, D. R. and L. F. Radke, J. Appl. Meteor., **29**, 970, 1990.  
Platt, C. M. R., J. Atmos. Sci., **30**, 1191, 1971.  
Platt, C. M. R. et al., J. Clim. Appl. Meteor., **44**, 729, 1987.  
Sassen, K., Bull. AMS, **72**, 1848, 1991a.  
Sassen, K., Appl. Opt., **24**, 3421, 1991b.

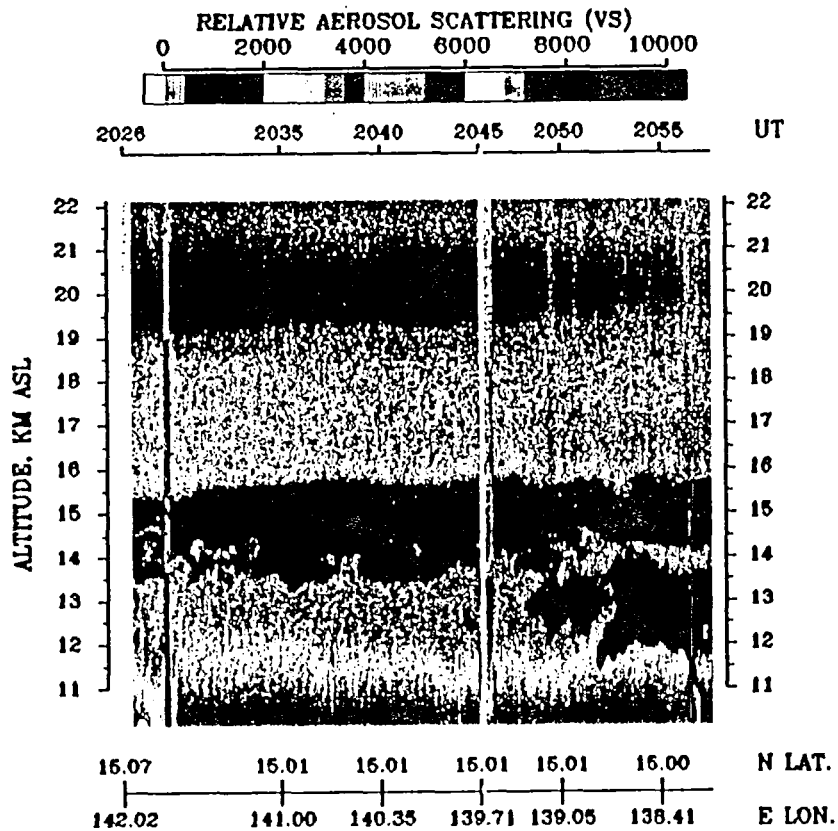


Figure 1. Relative aerosol backscattering from the visible lidar signals observed on October 14, 1991, from the DC-8 aircraft.

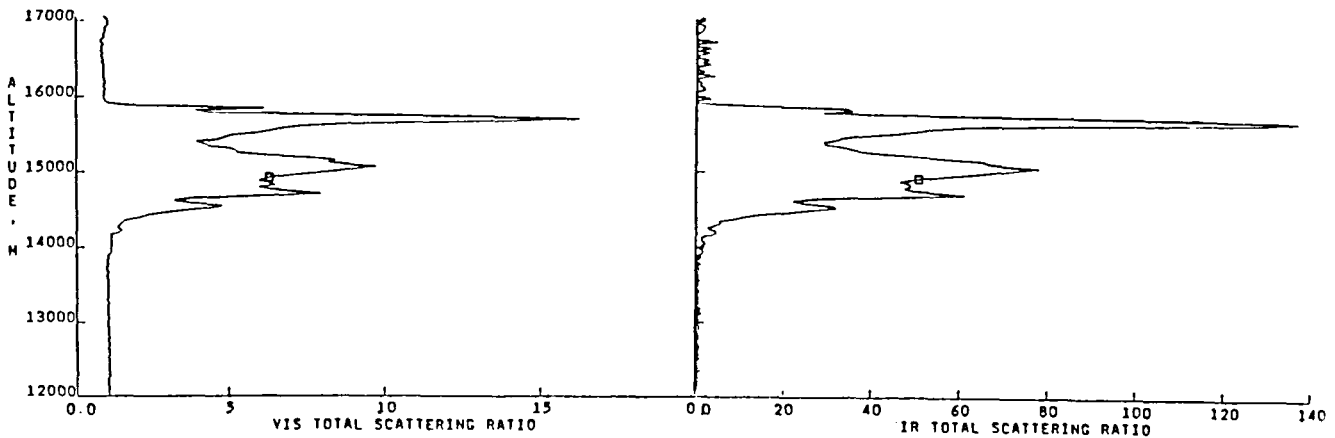


Figure 2. Visible and IR scattering ratio variations within a cirrus cloud observed on October 14, 1991.

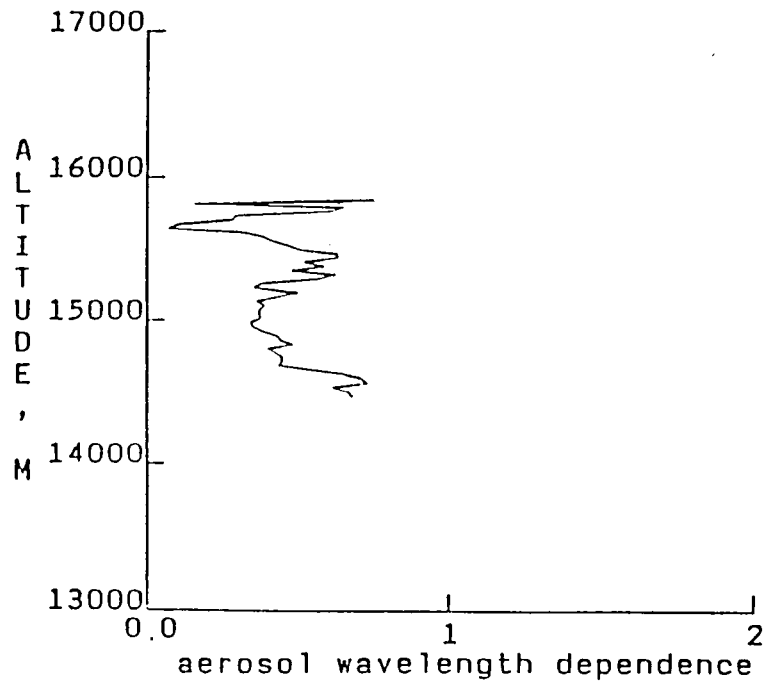


Figure 3. Aerosol wavelength dependence between visible and IR data shown in Figure 2.

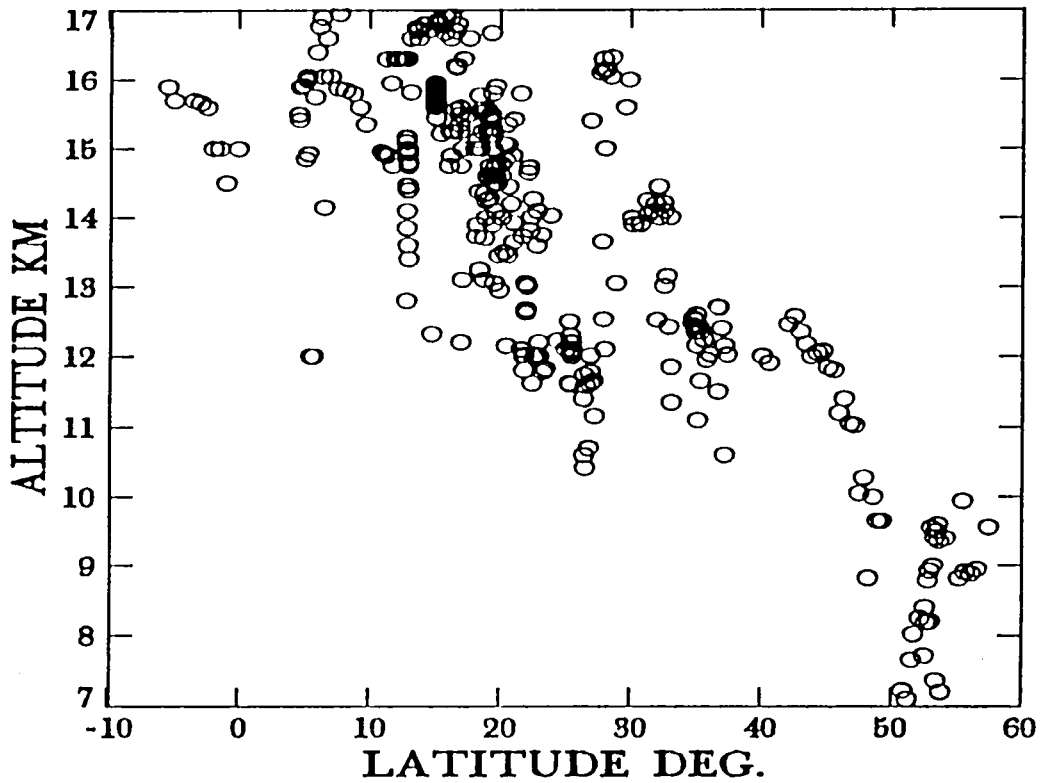


Figure 4. Variations of cirrus cloud top heights with latitude observed from lidar system onboard the DC-8 aircraft over the Pacific during September-October 1991 and on January 30, 1992.

# Diode - Pumped Nd:YAG Lidar for Airborne Cloud Measurements

A. Mehnert and Th. Halldorsson  
MBB/DASA  
P.O.Box 80 11 09  
D-8000 München 80  
Federal Republic of Germany

H.Herrmann, R.Häring\*, W.Krichbaumer, J.Streicher and Ch.Werner  
DLR - Institute of Optoelectronics  
D -8031 Oberpfaffenhofen  
Federal Republic of Germany  
\* Consultant

This work is concerned to the experimental method to separate scattering and to use it for the determination of cloud microphysical parameters. It is also the first airborne test of a lidar version related to the ATLID programme - ESA's scheduled spaceborne lidar.

The already tested DLR - Microlidar (1) was modified with the new diode-pumped laser and a faster data recording system was added. The system was used during the CLEOPATRA campaign in the DLR research aircraft Falcon 20 to measure cloud parameters.

The diode pumped Nd:YAG laser we developed for the Microlidar is a modification of the laser we introduced at the Lidar Congress at the "Laser 91" in Munich (2). Due to the requirements of the airborne Microlidar especially the EMC between the laser and the data acquisition system, we decided to use a rotating prism as a Q-switch instead of the pockels cell. Though the laser is not finally tested, we are hopeful to get output data similar to the data that resulted when we used the pockels cell as Q-switch element. Since the lidar system operates at the fundamental wavelength of the Nd:YAG (1.06  $\mu\text{m}$ ) the mentioned SHG-crystal is not inserted.

The laser consists of a Nd:YAG-Brewster-slab-crystal (DBS) with a triangular geometry. The so called zigzag slab is designed to have one internal reflection of the resonator mode inside the crystal, and therefore the baseline is 20 mm long, the thickness is 5 mm and the apex angle is on both sides the Brewster angle. The plan-concave resonator leads to a beam waist of  $w_0 = 0.4$  mm for the TEM<sub>00</sub> mode thus the divergence  $\theta$  for the fundamental mode is less than 2 mrad. A SDL 3230TA stacked quasi-cw laser diode array was used as a pump source. This diode is made of two linear arrays, each array capable of emitting 60W of optical power, for a pulse length of 200  $\mu\text{s}$  and a repetition rate of 100 Hz. This results in a total pulse energy of 24 mJ.

For electro-optically q-switching the laser we decided to use a pockels cell with a high optical damage threshold.

Some of the optical characteristics of the laser are shown in Fig.1. Remarkable is the

high optical-to-optical efficiency  $\eta_{\text{opt.-opt.}} = 43\%$  of the laser in free running operation, as well as the corresponding values for pure TEM<sub>00</sub>-operation ( $\eta_{\text{opt.-opt.}} = 21\%$ ) and for q-switched operation ( $\eta_{\text{opt.-opt.}} = 27\%$ ).

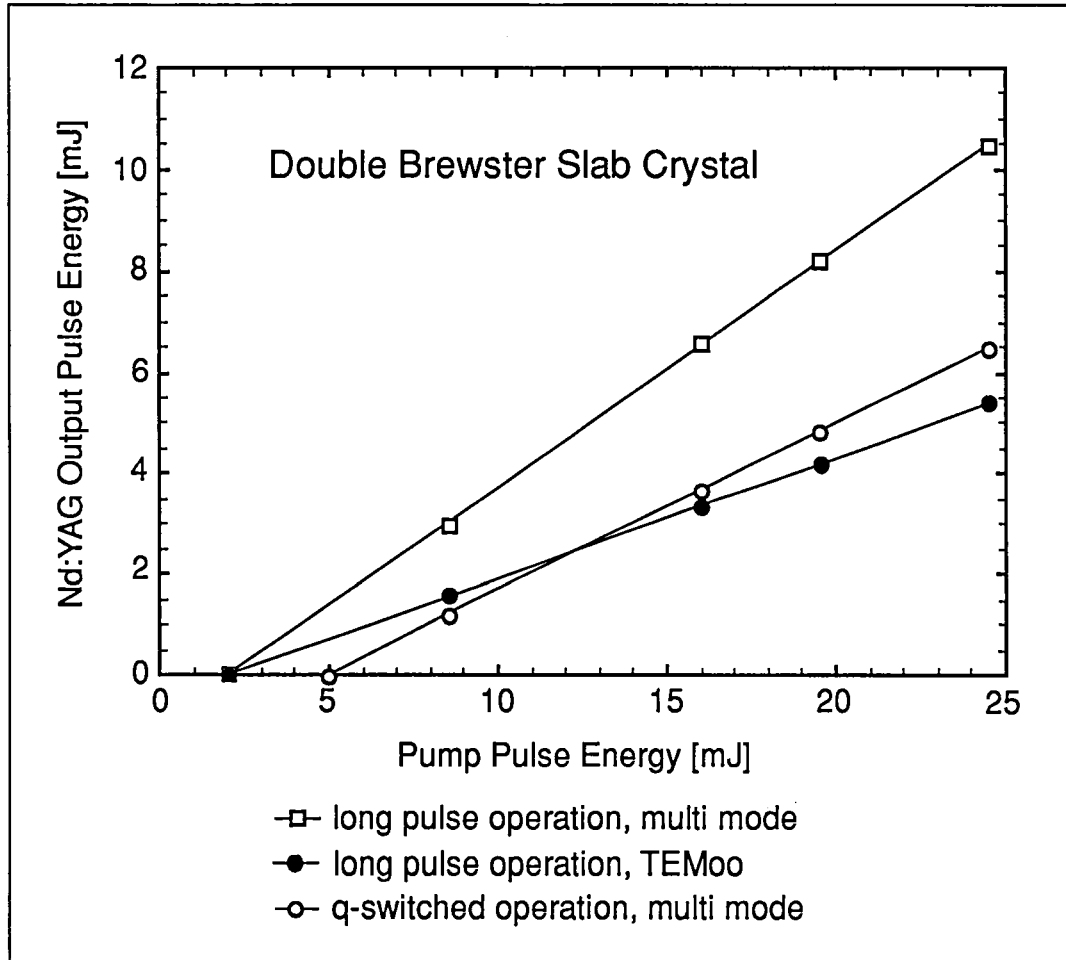


Fig.1: Optical Output Data of the Nd: YAG-DBS-Laser

These values correspond to 11 mJ pulse energy for free running operation (multimode), 5.3 mJ (TEM<sub>00</sub>), and 6.5 mJ for q-switched operation. These data are constant over the whole range of repetition rate of the laser diode (10 to 100 Hz). The pulse length in the free running mode is close to 200  $\mu\text{s}$  because of the very short pulse build-up-time. In the case of q-switched operation, pulse lengths <10 ns could be achieved.

To avoid optical damage of the laser components, we limited the pump pulse energy to 13 mJ for our intracavity frequency doubling experiments. We achieved 1.2 mJ of pulse energy at 0.532  $\mu\text{m}$  wavelength, which results in an opt.-opt. efficiency of  $\eta_{\text{opt.-opt.}} = 9\%$ .

The receiver is a Cassagrain telescope with the capability to detect multiple scattering and depolarization simultaneously. Figure 2 shows the schematic.

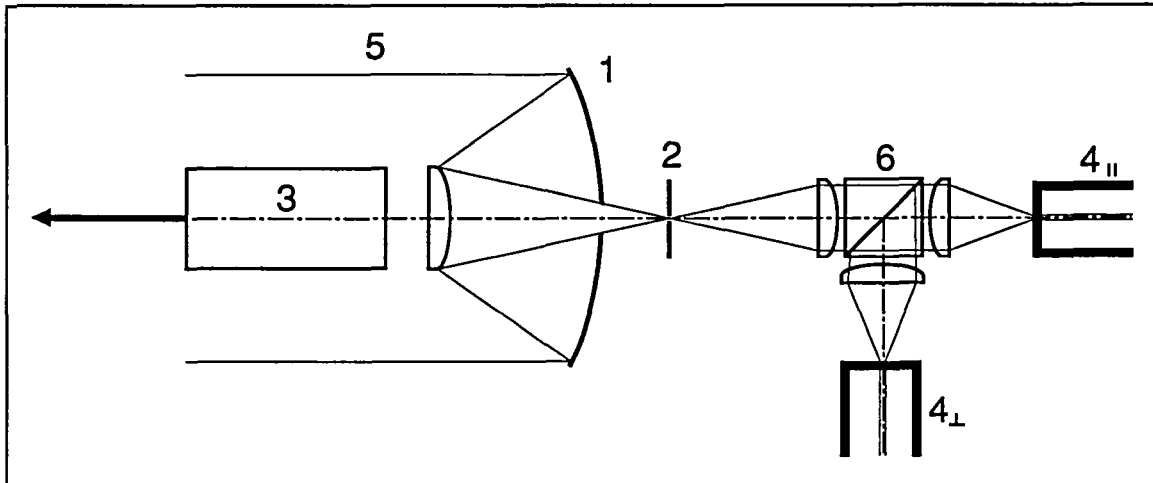


Figure 2: Schematic of the lidar

- 1 parabolic mirror
- 2 field stop
- 3 diode- pumped Nd:YAG laser
- 4 fibers adjusted to different field of views
- 5 receiver field of view
- 6 polarizing beam splitter

The fiber is used to separate single scattered radiation and the multiple scattered contribution. Two of such fibers are used to get the polarization sensitive information from clouds. The four end of the two fibers are given to PIN photodiodes. The electrical signal is stored on a 10 bit four channel transient recorder. For the airborne environment a PC was modified (Portax) and it transfers the digitized signals to a Winchester hard disk. A readout procedure was prepared to select the information which is useful and interesting for further processing. The pulse repetition rate which can be handled by the data system is 10 Hz.

- (1) Ch. Werner, J. Streicher, H. Herrmann, H.G. Dahn, Multiple Scattering Lidar Experiment Optical Engineering in press.
- (2) A. Mehnert, P. Peuser and N. Schmitt, Laser in Umweltmeßtechnik, Springer Verlag Berlin, page 201-205, (1992)



# REMOTE SENSING BY SPACEBORNE LIDAR AIDED BY SURFACE RETURNS<sup>1</sup>

J.A. Reagan and T.W. Cooley  
University of Arizona  
Department of Electrical & Computer Engineering  
Tucson, AZ 85721

## INTRODUCTION

Spaceborne lidar offers the possibility of global mapping of clouds and atmospheric aerosols. Mapping of cloud-top heights, multiple layers of thin clouds and the depth of the Planetary Boundary Layer (PBL), given sufficient aerosols, are applications that should be fairly easy to accomplish from space with even a modest lidar system. However, the constraints imposed on spaceborne lidar by large ranging distances, limited available power/weight, and fast moving platforms present significant challenges to achieving more quantitative retrievals such as extracting aerosol extinction profiles, PBL optical depths and cloud optical depths. This paper explores ways to take advantage of the strong signals available from ground/sea reflections to improve upon atmospheric aerosol and cloud retrievals as well as to distinguish certain surface types.

## LIDAR RELATIONS AND PARAMETERS

For a nadir viewing lidar operating at wavelength  $\lambda$ , the energy  $E_\lambda(z)$  received due to backscattering from range bin  $\Delta z$  at distance  $z$  from the lidar may be expressed as

$$E_\lambda(z) = \frac{E_0 A_R \beta_\lambda(z) T_\lambda^2(z) \Delta z}{z^2} \quad (1)$$

where  $E_0$  is the transmitted pulse energy,  $A_R$  is the effective receiver area,  $\beta_\lambda(z)$  is the atmospheric unit volume backscattering coefficient at range  $z$  for wavelength  $\lambda$ , and  $T_\lambda^2(z)$  is the atmospheric round-trip transmittance to and from range  $z$ . The range bin  $\Delta z$  equals  $ct_i/2$  where  $c$  is the speed of light and  $t_i$  is the effective integration time set by the receiver system bandwidth or the transmitted pulse duration, whichever is larger.

Scattering by a hard surface at range  $z_s$ , such as the earth's surface, yields a signal

$$E_\lambda(z_s) = \frac{E_0 A_R R_\lambda T_\lambda^2(z_s)}{z_s^2} \quad (2)$$

where  $R_\lambda$ , the surface backscatter coefficient, which takes the place of  $\Delta z \beta_\lambda(z)$  in eq. (1).

---

<sup>1</sup>This work is supported under the NASA Graduate Student Researchers Program and the LITE Science Steering Group, Langley Research Center.

The received signal can be expressed in terms of the number of primary photoelectrons  $n_\lambda$  generated by the receiver photodetector by multiplying  $E_\lambda$  by  $\lambda\delta_\lambda/hc$  where  $h$  is Planck's constant,  $\delta_\lambda$  is the photodetector quantum efficiency, and  $c$  and  $\lambda$  are as defined earlier. Random noise due to the fluctuating generation rate of the signal charge carriers  $n_\lambda$ , as well as charge carriers due to received background radiation,  $n_{\lambda B}$ , and in electronic detector noise,  $n_{\lambda D}$ , yield an *rms* signal-to-noise ratio of the form

$$S/N = \frac{n_\lambda}{\sqrt{n_\lambda + n_{\lambda B} + n_{\lambda D}}} . \quad (3)$$

Under strong signal conditions where  $n_\lambda$  is much larger than  $n_{\lambda B} + n_{\lambda D}$ ,  $S/N$  reaches the optimal level  $S/N = \sqrt{n_\lambda}$ . Conversely,  $n_\lambda$  must exceed the noise floor set by  $\sqrt{n_{\lambda B} + n_{\lambda D}}$  to yield a detectable signal, although signal averaging or photon counting over many lidar returns can be used to improve poor  $S/N$  values.

The signal count can be raised by increasing  $E_0$ ,  $A_R$  or  $\delta_k$ , although the background count  $n_{\lambda B}$  is also increased as  $A_R$  and  $\delta_k$  are increased. The background count is chiefly of concern for daytime operation for which  $n_{\lambda B}$  is still quite large even for lidar receivers with very narrow fields-of-view (FOV's  $\sim 1$  milliradian) and extremely narrow filter bandwidths ( $\Delta\lambda_f \sim 0.1nm$ ). The internal detector noise count  $n_{\lambda D}$  can be kept very small for photomultiplier (PMT) detectors, but it is excessively large for avalanche photodiode (APD) type detectors. Nominal lidar system parameter values for a shuttle-borne lidar experiment such as LITE have been given by [1], [2]. For representative example computations, the product  $E_0 A_R$  is assumed to be  $0.03 Jm^2$ ,  $\delta_k$  to be 20% and  $n_{\lambda B} + n_{\lambda D} = 2 \times 10^4/km$  for worst case conditions of daytime operation. Wavelengths are assumed to be 532 nm and 1064 nm, the doubled and fundamental wavelengths for a Nd:YAG laser transmitter. High performance PMT's are available for the 532 nm wavelength, but APD's, even with their poor internal noise characteristics, are the best choice for the 1064 nm wavelength.

## EXAMPLE RETURN SIGNALS

The surface backscatter coefficient,  $R_\lambda$ , can easily vary over a decade or more depending on surface type. For ground reflections,  $R_\lambda$  may be modeled approximately by  $R_\lambda \approx \rho/\pi$  where  $\rho$  is the surface albedo; by using the factor  $1/\pi$ , it is assumed that the reflection is approximately Lambertian. Water reflections are neither perfectly specular nor Lambertian. For modeling purposes, it appears that  $R_\lambda \approx 0.05$  is a reasonable choice for approximating both typical water surfaces and a number of ground types.

Example signal counts,  $n_\lambda$ , computed for returns from the earth's surface for a lidar height of 300 km are given in Table 1. Atmospheric return counts, based on the 1964 Elterman model [3], are given as well for layers of thickness  $\Delta z = 1 km$  and  $\Delta z = 150m$  immediately adjacent to the surface. Signal to noise,  $S/N$ , values are also listed for the various counts. From the table, it can be seen that the surface returns are immensely greater than the adjacent 150m layer atmospheric returns. In particular, the  $S/N$  values for both the 532 nm and 1064 nm surface returns are large enough to permit quantitative application of the

surface signals on a per shot basis. This is important because averaging over many lidar returns may not greatly improve the surface signal statistics due to variability in terrain/surface conditions under the moving lidar platform. Spatial averaging over the relatively large surface-level lidar footprint ( $\sim 300$  m) may provide rather consistent surface returns over water and fairly homogeneous ground surfaces.

## WAYS TO EMPLOY THE SURFACE RETURNS

Reflection of the transmitted lidar pulse by the earth's surface presents several opportunities for both investigating surface properties and aiding in the recovery of atmospheric information. Different opportunities and problems are presented for ground reflections as opposed to water reflections. In either case, the surface return is large enough for the 532 nm and 1064 nm wavelengths to provide a very useful signal level. Specific applications of surface returns that appear to be well worth considering are highlighted below. Additional details and discussion about the various applications noted here will be given in the conference presentation of this paper.

### Water Reflection Applications

- Retrieval of  $R_\lambda$  at 1064 nm - For clear conditions,  $T_\lambda$  is close to one ( $\sim 0.9$ ) and can be fairly accurately modeled permitting retrieval of  $R_\lambda$ . Knowing  $R_\lambda$  can provide information about ocean state and winds.
- Retrieval of  $T_\lambda$  at 532 nm - For clear conditions and  $R_\lambda$  retrieved at 1064 nm as noted above,  $T_\lambda$  can then be recovered at 532 nm as  $R_\lambda$  will be nearly the same for both wavelengths.
- Retrieval of ratio  $T_{\lambda_1}/T_{\lambda_2}$  - Regardless of whether the atmosphere is quite clear or not,  $R_\lambda$  will be effectively the same at 532 nm and 1064 nm for a water reflection, permitting retrieval of  $T_{\lambda_1}/T_{\lambda_2}$  by ratioing the lidar returns for the two wavelengths. The spectral transmittance ratio can be used to assess aerosol loading.

### Ground Reflection Applications

- Retrieval of  $R_\lambda$  at 1064 nm - For clear conditions, as with the water reflection case,  $R_\lambda$  can be estimated fairly well by modeling  $T_\lambda$  which will be close to one. Knowing  $R_\lambda$  will permit limited identification of different terrain types as well as establish a climatology for  $R_\lambda$  that could be useful in estimating  $T_\lambda$  for other occasions when the atmosphere is not clear.
- Retrieval of reflectance ratio  $R_{\lambda_1}/R_{\lambda_2}$  - By employing model atmosphere assumptions or auxiliary data to estimate  $T_{\lambda_1}/T_{\lambda_2}$ , the reflectance ratio  $R_{\lambda_1}/R_{\lambda_2}$  can be inferred from the ratio of returns for 532 nm and 1064 nm. As  $R_{\lambda_1}/R_{\lambda_2}$  changes significantly for different surfaces, even obtaining a rough estimate of  $R_{\lambda_1}/R_{\lambda_2}$  can be useful.

### Cloud/Fog Applications

- Detection of fog layers - The ratio of the atmospheric return from the layer adjacent to the surface to the surface return can be used to detect the presence of fogs and strong hazes near the earth's surface.

- Retrieval of cloud/fog transmittance - By using an assumed value for  $R_\lambda$ ,  $T_\lambda$  can be estimated for clouds/fogs that are not too optically thick to mask the substantial surface return. Even for only a poor estimate of  $R_\lambda$ , useful information can still be obtained about  $T_\lambda$ .

#### Aerosol Applications

- Retrieval of aerosol profiles - Estimates of  $T_\lambda$  and the ratio  $T_{\lambda 1}/T_{\lambda 2}$  obtained from the various approaches noted above can be used as boundary condition and constraint data in lidar equation solutions for retrieving aerosol profiles.
- Lidar Calibration - Lidar returns from surfaces with known reflectances (e.g., White Sands, NM), coupled with auxiliary transmittance data, can be used to provide the calibration necessary for most aerosol profile retrieval techniques.

#### REFERENCES

- [1] P.B. Russell, B.M. Morley, J.M. Livingston, G.W. Grams, and E.M. Patterson, "Orbiting lidar simulations. 1: Aerosol and cloud measurements by an independent-wavelength technique," *Appl. Opt.*, Vol. 21, pp. 1541-1553, May, 1982.
- [2] R.H. Couch et al., "Lidar In-Space Technology Experiment (LITE): NASA's first in-space lidar system for atmospheric research," *Opt. Engr.*, Vol. 30, pp. 88-95, 1991.
- [3] L. Elterman, "Parameters for attenuation in the atmospheric windows for fifteen wavelengths," *Appl. Opt.*, Vol. 3, pp. 745-749, 1964.

TABEL 1. PROPERTIES OF SURFACE AND NEAR SURFACE RETURNRS

$$E_0 A_R = 0.03, \delta_\lambda = 0.2, n_{\lambda D} + n_{\lambda B} = 2 \times 10^4 / km$$

Reflecting Element	$\lambda = 532 \text{ nm}$ $T_\lambda^2 = 0.5406$		$\lambda = 1064 \text{ nm}$ $T_\lambda^2 = 0.7302$	
	$n_\lambda$	$S/N$	$n_\lambda$	$S/N$
Surface ( $R_\lambda = 0.05$ ; $\Delta z = 150\text{m}$ )	4823	54.5	13,028	102.9
1 km $\Delta z$ over surface	740	5.1	1197	8.2
150m $\Delta z$ over surface	111	2.0	179	3.2

# NWP IMPACT OF CLOUD TOP AND BOUNDARY LAYER WINDS FROM A SATELLITE BORNE LIDAR: AN OBSERVING SYSTEM SIMULATION EXPERIMENT<sup>1</sup>

R.G. Isaacs, C. Grassotti, R.N. Hoffman, M. Mickelson, T. Nehrkorn, and J.-F. Louis  
Atmospheric and Environmental Research, Inc., Cambridge, Massachusetts, 02139 USA

## 1. INTRODUCTION

Observing systems simulation experiments (OSSEs) provide a powerful tool to assess the impact of proposed satellite borne observing systems on meteorological applications models (Arnold and Dey, 1986). Here we describe the results of an OSSE conducted to assess the impact of data from a low power lidar wind sensor on the forecast accuracy of a global spectral numerical weather prediction (NWP) model, the Air Force Geophysics Laboratory Global Data Assimilation System (Grassotti et al, 1991). The instrument would be operating at near-infrared wavelengths thereby increasing the backscatter signal relative to a comparable infrared lidar. Since it would also operate at lower energy, its resolving power is not expected to be as great and retrieved wind profiles are not likely to be as complete, with measurements primarily at or near cloud tops, from cirrus return, and in the marine boundary layer. This instrument may be seen as a potentially lower cost alternative to some of the other lidar instruments which are currently planned such as the Laser Atmospheric Wind Sounder (LAWS) (see Huffaker et al, 1984). The trade-off is that between system complexity and potential payback measured in terms of positive impact on numerical weather prediction (NWP) forecast accuracy. For the more complex lidar wind sounder, impacts can be ascertained from our previous experiment based on the WINDSAT concept (Hoffman et al, 1990).

## 2. APPROACH

An extended 20 day forecast of the ECMWF grid point model (nature run) serves ground truth for cloud diagnosis and for verification. The simple lidar wind sounding instrument has been assumed to be aboard the DMSP polar orbiting platform with observational coverage similar to the SSM/T sounder. Three types of returns are treated: (1) cirrus cloud, (2) liquid water cloud, and (3) marine boundary layer aerosol. Two line of sight velocity measurements, with their own intrinsic errors are required to uniquely determine the two-dimensional horizontal wind vector. Errors of the u and v components are treated as a function of both distance to the satellite subtrack as well as the orientation of the satellite track with respect to lines of latitude and longitude. This results in measured wind profiles which contain observations at one or several levels, but never complete profiles, and which reflect the local geophysical conditions (i.e. cloudiness). The errors associated with each observation are a function of the viewing geometry and the actual source of the lidar backscatter: cirrus, water cloud, or marine boundary layer aerosol. Using the Geophysics Laboratory (GL) Global Data Assimilation System, we insert the simulated wind data at 6 hour intervals into the assimilation system for a period of 7 days. Forecasts of 4 days in length are run using the GL Global Spectral Model (Brenner et al., 1982, 1984) with initial conditions provided by analyses valid at various points during the assimilation run.

## 3. OSSE PROCEDURE

The procedure is summarized in Figure 1, which shows the control simulation, the lidar simulation and respective forecasts with the nature run or truth initial state.

---

<sup>1</sup>Sponsored by the Geophysics Directorate, Phillips Laboratory under contract number F19628-89-C-0137.

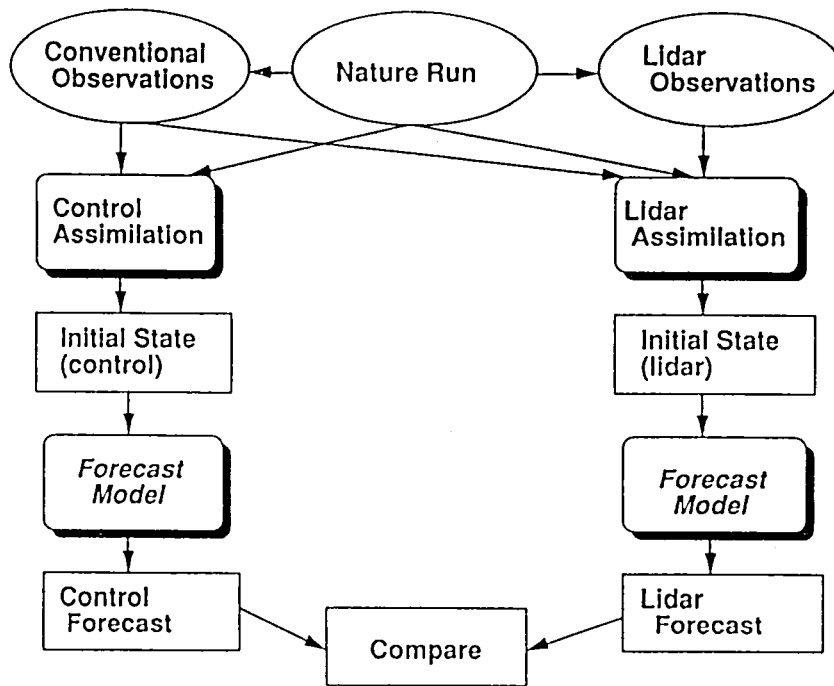


Figure 1. Lidar OSSE Procedure

#### 4. DATA SIMULATION

There are essentially two steps in the process: (a) identifying where lidar data is available and extracting it from the nature run (perfect lidar data) and (b) assigning appropriate measurement error or noise to the lidar data to accomplish a realistic simulation.

##### 4.1 Perfect Lidar Data

As a preliminary to accomplishing step (a), fields of temperature, relative humidity, height, and u and v wind components have been extracted from the OSSE nature run for each 6 hour time period of the assimilation cycle. This grid uses the orbital geometry of the DMSP and is consistent with a 45 degree scan given a 1700 km swath width. Cirrus clouds are diagnosed from both the relative humidity and temperature profile at the observing location. Liou et al. (1990) have proposed a simple criterion for the presence of cirrus cloud. Ice clouds are present if both the relative humidity and temperature fall above and below their critical values, respectively. A threshold relative humidity is calculated as a function of ambient temperature. We have modified the criterion to reproduce the fall time period zonal climatology of the SAGE data results of Woodbury and McCormick (1986). We have also assumed that cirrus clouds are sufficiently transmissive so that the presence of cirrus does not necessarily preclude returns from lower levels. Liquid water clouds are diagnosed using the Geleyn scheme (Geleyn, 1981) using the same critical relative humidity values as in the nature run. A measurement occurs if the cloud fraction at a particular level as seen from the satellite (assuming random overlap) exceeds a critical value. Finally, a measurement in the marine boundary layer results if, again, the fraction of the lowest layer seen from above exceeds a critical value. This measurement is considered to be an average of the wind at the lowest two mandatory pressure levels (1000 and 850 mb).

##### 4.2 Lidar data errors

Lidar wind data errors will depend on the sensor characteristics as well as orbital data. To provide an estimate of wind vector errors for a simple lidar, an instrument simulation model has been applied. Optical properties of the clouds are required to ultimately assign a wind retrieval error. Properties of liquid water clouds assume a simple stratus or stratocumulus drop size distribution. The boundary layer aerosol model is a marine boundary layer model. We have not considered the relative humidity dependence of the aerosol size distribution. The estimation of cirrus optical properties including extinction

and the desired lidar backscatter cross sections were based on the parameterization of the cirrus particle size spectrum by Heymsfield and Platt (1984). This results in one class of size distribution corresponding to "warm" and "cold" cirrus, respectively. This is consistent with a change in lidar extinction to backscatter ratio noted by Platt and Dilley (1981). We exploit this dependence to simplify our treatment of the temperature dependence of the cirrus backscatter and assignment of simulated wind errors. To calculate backscatter coefficients we adopt the optical constants for ice from Warren (1984). The backscatter and extinction coefficients corresponding to the temperature dependent size distributions described above are evaluated using the Mie theory algorithm of Shettle (pers. communication). Although the Mie theory is strictly applicable to spherical particles a comparison of asymmetry factors calculated by Takano and Liou (1989) for hexagonal crystals and equivalent ice spheres suggests that, for our purposes, the error is not significant.

## 5. DISCUSSION OF RESULTS

The specific results of the OSSE are summarized by these specific findings:

### *Synoptic maps:*

- Reduction in analysis and forecast errors of 500hPa geopotential height in the southern hemisphere by factors of 2-3;
- Most of the data impact on vector wind analysis and forecast in the southern hemisphere with wind vector errors of 20-30  $\text{ms}^{-1}$  reduced to 10  $\text{ms}^{-1}$ ;
- Again most impact in the southern hemisphere extratropics with large areas of errors greater than 50% in the CONTROL experiment reduced in the LIDAR analysis. Similar results for humidity forecasts with improved specification of the horizontal motion field leading to a better moisture forecast.

### *Time evolution of forecast and analysis error:*

- Global reduction of the 500hPa height analysis error by a factor of two (from 25 m to 12 m), most dramatic in the southern hemisphere. A global increase in accuracy for a three day forecast by the equivalent of 12 hours relative to control (36 hours in the southern hemisphere extratropics);
- A thirty percent reduction in the error of the 850 hPa zonal wind component with a forecast predictability improvement in the southern hemisphere of up to 48 hours;
- Consistent positive impact on the analysis of 850 hPa relative humidity in the southern hemisphere with forecast predictability increases of 24 to 72 hours compared to control.

### *Averaged forecast error:*

- Global improvement of the 500 hPa height forecast (compared to CONTROL) by 1 day (2-2.5 days in the southern hemisphere);
- Global zonal wind forecast error improvements of 0.5 and 1 days and at 850 hPa and 200 hPa, respectively. (1-1.5 days and 2 days, respectively, in the southern hemisphere);
- Improvements in the 850 hPa humidity forecasts by 1-1.5 days.

We have also performed an OSSE to evaluate the impact of a WINDSAT type instrument (Hoffman et al, 1990). In the examination of southern hemisphere results, a meaningful comparison of WINDSAT and LIDAR impacts can be made. The scaled down LIDAR system reduces 500 hPa geopotential height analysis errors by between 1/2 and 3/4 that of the WINDSAT system. Predictability increases for LIDAR are about one day less than WINDSAT. Zonal wind improvements at 850 hPa from LIDAR are about 1/2 of WINDSAT.

## 6. ACKNOWLEDGEMENT

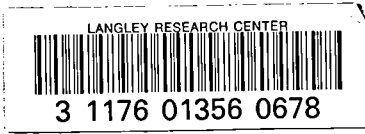
The authors thank their colleagues D. Hogan and D. Kenyon at GE Astro Space Division, Princeton, NJ for providing lidar wind error estimates.

## 7. REFERENCES

- Arnold, C.P., and C.H. Dey, 1986: Observing systems simulation experiments: Past, present, and future. Bull. Amer. Meteor. Soc., 67, 687-695.
- Brenner, S., C.-H. Yang and S.Y.K. Yee, 1982: The AFGL spectral model of the moist global atmosphere: Documentation of the baseline version. AFGL-TR-82-0393, AFGL, 65 pp. [NTIS ADA129283]
- Brenner, C.-H. Yang and K. Mitchell, 1984: The AFGL global spectral model: Expanded resolution baseline version. AFGL-TR-84-0308, AFGL. [NTIS ADA160370]
- Gelyn, J.-F., 1981: Some diagnostics of the cloud radiation interaction in ECMWF forecasting models. In workshop on Radiation and Cloud-Radiation Interaction in Numerical Modeling, ECMWF, Reading, UK, pp. 135-161.
- Grassotti, C., R. G. Isaacs, R. N. Hoffman, M. Mickelson, T. Nehr Korn, J.-F. Louis, 1991: A Simple Doppler Wind Lidar Sensor: Simulated Measurements and Impacts in a Global Assimilation and Forecast System. PL-TR-91-2253, Phillips Laboratory, Hanscom AFB, MA 01731, 98 pp.
- Heymsfield, A.J. and C.M.R. Platt, 1984: A parameterization of the particle size spectrum of ice clouds in terms of the ambient temperature and the ice water content. J. Atmos. Sci., 41, 5, pp. 846-855.
- Hoffman, R.H., C. Grassotti, R.G. Isaacs, J.-F. Louis, T. Nehr Korn and D.C. Norquist, 1990: Assessment of the Impact of Simulated Satellite Lidar Wind and Retrieved 183 GHz Water Vapor Observations on a Global Data Assimilation System. Monthly Weather Review, 118, 12, 2513-2542.
- Huffaker, R.M. et al., 1984: Feasibility studies for a global wind measuring satellite system (WINDSAT); analysis of simulated performance. Appl. Optics, 23, 2523.
- Liou, K.N., Y. Takano, S.C. Ou, A. Heymsfield, and W. Kreiss, 1990: Infrared transmission through cirrus clouds: a radiative model for target detection. Applied Optics, 29, 13, pp. 1886-1896.
- Platt, C.M.R., and A.C. Dilley, 1981: Remote sounding of high clouds. IV: Observed temperature variations in cirrus optical properties. J. Atmos. Sci., 38, 1069-1082.
- Takano, Y., and K.-N. Liou, 1989: Solar radiative transfer in cirrus clouds. Part I: Single-scattering and optical properties of hexagonal ice crystals. J. Atmos. Sci., 46, 1, pp. 3-19.
- Woodbury, G.E. and M.P. McCormick, 1986: Zonal and geographical distributions of cirrus clouds determined from SAGE data. J. Geophys. Res., 91 D2, pp. 2775-2785.
- Warren, S.G., 1984: Optical constants of ice from the ultraviolet to the microwave. Appl. Optics, 23:8, 1206-1225.

REPORT DOCUMENTATION PAGE			Form Approved OMB No. 0704-0188											
Public reporting burden for this collection of information is estimated to average 1 hour per response, including the time for reviewing instructions, searching existing data sources, gathering and maintaining the data needed, and completing and reviewing the collection of information. Send comments regarding this burden estimate or any other aspect of this collection of information, including suggestions for reducing this burden, to Washington Headquarters Services, Directorate for Information Operations and Reports, 1215 Jefferson Davis Highway, Suite 1204, Arlington, VA 22202-4302, and to the Office of Management and Budget, Paperwork Reduction Project (0704-0188), Washington, DC 20503.														
1. AGENCY USE ONLY (Leave blank)	2. REPORT DATE July 1992	3. REPORT TYPE AND DATES COVERED Conference Publication												
4. TITLE AND SUBTITLE Sixteenth International Laser Radar Conference			5. FUNDING NUMBERS WU 665-45-20-21											
6. AUTHOR(S) M. P. McCormick, Editor														
7. PERFORMING ORGANIZATION NAME(S) AND ADDRESS(ES) NASA Langley Research Center Hampton, VA 23665-5225			8. PERFORMING ORGANIZATION REPORT NUMBER L-17126											
9. SPONSORING/MONITORING AGENCY NAME(S) AND ADDRESS(ES) U.S. Air Force Office of Scientific Research, Washington, DC, 20035; NASA Langley Research Center, Hampton, VA 23665; the U.S. Air Force Phillips Laboratory, Hanscomb, MA 02106; the American Meteorological Society, Boston, MA 02108; and the Optical Society of America, Washington, DC, 20036.			10. SPONSORING/MONITORING AGENCY REPORT NUMBER NASA CP-3158, Part 1											
11. SUPPLEMENTARY NOTES Abstracts of conference held at Cambridge, Massachusetts, July 20-24, 1992.														
12a. DISTRIBUTION/AVAILABILITY STATEMENT  Unclassified-Unlimited  Subject Category 35			12b. DISTRIBUTION CODE											
13. ABSTRACT (Maximum 200 words) This publication contains extended abstracts of papers presented at the 16th International Laser Radar Conference, held in Cambridge, Massachusetts, July 20-24, 1992. One hundred ninety-five papers were presented in both oral and poster sessions. The topics of the conference sessions were:  <table border="0" style="width: 100%;"> <tr> <td style="width: 50%;">1. Mt. Pinatubo Volcanic Dust Layers Observations</td> <td style="width: 50%;">6. Wind Measurements and Measurement Systems</td> </tr> <tr> <td>2. Global Change/Ozone Measurements</td> <td>7. Imaging and Ranging</td> </tr> <tr> <td>3. GLOBE/LAWS/LITE</td> <td>8. Water Vapor Measurements</td> </tr> <tr> <td>4. Mesospheric Measurements and Measurement Systems</td> <td>9. Systems and Facilities</td> </tr> <tr> <td>5. Middle Atmosphere</td> <td>10. Laser Devices and Technology</td> </tr> </table> This conference reflects the breadth of research activities being conducted in the lidar field. These abstracts address subjects from lidar-based atmospheric investigations relating to global change to the development of new lidar systems and technology.					1. Mt. Pinatubo Volcanic Dust Layers Observations	6. Wind Measurements and Measurement Systems	2. Global Change/Ozone Measurements	7. Imaging and Ranging	3. GLOBE/LAWS/LITE	8. Water Vapor Measurements	4. Mesospheric Measurements and Measurement Systems	9. Systems and Facilities	5. Middle Atmosphere	10. Laser Devices and Technology
1. Mt. Pinatubo Volcanic Dust Layers Observations	6. Wind Measurements and Measurement Systems													
2. Global Change/Ozone Measurements	7. Imaging and Ranging													
3. GLOBE/LAWS/LITE	8. Water Vapor Measurements													
4. Mesospheric Measurements and Measurement Systems	9. Systems and Facilities													
5. Middle Atmosphere	10. Laser Devices and Technology													
14. SUBJECT TERMS Lidar, Laser radar, Remote sensing, Atmospheric measurements			15. NUMBER OF PAGES 409											
			16. PRICE CODE A18											
17. SECURITY CLASSIFICATION OF REPORT Unclassified	18. SECURITY CLASSIFICATION OF THIS PAGE Unclassified	19. SECURITY CLASSIFICATION OF ABSTRACT	20. LIMITATION OF ABSTRACT											

National Aeronautics and  
 Space Administration  
 Code JTT  
 Washington, D.C.  
 20546-0001  
 Official Business  
 Penalty for Private Use, \$300



SPECIAL FOURTH-CLASS RATE  
 POSTAGE & FEES PAID  
 NASA  
 PERMIT No. G27



**DO NOT REMOVE SLIP FROM MATERIAL**

Delete your name from this slip when returning material to the library.

NAME	DATE	MS
<del>[REDACTED]</del>	<del>[REDACTED]</del>	<del>[REDACTED]</del>
<del>[REDACTED]</del>	<del>[REDACTED]</del>	<del>[REDACTED]</del>
VANN, LELIA	5/1/2000	475
<del>[REDACTED]</del>	<del>[REDACTED]</del>	<del>[REDACTED]</del>
Library	8/26/04	185

NASA Langley (Rev. Dec. 1991) RIAD N-75

ER: If Undeliverable (Section 158  
 Postal Manual) Do Not Return